CHAPTER 01: General Introduction on Oxygenases

1.1. Introduction

Non-haem iron (Fe)-dependent oxygenases constitute a large group of redox-enzyme family (1). These oxygenases can either be monooxygenases utilising single oxygen atom (*e.g.* cytochrome P450 monooxygenases) or be dioxygenases incorporating both the atoms of molecular oxygen into the substrate (*e.g.* intradiol cleaving catechol dioxygenases) (1,2). Alternatively, the Fe-dependent oxygenases can either be di-iron-dependent (*e.g.* methane monooxygenases) or mono-iron-dependent (*e.g.* lipooxygenase) (1). Mono-iron-dependent oxygenases again can be divided into two subgroups: those requiring Fe(III), important examples of which include lipooxygenases, intradiol cleaving catechol dioxygenases, and those requiring Fe(II), examples of which may include extradiol cleaving catechol dioxygenases, tyrosine or phenylalanine hydroxylases, benzene or naphthalene dioxygenases and 2-oxoglutarate (2OG)-dependent oxygenases (1).

'2OG-dependent oxygenases' employ the TCA (citric acid or tricarboxylic acid) cycle intermediate 2OG (or α-ketoglutarate) as a co-substrate in addition to the co-factor iron (Fe(II)) to oxidise their substrates while producing CO_2 and succinate as by-products (3). Over the past few decades, 2OG oxygenases have emerged as a large enzyme family, some members of which are potential therapeutic targets (4). The first identified 2OG-dependent oxygenases are the collagen prolyl-4-hydroxylases (CP4H), which had been targeted for treatment of fibrotic disease (5-7). The early work on CP4H highlighted the therapeutic potential of 2OG oxygenases, though initial studies were not able to identify any clinically useful inhibitors (5-7). Later it was found that 2OG oxygenases are in fact present in almost all living organisms. To date ≥ 60 2OG oxygenases have been identified in humans (3,4). Subsequent works have identified 2OG oxygenases that are key regulators of multiple biologically important processes, both in

eukaryotes and prokaryotes, including roles in nucleic acid repair, fatty acid metabolism, hypoxia, obesity, and in secondary metabolism (3,4).

1.2. Structural and Mechanistic Overview of 2OG Oxygenases

2OG oxygenases have functionally characteristic domains; these include ARID (AT-rich interaction domain), JmjC, JmjN, PHD (plant homeobox domain), tudor, TPR (tetratricopeptide repeat), and WH (winged-helix) domains. (Figure 1.1) (8). The JmjC domain is the catalytic domain and the additional domains, *i.e.*, PHD, JmjN, tudor, TPR, and WH are involved in substrate binding as well as in the interaction with other proteins (Figure 1.1) (3,8). A hallmark feature of this superfamily is the presence of a double-stranded β-helix (DSBH) or jelly roll or cupin fold forming the core fold (Figure 1.2) (3,8). The right-handed class I DSBH fold present in the 2OG oxygenases harbours the conserved iron binding residues HxD/E…H (also known as catalytic triad) (8). The catalytic triad (also known as facial triad) coordinates the active-site metal co-factor, Fe(II) (Figure 1.2) (8). The octahedral coordination of Fe(II) is fulfilled by the cosubstrate 2OG and one molecule of water (Figure 1.2**B**) (8). The oxygen atoms of the 2OG C-1 carboxylate and C-2 carbonyl groups coordinate the active-site metal (Fe(II)). Variation in the coordination of the carboxylate group with respect to the histidine residues is a noteworthy feature of 2OG oxygenases and has been observed previously (Figure 1.2**B**) (8,9). The 2OG C-5 carboxylate group interacts with a basic residue located at subfamily-conserved position on the DSBH fold (Figure 1.2) (8). In a vast number of studied cases, binding of 2OG facilitates binding of the substrate at the catalytic site resulting in the formation of a quaternary enzyme-iron-2OG-substrate complex to which O_2 finally binds (Figure 1.3) (10,11). Next, oxidative decarboxylation of 2OG occurs through a peroxo-intermediate yielding a reactive Fe(IV)-oxo species (Figure 1.3). Finally, the event of 2OG oxygenase catalysis is completed by the release of modified product, carbon dioxide and succinate with concomitant reduction of Fe(IV) to Fe(II) (Figure 1.3) (10,11).

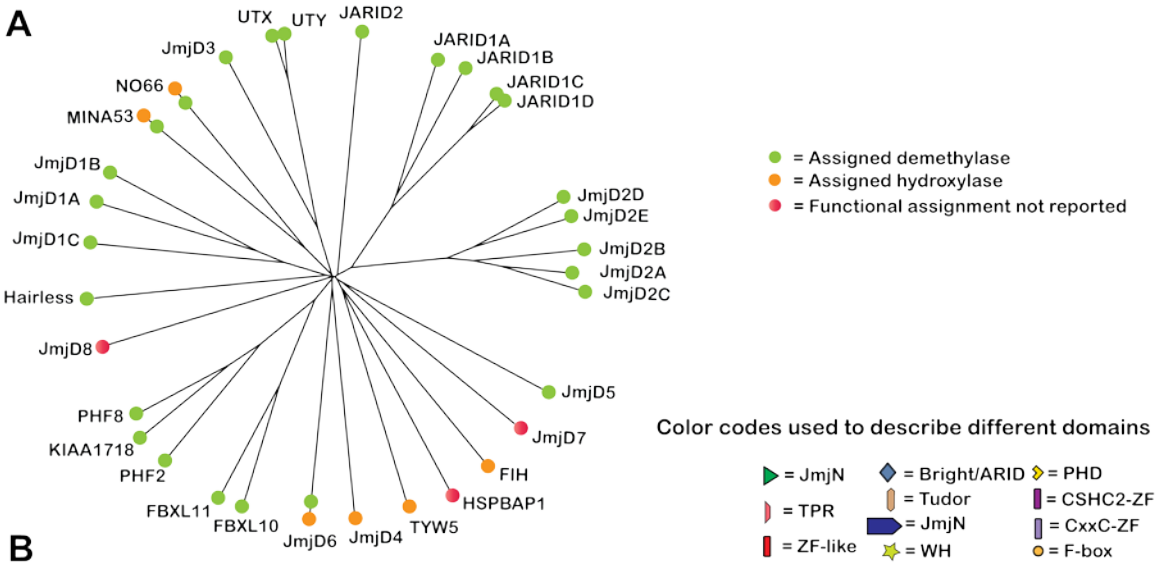

B

Gene	Domain Architecture	Protein Name	UniProtKB Accession Number
MINA53		MYC induced nuclear antigen	Q8IUF8
NO66		Nuclear protein 66	Q9H6W3
JmjD3/KDM6B		Jumonji domain containing protein 3	O15054
UTX/KDM6A		Ubiquitously transcribed tetratricopeptide repeat protein, chromosome X	O15054
UTY		Ubiquitously transcribed tetratricopeptide repeat protein, chromosome Y	O14607
JARID2/JMJ		Jumonji/ARID domain containing protein 2/Protein Jumonji	Q92833
JARID1A/RBBP2/KDM5A		Jumonji, AT rich interactive domain 1A	P29375
JARID1B/KDM5B		Jumonji, AT rich interactive domain 1B	Q9UGL1
JARID1C/KDM5C		Jumonji, AT rich interactive domain 1C	P41229
JARID1D/KDM5D		Jumonji, AT rich interactive domain 1D	Q9BY66
JmjD2D/KDM4D		Jumonji domain containing protein 2D	Q6B0I6
JmjD2E/KDM4E		Jumonji domain containing protein 2E	B2RXH2
JmjD2B/KDM4B		Jumonji domain containing protein 2B	P29375
JmjD2A/KDM4A		Jumonji domain containing protein 2A	O75164
JmjD2C/KDM4C		Jumonji domain containing protein 2C	O94953
JmjD5		Jumonji domain containing protein 5	Q8N371
JmjD7		Jumonji domain containing protein 7	P0C870
FIH		Factor Inhibiting hypoxia inducible factor 1-alpha	Q9NWT6
HSPBAP1/PASS1		HSPB1-associated protein 1	Q96EW2
TYW5		tRNA wybutosine-synthesizing protein 5	A2RUC4
JmjD4		Jumonji domain containing protein 4	Q9H9V9
JmjD6		Jumonji domain containing protein 6	Q6NYC1
FBXL10/JHDM1B/KDM2B		F-box and leucine-rich repeat protein 10	Q8NHM5
FBXL11/JHDM1A/KDM2A		F-box and leucine-rich repeat protein 11	Q9Y2K7
PHF2/JHDM1E		PHD finger protein 2	O75151
KIAA1718/JHDM1D/KDM7		Lysine-specific demethylase 7	Q6ZMT4
PHF8/KIAA1111		PHD finger protein 8	Q9UPP1
JmjD8		Jumonji domain containing protein 6	Q96S16
Hairless		Protein hairless	O43593
JmjD1C/JHD2C		Jumonji domain containing protein 1C	Q15652
JmjD1A/KDM3A		Jumonji domain containing protein 1A	Q9Y4C1
JmjD1B/KDM3B		Jumonji domain containing protein 1B	Q7LBC6

FIGURE 1.1. **Phylogenetic relationships and domain architectures of human 2OG oxygenases.** (A) A Phylogenetic tree showing the relative positioning of the human demethylases (green circle), hydroxylases (orange circle), and oxygenases with no assigned function (red circle). The tree is constructed using Archaeptaryx v.0.9812 from ClustalW-aligned human 2OG oxygenase protein sequences (12,13). (B) Domain architectures of the human 2OG oxygenases. ARID = AT-rich interaction domain, PHD = plant homeobox domain, TPR = tetratricopeptide repeat, WH = winged-helix, ZF = zinc finger. [Figure adapted from Klose *et al.* (14)]

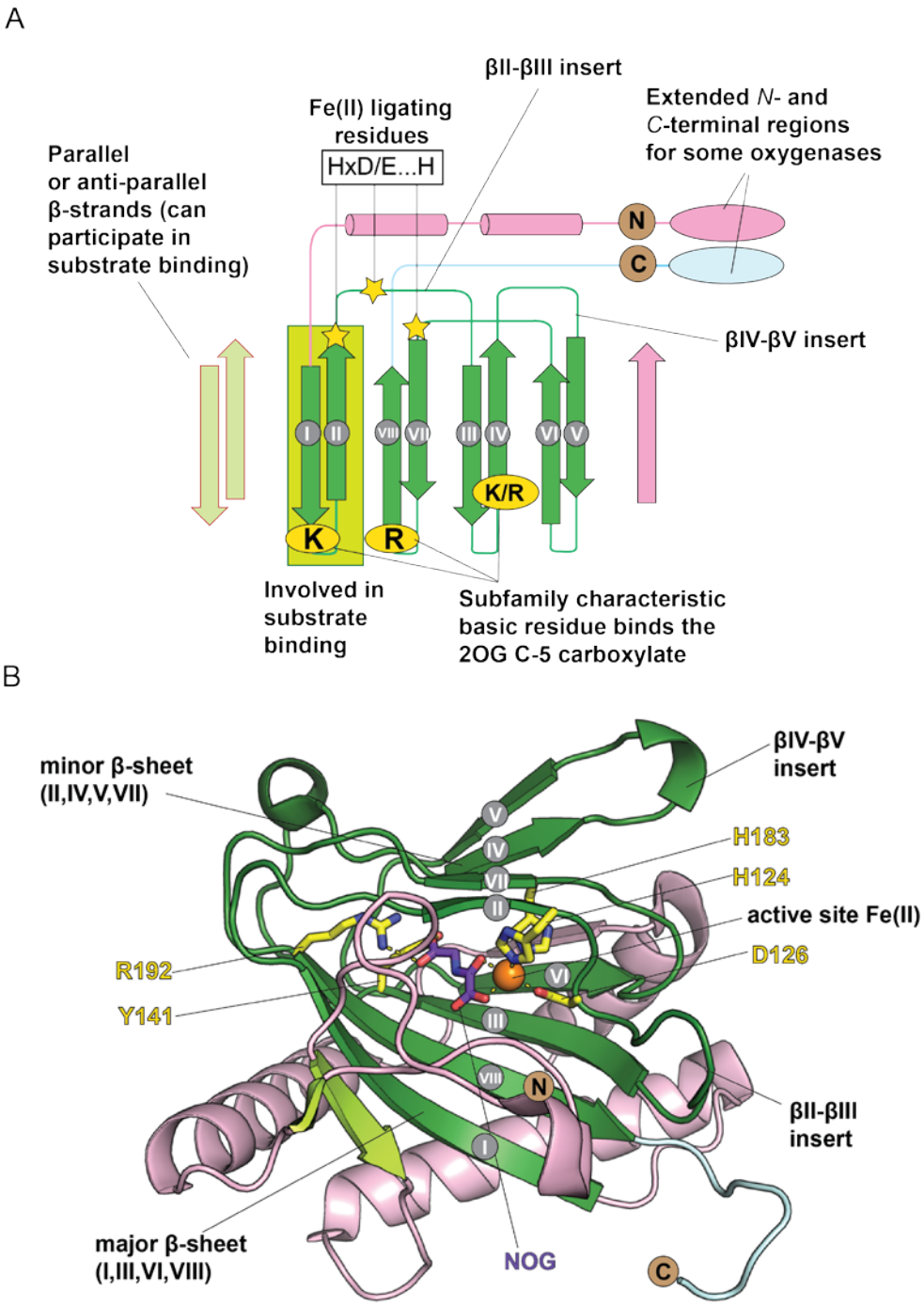

FIGURE 1.2. **2OG Oxygenases contain a core DSBH fold with conserved Fe(II)- and 2OG-binding sites.** (A) Composite topology diagram for 2OG oxygenases showing the core DSBH (green, I-VIII), *N*-terminal region (pink), *C*-terminal region (pale cyan), iron-binding residues (yellow stars), and 2OG-binding residues (yellow ovals). The βII-βIII and βIV-βV inserts that are sometimes involved in substrate binding are identified. (B) View of a structure of PPHD (*Pseudomonas* Prolyl-Hydroxylase Domain containing protein, PDB:

4IW3) from *Pseudomonas putida.* Fe(II) is in an orange sphere; 2OG in purple sticks; secondary structures colored as (A). [Figure adapted from Islam *et al.* (3)].

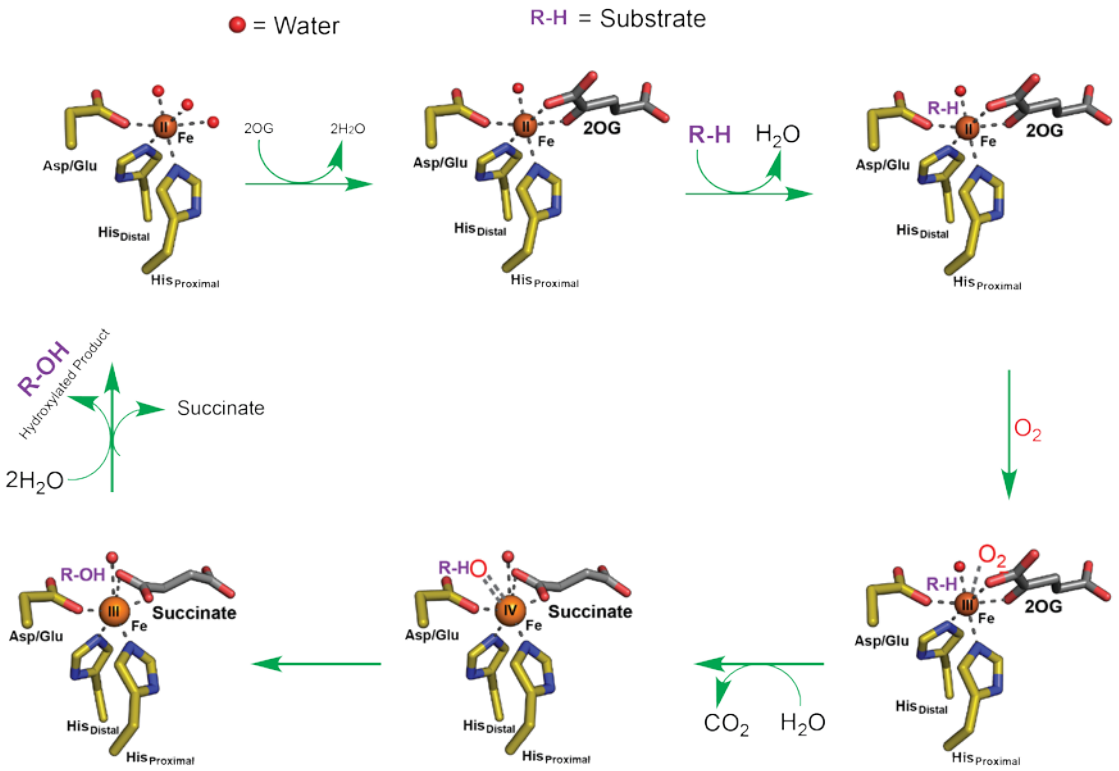

FIGURE 1.3. **Mechanistic scheme of hydroxylation as catalysed by 2OG oxygenases.** Following bidentate coordination of 2OG to the Fe(II), the substrate binds such that the C-H bond to be oxidized is positioned proximal to the Fe(II). Substrate-binding weakens the binding of Fe-ligated water, providing a vacant coordination site for O_2 to bind. Oxidative decarboxylation of 2OG forms succinate, CO_2 and an Fe(IV)-oxo intermediate. The Fe(IV)-oxo intermediate reacts with the proximal C-H to form an alcohol, with concomitant reduction of the Fe(IV) to Fe(II). Succinate is released concomitantly with loss of the hydroxylated product.

1.3. Structural and Mechanistic Overview of HPPD

4-hydroxyphenylpyruvate dioxygenase (HPPD) is a non-haem iron (Fe(II)) and 2-oxoacid-dependent oxygenase whose catalytic activity in part is mechanistically related to those of 2OG oxygenases (10,15). HPPD belongs to the extradiol dioxygenase enzyme family, which has a H...x…H…x…E catalytic triad (Figure 1.4) (15). HPPD does not have a DSBH fold (10,15), instead the HPPD structure is comprised of two twisted β-sheets (each consisting of 8 β-strands) with its metal-binding residues located within the *C*-terminal β-sheets (Figure 1.4**A**) (15). The HPPD structural features are strictly conserved from humans through to animals (15).

HPPD catalyses the conversion of 4-hydroxyphenylpyruvic acid (HPPA) to 2,5-dihydroxyphenyl acetic acid or homogentisic acid (HMGA), the second step of the tyrosine catabolism pathway [Figure 9.1, **Chapter 09**] (15). In the course of transformation of HPPA to HMGA, HPPD catalyses decarboxylation, aromatic ring hydroxylation and substituent migration reactions in a single step analogous to P450 hydroxylases and pterin dependent oxygenases (Figure 1.4**B**) (15). Like the 2OG oxygenases, HPPD also catalyses substrate oxidation through a high energy Fe(IV)-oxo intermediate species, which is formed during oxidative decarboxylation of the substrate (Figure 1.4**B**) (10,15). Interestingly, HPPD does not require 2OG; the substructure of 2OG is contained within the structure of HPPA (Figure 1.4**B**) (10,15).

HPPD is mainly targeted for the development of herbicides in the agrochemical industry. Inhibitors of plant-HPPD including mesotrione, nitisinone, and sulcotrione are potential herbicides. Nitisinone was later found to be effective in the treatment of type I tyrosinemia by inhibiting human HPPD. Since then, nitisinone has been used for the treatment of type I tyrosinemia and alkaptonuria. (15) [more detail on HPPD is in **Chapter 09**].

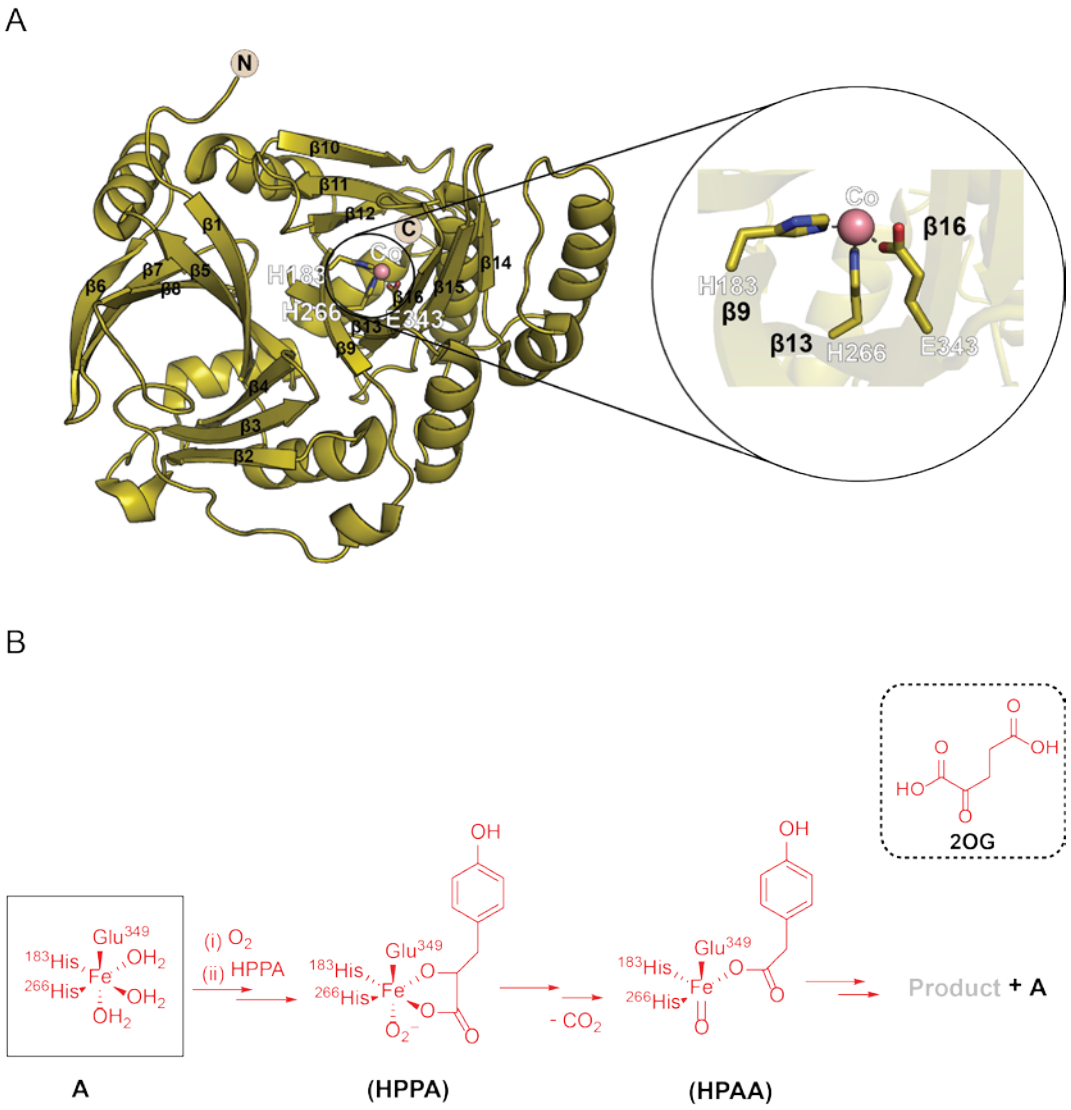

FIGURE 1.4. **Structural and mechanistic properties of HPPD**. (A) Cartoon view of human HPPD (PDB: 3ISQ) showing the location of His^{183}, His^{266}, and Glu^{349} (H....x.…H...x.…E) on β9, β13, and β16 of the *C*-terminal β-sheet, respectively. (B) Mechanistic overview of HPPD catalysis.

1.4. Overview of 2OG Oxygenase Functions

In both plants and animals, 2OG oxygenases target a wide variety of substrates ranging from small molecules to macromolecules, which suggests that they have a broad substrate specificity (3). In animals (including humans), 2OG oxygenases catalyse either hydroxylation of unactivated C-H bonds or demethylation of *N*-methyl group *via* hydroxylation on the targeted residues of the protein substrates, which include collagens,

histones, splicing regulators, transcription factors (hypoxia inducible factors (HIFs)), ribosomal proteins, and many more (3). 2OG oxygenases also catalyse demethylation of methylated nucleobases of nucleic acids (3). Types of reactions that 2OG oxygenases catalyse are also very exotic, which include desaturation, oxidative cyclisation, rearrangements, and halogenations (3). The highly diverse catalytic ability of 2OG oxygenases enables biosynthetic production of many secondary metabolites in plants and prokaryotes including antibiotics, gibberellins, ethylene, and flavonoids.

1.4.1. 2OG Oxygenases Acting on Protein Targets

Studies on collagen biosynthesis led to the pioneering discovery of a 2OG-dependent oxygenase, collagen C-4 prolyl hydroxylase (CP4H), which catalyses the hydroxylation of C-4 of collagen triple helix proline residues (Figure 1.5) (5-7). Like other 2OG oxygenases, catalytic activity of CP4H is also reported to be stimulated by ascorbate (6,7). Ascorbate deficiency leads to scurvy *via* mechanisms resulting in impaired connective tissue formation, possibly due to impaired CP4H activity (6,7). Subsequent studies also identified other collagen-modifying 2OG oxygenases, procollagen prolyl C-3 hydroxylases (CP3H) or the leprecans (LEPREs) (Figure 1.5) (6,7). However, unlike CP4H, the catalytic activity of CP3H/LEPREs has not been found to impact collagen properties strongly, except destabilisation of the collagen fold (6,7). Other 2OG oxygenase collagen-modifying enzymes, procollagen lysyl-hydroxylases (PLODs), which catalyse C-5 hydroxylation of lysine residues involved in cross-linking in procollagen, were also identified in subsequent works (6,7). Notably, mutations in PLODs result in Ehlers-Danlos disease, a connective tissue disorder (6,7).

JmjC domain containing protein 6, JMJD6 was reported as a lysyl-hydroxylase in 2009 by Webby *et al.* (16). JMJD6 catalyses the hydroxylation of lysine residues of histone proteins, arginine-serine (RS)-rich domains of splicing regulatory (SR) proteins LUC7L2 (putative RNA binding protein luc-7-like 2), CROP (cisplatin resistance-associated overexpressed protein), U2AF65 (u2 small nuclear ribonucleoprotein auxiliary

factor 65 kDa subunit) (Figure 1.5) (16). Subsequent report on JMJD6 suggests it may have a role in tumorigenesis by hydroxylating a lysine residue (Lys^{382}) of tumour suppressor p53 (17). Although the catalytic activity of JMJD6 was linked to the hypoxic response by observed-interaction between JMJD6 and VHL, no direct evidence for JMJD6-mediated hydroxylation of VHL lysine residues has been reported yet (18).

Like JMJD6, 2OG oxygenases JMJD4 and JMJD7 are recently identified as lysyl-hydroxylases (19,20). JMJD4 catalyses the hydroxylation of lysine residues in eukaryotic release factor 1 (eRF1) (20) (Figure 1.5), while JMJD7 catalyses lysyl-hydroxylation of two members of the translation factor (TRAFAC) family of GTPases: developmentally regulated GTP binding proteins 1 and 2 (DRG1-2) (19).

Of the 2OG-dependent hydroxylases identified, PHDs (prolyl hydroxylases) and FIH (asparaginyl hydroxylase) are probably the mostly studied owing to their direct connection with biology (2,21). In animals (including humans), oxygen availability inside cells is controlled by a set of genes including those encoding for hypoxia inducible factors (HIFs) (2,21). In humans, HIF-1α and HIF-2α together trigger the transcription of genes encoding for EPO (erythropoietin) and VEGF (vascular endothelial growth factor) in response to low oxygen availability. HIF levels are regulated by the post-translational hydroxylation of HIF, catalysed by Fe(II)- and 2OG-dependent oxygenases: HIF prolyl hydroxylases (PHDs or EGLN1-3) and HIF asparaginyl hydroxylase (FIH) (2,21). PHDs and FIH catalyse hydroxylation of proline and asparagine residues of HIF-α, respectively (Figure 1.5) (2,21-23). The key regulators are the PHDs, which catalyse prolyl-4-hydroxylation of either or both *N*- and *C*-terminal oxygen-dependent degradation domains (NODD and CODD, respectively) of HIF-α, thereby increasing the affinity of HIF-α binding (~ 1000 fold) to VHL (von Hippel-Lindau) protein and finally mediating the proteasomal degradation of HIF-α (22).

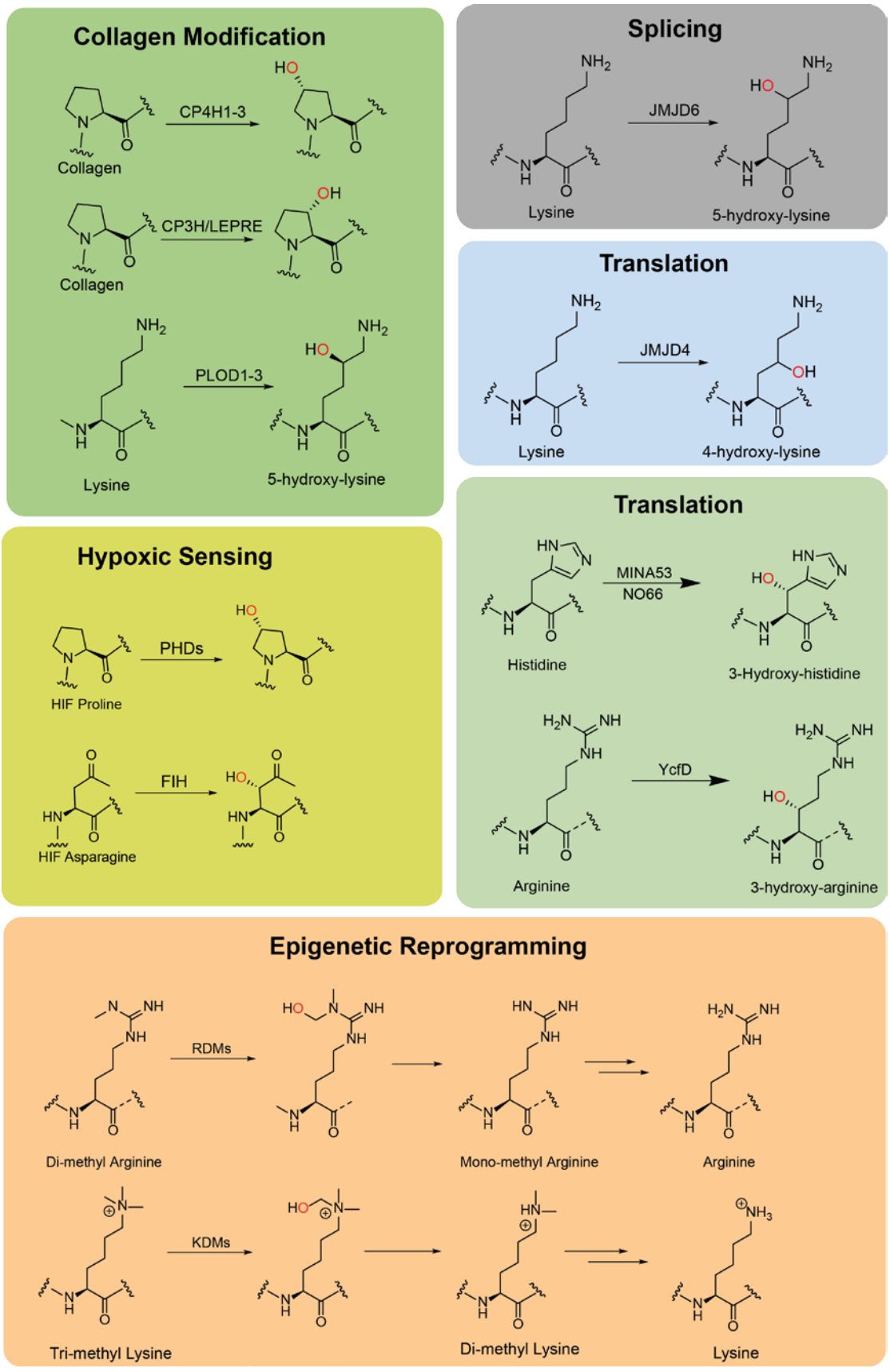

FIGURE 1.5. **Protein substrates for 2OG oxygenases.**

In addition, FIH catalyses the hydroxylation of an asparagine residue within the *C*-terminal transcriptional activation domain (CAD) of HIF-α, which blocks the interaction between HIF-α and the transcriptional co-activator proteins CBP/p300 thereby decreasing HIF-mediated transcription (23). To note, FIH was the first JmjC domain containing 2OG-dependent oxygenase structure to be determined (23). However, since its discovery the substrate-selectivity of FIH has been promiscuous compared to the PHDs. In addition to HIF asparaginyl-hydroxylation, FIH can also, albeit weakly, catalyse hydroxylation of asparagine, aspartate, and histidine residues within ankyrin repeat domain proteins (ARD) (3,23).

After the identification of prolyl-hydroxylase PHDs, another prolyl-hydroxylase OGFOD1 (human uS12 prolyl 3-hydroxylase) was identified (24). OGFOD1 catalyses the C-3 hydroxylation of proline residue within the ribosomal protein S23 (RPS23) in human and likely in other animals. A yeast homologue of OGFOD1, TPA1, catalyses sequential hydroxylation of C-3 and C-4 in RPS23 (24).

Like OGFOD1, MINA53 (MYC-induced nuclear antigen 53) and NO66 (nucleolar protein 66) also target ribosomal proteins RPL27 and RPL8, respectively (25). In contrast to OGFOD1, MINA53 and NO66 catalyse C-3 hydroxylation of histidine residues (Figure 1.5) (25). A bacterial homologue of MINA53 and NO66, ycfD, catalyses the C-3 hydroxylation of an arginine residue within the ribosomal protein RPL16 (Figure 1.5) (25). Crystallographic studies have revealed that in addition to their catalytic *N*-terminal JmjC domain, these ribosomal oxygenases (ROXs) possess a bridging dimerisation domain and a *C*-terminal winged-helix (WH) domain (Figure 1.1) (25). ROXs are also reported to regulate growth, possibly *via* interacting with nucleic acids (25).

The human JMJD5 enzyme has recently been identified as to catalyse hydroxylation of an arginine residue of ribosomal protein RpS6 (40S ribosomal protein) and an arginine residue of RCCD1 (regulator of chromosome condensation domain-containing protein 1) (26). JMJD5 is reported to play an important role in

osteoclastogenesis *via* interaction with NFATc1 (nuclear factor of activated T-cells calcineurin-dependent 1) (27).

Apart from the studies on PHDs and FIH, 2OG-dependent JmjC histone lysine demethylases (KDMs) are probably the most vastly studied 2OG oxygenases, which have important physiological roles including in epigenetic regulation (14). KDMs catalyse the demethylation of mono-, di-, and tri-methylated lysine residue(s) of histone proteins, which proceeds *via* initial *N*-methyl group hydroxylation followed by fragmentation of the resulting unstable hemiaminal intermediate (as yet not directly observed) to give formaldehyde (Figure 1.5) (14). Mutations in the genes encoding for the KDMs cause multiple diseases including mental diseases, mid-line defects, and cancers (14).

Recent biochemical studies have revealed that some of the JmjC KDMs can also catalyse demethylation of methylated-arginine residues within histones (28). JMJD6 is also reported to be an arginine demethylase of histones (29), estrogen receptor α (ERα) (30), RNA helicase A (31), and heat-shock protein 70 kDa (32), though these assignments have been controversial (33). 2OG hydroxylases JMJD5, MINA53, and NO66 are also assigned as histone lysine demethylases (primarily by antibody-based studies); direct demethylase activity for these enzymes has not been observed by others (3). In addition to the 2OG-dependent demethylases, another class of lysine-specific demethylases (LSDs) are also identified. LSDs employ a flavin co-factor to catalyse demethylation of mono- as well as di-N^{ε}-methylated lysine residues of histone proteins (14).

1.4.2. 2OG Oxygenases Acting on Nucleic Acids

2OG oxygenases that catalyse nucleic acid modifications include AlkB homologues (ABHs), fat mass and obesity associated protein (FTO), tRNA wybutosine-synthesizing protein (TYW5) and ten-eleven translocation protein (TETs) (3). ABH-mediated demethylation reaction on methylated-DNA and/or RNA proceeds *via* oxidation of an *N*-

methyl group, yielding formaldehyde (Figure 1.6) analogous to the *N*-demethylation processes of JmjC KDMs (Figure 1.5) (3). AlkB homologues are widely distributed across prokaryotes and eukaryotes, with nine AlkB homologues in humans (ABH1-8 and FTO) (3). ABH2/3 catalyse demethylation on 1meA and 3meC of DNA and RNA (Figure 1.6), while ABH5 and FTO catalyse N-methyl RNA demethylation (3) (Figure 1.6). Their catalytic activities are linked to various physiological functions including nucleic acid repair, circadian rhythm, and obesity (3). Another nucleic acid-modifying enzyme that also requires 2OG for its catalytic activity is TYW5, which catalyses the hydroxylation of the unusual wybutosine at the wobble position of certain tRNA, yielding hydroxywybutosine (Figure 1.6) (3). ABH8 catalyses the 5-methylcarboxymethyl uridine (mcm5U) in tRNA, while the substrate mcm5U is produced by the methyl transferase domain of ABH8 (3). The catalytic activities of both TYW5 and AlkBH8 are essential in maintaining translational accuracy (3). Like the AlkBH2/3, the TET enzymes also target both DNA and RNA to catalyse the oxidation of 5-methylcytosine (Figure 1.6). TET-mediated modification to DNA plays role in epigenetic regulations (3).

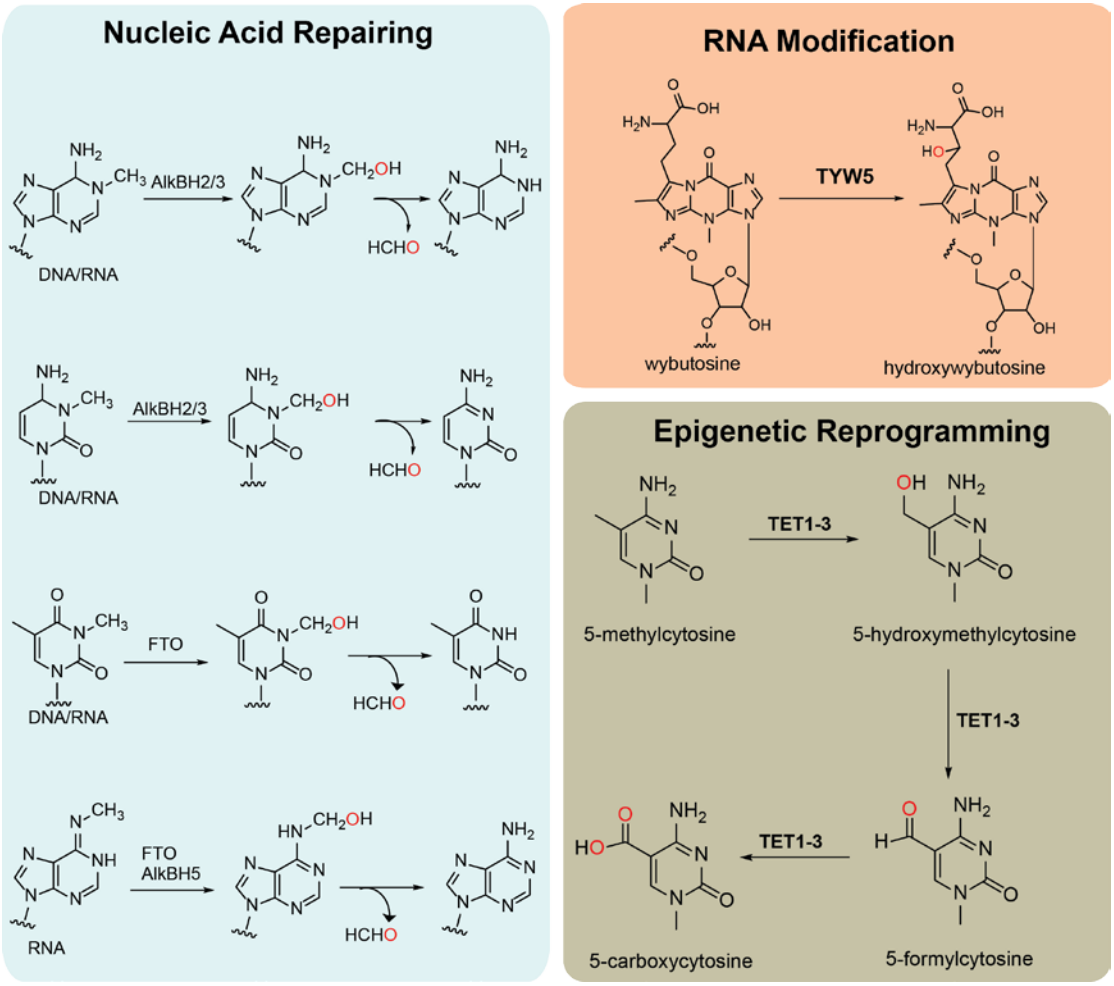

FIGURE 1.6. **Known nucleic acid substrates of human 2OG oxygenases.**

1.4.3. 2OG Oxygenases in Small Molecule Oxidation

As discussed earlier, the catalytic diversity of 2OG oxygenases is reflected by their ability to modify small molecules. These modifications are of both biological and commercial importance (3). One particular example of mechanistic interest is the EFE (ethylene forming enzyme) from *Pseudomonas* spp. that catalyses arginine C-5 hydroxylation, uncoupled 2OG turnover, and oxidative fragmentation of 2OG to give ethylene (Figure 1.7) (3).

2OG oxygenases also play key roles in the biosynthesis of plant hormones, *i.e.* gibberellins that can be considered as a classical example of catalytic flexibility of 2OG oxygenases, which proceeds *via* hydroxylation, desaturation, and methyl group oxidation

reactions (Figure 1.7) (3). Catalytic flexibility is also reflected in the FNS (flavone synthase 1)-catalysed biosynthesis of flavonoids (Figure 1.7), which plants use for attraction as well as protection purposes (3).

Halogenations by the 2OG-dependent halogenases occur by installing chlorine or bromine atom on *sp3*-hybridized carbon centres (Figure 1.7). Of the halogenases identified, SyrB2 from *Pseudomonas syringae* catalyses the chlorination of L-threonine. In comparison, the most recently discovered halogenase WelO5 chlorinates C-13 of 12-epi-fischerindole U to yield 12-epi-fischerindole G (Figure 1.7) (3).

DAOCS (deacetoxycephalosporin C synthase) catalyses the formation of cephalosporin antibiotics *via* D- to L-α-aminoadipoyl sidechain epimerisation followed by oxidative ring expansion of the penicillin N-amide thiazolidone ring (Figure 1.7). 2OG oxygenases also catalyse the biosynthesis of β-lactam antibiotics, carbapenems and clavams (3) (Figure 1.7).

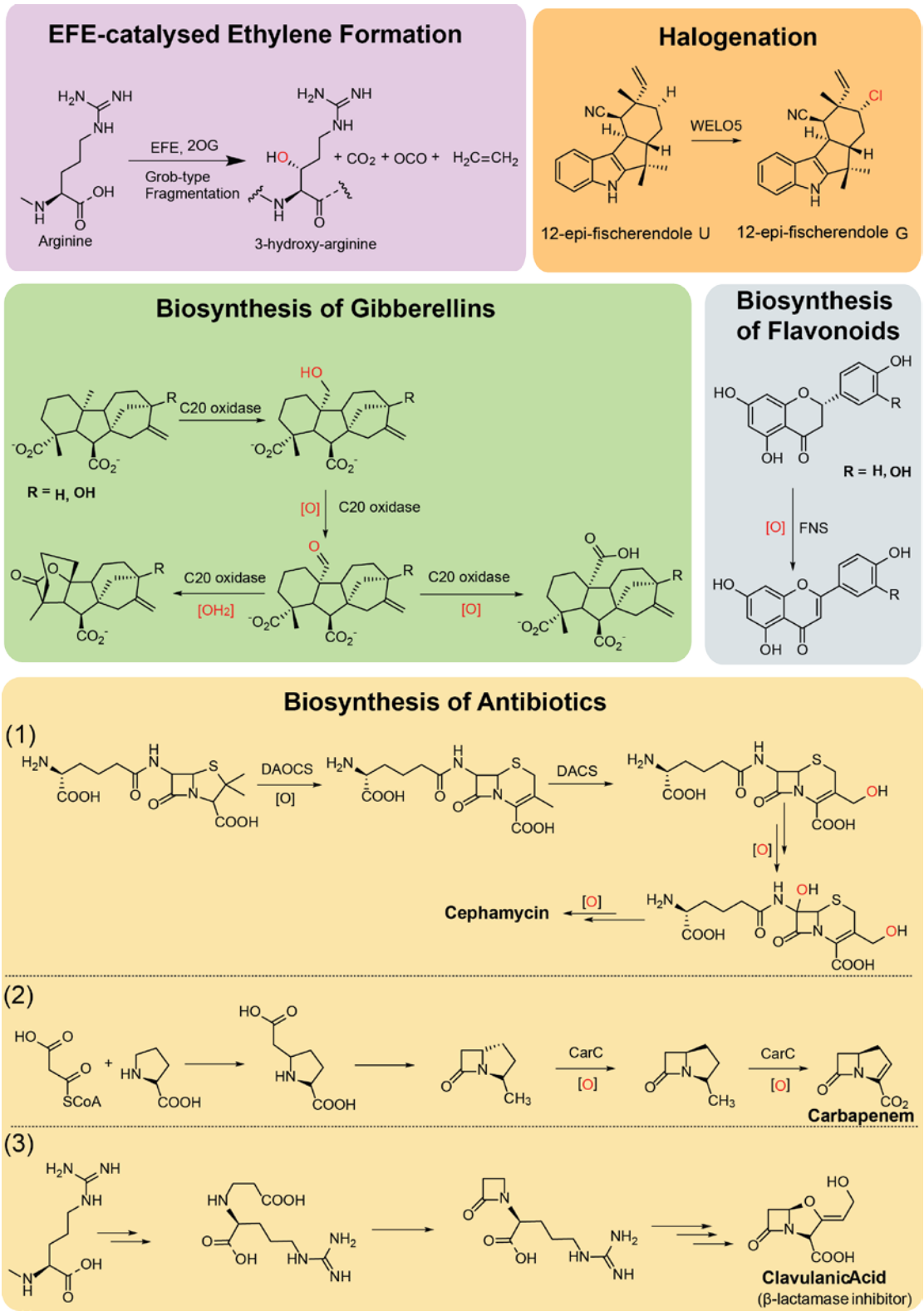

FIGURE 1.7. **Biocatalytic reactions on small molecules as are catalysed by 2OG oxygenases.** DACS = deacetylcephalosporin C synthase.

1.4.4. 2OG Oxygenases in Lipid Metabolism

2OG oxygenases regulate the fatty acid metabolism pathway *via* biosynthesis of L-carnitine during two steps: first is the hydroxylation of trimethyllysine catalysed by N^{ε}-trimethyllysine hydroxylase (TMLH) and the second is the hydroxylation of γ-butyrobetaine catalysed by γ-butyrobetaine hydroxylase (BBOX) (Figure 1.8) (3).

Phytanyl-CoA-hydroxylase (PAHX) is another important 2OG oxygenase for both animals and plants, which catalyses the C-2 hydroxylation of phytanoyl coenzyme A to form pristanal, an important step in the degradation pathway of chlorophyll (Figure 1.8). Mutations to the *PAHX* gene cause Refsum Disease, the symptoms of which are associated with the elevated levels of phytanoic acid (3).

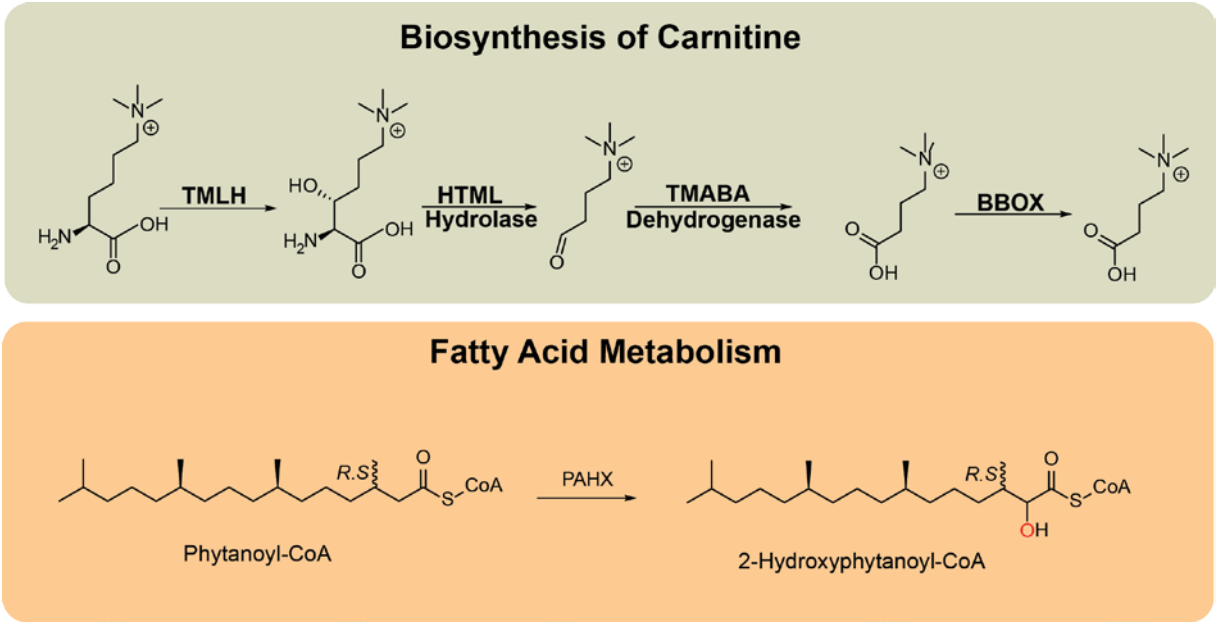

FIGURE 1.8. **2OG oxygenase-catalysed oxidation in lipid molecules.** TMABA = Trimethylaminobutyraldehyde.

1.5. Objectives

The objectives of this work were to both structurally and functionally characterise the 2-oxoacid-dependent oxygenases JMJD5, JMJD6, and HPPD.

JMJD6 was controversially identified by Fadok *et al.* as a phosphatidylserine receptor (PSR) to be involved in apoptosis (34). Subsequent works however established that PSR is not a membrane protein instead is a nuclear protein having similar domain architecture to those of Fe(II)- and 2OG-dependent oxygenases (35,36). Since then, PSR has been named as 2OG- and Fe(II)-dependent oxygenase JMJD6 (35,36). JMJD6 is localised in the nucleus of the cell and is reported to play an essential role in growth development (37). *JMJD6*-knockout mice die around birth, which is attributed by severe growth-impairment of organs including heart, brain, lung, kidney, and eye (37). Important biological functions are also reported to be regulated by the enzymatic-function of JMJD6, which include pre-mRNA splicing (38), transcription (39), and cancer (17,30). Nevertheless, the functional assignment of JMJD6 is still a controversy, as is mentioned earlier. Chang *et al.* first assigned JMJD6 with a histone arginine-demethylase function in 2007 (29). Although the interaction of JMJD6 with histones was later observed by several other groups, its arginine-demethylase function was non-reproducible (16,40). Instead of demethylase, JMJD6 was found as a hydroxylase catalysing the hydroxylation reaction of lysine residues of histones (16,40). JMJD6 was also reported to hydroxylate lysine residues of the SR proteins LUC7L2, CROP, U2AF65, and tumour suppressor p53 (33).

Similar to JMJD6, knockout of *JMJD5* has also been found lethal to embryos (41,42). Apart from the role in growth, JMJD5 impacts multiple biological functions including circadian rhythm (43), glucose metabolism (44), chromosome stability (45), osteoclastogenesis (27), regulation of tumour suppressor p53 (41,46), regulation of mitosis (41), and cancer (47,48). Nevertheless, the biochemical function of JMJD5 is elusive. Initially, JMJD5 was reported by a couple of groups as an arginine-demethylase, whereas this arginine-demethylase activity has still been non-reproducible by others (27,41,48,49). Therefore, addressing the following issues related to the controversial functional-assignments of both JMJD5 and JMJD6 is very timely:

- Are both JMJD5 and JMJD6 demethylases or if not, are unreliable antibody-based studies the basis of reporting these two enzymes as demethylases?
- What is the kinetic relationship between JMJD6 and SR proteins?
- How selective is the JMJD6-catalysed hydroxylation of lysine residues of reported substrates?
- If JMJD6 interacts with VHL and ERα, could JMJD6-mediated hydroxylation of lysine residue(s) of these proteins be the basis of these interactions?
- Provided the *C*-terminal region of JMJD6 is crucial for its cellular localisation and oligomerisation, is there any other role that it can play in, *e.g.* catalytic activity of JMJD6?
- Is the active-site structure of JMJD6 different from the other 2OG oxygenases as it is reported to catalyse both hydroxylation and demethylation reactions?
- If JMJD5 is not a demethylase, then what are the targets of JMJD5?
- Can selective and non-selective 2OG oxygenase inhibitors inhibit both JMJD5 and JMJD6?

Although HPPD does not require 2OG for its enzymatic activity, its catalytic activity is mechanistically related to those of 2OG oxygenases and is of paramount importance from both pharmaceutical and agrochemical industry perspectives (15). HPPD has been a potential target over the last few decades owing to the pharmaceutical importance of its known inhibitors. Nevertheless, the biochemistry of human HPPD is less understood compared to the non-human homologues. Therefore, it would be beneficial to know the kinetic relationship between human HPPD and its reported inhibitors. Moreover, inhibition studies of human HPPD may also have scope to develop new inhibitors with greater potency. Furthermore, structures of human HPPD in complex with inhibitors may add further insights into the SAR (structure-activity-relationship) of HPPD inhibitors.

CHAPTER 02: Role of its *C*-Terminal Polyserine Domain in JMJD6 Activity

2.1. Introduction

JMJD6 has a JmjC or cupin metalloenzyme-like domain (35). Like factor inhibiting HIF (FIH), JMJD6 has only one catalytic domain (*i.e.*, a JmjC domain) comprising residues approximately Pro^{141}-Gln^{296}. In addition to its catalytic domain, other notable regions of JMJD6 include three potential nuclear localization sequences (NLSs; residues Pro^{141}-Lys^{145}, Lys^{167}-Pro^{171}, and Arg^{373}-Arg^{378}), an AT-hook motif (residues Lys^{300}-Ser^{309}), a SUMOylation site (residues Leu^{316}-Asp^{319}), and a polyserine (polyS) domain (residues Ser^{340}-Ser^{359} including 4 aspartate residues) (35) (Figure 2.1).

These structural features are apparently highly conserved in JMJD6 homologues from humans to lower animals (33) (Figure 2.1). The NLSs and polyS domain of JMJD6 have been previously associated with its cellular localisation (50,51). In 2004, Cui *et al.* reported that JMJD6 is localised in the nucleus of cells due to the presence of its NLSs (50). In 2013, Wolf *et al.* reported that splice-variants of JMJD6 show bidirectional shuttling between the nucleoplasm and nucleolus of HeLa cells, and that this bidirectional shuttling is regulated by the polyS domain (51). *C*-Terminally truncated JMJD6 (*i.e.*, residues 1-362) retaining the polyS domain appears in the nucleus of HeLa cells, similar to the full-length JMJD6 (*i.e.,* residues 1-403). Conversely, a splice variant of JMJD6 (aa 1-337) lacking the polyS domain appears in the nucleolus, but not in the nucleus (51).

The oligomerisation state of JMJD6 has also been reported to be dependent on its polyS domain (51). Using three variants of His_6-tagged JMJD6 produced in *Escherichia coli*, it was shown by transmission electron microscopy (TEM) that the oligomerization status of JMJD6 changes with the presence or absence of the *C*-terminal polyS domain. Full-length and a *C*-terminally truncated variants of JMJD6, both containing the polyS domain, appeared as heptamers of dimers. In contrast, a *C*-terminally truncated version lacking the polyS domain appeared as filamentous structures (51).

The objective of the work described in this study was to examine the impact of the polyS domain of JMJD6 on biochemical properties of JMJD6 apart from oligomerization, including effects on:

i. Binding of its cosubstrate 2OG, and

ii. Its C-5 lysine hydroxylation activity

JMJD6 has been reported to catalyse the lysine hydroxylation of splicing-regulatory (SR) proteins in an Fe(II)- and 2OG-dependent manner (16). The apparent K_m for 2OG was reported as 39 µM against full-length JMJD6 (36). The objective of this study was to see if removal of the *C*-terminal polyS domain impacts on the affinity for 2OG, and hence on the hydroxylation activity of JMJD6. A plan was also to check the catalytic activity of multiple JMJD6-variants against the reported substrates of JMJD6. Investigating the oligomerization status of JMJD6 using native mass spectrometry was also of interest.

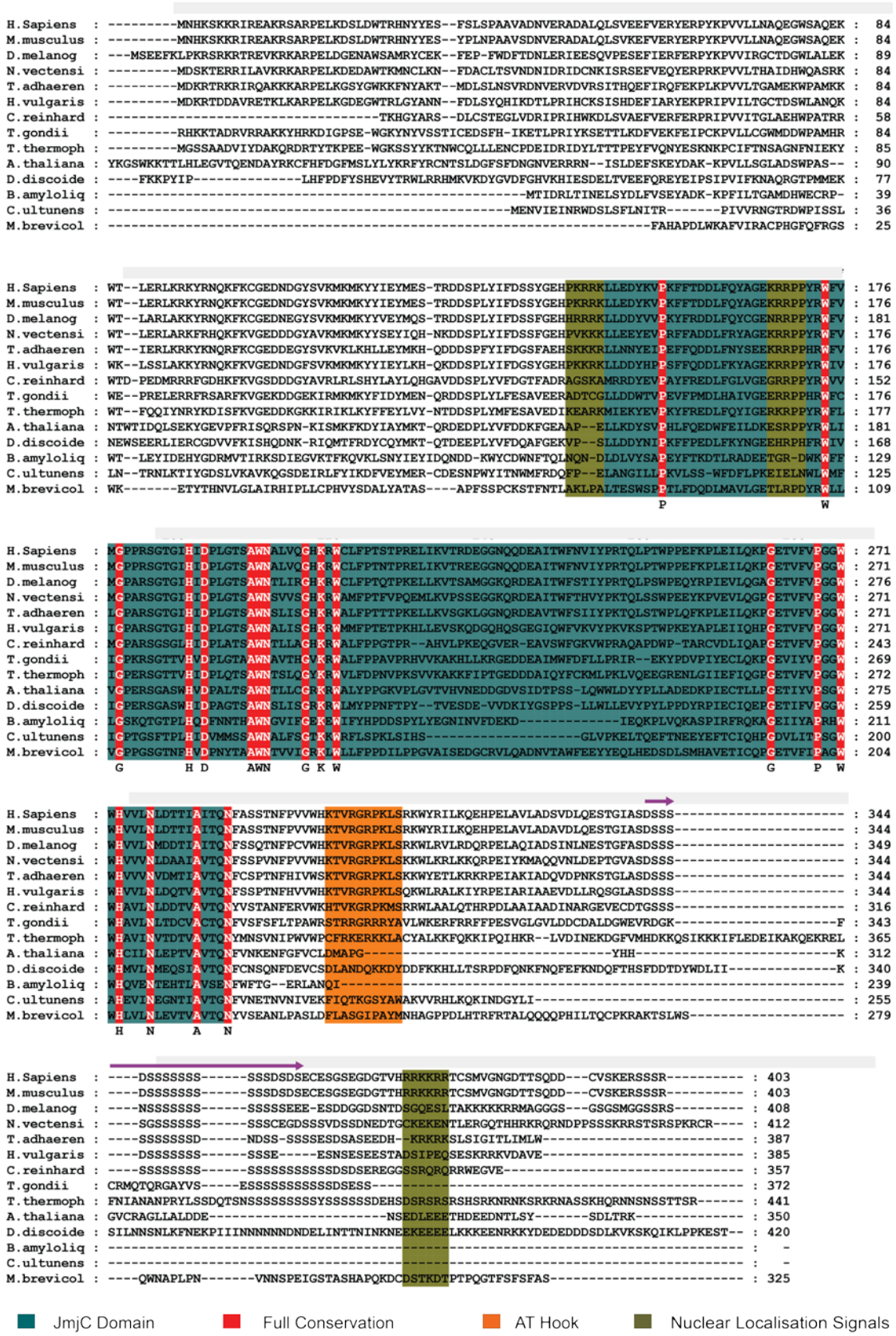

FIGURE 2.1. **The JMJD6 *C*-terminal polyS domain is conserved from humans to lower animals.** Clustal alignment of JMJD6 sequences from *Homo sapiens*, *Mus*

musculus, *Drosophila melanogaster*, *Nematostella vectensis*, *Trichoplax adhaerens*, *Hydra vulgaris*, *Chlamydomonas reinhardtii*, *Toxoplasma gondii*, *Tetrahymena thermophila*, *Arabidopsis thaliana, Dictyoselium discoideum*, *Bacillus amyloliquifaciens Clostridium ultunense*, and *Monosiga brevicollis*. Purple arrow above the alignment indicates the polyS domain.

2.2. Optimization of Purification Conditions of JMJD6

This study began with expressing the *JMJD6* gene and purifying full-length JMJD6 protein (aa 1-403, $JMJD6^{FL}$). DNA encoding for *N*-terminally His_6-tagged full-length JMJD6 protein was in the expression vector pET-28a(+) and the construct was made by Dr. Celia J. Webby (Chemistry Research Laboratory, University of Oxford). This construct was then transfected into *E. coli* Rosetta 2(DE3) competent cells following standard transformation conditions (**Chapter 10**); expression and purification followed the reported procedure (16,36). The purified enzyme was then tested for catalytic activity against a 12-residues long peptide fragment from the luc 7-like protein 2 ($LUC7L2_{267-278}$) in hydroxylation assays (**Chapter 10**). LUC7L2 is a SR protein and was previously reported as substrate of JMJD6, where the residue Lys^{269} of LUC7L2 is hydroxylated by JMJD6 (16). However, the JMJD6 enzymes purified by following the reported procedures were catalytically not very active (Figure 2.2).

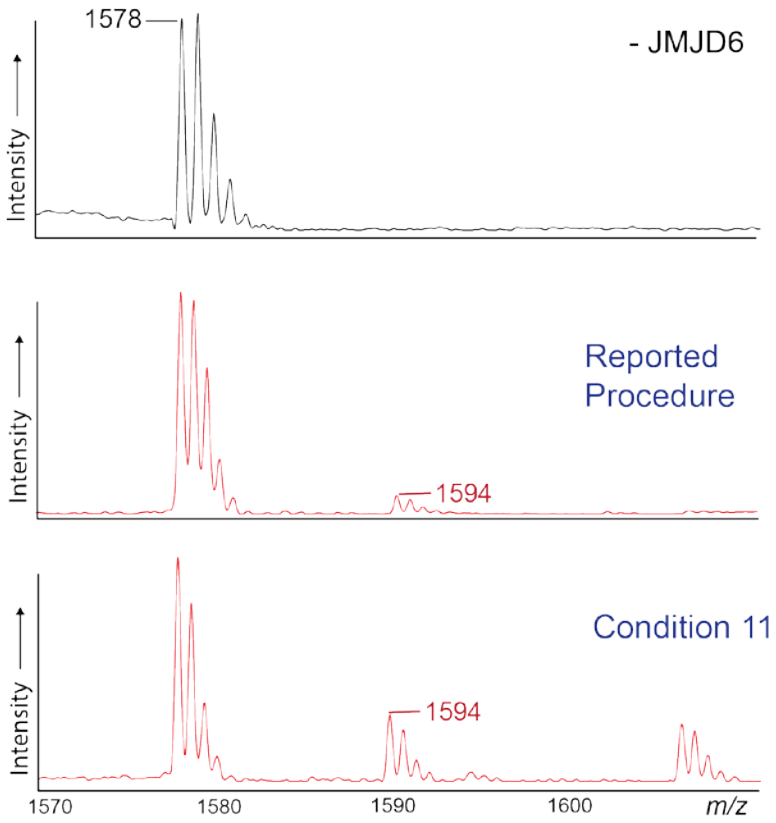

FIGURE 2.2. **Comparative hydroxylation activity of JMJD6**. MALDI-TOF spectra showing hydroxylated substrates catalyzed by JMJD6 that were produced following the reported procedure (16,36) and the procedure optimised in this study, which is described in the following section. The black subfigure represents the reaction without JMJD6.

Subsequent studies were then carried out to purify active JMJD6. First, *JMJD6* gene was overexpressed in *E.coli* following various conditions (Table 2.1). The cells were harvested and used for purification of JMJD6. The activities of the purified JMJD6 proteins were then tested as before. JMJD6, expressed and purified following condition **11** (Table 2.1), appeared comparatively more active than that from the other procedures. However, only ~25% of hydroxylation of the substrate was observed (Figure 2.2).

Table 2.1. Optimization and purification conditions for JMJD6

Batch	Expression/Induction Conditions			Purification Conditions			Activity
	Competent Cells	IPTG (mM)	Induction Temperature (°C)	Buffers*	Additives in Buffers	Column†	
01	BL21 (DE3)	0.5	25	A	0.2 mM TCEP	HisTrap Superdex 75	Inactive
02	Rosetta 2 (DE3)	0.5	25	A	0.2 mM TCEP	HisTrap Superdex 75	Inactive
03	Rosetta 2 (DE3)	0.5	25	A	0.2 mM TCEP	HisTrap Superdex 200	Inactive
04	Rosetta 2 (DE3)	0.5	25	B	0.2 mM TCEP	HisTrap No SEC	Inactive
05	Rosetta 2 (DE3)	0.5	25	C	0.2 mM TCEP	HisTrap No SEC	Inactive
06	Rosetta 2 (DE3)	0.5	25	C	0.2 mM TCEP 0.1% NP40	HisTrap Superdex 200	Inactive
07	Rosetta (DE3)-pLysS	0.5	25	D	1 mM TCEP	HisTrap Superdex 200	Inactive
08	Rosetta 2 (DE3)	0.5	25	C	0.2 mM TCEP 0.1 mM PMSF	HisTrap Superdex 200	Inactive
09	Rosetta 2 (DE3)	0.5	25	E	-	S Sepharose Ni-TED Superdex 200	Inactive
10	Rosetta 2 (DE3)	0.5	16	C	0.1% NP40 0.1 mM PMSF	HisTrap Superdex 200	Moderately Active
11	Rosetta 2 (DE3)	0.1	16	C	0.1% NP40 0.1 mM PMSF	HisTrap Superdex 200	Moderately Active

***Buffer Compositions:**

A: BB-50 mM Tris pH 7.5, 200 mM NaCl, 10% glycerol+10 mM imidazole; EB- BB with 500 mM imidazole, GFB-BB without imidazole.
B: BB-20 mM Tris pH 7.5, 500 mM NaCl, 5% glycerol; EB-BB+500 mM imidazole; GFB-BB with 50 mM Tris pH 7.5
C: BB-50 mM Tris pH 7.5, 300 mM NaCl, 10% glycerol,10 mM imidazole; EB- BB with 500 mM imidazole; GFB-BB without imidazole
D: BB-50 mM HEPES 7.5,500 mM NaCl,10% glycerol,10 mM imidazole; EB-BB with 500 mM imidazole; GFB-50 mM Tris pH 7.5, 500 mM NaCl, 10% glycerol
E: Buffer 01- 100 mM MES pH 5.8 and 5% glycerol; Buffer 02-Buffer 01 + 100 mM NaCl; Buffer 03-Buffer 01+1 M NaCl; EB-Buffer 01 + 500 mM imidazole and 500 mM NaCl; GFB-50 mM Tris 7.0, 500 mM NaCl and 5% glycerol

[**BB-Binding Buffer, EB-Elution Buffer, GFB-Gel Filtration Buffer**]

†Column

IMAC: Immobilised metal ion affinity chromatography (HisTrap, Ni-TED)
SEC: Size-exclusion chromatography (Superdex® 75, Superdex® 200)
Cation Exchange column: S Sepharose

It was then hypothesized that a contamination with Ni(II) or non-specific protein aggregation could be the reason why the produced JMJD6 enzyme was not fully-active. To test this hypothesis, modifications to the purification conditions were made including using various concentrations of imidazole, sodium chloride, and detergents (Tween 20, Triton X100, Nonidet P40).

Based on the analyses of MALDI-TOF spectra, it was found that the concentration of sodium chloride has a strong impact on the catalytic activity of JMJD6 (Figure 2.3**A**). JMJD6 enzyme, purified using 200 mM sodium chloride, was found to be relatively more active than that purified using 300 mM sodium chloride. Moreover, hydroxylation activity was completely abrogated in the presence of 500 mM sodium chloride (Figure 2.3**A**). Hydroxylation assays were carried out in the presence of various concentrations of imidazole; no effect of imidazole on JMJD6-activity was observed (Figure 2.3**B**). Amongst the detergents tested, Nonidet P40 (NP40) had little or no effect on catalytic activity. In contrast, Tween 20 and Triton X100 appeared to inhibit activity (Figure 2.3**C**). Henceforth, NP40 was incorporated into the purification buffers.

Based on the results obtained from the optimization of purification conditions, it was decided to use 200 mM sodium chloride, 500 mM imidazole, and NP40 in the purification buffers of JMJD6.

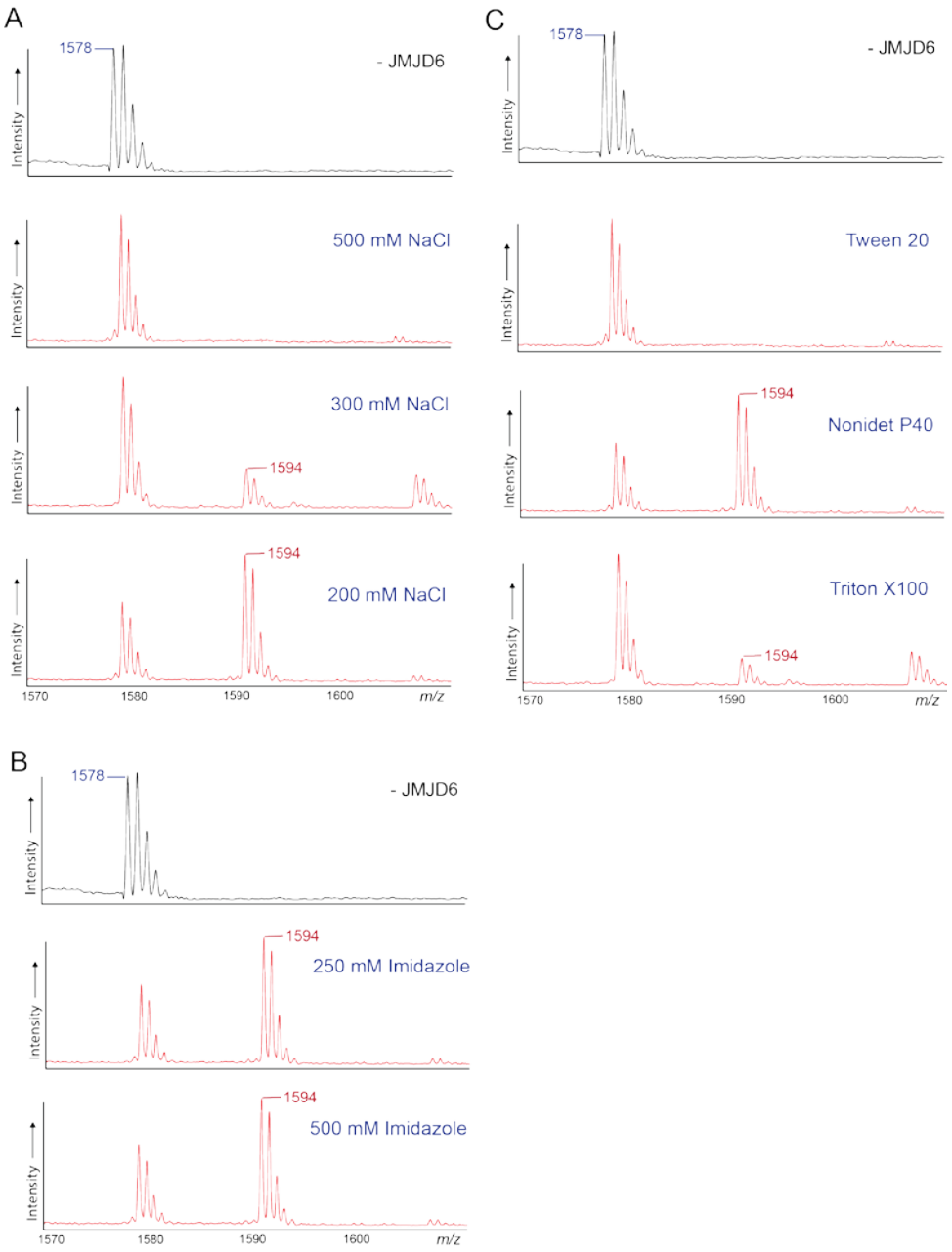

FIGURE 2.3. **Effects of sodium chloride, imidazole, and detergents on JMJD6 activity**. MALDI-TOF spectra showing the effects of (A) sodium chloride, (B) imidazole, and (C) detergents on catalytic activity of JMJD6. The black subfigures represent reactions without enzyme. Activity testing was carried out following the hydroxylation assay procedures described in Chapter 10.

The purification was then performed using a 10 mL Ni-TED column instead of a 5 mL HisTrap column, whilst keeping other conditions unchanged. Interestingly, the hydroxylation activity of the purified JMJD6 was found to be improved when using the Ni-TED column (Figure 2.4**A**). This result suggests that metal-leaching might have occurred during the purification using HisTrap column. To confirm this, apo-form of JMJD6 proteins was produced (**Chapter 10**). The activity of EDTA-treated JMJD6 protein was then tested in the hydroxylation assay with added Fe(II). JMJD6, treated by EDTA, was found to be more active than the untreated-form resulting near to complete hydroxylation of $LUC7L2_{267\text{-}278}$ after 30 minutes of incubation at 37 °C(Figure 2.4**A**). JMJD6 was also purified using HEPES buffer instead of Tris keeping the other components unchanged. However, no significant impact of buffer component on catalytic activity of JMJD6 was observed (Figure 2.4**B**).

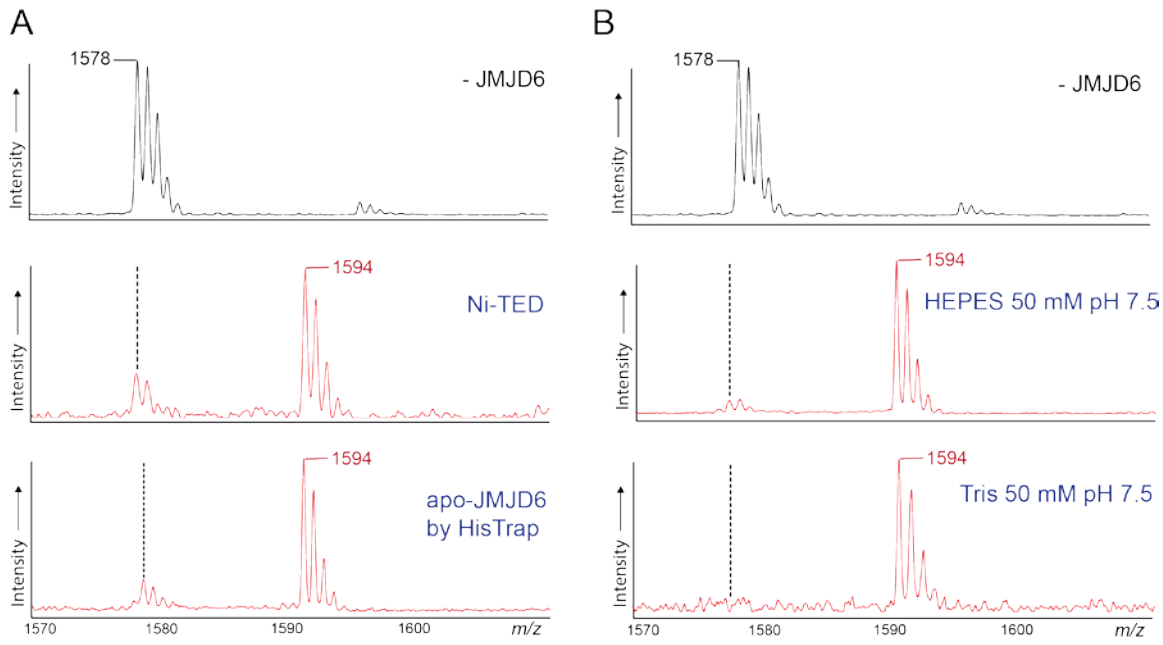

FIGURE 2.4. **Optimization of buffer and column for JMJD6 purification**. MALDI-TOF spectra showing the hydroxylation activities of JMJD6 purified (A) on various columns and (B) using various buffer components. Black subfigures represent reactions without JMJD6. Activity testing was carried out following the hydroxylation assay procedures described in Chapter 10.

2.3. Optimisation of JMJD6 Construct for Activity

To investigate the role of the PolyS domain, three constructs of JMJD6 (Figure 2.5) previously made by Dr. Celia J Webby (Chemistry Research Laboratory, University of Oxford) were used: full-length JMJD6 (aa 1-403; $JMJD6^{FL}$), *C*-terminally truncated JMJD6 with the polyS domain (aa 1-362; $JMJD6^{\Delta 363-403}$), and *C*-terminally truncated JMJD6 without the polyS domain (aa 1-343; $JMJD6^{\Delta 344-403}$). These three variants of JMJD6 were used to produce the recombinant JMJD6 in *E. coli*, which were purified according to the optimized procedures.

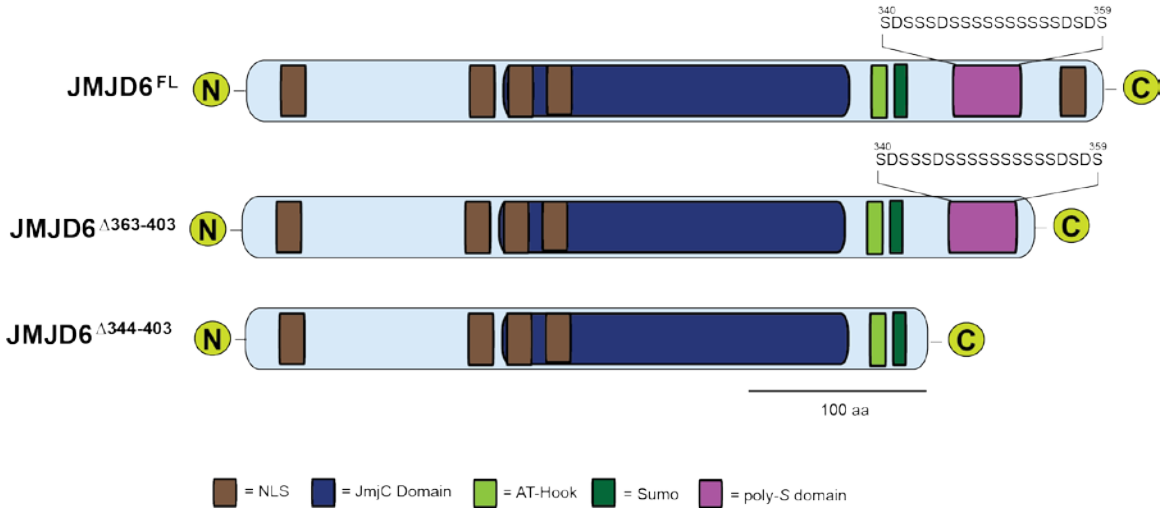

FIGURE 2.5. **JMJD6 variants used to assess the role of polyS domain.** Domain architectures of the three JMJD6 variants showing the location of polyS domain along with other domains.

Before conducting the kinetic studies, it was important to ensure that the overall folding-property of these JMJD6 variants was not impacted by the deletion of the *C*-terminal residues, including the polyS domain.

2.3.1. Study of Folding Properties of JMJD6 Variants

Several techniques are commonly used to study protein folding both *in vitro* and in cells including nuclear magnetic resonance (NMR) spectroscopy, Raman spectroscopy, labeling with dyes, and fluorescence resonance energy transfer (FRET) spectroscopy (52). Circular dichroism (CD) spectroscopy has been a widely used method to study protein folding property owing to its simple operation procedure and low sample requirement (53). Data generated by CD spectroscopy are often easy to interpret (53), hence was employed to study JMJD6. Far-ultraviolet CD spectroscopy is a useful technique to study protein folding (53). α-Helical region shows positive bands at 193 nm and negative bands at 222 nm and 208 nm; anti-parallel β-sheets show positive bands at 195 nm and negative bands at 218 nm; disordered proteins show low ellipticity above 210 nm and negative bands near 195 nm (53).

Purified JMJD6 variants were analysed by CD spectroscopy to see whether the deletion of polyS domain caused any change in secondary structure (Figure 2.6). JMJD6 variants were buffer exchanged into a buffer suitable for CD spectroscopy (*i.e.*, 10 mM phosphate buffer, pH 8.0) and diluted to 0.1 mg/mL (**Chapter 10**). The spectra of the variants showed signals indicating similar folding patterns (Figure 2.6**A**). The observations including a negative absorption at ~222 nm (222.5 nm for $JMJD6^{FL}$, 221.5 nm for $JMJD6^{\Delta 363\text{-}403}$ and $JMJD6^{\Delta 344\text{-}403}$) and a positive absorption at ~193 nm (194.5 nm for $JMJD6^{FL}$, 196.0 nm for $JMJD6^{\Delta 363\text{-}403}$ and 193.0 nm for $JMJD6^{\Delta 344\text{-}403}$) indicated the presence of α-helical regions. Positive absorption values at ~195 nm indicated the presence of β-sheet in JMJD6 (Figure 2.6**A**). Overall, these results suggest that the deletion of the polyS domain does not change the overall folding property of JMJD6, and therefore any changes in catalytic activity likely result from presence/absence of polyS domain instead of misfolding.

Next, melting temperature (T_m) of the JMJD6 variants were determined by applying temperatures ranging from 18 to 68 ºC (**Chapter 10**). Interestingly, $JMJD6^{\Delta 363\text{-}403}$

was found to be more stable (T_m of 44.3 ± 0.08 ºC) than JMJD6^{FL} (41.0 ± 0.26 ºC) or JMJD6$^{\Delta 344\text{-}403}$ (39.4 ± 0.1 ºC) (Figure 2.6**B**). The unfolded proteins were then exposed to a decreasing temperature gradient from 68 to 18 ºC to test if refolding occurred. Although the position of corresponding peaks representing α-helices and β-sheets appeared to be shifted slightly, overall secondary structures of the variants appeared unchanged (Figure 2.6**B**). This observation demonstrates that JMJD6 proteins can refold following thermal denaturation, irrespective of the presence or absence of the polyS domain. Refolded proteins obtained thereafter were tested for activity in the hydroxylation assay (**Chapter 10**). Interestingly, all three variants of JMJD6 with/out the polyS domain showed little or no hydroxylation activity (**Appendix 01**), suggesting that the JMJD6 variants probably lost their catalytic activities due to thermal denaturation.

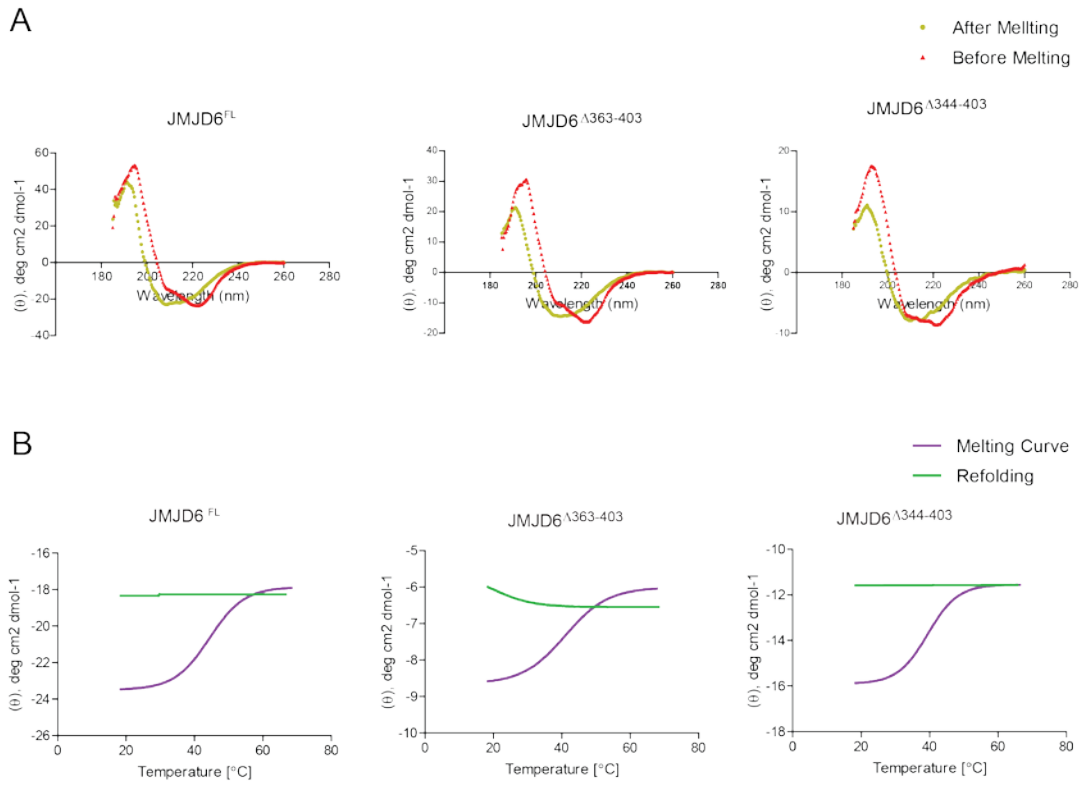

FIGURE 2.6. **The *C*-terminal polyS domain enhances JMJD6 stability**. (A, B) CD spectra showing the overall folding properties of the three JMJD6 variants, as measured in the far-UV region (185-260 nm). Melting and refolding curves were measured following

the procedures described in Chapter 10. Values represent mean ± standard deviation (SD)

2.3.2. 2OG Turnover Assays Catalysed by JMJD6 Variants

2OG turnover assay (*i.e.*, monitoring the enzymatic conversion of 2OG to succinate) is a useful means of testing the activity of 2OG oxygenases (28). Turnover may be either substrate-dependent (*i.e.*, coupled turnover), substrate-independent (*i.e.*, uncoupled turnover), or a mixture of both (28).

JMJD6 variants were tested by the 2OG turnover assays to see if the presence/absence of polyS domain can influence cosubstrate recognition. Differences in the rate of 2OG turnover catalysed by the JMJD6 variants were observed (Table 2.2, Figure 2.7). In the absence of substrate, JMJD6$^{\Delta 344\text{-}403}$-catalysed reaction resulted in only 0.5 µM of succinate after 1.5 h, which was less than those catalysed by JMJD6$^{\Delta 363\text{-}403}$ (6.4 µM) or JMJD6^{FL} (0.9 µM) (Figure 2.7). In the presence of substrate, the amounts of succinate produced were 1.8, 3.6, and 8.4 µM, respectively (Figure 2.7). These data suggest that the polyS domain of JMJD6 is important for the optimal conversion of 2OG to succinate. Interestingly, succinate formation was higher for JMJD6$^{\Delta 363\text{-}403}$ than JMJD6^{FL}, albeit both contained the polyS domain.

Table 2.2. 2OG turnover results as catalyzed by JMJD6 variants. 2OG (400 µM) and JMJD6 (10 µM) were allowed to react inside 2 mm NMR tubes either in absence or presence of substrate peptide LUC7L2$_{267\text{-}278}$ (NPKRSRSREHRR) for 1.5 hour (**Chapter 10**). Values represent mean ± SD (standard deviation).

Protein	Succinate (µM)	
	Without Substrate	With Substrate
JMJD6^{FL}	0.9 ± 0.03 (12.3 ± 0.04)*	3.6 ± 0.03 (44.0 ± 0.06)*
JMJD6$^{\Delta 363\text{-}403}$	6.4 ± 0.02 (8.0 ± 0.03)*	8.4 ± 0.02 (39.2 ± 0.02)*
JMJD6$^{\Delta 343\text{-}403}$	0.5 ± 0.02 (1.6 ± 0.05)*	1.8 ± 0.03 (5.8 ± 0.03)*

*2OG turnover catalysed by EDTA-treated JMJD6.

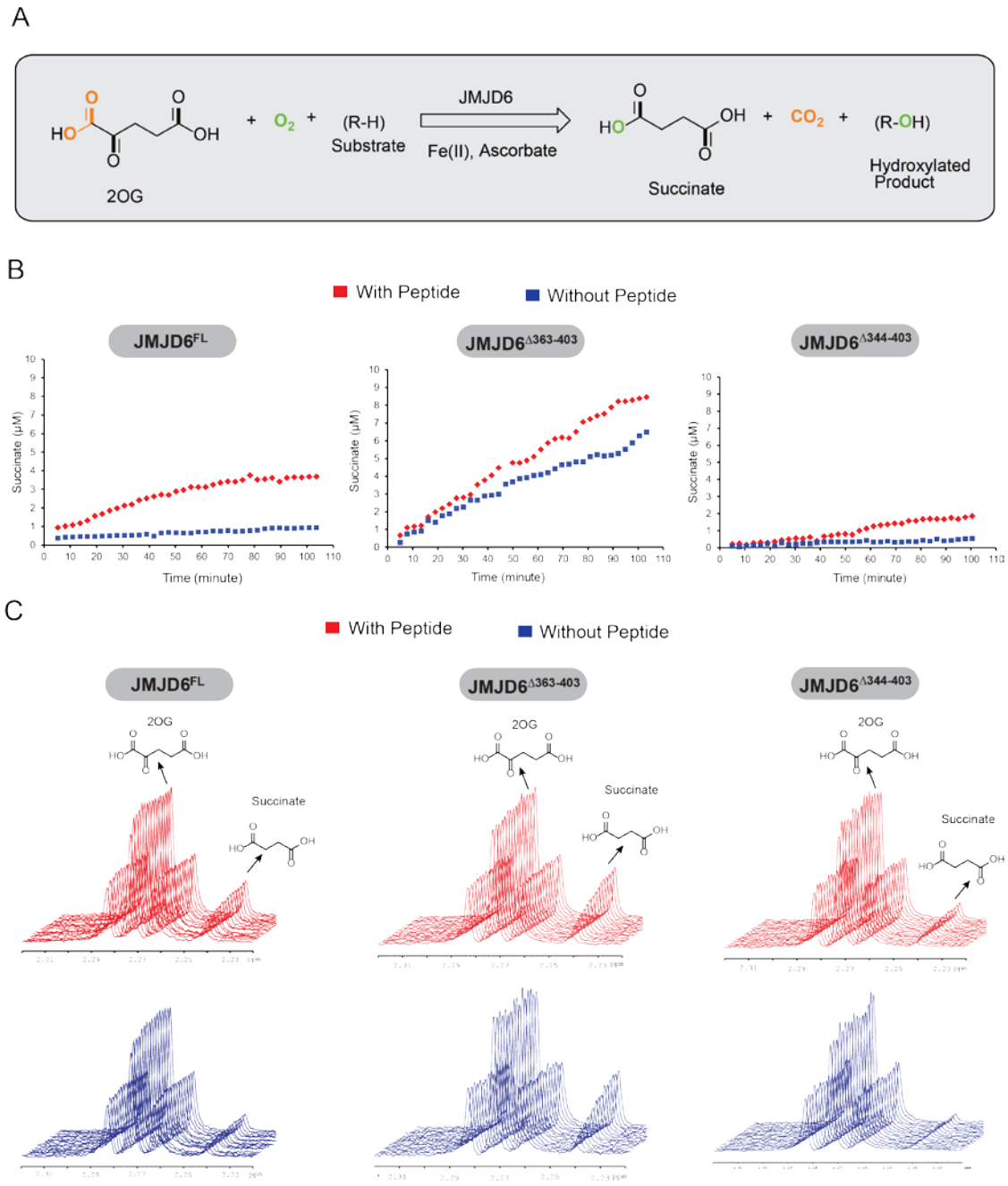

FIGURE 2.7. **2OG turnover assays**. (A) Reaction scheme showing the conversion of 2OG to succinate as catalyzed by JMJD6. (B) The plots show the level of succinate formation catalyzed by three JMJD6 variants. (C) NMR spectra showing the decrease in intensities of 2OG signals, whereas signals for succinate increase over time. Values represent mean (n = 3) ± SD.

2OG conversion assays were thereafter performed using EDTA-treated JMJD6 variants. In this case, the amount of succinate, produced under the same experimental

conditions, was an order of magnitude higher than those obtained previously (Table 2.2, Figure 2.8). As above, the construct lacking the polyS domain was found to be the least active. This suggests that removing the residual metal from the active site, which can be a result of metal-leaching during purification, is essential for fully active forms of JMJD6 as observed earlier. Furthermore, succinate formation was higher in the presence of the substrate, suggesting JMJD6 binds its cosubstrate 2OG more strongly in presence of its substrate.

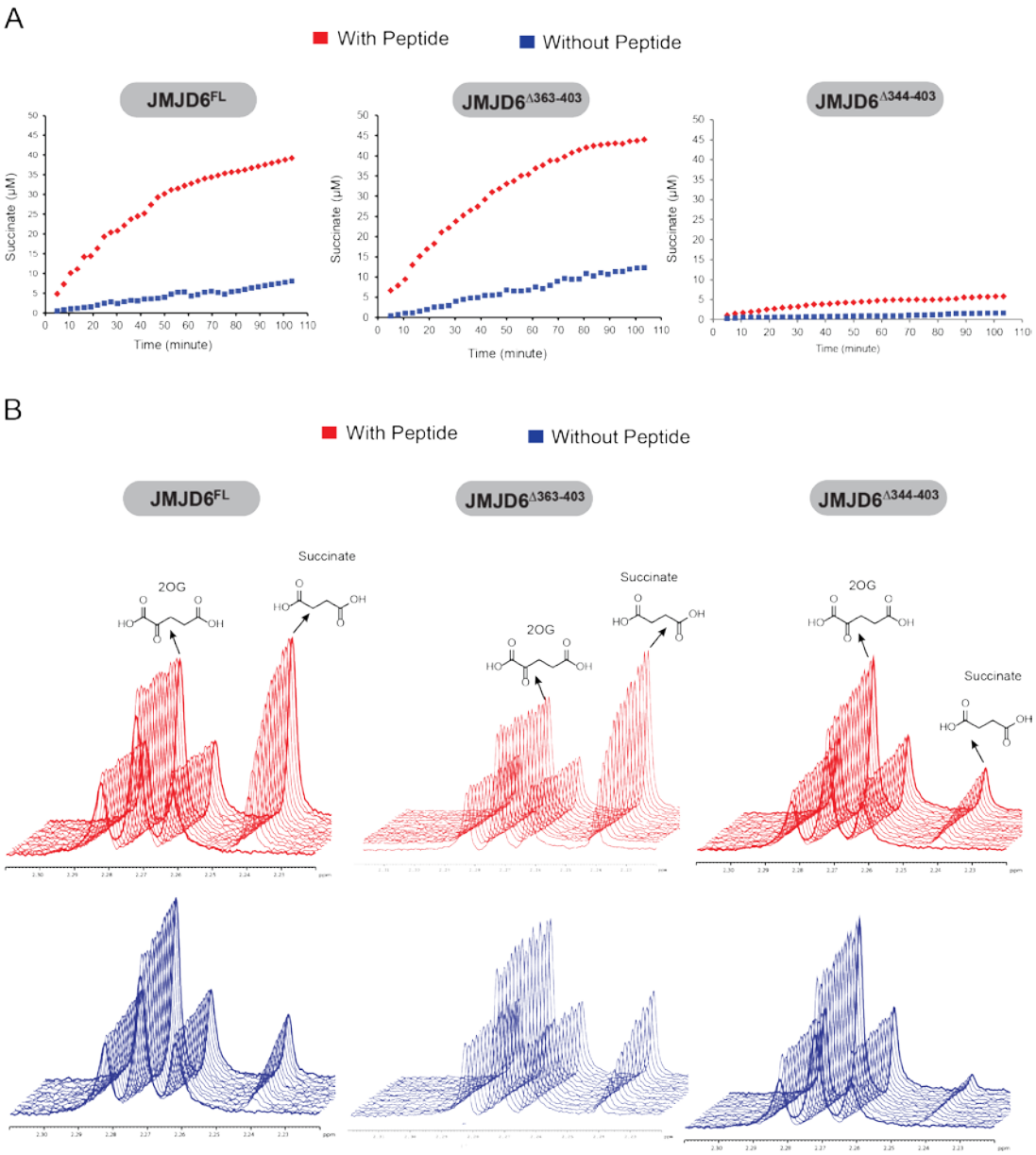

FIGURE 2.8. **2OG turnover assays catalysed by EDTA-treated JMJD6**. (A) The plots show the levels of succinate formation as catalyzed by the three variants of JMJD6

treated with EDTA. (B) NMR spectra showing the decrease in 2OG signals and increase in succinate signals over time. Values represent mean (n = 3) ± SD.

2.3.3. Binding Assay between 2OG and JMJD6 Variants

To investigate the interaction between 2OG and the variants of JMJD6, binding constants (K_D) were determined. Several biophysical methods have been developed as binding assays for 2OG oxygenases including non-denaturing electrospray ionization-mass spectrometry (ESI-MS), protein X-ray crystallography, isothermal titration calorimetry (ITC), surface plasmon resonance (SPR), circular dichroism (CD) spectroscopy, electron paramagnetic resonance (EPR) spectroscopy, and protein NMR spectroscopy (4). In this study, an NMR-based binding assay was used owing to its accuracy and simplicity (54,55).

2OG was titrated against increasing concentrations of JMJD6 in the presence of Zn(II) (**Chapter 10**). JMJD6$^{\Delta 363\text{-}403}$ was added until the methylene proton signals of 2OG completely disappeared, indicating complete 2OG binding (55). Under these conditions, the ^{1}H NMR spectra were dominated by signals due to the protein, which interfered with the 2OG signals. To overcome this, the Carr-Purcell-Meiboom-Gill (CPMG) pulse sequence coupled with periodic refocusing of J evolution by coherence transfer (PROJECT) method was applied for spectral editing (56,57). The extent of 2OG (%) bound to JMJD6 was calculated, and the values were plotted against the concentration of JMJD6 using Origin^{TM} (55). The apparent binding constant of the reporter ligand, 2OG (K_D^{app}), was then calculated following the equation described by Morton *et al.* (58) (**Chapter 10**)

Variation in the binding affinities for 2OG by the JMJD6 variants was observed. The K_D^{app} of 2OG for JMJD6$^{\Delta 363\text{-}403}$ was 3.0 µM, while the K_D^{app}s for JMJD6^{FL} and JMJD6$^{\Delta 344\text{-}403}$ were 2.3 µM and 3.5 µM, respectively (Figure 2.9). Constructs retaining the *C*-terminal polyS domain appeared to bind 2OG more strongly than the construct without

the polyS domain (assuming K_D reflects binding), consistent with the 2OG turnover experiments.

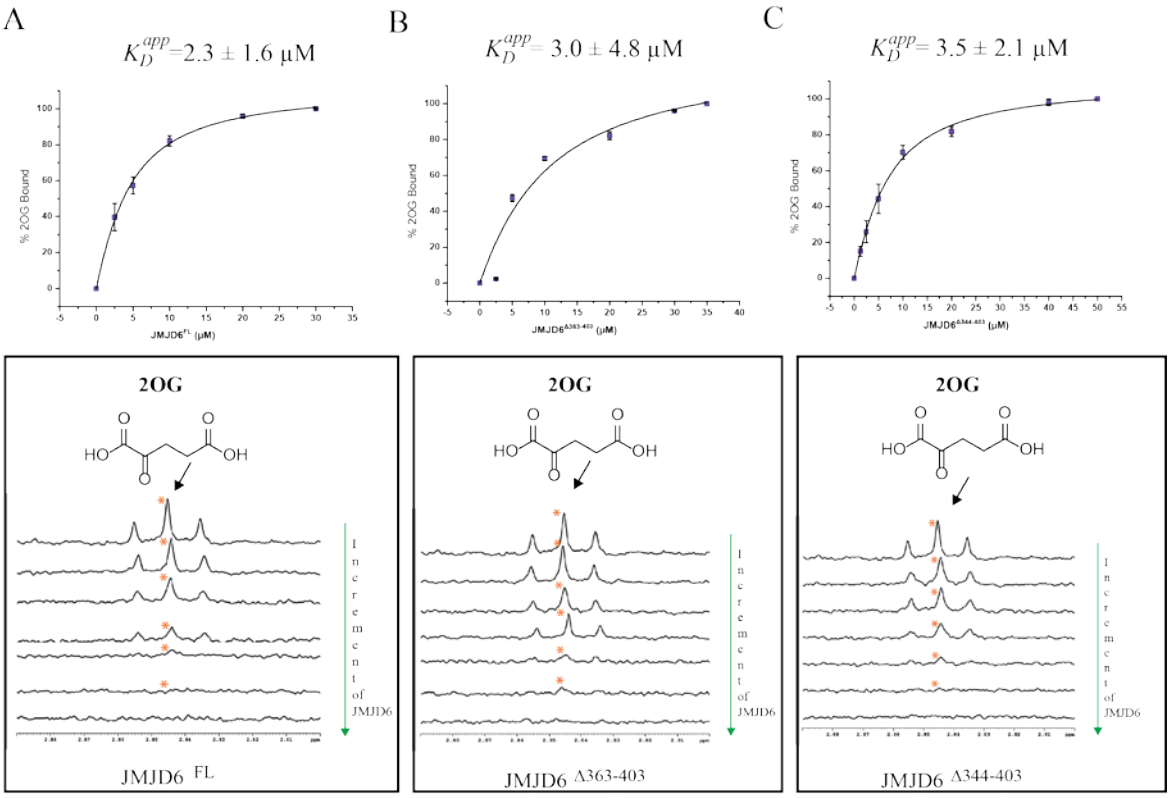

FIGURE 2.9. **Binding experiments between JMJD6 and co-substrate 2OG by NMR.** Curves show the titration of 2OG against varied concentrations of variants (A) JMJD6^{FL}, (B) JMJD6$^{\Delta 363\text{-}403}$, and (C) JMJD6 $^{\Delta 344\text{-}403}$. Insets show the NMR spectra of 2OG signals disappearing with the addition of JMJD6. 10 µM 2OG was titrated against increasing concentrations of EDTA-treated JMJD6 (0-60 µM) with added Zn(II) (200 µM). Values represent mean (n = 3) ± SD.

Furthermore, these results indicate a relatively tight binding interaction between JMJD6 and 2OG, comparable to HIF prolyl hydroxylase PHD2 (K_D = 0.9 µM) and HIF asparaginyl hydroxylase FIH (K_D = 4.0 µM) (55). Studies were next carried out to investigate the impact of the polyS domain on the catalytic activity of JMJD6.

2.3.4. Testing of Hydroxylation Activity of JMJD6 Variants

Hydroxylation of lysine residues is an important post-translational modification (PTM) that is catalysed by 2OG oxygenases including JMJD6 and collagen lysyl-hydroxylases (PLODs) (33). PLOD-catalyzed lysyl hydroxylation occurs in the endoplasmic reticulum whereas JMJD6-catalyzed hydroxylation is reported to occur in the nucleus (33). Notably, previously carried out NMR studies revealed that JMJD6 catalyzes hydroxylation of C-5 position of lysine residues of SR proteins. However, lysine hydroxylation by PLODs give products with the (*2S,5R*)-stereochemistry, whereas JMJD6 hydroxylates lysine with the (*2S,5S*)-stereochemistry (33) (Figure 2.10).

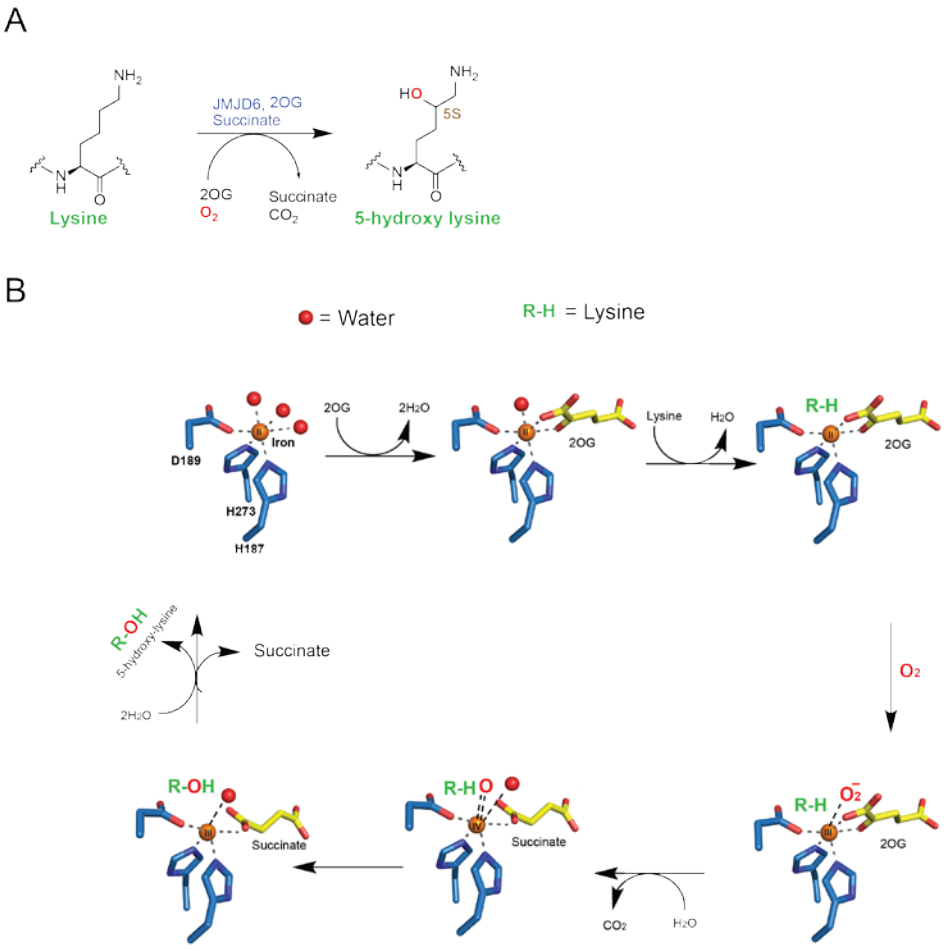

FIGURE 2.10. **The JMJD6-catalysed lysine hydroxylation.** (A) The scheme shows the JMJD6-catalyzed lysine hydroxylation reaction. (B) Insights into the mechanism of the

hydroxylation reaction catalyzed by JMJD6; one atom of O_2 is incorporated into lysine (R-H), driven by the oxidative decarboxylation of 2OG to succinate.

The purpose of this study was to investigate the effect of the presence/absence of *C*-terminal polyS domain on the JMJD6-catalysed lysine hydroxylation (if any). In order to do so, hydroxylation assays were carried out using JMJD6 variants where $LUC7L2_{267-278}$ (NPKRSRSREHRR) was used as the substrate and MALDI-TOF MS was used to quantify the results. Analyses of the MALDI spectra revealed that the JMJD6 variants with the polyS domain were more active than the variant without it (Figure 2.11), in agreement with the 2OG turnover assay results (Figure 2.7 and 2.8). $JMJD6^{FL}$ (88% ± 2.1%) and $JMJD6^{\Delta 363-403}$ (90% ± 3.2%) were apparently 2.2 and 2.3-fold more active, respectively (Figure 2.11**A** and 2.11**B**), than $JMJD6^{\Delta 344-403}$ (39% ± 1.2%) (Figure 2.11**C**).

The activity of the JMJD6 variants was also tested using a 15-mer peptide from histone 4 ($H4R3(me2a)_{1-15}$: SGR(me2a)GKGGKGLGKGGA), which is a reported substrate of JMJD6 (16). In this case also, hydroxylation activity was enhanced due to the presence of the polyS domain (Figure 2.11). Interestingly, both lys^8 and lys^5 were hydroxylated by $JMJD6^{\Delta 363-403}$ whereas only lys^5 was observed to be hydroxylated by $JMJD6^{FL}$ suggesting variant $JMJD6^{\Delta 363-403}$ is more active than the variant $JMJD6^{FL}$ due to a reason that is still unclear.

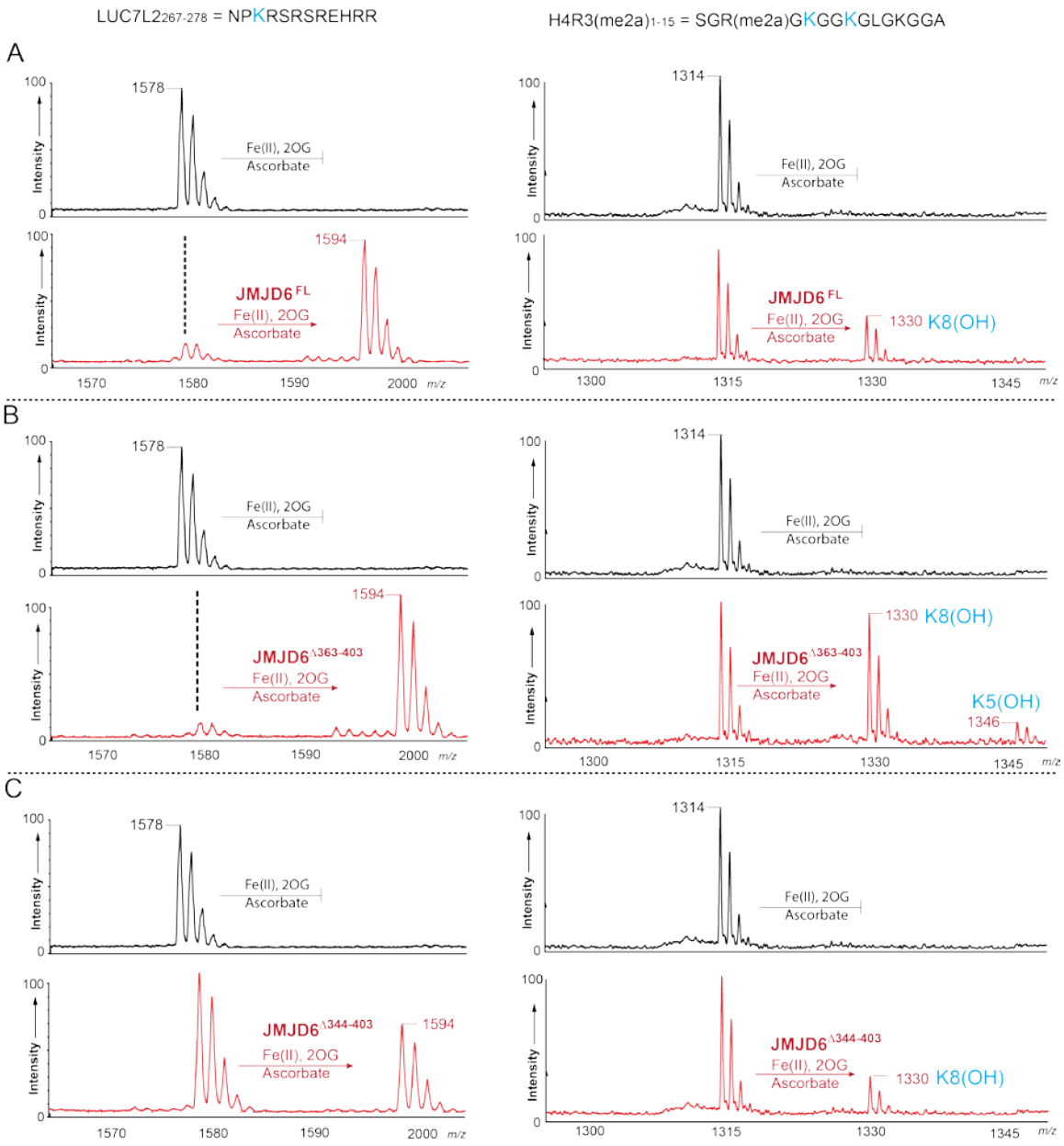

FIGURE 2.11. **Lysine hydroxylation activity of JMJD6**. MALDI-TOF mass spectra showing peaks for peptides alone (black subfigures) and peptides incubated with JMJD6 variants (red subfigures): panel A, JMJD6^{FL}; panel B, JMJD6$^{\Delta 363-403}$; panel C, JMJD6$^{\Delta 344-403}$. The hydroxylated residues in each peptide were assigned based on the observed MS/MS analyses, which is discussed in Chapter 03. Hydroxylation assays comprising 10 µM JMJD6 variants, 500 µM 2OG, 100 µM Fe(II), 400 µM ascorbate, and 100 µM substrate peptide were carried out following the procedures described in Chapter 10.

2.4. Apparent Kinetic Parameters (K_m^{app}) of 2OG and Fe(II)

MALDI-TOF MS has been widely used to carry out kinetic studies of 2OG oxygenases (59,60) and was used to carry out the kinetic studies described in this chapter. It was of particular interest to determine the apparent kinetic parameters (K_m^{app}) of cosubstrate 2OG and co-factor Fe(II) with the JMJD6 variants.

In the case of K_m^{app} determination for 2OG, the concentration of 2OG was varied (0-150 µM) whilst the concentrations of the other reagents were kept constant (**Chapter 10**). The K_m^{app} of 2OG for JMJD6^{FL} was found to be 31 µM (Figure 2.12**A**), comparable to a previously reported value (36). However, K_m^{app} values for JMJD6$^{\Delta 363\text{-}403}$ and JMJD6$^{\Delta 344\text{-}403}$ were 24 and 45 µM, respectively (Figure 2.12), indicating again an impact of the polyS domain on the kinetic relationship between JMJD6 and its cosubstrate. This result further shows analogy with an earlier finding that the polyS domain increases the affinity of JMJD6 for 2OG. Interestingly, the JMJD6$^{\Delta 363\text{-}403}$ variant was found to be more active than JMJD6^{FL} (both contained the polyS domain). Henceforth, the variant JMJD6$^{\Delta 363\text{-}403}$ was used in kinetic studies. The K_m^{app} of Fe(II) for JMJD6$^{\Delta 363\text{-}403}$ was similarly determined (**Chapter 10**), resulting in a value of 62.3 µM (Figure 2.12**D**) when using LUC7L2$_{267\text{-}278}$ (NPKRSRSREHRR) as a substrate.

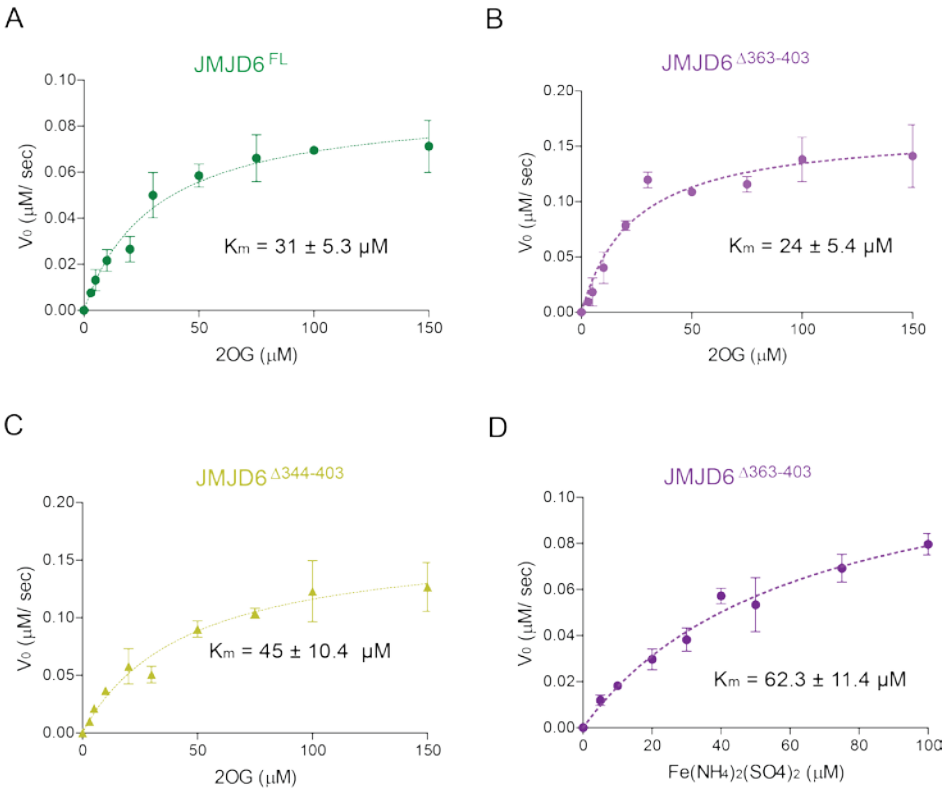

FIGURE 2.12. **Apparent kinetic parameters (K_m^{app}) for 2OG and Fe(II).** The K_m^{app} of 2OG was measured with (A) JMJD6^{FL}, (B) JMJD6$^{\Delta 363-403}$, and (C) JMJD6$^{\Delta 344-403}$. (D) The K_m^{app} of Fe(II) was measured with JMJD6$^{\Delta 363-403}$. Kinetic parameters were measured following *steady-state* kinetic assay procedures described in Chapter 10. Values represent mean (n = 3) ± SD.

K_ms for 2OG and Fe(II) with other 2OG-dependent hydroxylases have also been determined previously by different groups including us following the same MALDI-TOF-based method (59-61). In the case of HIF prolyl hydroxylase PHD2 (concentration used was 4 μM), 2OG K_m^{app} values of 13, 30, 9, and 17 μM were found against substrates HIF-1α CODD, HIF-1α NODD, HIF-2α CODD, and HIF-2α CODD, respectively (60). In contrast, the 2OG K_m^{app} values were found to be 110 and 19 μM for the HIF asparaginyl hydroxylase FIH (concentration used was 0.1-5 μm) using HIF-1α CAD and HIF-2α CAD as substrates, respectively (60). Kinetic studies with the 2OG-dependent hydroxylase OGFOD1 (which catalyzes prolyl hydroxylation of the small ribosomal subunit protein uS12, RPS23) yielded a K_m^{app} value of 25 μM for 2OG against 1 μM of enzyme (59).

Based on these results, the sensitivity of JMJD6 for 2OG resembles more closely to PHD2 and OGFOD1 rather than FIH. Furthermore, the $K_m^{Fe(II)}$ of JMJD6 was higher compared to K_m^{2OG}, suggesting JMJD6 requires a greater amount of Fe(II) for activity.

2.5. Activity Testing of Catalytic Variants of JMJD6

Like other 2OG oxygenases, metal binding by JMJD6 involves three residues: His^{187}, Asp^{189}, and His^{273} (36). Three catalytic variants of the $JMJD6^{\Delta 363-403}$ replacing these metal binding residues by alanine were made for activity testing. These variants were then expressed and purified following the same procedures as used for wild-type JMJD6 (**Chapter 10**).

2.5.1. 2OG Turnover Assays

Initially, the activities of these catalytic-variants of JMJD6 were tested using the 2OG turnover assay (28). NMR spectra revealed the formation of succinate in the reaction with the mutant $JMJD6^{\Delta 363-403}$D189A demonstrating that this variant of JMJD6 is active with respect to 2OG turnover. Nevertheless, the level of succinate formation was very low compared to the wild-type suggesting a very weak activity. Moreover, 2OG turnover by this mutant was completely abolished in presence of $LUC7L2_{267-278}$, which further indicates the weak/no activity of this variant. The other two variants, $JMJD6^{\Delta 363-403}$H187A and $JMJD6^{\Delta 363-403}$H273A, were also found catalytically inactive in the 2OG turnover assay (Figure 2.13).

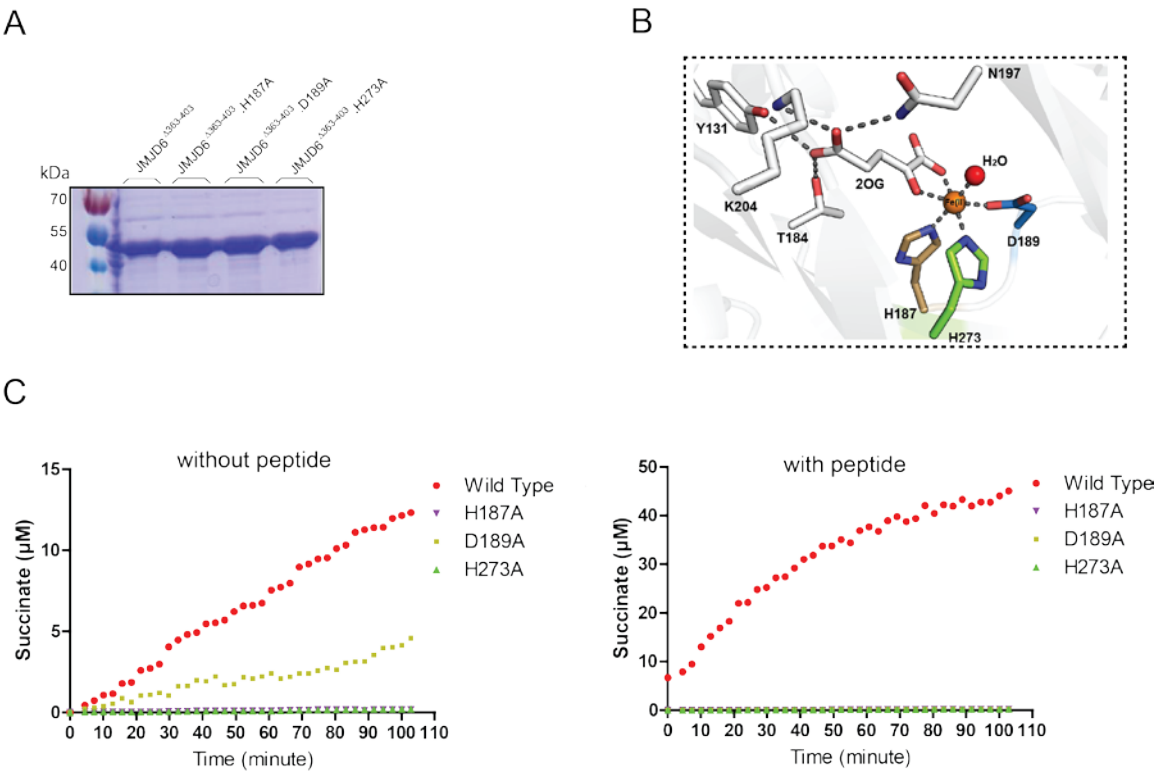

FIGURE 2.13. **Activity testing of metal binding variants of JMJD6.** (A) SDS-PAGE analyses of the wild-type and the metal binding variants of JMJD6$^{\Delta 363\text{-}403}$. (B) A view of the active-site residues of JMJD6 showing residue H187 (sand stick), D189 (blue stick), and H273 (green stick) that were replaced by alanine. (C) Plots showing the rate of formation of succinate catalyzed by wild-type and metal binding variants of JMJD6 proteins as measured by NMR; the substrate used in this experiment was LUC7L2$_{267\text{-}278}$: NPKRSRSREHRR (**Chapter 10**). Values represent mean (n = 3) ± SD.

2.5.2. Binding Assays with 2OG

To gain a more detail understanding on the binding mode of 2OG with the catalytic variants, the apparent binding constants (K_D^{app}) were determined following the same NMR-based method as before (55). Measured values of K_Ds were 24.7, 82.7, and 101.9 μM for JMJD6$^{\Delta 363\text{-}403}$H187A, JMJD6$^{\Delta 363\text{-}403}$D189A, and JMJD6$^{\Delta 363\text{-}403}$H273A, respectively (Figure 2.14). The obtained K_D^{app} values were an order of magnitude higher than that of the wild-type JMJD6 (3 μM) (section 2.3.3), suggesting JMJD6 requires all of its three metal binding residues to bind its cosubstrate 2OG.

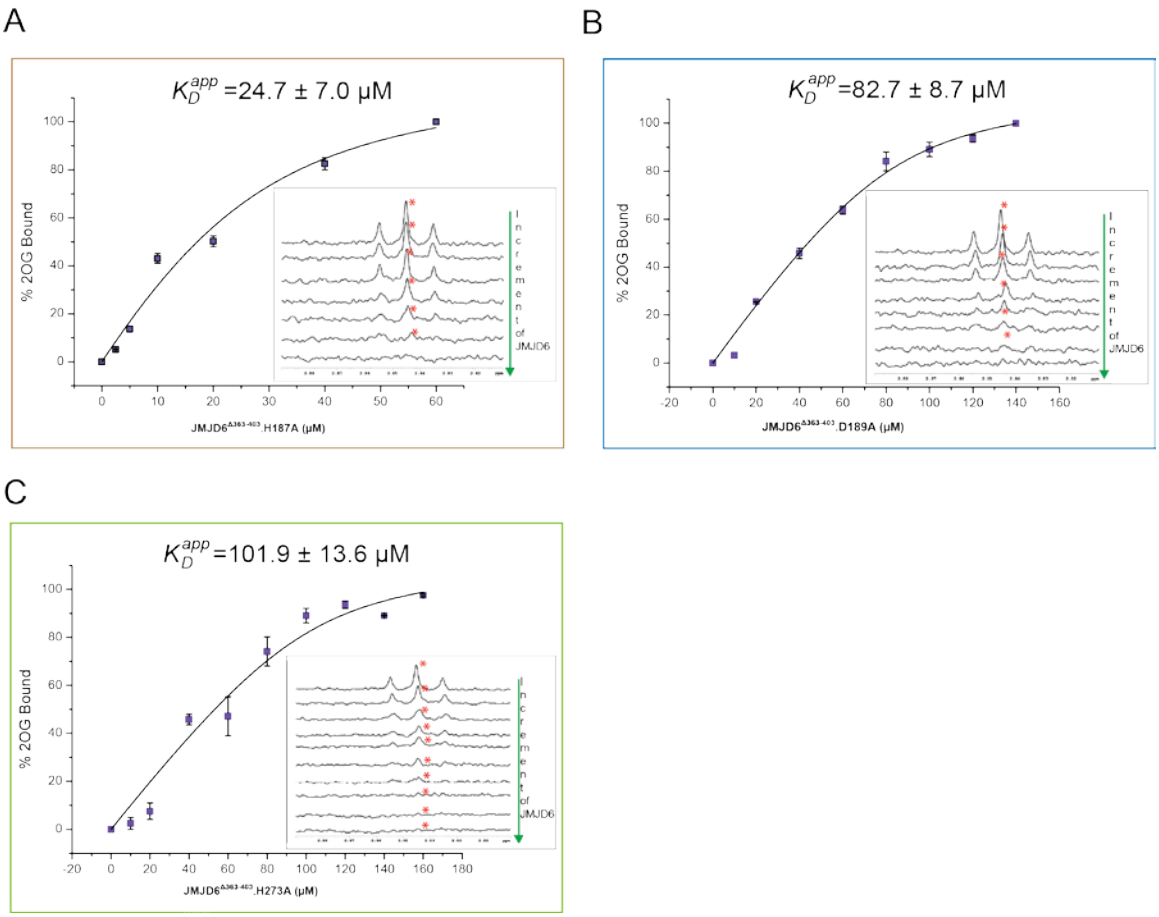

FIGURE 2.14. **Binding experiments between 2OG and the metal binding variants of JMJD6**. Curves used to determine the binding constants of 2OG for (A) JMJD6$^{\Delta 363\text{-}403.}$H187A, (B) JMJD6$^{\Delta 363\text{-}403.}$D189A, and (C) JMJD6$^{\Delta 363\text{-}403.}$H273A. Binding assays were carried out following the NMR-based binding assay described in Chapter 10. Values represent mean (n = 3) ± SD.

2.5.3. Hydroxylation Assays

Next, activity was tested using the MALDI-TOF based hydroxylation assay following the slightly modified procedures described previously (59-61) (**Chapter 10**). Spectra of MALDI-TOF MS also revealed the similar inactivity of the metal binding variants (Figure 2.15) to those observed in 2OG turnover assay. Therefore, it can be implied that JMJD6 requires all of its three metal binding residues for full catalytic activity.

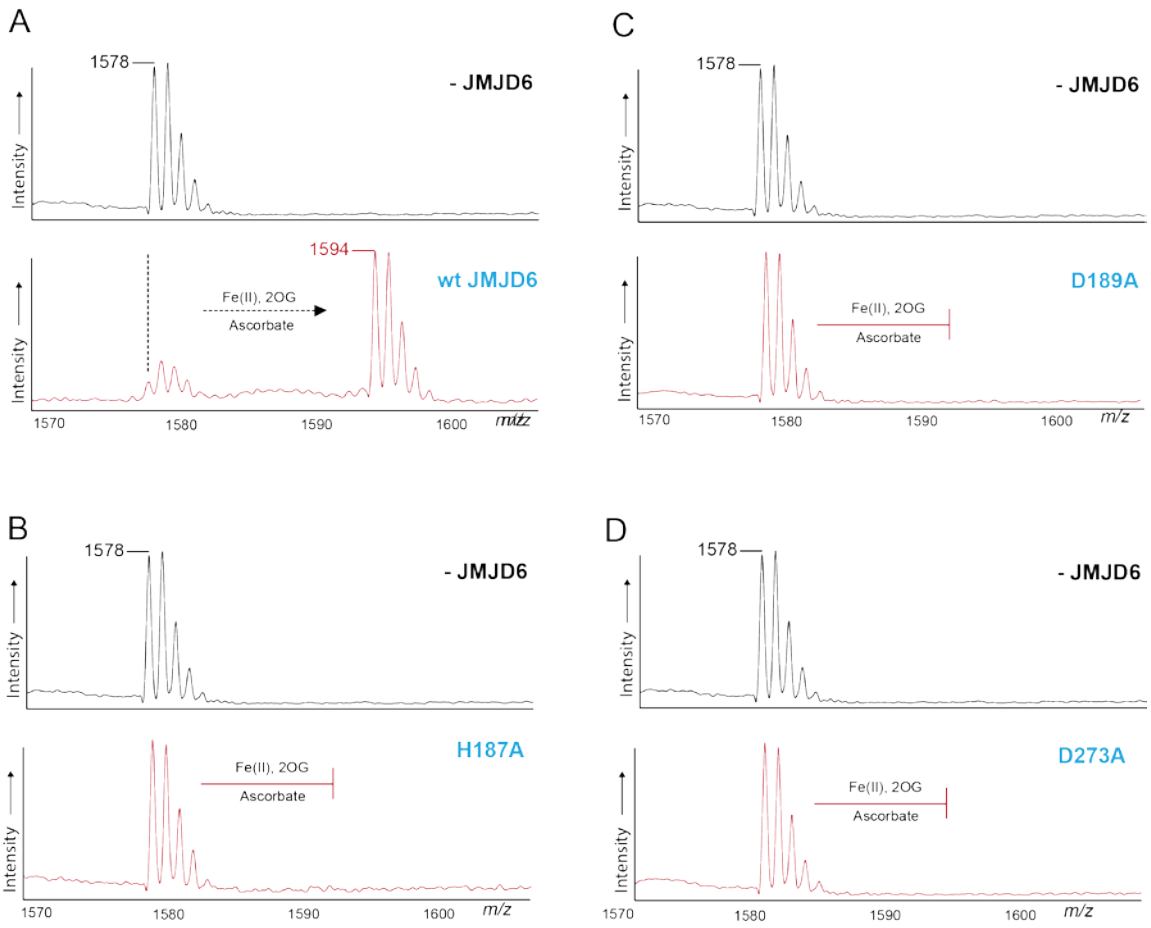

FIGURE 2.15. **Activity testing of metal binding variants of JMJD6 by MALDI-TOF MS.** MALDI-TOF spectra showing the relative hydroxylation of LUC7L2$_{267-278}$ catalyzed by: (A) wild-type JMJD6$^{\Delta 363-403}$, (B) JMJD6$^{\Delta 363-403}$·H187A, (C) JMJD6$^{\Delta 363-403}$·D189A, and (D) JMJD6$^{\Delta 363-403}$·H273A in an Fe(II)- and 2OG-dependent manner. Activity testing was performed following the hydroxylation assay described in Chapter 10.

2.6. Effect of Ascorbic Acid on JMJD6 Activity

It was shown previously using MALDI-TOF-based hydroxylation assay that JMJD6 requires Fe(II) and 2OG for its lysyl-hydroxylase activity with the SR protein LUC7L2 (16). It was also reported that JMJD6 requires ascorbate for its demethylase activity (29); based on Western blot analysis using antibody α-H4R3me1, it was reported that wild-type JMJD6 is unable to catalyze the demethylation reaction on peptide fragment $H4R3(me2)_{1-30}$ in the absence of ascorbate (29). Hence, conflicts arouse; catalytic role of JMJD6 should not be limited on the presence/absence of ascorbate in the reaction buffer. Experiments were therefore carried out to investigate if the lysyl-hydroxylase activity of wild-type JMJD6 depends on ascorbate or not. The results showed similar level of near to complete hydroxylation of $LUC7L2_{267-278}$ catalysed by $JMJD6^{\Delta 363-403}$ in the absence of ascorbate (Figure 2.16). Further, assays were also conducted using a peptide fragment of H4 protein corresponding to residues 1-15 ($H4_{1-15}$) (29). In this case also, activity of JMJD6 was found to be unaffected due to the absence of ascorbate (Figure 2.16**B**). It may therefore be concluded that, at least under the experimental conditions used, the catalytic activity of JMJD6 is not ascorbate-dependent.

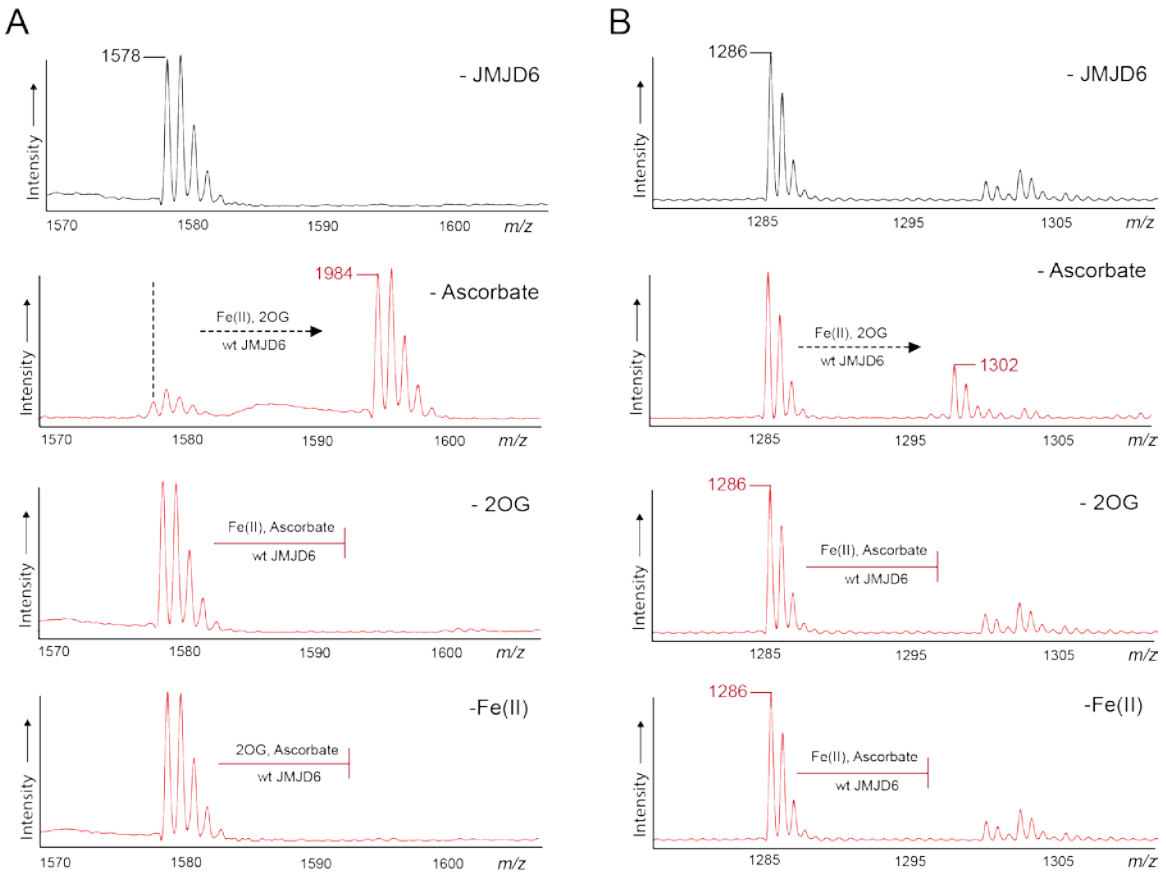

FIGURE 2.16. **Effect of ascorbate on the hydroxylation activity of JMJD6**. MALDI-TOF spectra showing the lysyl-hydroxylase activity of JMJD6 tested on (A) $LUC7L2_{267-278}$ and (B) $H4_{1-15}$ in the presence and absence of ascorbate. Activity assays were carried out following the hydroxylation assay procedures described in Chapter 10.

2.7. Impact of the PolyS Domain on JMJD6 Oligomerization

Some 2OG oxygenases have been observed to form various types of oligomers in solution as mediated by their *C*- and *N*-termini (62). γ-Butyrobetaine hydroxylase (BBOX) remains principally as a dimer in solution; interactions involved in dimerization comprise the *N*-terminal Zn(II) binding domain (63). In contrast, factor inhibiting HIF (FIH) forms a dimer, as mediated by two *C*-terminal α-helices (64).

JMJD6 forms a heptamer of dimers in solution, unlike any other studied 2OG oxygenases (51). Moreover, the JMJD6 oligomers have been shown to be resistant to denaturing conditions, and are clearly visible on SDS-PAGE gels (33). The oligomeric

properties of JMJD6 has been investigated previously by techniques including: TEM, western blotting, co-immunoprecipitation and fluorescence two-hybrid assays (33). Quantitative SEC and non-denaturing MS were used in this study to investigate the oligomerisation status of the JMJD6 variants.

2.7.1. Quantitative SEC

Full-length JMJD6 ($JMJD6^{FL}$) was analysed by an analytical gel filtration column (30 mL, GE Healthcare) which had been calibrated with standard molecular weight markers using the reported procedures (65,66) (**Chapter 10**). The calculated molecular weight of $JMJD6^{FL}$ with a His_6-tag is 48.6 kDa. However, the elution volume suggested that JMJD6 remains in solution as approximately a 14-mer (~620 kDa, corresponding to 10.78 mL) and a hexamer (~296 kDa, corresponding to 12.21 mL) (Figure 2.17**A**). By contrast, variant $JMJD6^{\Delta 344\text{-}403}$ lacking the polyS domain eluted at 15.43 mL, which indicates a molecular weight consistent with a $JMJD6^{\Delta 344\text{-}403}$ monomer (42.124 kDa) (Figure 2.17**A**).

2.7.2. Nanoelectrospray Ionisation-Mass Spectrometry (nESI-MS)

The oligomerization status of $JMJD6^{FL}$ was then analysed by nanoelectrospray ionization-mass spectrometry (nESI-MS) (Dr. Joseph Gault, Professor Dame Carol Robinson Group, Chemistry Research Laboratory, University of Oxford). nESI-MS is an emerging technique for studying macromolecules (67). In particular, the nanoelectrospray quadrupole time-of-flight (Q-ToF) MS has gained significant attention due to its ability to probe intact proteins with high resolution (68). Based on our initial findings and previously reported evidence of higher oligomeric status (~680 kDa), JMJD6 was also considered as a good candidate to be monitored by nESI-MS.

The resulting spectrum indicated that JMJD6 exists in solution as mixtures of monomeric, dimeric, trimeric, tetrameric and higher oligomeric forms (Figure 2.17**B**). The different results using SEC and nESI-MS may reflect different assay conditions, but both imply mixtures of oligomeric forms.

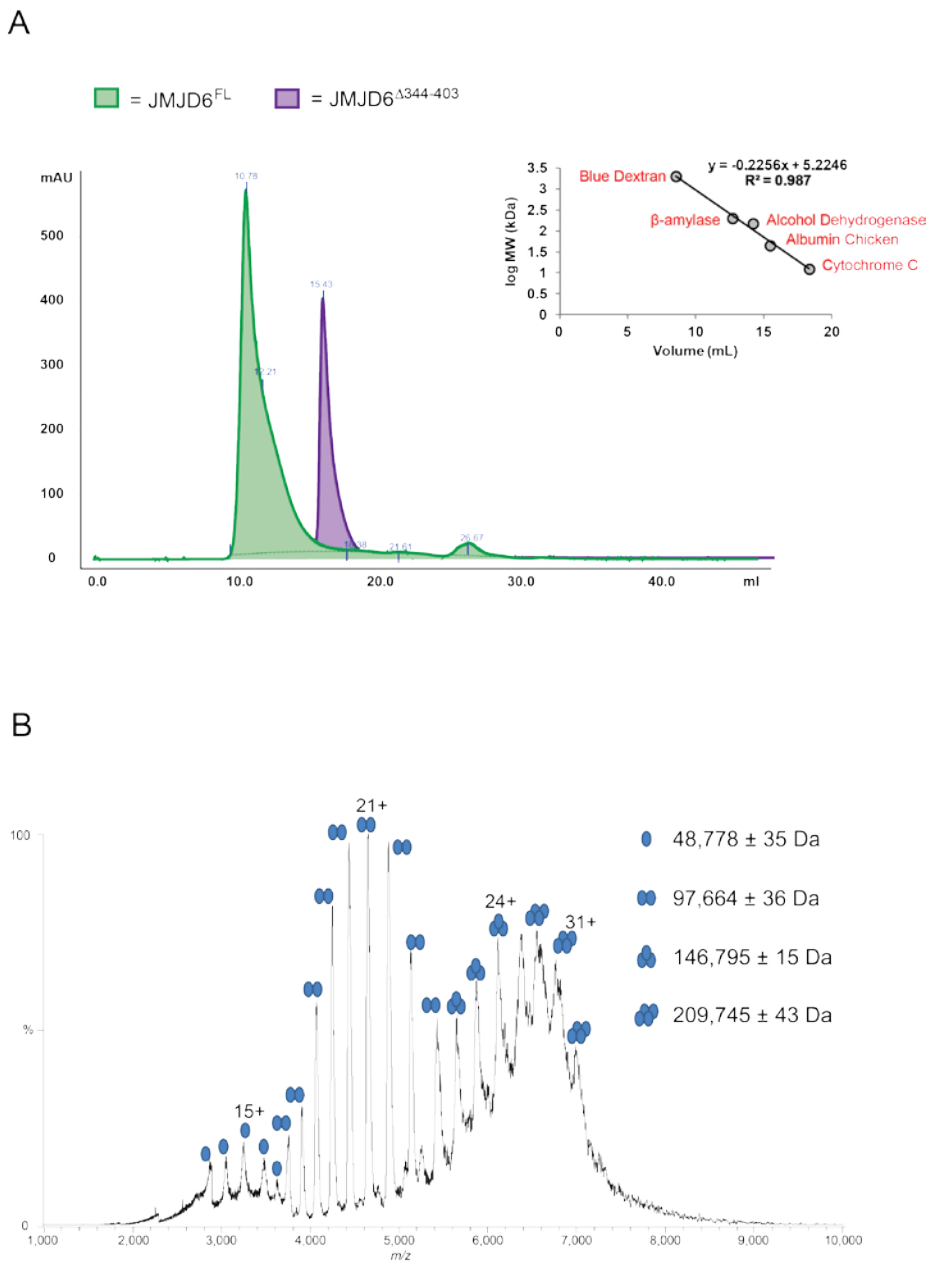

FIGURE 2.17. **Oligomerization properties of JMJD6.** (A) JMJD6 was loaded onto a 30 mL analytical SEC column, the elution volume was indicative of ~14-mer and ~6-mer oligomers in case of JMJD6^{FL} and monomer in case of JMJD6$^{\Delta 344-403}$. (B) nESI-MS spectrum of JMJD6^{FL} showing the presence of monomeric, dimeric, trimeric, tetrameric, and higher oligomeric forms.

CHAPTER 03: Kinetic Investigation for Substrate Selectivity of JMJD6

3.1. Introduction

Since its controversial identification by Fadok *et al.* in 2000 as a cell surface receptor involved in apoptotic cell death (34), a wide variety of cellular functions of JMJD6 have been reported *e.g.* pre-mRNA splicing, transcriptional pause release, and cancer (16,17,30,38,39). A wide variety of targets for JMJD6 inside cells are also identified, which include splicing regulatory (SR) proteins U2AF65 (U2 small nuclear ribonucleoprotein auxiliary factor 65 kDa subunit), LUC7L2 (putative RNA binding protein luc 7-like 2), CROP (cisplatin resistance-associated overexpressed protein) (16,69), histones (H2A/H2B, H3, and H4) (16,29,40), tumour suppressor p53 (17), estrogen receptor α (ERα) (30), heat-shock protein 70 kDa (HSP70) (32), and RNA helicase A (RHA) (31). Although histone proteins have been reported as substrates of JMJD6 (16,29,40), any direct evidence for epigenetic regulation by JMJD6 has not been reported yet. Substrate-selectivity of JMJD6 therefore appears widespread and thus promiscuous (33).

The objective of the works described in this chapter was to investigate the enzymatic function of JMJD6. In addition, it was planned to carry out a comprehensive kinetic study of JMJD6 using validated substrates. The nature of the interaction between JMJD6 and its substrates was of interest as the results may also be helpful to improve crystallographic studies. It was also planned to test the lysyl-hydroxylase or argininyl-demethylase activity of JMJD6 on its recently reported (during the course of this work) substrates *e.g.* VHL, p53, HSP70, ERα (17,18,30,32).

3.2. Is JMJD6 a Bifunctional Arginine Demethylase and Lysyl Hydroxylase?

The *N*-methyl arginine demethylase activity of JMJD6$^{\Delta 363\text{-}403}$ against three histone peptides (H3R2$_{1\text{-}25}$, H4R3$_{1\text{-}30}$ and H4R3(me2s)$_{1\text{-}18}$-Biotin) was first investigated following the reported procedures (29,32,39). Peptides H3R2(me2s)$_{1\text{-}25}$, H4R3(me2s)$_{1\text{-}30}$, and

H4R3(me2s)$_{1-18}$-Biotin were purchased from GL Biochem (GL Biochem, Shanghai, China). However, positive control reactions contained JMJD2E in place of JMJD6, as JMJD2E is a 2OG- and Fe(II)-dependent demethylase capable of catalysing demethylation of mono- as well as di-methylated arginine residues of both H3 and H4 (28). On the other hand, negative control reactions contained all the reaction components except an enzyme. MALDI-TOF analyses of the reaction products revealed +16 Da mass shifts in the presence of JMJD6 with each of the substrate tested, corresponding to an addition of oxygen alone (Figure 3.1). In contrast, JMJD2E-catalyzed demethylation of the methylated arginine (-14 Da shift) was found under the same reaction conditions with each of the peptide tested (Figure 3.1).

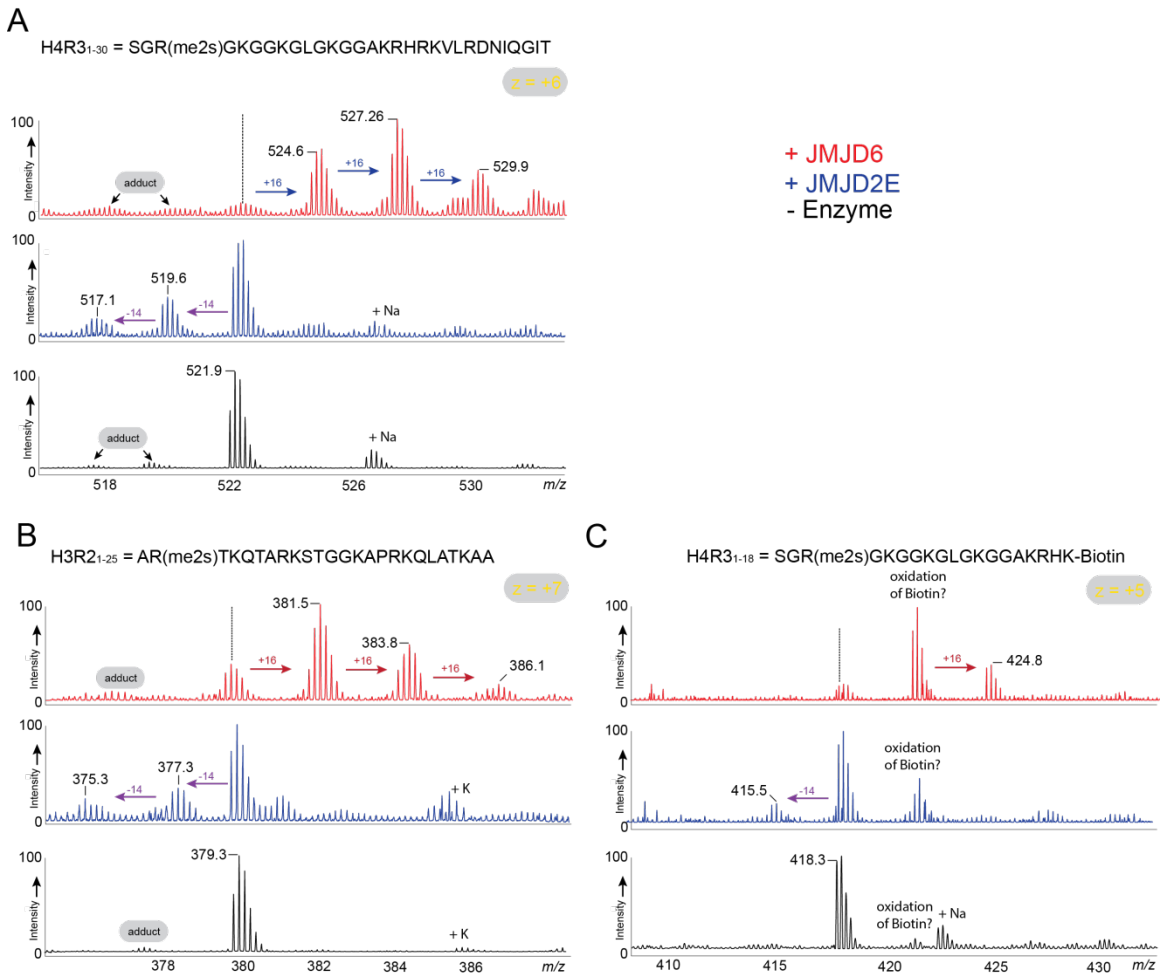

FIGURE 3.1**. JMJD6 is a lysyl-hydroxylase**. MALDI spectra showing the appearance of peaks with +16 Da shifts in mass demonstrating hydroxylation in JMJD6-treated histone

peptides (red spectra). By contrast, peaks corresponding to -14/-28 Da shift for JMJD2E-treated peptides manifest demethylation (blue spectra). Black spectra are of the peptides in presence of other reaction components except enzyme. Note the lack of evidence for demethylation by JMJD6; *i.e.*, the lack of a -14 Da peak in reactions catalysed by JMJD6. Experiments were carried out following the demethylation assay procedure described in Chapter 10.

Attempted demethylation reactions were also performed using JMJD6$^{\Delta 363\text{-}403}$ purified following the reported procedures (32,39). However, no evidence for demethylation activity of JMJD6 was observed (**Appendix 02**). The other two constructs of JMJD6 (JMJD6$^{\Delta 344\text{-}403}$ and JMJD6^{FL}) used for biochemical characterization (**Chapter 02**) were also used in attempted demethylation reactions. Again, demethylation was not observed (**Appendix 03**). Studies were then performed with/out ascorbate, because in previously reported assay, it was shown that JMJD6 requires ascorbate to perform its demethylation activity on histone peptides (29). There was still no evidence for demethylation under the conditions used (**Appendix 04**). Moreover, only peaks corresponding to +16, +32, and +48 Da shift in mass were observed in the JMJD6-catalysed peptides. Note the observed JMJD6-catalysed modifications of the histone peptide are consistent with the analyses carried out by other groups (16,29). These results further support the earlier proposal that ascorbate cannot regulate the enzymatic activity of JMJD6, consistent with a previous report where JMJD6 was shown to catalyse Lys^{15} and Lys^{276} of endogenous U2AF65 in absence of ascorbate (69). Therefore, if the lysyl-hydroxylase activity of JMJD6 doesn't depend on ascorbate, it would be expected that its demethylase activity would also not depend on it.

Further investigations were carried out to know the regiochemistry of hydroxylation of the histone peptides. In order to do so, JMJD6-treated peptides were subjected to CID (collision induced dissociation)- and ETD (electron transfer dissociation)-based fragmentation using a liquid chromatography-mass spectrometry (LC-

MS) (16,29). The results were analysed in light of the original chromatograms, mass spectra and the corresponding mass spectra and ion tables of the fragmented ions generated by PEAKS 8.0 (Elisabete Pires, MS Facility, Chemistry Research Laboratory, University of Oxford).

In case of unmodified H3R2(me2s)$_{1-25}$, LC was able to detect the peptide (m/z = +7) with almost 100% coverage of the fragmented ions generated by PEAKS 8.0 (Figure 3.2). In the case of JMJD6-treated peptide (m/z = +7) in which case, MALDI spectra revealed peaks corresponding to triple hydroxylation (Figure 3.1), LC-MS followed by LC-MS/MS further provided evidence that JMJD6 indeed catalysed hydroxylation of Lys^{14}, Lys^{9}, and Lys^{4} (in order of preference) (Figure 3.3). In contrast, analysis of the JMJD2E-treated H3R2(me2s)$_{1-25}$ (m/z = +7) provided evidence for the removal of a single methyl group from symmetrically di-methylated Arg^{2} (Figure 3.4).

LC-MS analysis of H4R3(me2s)$_{1-30}$, treated with JMJD6, revealed that the peptide was modified by a +32 Da shift in mass, suggesting a possible double hydroxylation (Figure 3.6). MS/MS analysis of the modified peptide thereafter confirmed the hydroxylation of Lys^{8} and Lys^{5} (in order of preference) (Figure 3.6**C**). MS/MS analyses of only H4R3(me2s)$_{1-30}$ (Figure 3.5**C**) or JMJD2E-treated H4R3(me2s)$_{1-30}$ (Figure 3.7**C**) revealed no modification or demethylation, respectively. Similarly, MS/MS analysis of another H4 peptide H4R3(me2s)$_{1-18}$-Biotin revealed that JMJD6 hydroxylates Lys^{8} (Figure 3.9). Analyses of H4R3(me2s)$_{1-18}$-Biotin and JMJD2E-treated H4R3(me2s)$_{1-18}$-Biotin showed no modification and demethylation, respectively (Figure 3.8 and 3.10). To note, chromatograms coupled with the corresponding mass spectra of the fragmented ions that represent a single modification (*e.g.* hydroxylation/demethylation) were also analysed to complement our results (**Appendix 05**).

Collectively, these results reveal that JMJD6, at least under the tested conditions, is only a lysyl-hydroxylase and not a bifunctional hydroxylase/demethylase.

A

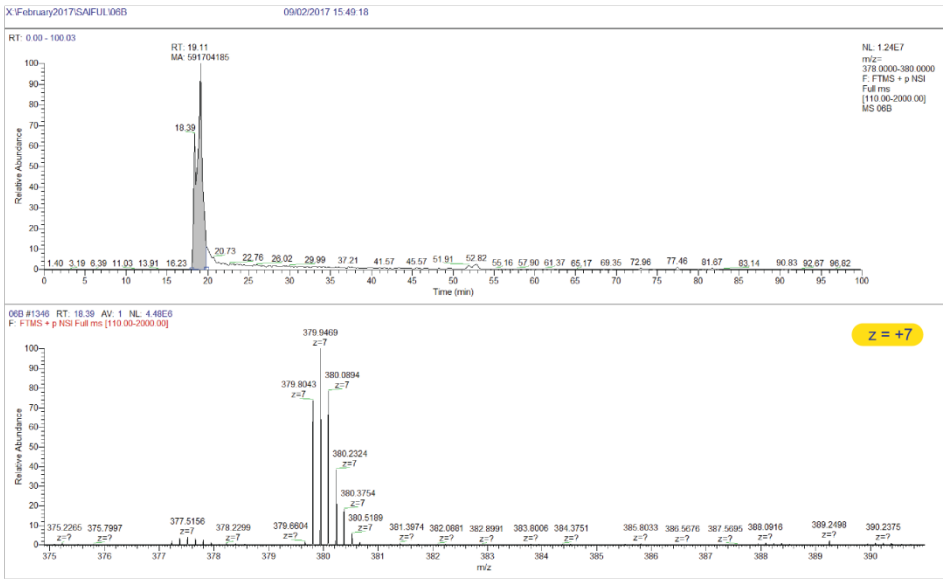

B

#	b (2+)	c (2+)	Seq	y (2+)	z (2+)	#
1	36.52	45.04	A			26
2	128.59	137.10	R(+28.03)	1327.15	1319.69	25
3	179.11	187.26	T	1235.61	1227.63	24
4	243.16	251.67	K	1184.69	1175.21	23
5	307.19	315.70	Q	1120.14	1113.07	22
6	357.71	366.23	T	1056.62	1048.58	21
7	393.23	402.07	A	1006.09	998.50	20
8	471.28	480.08	R	970.89	963.03	19
9	535.05	543.84	K	892.45	883.43	18
10	579.20	587.68	S	827.59	819.78	17
11	629.51	638.53	T	784.94	776.90	16
12	657.21	666.23	G	734.44	726.73	15
13	685.42	695.24	G	705.54	697.91	14
14	749.44	759.22	K	677.42	669.76	13
15	785.96	795.32	A	612.77	605.67	12
16	834.48	842.18	P	577.81	569.67	11
17	912.53	921.50	R	529.32	520.81	10
18	976.98	985.38	K	451.27	442.76	9
19	1040.57	1049.46	Q	387.23	378.71	8
20	1096.88	1106.53	L	323.20	314.68	7
21	1132.96	1142.01	A	266.65	258.14	6
22	1183.05	1192.18	T	231.14	222.62	5
23	1247.24	1256.13	K	180.61	172.10	4
24	1283.12	1291.58	A	116.56	108.05	3
25	1318.76	1327.15	A	81.05	72.53	2
26			A	45.53	37.01	1

C

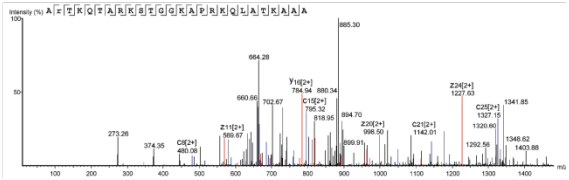

FIGURE 3.2. **LC-MS/MS analysis of H3R2(me2s)$_{1-25}$: AR(me2s)TKQTARKSTGGKAPR KQLATKAA without enzyme treatment.** (A) LC-MS chromatogram and the corresponding mass spectrum displaying the unmodified peptide (m/z = +7). (B) Ion table generated by PEAKS 8.0 showing the coverage for *b*, *y* (CID) and *c*, *z* (ETD) ions of the fragmented peptide. (C) Spectrum of the fragmented ions corresponding to the ion table further confirms the existence of the predicted ions with good intensities. The samples were analysed with technical triplicates following the procedure described in Chapter 10.

A

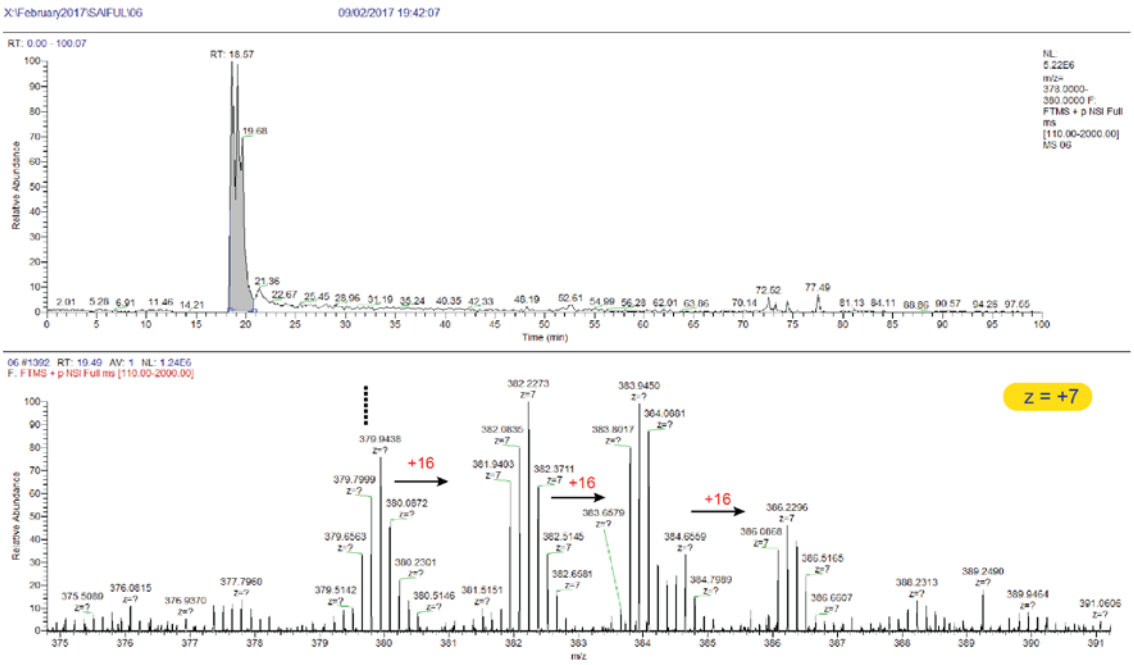

B

#	b (2+)	c (2+)	Seq	y (2+)	z (2+)	#
1	36.52	45.04	A			25
2	128.59	137.10	R(+28.03)	1315.77	1307.25	24
3	179.11	187.26	T	1223.06	1215.19	23
4	251.16	259.67	K(+16.00)	1173.77	1164.57	22
5	315.19	323.70	Q	1101.45	1092.48	21
6	365.71	374.34	T	1036.99	1027.87	20
7	401.76	409.74	A	986.58	978.85	19
8	479.67	487.68	R	950.44	943.39	18
9	551.86	560.11	K(+16.00)	873.54	864.55	17
10	595.81	603.56	S	801.53	792.19	16
11	645.74	654.00	T	757.40	749.71	15
12	674.37	682.57	G	707.69	698.77	14
13	702.75	711.69	G	678.41	670.23	13
14	774.81	783.86	K(+16.00)	649.74	641.71	12
15	809.18	818.72	A	577.97	569.58	11
16	858.07	867.00	P	542.59	534.78	10
17	936.56	945.05	R	494.43	485.54	9
18	1000.08	1009.69	K	415.51	407.24	8
19	1064.61	1073.59	Q	351.71	343.19	7
20	1120.52	1129.67	L	288.30	279.16	6
21	1156.73	1164.57	A	231.14	222.62	5
22	1207.19	1215.71	T	195.62	187.26	4
23	1270.96	1279.76	K	145.09	136.58	3
24	1306.76	1314.58	A	81.05	72.53	2
25			A	45.53	37.01	1

C

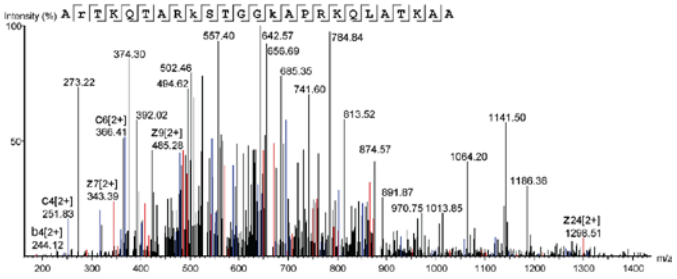

FIGURE 3.3. **LC-MS/MS analysis of JMJD6-tretaed H3R2(me2s)$_{1\text{-}25}$: AR(me2s)TKQT ARKSTGGKAPRKQLATKAA.** (A) LC-MS chromatogram and the corresponding mass spectrum displaying the modified peptide (m/z = +7). (B) Ion table generated by PEAKS 8.0 showing the coverage for *b*, *y* (CID) and *c*, *z* (ETD) ions of the fragmented peptide. (C) Spectrum of the fragmented ions corresponding to the ion table further confirms the existence of the predicted ions with good intensities. The samples were analysed with technical triplicates following the procedure described in Chapter 10.

A

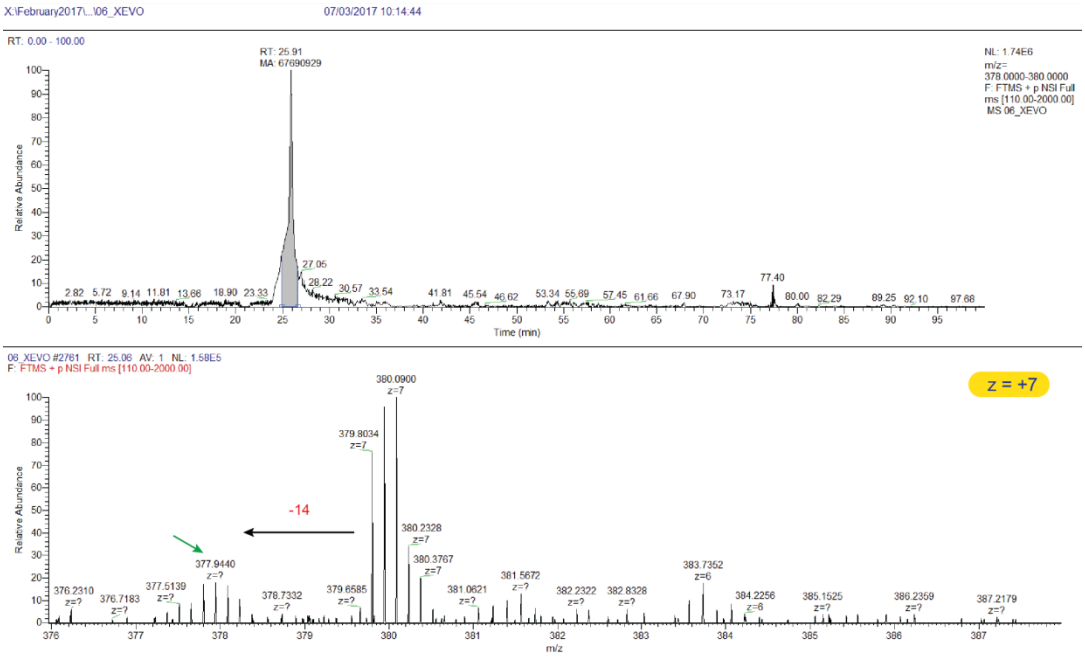

B

#	b (2+)	c (2+)	Seq	y (2+)	z (2+)	#
1	36.52	45.04	A			25
2	121.59	130.17	R(+14.03)	1284.77	1275.99	24
3	172.11	180.63	T	1199.85	1191.48	23
4	236.16	244.67	K	1149.57	1140.66	22
5	300.19	308.70	Q	1085.13	1076.84	21
6	350.71	359.02	T	1020.87	1012.59	20
7	386.19	394.52	A	970.67	961.85	19
8	463.96	472.80	R	935.06	926.93	18
9	528.33	536.84	K	856.85	848.90	17
10	571.38	580.36	S	792.96	784.22	16
11	622.37	630.88	T	749.26	741.34	15
12	650.88	659.39	G	698.82	690.17	14
13	679.79	687.90	G	670.13	661.89	13
14	743.44	751.72	K	642.10	633.69	12
15	778.96	787.47	A	577.71	569.58	11
16	827.28	835.69	P	542.57	533.82	10
17	905.53	913.79	R	493.38	485.47	9
18	969.82	978.14	K	415.34	407.42	8
19	1033.82	1042.03	Q	352.05	343.25	7
20	1090.15	1098.62	L	287.18	279.16	6
21	1125.96	1133.77	A	231.14	222.62	5
22	1176.54	1184.45	T	195.62	187.20	4
23	1240.52	1248.76	K	145.09	136.58	3
24	1275.99	1283.97	A	81.05	72.53	2
25			A	45.53	37.01	1

C

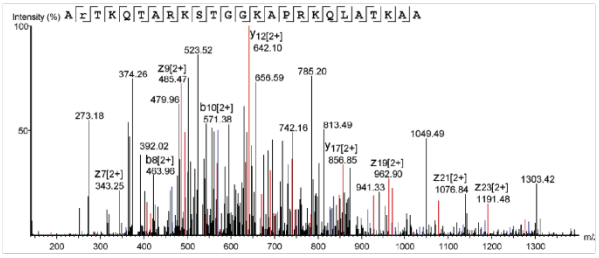

FIGURE 3.4. **LC- MS/MS analysis of JMJD2E-tretaed H3R2(me2s)$_{1\text{-}25}$: A<u>R</u>(me2s)TKQ TARKSTGGKAPRKQLATKAA.** (A) LC-MS chromatogram and the corresponding mass spectrum displaying the modified peptide (m/z = +7). (B) Ion table generated by PEAKS 8.0 showing the coverage for *b*, *y* (CID) and *c*, *z* (ETD) ions of the fragmented peptide. (C) Spectrum of the fragmented ions corresponding to the ion table further confirms the existence of the predicted ions with good intensities. The samples were analysed with technical triplicates following the procedure described in Chapter 10.

A

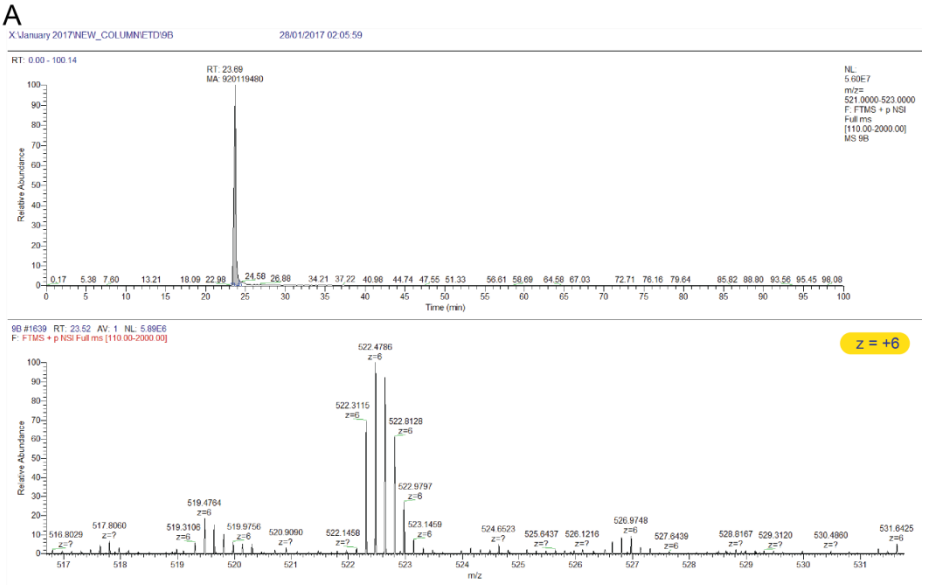

B

#	b (2+)	c (2+)	Seq	y (2+)	z (2+)	#
1	44.52	53.03	S			30
2	73.03	81.54	G	1521.66	1512.95	29
3	165.10	173.61	R(+28.03)	1493.39	1484.87	28
4	193.61	202.12	G	1401.63	1393.16	27
5	257.65	266.17	K	1372.81	1363.61	26
6	286.17	295.25	G	1309.16	1300.46	25
7	314.68	323.19	G	1279.87	1272.17	24
8	378.72	387.37	K	1251.74	1242.77	23
9	407.23	416.05	G	1187.70	1178.51	22
10	463.78	472.53	L	1158.84	1150.67	21
11	492.29	501.07	G	1102.64	1094.18	20
12	556.33	565.04	K	1074.13	1065.55	19
13	584.85	593.60	G	1010.37	1001.57	18
14	613.40	621.84	G	981.71	973.06	17
15	649.00	657.66	A	953.06	944.55	16
16	712.92	721.72	K	916.81	909.75	15
17	790.83	799.73	R	853.80	845.77	14
18	859.50	867.90	H	775.45	767.12	13
19	937.34	946.07	R	707.21	698.40	12
20	1001.60	1010.37	K	629.37	620.47	11
21	1051.13	1059.92	V	565.04	556.31	10
22	1107.68	1116.10	L	515.28	506.77	9
23	1185.81	1194.72	R	458.74	450.82	8
24	1242.77	1251.75	D	380.69	372.18	7
25	1300.46	1309.16	N	323.18	314.66	6
26	1356.09	1364.74	I	266.16	257.64	5
27	1420.83	1429.35	Q	209.61	201.10	4
28	1449.57	1458.50	G	145.59	137.07	3
29	1505.89	1514.40	I	117.07	108.56	2
30			T	60.53	52.02	1

C

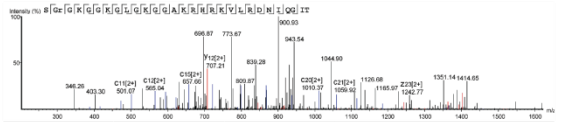

FIGURE 3.5. **LC-MS/MS analysis of H4R3(me2s)$_{1-30}$: SGR(me2s)GKGGKGLGKGGAK RHRKVLRDNIQGIT without enzyme treatment.** (A) LC-MS chromatogram and the corresponding mass spectrum displaying the unmodified peptide (m/z = +6). (B) Ion table generated by PEAKS 8.0 showing the coverage for *b*, *y* (CID) and *c*, *z* (ETD) ions of the fragmented peptide. (C) Spectrum of the fragmented ions corresponding to the ion table further confirms the existence of the predicted ions with good intensities. The samples were analysed with technical triplicates following the procedure described in Chapter 10.

A

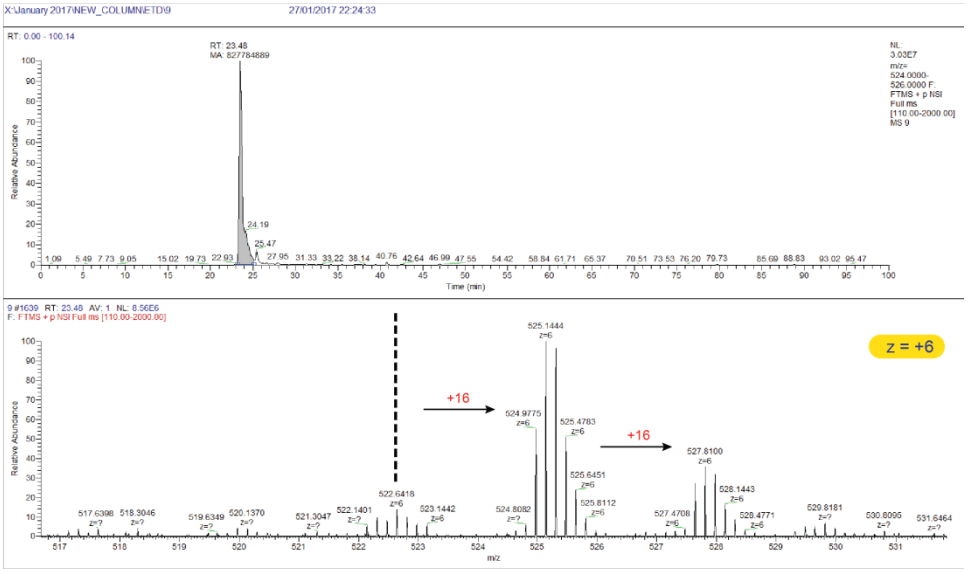

B

#	b (2+)	c (2+)	Seq	y (2+)	z (2+)	#
1	44.52	53.03	S			30
2	73.03	81.54	G	1537.90	1529.00	29
3	165.10	173.61	R(+28.03)	1509.39	1501.32	28
4	193.61	202.12	G	1417.32	1409.10	27
5	265.65	274.17	K(+16.00)	1388.36	1380.30	26
6	294.17	302.68	G	1316.57	1308.60	25
7	322.68	331.19	G	1288.25	1280.09	24
8	394.23	403.33	K(+16.00)	1259.74	1250.84	23
9	423.64	431.40	G	1187.76	1179.18	22
10	479.78	488.68	L	1159.18	1150.41	21
11	508.78	516.76	G	1102.96	1094.13	20
12	571.89	581.21	K	1073.88	1065.49	19
13	600.40	609.36	G	1009.97	1001.57	18
14	629.36	637.87	G	981.17	973.41	17
15	664.42	673.39	A	953.47	944.89	16
16	728.92	737.18	K	917.14	909.25	15
17	806.84	815.89	R	853.23	844.93	14
18	875.50	884.20	H	775.83	767.33	13
19	953.47	962.34	R	706.88	698.61	12
20	1017.51	1026.11	K	628.87	620.68	11
21	1067.13	1075.65	V	564.99	556.31	10
22	1123.45	1131.88	L	515.28	507.23	9
23	1201.48	1209.89	R	458.74	450.18	8
24	1259.24	1267.75	D	380.69	372.18	7
25	1316.57	1324.78	N	323.30	314.66	6
26	1372.80	1381.32	I	266.16	257.64	5
27	1436.35	1445.35	Q	209.61	201.10	4
28	1465.34	1473.86	G	145.59	137.07	3
29	1521.88	1530.40	I	117.07	108.56	2
30			T	60.53	52.02	1

C

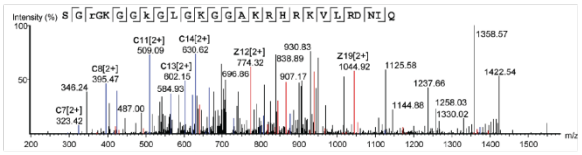

FIGURE 3.6. **LC-MS/MS analysis of JMJD6-treated H4R3(me2s)$_{1-30}$: SGR(me2s)GKG GKGLGKGGAKRHRKVLRDNIQGIT.** (A) LC-MS chromatogram and the corresponding mass spectrum displaying the modified peptide (m/z = +6). (B) Ion table generated by PEAKS 8.0 showing the coverage for *b*, *y* (CID) and *c*, *z* (ETD) ions of the fragmented peptide. (C) Spectrum of the fragmented ions corresponding to the ion table further confirms the existence of the predicted ions with good intensities. The samples were analysed with technical triplicates following the procedure described in Chapter 10.

A

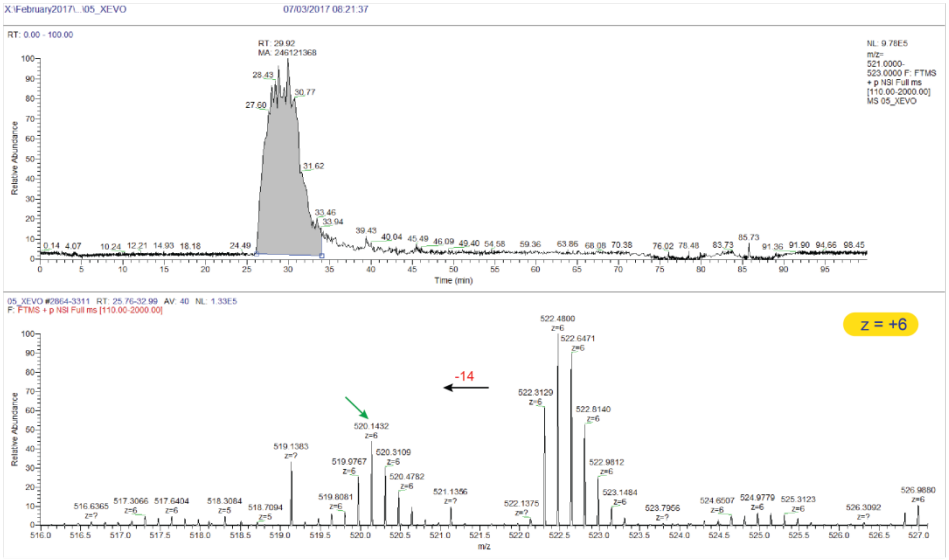

B

#	b (2+)	c (2+)	Seq	y (2+)	z (2+)	#
1	44.52	53.03	S			30
2	73.03	81.54	G	1514.61	1506.08	29
3	158.10	166.59	R(+14.00)	1486.37	1477.66	28
4	186.59	195.11	G	1401.80	1393.12	27
5	250.64	259.20	K	1372.43	1364.65	26
6	279.15	287.57	G	1308.76	1299.78	25
7	307.66	316.32	G	1280.57	1272.04	24
8	371.59	380.38	K	1251.70	1242.91	23
9	400.22	408.91	G	1187.70	1179.18	22
10	456.76	465.23	L	1158.96	1151.06	21
11	485.52	493.96	G	1102.64	1094.44	20
12	549.32	557.83	K	1073.94	1065.38	19
13	578.08	586.61	G	1009.91	1001.99	18
14	606.65	615.09	G	981.50	973.06	17
15	642.28	650.64	A	952.76	944.89	16
16	705.91	714.58	K	917.70	909.31	15
17	783.96	792.35	R	853.17	844.88	14
18	852.49	860.90	H	775.45	767.30	13
19	930.39	938.86	R	706.56	698.30	12
20	994.58	1003.10	K	628.87	620.35	11
21	1043.88	1052.46	V	564.82	556.31	10
22	1100.43	1109.17	L	515.28	506.53	9
23	1178.57	1187.07	R	458.74	450.23	8
24	1236.23	1244.74	D	380.38	372.41	7
25	1293.25	1301.76	N	323.18	314.66	6
26	1349.79	1358.42	I	266.16	257.64	5
27	1414.05	1422.19	Q	209.61	201.10	4
28	1442.81	1450.72	G	145.59	137.07	3
29	1498.73	1507.26	I	117.07	108.56	2
30			T	60.53	52.02	1

C

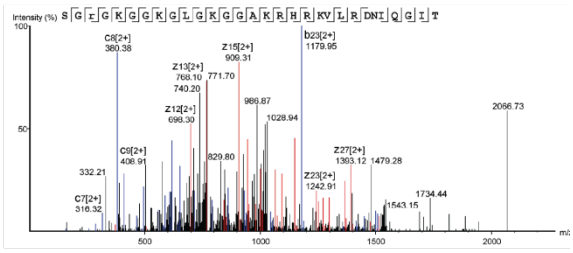

FIGURE 3.7. **LC-MS/MS analysis of JMJD2E-treated H4R3(me2s)$_{1-30}$: SGR(me2s)GK GGKGLGKGGAKRHRKVLRDNIQGIT.** (A) LC-MS chromatogram and the corresponding mass spectrum displaying the modified peptide (m/z = +6). (B) Ion table generated by PEAKS 8.0 showing the coverage for *b*, *y* (CID) and *c*, *z* (ETD) ions of the fragmented peptide. (C) Spectrum of the fragmented ions corresponding to the ion table further confirms the existence of the predicted ions with good intensities. The samples were analysed with technical triplicates following the procedure described in Chapter 10.

A

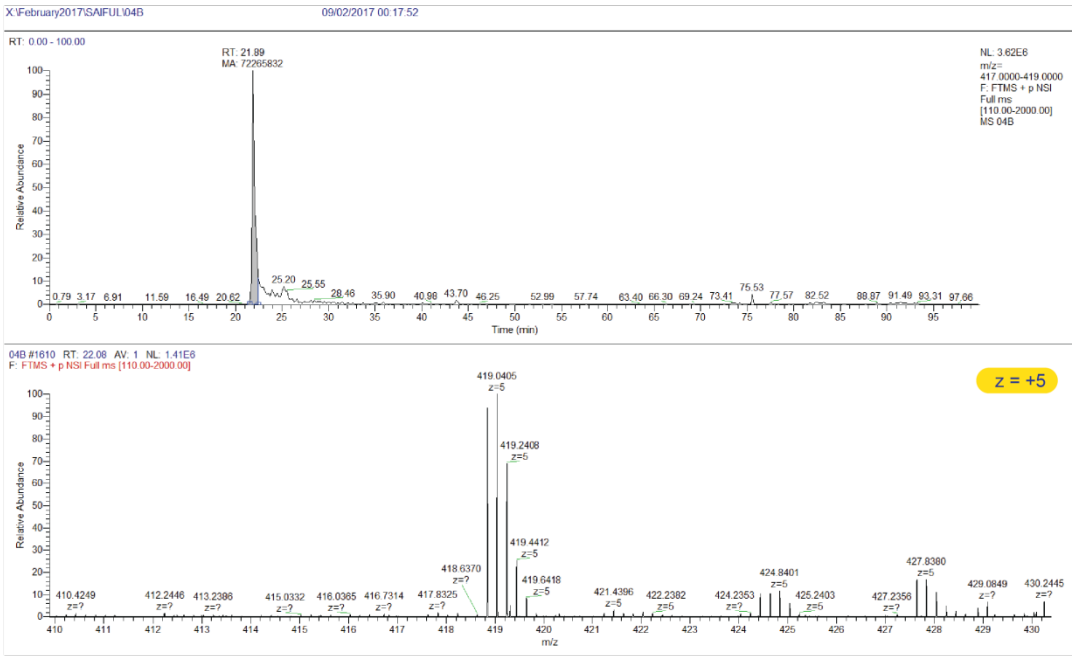

B

#	b (2+)	c (2+)	Seq	y (2+)	z (2+)	#
1	44.52	53.03	S			20
2	73.03	81.54	G	967.09	958.58	19
3	165.10	173.61	R(+28.03)	938.58	929.79	18
4	193.61	202.12	G	846.51	838.00	17
5	257.65	266.35	K	818.00	809.54	16
6	286.40	295.16	G	753.95	745.44	15
7	314.83	323.59	G	725.44	716.93	14
8	378.72	387.14	K	696.93	688.62	13
9	407.23	415.75	G	632.89	624.48	12
10	463.78	472.53	L	604.37	595.86	11
11	492.29	500.96	G	547.83	539.38	10
12	556.33	564.85	K	519.32	510.49	9
13	584.85	593.51	G	455.27	446.76	8
14	613.63	622.05	G	426.76	418.25	7
15	648.87	657.39	A	398.08	389.64	6
16	712.92	721.90	K	362.73	354.22	5
17	790.97	799.90	R	298.69	290.17	4
18	859.50	868.44	H	220.64	212.12	3
19	937.55	946.07	R	152.11	143.59	2
20			K	74.06	65.54	1

C

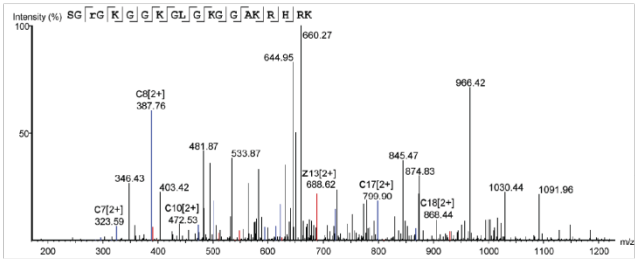

FIGURE 3.8. **LC-MS/MS analysis of H4R3(me2s)$_{1-19}$: SGR(me2s)GKGGKGLGKGGAK RHK-Biotin without enzyme treatment.** (A) LC-MS chromatogram and the corresponding mass spectrum displaying the unmodified peptide (m/z = +5). (B) Ion table generated by PEAKS 8.0 showing the coverage for *b*, *y* (CID) and *c*, *z* (ETD) ions of the fragmented peptide. (C) Spectrum of the fragmented ions corresponding to the ion table further confirms the existence of the predicted ions with good intensities. The samples were analysed with technical triplicates following the procedure described in Chapter 10.

A

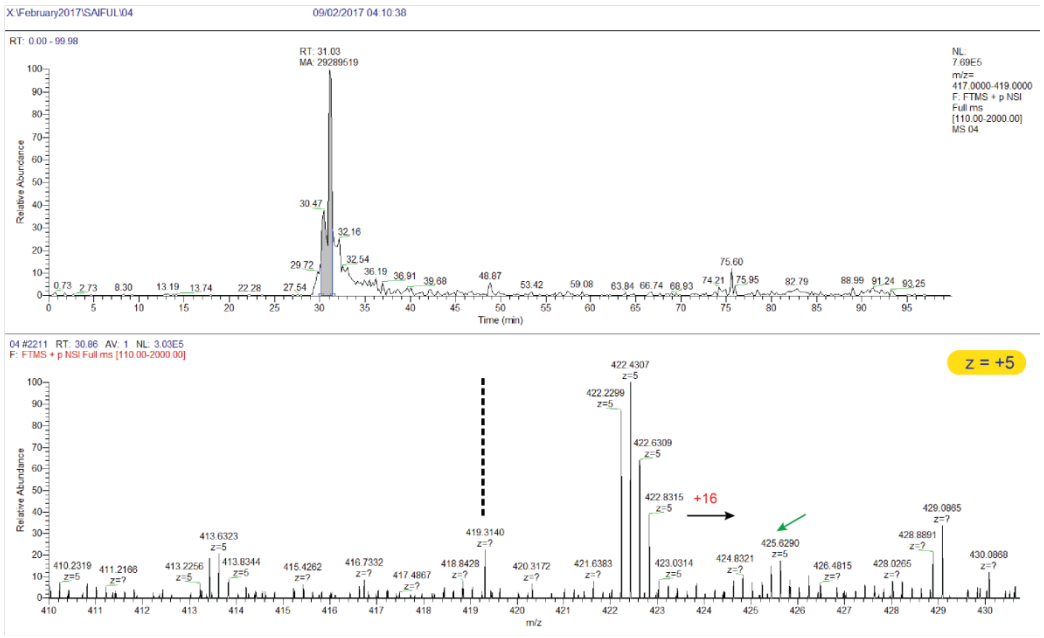

B

#	b (2+)	c (2+)	Seq	y (2+)	z (2+)	#
1	44.52	53.03	S			20
2	73.03	81.54	G	975.09	966.57	19
3	165.10	173.61	R(+28.03)	946.58	937.73	18
4	193.61	202.12	G	854.51	846.00	17
5	257.65	266.17	K	826.00	817.49	16
6	286.02	294.93	G	761.95	753.52	15
7	314.47	323.42	G	733.44	724.93	14
8	386.67	395.43	K(+16.00)	704.93	696.42	13
9	415.23	423.75	G	632.61	624.37	12
10	472.25	480.54	L	604.37	595.86	11
11	500.29	508.66	G	547.83	539.18	10
12	564.69	572.85	K	519.21	511.24	9
13	592.83	601.36	G	454.92	447.19	8
14	621.14	629.51	G	426.51	418.25	7
15	656.87	665.51	A	397.94	389.74	6
16	720.82	729.68	K	362.73	354.22	5
17	798.97	807.36	R	298.69	290.17	4
18	867.74	875.59	H	220.64	212.12	3
19	945.55	954.07	R	152.11	143.59	2
20			K	74.06	65.54	1

C

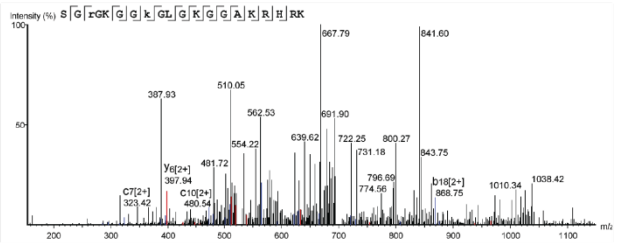

FIGURE 3.9. **LC-MS/MS analysis of JMJD6-treated H4R3(me2s)$_{1-19}$: SGR(me2s)GK GGKGLGKGGAKRHK-Biotin.** (A) LC-MS chromatogram and the corresponding mass spectrum displaying the modified peptide (m/z = +5). (B) Ion table generated by PEAKS 8.0 showing the coverage for *b*, *y* (CID) and *c*, *z* (ETD) ions of the fragmented peptide. (C) Spectrum of the fragmented ions corresponding to the ion table further confirms the existence of the predicted ions with good intensities. The samples were analysed with technical triplicates following the procedure described in Chapter 10.

A

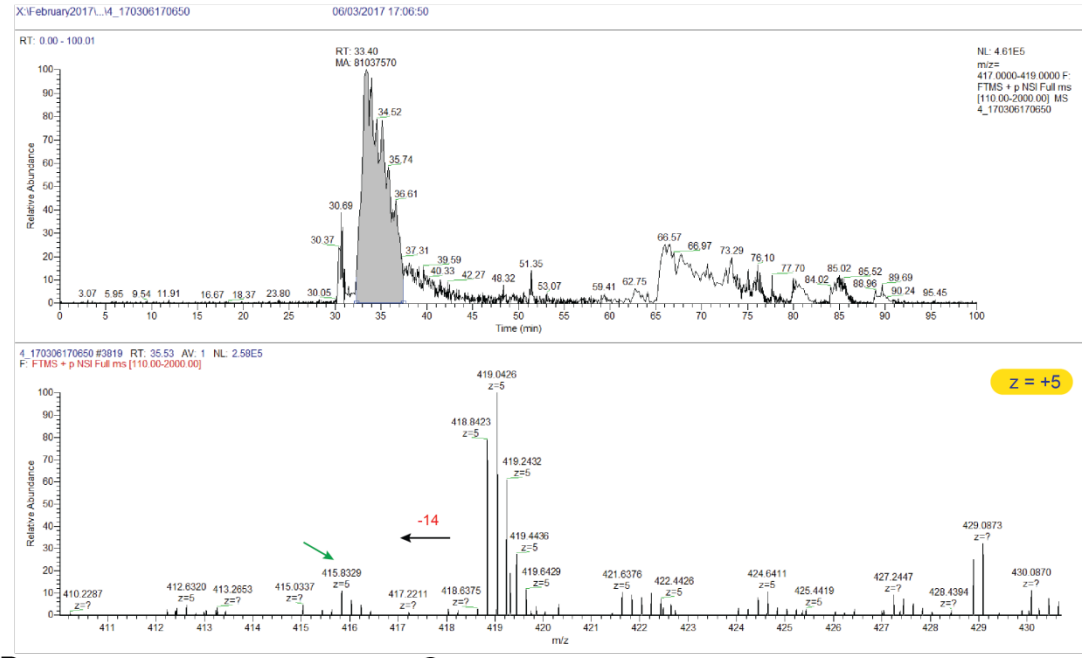

B

#	b (2+)	c (2+)	Seq	y (2+)	z (2+)	#
1	44.52	53.03	S			20
2	73.03	81.54	G	960.07	951.56	19
3	158.20	166.59	R(+14.00)	931.68	922.65	18
4	186.59	195.11	G	846.47	838.13	17
5	250.64	259.27	K	818.00	809.74	16
6	279.15	287.81	G	753.50	745.86	15
7	307.66	316.50	G	725.44	716.70	14
8	371.71	380.36	K	696.69	688.42	13
9	400.22	408.82	G	632.89	624.16	12
10	456.76	465.46	L	604.46	595.86	11
11	485.69	494.14	G	547.83	539.35	10
12	549.42	557.78	K	519.32	510.81	9
13	577.59	586.14	G	455.27	446.76	8
14	606.70	614.75	G	426.76	418.25	7
15	642.23	650.25	A	398.06	389.29	6
16	705.91	714.50	K	363.19	354.22	5
17	784.43	792.68	R	298.69	289.71	4
18	852.80	861.31	H	220.64	212.12	3
19	930.54	939.05	R	152.11	143.59	2
20			K	74.06	65.54	1

C

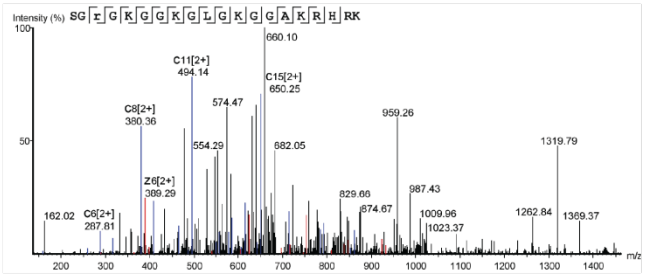

FIGURE 3.10. **LC-MS/MS analysis of JMJD2E-treated H4R3(me2s)$_{1-19}$: SGR(me2s)GK GGKGLGKGGAKRHK-Biotin.** (A) LC-MS chromatogram and the corresponding mass spectrum displaying the modified peptide (m/z = +5). (B) Ion table generated by PEAKS 8.0 showing the coverage for *b*, *y* (CID) and *c*, *z* (ETD) ions of the fragmented peptide. (C) Spectrum of the fragmented ions corresponding to the ion table further confirms the existence of the predicted ions with good intensities. The samples were analysed with technical triplicates following the procedure described in Chapter 10.

3.3. Does Methylation Interfere with Hydroxylation Activity of JMJD6?

Given that JMJD6 hydroxylates Lys^{9}, Lys^{14}, and Lys^{4} of the isolated peptide $H3R2(me2s)_{1-25}$ (Figure 3.3), attempts were then made to investigate the hydroxylation activity of JMJD6 on another fragment of H3 corresponding to residues 1-17 with a mono-methyl lysine residue at position 9 ($H3K9(me1)_{1-17}$). In this case also, no evidence for demethylation by any of the variants of JMJD6 was observed (Figure 3.11). However, the level of hydroxylation catalysed by the JMJD6 variants were found to be lowered in this case due to the presence of the methyl group at Lys^{9} (Figure 3.11). Instead of double/triple hydroxylation (+32/+48 Da shift in mass) as was observed in the case of $H3_{1-25}$ or $H3R2(me2s)_{1-25}$ (Figure 3.3 and 3.12), only very small peaks corresponding to +16 Da shift in the mass of the peptide were observed in the MALDI spectra, suggesting non-spontaneous hydroxylation by JMJD6 (Figure 3.11). These results indicate weak binding between $H3K9(me1)_{1-17}$ and JMJD6, which might be due to the steric hindrance posed by the methylated lysine (K9me1).

It can therefore be inferred that JMJD6 preferably hydroxylates its targeted lysine residues only when they are unmodified.

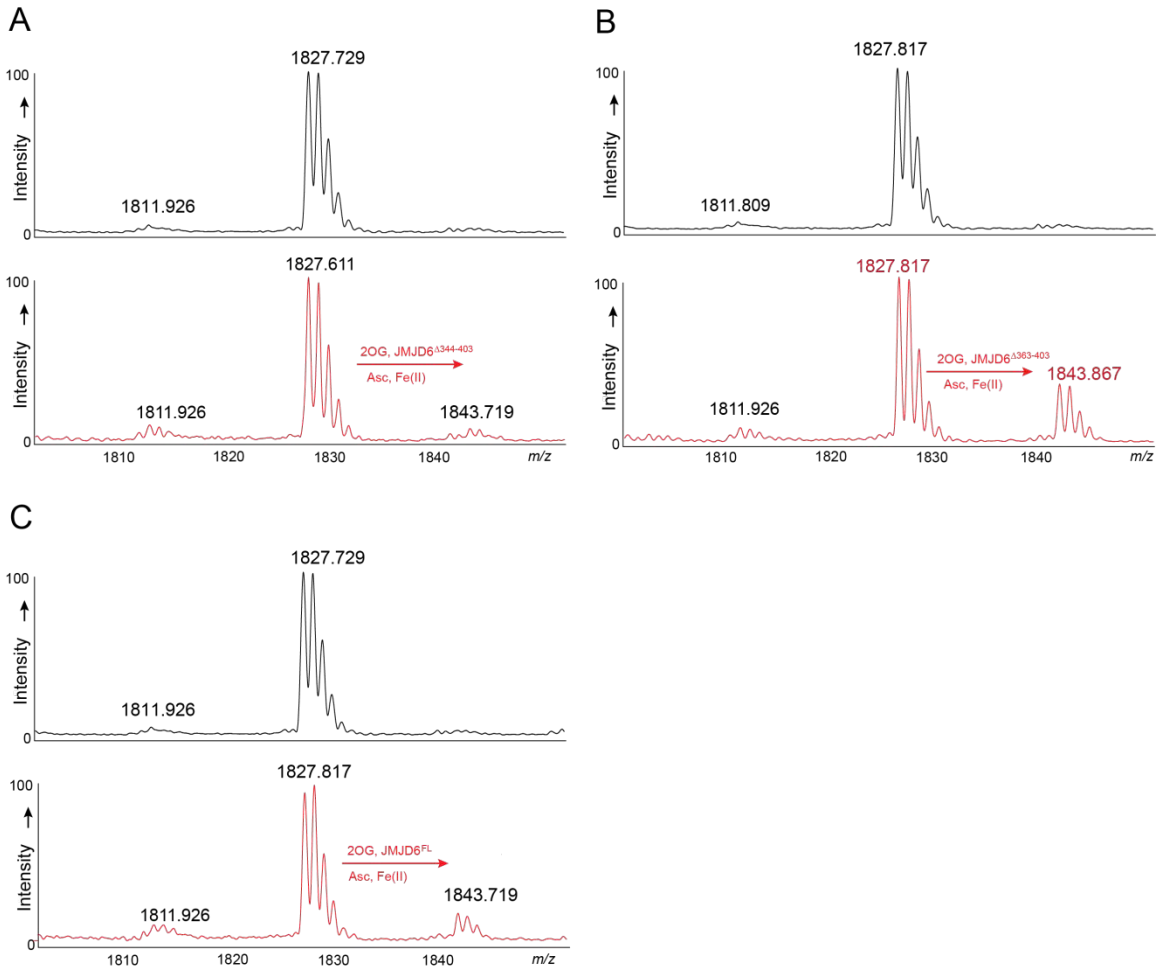

FIGURE 3.11. **Testing the hydroxylation/demethylation activity of JMJD6 on peptide H3K9(me1)$_{1\text{-}17}$: ARTKQTARK(me1)STGGKAPR.** MALDI-TOF spectra showing a relatively low level of hydroxylation, but no demethylation on H3K9(me1)$_{1\text{-}17}$, as was catalysed by (A) JMJD6$^{\Delta 344\text{-}403}$, (B) JMJD6^{FL}, and (C) JMJD6$^{\Delta 363\text{-}403}$. Experiments were carried out following the MALDI-TOF-based assay procedure described in Chapter 10.

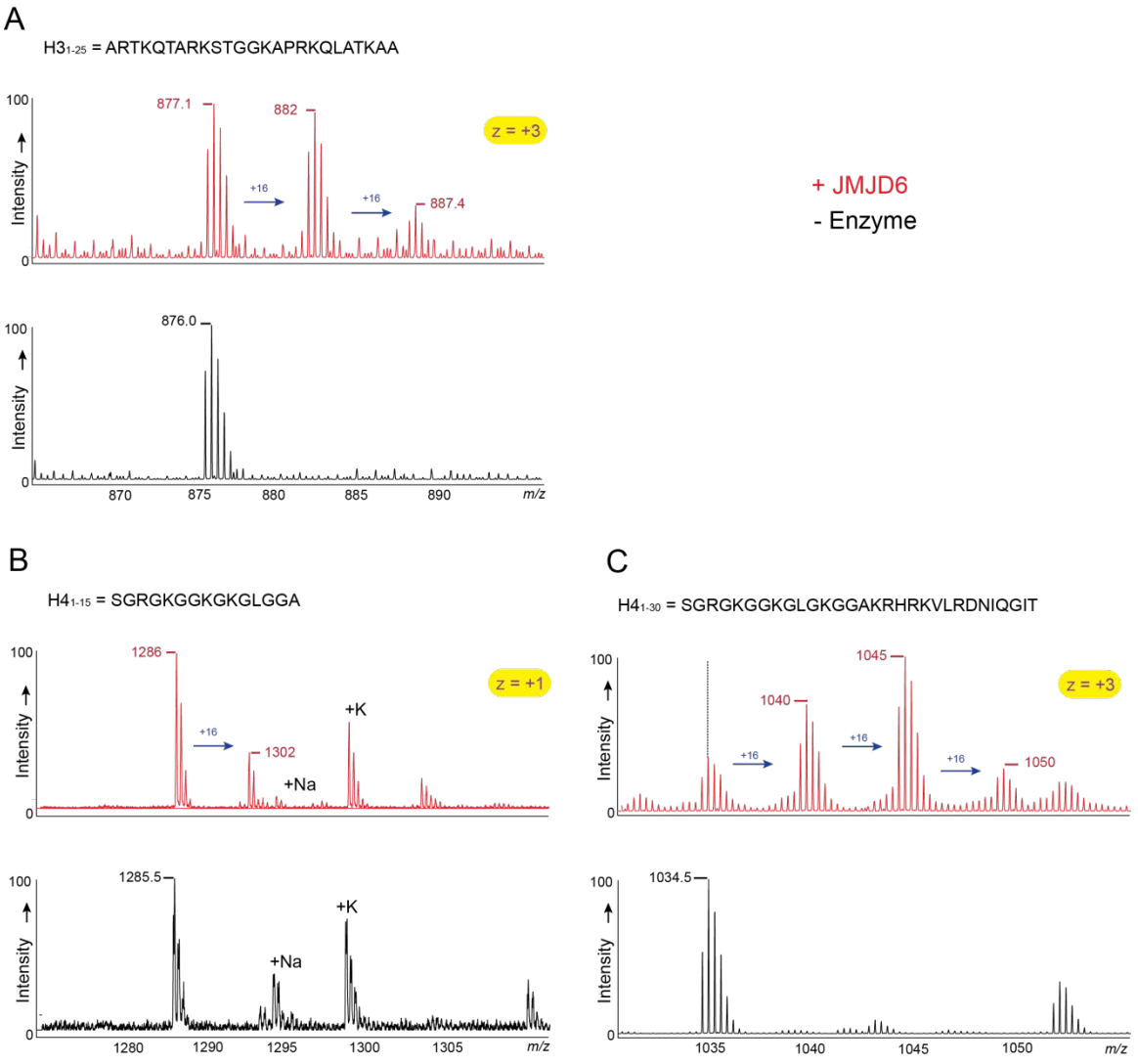

FIGURE 3.12. **Testing of hydroxylation activity of JMJD6$^{\Delta 363\text{-}404}$ on unmodified histone peptides.** MALDI-TOF spectra showing hydroxylation on histone peptides (A) $H3_{1\text{-}25}$, (B) $H4_{1\text{-}15}$, and (C) $H4_{1\text{-}30}$ as catalysed by JMJD6$^{\Delta 363\text{-}403}$. Experiments were carried out following the hydroxylation assay procedure described in Chapter 10.

3.4. Can JMJD6 Hydroxylate Modified Lysine Residue?

The findings that JMJD6 cannot recognize modified lysine further raised the question: can JMJD6 hydroxylate any of the lysine analogues? To investigate, $LUC7L2_{267\text{-}278}$ (NPKRSRSREHRR) peptides with analogues of lysine at position 269 (Lys^{269}) were tested against JMJD6. Peptides were synthesized in the laboratory of Dr. Jasmin Mecinovic (Institute of Molecules and Materials, Radboud University Nijmegen, The Netherland). However, MALDI-TOF analyses of the peptides, treated by JMJD6 in the presence of Fe(II), 2OG and ascorbate, revealed that JMJD6-catalysed hydroxylation is selective only for the unmodified lysine (Figure 3.13).

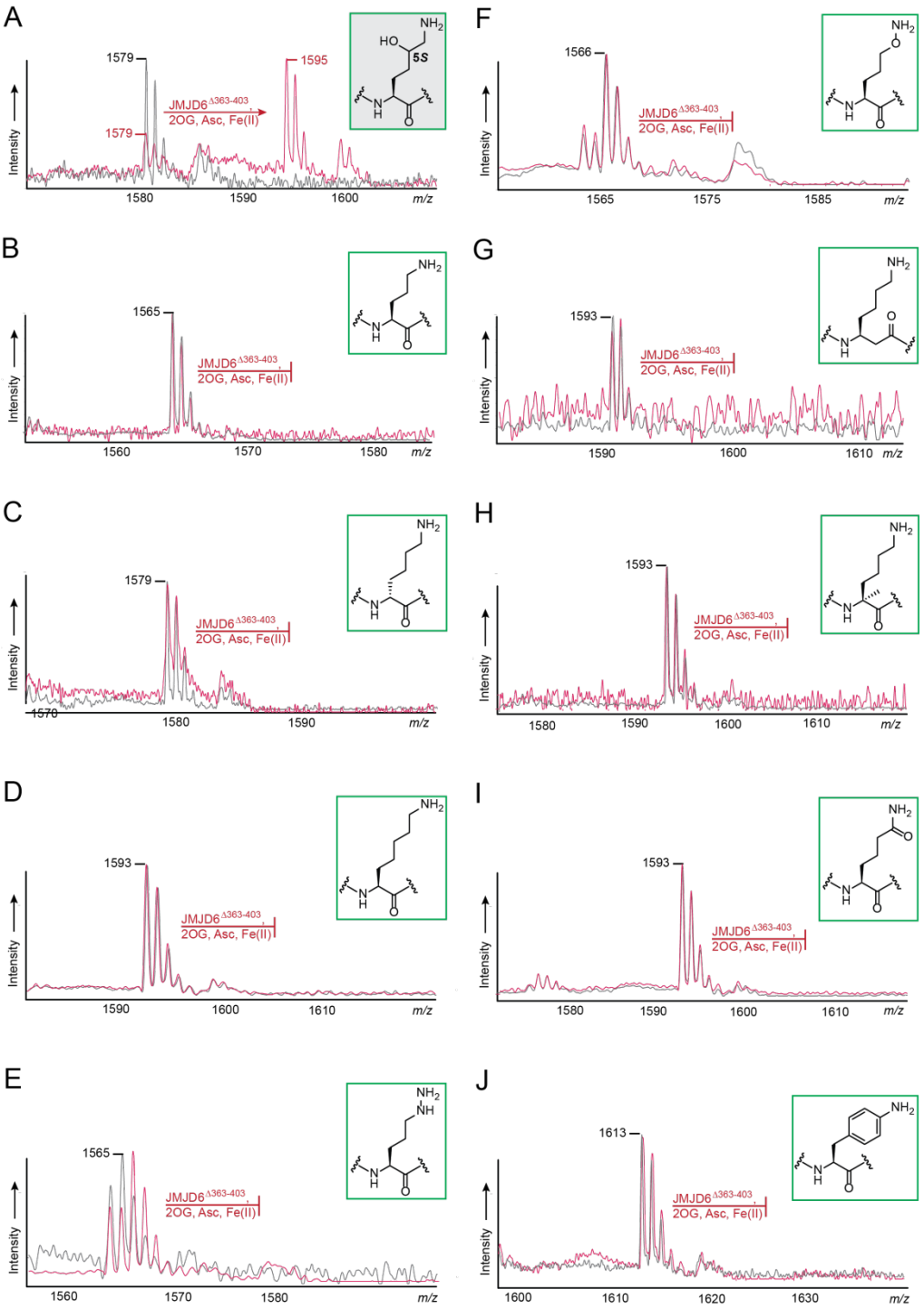

FIGURE 3.13. **Testing hydroxylation activity of JMJD6 on LUC7L2$_{267-278}$ (NPKRSRSREHRR) with various lysine analogues at position 269.** MALDI-TOF spectra revealing that JMJD6-catalysed hydroxylation of LUC7L2$_{267-278}$ is selective only to (A) L-lysine, not to any other modified forms of lysine (B-J)**.**

3.5. Studies on JMJD6-Catalysed Hydroxylation of Lysine Residue in SR Proteins

Recent work by Heim *et al.* has reported that JMJD6 targets lysine residues from multiple arginine-serine (RS)-rich regions of the SR proteins (70). They also showed, based on studies with multiple SR- and SR-related proteins, that JMJD6 selectively interacts with the RS regions of U2AF65, LUC7L2, SRSF11 (serine/arginine-rich splicing factor 11), and Acinus S' (apoptotic chromatin condensation inducer in the nucleus) but not with the RS region of SRSF1 (70). It was thus of interest of this study to investigate the kinetic *cross-talk* between the SR proteins and JMJD6. Although PUF60 (poly(U)-binding-splicing factor 60) does not have any RS-rich region, this protein was selected because a previous study had shown endogenous interaction between JMJD6 and PUF60 (70). Synthetic peptides of the SR proteins comprising residues from the RS-rich regions (Figure 3.14) were therefore made and were tested against JMJD6.

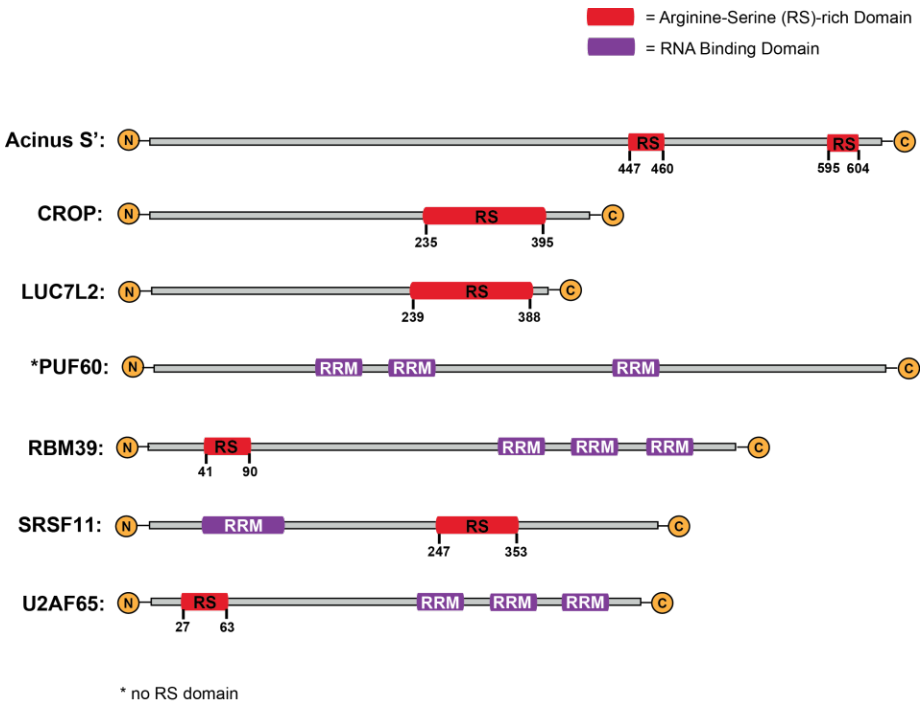

FIGURE 3.14. **Domain architectures of JMJD6-targeted SR proteins**.

3.5.1. Optimisation of JMJD6/Substrate Concentrations for Kinetic Study

To carry out this study, MALDI-TOF MS was used to analyse the reaction products. Signal to noise ratio is a drawback of MALDI-based experiments, which can interfere with low intensity signals (71). To identify the best enzyme: substrate ratio and to optimize the signal to noise, hydroxylation assays were carried out using various enzyme: substrate ratios (Figure 3.15). Reactions were carried out for 30 minutes at 37 °C with a 12-residues peptide from LUC7L2 protein ($LUC7L2_{267\text{-}278}$: NPKRSRSREHRR) as the substrate. Finally, an optimal enzyme: substrate ratio of 1:10 was chosen to be used in the kinetic studies. At this enzyme: substrate ratio, the percentage of hydroxylated $LUC7L2_{267\text{-}278}$ after 4 minutes was >25% and after 30 minutes was >95% (Figure 3.15). This demonstrates that enzyme: substrate of 1:10 is workable in the kinetic studies provided a potential substrate for JMJD6 is used.

3.5.2. End-point Hydroxylation Assays with the SR Proteins

Synthetic peptides were then tested as substrates of JMJD6 at a 1:10 enzyme: substrate ratio. MALDI-TOF analyses of the products revealed JMJD6-dependent peaks with +16 Da shifts in mass corresponding to hydroxylation only (Table 3.1). However, no JMJD6-dependent derivative corresponding to hydroxylated $PUF60_{495\text{-}510}$ (+16 Da shift in mass) was formed, suggesting JMJD6 doesn't hydroxylate Lys^{502} of PUF60 under the reaction conditions and with the peptide fragment used.

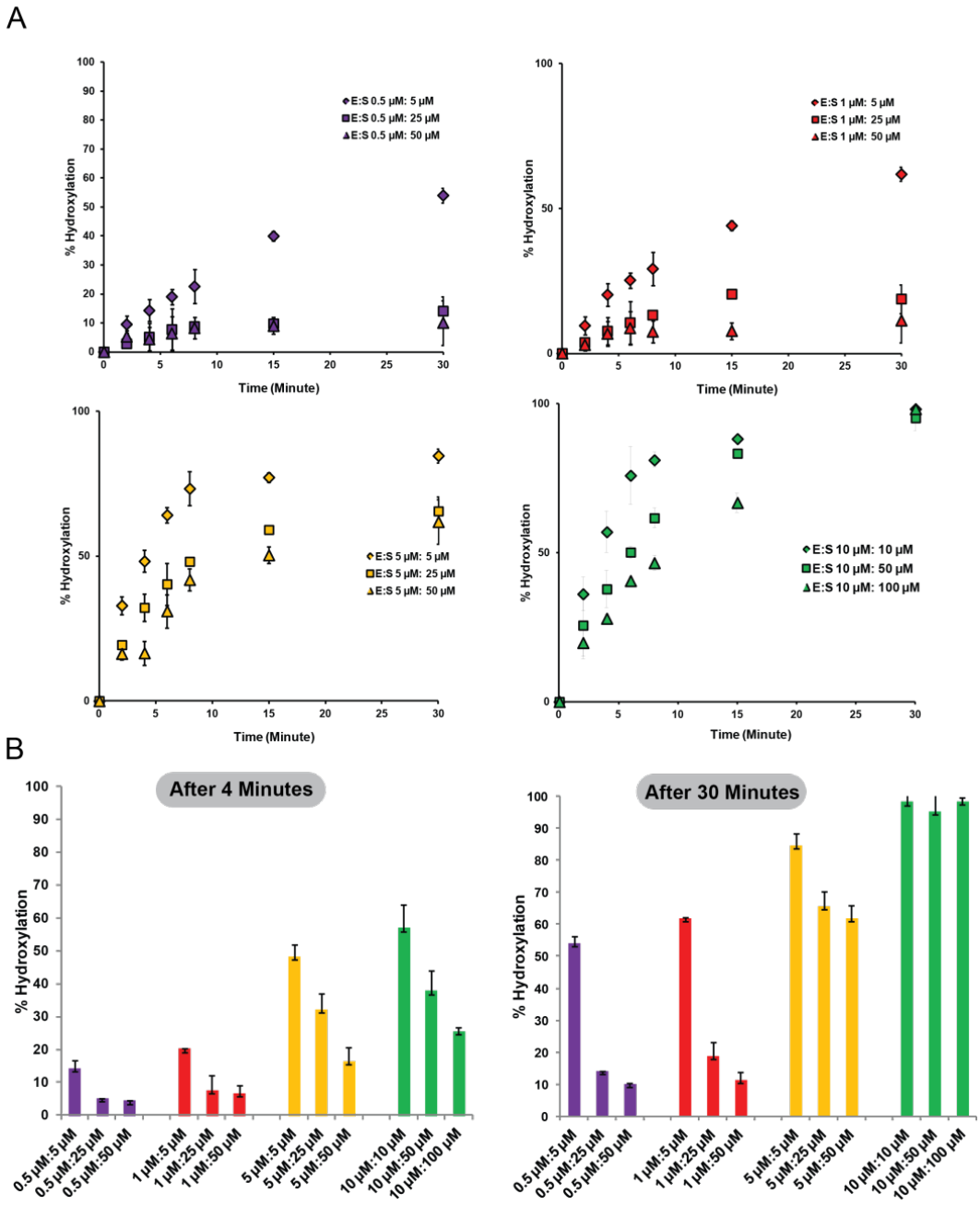

FIGURE 3.15. **Optimization of JMJD6/Substrate concentrations for kinetic studies**. (A) Plots showing the time-course hydroxylation assays for various concentrations of JMJD6 and the substrate LUC7L2$_{267\text{-}278}$ (NPKRSRSREHRR). (B) Bar charts show the percent hydroxylation of LUC7L2 after 4 minutes and 30 minutes. Experiments were carried out following the hydroxylation assay procedure described in Chapter 10. Values represent mean (n = 3) ± standard deviation (SD).

Table 3.1. JMJD6-catalysed hydroxylation of peptides derived from SR proteins. Experiments were carried out following the hydroxylation assay procedure described in Chapter 10. Values represent mean (n = 3) ± SD.

Peptide	Accession	Sequence	Hydroxylation (%)
LUC7L2$_{267-278}$	Q9Y383	NPKRSRSREHRR	98.5 ± 4.8
U2AF65$_{21-35}$	P26368	ENRHRKRSHSRSRSR	74.7 ± 4.1
U2AF65$_{30-46}$		SRSRSRDRKRRSRSRDR	72.4 ± 6.5
U2AF65$_{55-70}$		RDRRRRSKPLTRGAK	61.0 ± 6.4
CROP$_{311-325}$	Q95232	SRDHKRSRSRERRRS	89.3 ± 1.9
CROP$_{341-355}$		RKHRSRSRDRRRSKS	92.7 ± 6.9
CROP$_{357-370}$		DRKSYKHRSKSRDR	88.7 ± 4.9
LUK7L1$_{287-298}$	Q9NQ29	SRERRKL SRSRSR	18.3 ± 3.1
SRSF11$_{271-282}$	Q05519	SRSRRRSHSKSR	33.6 ± 1.8
SRSF11$_{286-298}$		RSKSPRRRRSHSR	97.5 ± 5.0
SRSF11$_{298-310}$		ERGRRSRSTSKT	6.4 ± 0.9
SRSF11$_{347-360}$		RSRSGTRSPKKPSR	97.0 ± 2.2
SRSF11$_{358-372}$		RSPKRKLSRSPSPR	44.1 ± 3.9
RBM39$_{31-42}$	Q14498	RSKKRKKSKS RS	99.0 ± 0.7
RBM39$_{38-50}$		SKSRSRSHERKRS	79.0 ± 8.9
RBM39$_{49-61}$		RSKSKERKRSRD	37.0 ± 7.6
RBM39$_{71-82}$		RKRSRSKERRRS	87.6 ± 7.0
RBM$_{121-132}$		SRRRSRSKSPFR	82.5 ± 5.6
Acinus$_{447-460}$	Q9UKV3	PRSRSRSRDRRRKE	25.6 ± 2.8
Acinus$_{595-604}$		KRHSRSRSRS	12.5 ± 3.0
PUF60$_{495-510}$	Q9UHX1	RVIIYQEKQGEEEDAE	0 ± 0.0

3.5.3. Alanine Scanning of Peptides Derived from SR Proteins

Most of the peptides synthesized from the RS regions of SR proteins contain more than one lysine residue (and hence potential site for hydroxylation). Indeed, peaks with +32 Da as well as +48 Da shifts were observed in some cases (Figure 3.16-3.21). These results suggest that JMJD6 can target more than one lysine residue within RS regions of SR proteins. To investigate the targeted lysine residue(s) of JMJD6, alanine variants of the peptides were thereafter made. These peptides were then tested for $JMJD6^{\Delta 363-403}$-catalysed hydroxylation. The targeted lysine residue(s) were identified based on the absence of hydroxylated peak owing to the presence of alanine in the corresponding position of lysine. For example, in case of $LUC7L2_{267-278}$ and $LUC7L1_{287-298}$, respectively ~98% and ~10% hydroxylation were observed in presence of JMJD6 (Figure 3.16). But both of the peaks corresponding to +16 Da shifts disappeared completely in case of $LUC7L2_{267-278}$K269A (Figure 3.16**A**) or $LUC7L1_{287-298}$K292A (Figure 3.16**B**), suggesting that JMJD6-dependent modifications of these peptides are due to the hydroxylation of Lys^{269} and Lys^{292}, respectively (Figure 3.16).

Similarly, JMJD6-dependent hydroxylation was also observed for peptide fragments $U2AF65_{21-35}$ and $U2AF65^{30-46}$ where the hydroxylation was apparently specific to Lys^{26} and Lys^{38}, respectively (Figure 3.17). In case of $U2AF65_{55-70}$, peaks corresponding to +16 as well as +32 Da shifts were observed in the MALDI-TOF spectrum. Complete abrogation of hydroxylation was achieved when both Lys^{62} and Lys^{70} were replaced by alanine residues (Figure 3.17**C**). This suggests that JMJD6 hydroxylates both Lys^{62} and Lys^{70}, but preferentially Lys^{62} of U2AF65.

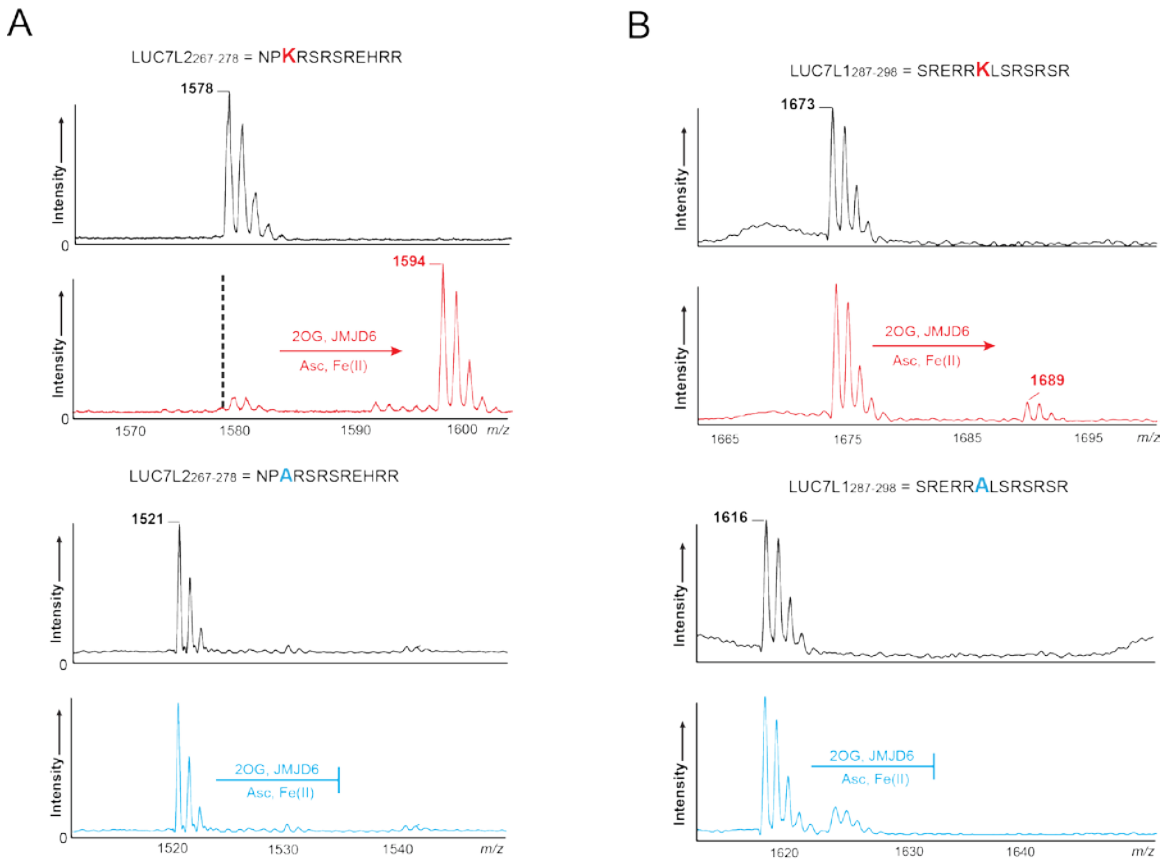

FIGURE 3.16. **Alanine variants of peptides from LUC7L proteins tested against JMJD6 to identify the targeted lysine residues.** MALDI-TOF spectra of JMJD6-treated wild-type and alanine variants of (A) LUC7L2$_{267-278}$ and (B) LUC7L1$_{287-298}$ show that the observed hydroxylated peaks (+16 Da shift in mass) are specific to Lys^{269} and Lys^{292}, respectively, not to any other residues. Experiments were carried out in triplicate (n = 3) following the hydroxylation assay procedure described in Chapter 10.

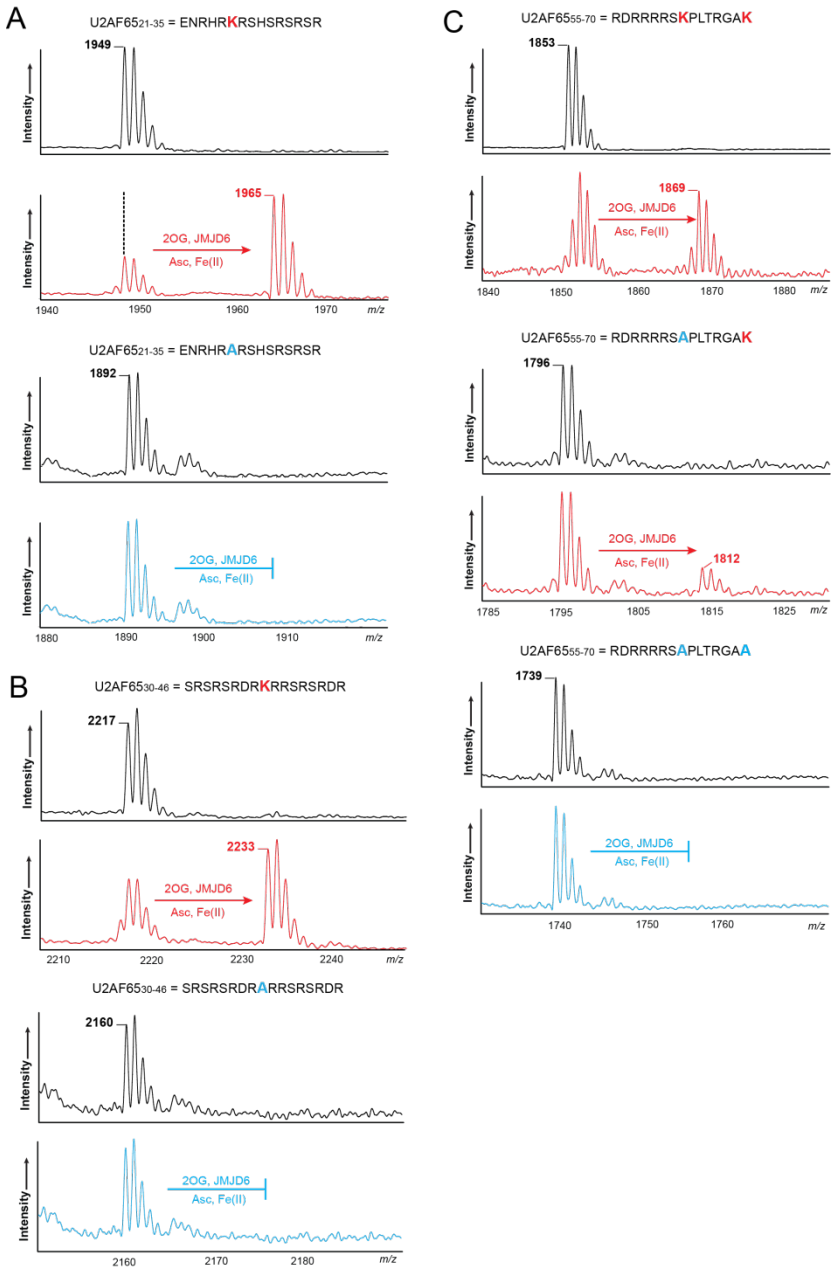

FIGURE 3.17. **Alanine variants of peptides from U2AF65 protein tested against JMJD6 to identify the targeted lysine residues.** MALDI-TOF spectra of JMJD6-treated wild-type and alanine variants of U2AF65 show that the observed hydroxylated peaks (+16 Da shift in mass) are specific to Lys^{26}, Lys^{38}, Lys^{62}, and Lys^{70}, not to any other residues of U2AF65. Experiments were carried out in triplicate (n = 3) following the hydroxylation assay procedure described in Chapter 10.

Alanine scanning of peptide fragments $CROP_{311-325}$ and $CROP_{357-370}$ further revealed that JMJD6 hydroxylates Lys^{315} and Lys^{359}, respectively (Figure 3.18**A** and 3.18**B**). Although 2 more lysine residues are present in $CROP_{357-370}$, no binding between JMJD6 and these lysine residues was observed in the hydroxylation assay, demonstrating that JMJD6 selectively hydroxylates Lys^{359} (Figure 3.18**C**). MALDI-TOF analyses of another peptide fragment of CROP (wild-type and alanine variants) revealed that JMJD6 preferentially hydroxylates Lys^{342} among its two targets, Lys^{342} and Lys^{354} (Figure 3.18**B**).

Likewise, assigning the targeted residues in peptides $SRSF11_{271-282}$, $SRSF11_{286-298}$, and $SRSF11_{298-310}$ responsible for showing +16 Da modification was straightforward as each had only one lysine residue. When the alanine variants of these peptides ($SRSF11_{271-282}$K280A, $SRSF11_{286-298}$K288A, and $SRSF11_{298-310}$K309A) were tested against JMJD6, no modification was observed (Figure 3.19). This confirms that JMJD6 indeed hydroxylates Lys^{280}, Lys^{288}, and Lys^{309}, respectively (Figure 3.19**A**, 3.19**B** and 3.19**C**). In contrast, JMJD6 appeared to target more than one lysine residues from residues 347-372 of SRSF11 (Figure 3.19). MALDI-TOF analyses of wild-type and alanine variants of peptides corresponding to residues 347-372 revealed that JMJD6 targets Lys^{356}, Lys^{357}, Lys^{362}, and Lys^{364}, with a preference for Lys^{356} and Lys^{362} only (Figure 3.19**D** and 3.19**E**).

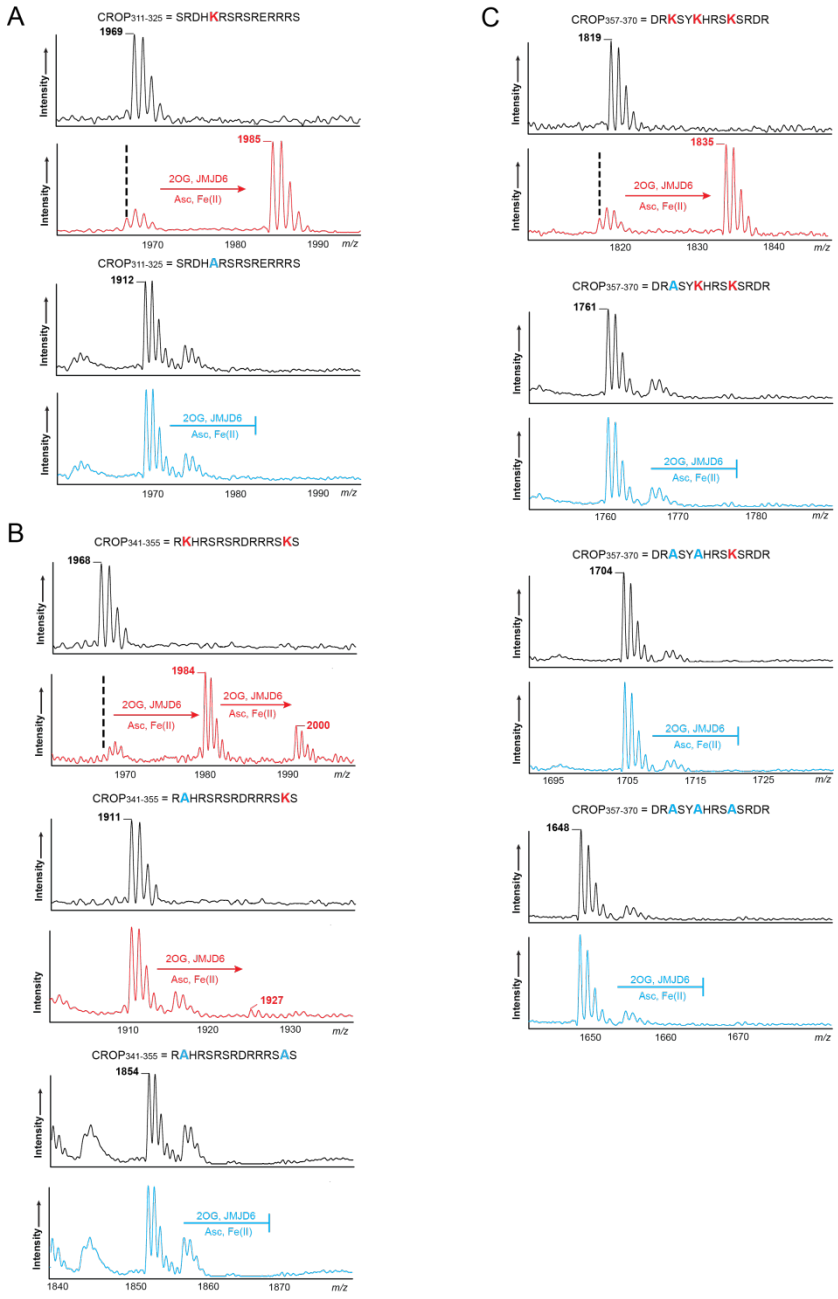

FIGURE 3.18. **Alanine variants of peptides from CROP protein tested against JMJD6 to identify the targeted lysine residues.** MALDI-TOF spectra of JMJD6-treated wild-type and alanine variants of CROP show that the observed hydroxylated peaks (+16 Da shift in mass) are specific to Lys^{315}, Lys^{342}, Lys^{354}, and Lys^{359}, not to any other residues. Experiments were carried out in triplicate (n = 3) following the hydroxylation assay procedure described in Chapter 10.

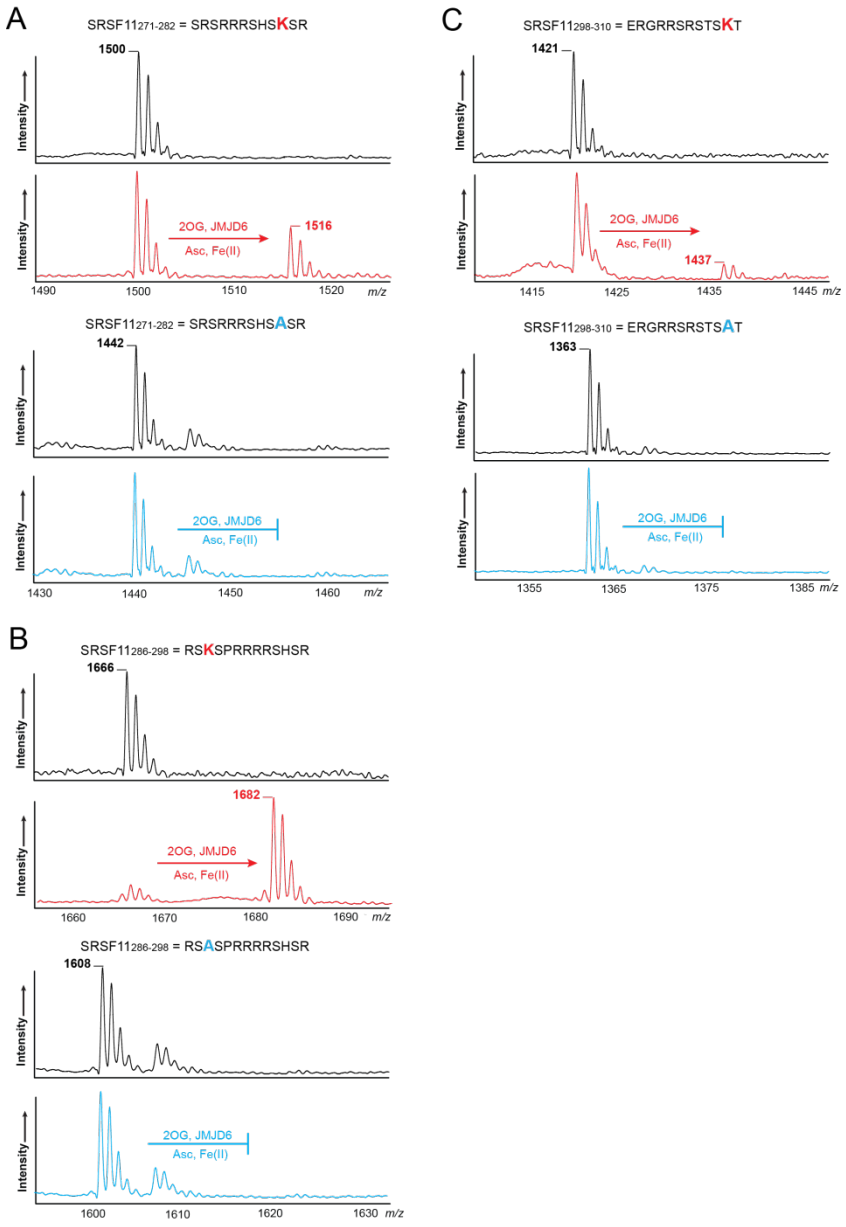

FIGURE 3.19. **Alanine variants of peptides from SRSF11 protein tested against JMJD6 to identify the targeted lysine residues.** MALDI-TOF spectra of JMJD6-treated wild-type and alanine variants of SRSF11 show that the observed hydroxylated peaks (+16 Da shift in mass) are specific to Lys^{280}, Lys^{288}, Lys^{309}, Lys^{356}, Lys^{357}, Lys^{362}, and Lys^{364}, not to any other residues of SRSF11. Experiments were carried out in triplicate (n = 3) following the hydroxylation assay procedure described in Chapter 10.

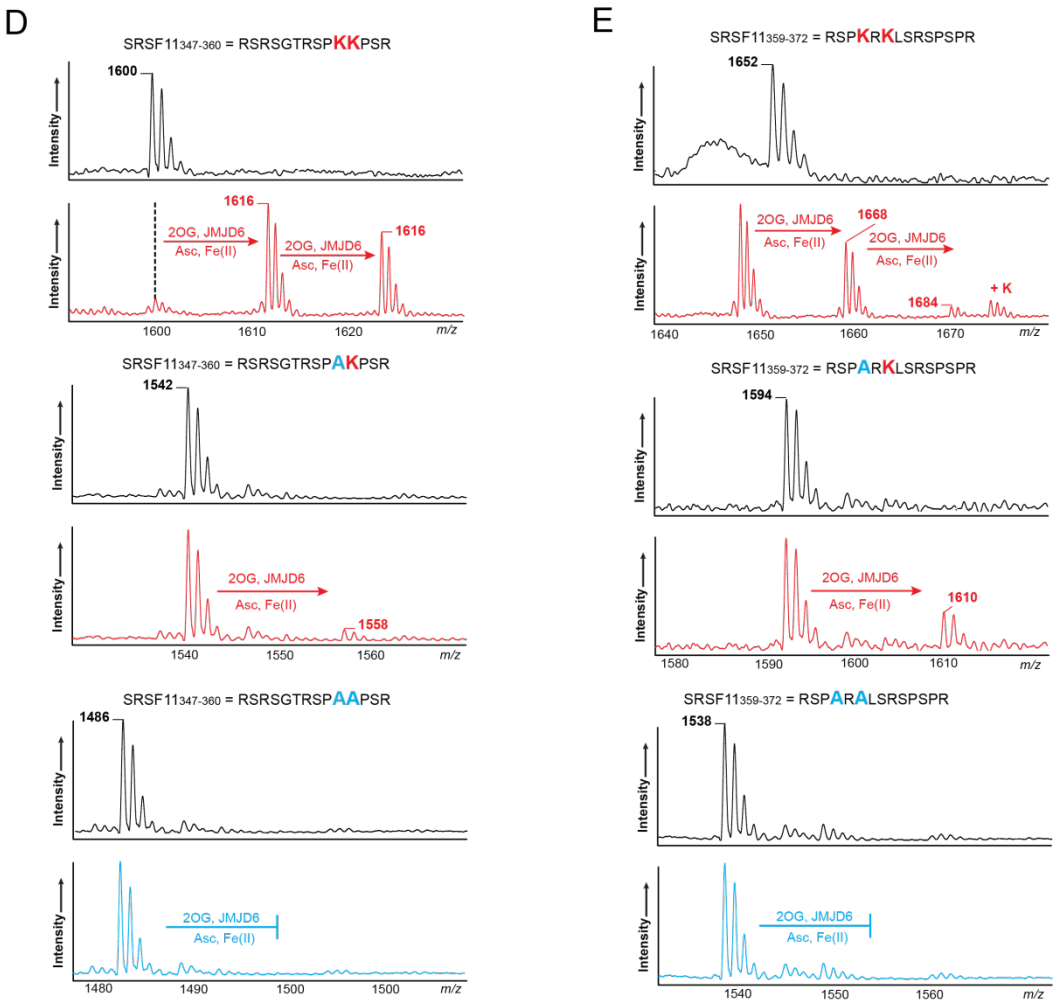

FIGURE 3.19. **continues … … ….**

Unlike the other targets of JMJD6, the SR region of RBM39 has relatively more lysine residues. For example, peptide fragment $RBM39_{31-42}$ has five lysine residues (Figure 3.20**A**). After replacement of each lysine systematically by an alanine residue followed by testing the alanine variants against JMJD6, it was found that JMJD6 targets Lys^{33}, Lys^{34}, and Lys^{36} with an order of preference as: Lys^{36} > Lys^{34} > Lys^{33} (Figure 3.20**A**). Similarly, multiple targets of JMJD6 from residues of 50-82 of RBM39 were identified (Figure 3.20).

MALDI-TOF analyses of the wild-type and alanine variants imply that JMJD6 can hydroxylate Lys^{39}, Lys^{48}, Lys^{51}, Lys^{53}, Lys^{56}, Lys^{72}, and Lys^{77}, with an inclination toward Lys^{39} and Lys^{72} (Figure 3.20**B**, 3.20**C**, and 3.20**D**). Residues Lys^{51}, Lys^{53}, and Lys^{56} did

not appear as good target for hydroxylation compared to other lysine residues (Figure 3.20**C**). However, peptide fragment RBM39$_{121\text{-}132}$ appeared as a relatively good substrate for JMJD6 with ~95% conversion to its hydroxylated derivative, catalysed by JMJD6 (Figure 3.20E). Further analysis with its alanine variant RBM39$_{121\text{-}132}$K128A showed that the hydroxylated residue is Lys^{128} (Figure 3.20**E**).

Next, wild-type and alanine variants of peptides corresponding to RS-regions of Acinus S' were synthesized. Although JMJD6-dependent hydroxylation specific to residues Lys^{459} and Lys^{595} were observed, the level of hydroxylation was not very high (~12-25%) (Figure 3.21). This demonstrates, at least under the hydroxylation assay conditions used, that Acinus S' is not a good substrate for JMJD6.

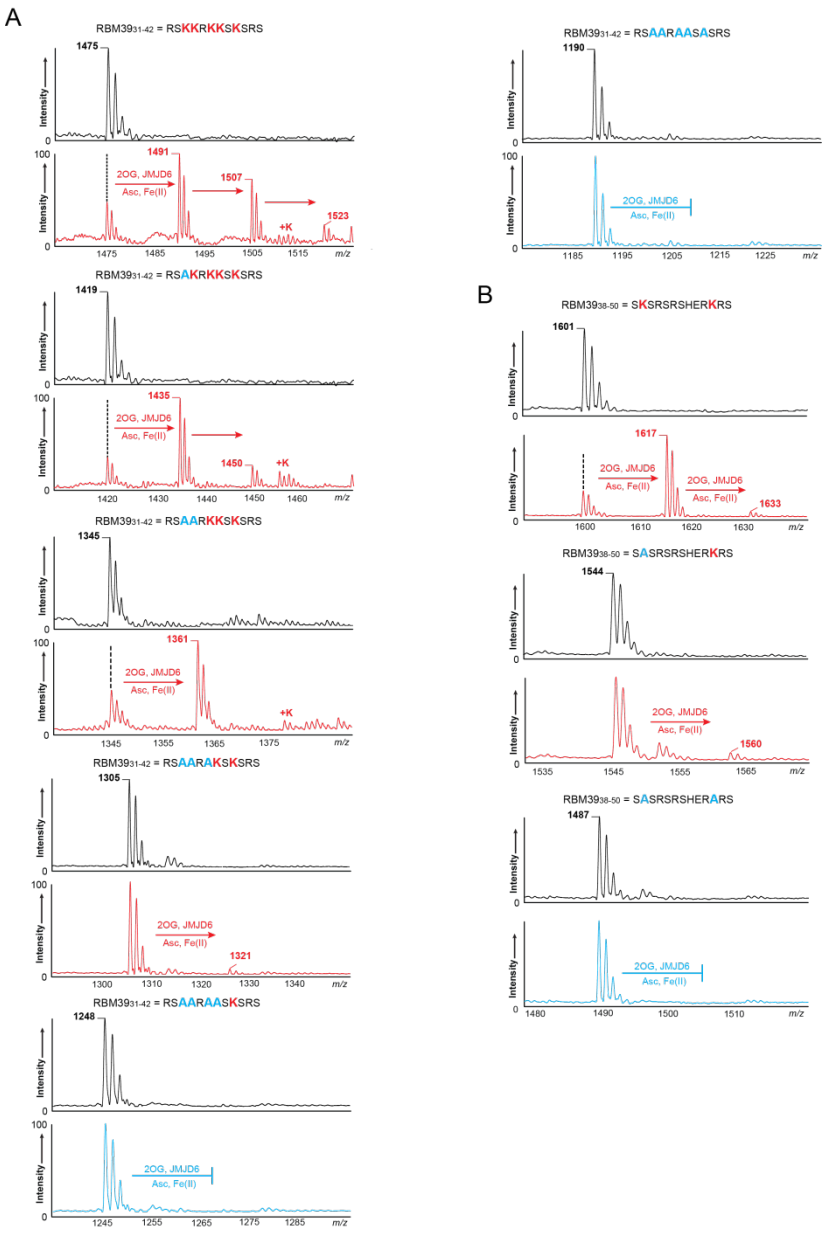

FIGURE 3.20. **Alanine variants of peptides from RBM39 protein tested against JMJD6 to identify the targeted lysine residues.** MALDI-TOF spectra of JMJD6-treated wild-type and alanine variants of RBM39 show that the observed hydroxylated peaks (+16 Da shift in mass) are specific to Lys^{33}, Lys^{34}, Lys^{36}, Lys^{39}, Lys^{48}, Lys^{56}, Lys^{72}, Lys^{77}, and Lys^{128}, not to any other residues of RBM39. Experiments were carried out in triplicate (n = 3) following the same hydroxylation assay procedure described in Chapter 10.

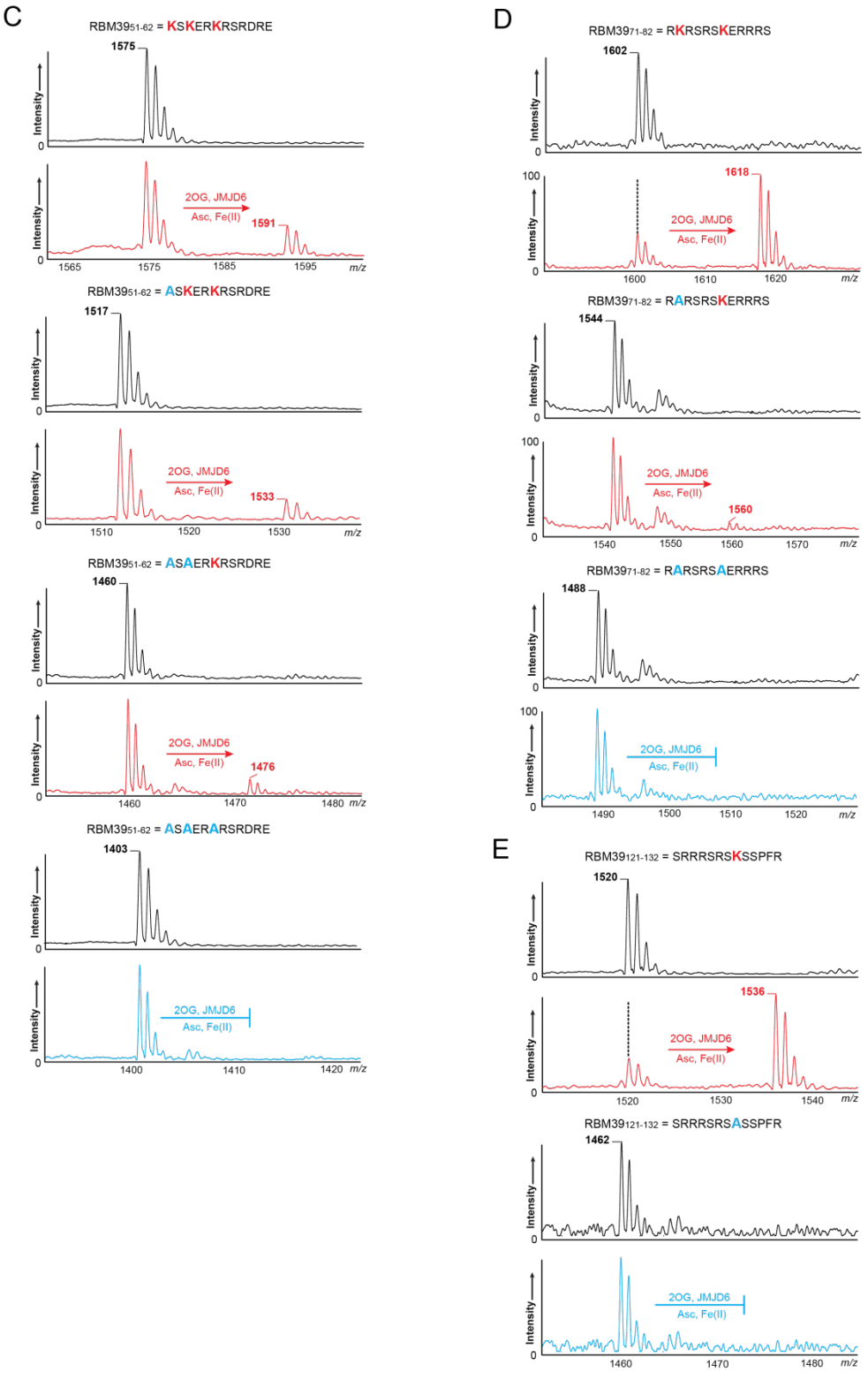

FIGURE 3.20. **continues… … …**

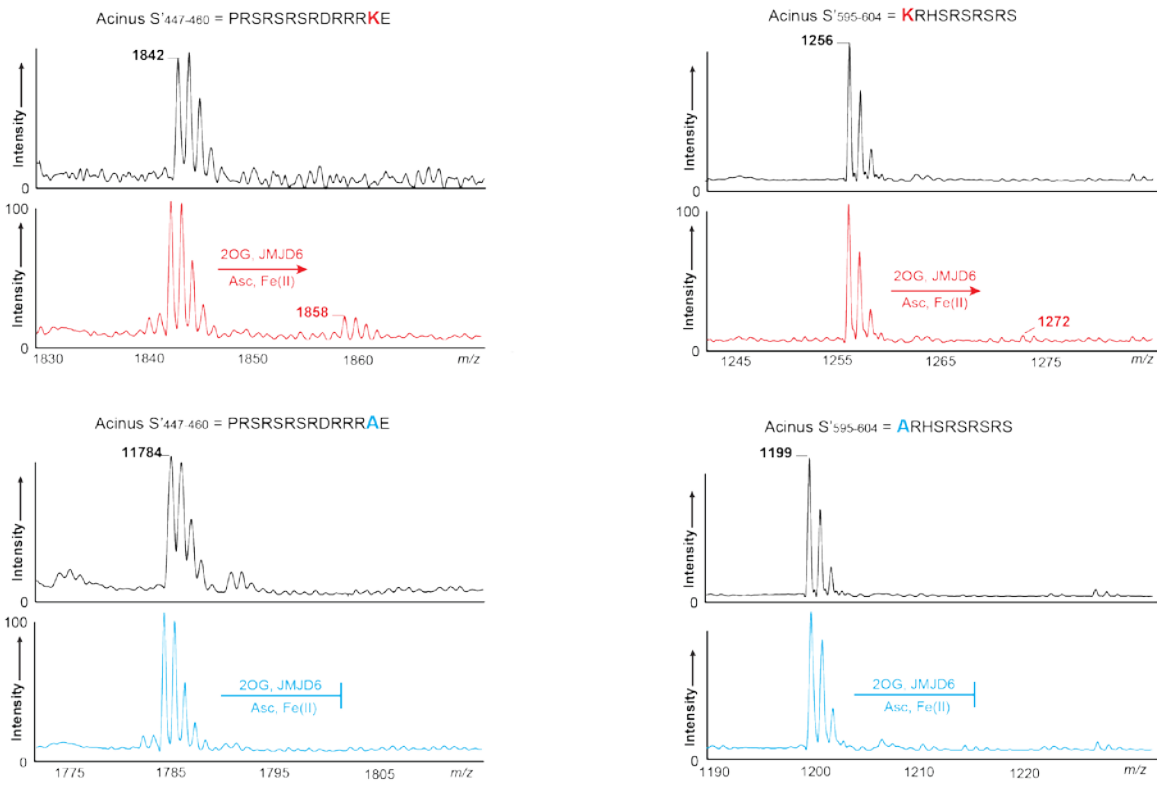

FIGURE 3.21. **Alanine variants of peptides from Acinus S' proteins tested with JMJD6 to identify the targeted Lysine.** MALDI-TOF spectra of JMJD6-treated wild-type and alanine variants of Acinus S' show that the observed hydroxylated peaks (+16 Da shift in mass) are specific to Lys^{459} and Lys^{595}. Experiments were carried out in triplicate (n = 3) following the hydroxylation assay procedure described in Chapter 10.

3.6. *Steady-state* Kinetic Studies with the SR Proteins

3.6.1. Time-course Hydroxylation Assay to Determine Linear Range

We next sought to carry out time-course hydroxylation assays using the synthetic peptides of SR proteins, in part with a view, to identify the linear region of the hydroxylation reactions. Assays were carried out at 1:10 enzyme: substrate ratio following the standard hydroxylation assay procedure. Reactions were allowed to continue for 30 minutes under 37 °C whilst withdrawing 5 µL samples from each reaction at various time intervals (*e.g.* 2, 4, 6, 8, 12, 15 and 30 minutes). The results showed that the peptides were hydroxylated by JMJD6 at different rates (Figure 3.22). However, in most of the

cases, reactions reached a plateau after ~8 minutes. Therefore, peptides showing ≥ 25% hydroxylation after 6 minutes were considered for further *steady-state* kinetic studies.

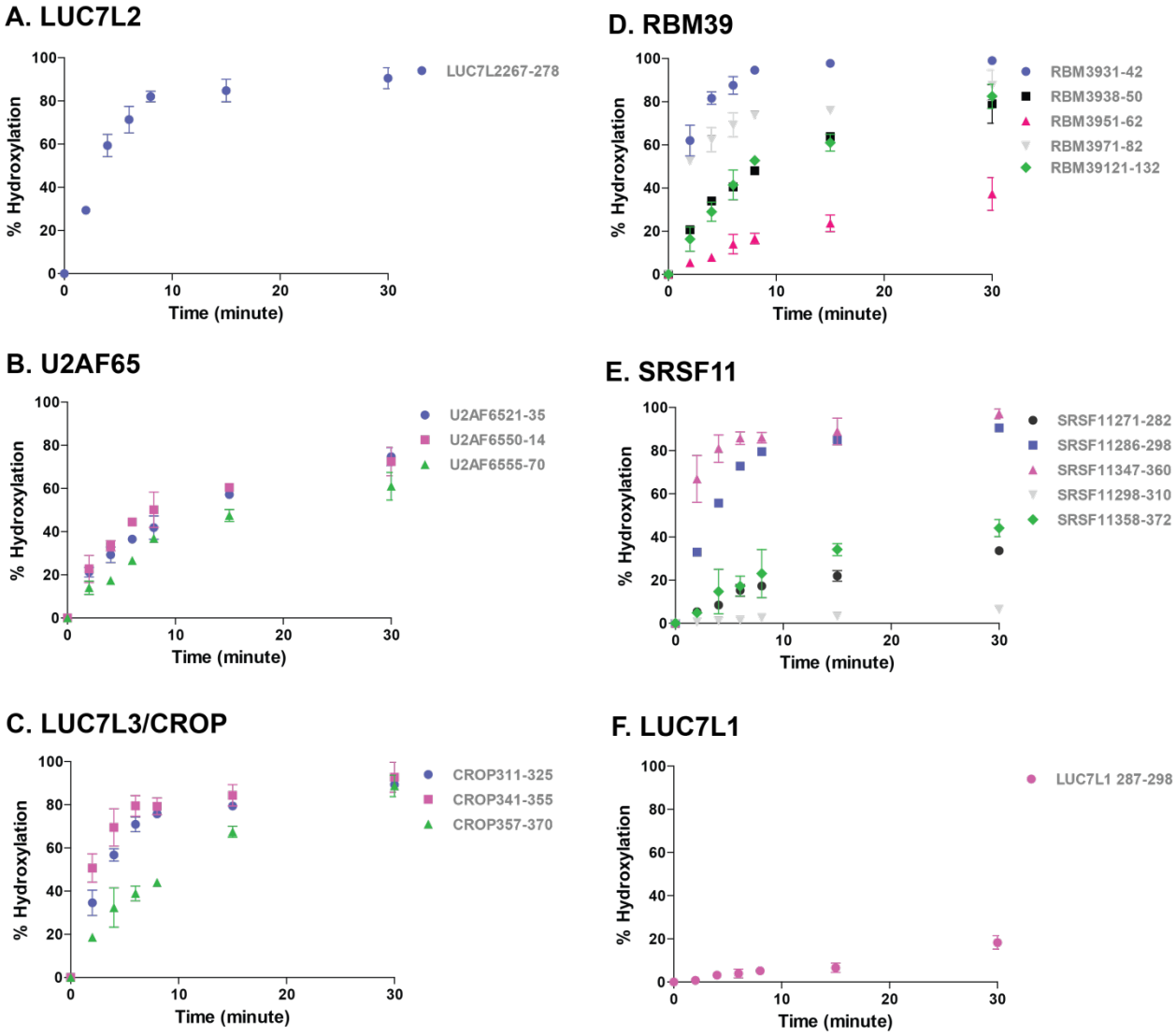

FIGURE 3.22. **Time-course hydroxylation assay of JMJD6 with SR proteins.** Plots showing the time-course hydroxylation of the peptide fragments of SR proteins (A) LUC7L2, (B) U2AF65, (C) LUC7L3, (D) RBM39, (E) SRSF11, and (F) LUC7L1. Note, each hydroxylation plot shows the initial linear region that was exploited later in *steady-state* kinetic studies. Experiments were carried out following the hydroxylation assay procedure described in Chapter 10. Values represent mean (n = 3) ± SD.

3.6.2. K_m Values Determination for the Peptide Fragments of SR Proteins

Kinetic studies of JMJDJ6 were then carried out using the peptide fragments of SR-proteins. Hydroxylation assays were carried out for 6 minutes at 37 °C in presence of increasing concentrations of peptides (0-400 µM) (**Chapter 10**). Reaction samples were withdrawn at 2, 4, and 6 minutes, then quenched by adding equivolume of 1% formic acid. MALDI-TOF MS was used to determine the relative quantities of unreacted substrates and hydroxylated products. Finally, the reaction rate (v_0) for each peptide calculated from apparent linear region was plotted as a function of peptide concentration using GraphPad PRISM and the kinetic parameters were obtained from the Michaelis-Menten equation (**Chapter 10**).

Kinetic parameters for JMJD6 hydroxylation of $LUC7L2_{267-278}$ were found to be: V_{max}, 0.1 µM.s^{-1}; K_m, 51 µM; k_{cat}, 106 s^{-1}; k_{cat}/K_m, 207.8 $\mu M^{-1}.s^{-1}$ (Table 3.2, kinetic data was calculated from figure 3.23). Of the peptide fragments of U2AF65, $U2AF65_{21-35}$ (K_m = 59 µM) was found to be better substrate than $U2AF65_{30-46}$ (K_m = 78 µM) and $U2AF65_{55-70}$ (K_m = 124 µM) (Table 3.2, kinetic data were calculated from figure 3.23). Peptide fragments from another SR protein, CROP, were also found to be hydroxylated with same efficiency by JMJD6 showing K_m values ~ 90 µM (Table 3.2, kinetic data were calculated from figure 3.23). Of the peptide fragments of SRSF11, JMJD6 hydroxylated $SRSF11_{358-372}$ with a relatively high efficiency with measured K_m and k_{cat}/K_m values 41 µM and 195.1 $\mu M^{-1}.s^{-1}$, respectively. In case of RBM39, different efficiencies of JMJD6-catalysed hydroxylation for different sequences were observed with measured K_m values ranging within 56-99 µM (Table 3.2, kinetic data were calculated from figure 3.23). Amongst the peptides, $RBM39_{31-42}$ was found to be relatively good, with a K_m value of 56 µM.

Table 3.2. Kinetic parameters for substrate peptides of JMJD6. Experiments were carried out following the *steady-state* kinetic assay procedure described in Chapter 10. Values represent mean (n = 3) ± SD.

Peptide	Sequence	Hydroxylation (%)	V_{max} (μM. s^{-1})	K_m (μM)	k_{cat} (x10^{-4}) (s^{-1})	k_{cat}/K_m (x 10^{-6}) ($\mu M^{-1}.s^{-1}$)
LUC7L2$_{267-278}$	NP**K**RSRSREHRR	98.5 ± 4.8	0.1	51 ± 4.6	106 ± 4	207.8
U2AF65$_{21-35}$	ENRHR**K**RSHSRSRSR	74.7 ± 4.1	0.04	59 ± 8.6	40 ± 2.2	68
U2AF65$_{30-46}$	SRSRSRDR**K**RRSRSRDR	72.4 ± 6.5	0.09	78 ± 14.8	92 ± 7.0	118
U2AF65$_{55-70}$	RDRRRRS**K**PLTRGAK	61.0 ± 6.4	0.04	124 ±	43 ± 5.2	34
CROP$_{311-325}$	SRDH**K**RSRSRERRRS	89.3 ± 1.9	0.19	71 ± 7.2	191 ± 6.6	269
CROP$_{341-355}$	R**K**HRSRSRDRRRSKS	92.7 ± 6.9	0.16	76 ± 13.3	165 ± 12	217
CROP$_{357-370}$	DR**K**SYKHRSKSRDR	88.7 ± 4.9	0.04	93 ± 20.6	39 ± 3.6	42
SRSF11$_{271-282}$	SRSRRRSHS**K**SR	**33.6 ± 1.8**	**Not Determined**			
SRSF11$_{286-298}$	RS**K**SPRRRRSHSR	90.5 ± 5.0	0.08	41 ± 6.6	80 ± 3.9	195.1
SRSF11$_{298-310}$	ERGRRSRSTS**K**T	**6.4 ± 0.9**	**Not Determined**			
SRSF11$_{347-360}$	RSRSGTRSP**K**KPSR	97.0 ± 2.2	0.14	92 ± 13.9	146 ± 9.6	158.7
SRSF11$_{358-372}$	RSP**K**RKLSRSPSPR	44.1 ± 3.9	0.17	76 ± 21.2	174 ± 18.9	228.9
RBM39$_{31-42}$	RSKKR**K**KSKSRS	99.0 ± 0.7	0.25	56 ± 9.6	255 ± 15.3	455
RBM39$_{38-50}$	S**K**SRSRSHERKRS	79.0 ± 8.9	0.28	71 ± 9.9	281 ± 14.8	395
RBM39$_{51-62}$	KSKER**K**RSRDRE	**37.0 ± 7.6**	**Not Determined**			
RBM39$_{71-82}$	R**K**RSRSKERRRS	87.6 ± 7.0	0.28	88 ± 8.7	284 ± 11.4	322
RBM39$_{121-132}$	SRRRSRS**K**SPFR	82.5 ± 5.6	0.3	99 ± 19.2	300 ± 23	303
LUC7L1$_{287-298}$	SRERR**K**LSRSRSR	**18.3 ± 3.1**	**Not Determined**			
Acinus$_{447-460}$	PRSRSRSRDRRR**K**E	25.6 ± 2.8	**Not Determined**			
Acinus$_{595-604}$	**K**RHSRSRSRS	12.5 ± 3.0	**Not Determined**			

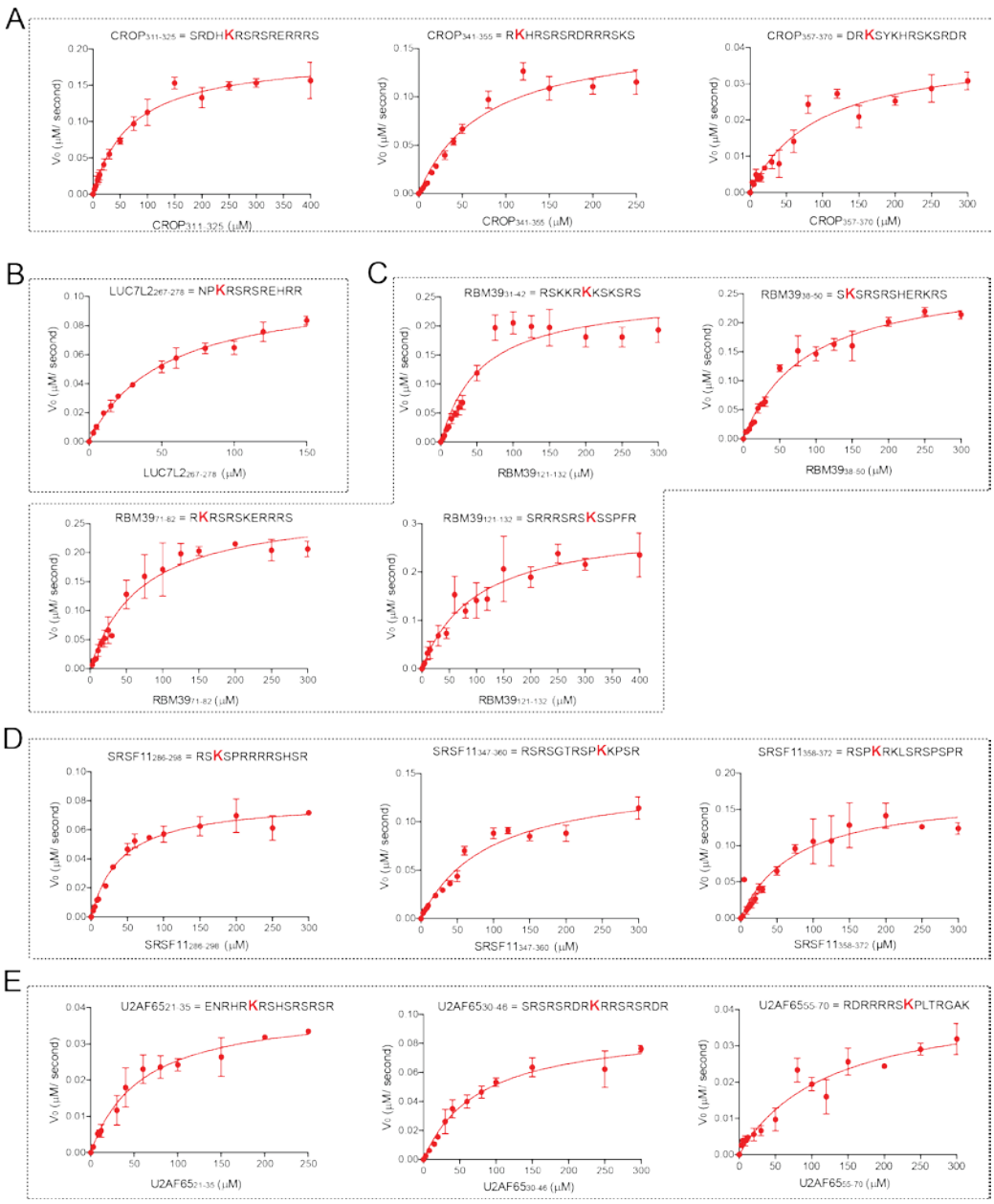

FIGURE 3.23. ***Steady-state*** **kinetic studies of JMJD6 using peptides from SR proteins**. Michaelis-Menten curves of the *steady-state* kinetic reactions between JMJD6 and peptides of SR proteins (A) CROP, (B) LUC7L2, (C) RBM39, (D) SRSF11, and (E) U2AF65. Experiments were carried out following the *steady-state* kinetic assay procedure described in Chapter 10. Values represent mean (n = 3) ± SD.

The K_m values for the JMJD6-catalysed hydroxylation reactions were 40-125 μM. Interestingly, JMJD6 appeared to prefer the peptides with a higher content of basic residues (and hence higher pI values). For example, of the peptide fragments,

SRSF11$_{286-298}$ has the highest number of basic residues (62% of the total residues, pI = 12.7) and hence shows the lowest K_m value (41 μM). On the other hand, U2AF65$_{55-70}$ has 53% basic residues (pI = 12.3) and thus shows a K_m value of 124 μM.

The length of the peptides was also found to have impact on JMJD6-catalysed hydroxylation activity, as was observed previously in the work by Koivunan *et al.* with PHD2 (72). Peptides with 12-13 amino acids (*e.g.* LUC7L2$_{267-278}$, SRSF11$_{286-298}$ and the measured K_m values were 51 and 41 μM, respectively) were found to be better substrates of JMJD6 than peptides containing ≥15 amino acids (U2AF65$_{30-46}$ and CROP$_{341-355}$ and the measured K_m values were 78 and 76 μM, respectively) (Table 3.2). This substrate recognition property of JMJD6 is quite different from other 2OG oxygenases including FIH for which, longer peptides are usually better substrates (60). For example, FIH was reported to hydroxylate 35-mer HIF-1α CAD near to completion whereas the level of hydroxylation was only 20% under the same reaction conditions when a 19-mer HIF-1α CAD was used. Similar results were observed with another substrate HIF-2α CAD as well (60).

The relative position of the targeted lysine residue within the peptide sequence also influenced the hydroxylation activity of JMJD6. Peptides with the targeted lysine close to their *N*-terminus showed lower K_m values than those having the targeted lysine in the middle or toward their *C*-terminus (Table 3.2). For example, peptide fragments LUC7L2$_{267-278}$ (NPKRSRSREHRR) and SRSF11$_{286-298}$ (RSKSPRRRRSHSR) have the lysine residues close to their *N*-termini and showed the lowest K_m values (51 and 41 μM, respectively). These two peptides have only one lysine residue, which further demonstrates that presence of more than one targeted lysine residue within the sequences is another factor that regulates the substrate recognition of JMJD6. An exception was observed in case of RBM39$_{31-42}$ (RSKKRKKSKSRS) which, although contains five lysine residues, is a good substrate of JMJD6 (near to complete hydroxylation and relatively a lower K_m value, 56 μM). It is proposed that its shorter length

made it a better substrate than others although the reason for this is unclear. Moreover, JMJD6 appeared to preferably hydroxylate Lys^{36} among its three targets (Lys^{33}, Lys^{34}, and Lys^{36}) in RBM; the other two lysine residues (Lys^{37} and Lys^{39}) were not targets of JMJD6 (Figure 3.17).

3.7. JMJD6 Hydroxylates Lys^{171} of the Tumour Suppressor VHL

Recently, it was reported that JMJD6 modifies tumour suppressor von Hippel-Lindau (VHL) protein (18). It was shown that knockdown of *JMJD6* in human JEG3 choriocarcinoma cell-lines increases the level of HIF-1α whereas decreasing VHL levels and *vice versa* (18). The same experiment was performed with JEG3 choriocarcinoma cell lines pre-exposed to a lysyl-hydroxylase inhibitor, minoxidil (18). VHL levels inside cells were found to be decreased upon minoxidil treatment. Based on this result, it was postulated that VHL is more stable inside cells when it is hydroxylated by JMJD6 (18). However, no evidence for hydroxylation by JMJD6 of any of the lysine residues of VHL was shown (18).

Experiments were then conducted in this study to determine whether JMJD6 can hydroxylate any of the lysine residues of VHL and if so, which lysine residue. To investigate, we tested fragments of VHL protein against $JMJD6^{\Delta 363\text{-}403}$ using hydroxylation assays. In order to carry out this study, three peptide-fragments from VHL protein ($VHL_{154\text{-}165}$: PVYTL**K**ERCLQV, $VHL_{166\text{-}177}$: VRSLV**K**PENYRR, and $VHL_{189\text{-}200}$: EDHPNVQ**K**DLER) spanning the three lysine residues within the peptide sequences were synthesized. The peptides were then tested against $JMJD6^{\Delta 363\text{-}403}$. MALDI-TOF analyses of the JMJD6-treated peptides revealed the presence of a hydroxylated species (peak with +16 Da shift) only in case of $VHL_{166\text{-}177}$, not in case of others (Figure 3.24). This result indicated that JMJD6 perhaps hydroxylated Lys^{171} upon incubation in presence of Fe(II) and 2OG. Hydroxylation assays were also performed using the alanine variant of $VHL_{166\text{-}177}$K171A and the wild-type $VHL_{166\text{-}177}$ in presence of 2,4-PDCA (a potent JMJD6 inhibitor, **Chapter 05**). The MALDI-TOF results revealed complete ablation of the

hydroxylated species in both cases (Figure 3.25). These results support Lys^{171} of VHL being a new target of JMJD6. In order to confirm, JMJD6-treated wild-type $VHL_{166-177}$ was subjected to LC-MS analysis. LC-MS/MS analysis of the fragmented product further confirmed that JMJD6 indeed hydroxylates Lys^{171} of VHL in the $VHL_{166-177}$ peptide (Figure 3.26).

Analysis of relative position of Lys^{171} in the reported VHL structure shows that the Lys^{171} position is completely exposed toward the exterior of the protein (Figure 3.24). Thus the overall results are consistent with the proposal of endogenous interaction between JMJD6 and VHL (18).

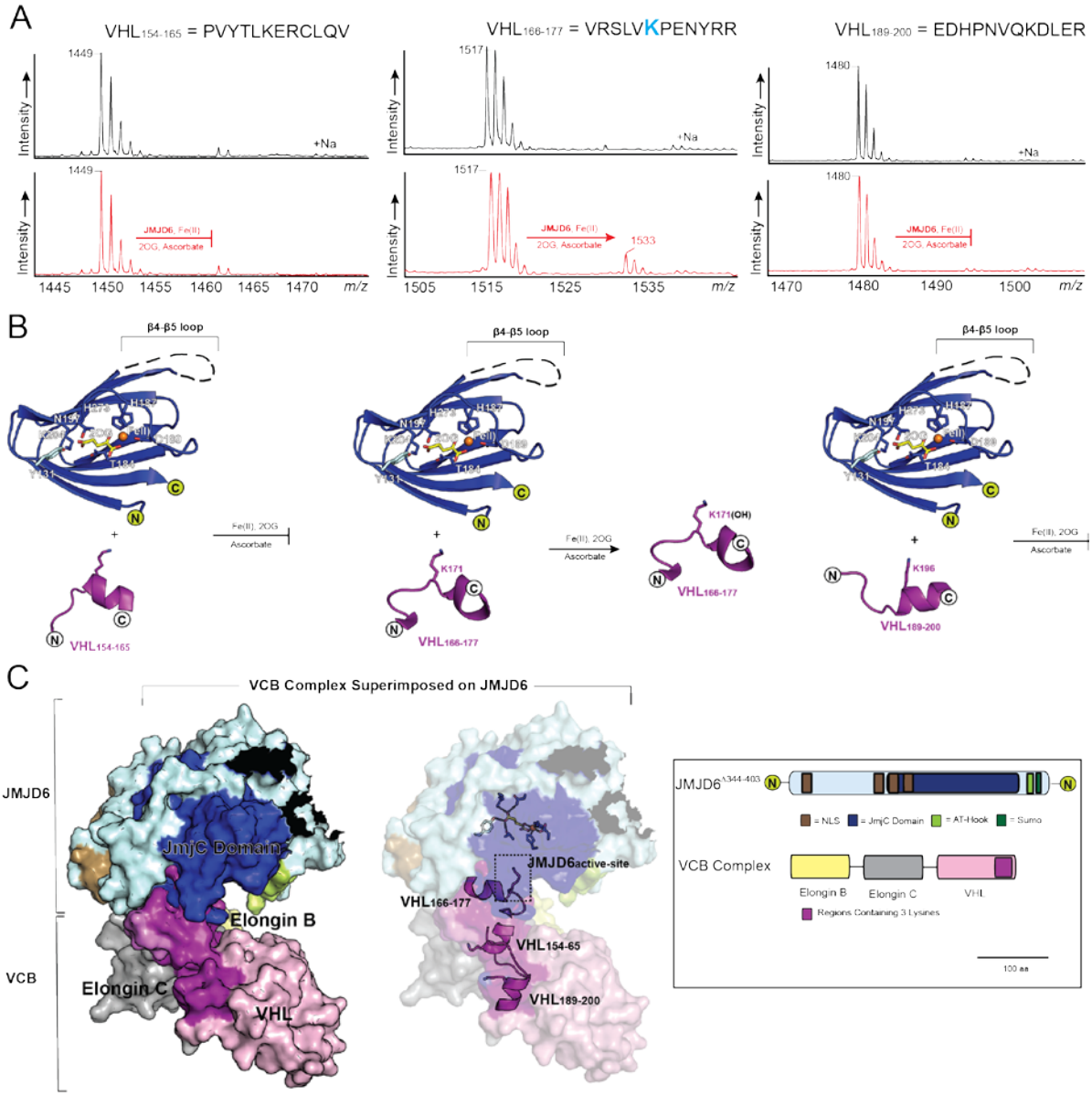

FIGURE 3.24. **Investigations of VHL as a substrate of JMJD6.** (A) MALDI-TOF mass spectra show that JMJD6-catalyzed modification occurs only on $VHL_{166-177}$, but not on $VHL_{154-165}$ or $VHL_{189-200}$. (B) Modelled cartoon representation showing the interactions between JMJD6 and $VHL_{166-177}$; structures used to model this interaction are a crystal structure of $JMJD6^{\Delta344-403}$.Fe(II).2OG complex (**Chapter 04**) and a crystal structure of VHL in complex with elongin B and elongin C (VCB complex) (PDB: 1VCB). (C) Surface and cartoon views of crystal structure of VHL (PDB: 1VCB) superimposed on $JMJD6^{\Delta344-403}$.Fe(II).2OG show that the position of Lys^{171} is exposed on the surface of VHL structure

(C). Colour coding: DSBH and active-site residues of JMJD6 as blue, 2OG as yellow, Fe(II) as orange sphere, VHL peptides and lysines as purple.

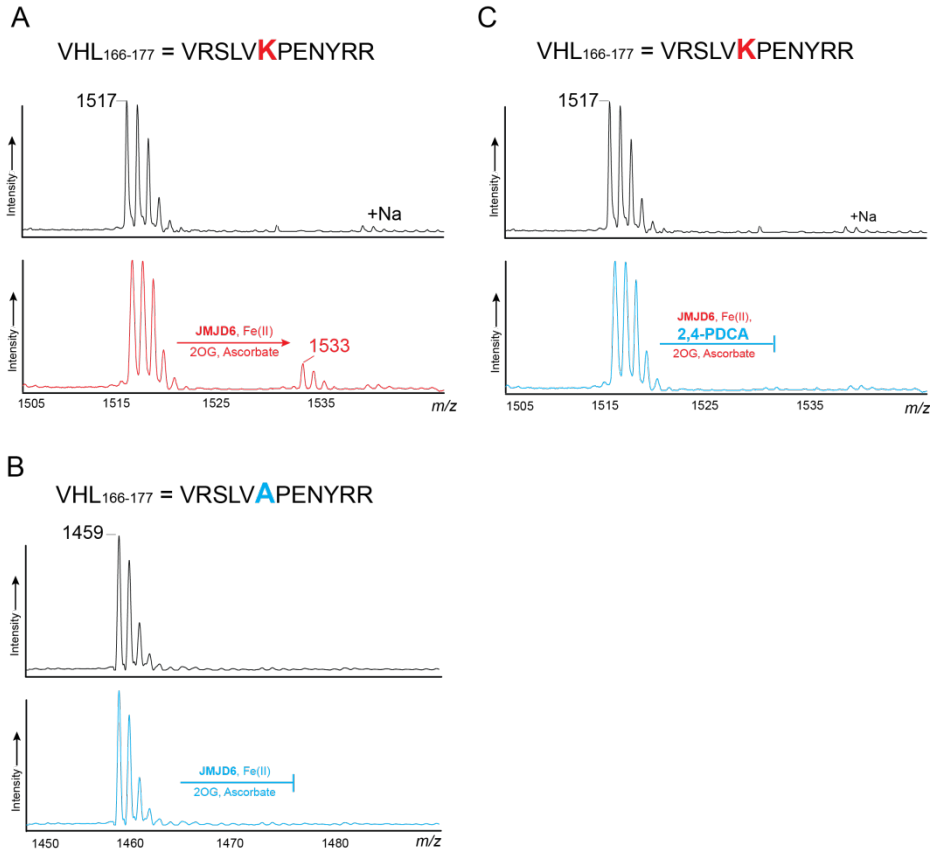

FIGURE 3.25. **Alanine scanning of VHL$_{166-177}$.** (A) MALDI-TOF spectra of JMJD6-treated wild-type VHL$_{166-177}$ shows a peak corresponding +16 Da shift in mass, which completely disappeared in case of (B) VHL$_{166-177}$K171A and (C) VHL$_{166-177}$ in presence of a JMJD6-inhibitor 2,4-PDCA. Experiments were carried out following the hydroxylation assay procedures described in Chapter 10.

A

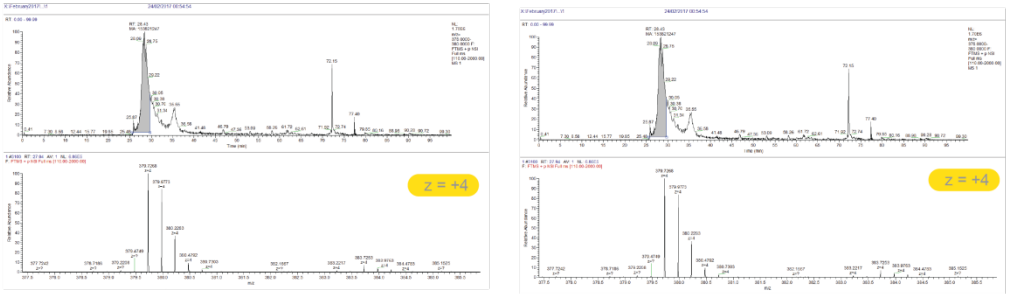

B

#	b (2+)	c (2+)	Seq	y (2+)	z (2+)	#
1	50.54	59.05	V			12
2	129.17	137.18	R	708.75	701.25	11
3	171.59	180.66	S	631.05	623.18	10
4	228.16	237.29	L	587.62	579.68	9
5	278.84	286.81	V	530.64	523.05	8
6	342.43	351.28	K	481.76	473.17	7
7	391.30	399.45	P	417.71	409.34	6
8	455.95	463.96	E	369.32	360.45	5
9	512.98	521.02	N	304.66	296.29	4
10	594.58	602.57	Y	247.25	239.27	3
11	672.60	680.69	R	165.65	157.91	2
12			R	88.06	79.55	1

#	b (2+)	c (2+)	Seq	y (2+)	z (2+)	#
1	50.54	59.05	V			12
2	128.59	137.10	R	717.40	708.91	11
3	172.10	180.62	S	638.63	631.12	10
4	229.19	237.16	L	595.48	586.68	9
5	278.18	286.30	V	539.29	530.80	8
6	350.23	359.18	K(+16.00)	489.36	481.24	7
7	399.32	407.44	P	418.41	409.47	6
8	463.28	471.79	E	368.45	360.49	5
9	521.08	528.82	N	305.30	296.38	4
10	601.83	610.76	Y	247.23	239.20	3
11	680.16	688.61	R	166.11	158.00	2
12			R	88.06	79.55	1

C

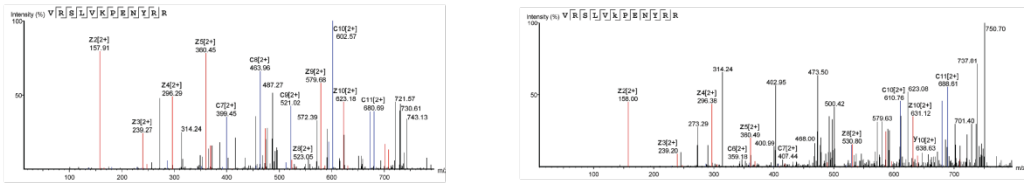

D

-JMJD6

```
  1  MPRKAASPEE AAGEPGPEEM EAGRPRPVLR SVNSREPSQV IFCNRSPRVV LPLWLNFDGE PQPYPILPPG TGRRIHSYRG
 81  HLWLFRDAGT HDGLLVNQTE LFVPSLNVDG QPIFANITLP VYTLKERCLQ VVRSLVKPEN YRRLDIVRSL YEDLEDYPSV

161  RKDIQRLSQE HLESQHLEEE P
```

+JMJD6

```
  1  MPRKAASPEE AAGEPGPEEM EAGRPRPVLR SVNSREPSQV IFCNRSPRVV LPLWLNFDGE PQPYPILPPG TGRRIHSYRG   HIDROXLYS (+16.00)
 81  HLWLFRDAGT HDGLLVNQTE LFVPSLNVDG QPIFANITLP VYTLKERCLQ VVRSLVKPEN YRRLDIVRSL YEDLEDYPSV

161  RKDIQRLSQE HLESQHLEEE P
```

FIGURE 3.26. **JMJD6 hydroxylates Lys^{171} of VHL (**VRSLVKPENYRR**)**. (A) LC-MS analysis of peptide VHL$_{166\text{-}171}$ shows peak with +16 Da shift only in presence of JMJD6. (B) PEAKS 8.0 generated ions *b, y* (CID) and *c, z* (EID) of the fragmented peptides show hydroxylated-Lys^{171} in the presence but not in the absence of JMJD6. (C) Spectra of the fragmented ions that correspond to the ion table. (D) PEAKS 8.0 generated sequence of full-length VHL protein also identifies the Lys^{171} as hydroxylated. Experiments were carried out following the hydroxylation assay procedures described in Chapter 10.

3.8. Evidence that JMJD6 Hydroxylates Lys^{382} of p53

p53 is accumulated in cells in response to genotoxic stresses and promotes transcription of a plethora of genes (73). The anti-tumorigenic activity of these gene-products is mediated by various cellular activities including cell cycle arrest, apoptosis, and cellular senescence (73). Balancing the activity of p53 is a decisive factor in determining cell life and death (73).

In 2014, it was reported that JMJD6 interacts with the tumor suppressor p53 (17). The catalytic activity of JMJD6 was reported to be essential to maintain the balance between the activating and suppressing role of p53 (17). It was shown that p53 is hydroxylated inside HCT116 cells. The level of hydroxylated p53 was reported to be increased (~6 fold) with the overexpression of JMJD6. Data from both MS and MS/MS showed that JMJD6 catalyses the hydroxylation of Lys^{382} of p53 in an Fe(II)- and 2OG-dependent manner.

It was thus of interest to test if JMJD6 protein, purified in this study, can accept p53 as a substrate. A fragment of p53 protein corresponding to residues 381-393 (p53: K<u>K</u>LMFKTEGPDSD) was tested with JMJD6$^{\Delta 363\text{-}403}$ (Figure 3.27). A shift (+16 Da) in mass was observed in the presence of JMJD6$^{\Delta 363\text{-}403}$ (Figure 3.27**A**), the intensity of which was more than that reported in the literature (17). Assays using JMJD6$^{\Delta 363\text{-}403}$ and p53$_{381\text{-}393}$K382A (K**A**LMFKTEGPDSD) were also performed with no hydroxylation being observed (Figure 3.27**B**). Similarly, hydroxylated peak was not observed when the assay was performed in the presence of 2,4-PDCA (a JMJD6 inhibitor, **Chapter 05**) (Figure 3.27**C**). Together, these results suggest JMJD6-dependent hydroxylation of p53$_{381\text{-}393}$, likely on residue Lys^{382}. MS/MS analysis of the substrate peptide after treatment with JMJD6$^{\Delta 363\text{-}403}$ further confirmed that JMJD6$^{\Delta 363\text{-}403}$ hydroxylates Lys^{382}.

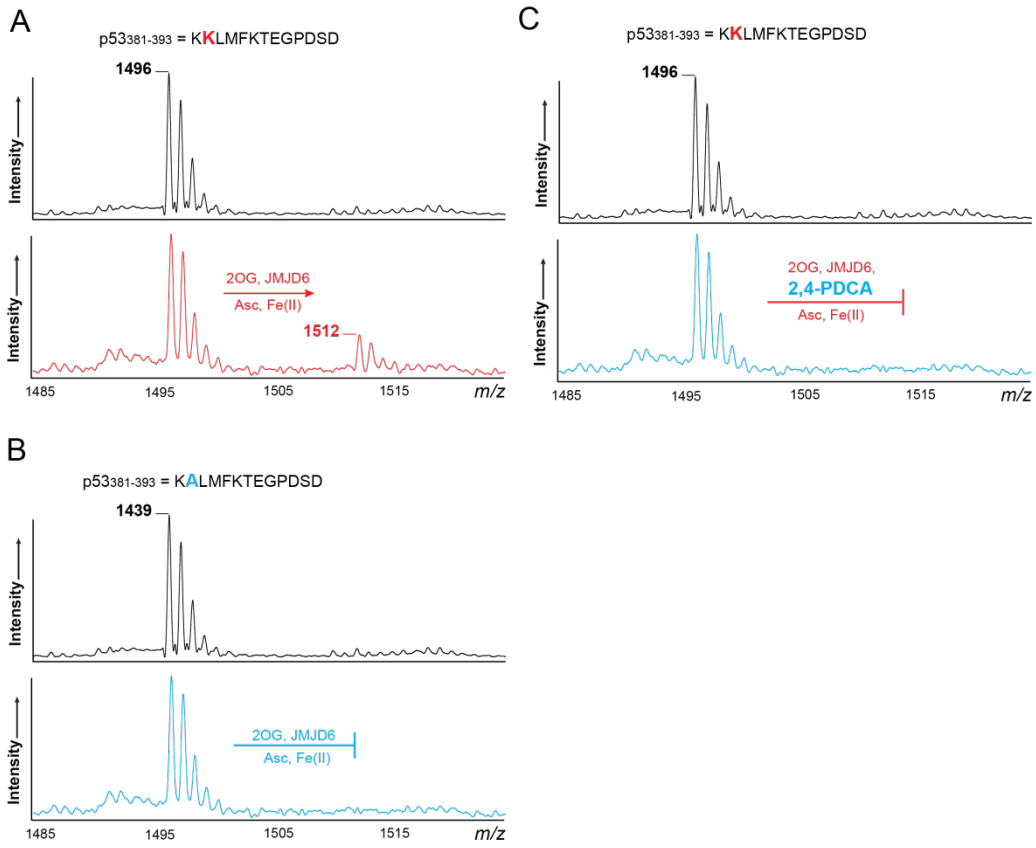

FIGURE 3.27. **Evidence of JMJD6-catalysed hydroxylation of Lys^{382} of p53**. MALDI-TOF spectra of JMJD6-treated (A) p53$_{381-393}$ (KKLMFKTEGPDSD), (B) p53$_{381-393}$K382A (K**A**LMFKTEGPDSD), and (C) p53$_{381-393}$ in presence of the JMJD6-inhibitor 2,4-PDCA suggesting that JMJD6-catalysed hydroxylation is specific to Lys^{382}, but not to any other residues. Experiments were carried out following the hydroxylation assay procedures described in Chapter 10.

3.9. JMJD6 Hydroxylates Lys^{252} and Lys^{257} of ERα

In 2014, JMJD6 was also reported to catalyse the removal of an *N*-methyl group from di-methylated (asymmetrically) Arg^{260}(me2a) within the estrogen receptor α (ERα) (30). It was therefore of interest to test whether JMJD6 enzyme produced in this study could reproduce the demethylation of the methylated Arg^{260} of ERα. To test this, a demethylation assay was carried out using a fragment of ERα corresponding to amino acid residues 251-262, where the assay procedure followed previous work (32). JMJD6-treated ERαR260(me2a)$_{251\text{-}262}$ was analysed by MALDI-TOF MS. No evidence for demethylation was observed (Figure 3.28**A**). A peptide fragment with symmetrically di-methylated arginine (ERαR260(me2s)$_{251\text{-}262}$) was also tested; the same result was observed, *i.e.*, no demethylation (Figure 3.28**B**). Further investigations were therefore carried out to investigate the functional link between JMJD6 and ERα.

In view of the initial negative findings of this study with respect to demethylation, it was of interest to test whether JMJD6 might hydroxylate the lysine residue(s) (Lys^{252} or Lys^{257} or both) around the targeted Arg^{260}. To test this hypothesis, peptide fragments corresponding to amino acid residues 251-262 of ERα including wild-type (MKGGIRKDRRGG) and alanine variants (M**A**GGIR**A**DRRGG **A**KGGIRKDRRGG, **A**KGGIR**A**DRRGG, and **AA**GGIRKDRRGG) were synthesized. MALDI-TOF analyses of wild-type and alanine variants of ERα$_{251\text{-}262}$ confirmed that JMJD6 can hydroxylate either Lys^{252} or Lys^{257} of ERα with a preference towards Lys^{252} in an Fe(II)- and 2OG-dependent manner (Figure 3.29).

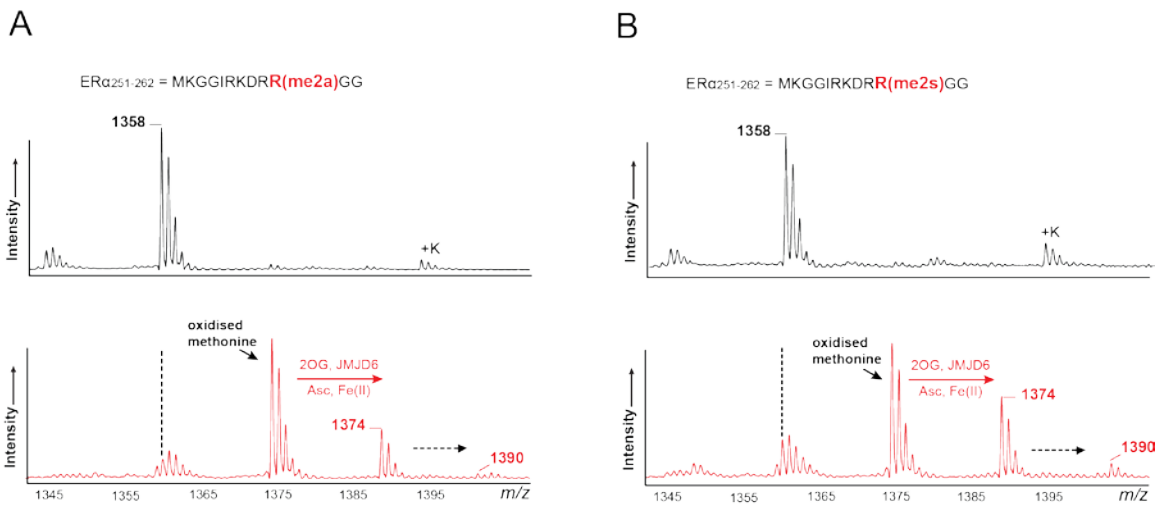

FIGURE 3.28. **Investigation of JMJD6-mediated demethylation on previously reported ERα peptides**. MALDI-TOF spectra of JMJD6-treated (A) ERαR260(me2a)$_{251-262}$ (MKGGIRKDRR(me2a)GG) and (B) ERαR260(me2s)$_{251-262}$ (MKGGIRKDRR(me2s)GG) revealed peaks with only +16 Da shifts, but no peak with -14 Da. Experiments were carried out following the demethylation assay procedures described in Chapter 10.

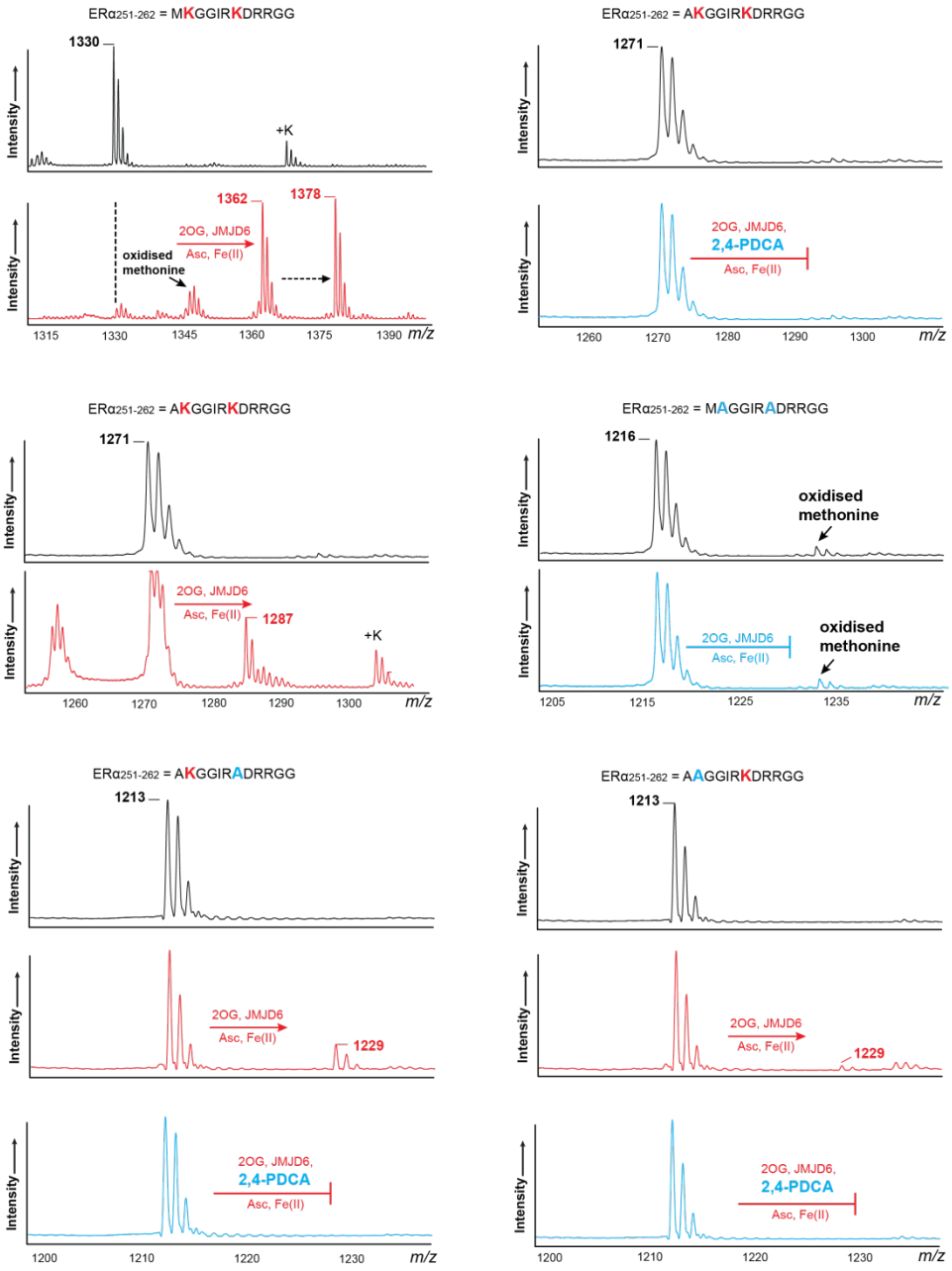

FIGURE 3.29. **JMJD6 hydroxylates Lys^{252} and Lys^{257} of ERα**. MALDI-TOF spectra of JMJD6-treated wild-type as well as alanine variants of ERα$_{251-262}$ indicating that JMJD6 hydroxylates both Lys^{252} and Lys^{257}**,** but preferentially Lys^{252}. Hydroxylated peaks corresponding to Lys^{252} and Lys^{257} disappeared in presence of a potent JMJD6 inhibitor, 2,4-PDCA. Experiments were carried out following the hydroxylation assay procedures described in Chapter 10.

3.10. Is HSP70 a New Substrate of JMJD6?

Heat-shock protein of 70 kDa (HSP70) is a molecular chaperone with a key role in preventing other proteins from misfolding (74). In 2015, another striking role of HSP70 in transcription was proposed by Gao *et al.*, when JMJD6-mediated demethylation of a highly conserved *N*-methylated arginine residue (R469) in HSP70 was reported to be a key factor in regulating the transcriptional regulation property of HSP70 (32). *In vitro* and *in vivo* results indicated that JMJD6 can catalyse the removal of a methyl group from R469(me1) of *N*-terminally biotinylated HSP70R469(me1)$_{463\text{-}475}$ (32).

The same fragment of HSP70 without biotinylation at the *N*-terminus was tested against three variants of JMJD6 using the demethylation assay. However, no evidence for demethylation by any of the JMJD6 proteins was observed (Figure 3.30). Demethylation attempts were also made using higher amount of JMJD6; yet no demethylation was observed (Figure 3.30).

These results suggest that JMJD6 does not catalyse HSP70 demethylation, at least under the conditions used in this study, which included use of a peptide fragment.

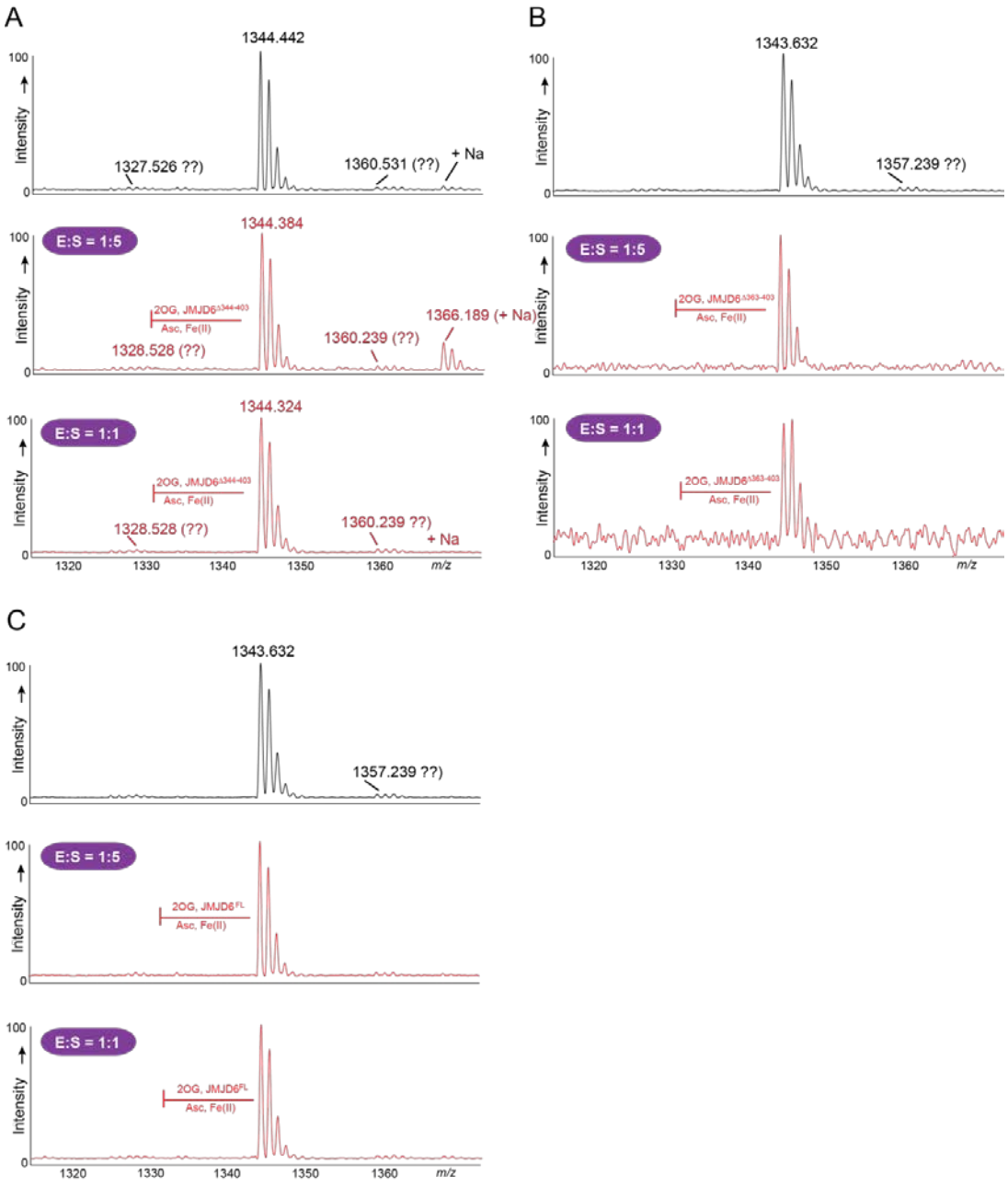

FIGURE 3.30. **Testing for the reported demethylation activity of JMJD6 on peptide fragment of HSP70, HSP70R469(me1)$_{463-475}$: GIPPAPR(me1)GVPQIE**. MALDI-TOF spectra revealing no evidence for demethylation on HSP70R469(me1)$_{463-475}$, as potentially catalysed by (A) JMJD6$^{\Delta 344-403}$, (B) JMJD6$^{\Delta 363-403}$, and (C) JMJD6^{FL}. Experiments were carried out following the demethylation assay procedures described in Chapter 10.

Table 3.3. List of peptides used in this study with observed position of modification(s) (underlined) catalysed by JMJD6

Peptide	Protein	Accession Code	Sequence	Modification
$H3_{1-25}$	H3	P68431	ARTKQTARKSTGGKAPRKQLATKAA	+16
$H3R2(me2s)_{1-25}$			AR(me2s)TKQTARKSTGGKAPRKQLATKAA	+16
$H3K9(me1)_{1-17}$			AR(me2s)TKQTARKSTGGKAPRKQLATKAA	+16
$H4_{1-15}$	H4	P62805	SGRGKGGKGLGKGGA	+16
$H4_{1-30}$			SGRGKGGKGLGKGGAKRHRKVLRDNIQGIT	+16
$H4R3(me2s)_{1-15}$			SGR(me2s)GKGGKGLGKGGA	+16
$H4R3(me2s)_{1-19}$-Biotin			SGR(me2s)GKGGKGLGKGGAKRHK-Biotin	+16
$H4R3(me2s)_{1-30}$			SGR(me2sme2s)GKGGKGLGKGGAKRHRKVLRDNIQGIT	+16
$LUC7L2_{267-278}$	LUC7L2	Q9Y383	NPKR SRSREHRR	+16
$U2AF65_{21-35}$	U2AF65	P26368	ENRHRKRSHSRSRSR	+16
$U2AF65_{30-46}$			SRSRSRDRKRRSRSRDR	+16
$U2AF65_{55-70}$			RDRRRRSKPLTRGAK	+16
$CROP_{311-325}$	CROP/ LUC7L3	Q95232	SRDHKRSRSRERRRS	+16
$CROP_{341-355}$			RKHRSRSRDRRRSKS	+16
$CROP_{357-370}$			DRKSYKHRSKSRDR	+16
$LUK7L1_{287-298}$	LUC7L1	Q9NQ29	SRERRKL SRSRSR	+16
$SRSF11_{271-282}$	SRSF11	Q05519	SRSRRRSHSKSR	+16
$SRSF11_{286-298}$			RSKSPRRRRSHSR	+16
$SRSF11_{298-310}$			ERGRRSRSTSKT	+16
$SRSF11_{347-360}$			RSRSGTRSPKKPSR	+16
$SRSF11_{358-372}$			RSPKRKLSRSPSPR	+16
$RBM39_{31-42}$	RBM39	Q14498	RSKKRKKSKS RS	+16
$RBM39_{38-50}$			SKSRSRSHERKRS	+16
$RBM39_{49-61}$			RSKSKERKRSRD	+16
$RBM39_{71-82}$			RKRSRSKERRRS	+16
$RBM_{121-132}$			SRRRSRSKSPFR	+16
$Acinus_{447-460}$	Acinus S'	Q9UKV3	PRSRSRSRDRRRKE	+16
$Acinus_{595-604}$			KRHSRSRSRS	+16
$PUF60_{495-510}$	PUF60	Q9UHX1	RVIIYQEKQGEEEDAE	No modification
$VHL_{154-165}$	VHL	P40337	PVYTLKERCLQV	No modification
$VHL_{166-177}$			VRSLVKPENYRR	+16
$VHL_{189-200}$			EDHPNVQKDLER	No modification
$P53_{381-393}$	P53	P04637	KKLMFKTEGPDSD	+16
$ERαR260(me2s)_{251-262}$	ERα	P03372	MKGGIRKDRR(me2s)GG	+16
$ERαR260(me2a)_{251-262}$			MKGGIRKDRR(me2a)GG	+16
$ERα_{251-262}$			MKGGIRKDRRGG	+16
$HSP70R469(me1)_{463-475}$	HSP70	P0DMV8	GIPPAPR(me1)GVPQIE	No modification

CHAPTER 04: Crystallisation and Structural Analysis of JMJD6

4.1. Introduction

The first crystal structure of JMJD6 was reported by Mantri *et al.* in 2010 (PDB: 3K2O) having monoclinic space group $P2_1$ and two molecules in the asymmetric unit (ASU) (36) (Figure 4.1**A**). In this work, SeMet-derivatised JMJD6 (aa 1-343) was crystallised using the sitting-drop vapour diffusion method, yielding a crystal which diffracted to 1.7 Å resolution. Attempts were also made to crystallise full-length JMJD6 (aa 1-403), but these were unsuccessful, possibly due to the disordered *C*-terminal regions comprising residues 340-403 (including the polyserine domain) (36). In this structure, an acetate molecule was observed bound in the predicted 2OG (2-oxoglutarate) *C*-5 carboxylate binding-site (Figure 4.1**A**). Subsequently, two more crystal structures of JMJD6 were determined by Hong *et al.*: one proposed to be in complex with Fe(III) (PDB: 3LD8) (Figure 4.1**B**) and another in complex with Fe(III) and 2OG (PDB: 3LDB) (Figure 4.1**C**) (note the redox state cannot be defined using crystallographic data alone) (75). The authors attempted to determine the structure of the *C*-terminal regions including the polyserine domain by crystallizing JMJD6 with Fab fragment obtained from a JMJD6-specfic monoclonal antibody. The resulting structures were refined to 2.7 Å (PDB: 3LD8) and 2.8 Å (PDB: 3LDB) resolution, respectively. However, the *C*-terminal regions were disordered. Further, in the JMJD6.Fe(III).2OG complex, the 2OG could not be modelled confidently due to its low occupancy (75). Thus, the available crystal structures do not provide a complete picture of the coordination chemistry between JMJD6 and its co-factor and cosubstrate. To date, there is no structural information regarding substrate recognition by JMJD6, highlighting the challenge that JMJD6 poses for structural characterization.

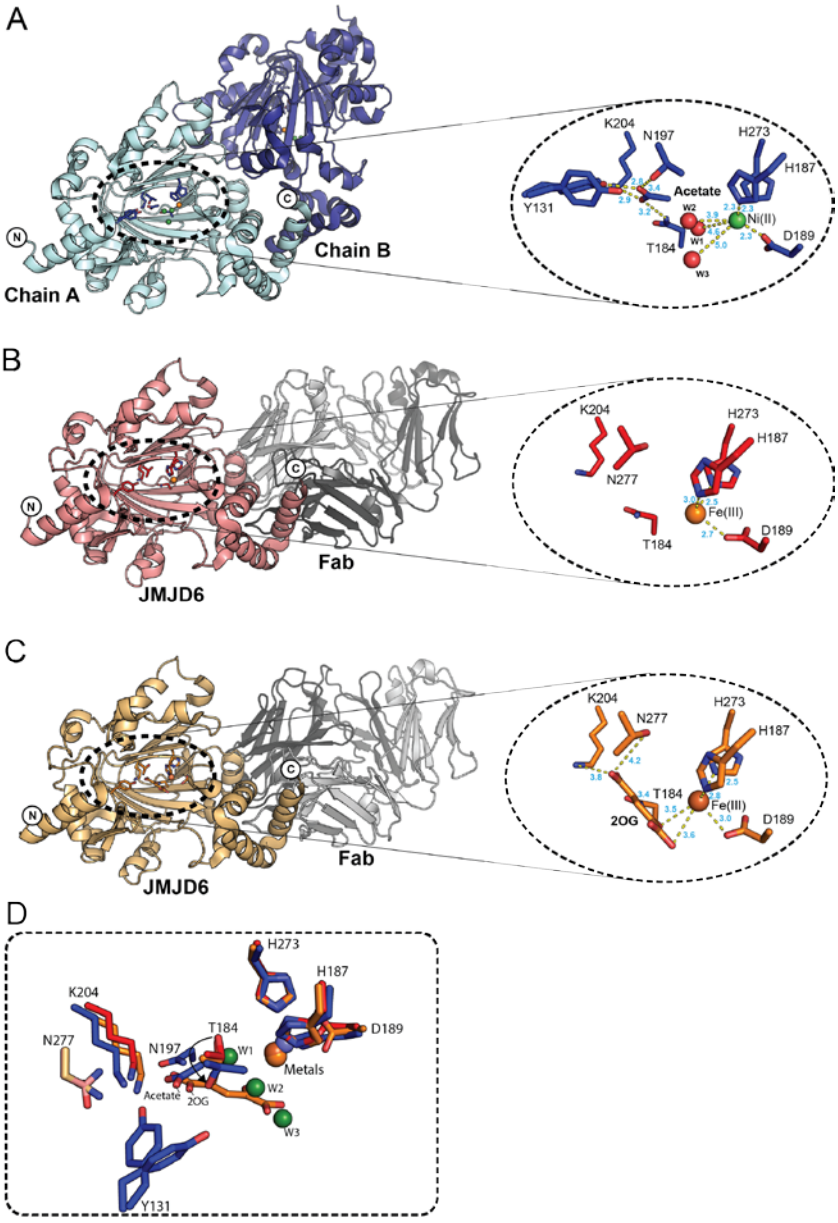

FIGURE 4.1. **Views from previously described crystal structures of JMJD6**. A crystal structure of a truncated version of (A) JMJD6 (aa1-343) in complex with Ni(II) and an acetate molecule. Crystal structures of JMJD6-Fab complexes containing (B) only Fe(III) (PDB: 3LD8) and (C) Fe(III) and 2OG (PDB: 3LDB) bound at the JMJD6 active site. (D) The positions of 2OG and residue Thr^{184} do not fully support the presence of the 2OG in the active site of the JMJD6.Fe(III).2OG structure (C). Note, the metal oxidation states were proposed.

The objectives of the crystallographic work described in this Chapter were therefore to determine the crystal structure of (i) a truncated version of JMJD6 (aa 1-343, JMJD6$^{\Delta 344-403}$) in complex with its co-factor Fe(II) and cosubstrate 2OG; (ii) JMJD6 in complex with different transition metals [*e.g.* Mn(II) and Ni(II)] and structural analogues of 2OG (e.g. *N*-oxalylglycine, NOG) to investigate possible conformational changes that may arise due to changes in the active-site metal and ligand; (iii) full-length JMJD6 (aa 1-403, JMJD6^{FL}); (iv) a truncated version of JMJD6 (aa 1 to 362, JMJD6$^{\Delta 363-403}$) retaining the polyserine (polyS) domain at its *C*-terminus, which was used to carry out the kinetic studies (**Chapter 03**).

4.2. Metal Screening by Differential Scanning Fluorimetry (DSF)

The use of transition metals to achieve catalytically inert conditions during crystallisation of metallo-enzymes is widely used (8). To identify a suitable transition metal for JMJD6 crystallisation, a metal-screening study was carried out. For this purpose, differential scanning fluorimetry (DSF) was used to investigate the binding properties of JMJD6 with transition metals including Co(II), Cu(II), Fe(II), Mn(II), Ni(II), and Zn(II) (**Chapter 10**).

DSF is widely used for investigating protein stability owing to its rapid and simple procedure (76). Furthermore, the amount of protein required for DSF is small (approx. 1 mg/96 well plate). In principle, proteins become unfolded upon exposure to increased temperature. In the DSF method, a fluorescent dye binds to hydrophobic regions of protein that are exposed upon unfolding. The unfolding can be detected by a change in fluorescence using a simple real-time PCR instrument. The change in fluorescence is plotted as a function of temperature to determine the inflection point (T_m) of the transition curves. The T_m (or stability) of a particular protein typically increases with metals, small molecules or peptides (76).

In this study, a previously reported procedure was modified to carry out metal-screening/T_m shift of JMJD6 (**Chapter 10**). EDTA-treated JMJD6 (JMJD6^{FL} and

JMJD6$^{\Delta 344\text{-}403}$) was used. In the case of JMJD6$^{\Delta 344\text{-}403}$, Cu(II) appeared to stabilize JMJD6 more than the other metals tested (Table 4.1, Figure 4.2). Conversely, JMJD6^{FL} was found to be mostly stabilized by Co(II) (Table 4.1, Figure 4.2).

Table 4.1. Results of metal-screening using DSF. 2 µM JMJD6 was incubated with various transition metals in 200 mM HEPES, pH 7.0 and the SYPRO dye solution (1X in buffer). The fluorescence readings were taken in steps of 1°C every minute between 25°C and 80°C (**Chapter 10**). Values represent mean ± standard deviation (SD).

	JMJD6$^{\Delta 343\text{-}403}$ (°C)	JMJD6^{FL} (°C)
No metal	47.9 ± 0.35	48.1 ± 0.41
Co(II)	56.4 ± 1.8	55.5 ± 0.34
Cu(II)	58.5 ± 0.42	53.4 ± 0.14
Fe(II)	50.6 ± 0.86	49.7 ± 0.6
Mn(II)	46.4 ± 0.58	48.7 ± 0.1
Ni(II)	54.0 ± 0.6	55.3 ± 0.17
Zn(II)	52.3 ± 0.4	52.0 ± 0.2

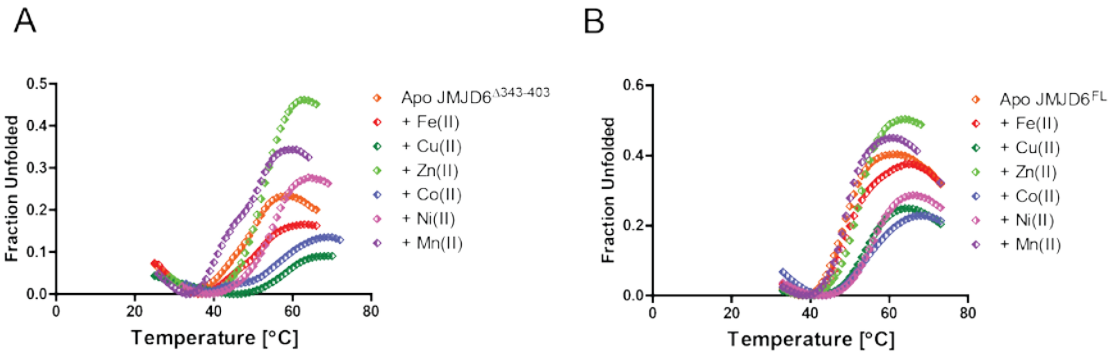

FIGURE 4.2. **JMJD6 metal screening assay using differential scanning fluorimetry**. Melting curves showing the induced stabilization of both (A) truncated and (B) full-length JMJD6 in the presence of various transition metals. Values represent mean ± standard deviation (SD).

4.3. Metal Screening by ITC

Isothermal titration calorimetry (ITC) was used to test the binding-thermodynamics of various metals with JMJD6. ITC is useful for investigating the thermal stability of proteins in the presence of metals, small molecules, and biomolecules (77). Given that JMJD6 already had shown variable affinities toward various transition metals (as shown by DSF), binding affinities of the metals were further analysed using ITC. The findings from DSF were consistent with the results obtained from ITC in that higher T_m is indicative for lower K_D. JMJD6 was found to bind Ni(II) and Cu(II) more strongly than Co(II) (K_D values of 2.41, 3.29, and 62.1 μM, respectively) (Table 4.2, Figure 4.3). Due to the tendency of Fe(II) to oxidize to Fe(III) in the presence of molecular oxygen, it was not feasible to carry out the corresponding experiment with Fe(II). The ITC results indicate that binding of metals to JMJD6 is substantially enthalpically driven.

Table 4.2. K_Ds of various metals for JMJD6 determined by ITC. Experiments were carried out following the procedures described in Chapter 10. Values represent mean (n = 3) ± SD.

	K_D (μM)	ΔG (kcal mol^{-1})	ΔH (kcal mol^{-1})	-TΔS (kcal mol^{-1})
Ni(II)	2.41 ± 0.62	-7.69 ± 0.16	-21.3 ± 2.23	13.6 ± 2.31
Cu(II)	3.29 ± 0.07	-7.49 ± 0.007	-20.8 ± 0.71	13.3 ± 0.71
Co(II)	62.1 ± 1.84	-5.74 ± 0.014	35.0 ± 1.13	29.3 ± 1.13

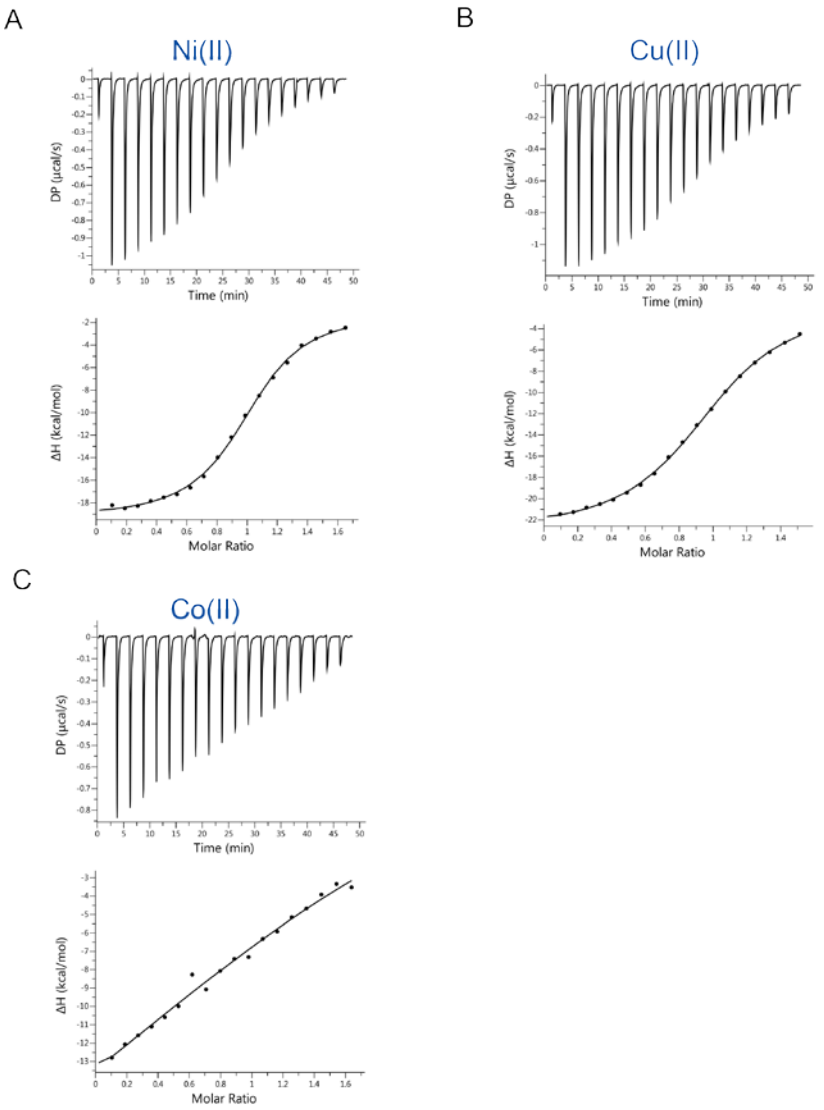

FIGURE 4.3. **ITC-based metal screening.** Isothermal calorimetric titration of binding of (A) Ni(II), (B) Cu(II), and (C) Co(II) with JMJD6. Experiments were carried out following the procedures described in Chapter 10.

4.4. Crystallisation of JMJD6

Crystallographic data collection, molecular replacement, and refinement for the crystal structures of JMJD6 described in this chapter were performed with the help of Dr. Michael A. McDonough (Chemistry Research Laboratory, University of Oxford), unless otherwise stated.

Attempts to crystallise JMJD6 protein started with a truncated construct, JMJD6$^{\Delta 344\text{-}403}$, that was previously crystallised by Mantri *et al.* (36). The protein used for these studies was purified according to the reported procedure (36); similar crystallisation strategies were used (36,75). Unfortunately, no suitable crystals were obtained using these conditions. Moreover, JMJD6 protein purified according to the reported procedure (36) was not very active (**Chapter 02**). Therefore, subsequent crystallographic studies used the proteins purified according to the optimized conditions (**Chapter 02**). Commercially available crystallisation broad screens, including Pact Premier, PEG Ion, Salt Rx, Crystal Screen, and Index were used for the crystallographic studies. In parallel to the crystallisation attempts with JMJD6$^{\Delta 344\text{-}403}$, attempts were made to crystallise full-length JMJD6^{FL} also.

4.4.1. Structure Determination of JMJD6$^{\Delta 344\text{-}403}$ in Complex with Ni(II) and 2OG

JMJD6$^{\Delta 344\text{-}403}$, purified using optimized conditions, was used for crystallisation by using the sitting-drop vapour-diffusion method (78). The complex of JMJD6.Ni(II).2OG was prepared by incubating JMJD6 (25 mg/mL) with approximately five fold excess of Ni(II) and 2OG on ice for one hour (**Chapter 10**). The crystallisation plates were prepared using an Art Robbins PHOENIX RE liquid dispenser with drops containing three different ratios of protein to crystallisation condition (*i.e.*, 2:1, 1:1, and 1:2, with drop volumes of 300 nL, 200 nL, and 300 nL, respectively). The first suitable crystallisation hit was obtained from the commercially available broad screen Crystal Screen (condition #30). Crystals appeared to grow in wells corresponding to the 2:1 ratio of protein: crystallisation buffer, which suggests a higher concentration of JMJD6 was required to induce crystal growth. Crystals were cryo-protected using a mixture of reservoir solution diluted with 20% glycerol (v/v) and subjected to synchrotron X-ray diffraction data collection at the Diamond Light Source (DLS). Although the crystals were of suitable size (~80x10 µM), they did not diffract well (4-5 Å resolution). The crystallisation conditions were then optimized with consideration of several crystallisation parameters, including pH of the

buffer, salt concentration, precipitant concentration, additive concentration, and incubation temperature.

The first crystal to diffract well was obtained from the optimised conditions: 0.1 M HEPES, pH 7.8, 0.9 M NaH_2PO_4, 0.7 M KH_2PO_4. The crystals grew after one week at 4 °C, and diffracted to a resolution of 3.0 Å. PHASER was used for molecular replacement (MR) (79) using JMJD6 (PDB: 3K2O) as a search model (36). A MR solution for structure of $JMJD6^{\Delta 344\text{-}403}$ was found in space group $P2_12_12_1$ with 4 molecules in the ASU (Figure 4.4**B**, Table 4.3). Structural models were improved by iterative cycles of manual building in COOT and crystallographic refinement in PHENIX (80).

Despite the relatively poor resolution data, the electron density maps were good enough to model Ni(II) (the oxidation state is assumed) at the metal centre and 2OG in the ligand-binding pocket (Figure 4.4). The octahedral coordination of Ni(II) was completed by the side chains of H187, D189, and H273, the C-1 carboxylate oxygen and C-2 ketone oxygen from 2OG, and a water molecule (Figure 4.4**C**). The residues responsible for binding the 2OG side chain at the active site were also visible. One of the oxygens of the 2OG C-5 carboxylate group appears to form hydrogen bonds to the side chains of residues Tyr^{131} (Y131) and Thr^{184} (T184) (Figure 4.4**C**). The other oxygen of the C-5 carboxylate appears to form hydrogen bonds with the side chains of Lys^{204} (K204) and the primary amide of Asn^{197} (N197) (Figure 4.4**C**).

Further attempts were made to obtain $JMJD6^{\Delta 344\text{-}403}$ crystals with better diffraction quality. Mn(II) and Fe(II) were also used in parallel to Ni(II). In particular, efforts were made to crystallise JMJD6 in complex with Fe(II) and 2OG. Crystallisation buffers were also optimized until crystals of better diffraction quality were obtained.

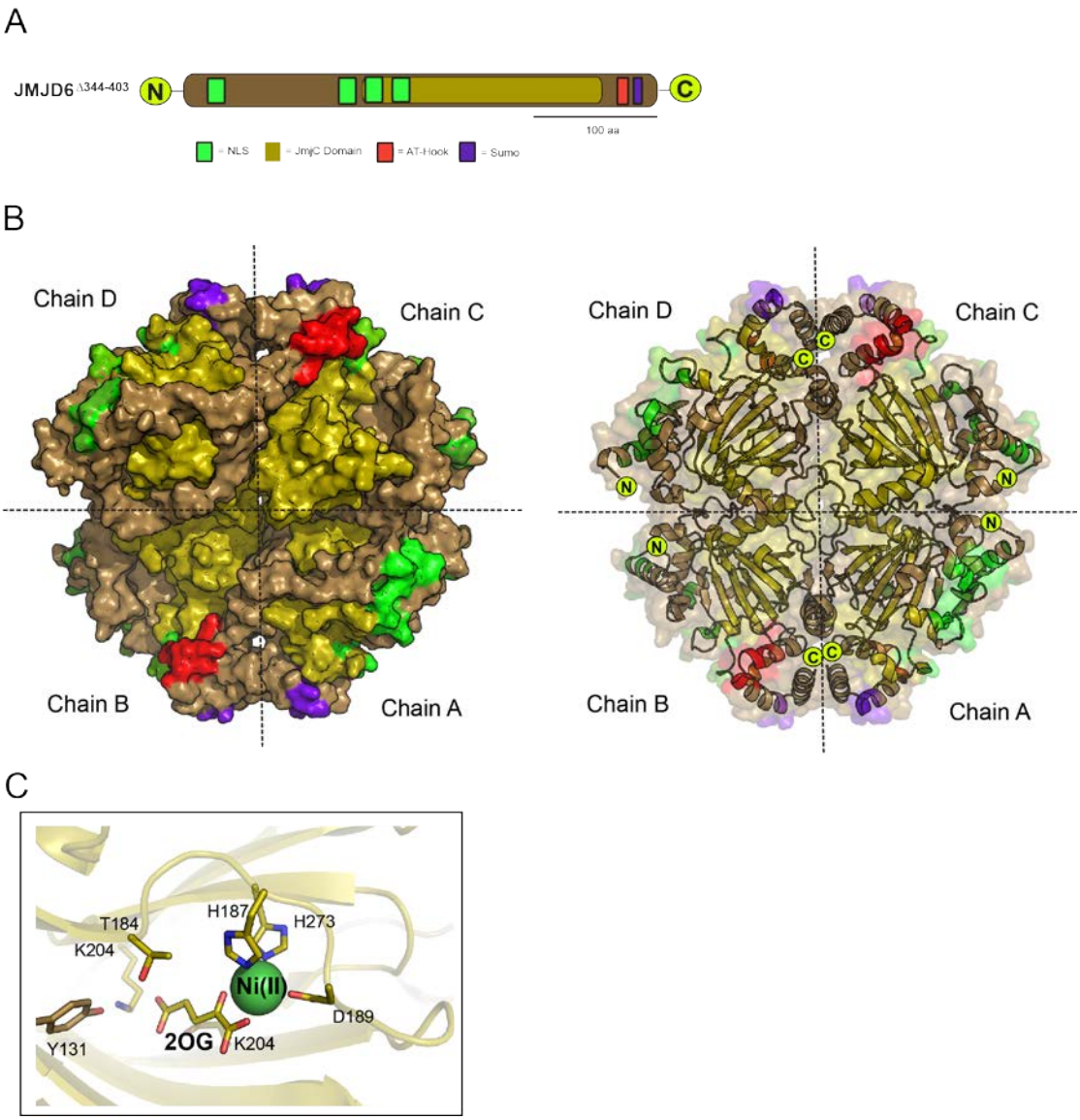

FIGURE 4.4. **Views from a crystal structure of JMJD6$^{\Delta 344\text{-}403}$ in complex with Ni(II) and 2OG**. (A) Domain architecture of JMJD6$^{\Delta 344\text{-}403}$. (B) Surface and cartoon views of a crystal structure of JMJD6$^{\Delta 344\text{-}403}$.Ni(II).2OG. (C) Close up view of the active-site including Ni(II) (green sphere), metal binding residues H187, D189, and H273 (olive and sand sticks), and 2OG (olive stick); 2OG appears to be bound in the active site with the help of residues Y131, T184, N197, and K204. NLS = nuclear localisation sequence, AT-hook = adenine-thymine rich hook/domain.

4.4.2. Structure Determination of JMJD6$^{\Delta 344\text{-}403}$ in Complex with Fe(II) and 2OG.

2OG oxygenases use Fe(II) and 2OG as a co-factor and cosubstrate, respectively, to enable catalysis (10). They enable activation of O_2 in order to modify a diverse range of primary substrates, which conjugates reacting with non-haem iron and cosubstrate 2OG to form the product(s), succinate, and CO_2 (10). From a mechanistic perspective, it is important to know how this superfamily of enzymes recognize their co-factor and cosubstrate. Although transition metals have been reported to displace the relatively weakly bound Fe(II) from the active sites of 2OG oxygenases and thereby forming a more stable complex, structures in complex with Fe(II) and 2OG reveal the catalytically relevant coordination chemistry of the catalytic site of 2OG oxygenases.

After numerous attempts, a crystal of JMJD6$^{\Delta 344\text{-}403}$ in complex with Fe(II) and 2OG was obtained using 0.1 M HEPES, pH 7.8, 0.7 M NaH_2PO_4, 0.9 M KH_2PO_4, 3% glycerol. The JMJD6$^{\Delta 344\text{-}403}$.Fe(II).2OG complex was formed by mixing the protein with Fe(II) and 2OG at a ratio of 1:5:5, respectively, under anaerobic conditions (**Chapter 10**). Crystals were grown by siting-drop vapour-diffusion method (78). In summary, JMJD6 protein (25 mg/mL) was mixed with a five-fold excess of Fe(II) [$(NH_4)_2Fe(SO_4)_2.6H_2O$] in crystallisation buffer equilibrated under anaerobic conditions. Next, a five-fold excess of 2OG was added to the enzyme/metal mixture. This mixture was then added to crystallisation buffer at a 1:1 ratio in the sitting drop wells of a 24-well crystallisation plate. The resulting crystals, which grew to a size of 50 x 50 µm after 2 weeks, diffracted to a resolution of 2.0 Å (Table 4.3). The diffraction data were automatically processed using Xia2/DIALS and a previously reported structure of JMJD6 (PDB: 3K2O) (36,79,80), resulting in a structure of truncated JMJD6 in the space group *$P12_11$* with 2 molecules in the ASU (Figure 4.5**B**, Table 4.3).

This structure revealed, for the first time, the catalytically relevant coordination chemistry at the active site of JMJD6; *i.e.*, with Fe(II) and 2OG bound at the active site. Structural features resembling the typical 2OG oxygenase 2-His-1-carboxylate metal-

binding motif were observed (Figure 4.5). The DSBH fold is composed of major and minor β-sheets (Figure 4.5**B**), as is observed in other 2OG oxygenases. A long βIV/βV loop/insert is present between residues Pro^{210} to Leu^{255} (P210-L255) (Figure 4.5**C**), an uncommon feature of the JMJD6 structure not observed in most of the 2OG oxygenases where this loop is usually shorter. Metal binding residues His^{187} and D^{189} are located in a loop between βII and βIII, while His^{273} is located in βVII (Figure 4.5**B**). The 2.0 Å resolution electron density maps clearly revealed that residues Tyr^{131}, Thr^{184}, Asn^{197}, and Lys^{204} are involved in 2OG binding (Figure 4.5**D**), consistent with the initial proposal made by Mantri *et al*., 2010 (36). These 2OG binding residues are also conserved throughout the 2OG oxygenase superfamily (8). Electron density within the active site also support the presence of Fe and 2OG (Figure 4.5**E**).

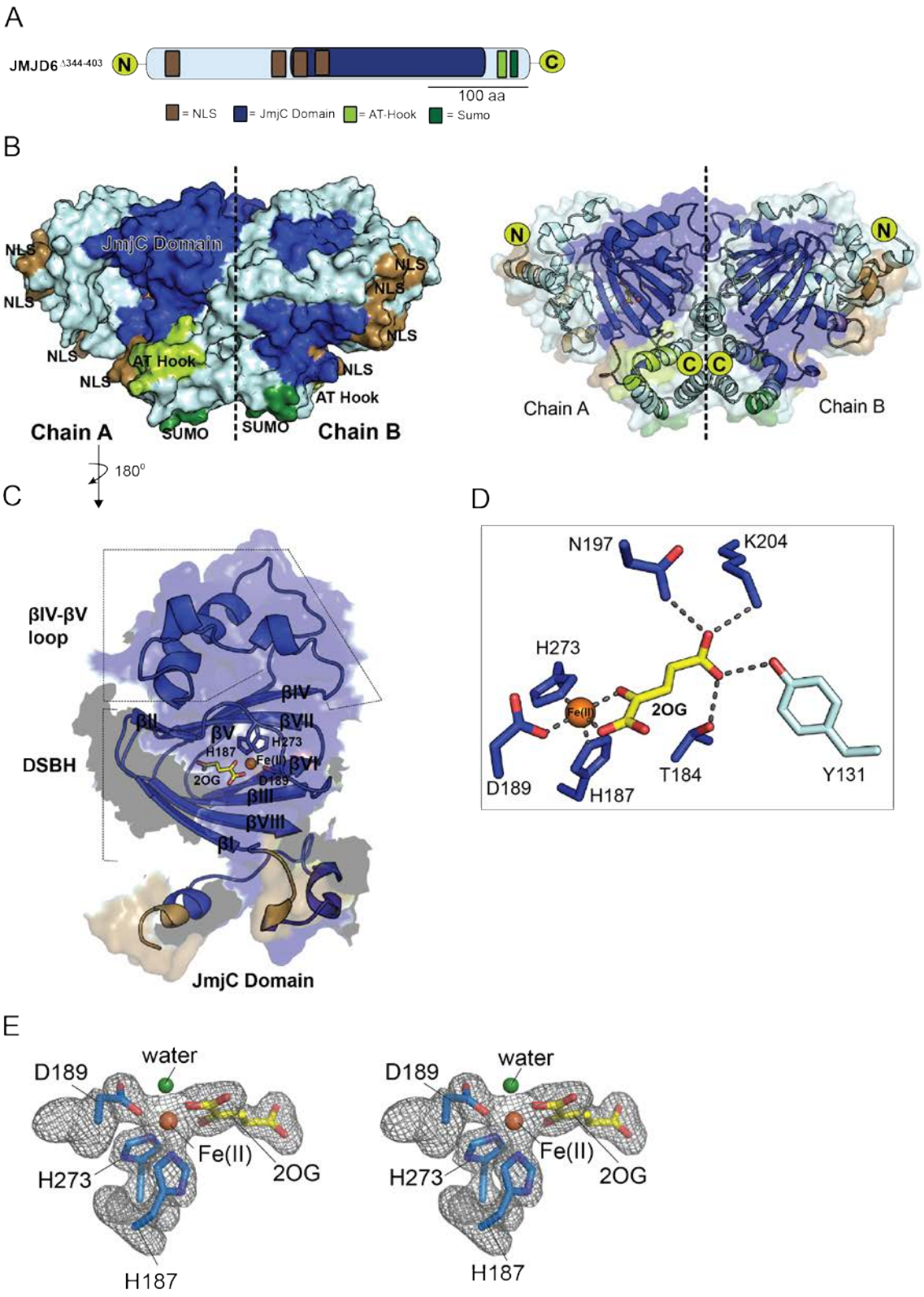

FIGURE 4.5. **Crystallographic studies of the JMJD6$^{\Delta 344\text{-}403}$.Fe(II).2OG complex**. (A) Domain architecture of the truncated version of JMJD6$^{\Delta 344\text{-}403}$. (B) Surface and cartoon representations of a crystal structure of JMJD6$^{\Delta 344\text{-}403}$.Fe(II).2OG complex; dotted lines

show the interfacial axis between two chains. (C) The JmjC domain, comprising the DSBH fold and a long βIV/βV-insert, is shown in overlaid cartoon and surface views. (D) Stick representation showing 2OG binding residues Y131, T184, N197, and K204; the active-site Fe is shown as an orange sphere. (E) Omit map contoured to 3.0σ of the active-site Fe(II), 2OG and the metal binding residues. NLS = nuclear localisation sequence, AT-hook = adenine-thymine rich hook/domain.

4.4.3. Structure Determination of Full-Length JMJD6

A suitable crystal of full-length JMJD6 (*i.e.*, aa 1-403, $JMJD6^{FL}$) was obtained using Mn(II) and NOG as surrogates for Fe(II) and 2OG, respectively. The crystal was grown at room temperature by siting-drop vapour-diffusion method (78) using a commercial screen (Index, condition #70) (Figure 4.6**A**). The crystal diffracted to a resolution of 3.8 Å at the DLS synchrotron facility in an orthorhombic space group $P2_12_12_1$ with unit cell dimensions a = 101.3, b = 142.1, c = 157.9 (Å), angles 90° and 4 molecules in the ASU (Table 4.3) (data were collected by Dr. Rasheduzzaman Chowdhury, Chemistry Research Laboratory, University of Oxford). MR using PHASER and iterative cycles of manual fitting and refinement using COOT and PHENIX, respectively, were used to obtain the final structure (79,80) (Figure 4.6**B**). Nevertheless, some regions of the structure of JMJD6, including part of the catalytic JmjC domain and the *C*-terminus, were not visible (Figure 4.6**B**).

Crystals were also obtained using the broad screens Pact Premier and PEG Ion, but the quality of diffraction was even poorer (Figure 4.6**C** and 4.6**D**). Therefore, the crystallisation conditions of the initial hit (using the broad scree Index) were optimized with the aim of obtaining larger crystals with higher diffraction quality.

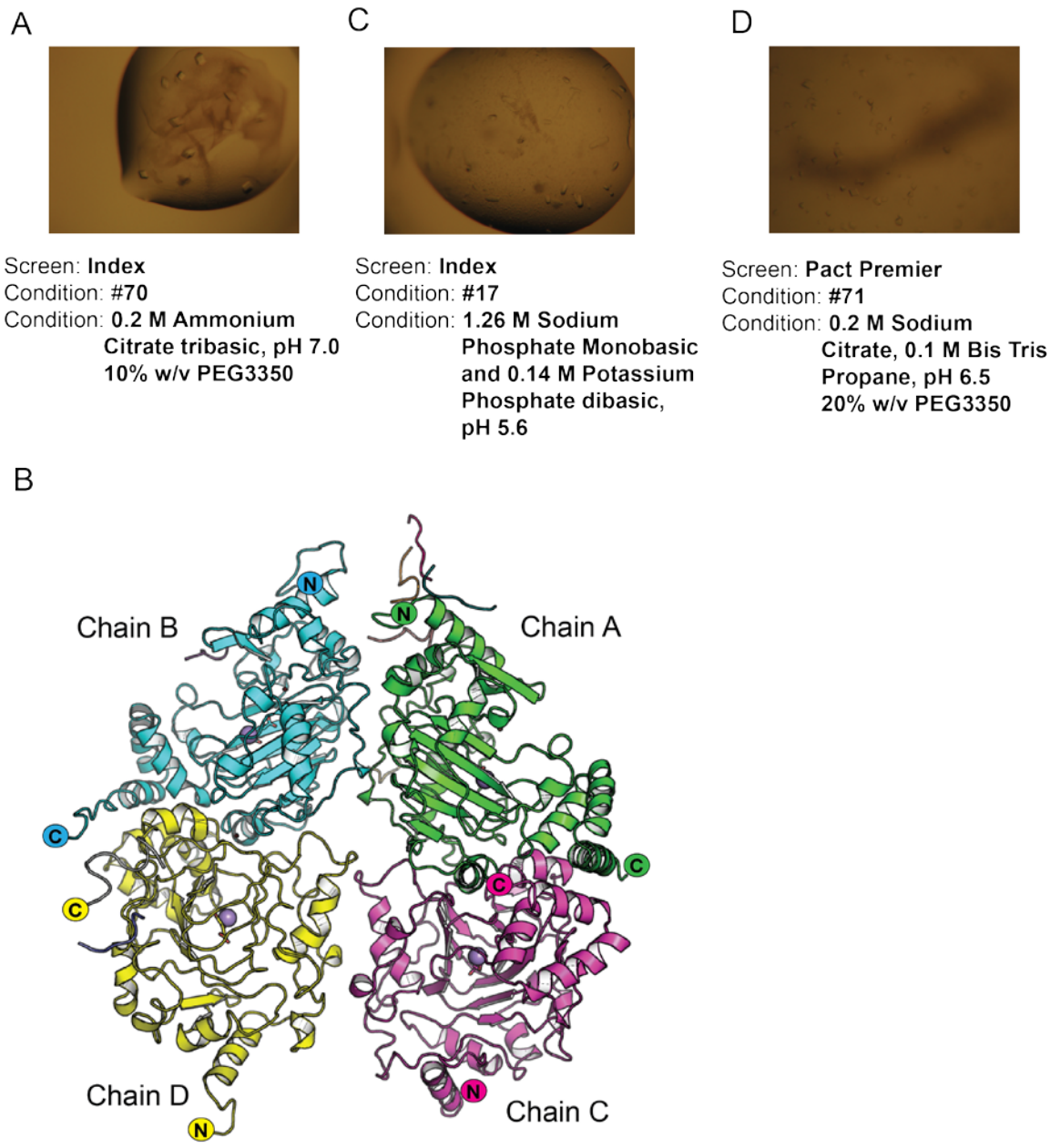

FIGURE 4.6. **Crystallographic Studies of JMJD6^{FL}**. (A) Images of crystals of full-length JMJD6 obtained using commercial screens. (B) View from a cartoon representation of a structure of JMJD6^{FL}.Mn(II).NOG complex with the four molecules in the ASU.

Based on the initial hits obtained from the commercial screens (Figure 4.6), optimisation by varying the composition of the crystallisation conditions was performed. A crystal of dimensions 80x60 µm was grown using crystallisation buffer containing 0.1 M HEPES, pH 7.7, 0.3 M sodium phosphate monobasic, 1.3 M potassium phosphate monobasic and 0.1 M ammonium citrate (Figure 4.7). The crystal diffracted to a resolution of 1.6 Å at the DLS synchrotron facility. After successful MR using PHASER and a previous structure of JMJD6 (*i.e.*, JMJD6$^{\Delta 344\text{-}403}$.Fe(II).2OG) as a model and iterative cycles of manual fitting and refinement using COOT and PHENIX, respectively (79,80), a structure of full-length JMJD6 protein was determined. This structure was in a monoclinic space group $P12_11$ with two protein molecules in the ASU (Figure 4.7, Table 4.3). Although the electron density map clearly showed the active-site Mn(II), it did not show the complete density for the ligand NOG (Figure 4.7**B**). Electron density for residues Ser^{335}-Arg^{403} was also not observed; therefore, it was not possible to model the *C*-terminal region including the polyS domain (Figure 4.7**A**). However, patches of electron density were observed around the *N*-terminal region of chain A, which may be of the residues from the *C*-terminus or from a symmetry or from an oligomeric neighbour. It is possible that degradation of full-length JMJD6 occurred during the course of crystallisation.

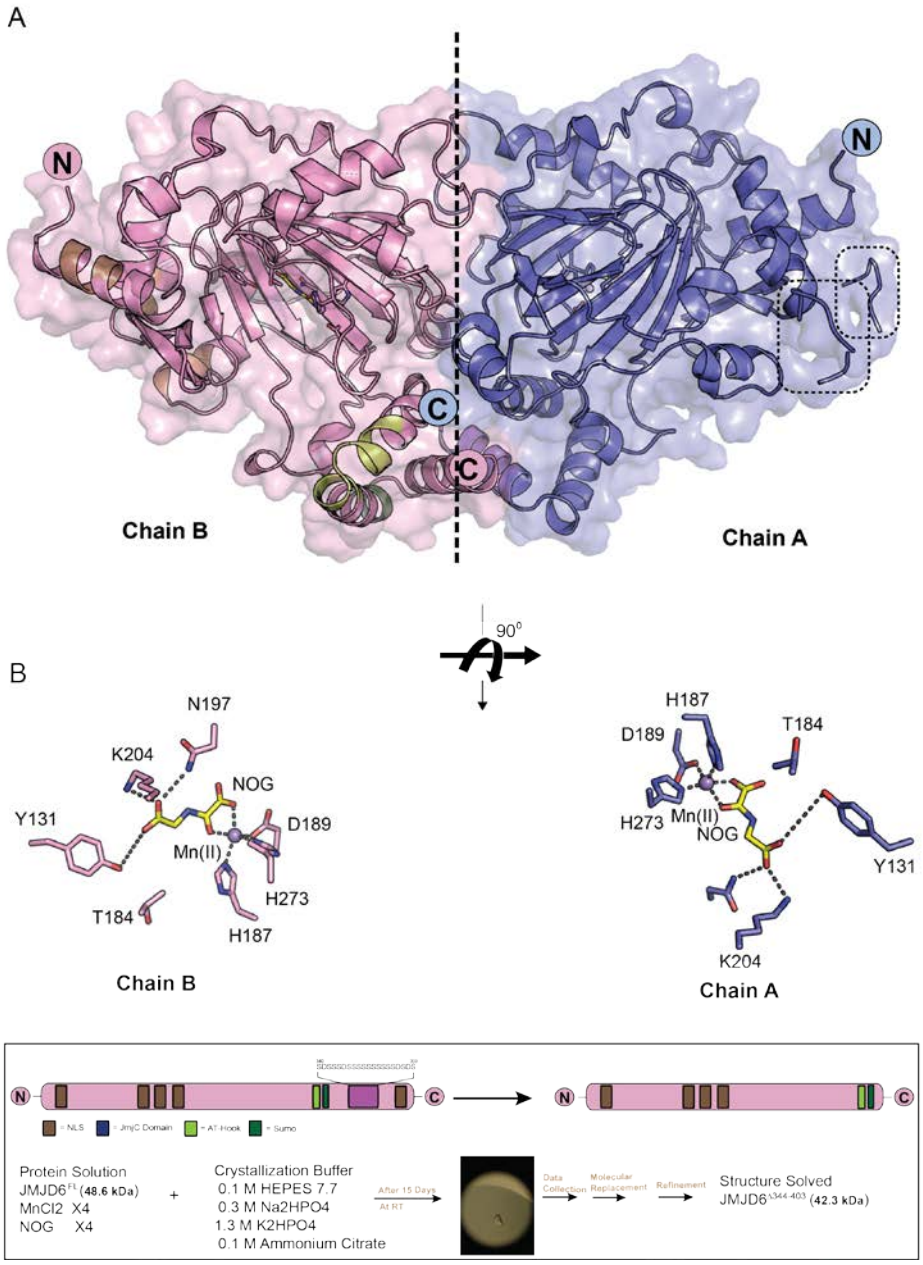

FIGURE 4.7. **Crystallographic analysis of full-length JMJD6**. (A) A cartoon and transparent surface representation from a structure of JMJD6^{FL}.Mn(II).NOG complex. (B) The active-site contains bound Mn(II) and NOG; inset shows the crystallisation buffer conditions used for JMJD6^{FL} which eventually led to the structure determination of JMJD6$^{\Delta 344\text{-}403}$. Note the discontinuous residues of the *C*-terminal regions (black dotted boxes) of full-length JMJD6 positioned around the *N*-terminal region of chain A.

Table 4.3. Crystallographic data collection and refinement statistics.

Protein	**JMJD6^{FL}.Mn(II).NOG**	**JMJD6$^{\Delta 344-403}$.Ni(II).2OG**	**JMJD6$^{\Delta 344-403}$.Fe(II).2OG**
X-Ray Source	DLS IO3	DLS IO4-1	DLS IO2
Wavelength (Å)	0.97625	0.92819	1.07206
Resolution (Å)	28.30-1.67 (1.71-1.67)*	80.40-3.09 (8.38-3.09)*	42.20-2.04 (9.12-2.04)*
Space Group	*$P12_11$*	*$P12_11$*	*$P12_11$*
Unit Cell Dimensions			
a, b, c	47.0, 97.1, 94.1	101.4, 142.0, 155.9	47.1, 96.9, 93.7
α, β, λ	90, 95.7, 90	90, 90, 90	90, 95.8, 90
Molecules per ASU	**2**	**4**	**2**
Wilson B Factor (A^2)	25.49	74.94	32.36
Reflections	96660 (6054)*	82801 (4138)*	53266 (3866)*
Completeness	98.6 (83.1)*	98.8 (98.2)*	99.8 (99.5)*
Multiplicity	6.7 (5.8)*	6.8 (6.9)*	6.7 (6.6)*
I/sI	16.6 (1.8)*	9.5 (1.3)*	9.7 (1.4)*
R_{merge}	0.056 (0.733)*	0.185 (1.444)*	0.130 (1.297)*
CC half	0.999 (75.1)*	0.992 (0.608)*	0.997 (0.569)*
R_{cryst}	0.1519	0.3656‡	0.1860
R_{free}	0.1739 (2.07)¥	0.3869 (2.42)¥‡	0.2119 (4.85)¥
Deviation from Idealized Geometry			
Bond Length (Å)	0.009	0.002	0.002
Bond angles (°)	1.015	0.468	0.543
Average B Factors			
All atoms	40.62	87.6	38.8
Protein	39.6	87.6	40.5
Ligand	66.0	94.5	32.6
Metal	33.4	63.4	23.9
Water	44.1	-	47.6
Ramachandran Plot			
Favored (%)	97.64	96.37	97.74
Allowed (%)	2.21	3.63	2.26
Disallowed (%)	0	0	0
Outlier (%)	0.15	0.0	0

* High resolution bin.

¥ Percentage of the total reflections used for R_{free} calculations.

‡ Data refined only for 3 cycles due to poor resolution and map quality.

4.5. Investigation of Degradation Potential of JMJD6

To investigate the degradation potentials of JMJD6, three JMJD6 constructs (*i.e.* $JMJD6^{FL}$, $JMJD6^{\Delta 363\text{-}403}$ and $JMJD6^{\Delta 344\text{-}403}$) were incubated at RT in the same buffer solutions that were used in crystallisation of $JMJD6^{FL}$. Protein samples were withdrawn every second day for up to 15 days, and analysed by SDS-PAGE. $JMJD6^{FL}$ and $JMJD6^{\Delta 363\text{-}403}$, both with the polyS domain, appeared to degrade over time and molecular weight of the degraded products resembled that of the truncated $JMJD6^{\Delta 344\text{-}403}$ (Figure 4.8**A**). On the other hand, the shorter construct $JMJD6^{\Delta 344\text{-}403}$ without the polyS domain showed no sign of degradation (Figure 4.8**A**). It was thus concluded that $JMJD6^{FL}$ and $JMJD6^{\Delta 363\text{-}403}$ underwent degradation. To confirm, samples were analysed by mass spectrometry (MS). MS analyses revealed masses of ~42 kDa for the degraded products of $JMJD6^{FL}$ and $JMJD6^{\Delta 363\text{-}403}$, which corresponded to the mass of the truncated $JMJD6^{\Delta 344\text{-}403}$ (Figure 4.8**B**). This further supports the proposed degradation of $JMJD6^{FL}$ and $JMJD6^{\Delta 363\text{-}403}$, which likely was triggered by the *C*-terminal regions including the polyS domain. Thus it is apparent that the *C*-terminal region of $JMJD6^{FL}$ is not observed by crystallography due to degradation. In 2012, Han *et al.* have also observed degradation of full-length JMJD6 protein using SDS-PAGE (81).

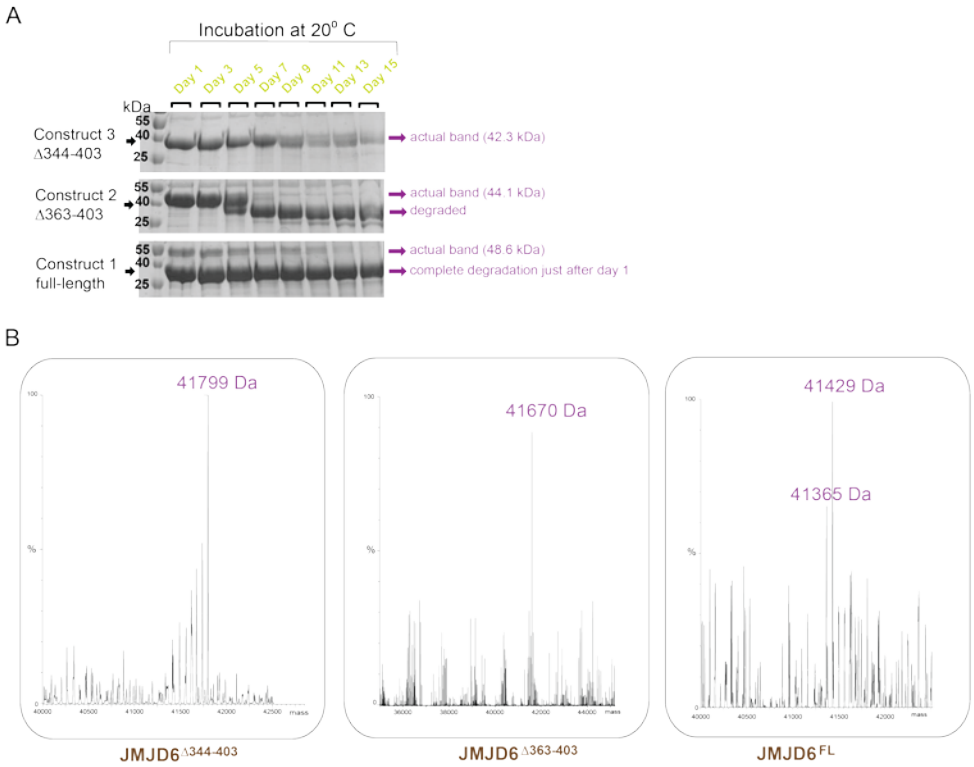

FIGURE 4.8. **Polyserine domain mediated degradation of JMJD6**. (A) SDS-PAGE analysis of samples of JMJD6 incubated at room temperature, showing time-dependent degradation. (B) Denatured MS spectra of the protein samples. Experiments were carried out following the procedures described in Chapter 10.

4.6. Active-Site Comparison between JMJD6 and other 2OG Oxygenases

To compare the active site of the complex JMJD6$^{\Delta 344\text{-}403}$.Fe(II).2OG to that of other 2OG oxygenases, the crystal structure of JMJD6$^{\Delta 344\text{-}403}$.Fe(II).2OG was superimposed on to FIH (HIF asparaginyl hydroxylase), PHD2 (HIF prolyl hydroxylase) and 2OG-dependent demethylases PHF8, KDM4A (JmjC domain containing protein 2A) (Figure 4.9).

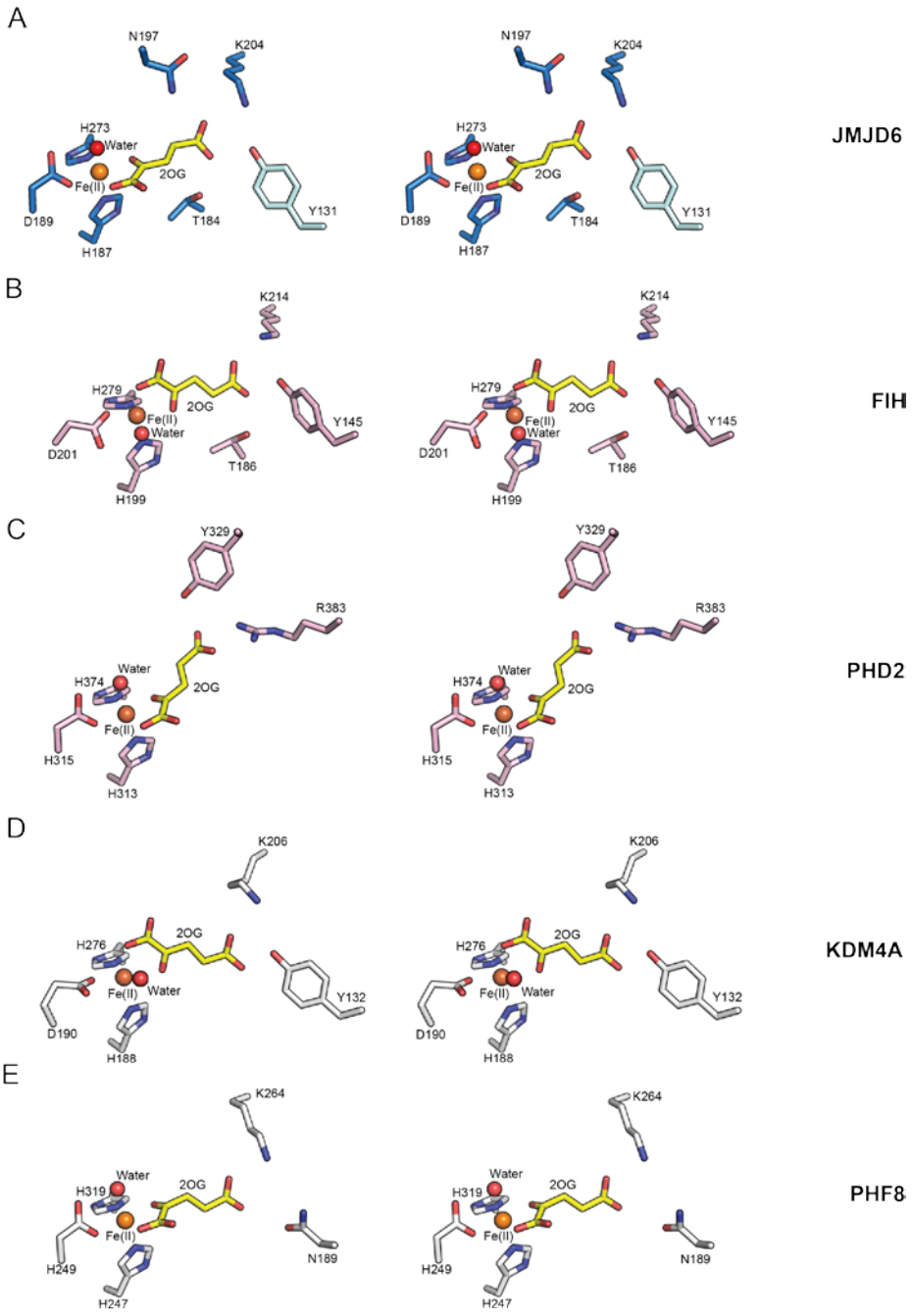

FIGURE 4.9. **Active-site comparison of JMJD6 with other 2OG oxygenases**. (A) Wall-eyed stereo view of the JMJD6$^{\Delta 344\text{-}403}$.Fe(II).2OG complex, compared to those of 2OG-dependent hydroxylases (B) FIH (PDB: 4Z2W), (C) PHD2 (PDB: 3OUJ) and 2OG-dependent demethylases (D) KDM4A (PDB: 2GP5), and (E) PHF8 (PDB: 3K3O).

In the case of JMJD6, 2OG was bound to the active site Fe(II) *via* the oxygens of the C-1 carboxylate and C-2 ketone, as is typical for many 2OG oxygenases. However, comparison shows that the orientation of 2OG bound to JMJD6 is different (Figure 4.9). In the case of JMJD6, the C-1 carboxylate of 2OG is positioned *trans* to the distal histidine His^{273} ($H273_{JMJD6}$), similar to HIF prolyl hydroxylase 2 (PHD2) ($H374_{PHD2}$) (Figure 4.9**C**) and histone lysine demethylase PHF8 ($H319_{PHF8}$) (Figure 4.9**E**), but different from HIF asparaginyl hydroxylase FIH (Figure 4.9**B**) and the histone lysine demethylase KDM4A (Figure 4.9**D**), where the C-1 carboxylate is positioned *trans* to the proximal histidine ($H199_{FIH}$ and $H188_{KDM4A}$).

4.7. Comparison Between the Crystal Structures of JMJD6$^{\Delta 343-403}$.Fe(II).2OG and JMJD6^{FL}.Mn(II).NOG

The crystal structure of JMJD6$^{\Delta 344-403}$.Fe(II).2OG was then compared to that of JMJD6^{FL}.Mn(II).NOG to check for differences (if any) in the active site (Figure 4.10). Both structures were determined in monoclinic space group *$P12_11$* with 2 molecules in the ASU (Figure 4.10). The interfacial regions between the two molecules (chain A and chain B) in the crystalline state were calculated to have similar buried surface areas of 2177 $Å^2$ and 2246 $Å^2$ for JMJD6$^{\Delta 344-403}$.Fe(II).2OG and JMJD6^{FL}.Mn(II)NOG, respectively (Table 4.4), as determined by PISA (Protein Interfaces Surfaces and Assemblies) (82). The Δ^iG values obtained from the PISA analysis were -15.8 kcal mol^{-1} and -15.4 kcal mol^{-1}, respectively (Table 4.4) suggesting the formation of stable complexes (82). In both cases, the molecules within the ASU interacted with each other through the helices α13, α4, loops between $3_{10}1/\beta I^{I}$, $\alpha 4/\beta I^{II}$, βIV/α8, and $\beta V/3_{10}10$ (Figure 4.10**C**, **4.**10**D**), analogous to what was observed by Mantri *et al.,* 2010 (36).

In contrast, conformational differences in the ligand-binding residues were observed (Figure 4.10**B**). At the active site of the crystal structure of JMJD6^{FL}.Mn(II).NOG, partial electron density for NOG was observed. The ligand-binding residues Tyr^{131} (Y131) and Thr^{164} (T184) were also found in different conformational

states compared to those observed in the structure of JMJD6$^{\Delta 344\text{-}403}$.Fe(II).2OG complex, despite similarity in the conformation of the metal binding residues (Figure 4.10**B** and **4.**5**D**).

Table 4.4. Calculation of buried surface area.

Structure	Chains	Symmetry Operation	Buried Surface Area (Å^2)	Δ^iG (kcal mol^{-1})	CSS*	Cα rmsd	Session ID
JMJD6$^{\Delta 344\text{-}403}$.Fe(II).2OG	A,B	x,y,z/x,y,z	2177	-15.8	0.130	1.03	228-9I-455**.**
JMJD6^{FL}.Mn(II).NOG	A,B	x,y,z/x,y,z	2246	-15.4	0.162	0.89	228-9I-455
3K2O (36)	A,B	x,y,z/x,y,z	2050	-16.6	0.126	-	

* Complex Formation Significance Score

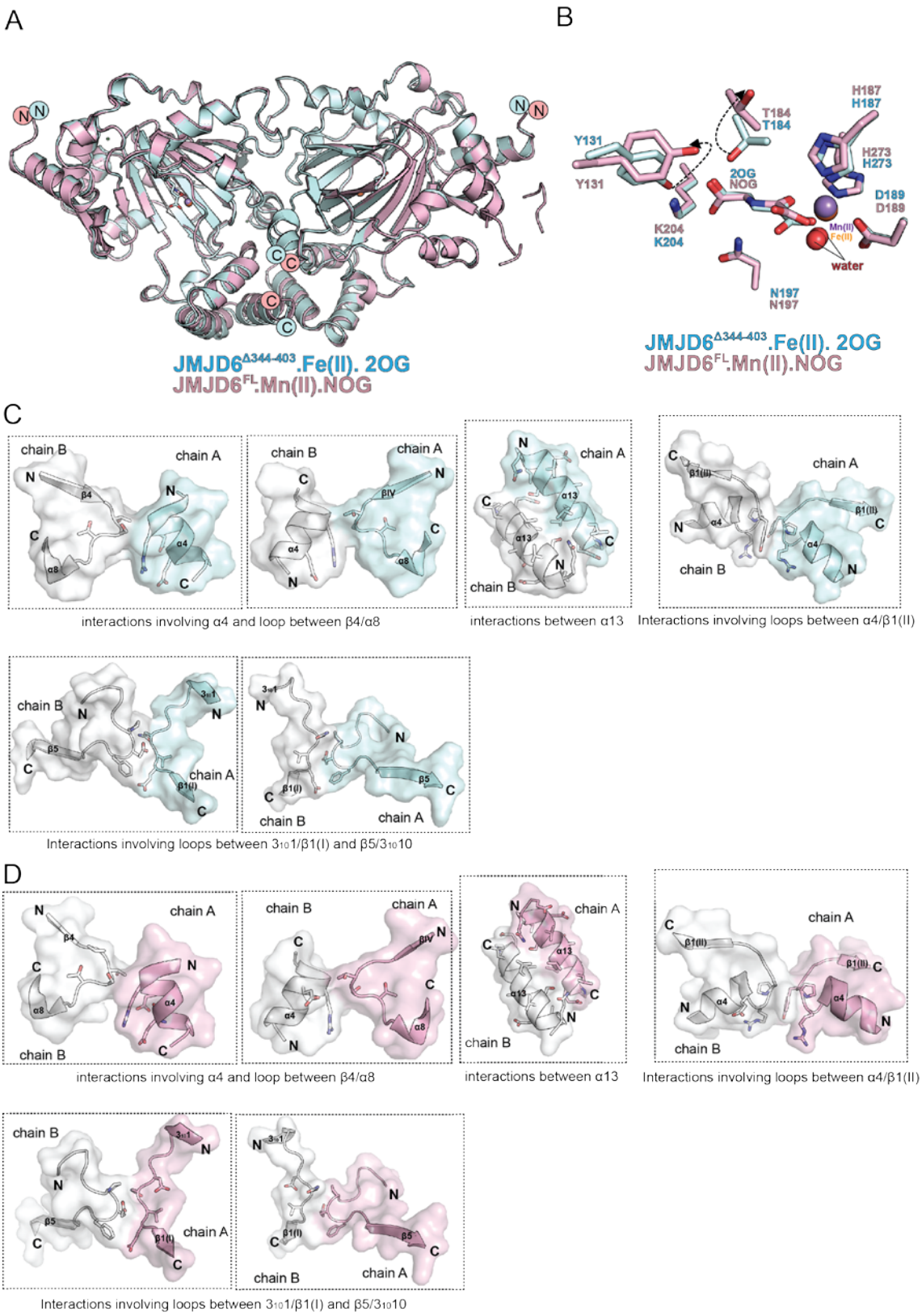

FIGURE 4.10. **Comparison of views from crystal structures of full length and truncated JMJD6**. (A) Views from the crystal structure of JMJD6$^{\Delta 344\text{-}403}$.Fe(II).2OG superimposed on that of JMJD6^{FL}.Mn(II).NOG. (B) Conformational changes of Tyr^{131} and

Thr^{184} in the structure of JMJD6^{FL} were observed. Similarity in the interfacial binding regions of two molecules (chain A and B) was observed in the structures of (C) JMJD6$^{\Delta 344\text{-}403}$ and (D) JMJD6^{FL}.

These two structures were compared to see if there were any differences in their respective secondary structures; *e.g.* α-helices, β-sheets and 3_{10} helices (Table 4.5). The JMJD6 structure determined by Mantri *et al.* (PDB: 3K2O) was used as a reference structure (36). Although the major and minor β-sheets appeared similar, differences in the 3_{10} helices were observed (Table 4.5).

Table 4.5. α-Helices and β-Sheets of the JMJD6 structures.

Residues	3K2O (36)	JMJD6$^{\Delta 344\text{-}403}$.Fe(II).2OG	JMJD6 ^{FL}.Mn(II).NOG
51-53	3_{10}2	Loop	Loop
153-157	3_{10}5	Loop	Loop
166-168	Loop	Helix	Loop
183-187	βII	βII (181-184)	Loop
189-193	3_{10}7	Loop	Loop
204-209	βIV	βIV	βIV
214-219	α8	α8 (215-218)	α8 (215-218)
231-245	α10	α10 (232-244)	α10 (232-244)
249-253	3_{10}10	Loop	Loop
255-259	βVI	βVI	βVI (256-259)
264-267	βVII	βVII (262-268)	βVII (262-268)
272-277	βVIII	βVIII (271-277)	βVIII (271-277)

CHAPTER 05: Inhibition Studies of JMJD6

5.1. Introduction

Human 2OG oxygenases are amenable to small molecule inhibition and are tractable targets for therapeutic inhibition. Collagen prolyl-4-hydroxylases (CP4H) were the first 2OG oxygenases to be targeted for therapeutic inhibition (5-7). Notably, the stability of the collagen triple helix fold is dependent on 4-hydroxyproline residues; the post-translational hydroxylation of proline residues in collagen is catalysed by CP4H. A decrease in the 4-hydroxyproline content of collagen leads to decreased structural stability, rendering it vulnerable to proteolytic cleavage and impairing its ability to interact with other components of the extracellular matrix. Derivatives of 2,5-pyridine dicarboxylic acid (2,5-PDCA) and N-oxalylglycine (NOG), which were subsequently found to be generic inhibitors of 2OG oxygenases, were initially found to potently inhibit CP4H, and were therefore considered lead compounds during the development of more potent inhibitors. However, efforts to develop therapeutically useful CP4H inhibitors have been unsuccessful, probably due in part to off-target effects (*i.e.*, non-specific inhibition of other 2OG oxygenases). There are also uncertainties regarding the mechanism of action of some of the inhibitors and also issues relating to long-term dosing (5-7). Inhibitors of the HIF prolyl hydroxylase domain proteins (PHDs) are in clinical trials for the treatment of anaemia, and orally active inhibitors of the KDM5 subfamily of JmjC histone lysine demethylases (KDMs) have been recently reported (83,84). A clinically used cardioprotective agent, meldonium (Mildronate, 2-(2-carboxylato-ethyl)-1,1,1-trimethylhydrazinium) inhibits BBOX1, though it may have other mechanisms of action (85,86). However, the development of 2OG oxygenase inhibitors is at a relatively early stage from a medicinal chemistry perspective, and more efforts must be made to discover selective leads. Recent progress in the understanding of 2OG oxygenase biology in humans has reinvigorated efforts to pursue them as potential medicinal targets in various

therapeutic areas. The primary objective of the work performed in this Chapter was to identify potential inhibitors for JMJD6.

2OG competitors are probably the most widely used 2OG oxygenase inhibitors, showing a broad scope of inhibition across most, if not all, 2OG oxygenases (4). 2OG competitors tested against JMJD6 are shown in Figure 5.1. In addition to the non-selective 2OG competitors, selective 2OG oxygenase inhibitors were also tested against JMJD6, which included selective PHD and KDM inhibitors (Figure 5.1). Tri-carboxylic acid (TCA) cycle intermediates were also tested for inhibition owing to their biological importance (Figure 5.1). Inhibitors with the tri-carbonyl group have been identified as potential inhibitors of 2OG oxygenase-related enzyme, HPPD (4-hydroxyphenylpyruvatedioxygenase), and are used as important herbicides in the agrochemical industry (**Chapter 09**). These tri-carbonyl inhibitors were also screened against JMJD6 for inhibition.

5.2. NMR Reporter Screening Methods

Several biophysical methods have been developed for binding assays between 2OG oxygenases and their ligands (including metal ions, small molecules, and other biomolecules) (4). In this study, a proton NMR-based (^{1}H NMR) binding assay was adopted due to its reliability and simplicity (55).

5.2.1. Ligand-Observed NMR-Based Competition Experiments for Inhibitor Screening

Ligand observed NMR-based methods are widely used to study protein-ligand interactions (55). An NMR-based binding competition assay was used for this work. This method provides qualitative and quantitative ‘apparently site-specific’ information about ligand binding. A CPMG (Carr-Pucell-Meiboom-Gill)-editing method was used to provide a means to distinguish between free and enzyme-bound 2OG (56,57).

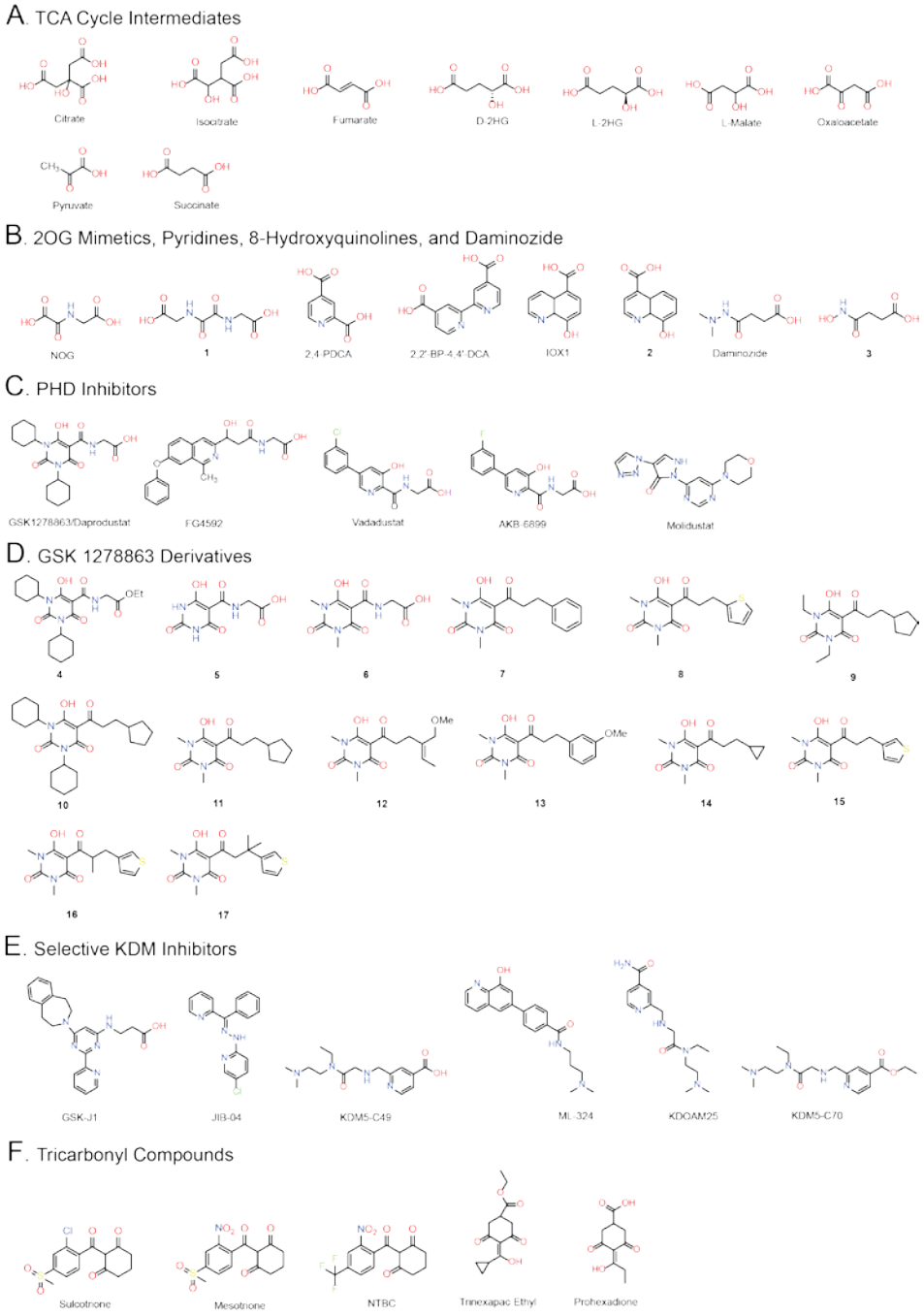

FIGURE 5.1. **Compounds tested for inhibition against JMJD6.**

To investigate the extent to which the ligands of interest compete with 2OG for the JMJD6 active site, a 2OG-displacement study was carried out using a single ligand concentration (Figure 5.2). A mixture of EDTA-treated JMJD6$^{\Delta 363\text{-}403}$ and Zn(II) was added to a mixture of 2OG and ligand of interest (**Chapter 10**). The subsequently obtained NMR

spectra were then analysed for the extent of recovery of the 2OG signal (if any), which was quantified to calculate 2OG displacement (%) (equation 5, **Chapter 10**).

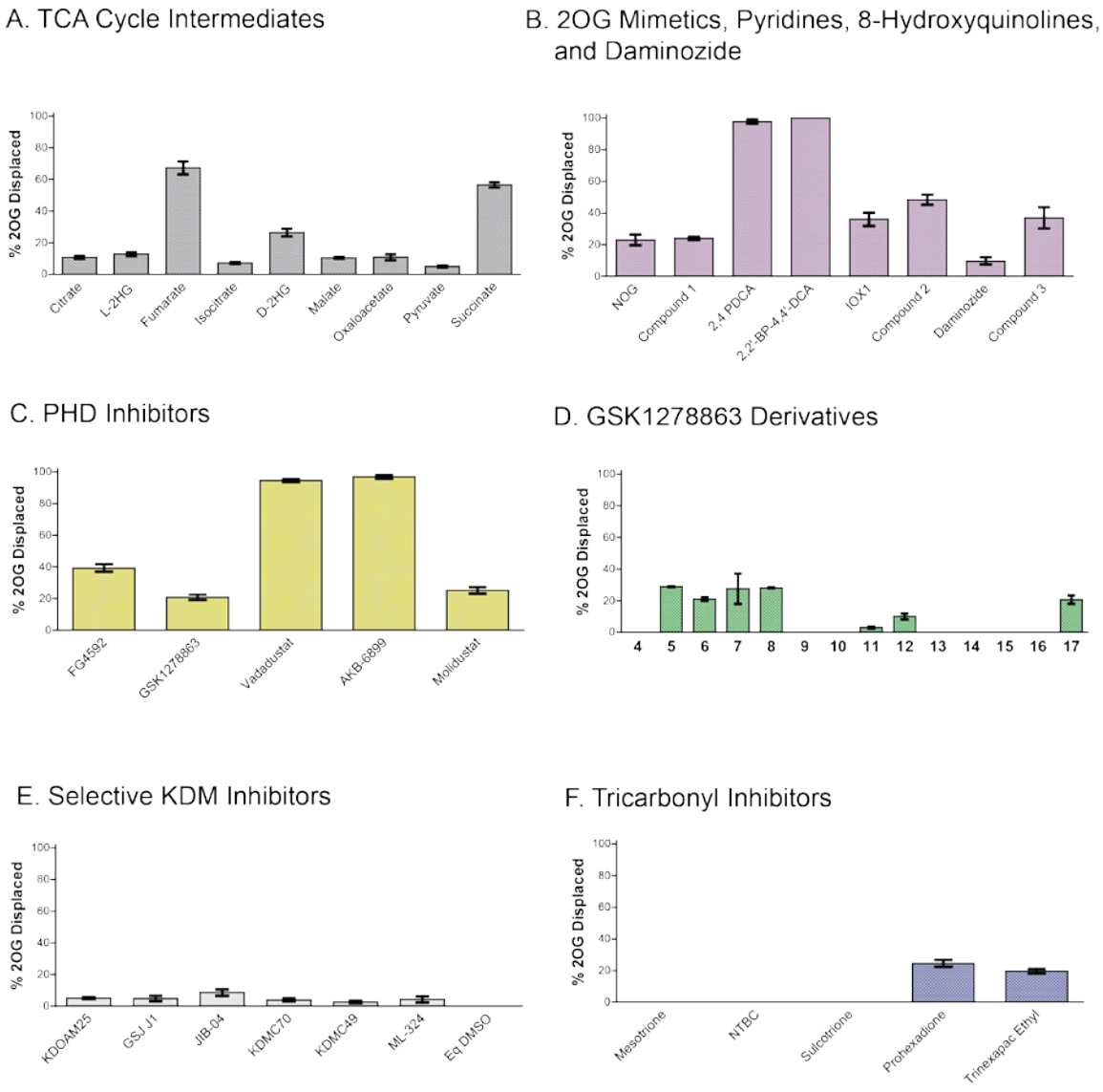

FIGURE 5.2. **Single-point 2OG displacement ligand binding assays *via* CPMG-edited ^{1}H NMR analyses of JMJD6.** Bar charts showing the extent of 2OG displacement for (A) TCA cycle intermediates, (B) 2OG mimetics, pyridines, 8-hydroxyquinolines, and daminozide, (C) selective PHD inhibitors, (D) GSK1278863 derivatives (E) selective KDM inhibitors, and (F) tri-carbonyl inhibitors. The assay mixtures contained 60 µM EDTA-treated JMJD6$^{\Delta 363\text{-}403}$, 200 µM Zn(II), 10 µM 2OG, and 400 µM of the ligand, all in 50 mM

Tris-D11, pH 7.0 in 10% D_2O (**Chapter 10**). Values represent mean (n = 3) ± standard deviation (SD).

The results revealed that of the tested TCA cycle intermediates, fumarate, D-2HG, and succinate compete with 2OG relatively strongly, displacing 68 ± 0.8%, 27 ± 0.9%, and 56 ± 1.1% 2OG, respectively (Figure 5.2). Previous studies with PHD2 and FIH also identified fumarate as a competitor of 2OG (55). Importantly, JMJD6 showed selectivity towards D-2HG over L-2HG, similar to FIH and PHD2 (55). This indicates that the active site of JMJD6 has similar properties to that of FIH and PHD2.

NOG and **1** (a dimer of NOG, Figure 5.1) displaced the JMJD6 bound 2OG only 23 ± 6% and 24 ± 1.7%, respectively (Figure 5.2). Binding of NOG to JMJD6 is weaker than binding with PHD2 and FIH, for which NOG displaces approximately 85% of 2OG under similar conditions (55). JMJD6 showed selectivity towards pyridines and quinolines, which is comparable to those of PHD2 also (~100 and ~50% 2OG displacement by pyridine-2,4-dicarboxylic acid and 5-Carboxy-8-hydroxyquinoline, respectively) (55). However, in the case of JMJD6, pyridine-2,4-dicarboxylic acid (2,4-PDCA) displaced 99 ± 2.1% 2OG, whereas its structural derivative2,2'-bipyridine-4,4'-dicarboxylic acid (2,4-BPDCA) displaced ~100% 2OG (Figure 5.2). 5-Carboxy-8-hydroxyquinoline (IOX1) and **2** (a structural derivative of IOX1) displaced only ~36% and ~48% of JMJD6-bound 2OG, respectively (Figure 5.2). IOX1 is reported to be a generic inhibitor for histone demethylases (87) and probably due to this reason showed relatively weak binding affinity for JMJD6. Conversely to JMJD6, relatively strong binding affinity of IOX1 for FIH (~75%) and PHD2 (~50%) has been observed previously (55). Another selective KDM inhibitor daminozide and its structural analogue **3** showed only ~10% and ~36% displacement of 2OG, respectively (Figure 5.2).

Of the 'selective' PHD inhibitors, Vadadustat and AKB-6899 were found to fully displace 2OG from the active site of JMJD6 (Figure 5.2). Further studies with derivatives of the PHD inhibitor GSK1278863/Daprodustat showed moderate levels of competition

with 2OG (Figure 5.2). Note, these compounds were tested against human uS12 prolyl 3-hydroxylase (OGFOD1) also (Cyrille Thinnes, DPhil Thesis, Chemistry Research Laboratory, University of Oxford) and were found to display inhibitory activity. The exact mechanism of binding of these compounds to JMJD6 however needs further investigation.

The interaction of JMJD6 with selective KDM inhibitors and various tri-carbonyl inhibitors (some of which have been used as herbicides and in the treatment of type I tyrosinemia) was next studied. But in the case of JMJD6, none of these compounds competed with 2OG even at 400 µM concentration (*i.e.*, a 40 fold excess compared to 2OG concentration) (Figure 5.2).

5.3. Binding Assay between JMJD6 and its Potential Inhibitors

To gain more information on the binding affinities of ligands, apparent binding constant (K_D^{app}) was thereafter determined by titration (55). K_D^{app} were determined for only those ligands showing substantial levels of 2OG displacements (≥50%). K_D^{app} is defined as the concentration of free inhibitor when 50% of the enzyme is bound to inhibitor in the presence of the reporter ligand (58). K_D^{app} was measured using the method previously described by Morton *et al.* (58) (**Chapter 10**). K_D^{app}s for fumarate and succinate were found to be 109 and 159 µM, respectively (Figure 5.3), suggesting that TCA cycle intermediates bind very weakly to JMJD6, as observed for PHD2 (55). In contrast, 2,4-PDCA and 2,4-BPDCA showed relatively tighter binding to JMJD6, having K_D^{app} values of 6 and 7 µM, respectively (Figure 5.4), again comparable to PHD2 (55). The K_D^{app} values for AKB-6899 and Vadadustat were found as 3 µM and 14 µM, respectively (Figure 5.5), suggesting that JMJD6 may have similar ligand-binding properties to PHD2.

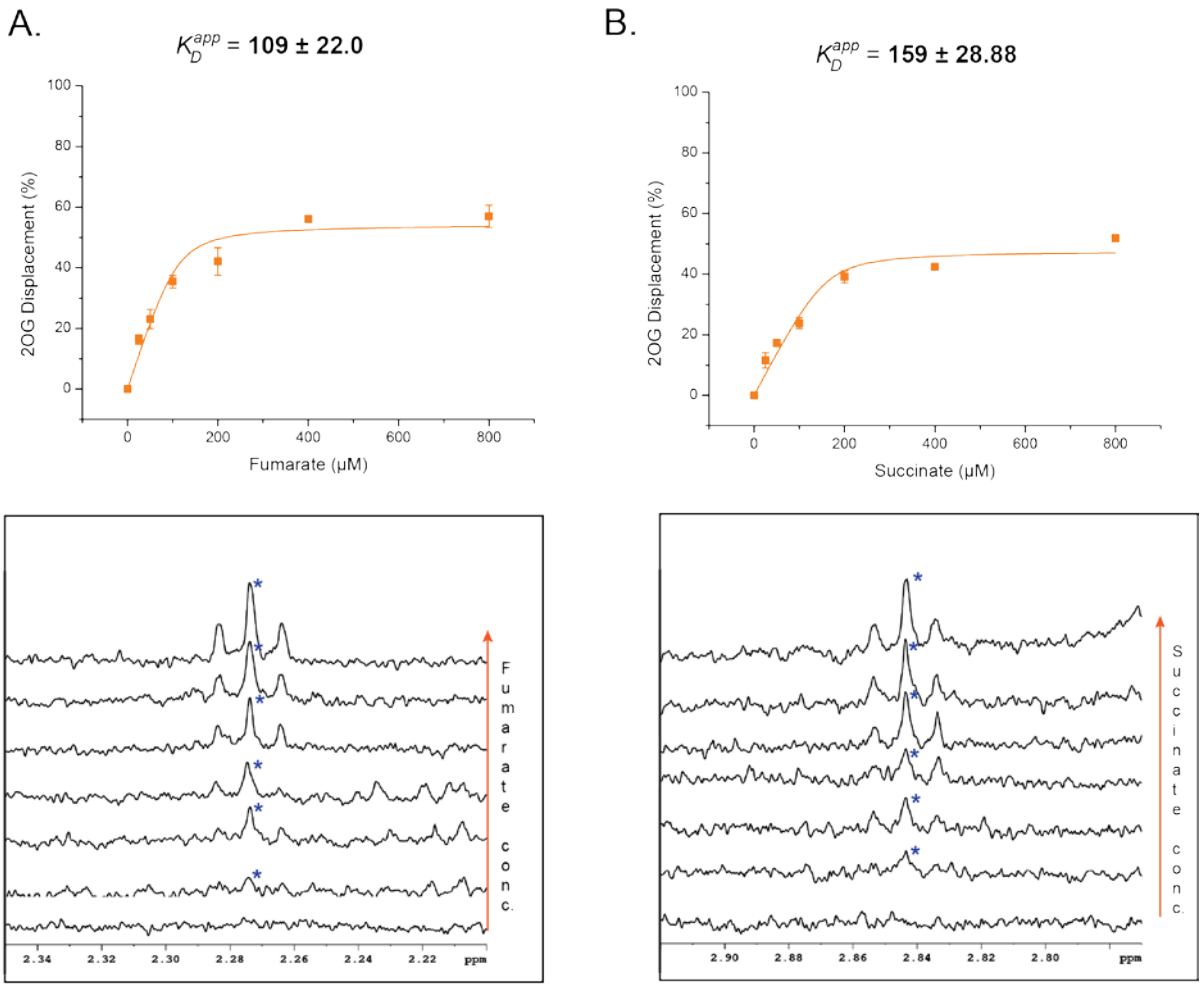

FIGURE 5.3. ***K_D^{app}* determination for TCA cycle intermediates binding to JMJD6**. Plots used for the determination of K_D^{app}s of (A) fumarate and (B) succinate; insets show the competitive titration between 2OG and the ligands. The assay mixtures contained 60 μM EDTA-treated JMJD6$^{\Delta 363\text{-}403}$, 200 μM Zn(II), 10 μM 2OG, 0-800 μM ligand, all in 50 mM Tris-D11, pH 7.0 in 10% D_2O (**Chapter 10**). Values represent mean (n = 3) ± SD.

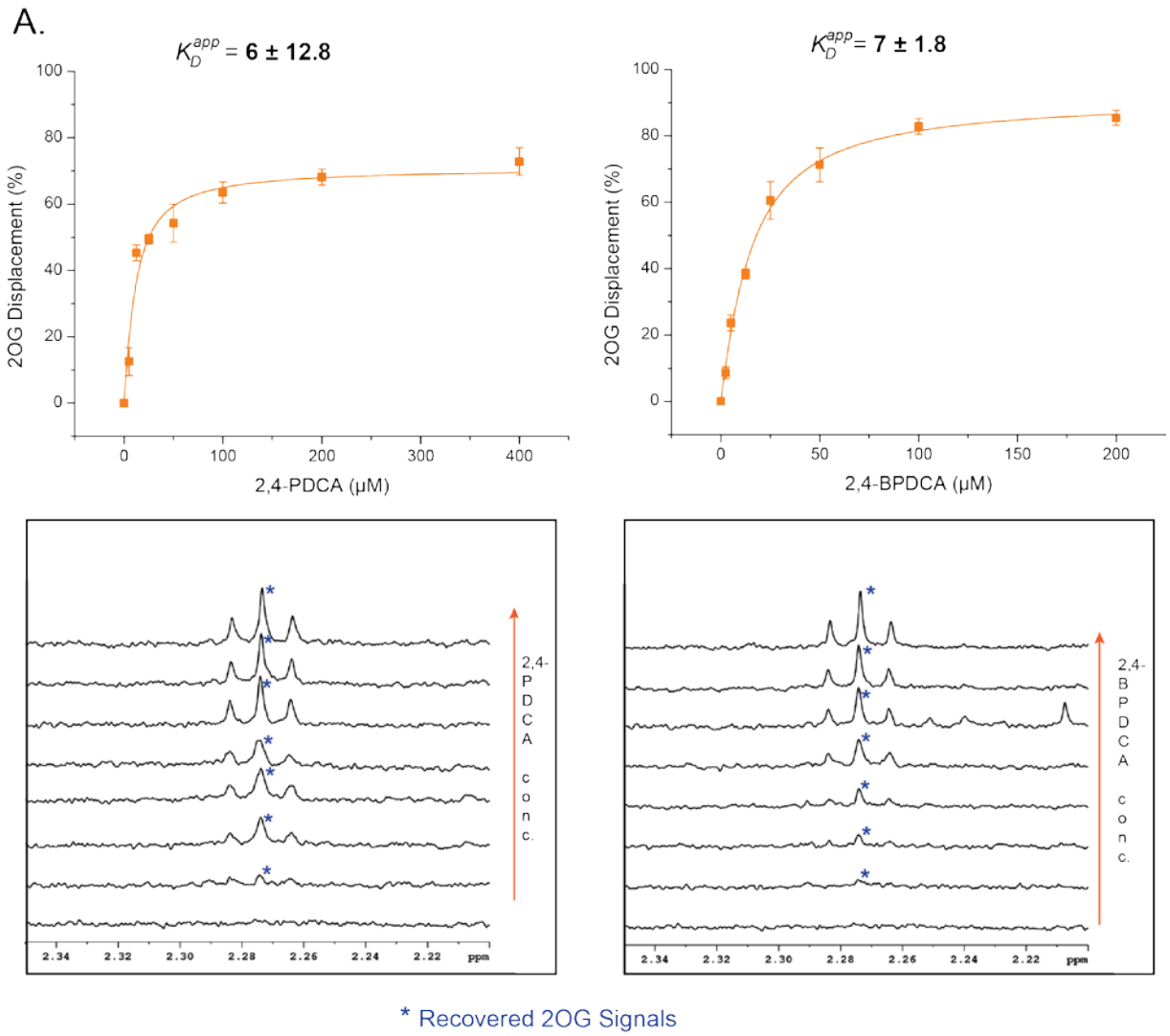

FIGURE 5.4. ***K_D^{app}* determination for pyridine derivatives binding to JMJD6**. Plots used for the determination of K_D^{app}s of (A) 2,4-PDCA and (B) 2,5-BPDCA; insets show the competitive titration between 2OG and the ligands. The assay mixtures contained 60 μM EDTA-treated JMJD6$^{\Delta 363\text{-}403}$, 200 μM Zn(II), 10 μM 2OG, 0-400 μM ligand, all in 50 mM Tris-D11, pH 7.0 in 10% D_2O (**Chapter 10**). Values represent mean (n = 3) ± SD.

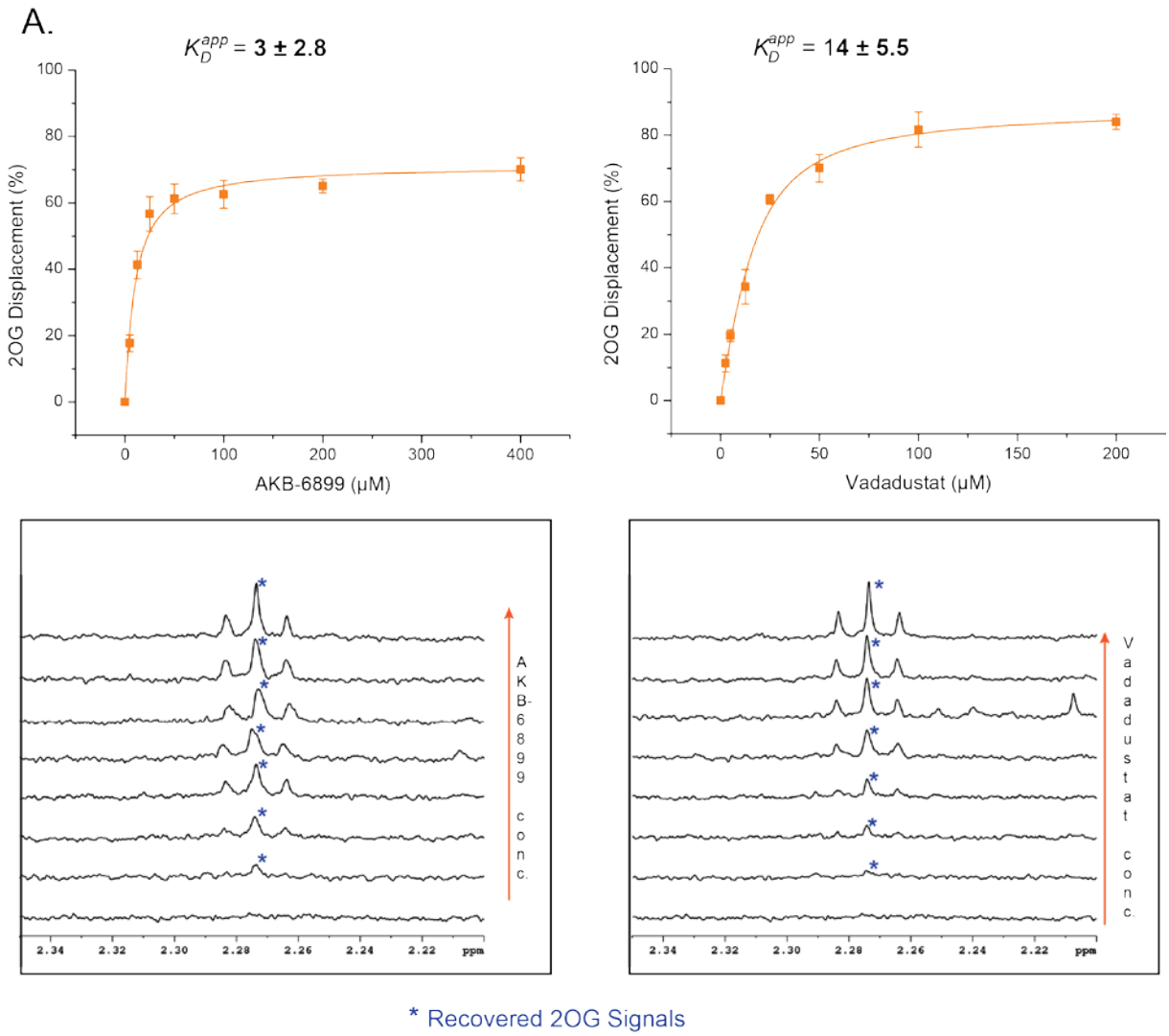

FIGURE 5.5. ***K_D^{app}* determination for PHD inhibitors binding to JMJD6**. Plots used for the determination of K_D^{app}s of (A) AKB-6899 and (B) Vadadustat; insets show the competitive titration between 2OG and the ligands (B). The assay mixtures contained 60 μM EDTA-treated JMJD6$^{\Delta 363\text{-}403}$, 200 μM Zn(II), 10 μM 2OG, 0-400 μM ligand , 50 mM Tris-D11, pH 7.0 in 10% D_2O (Chapter 10). Values represent mean (n = 3) ± SD.

5.4. MALDI-TOF MS-based Inhibition Study with JMJD6

MALDI-TOF (matrix-assisted laser desorption ionization-time of flight) has been widely used for carrying out inhibition studies with 2OG oxygenases (59,61). In this work also, a MALDI-TOF MS was used to detect the hydroxylated species (peaks with +16 Da shift in mass) formed from the enzyme-treated substrates in the presence of inhibitors (Figure 5.6).

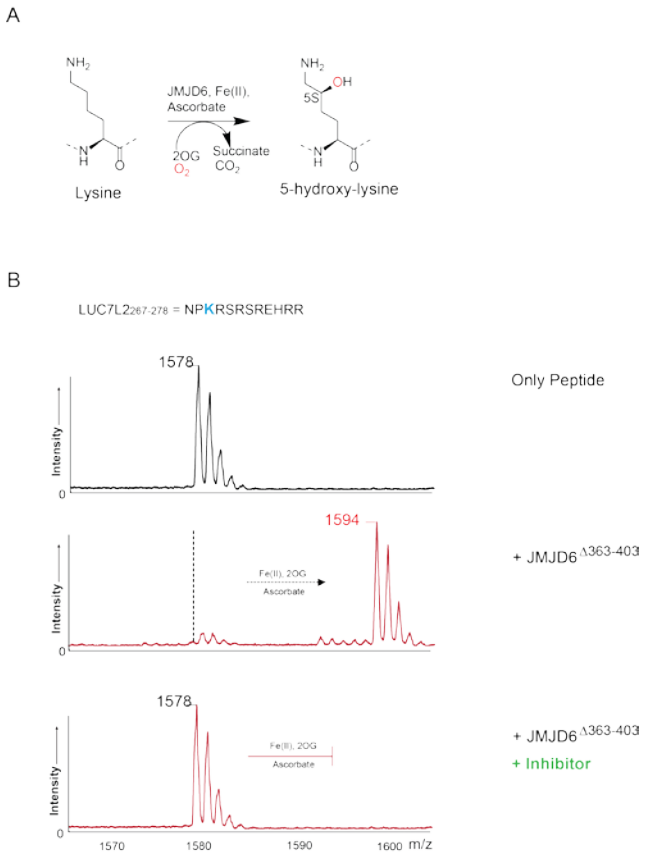

FIGURE 5.6. **MALDI-TOF MS-based inhibition assay of JMJD6**. (A) C-5 lysyl-hydroxylation as catalysed by JMJD6. (B) MALDI-TOF mass spectra showing the effect of inhibitors on the hydroxylation activity of JMJD6. Assay was carried out following the hydroxylation assay procedures described in Chapter 10.

5.4.1. End-point Inhibition assay using various compounds

Initially, inhibition assays were carried out in the presence of 0.1, 1, and 10 mM of the ligands (Figure 5.7). For most of the compounds tested, the degree of inhibition was found to be consistent with their corresponding 2OG-displacement values (Figure 5.2).

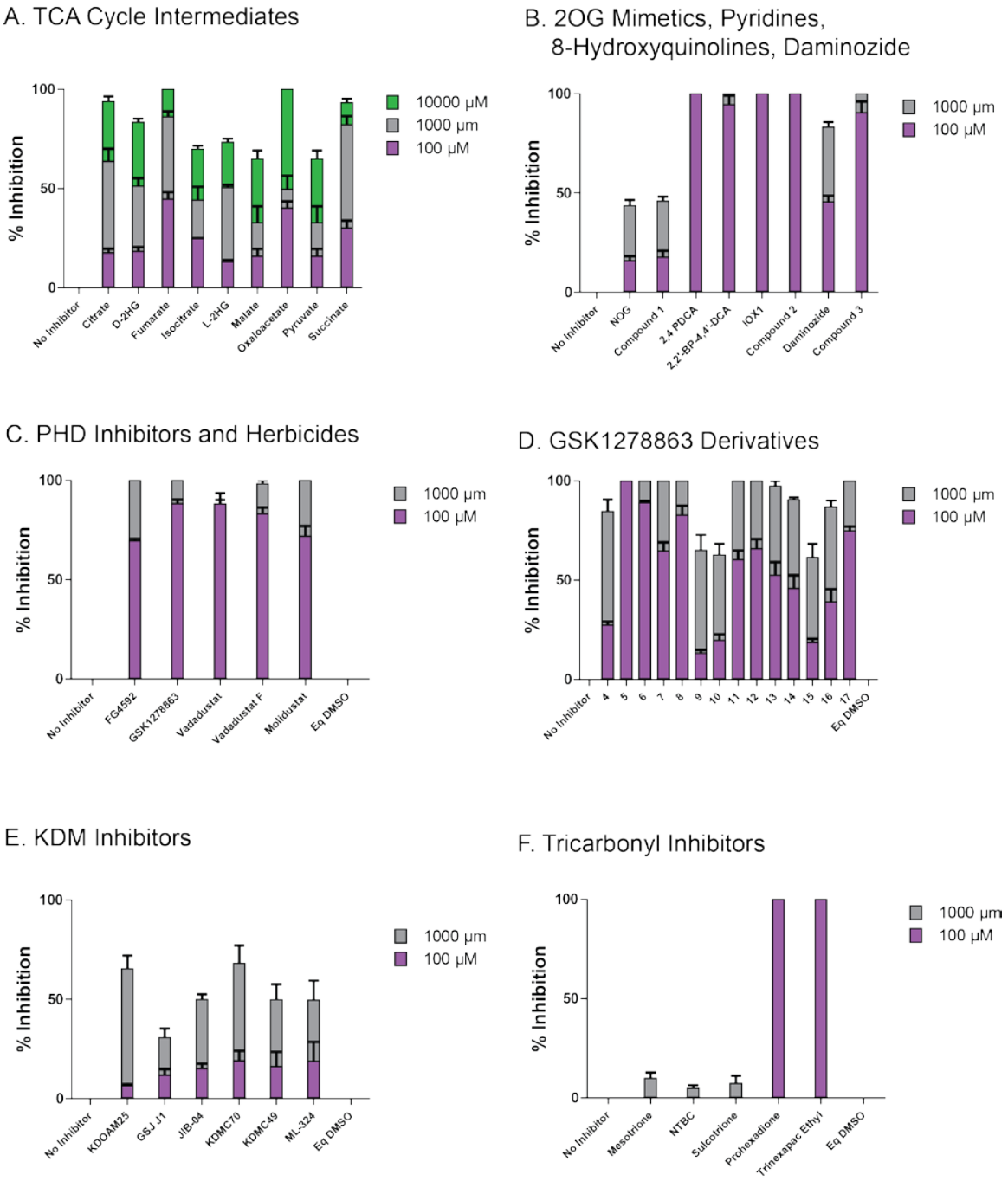

FIGURE 5.7. **End-point Inhibition study of JMJD6 using MALDI-TOF MS**. Bar charts showing the extent of JMJD6 inhibition by 0.1, 1, and 10 mM (A) TCA cycle intermediate,

(B) 2OG mimetics, pyridines, 8-hydroxyquinolines, and daminozide, (C) selective PHD inhibitors, (D) GSK1278863 derivatives, (E) selective KDM inhibitors, and (F) tri-carbonyl inhibitors. Values represent mean (n = 3) ± SD.

Half-maximal inhibitory concentration (IC_{50}) values were then measured for the inhibitors showing ≥ 50% inhibition at 0.1 mM concentration. Despite their poor binding affinities to JMJD6, TCA cycle intermediates were also considered for further inhibition studies owing to their biological importance.

5.4.2. IC_{50} Values Determination of the Compounds Tested against JMJD6

In agreement with other 2OG oxygenases, most TCA cycle intermediates showed IC_{50} values in the millimolar range (Table 5.1; IC_{50} values were calculated from data shown in Figure 5.8). However, fumarate (165 µM), oxaloacetate (204 µM), and succinate (261 µM) were more potent than other tested TCA cycle intermediates, indicating similarity to the findings with PHD2 and FIH (88,89). IC_{50} values for D- and L-hydroxyglutarate (D- and L-2HG) were 622 and 871 µM, respectively. Although weak, inhibition of JMJD6-catalyzed hydroxylation by these two enantiomers of hydroxyglutarate supports a possible connection between JMJD6 and cancer, as cancer cells with specific mutations in the isocitrate dehydrogenase (IDH) gene show substantially high levels of 2HG (90-92). Next, JMJD6 was also weakly inhibited by the generic 2OG oxygenase inhibitor NOG and its dimeric form **1** (IC_{50} 296 and 189 µM, respectively) (Table 5.1; IC_{50} values were calculated from data shown in Figure 5.9), whereas NOG has been reported to potently inhibit PHD2 and FIH (88,89). Conversely to NOG and **1**, JMJD6 was potently inhibited by IOX1 (IC_{50} 10 µM). A structural derivative of IOX1, **2**, was even more potent (IC_{50} 5 µM). As mentioned earlier, IOX1 is a broad-spectrum histone demethylase inhibitor (87). Nevertheless, similar potency of this compound against FIH and PHD2 has also been observed previously (55).

Table 5.1. IC_{50} values of the compounds tested against JMJD6. The IC_{50} values were determined following the hydroxylation assay procedure in the presence of various concentrations of the inhibitors as described in Chapter 10. Values represent mean (n = 3) ± SD.

TCA Cycle Intermediates	**IC_{50} (μM)**	**Derivatives of Daprodustat**	**IC_{50} (μM)**
Citrate	987 ± 1.3 μM	**4**	175 ± 1.5
D-2HG	622 ± 1.4 μM	**5**	19 ± 1.3
Fumarate	165 ± 1.4 μM	**6**	23 ± 1.2
Isocitrate	1055 ± 1.5 μM	**7**	43 ± 1.1
L-2HG	871 ± 1.5 μM	**8**	27 ± 1.4
Malate	5103 ± 2 μM	**9**	67 ± 1.2
Pyruvate	2377 ± 1.7 μM	**10**	58 ± 1.4
Oxaloacetate	204 ± 2.0 μM	**11**	135 ± 1.3
Succinate	261 ± 2.3 μM	**12**	163 ± 1.3
		13	214 ± 1.4
2OG mimetics, pyridines, 8-hydroxyquinoline, and daminozide	**IC_{50} (μM)**	**14**	22 ± 1.4
		PHD Inhibitors	**IC_{50} (μM)**
NOG	296 ± 1.9 μM	FG4592	23 ± 1.5 μM
1	189 ± 1.5 μM	GSK1278863	10 ± 1.2 μM
2,4 PDCA	13 ± 1.3 μM	Molidustat	74 ± 1.6 μM
2,4 BPDCA	6 ± 1.6 μM	Vadadustat	7 ± 1.6 μM
IOX1	10 ± 1.5 μM	AKB-6899	9 ± 1.5 μM
2	5 ± 1.3 μM	**Tricarbonyl compounds**	**IC_{50} (μM)**
Daminozide	94 ± 1.5 μM	Prohexadione calcium	6 ± 1.3
3	25 ± 2.0 μM	Trinexapac ethyl	6 ± 1.2

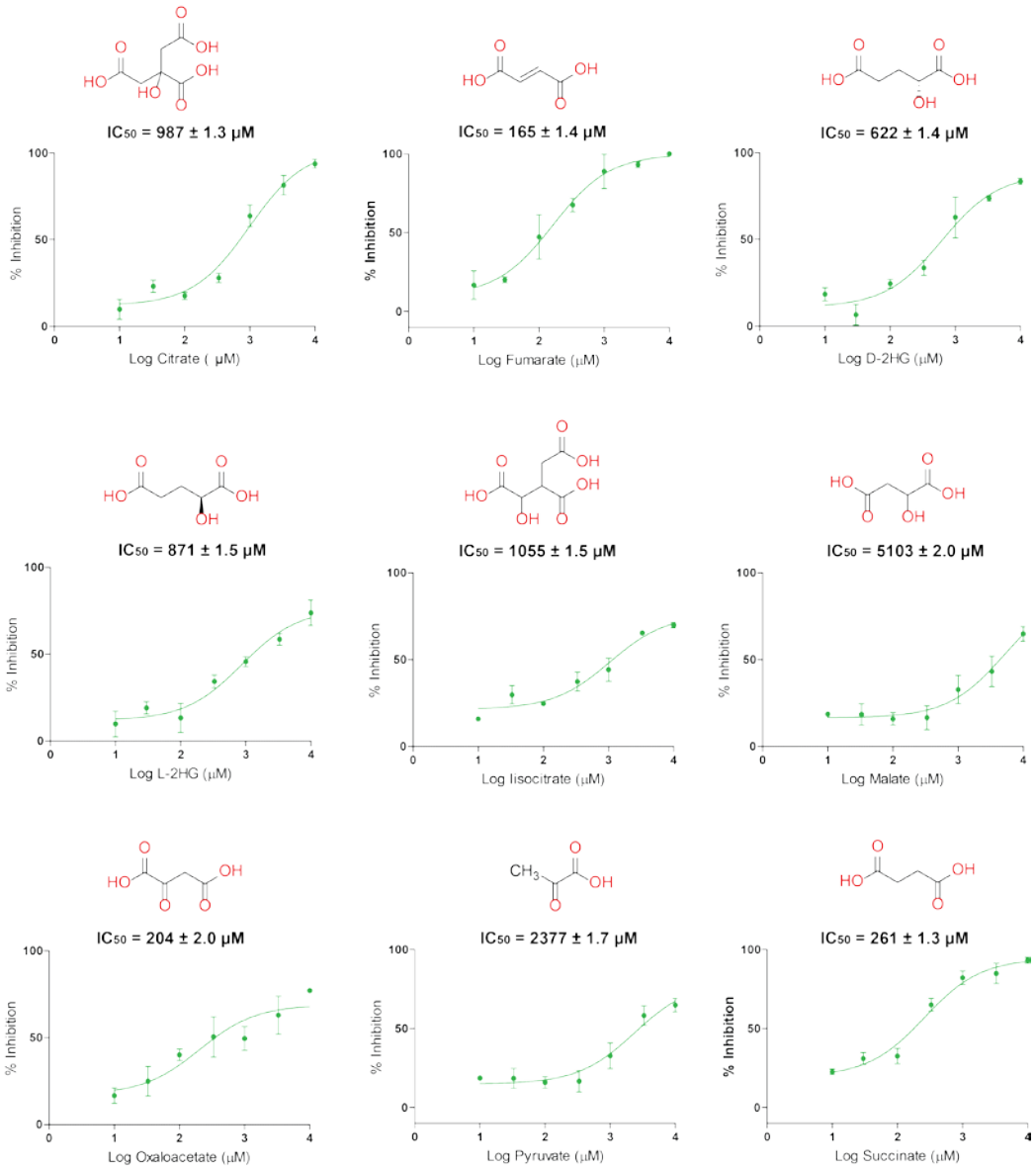

FIGURE 5.8. ***IC*$_{50}$ curves of the TCA cycle intermediates**. Inhibition assays were carried out using 10 µM JMJD6$^{\Delta 363\text{-}403}$, 24 µM 2OG (K_m of 2OG), 100 µM Fe(II), 400 µM ascorbate, and 100 µM LUC7L2$_{267\text{-}278}$ peptide (NPKRSRSREHRR) in the presence of inhibitors (0-10 mM) (**Chapter 10**). Values represent mean (n = 3) ± SD.

Like the quinolines, potent inhibitory activity against JMJD6 was also observed by the pyridine derivatives. 2,4-PDCA and 2,4-BPCA showed measured *IC*$_{50}$ values 13 and 6 µM, respectively (Table 5.1; *IC*$_{50}$ values were calculated from data shown in Figure 5.9). It is interesting that JMJD6 shows selectivity towards bipyridyl 2,4-BPDCA (Figure 5.1). Although, no inhibition data for 2,4-BPDCA, at least to date, has been reported against

any of the 2OG oxygenases, a series of structural derivatives of 2,4-BPDCA (Figure 5.10) have been reported to inhibit KDM4E with moderate to strong potency (93). Apart from these compounds, two close structural analogues of 2,4-BPDCA, *e.g.* 2,5-BPDCA and FG0041 (4-oxo-1,10-phenanthroline-3-carboxylate) (Figure 5.10), were also reported as potential 2OG oxygenase inhibitors (94-96). Both can inhibit CP4H *in vitro* and in cells by binding to the active site metal (95) whereas the latter shows inhibition against PHD2 (96) and FIH (94) also. Notably, non-denaturing ESI-MS and crystallographic studies showed that bipyridyl compounds coordinate the active-site Fe(II) (93).

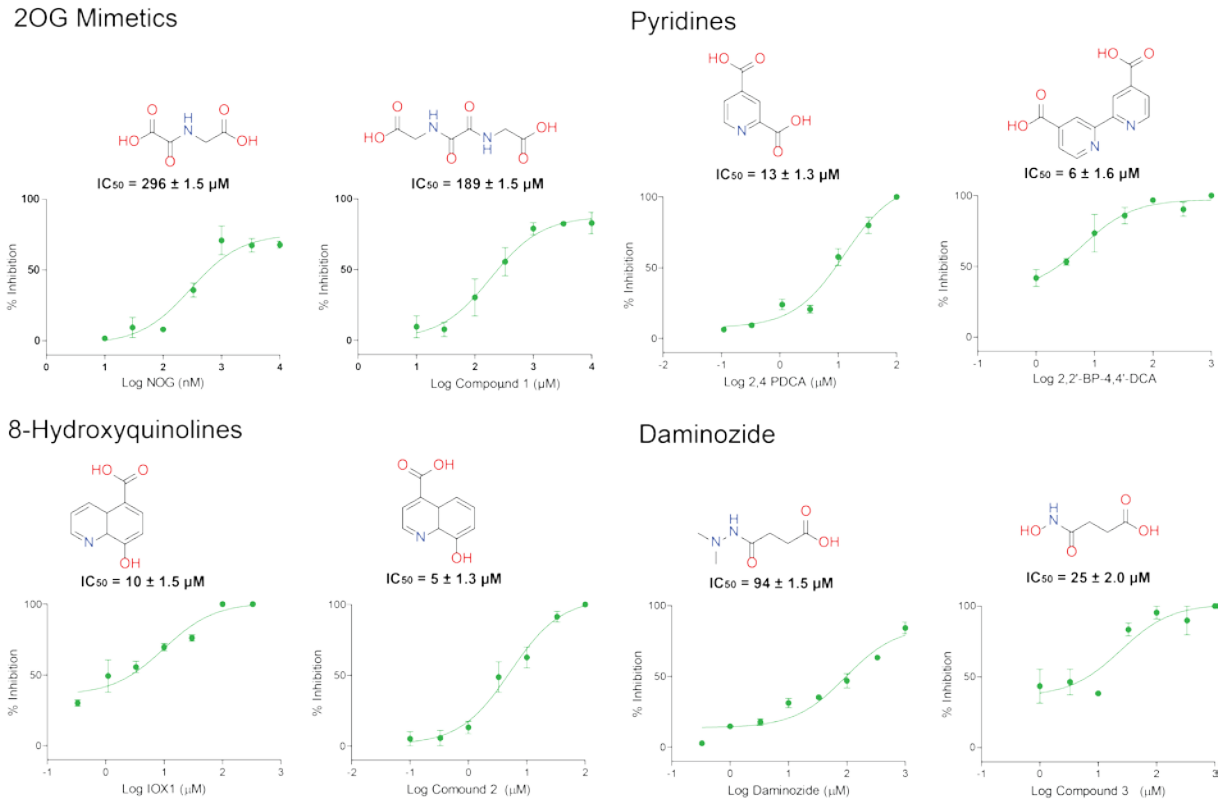

FIGURE 5.9. ***IC*$_{50}$ curves of the 2OG mimetics, 8-hydroxyquinolines, pyridines, and daminozide.** Inhibition assays were carried out using 10 μM JMJD6$^{\Delta 363\text{-}403}$, 24 μM 2OG (K_m of 2OG), 100 μM Fe(II), 400 μM ascorbate, and 100 μM LUC7L2$_{267\text{-}278}$ peptide (NPKRSRSREHRR) in the presence of inhibitors (0-10 mM) (**Chapter 10**). Values represent mean (n = 3) ± SD.

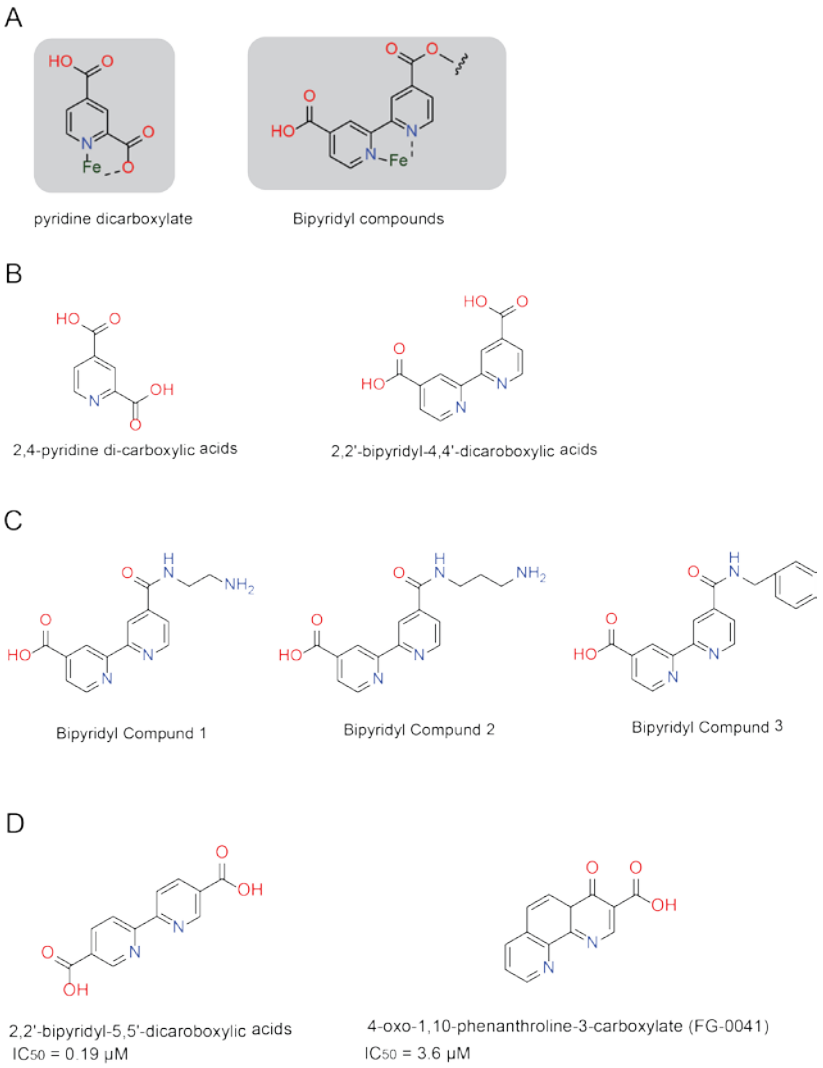

FIGURE 5.10. **Pyridyl and bipyridyl inhibitors of 2OG oxygenases**. (A) Structural studies of 2OG oxygenases in complex with pyridyl and bipyridyl inhibitors show that they occupy the same binding site as 2OG *via* chelation to the active-site Fe(II) (93). (B) Pyridyl compounds tested for JMJD6 inhibition. (C) Bipyridyl compounds reported to inhibit KDM4E (93). (D) Bipyridyl compounds reported to inhibit CP4H, PHD2 and FIH (94-96).

Daminozide, once a plant growth retardant (but withdrawn later due to toxicity) and a selective KDM inhibitor (97), was also tested against JMJD6 for inhibition. Unlike the quinoline and pyridine derivatives, daminozide was able to inhibit JMJD6 only weakly. The measured IC_{50} value was 94 µM (Table 5.1; IC_{50} values were calculated from data shown in Figure 5.9) supporting that daminozide is a highly selective inhibitor of

demethylases, and not of hydroxylases. Surprisingly, a very close structural derivative of daminozide, **3** (Figure 5.1) appeared to inhibit JMJD6 (IC_{50} = 25 µM) (Table 5.1; IC_{50} values were calculated from data shown in Figure 5.9). Interestingly, **3** has also been shown to inhibit PHD2 with a comparable potency (IC_{50} 20 µM) (97). Taken together with the exception of NOG, the other 2OG competitors showed moderate to strong inhibition of JMJD6.

Next, the sensitivity of JMJD6 to PHD inhibitors was tested. Except for Molidustat (IC_{50} 74 µM), the PHD inhibitors appeared to inhibit JMJD6 with relatively strong potency with measured IC_{50} values less than 25 µM (Table 5.1, IC_{50} values were calculated from data shown in Figure 5.11). A set of structural derivatives of Daprodustat (Figure 5.1) was also screened. Despite only weakly competing with JMJD6-bound 2OG (Figure 5.2), compounds **6-9,** and **17** potently inhibited JMJD6 (Table 5.1, IC_{50} values were calculated from data shown in Figure 5.12). This suggests that compounds **6-9**, and **17** probably inhibited JMJD6 activity by binding at an allosteric site (97) or by ejecting the active-site Fe(II) as was observed in the case of some KDM inhibitors (98). As already mentioned earlier, these compounds showed potent inhibition against OGFOD1 (Cyrille Thinnes, D.Phil Thesis, Chemistry Research Laboratory, University of Oxford), yet the mechanism of inhibition is still unknown. Nevertheless, overall data suggest that JMJD6 is not susceptible to KDM inhibitors, but may be inhibited by PHD inhibitors.

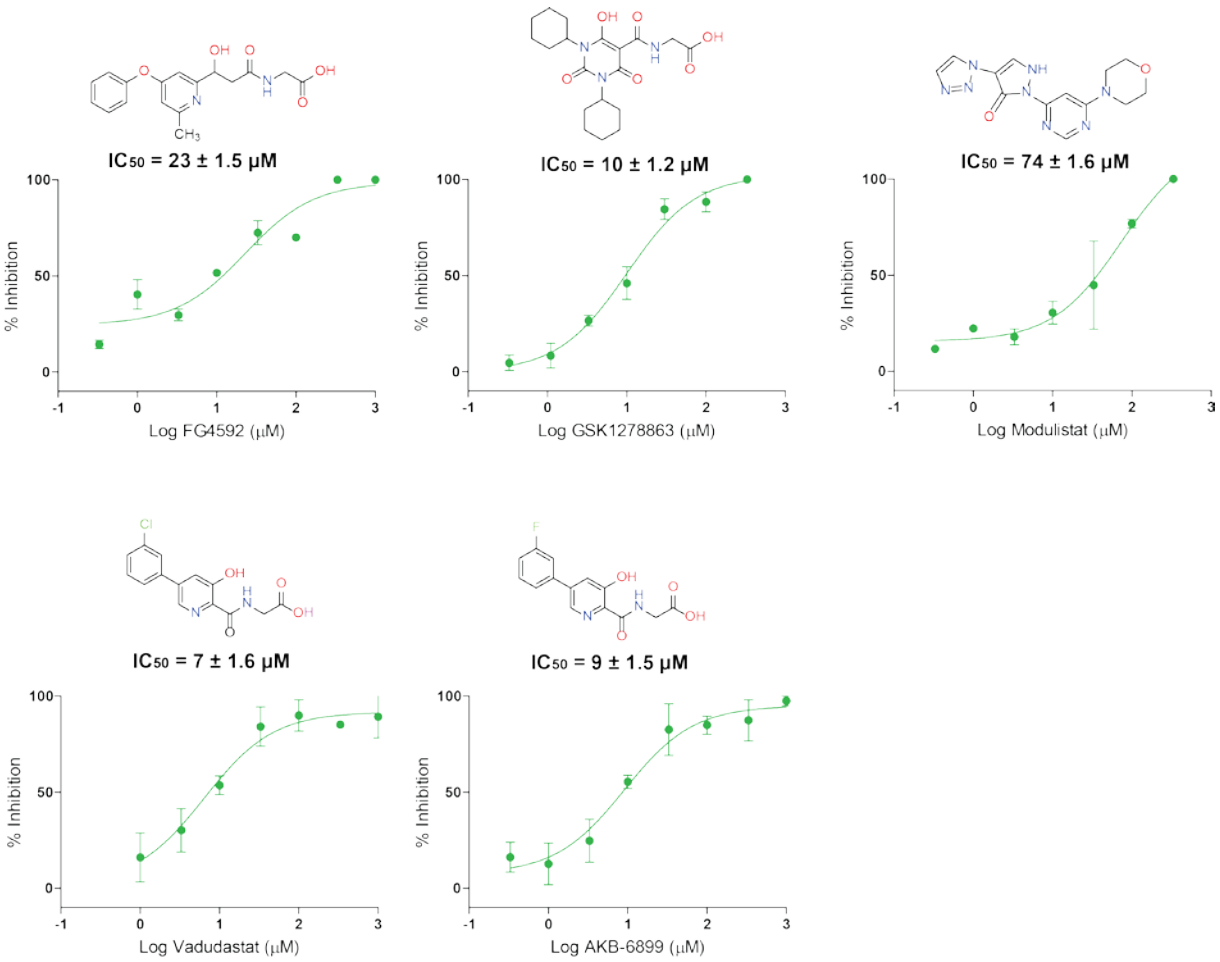

FIGURE 5.11. ***IC*$_{50}$ curves of the selective PHD inhibitors**. Inhibition assays were carried out using 10 µM JMJD6$^{\Delta 363\text{-}403}$, 24 µM 2OG (K_m of 2OG), 100 µM Fe(II), 400 µM ascorbate, and 100 µM LUC7L2$_{267\text{-}278}$ peptide (NPKRSRSREHRR) in the presence of the inhibitors (0-1 mM) (**Chapter 10**). Values represent mean (n = 3) ± SD.

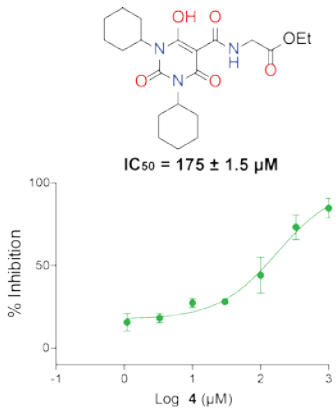

IC_{50} = 175 ± 1.5 µM

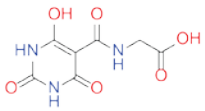

IC_{50} = 19 ± 1.3 µM

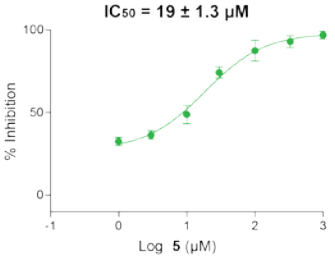

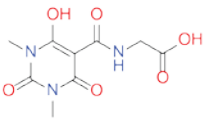

IC_{50} = 23 ± 1.2 µM

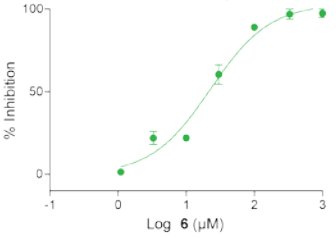

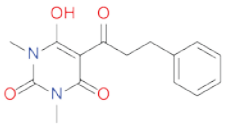

IC_{50} = 43 ± 1.1 µM

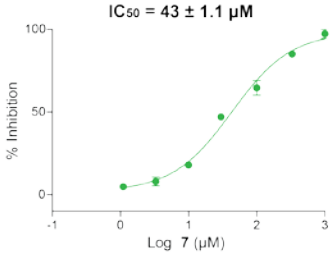

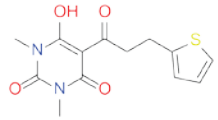

IC_{50} = 27 ± 1.4 µM

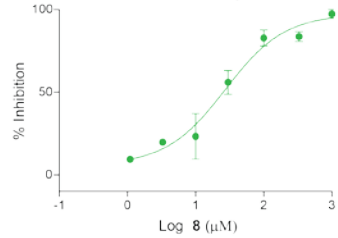

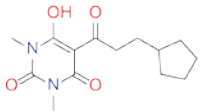

IC_{50} = 67 ± 1.2 µM

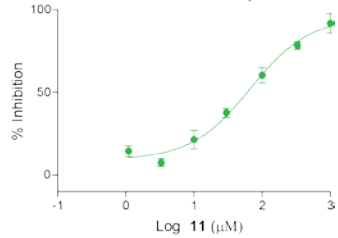

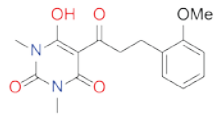

IC_{50} = 58 ± 1.4 µM

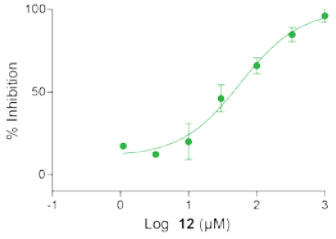

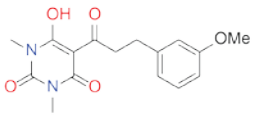

IC_{50} = 135 ± 1.3 µM

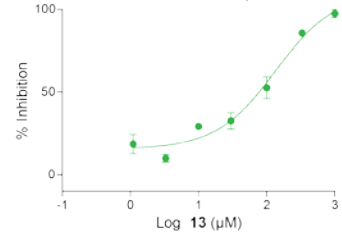

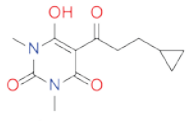

IC_{50} = 163 ± 1.3 µM

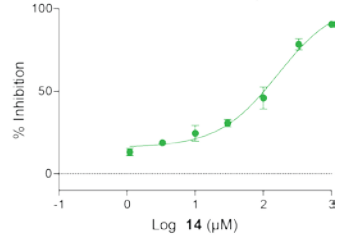

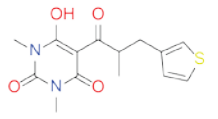

IC_{50} = 214 ± 1.4 µM

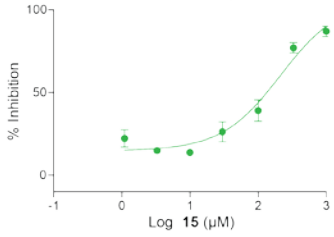

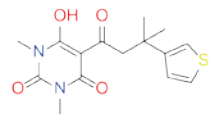

IC_{50} = 22 ± 1.4 µM

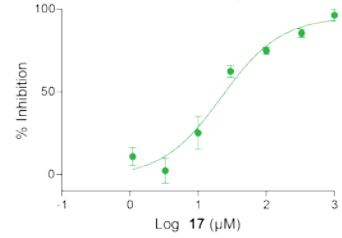

FIGURE 5.12. ***IC*$_{50}$ curves of the structural analogues of Daprodustat.** Inhibition assays were carried out using 10 µM JMJD6$^{\Delta 363\text{-}403}$, 24 µM 2OG (K_m of 2OG), 100 µM Fe(II), 400 µM ascorbate, and 100 µM LUC7L2$_{267\text{-}278}$ peptide (NPKRSRSREHRR) in the presence of the inhibitors (0-1 mM) (**Chapter 10**). Values represent mean (n = 3) ± SD.

The tri-carbonyl inhibitors prohexadione calcium and trinexapac ethyl appeared to inhibit JMJD6 relatively strongly (Table 5.1, Figure 5.13), despite showing only 20% displacement of JMJD6-bound 2OG by NMR (Figure 5.2). This indicates the likely prevalence of an alternative inhibition mechanism (97,98).

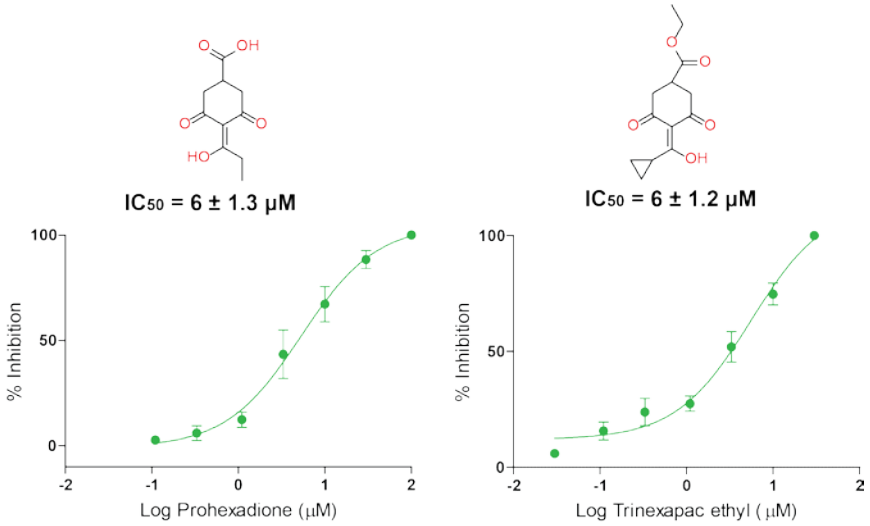

FIGURE 5.13. ***IC*$_{50}$ curves of the tri-carbonyl inhibitors**. Inhibition assays were carried out using 10 µM JMJD6$^{\Delta 363\text{-}403}$, 24 µM 2OG (K_m of 2OG), 100 µM Fe(II), 400 µM ascorbate, and 100 µM LUC7L2$_{267\text{-}278}$ peptide (NPKRSRSREHRR) in the presence of the inhibitors (0-1 mM) (**Chapter 10**). Values represent mean (n = 3) ± SD.

CHAPTER 06: Structure Determination of JMJD6 in Complex with Inhibitors

6.1. Introduction

The majority of 2OG oxygenase active-site contains a HxD/E…x_n…H iron binding motif comprising one aspartyl/glutamyl and two histidyl residues (8). Most 2OG oxygenase inhibitors have been reported to target the active-site Fe(II) and proximal cavities, often including the co-substrate binding sites (4). Crystal structures of factor inhibiting HIF (FIH) in complex with the cosubstrate 2OG (2-oxoglutarate) (PDB: 1H2L) and a broad spectrum 2OG oxygenase inhibitor NOG (N-oxalylglycine) (PDB: 1H2K) clearly reveal that NOG occupies the same binding pocket as 2OG (Figure 6.1) (64). Inhibitors that simultaneously target the cosubstrate- and substrate-binding residues, and hence compete with both substrates for their binding-pockets, have been subsequently developed (Figure 6.1). For example, a crystal structure of γ-butyrobetaine hydroxylase (BBOX) in complex with the inhibitor AR692B (PDB: 4C8R) reveals the latter to occupy both the substrate and the cosubstrate binding pockets (NOG substituting for 2OG in this case) (PDB: 3MS5, 3O2G) (Figure 6.1) (99). Selective inhibitors have been developed by exploiting differences around and within the binding pocket of the 2OG cosubstrate. A crystal structure of FIH in complex with the selective inhibitor N-oxalyl-D-phenylalanine (NOFD) reveals why it is selective for FIH over HIF prolyl hydroxylase (PHD2) (Figure 6.2**A**) (100). Crystal structures of KDM4A in complex with inhibitors N-oxalyl-D-(O-benzyl)tyrosine) (NOBT) and (4'-[(2-aminoethyl)carbamoyl]-2,2'-bipyridine-4-carboxylic acid) indicate why these compounds are selective for KDM4A over the JmjC hydroxylases (Figure 6.2**B**, 6.2**C**) (93,101). A crystal structure of PHD2 in complex with (N-[(1-chloro-4-hydroxyisoquinolin-3-yl)carbonyl]glycine) is also shown in figure 6.2**D** and reveals why this compound weakly inhibits FIH compared to its more potent inhibition on PHD2 (102).

The work described in this Chapter aimed to better understand the binding modes of the JMJD6-inhibitors identified in Chapter 5. Prior to this study, there was no crystal structure

of JMJD6 in complex with inhibitors. Given the chemical interest in 2OG oxygenase inhibition, obtaining structures of JMJD6/inhibitor complexes was therefore of interest.

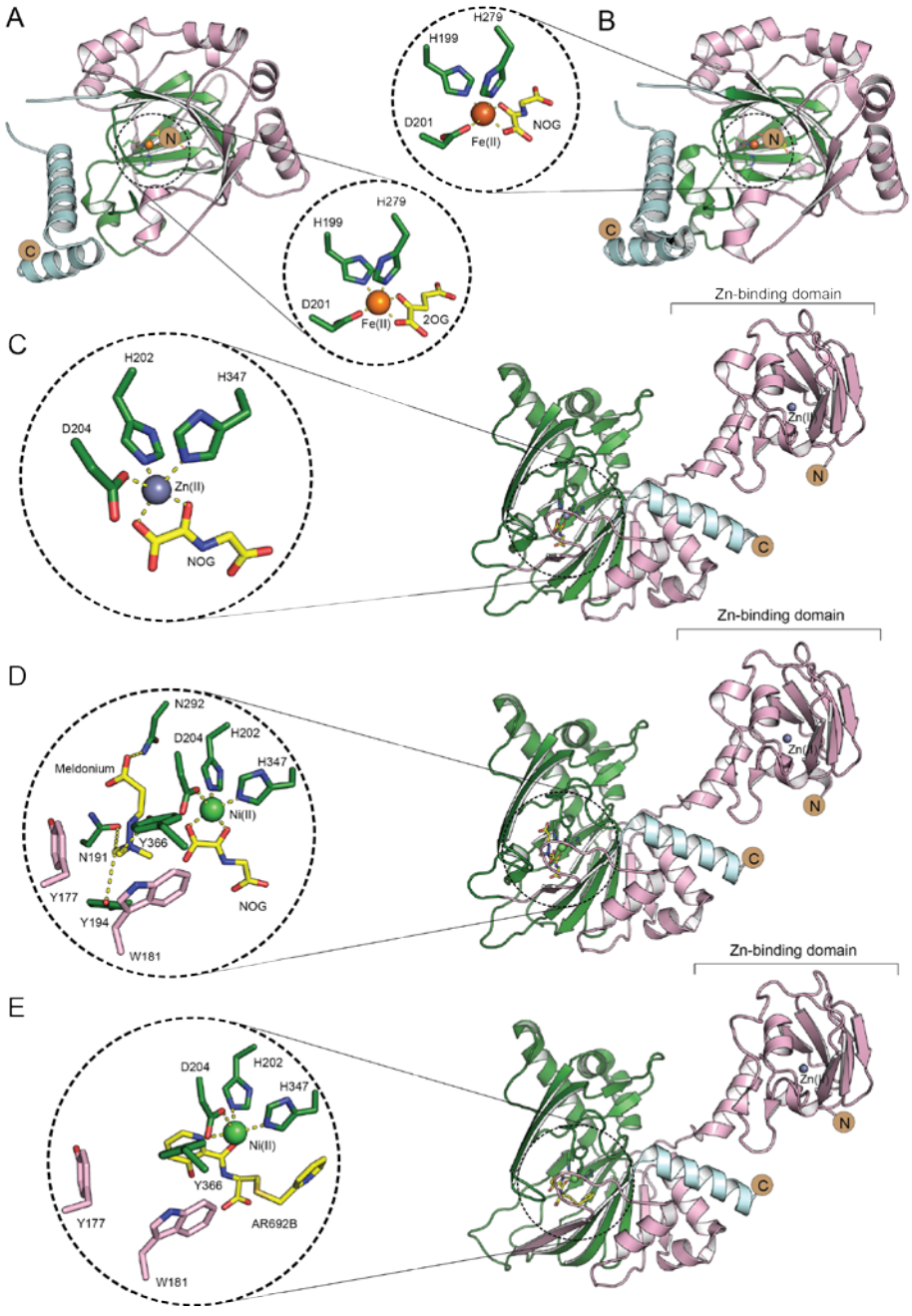

FIGURE 6.1. **Examples of inhibitors occupying cosubstrate and substrate binding pockets**. Views from crystal structures of (A) FIH in complex with 2OG (PDB: 1H2L), (B) FIH in complex with NOG (PDB: 1H2K), (C) BBOX in complex with NOG (3O2G), (D) BBOX in complex with NOG and the inhibitor/substrate meldonium (PDB: 3MS5), and (E) BBOX in complex with the inhibitor AR692B (PDB: 4C8R). Color code: JmjC domain as

green; *N*-terminal regions as light pink; *C*-terminal regions as pale cyan; ligands yellow, Ni(II), Zn(II), and Fe(II) as green, purple, and orange spheres, respectively.

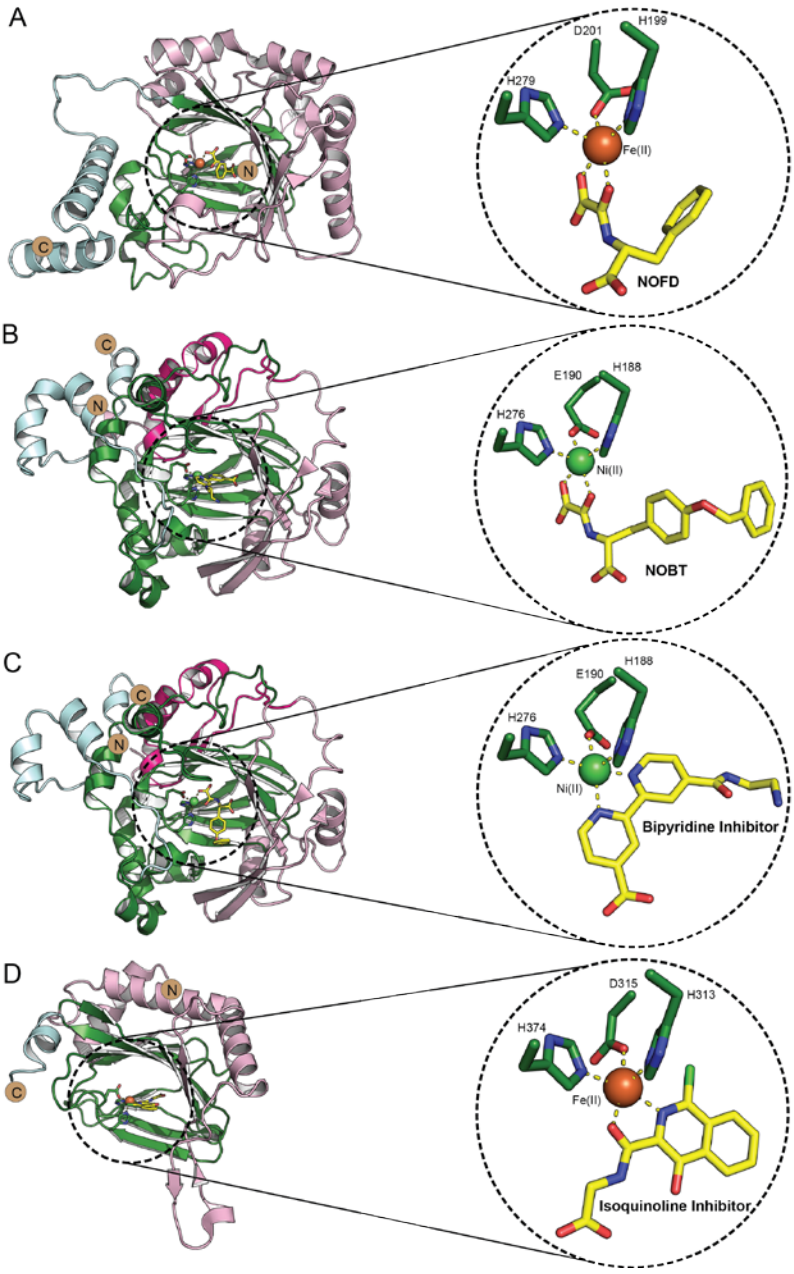

FIGURE 6.2. **Examples of selective inhibitors of 2OG oxygenases**. Cartoon representations of: (A) FIH in complex with selective inhibitor NOFD (PDB: 1YCI); (B) KDM4A in complex with the inhibitor NOBT (PDB: 2WWJ); (C) KDM4A in complex with a bipyridyl inhibitor (PDB: 3PDQ); (D) PHD2 in complex with a selective isoquinoline inhibitor (PDB: 3HQU), which does not inhibit FIH. Color code: similar to figure 1. NOBT and the bipyridyl compounds are selective KDM4A inhibitors (93,101).

6.2. Structure Determination of JMJD6 in Complex with Inhibitors

Crystallographic data collection, molecular replacement, and structure refinement for the crystal structures of JMJD6.inhibitor complexes described in this Chapter were performed with the help of Dr. Michael A. McDonough (Chemistry Research Laboratory, University of Oxford), unless otherwise stated.

Attempts to co-crystallize JMJD6 with inhibitors were carried out by sitting-drop vapour-diffusion method (78) using the construct JMJD6$^{\Delta 344\text{-}403}$ and previously optimized crystallisation conditions (**Chapter 04**). In summary, crystal structures of JMJD6$^{\Delta 344\text{-}403}$ in complex with 4 inhibitors (NOG, 2,4-PDCA, fumarate, and succinate) were determined. These inhibitors are relatively 'generic' and have also been reported to inhibit other 2OG oxygenases with moderate to strong potency (4). Crystal structures for some of them are reported in complex with other 2OG oxygenases also (Table 6.1).

Despite their weak binding at the active-site of JMJD6 (except 2,4-PDCA), crystal structures of JMJD6 in complex with NOG, 2,4-PDCA, fumarate, and succinate were determined (Table 6.2, Figure 6.3). Crystal structure of JMJD6$^{\Delta 344\text{-}403}$ in complex with Mn(II) (catalytically inactive Mn(II) was used as the Fe(II) surrogate) and the inhibitor NOG was first determined, which diffracted to 2.2 Å resolution (Table 6.2). Molecular replacement (MR) produced a solution for the structure in the orthorhombic space group $C222_1$ with 4 molecules (mol) per asymmetric unit (ASU) (Figure 6.3). The unit cell dimensions are a=77.6, b=214.0, c=215.2 (Å) and angles α=β=□= 90 (θ). Another JMJD6 crystal structure in complex with 2,4-PDCA was determined in the same space group $C222_1$ and crystal packing (4mol/ASU) (data collection for the JMJD6$^{\Delta 344\text{-}403}$.Mn(II).2,4-PDCA complex was performed by Dr. Rasheduzzaman Chowdhury, Chemistry Research Laboratory). The unit cell dimensions in this case were a=76.6, b=211.5 c=212.4 (Å) and angles 90^0 (Table 6.2).

Table 6.1. A sample of reported crystal structures of human 2OG oxygenases in complex with their inhibitors.

Abbreviation	Full Name	PDB ID	Active Site Metal	Ligand	Resolution (Å)	ASU	Reference
FIH	Factor inhibiting hypoxia-inducible factor	1H2K	Fe(II)	NOG	2.15	1	(64)
		2CGO	Fe(III)	Fumarate	2.4	1	(88)
		2CGN	Fe(III)	Succinate	2.4	1	(88)
		2W0X	Fe(II)	2,4-PDCA	2.12	1	(103)
PHD2	Prolyl hydroxylase domain 2	3HQR	Mn(II)	NOG	2.0	1	(102)
OGFOD1	Human uS12 prolyl 3-hydroxylase	4NHX	Mn(II)	NOG	2.11	1	(59)
OGFOD1	Human uS12 prolyl 3-hydroxylase	4NHY	Mn(II)	2,4-PDCA	2.6	4	(59)
BBOX	γ-butyrobetaine hydroxylase	3O2G	Zn(II)	NOG	1.78	1	(99)
JMJD2A	JmjC domain containing protein 2A	2P5B	Fe(II)	NOG	1.99	2	(104)
		5FYH	Mn(II)	Fumarate	2.3	2	(99)
		5FYC	Ni(II)	Succinate	2.2	2	(99)
		2VD7	Ni(II)	2,4-PDCA	2.25	2	(105)
JMJD2B	JmjC domain containing protein 2B	4LXL	Ni(II)	2,4-PDCA	1.87	1	(99)
JMJD2D	JmjC domain containing protein 2B	4D6Q	Ni(II)	2,4-PDCA	1.29	1	(99)
FTO	Fat mass and obesity associated protein	4IDZ	Ni(II)	NOG	2.46	1	(106)
		4IE0	Zn(II)	2,4-PDCA	2.53	1	(106)
ALKBH5	Alkylated DNA repair protein alkB homolog 5	4NRQ	Mn(II)	2,4-PDCA	2.5	1	(107)

Table 6.2. Crystallographic data collection and refinement statistics.

Protein	JMJD6.Mn(II). NOG	JMJD6.Mn(II). 2,4-PDCA	JMJD6.Mn(II). Succinate	JMJD6.Mn(II). Fumarate
X-Ray Source	DLS IO4-1	DLS IO2	DLS IO3	DLS IO3
Wavelength (Å)	0.92819	0.9798	1.0077	0.97947
Resolution (Å)	51.90-2.29 (6.20-2.29)*	47.41-2.80 (2.70-2.80)*	101.40-2.98 (8.00-2.98)*	212.60-2.66 (7.20-2.66)*
Space Group	$C222_1$	$C222_1$	$P2_12_12_1$	$C222_1$
Unit Cell Dimensions				
a, b, c	77.6, 214.0, 215.2	76.6, 211.5, 212.4	101.4, 142.0, 155.9	77.0, 211.3, 212.6
α, β, λ	90, 90, 90	90, 90, 90	90, 90, 90	90, 90, 90
Molecules per ASU	**4**	**4**	**4**	**4**
Wilson B Factor (A^2)	51.01	49.72	76.57	54.51
Reflections	80933	49740 (4892)*	46772	50017
Completeness	100 (100)*	100 (100)*	100 (100)*	100 (99.8)*
Multiplicity	13.17 (13.4)*	9.3 (9.0)*	13.3 (14.0)*	20 (20.8)*
I/sI	10.4 (1.3)*	10.7 (1.5)*	10.2 (1.6)*	13.3 (2.1)*
R_{merge}	0.176 (0.34)*	0.165 (1.211)*	0.24 (2.4)*	0.22 (2.06)*
R_{meas}(I)	0.184 (2.44)*	0.174 (0.00)*	0.25 (2.4)*	0.23 (2.12)*
CC half	0.99 (0.62)*	0.99 (0.585)*	0.99 (0.56)*	0.99 (.75)*
R_{cryst}	0.2444	0.2437	0.2130	0.2299
R_{free}	0.2746 (4.92)¥	0.2868 (5.23)¥	0.2563 (4.93)¥	0.2652 (4.79)¥
Deviation from Idealized Geometry				
Bond Length (Å)	0.003	0.003	0.003	0.002
Bond angles (°)	0.601	0.55	0.536	0.486
Average B Factors				
All atoms	70.8	58.9	101.2	69.8
Protein	71.1	58.8	102.0	70.1
Ligand	51.6	52.5	100.2	53.0
Metal	41.8	48.4	61.3	40.3
Water	56	50.8	61.0	50.2
Ramachandran Plot				
Favored	97.45	96.9	96.1	97.74
Allowed	2.55	3.02	3.75	2.19
Disallowed	0	0	0	0
Outlier	0.0	0.08	0.16	0.08

* High resolution bin.

¥ Percentage of the total reflections used for R_{free} calculations.

Despite the relatively weaker JMJD6 inhibition potency of TCA cycle intermediates, co-crystallisation of the TCA cycle intermediates was attempted, which eventually determined crystal structures of JMJD6 in complex with fumarate and succinate (Table 6.2, Figure 6.3). The JMJD6.Mn(II).succinate complex was crystallized in the orthorhombic space group $P2_12_12_1$ with 4mol/ASU and diffracted to 2.9 Å resolution with unit cell dimensions a=101.4, b=142.0 and c=155.9 (Å) and angles 90^0 (Figure 6.3). By contrast, crystals of JMJD6 in complex with fumarate diffracted to 2.6 Å resolution and indicated a $C222_1$ space group with 4mol/ASU (Table 6.2, Figure 6.3), similarly to the JMJD6 structures with NOG and 2,4-PDCA (Table 6.2).

Superimposition of the JMJD6-inhibitor complexes onto the crystal structure of JMJD6 reported by Mantri *et al.* (36) reveals a similar backbone conformation for the major (βI, βIII, βVI, βVIII) and minor (βII, βIV, βV, βVII) β-sheets (Figure 6.4). No change is observed either in the α-helices or in the 5 extra β-strands at the *N*-termini (Figure 6.4). Although the construct used for crystallographic studies was a truncated JMJD6 comprising residues 1 to 343, only residues 1 to 336 were observed in the structures with NOG, fumarate, and 2,4-PDCA (Figure 6.4). Exceptionally in case of the structure with succinate, 5 more residues (LVPRG) from the His_6-Tag at the *N*-terminus and 4 more residues (Gly^{337}-Ser^{340}) at the *C*-terminus are also observed (Figure 6.4**E**).

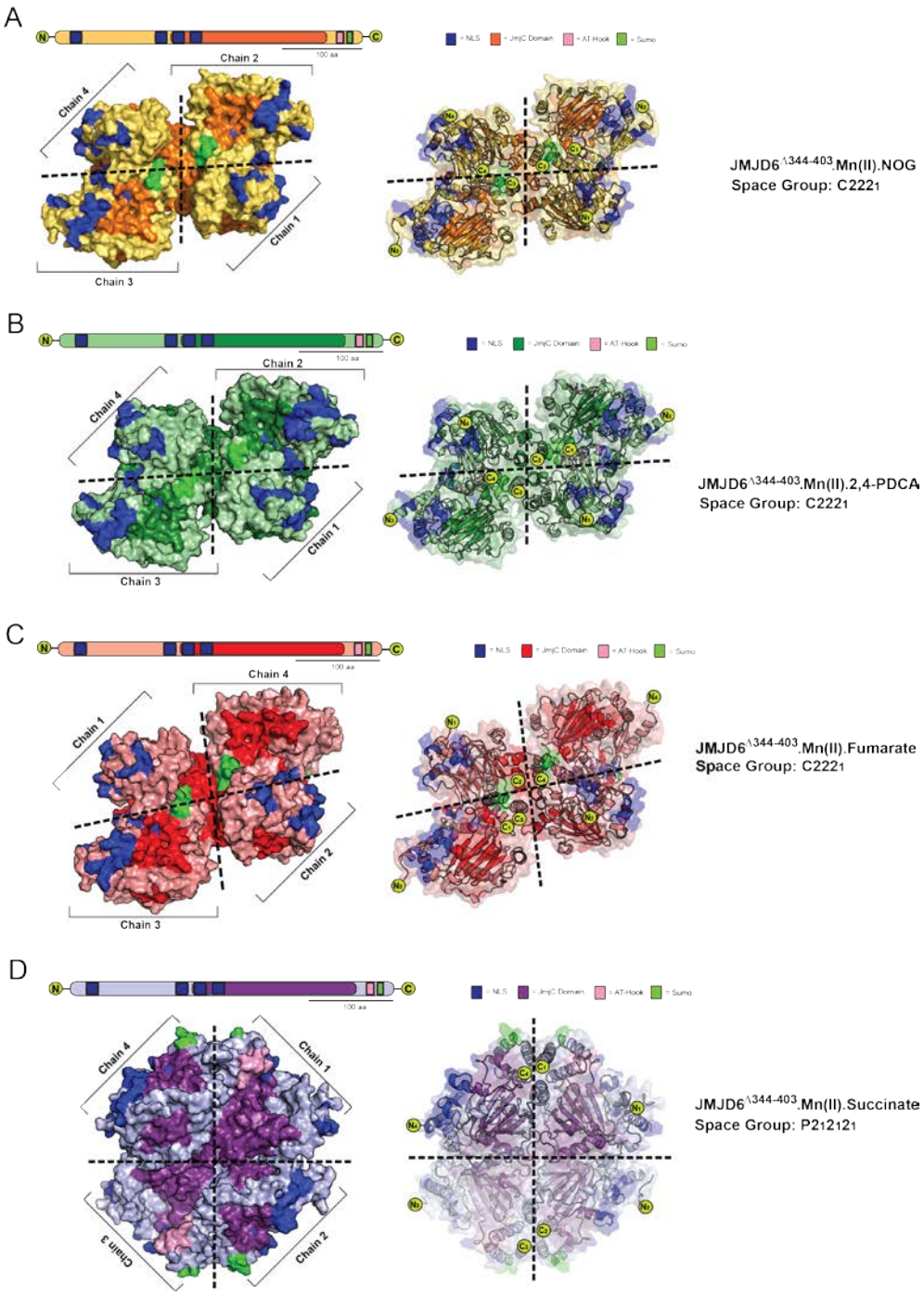

FIGURE 6.3. **JMJD6 in complex with inhibitors.** Surface and cartoon representations of crystal structures of JMJD6 in complex with (A) NOG, (B) 2,4-PDCA, (C) fumarate, and (D) succinate. Dotted lines indicate the interfacial axis between molecules in the ASU.

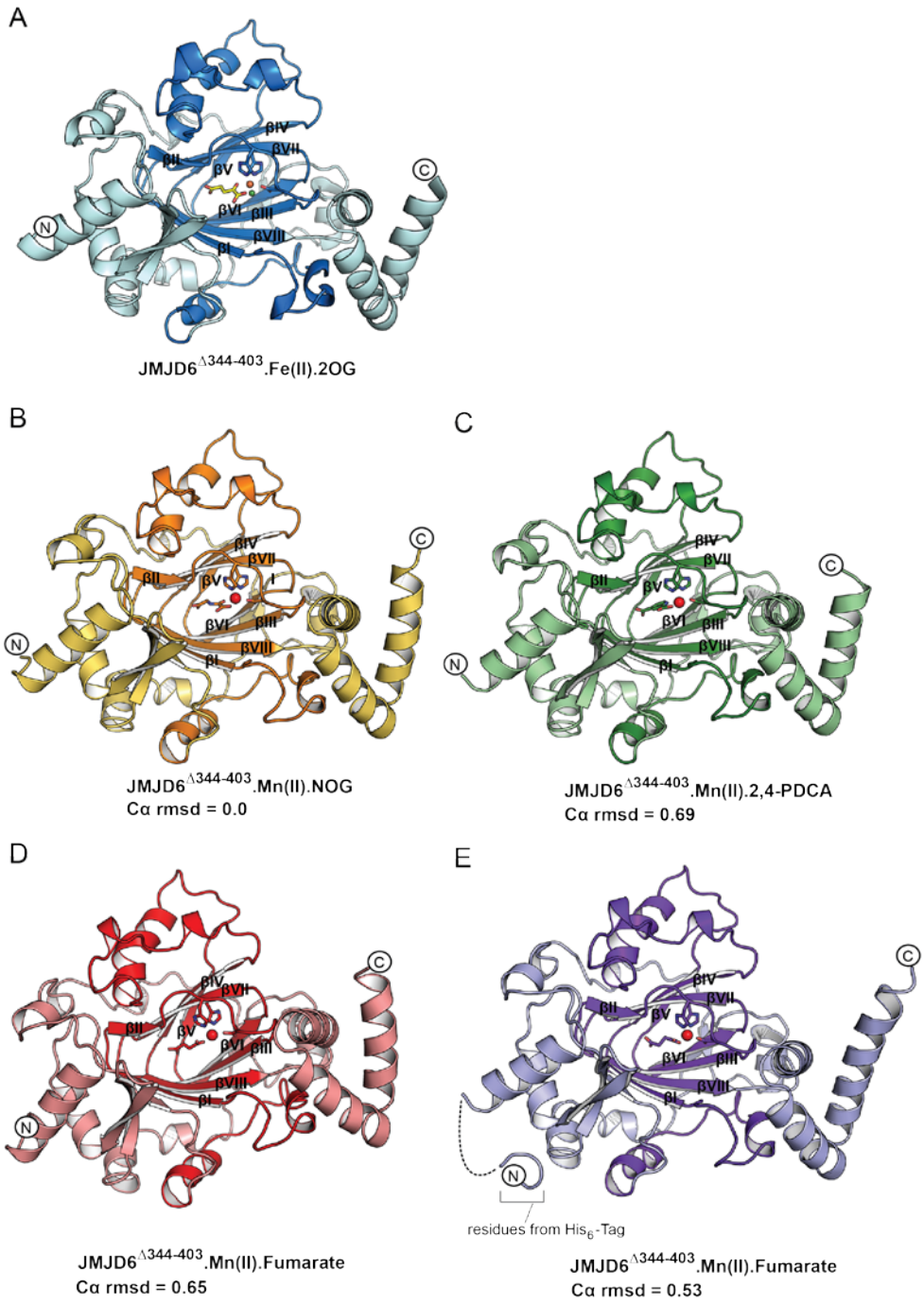

FIGURE 6.4. **Comparison of overall folds of JMJD6.inhibitor complex structures.** Cartoon representations of crystal structures of JMJD6 in complex with (A) NOG, (B) 2,4-PDCA, (C) fumarate, and (D) succinate. No change in overall structure of JMJD6 was observed.

6.3. Comparative Studies on Crystal Packing of JMJD6.Inhibitor Complexes

The structures were then analysed for potential changes (if any) in the oligomerization state within the crystals. Variation in the interacting regions between molecules within the crystal packing was observed for the JMJD6 structures with NOG ($C222_1$), 2,4-PDCA ($C222_1$), fumarate ($C222_1$), and succinate ($P2_12_12_1$) (Table 6.3), as determined using PISA (Protein Interfaces Surfaces and Assemblies) (82). Next, the interacting regions between the molecules comprising the ASU were analysed for both the $C222_1$ and $P2_12_12_1$ crystal forms. In order to do this, the structure in complex with NOG (space group: $C222_1$) was compared with that in complex with succinate (space group: $P2_12_12_1$) (Figure 6.5). Relatively more buried surface area between the molecules (chain A, B, C, and D) was observed in case of $P2_12_12_1$ crystal form than $C222_1$ (Figure 6.5), suggesting that the interaction between the molecules within each ASU in the $P2_12_12_1$ packing system is stronger than those in the $C222_1$. Notably, the interacting regions between the molecules in the $P2_12_12_1$ crystal form resemble those of the $P12_11$ crystal form observed for the crystal structures of JMJD6$^{\Delta 344\text{-}403}$.Fe(II).2OG and JMJD6^{FL}.Mn(II).NOG (**Chapter 04**).

Table 6.3. Calculation of buried surface area within the crystal structures.

Structure	Chains	Symmetry Operation	Buuried Surface Area ($Å^2$)	$\Delta\ ^iG$ (kcal mol^{-1})	CSS*	Session ID
JMJD6$^{\Delta 344\text{-}403}$.Mn(II). NOG	C/A	x,y,z/x,y,z	1027	-7.0	0.111	592-9I-MDK.
	D/B	x,y,z/x,y,z	769	-5.8	0.111	
	C/A	x,y,z/$x^{-1/2}$,-$y^{-1/2}$,-z	747	-5.0	0.046	
	B/D	x,y,z/$x^{-1/2}$,-$y^{-1/2}$,-z	276	-0.5	0.005	
	A/D	x,y,z/x^{-1},y,z	273	-3.5	.0.068	
	C/B	x,y,z/x-1,y,z	188	-2.5	0..068	
JMJD6$^{\Delta 344\text{-}403}$.Mn(II). 2,4-PDCA	A/C	x,y,z/$x^{-1/2}$,-$y^{-1/2}$,-z	984	-5.9	0.078	592-9I-MDK.
	B/D	x,y,z/$x^{-1/2}$,-$y^{-1/2}$,-z	973	-6.2	0.078	
	D/B	x,y,z/x,y,z	837	-6.9	0.055	
	C/A	x,y,z/x,y,z	337	-0.4	0.055	
	D/C	x,y,z/x-1,y,z	277	-2.8	0.038	
	B/A	x,y,z/x-1,y,z	251	-2.7	0.038	
JMJD6$^{\Delta 344\text{-}403}$.Mn(II). Fumarate	C/A	x,y,z/x,y,z	2751	-0.2	0.0	592-9I-MDK.
	D/B	x,y,z/x,y,z	2741	-2.4	0.0	
	C/B	x,y,z/x,y,z	858	-7.1	0.0	
	D/A	x,y,z/x,y,z	858	-6.8	0.0	
JMJD6$^{\Delta 344\text{-}403}$.Mn(II). Succinate	D/A	x,y,z/x,y,z	2193	-10.8	0.292	592-9I-MDK.
	C/B	x,y,z/x,y,z	1955	-14.3	0.292	
	B/A	x,y,z/x^{-1},y,z	1047	-10.2	0.104	
	C/D	x,y,z/x^{-1},y,z	412	-0.7	0.007	
	B/D	x,y,z/x^{-1},y,z	240	-3.0	0.031	
	C/A	x,y,z/x^{-1},y,z	237	-3.3	0.033	

* Complex Formation Significance Score.

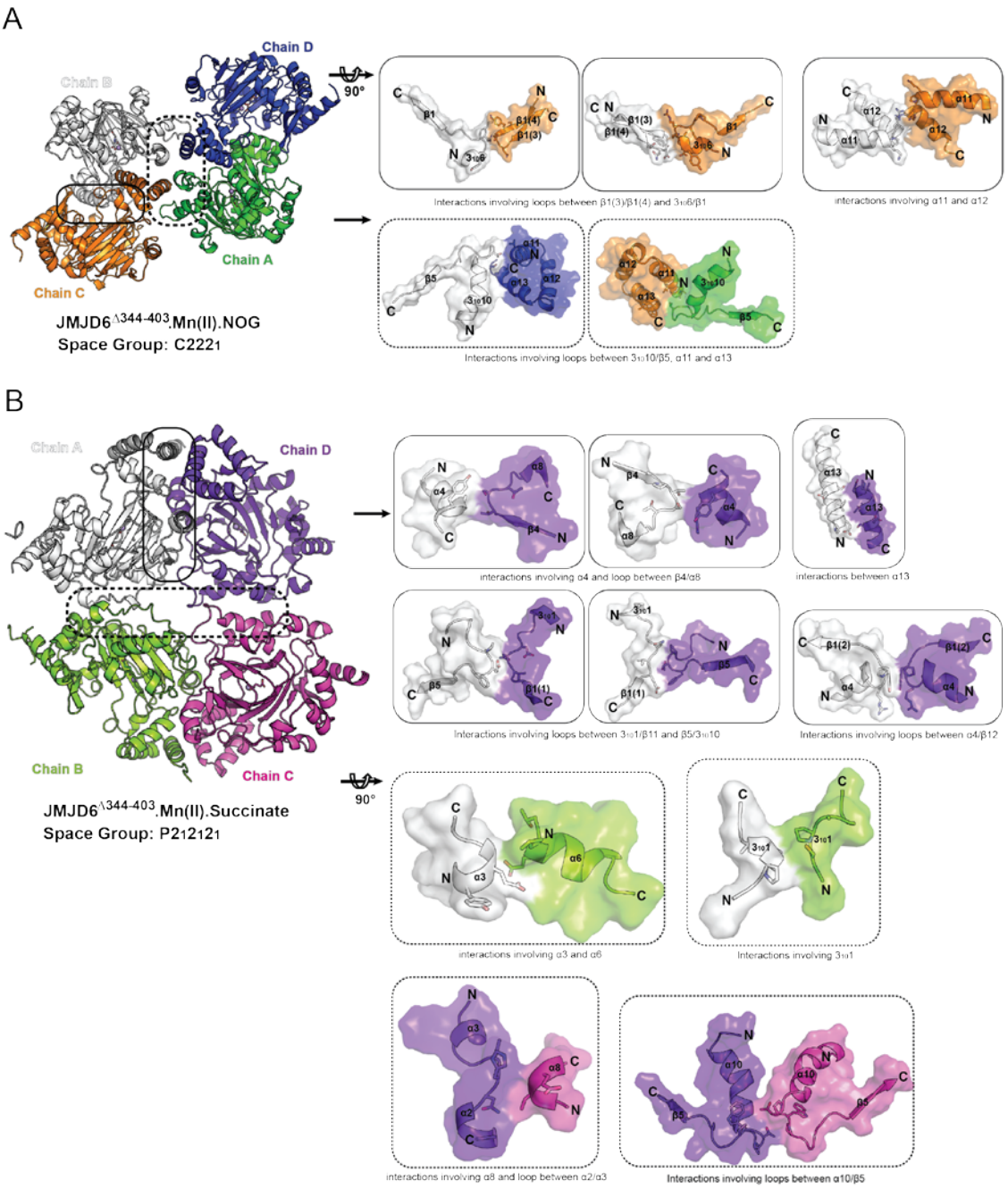

FIGURE 6.5. **Interactions within the ASU**. Comparatively less interactions between individual molecule within the ASU are observed in case of the (A) $C222_1$ compared to the (B) $P2_12_12_1$ crystal form.

6.4. Structural Insights into the Binding Mode of JMJD6 Inhibitors

The broad-spectrum 2OG oxygenase inhibitors NOG and 2,4-PDCA are reported to occupy the 2OG binding pocket (4). TCA cycle intermediates have also been reported to displace 2OG from the active-site (4). Therefore, these inhibitors were predicted to target the active-site metal and the adjacent 2OG binding residues in the case of JMJD6. In 2010, Mantri *et al.* reported the first crystal structure of JMJD6, but were unable to unequivocally identify 2OG binding residues due to the presence of an acetate ion in place of NOG (both present in the crystallisation conditions), emphasizing the weak inhibition properties of NOG towards JMJD6 (36). Mantri *et al*. proposed residues Tyr^{131}, Thr^{184}, Asn^{197}, and Lys^{204} as the 2OG binding residues of JMJD6. In the same year, Hong *et al.* reported that 2OG binds at the active-site of JMJD6 by interacting with the residues Ser^{184}, Lys^{204}, and Asn^{277} in an unusual and incompletely described mode, which is not observed in other 2OG oxygenases (75). The structure of JMJD6.Fe(II).2OG determined in this study (**Chapter 04**) reveals the active-site metal and 2OG coordination mode for JMJD6. However in this Chapter, an understanding of the active-site coordination of JMJD6 is further extended by crystal structures of JMJD6 in complex with four different inhibitors.

When the active-site binding modes of the inhibitors of JMJD6 were compared, similarity was observed among the interacting residues (Figure 6.6). The electron density maps revealed that NOG was bound at the active-site of JMJD6 by interacting with the active-site Mn(II) and residues Tyr^{131}, Thr^{184}, Asn^{197}, and Lys^{204}, similarly to that observed for 2OG binding (Figure 6.6). In addition, the metal ligated water in the NOG structure did not appear to be surrounded by two extra water molecules (Figure 6.6) as observed in the $JMJD6^{\Delta 344\text{-}403}$.Fe(II).2OG structure (Figure 4.5, **Chapter 04**). Similar binding modes were also observed with other inhibitors. Notably, the inhibition kinetics of the inhibitors differ (**Chapter 05**).

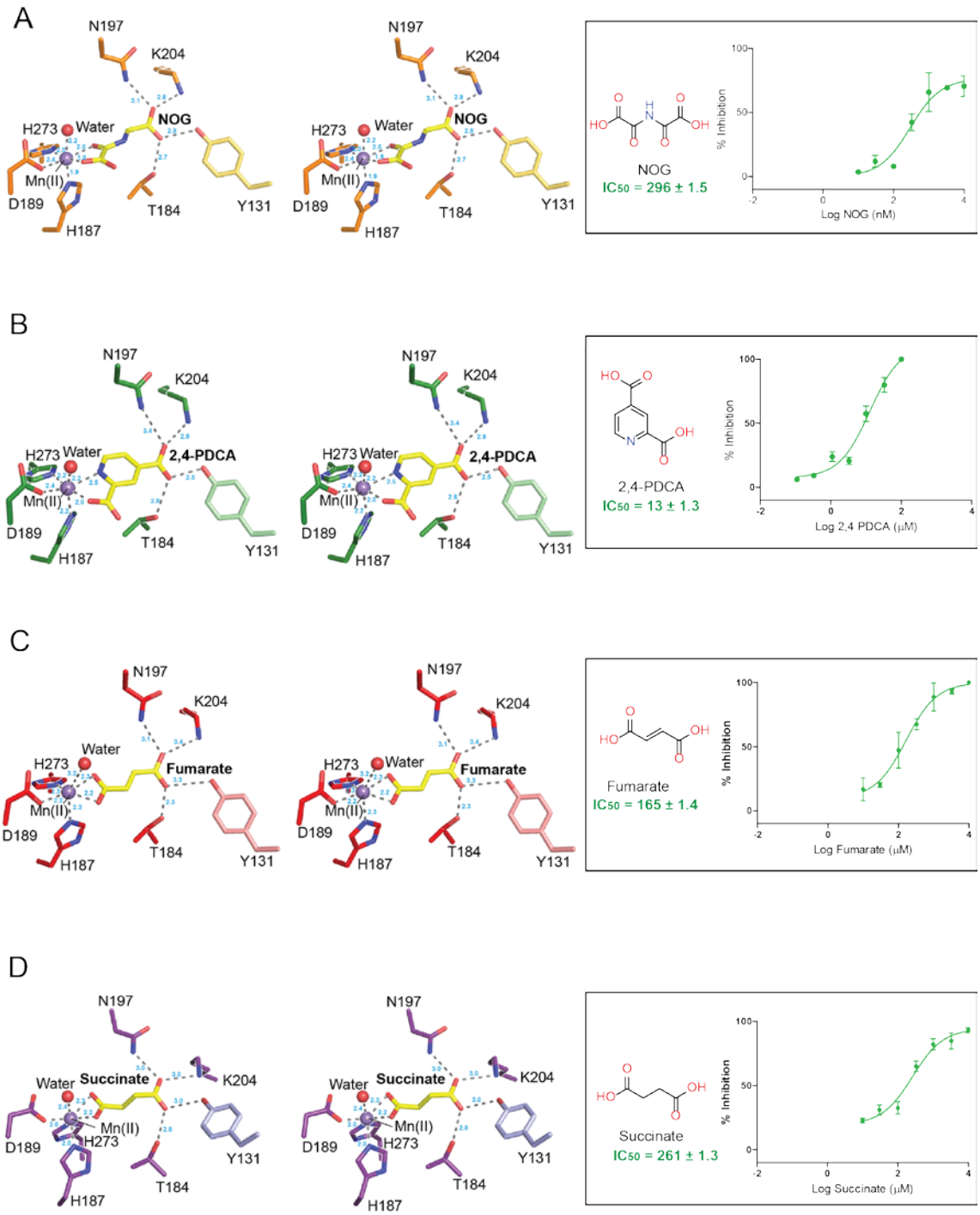

FIGURE 6.6. **Insights into the binding-modes of inhibitors at the active site of JMJD6.** Wall-eyed stereo views of the crystal structures of JMJD6 in complex with inhibitors (A) NOG, (B) 2,4-PDCA, (C) fumarate, and (D) succinate. Insets show the corresponding *IC*$_{50}$ curves.

6.5. Comparison of JMJD6.Inhibitor Complex Structures with Other 2OG Oxygenases

Having identified that NOG is a very weak inhibitor of JMJD6, the binding mode of NOG with JMJD6 was compared with that of other 2OG oxygenases. The reported IC_{50} values of NOG are 2 µM, 8 µM, 17 µM, and 75 µM for FIH (108), PHD2 (94), KDM4A (108), and KDM4E (109), respectively. To gain insights into the structural differences between these enzymes in complex with NOG, the structure of JMJD6.Mn(II).NOG was superimposed on those of FIH.Fe(II).NOG and KDM4A.Ni(II).NOG (Figure 6.7). In the case of JMJD6, the NOG C-1 carboxylate oxygen is positioned *trans* to the distal histidine His^{273} ($H273_{JMJD6}$) (Figure 6.7**B**). In contrast, the NOG C-1 carboxylate oxygen in FIH and KDM4A (PDBs: 4Z1V, 2OQ7, respectively) are positioned *trans* to their proximal histidine residues ($H199_{FIH}$, $H188_{KDM4A}$). One of the NOG C-5 carboxylate oxygens forms a hydrogen bond with Tyr^{131} ($Y131_{JMJD6}$) while the other oxygen forms a hydrogen bond with Lys^{204} ($K204_{JMJD6}$) of JMJD6, a feature common in other 2OG oxygenases including FIH ($Y145_{FIH}$, $K214_{FIH}$) and KDM4A ($Y132_{KDM4A}$, $K206_{KDM4A}$) (4) (Figure 6.7). In addition, an amide ($N197_{JMJD6}$ and $N198_{KDM4A}$) is positioned to form hydrogen bonds with one of the NOG C-5 carboxylate oxygens (Figure 6.7). Binding of NOG to KDM4A is apparently strengthened by the presence of three hydrophobic residues: $Y177_{KDM4A}$, $F185_{KDM4A}$ and $W208_{KDM4A}$.

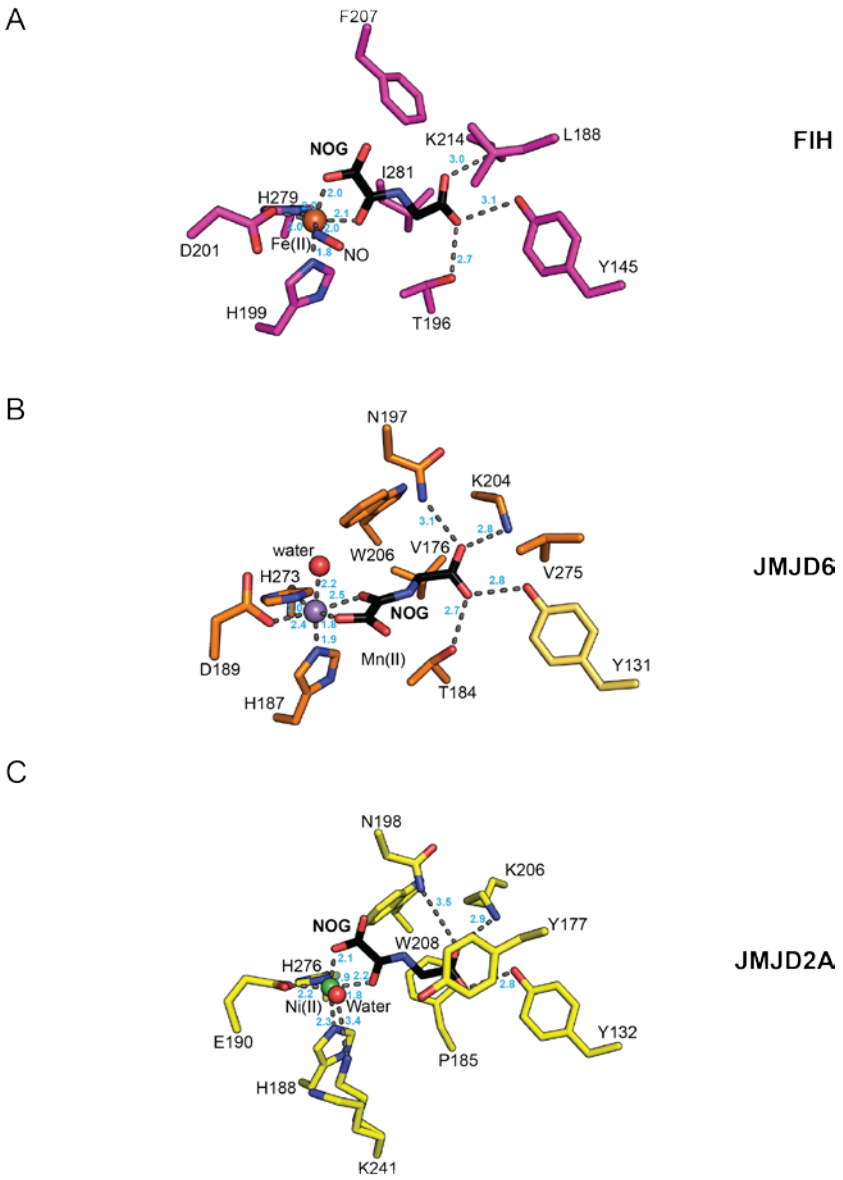

FIGURE 6.7. **Comparison of the crystal structures of JMJD6 with FIH and KDM4A in complex with NOG**. The figures show sticks representation of crystal structures of NOG bound to the active-sites of (A) FIH (PDB: 4Z1V), (B) JMJD6, and (C) KDM4A (PDB: 2OQ7).

2,4-PDCA is a relatively potent and broad spectrum inhibitor of 2OG oxygenases (4) and was found as a potent inhibitor for JMJD6 also (~95% 2OG displacement, IC_{50} value of 13 μM, **Chapter 05**). Crystals of JMJD6.Mn(II).2,4-PDCA grew under the same conditions as JMJD6.Mn(II).NOG. Similarly to 2OG and NOG, 2,4-PDCA binds to the active-site Mn(II) *via* bidendate coordination; the pyridinyl nitrogen coordinates Mn(II) *trans* to the acidic residue $D189_{JMJD6}$, and one of the C-2 carboxylate oxygens coordinates *trans* to the distal histidine $H273_{JMJD6}$ (Figure 6.8**B**). The C-4 carboxylate oxygens form hydrogen bonds with the 2OG binding residues $Y131_{JMJD6}$, $T184_{JMJD6}$, $N197_{JMJD6}$, and $K204_{JMJD6}$. The octahedral coordination of $Mn(II)_{JMJD6}$ is completed by a water molecule. When this structure was compared with the crystal structures of KDM4A.Ni(II).2,4-PDCA (PDB: 2VD7) and FIH.Fe(II).2,4-PDCA (PDB: 2W0X), more resemblance was observed to KDM4A than to FIH (Figure 6.8).

As was observed with NOG, $Y177_{KDM4A}$, $F185_{KDM4A}$ and $W208_{KDM4A}$ are positioned to make hydrophobic interactions with the pyridine ring of 2,4-PDCA, ensuring its firm anchoring inside the 2OG binding pocket of KDM4A (Figure 6.8**C**). $K241_{KDM4A}$ and $Y177_{KDM4A}$ interact with the non-metal ligated C-2 carboxylate oxygen of 2,4-PDCA (Figure 6.8**C**). Furthermore, $N198_{KDM4A}$ was refined in two different conformations: one positioned to form a hydrogen bond with the metal coordinated water and the other to form a hydrogen bond with one of the C-4 carboxylate oxygens (Figure 6.8**C**). In contrast, 2,4-PDCA appears to be bound relatively weakly to FIH and JMJD6 (Figure 6.8**A, 6.**8**B**). Instead of three hydrophobic residues, only one hydrophobic residue ($W206_{JMJD6}$, $F207_{FIH}$) is positioned to form a hydrophobic interaction with the pyridine ring. Although two more hydrophobic residues ($V176_{JMJD6}$, $V275_{JMJD6}$ and $L188_{FIH}$, $I281_{FIH}$) are also present around 2,4-PDCA, their distances are not suitable for interactions with the pyridine ring. This may rationalize why 2,4-PDCA is a relatively weak inhibitor of JMJD6 (IC_{50} = 13 μM) and FIH (IC_{50} = 30 μM), but is a relatively potent inhibitor of KDM4A (IC_{50} = 1.4 μM).

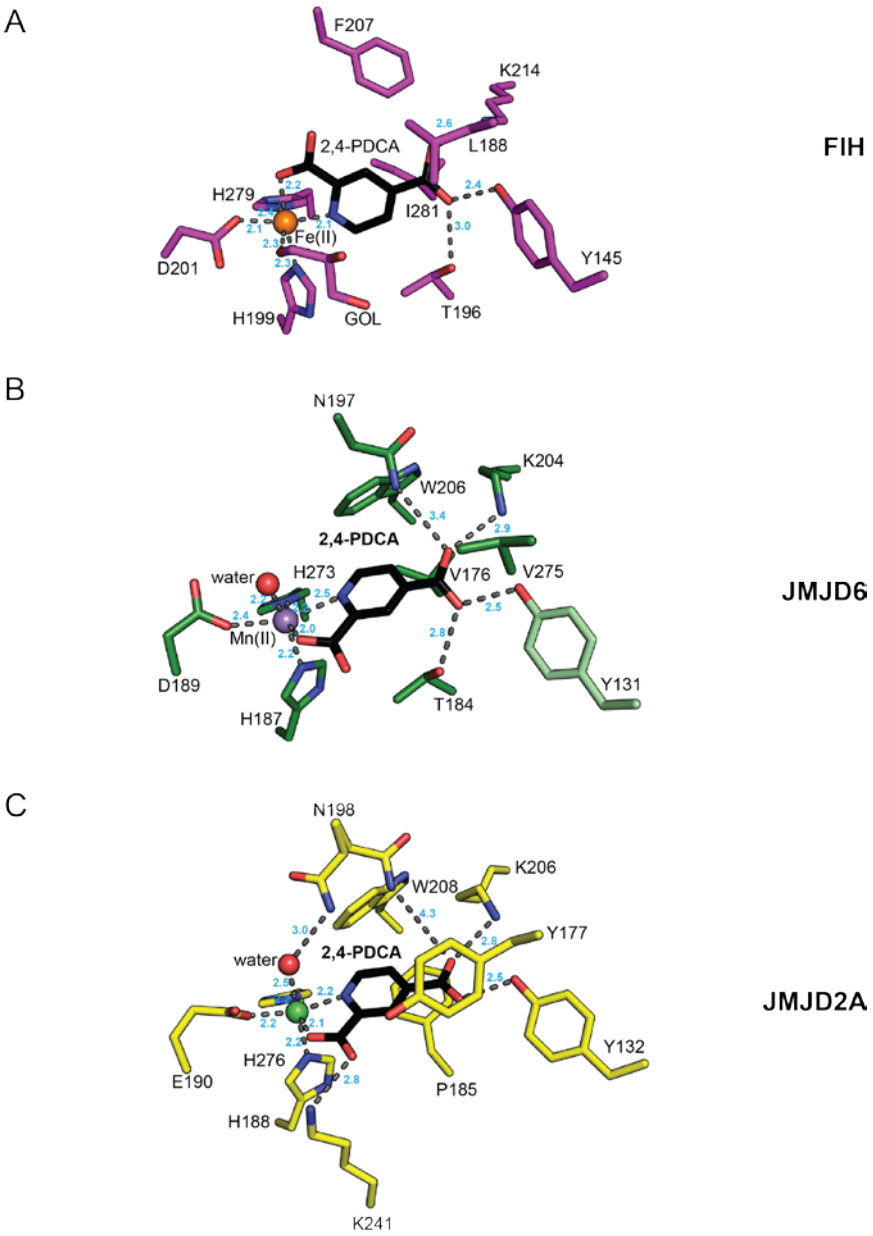

FIGURE 6.8. **Comparison of crystal structures of JMJD6 with FIH and KDM4A in complex with 2,4-PDCA**. The figure shows stick representations of 2,4-PDCA bound to the active-sites of (A) FIH (PDB: 2W0X), (B) JMJD6, and (C) KDM4A (PDB: 2VD7).

Similar binding modes to those for 2OG/NOG are observed for fumarate and succinate (Figure 6.9, 6.10), *i.e.*, apparently relatively tight binding at the active-site of KDM4A, but relatively weaker in the case of FIH and JMJD6.

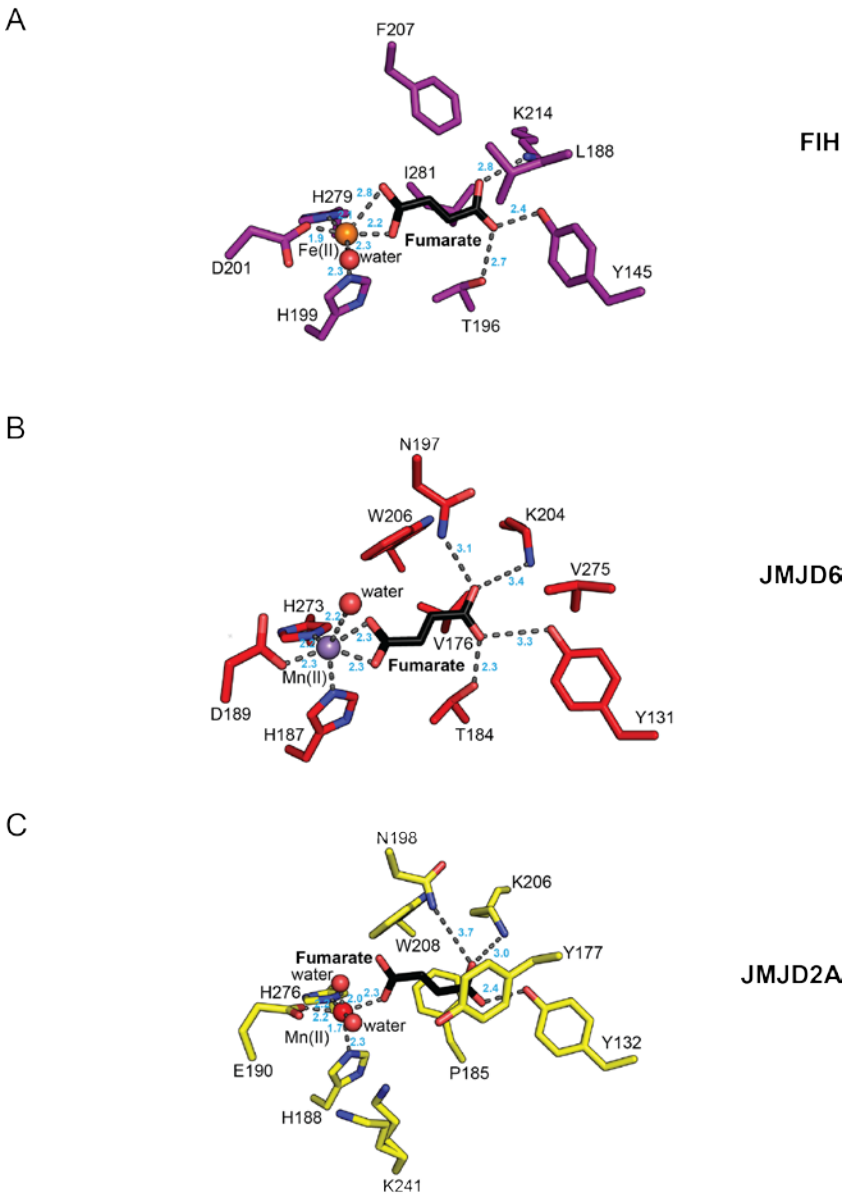

FIGURE 6.9. **Comparison of crystal structure of JMJD6 with FIH and KDM4A in complex with fumarate**. The figure shows stick representations of crystal structures of (A) FIH (PDB: 2CGO), (B) JMJD6, and (C) KDM4A (PDB: 5FYH) with the inhibitor fumarate bound to the active-site.

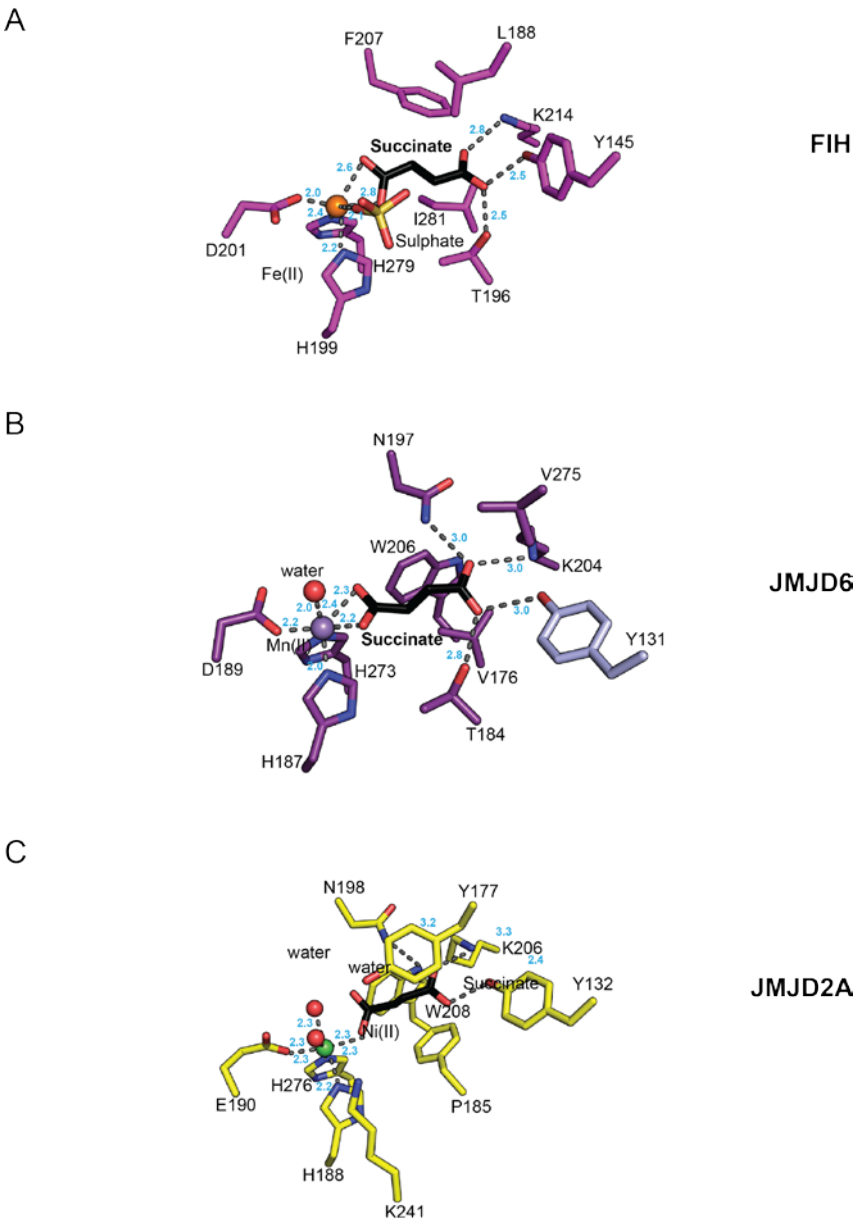

FIGURE 6.10. **Comparison of crystal structure of JMJD6 with FIH and KDM4A in complex with succinate**. The figures show stick representations of (A) FIH (PDB: 2CGN), (B) JMJD6, (C) KDM4A (PDB: 5FYC) in complex with succinate bound to the active-site.

6.6. Ligand-binding Groove in JMJD6 Structure

In addition to the differences in the observed binding-modes of the inhibitors at their active-sites, differences in the overall structures of JMJD6, FIH and KDM4A were also observed. A groove next to the active sites is present in both FIH and KDM4A structures (Figure 6.11), which creates additional space adjacent to C-4 of NOG. This 'C4-groove' has successfully been exploited in the design of selective inhibitors of both these enzymes; *i.e.* NOFD for FIH (Figure 6.2**A**, 6.11**A**) and NOBT for KDM4A (Figure 6.2**B**, 6.11**B**). When a comparison was made with the structure of JMJD6, no such C4-groove is apparent. Instead, a comparatively narrow groove next to the C-1 of NOG is present (Figure 6.11**C**). Moreover, the 'C-1 groove' of JMJD6 seems buried within the structure whereas the C-4 grooves of FIH and KDM4A are more exposed on the surface. The C-4 groove likely does not contribute to the binding of NOG with FIH or KDM4A, but may have a role in binding selective inhibitors of these enzymes (Figure 6.11**A**, 6.11**B**).

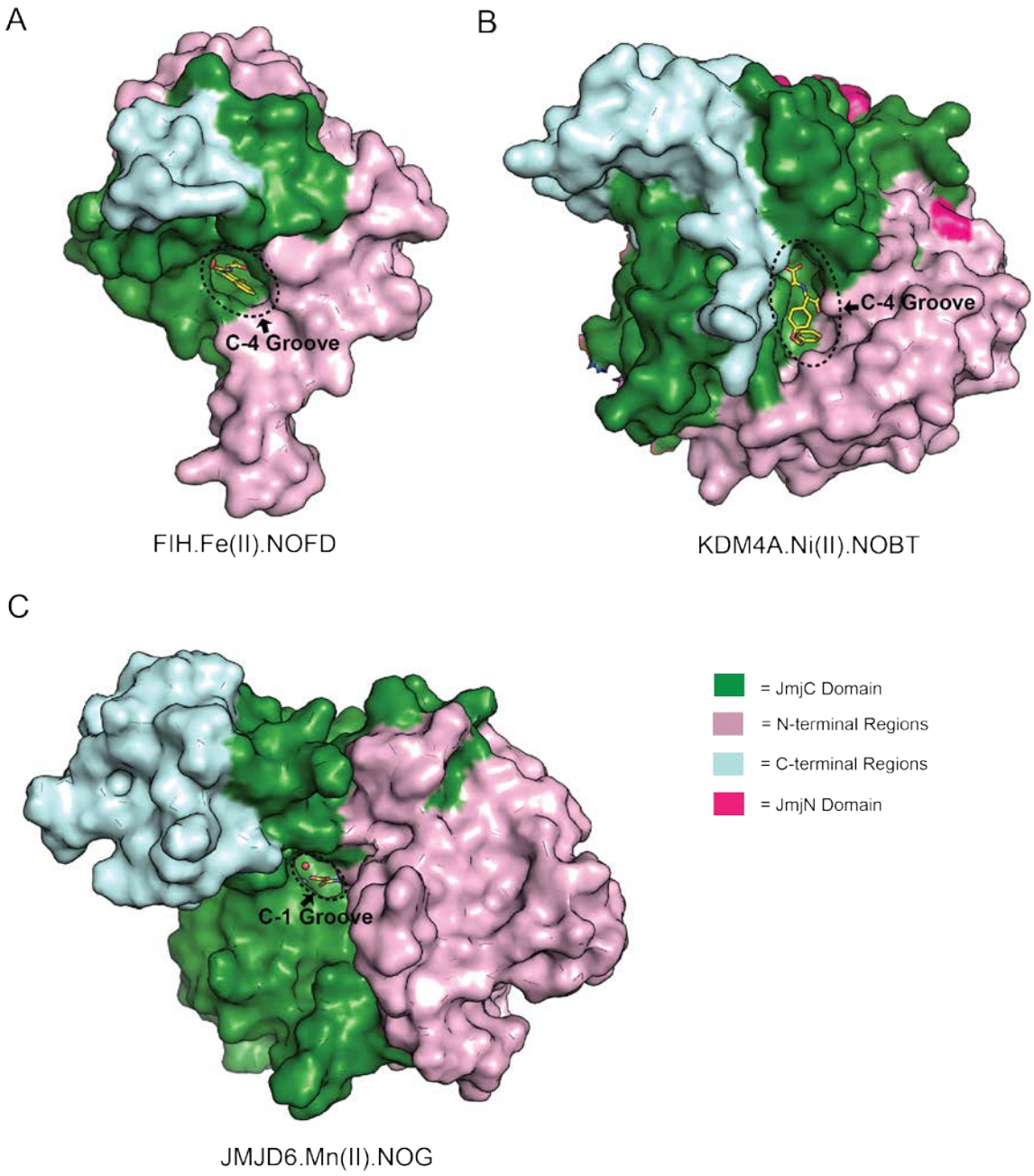

FIGURE 6.11. **Ligand-binding grooves**. Surface representations of crystal structures showing C-4 grooves in (A) FIH (PDB: 1YCI), (B) KDM4A (PDB: 2WWJ). Instead of C-4, a C-1 groove is seen in (C) JMJD6 structure, which is comparatively narrower and smaller.

Chapter 07: Investigation of Substrate Selectivity of JMJD5

7.1. Introduction

JmjC domain containing protein 5 (JMJD5) was first identified as a histone lysine demethylase that catalyses the demethylation of H3K36me2; hence is also known as KDM8 (110,111). In 2010, studies by Hsia *et al.* showed that JMJD5 can act as demethylase and that its demethylase activity is linked to the cancer cell progression (110). The demethylase activity of JMJD5 was also evidenced in subsequent work where it was reported to have important roles in other biological functions including growth development (42,111) and circadian rhythm (43). The initial assignment of JMJD5 as a demethylase was challenged by subsequent works and it was reported that the demethylase activity of JMJD5 is not reproducible (19,27,111). Instead, a JMJD5-mediated hydroxylation of NFATc1 was suggested and JMJD5 was proposed to have a role in osteoclastogenesis (27).

In our laboratory, peptide fragments from the *N*-terminal regions of histone proteins (H2A/H2B, H3, H4) with methylated lysines (mono-, di-, and tri-) were tested as potential substrates for JMJD5 (Dr. Sarah Wilkins, Chemistry Research Laboratory, University of Oxford), but no evidence for demethylation activity of JMJD5 was observed. Subsequently, extensive screening of ~1000 peptide fragments derived from human ribosomal protein was carried out by Dr. Wei Ge (Chemistry Research Laboratory, University of Oxford). From this high throughput peptide screening, a peptide from the 40S ribosomal protein RpS6 was observed to undergo a JMJD5-dependent mass shift of +16 Da, suggesting hydroxylation. Subsequent studies by Dr. Sarah Wilkins including alanine scanning and NMR (nuclear magnetic resonance) spectroscopy of peptide fragment of RpS6 ($RpS6_{129-144}$: VPRRLGPKRASRIRKL) led to the finding that JMJD5 catalyses C-3 (3*R*) hydroxylation of Arg^{137} of RpS6 (26). Analogously, argininyl-hydroxylase activity of JMJD5 was also identified on another peptide fragment of RCCD1 (regulator of chromosome condensation domain-containing protein 1, $RCCD1_{134-150}$) (26).

RCCD1 has been previously reported to regulate chromatin stability *via* interaction with JMJD5 (112).

The main objective of the work described in this Chapter was to investigate the structural basis of the argininyl-hydroxylase activity of JMJD5. X-ray crystallography was used in the structural studies of JMJD5 in complex with the peptide fragments of both RpS6 and RCCD1.

7.2. Identification of Preferred Substrate of JMJD5 between RpS6 and RCCD1

The study began with producing full-length JMJD5 protein (aa 1-416, $JMJD5^{FL}$) following an optimised procedure (**Chapter 10**). The hydroxylation activity of JMJD5 was then tested using peptide fragments of the substrates; *i.e.*, $RpS6_{129-144}$, $RCCD1_{133-148}$, and $RCCD1_{134-150}$. The results of MALDI-TOF-based hydroxylation assays revealed that $RpS6_{129-144}$ is a better substrate of JMJD5 than $RCCD1_{133-148}$ or $RCCD1_{134-150}$ (Figure 7.1). Near to complete hydroxylation of $RpS6_{129-144}$, catalysed by $JMJD5^{FL}$, was observed under the standard assay conditions (**Chapter 10**). In contrast, only ~30% hydroxylation was observed with $RCCD1_{133-148}$ or $RCCD1_{134-150}$ under the same experimental conditions (Figure 7.1). Moreover, JMJD5-dependent hydroxylation of $RpS6_{129-144}$ was found to be unaffected by the presence of $RCCD1_{133-148}$ or $RCCD1_{134-150}$ (Figure 7.1**A**), while hydroxylation of $RCCD1_{133-148}$ and $RCCD1_{134-150}$ were significantly reduced by the presence of $RpS6_{129-144}$ (Figure 7.1**B** and 7.1**C**). These results indicated toward a preference of JMJD5 for $RpS6_{129-144}$ over $RCCD1_{133-148}$ or $RCCD1_{134-150}$ for hydroxylation, at least with the amino acid sequences and the experimental conditions used.

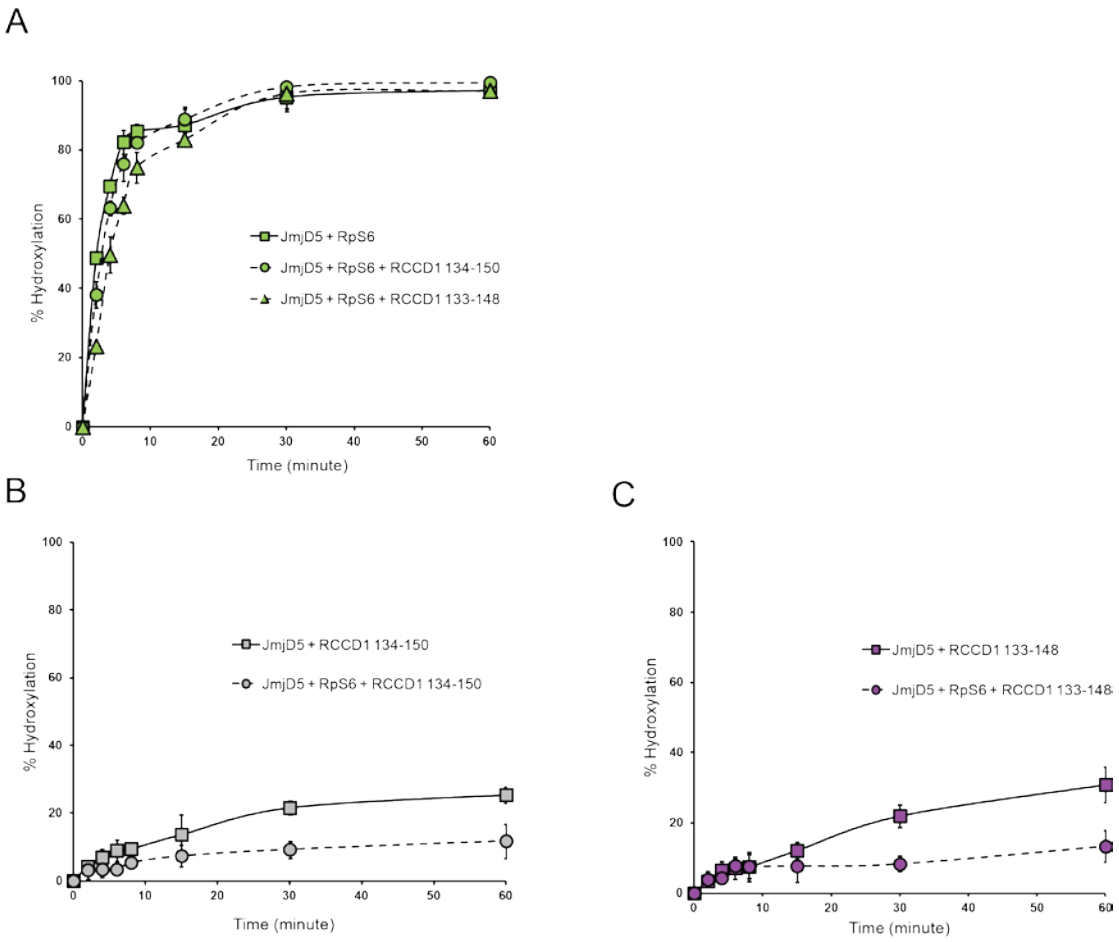

FIGURE 7.1. **Competitive hydroxylation assays of JMJD5 using peptide fragments of RCCD1 and RpS6**. Plots showing hydroxylation rates of (A) $RpS6_{129-144}$, (B) $RCCD1_{134-150}$, and (C) $RCCD1_{133-148}$ as catalysed by $JMJD5^{FL}$. Experiments were carried out following the hydroxylation assay procedure described in Chapter 10. Values represent mean (n = 3) ± standard deviation (SD).

7.3. *Steady-state* Kinetic Studies of $JMJD5^{FL}$ with $RpS6_{129-144}$, $RCCD1_{133-148}$, and $RCCD1_{134-150}$

To gain more insights into the substrate preference of JMJD5, *steady-state* kinetic studies were performed. First, K_m values of the cosubstrate 2OG and the co-factor Fe(II) were determined following the *steady-state* kinetic assay procedure (**Chapter 10**). The K_ms of 2OG and Fe(II) were found to be 9.5 and 2.7 μM, respectively (Table 7.1, Figure 7.2). Likewise, the K_m of $JMJD5^{FL}$-catalysed hydroxylation reaction of $RpS6_{129-144}$ was

determined and found to be 61 μM (Table 7.1, Figure 7.2**B**). By contrast, the measured K_m values were 512 and 526 μM for $RCCD1_{133-148}$ and $RCCD_{134-150}$, respectively (Figure 7.2**C** and 7.2**D**). K_m of $RpS6_{129-144}$ is thus an order of magnitude lower than those of $RCCD1_{133-148}$ and $RCCD_{134-150}$, consistent with the observation that $RpS6_{129-144}$ is a better substrate of JMJD5 than either $RCCD1_{133-148}$ or $RCCD_{134-150}$.

Table 7.1. *Steady-state* kinetic parameters of $JMJD5^{FL}$-catalysed argininyl-hydroxylase reactions of $RpS6_{129-144}$, $RCCD1_{133-148}$, and **$RCCD1_{134-150}$.** Experiments were carried out following the hydroxylation assay procedures described in Chapter 10. Values represent mean (n = 3) ± SD.

	V_{max} . μMs^{-1}	K_m .μM	k_{cat} .s^{-1}	k_{cat}/K_m .s^{-1}μM^{-1}
2OG	-	9.5 ± 2.0	-	-
Fe(II)	-	2.7 ± 0.7	-	-
$RpS6_{129-144}$	0.1695	61 ± 7.0	0.01695	280.6
$RCCD1_{133-148}$	0.3845	512 ± 25.0	0.03845	75.0
$RCCD1_{134-150}$	0.3968	526 ± 25.0	0.03968	75.4

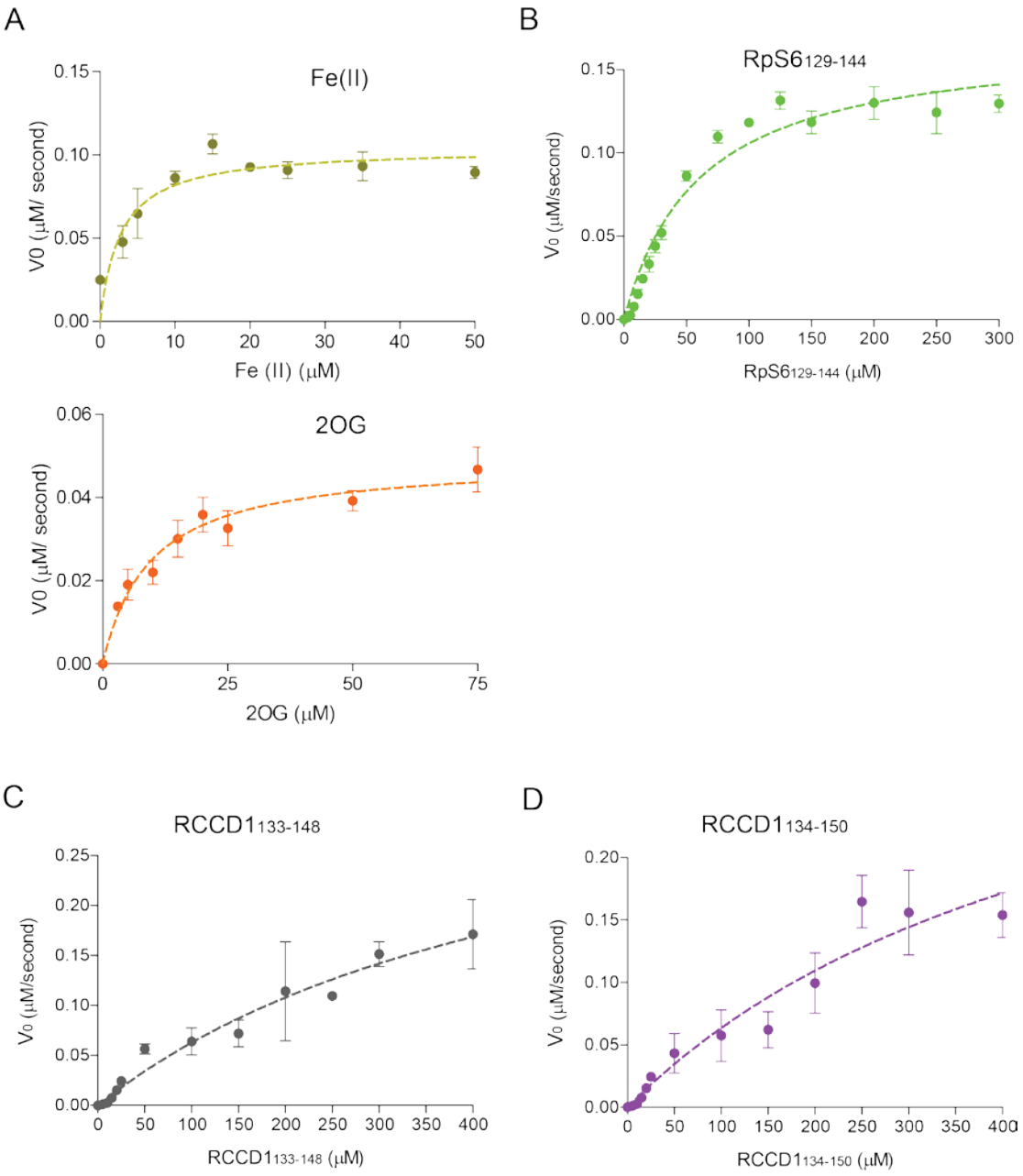

FIGURE 7.2. ***Steady-state*** **kinetic studies of JMJD5^{FL} using peptide fragments of RpS6 and RCCD1 as substrates**. Michaelis-Menten plots of JMJD5^{FL}-catalysed hydroxylation of (A-B) RpS6$_{129-144}$ (VPRRLGPKRASRIRKL), (C) RCCD1$_{133-148}$, (RLPLLPCARAYVSPRA) and (D) RCCD1$_{134-150}$ (LPLLPCARAYVSPRAPF) that were used to determine the kinetic parameters for the respective variables. Experiments were carried out following the *steady-state* kinetic assay procedure described in Chapter 10. Values represent mean (n = 3) ± SD.

7.4. Crystallographic Studies of JMJD5.Substrate Complexes

Crystallographic studies including crystallisation, data collection, structure solution and refinement of the crystal structures described in this Chapter were carried out by Dr. Rasheduzzaman Chowdhury, Chemistry Research Laboratory, University of Oxford.

The sitting-drop vapour-diffusion method was used in all crystallisation attempts of JMJD5.substrtae complexes (78). In addition to the full-length version ($JMJD5^{FL}$), two truncated versions of JMJD5 (aa 153-416, $JMJD5^{\Delta 1\text{-}152}$ and aa 183-414, $JMJD5^{\Delta 1\text{-}182}$) were also used in crystallisation attempts where synthetic peptides derived from RpS6 (corresponding to residues 129-144, $RpS6_{129\text{-}144}$) and RCCD1 (corresponding to residues 134-150, $RCCD1_{134\text{-}150}$) were used as substrates. Mn(II) and NOG respectively replaced Fe(II) and 2OG to achieve catalytic inertness. Putative complexes of JMJD5.Mn(II).NOG.$RpS6_{129\text{-}144}$/$RCCD1_{134\text{-}150}$ were formed by incubating JMJD5 enzyme (25-30 mg/mL) with the other components (in excess) on ice for 1-5 hours; crystallisation plates were made using a crystallisation robot (ARI Instruments) (**Chapter 10**). Crystals of ~ 300x20 µM were obtained which diffracted to 1.2-2.0 Å resolution using synchrotron radiation at Diamond Light Source (DLS). Molecular replacement (MR) using PHASER and the previously reported crystal structure of JMJD5 (PDB: 4GJZ) as a model, followed by refinement using PHENIX were performed (49,79,80) in order to obtain the crystal structures of JMJD5.

The first JMJD5.substrate complex structure was of the complex $JMJD5^{\Delta 1\text{-}182}$.Mn(II).NOG.$RpS6_{129\text{-}144}$; this diffracted to 1.45 Å resolution and was in orthorhombic space group $P2_12_12_1$ (Table 7.3). Electron density was observed only for the targeted arginine residue (Arg^{137}) of $RpS6_{129\text{-}144}$ at the active-site of $JMJD5^{\Delta 1\text{-}182}$ (Figure 7.3). Interestingly, the electron density of Arg^{137} implied the presence of two conformations of its side-chain: a productive conformation (Arg^{137} is directed towards the active-site) and a non-productive conformation (Arg^{137} is directed away from the active-site) (Figure 7.3). The C-3 of the Arg^{137} side-chain in the productive conformation is directed toward the

active-site metal suggesting that this conformation is catalytically relevant. By contrast, the position of C-3 in the non-productive conformation of the Arg^{137} is directed away from the active site. In both cases, the argininyl-guanidino group form a salt bridge with the Glu^{238} carboxylate. The binding of the Arg^{137} is further supported by π-stacking from Tyr^{243} (Figure 7.3).

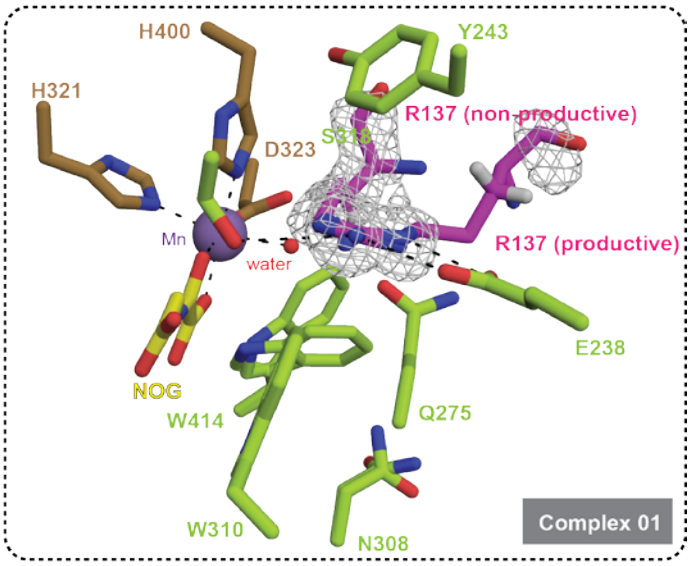

JMJD5$^{\Delta 1\text{-}182}$.Mn(II).NOG.RpS6$^{129\text{-}144}$

FIGURE 7.3. **JMJD5.RpS6 complex structure.** View from crystal structure of JMJD5$^{\Delta 1\text{-}182}$ in complex with RpS6$_{129\text{-}144}$: VPRRLGPKRASRIRKL. Note the targeted arginine residue (R^{137}) is apparently present in both productive as well as non-productive conformations of its side-chain. Difference-map of electron density (F_o-F_c omit map, grey) for substrates are contoured to 3σ.

Attempts were then made to obtain the structures of other JMJD5.substrate complexes using various concentrations of peptide, Mn(II), NOG and different crystallisation conditions. However, structures with RpS6$_{129\text{-}144}$ bound to JMJD5$^{\Delta 1\text{-}182}$ were not obtained. This might possibly be due to the conformational flexibility of the complex or the transient unstable nature of JMJD5$^{\Delta 1\text{-}182}$.RpS6$_{129\text{-}144}$/RCCD1$_{134\text{-}150}$ complexes,

evidence for the latter may be due to relatively high K_m value of the RpS6 peptide (Figure 7.2**B**). Thus, an alternative approach to form possibly more stable JMJD5-substrate complex was applied using *site-specific* cross-linking strategy. Notably, cross-linking strategy has been successfully used in crystallising ribosomal oxygenases MINA53, NO66, and YcfD in complex with peptide-fragments of their substrates RPL27A, RPL8, and RPL16, respectively, where the substrates displayed relatively higher K_m values (> 50 μM) (25).

7.5. JMJD5.RpS6 Complex Formation by *Site-specific* Cross-linking Strategy

In attempts to achieve *site-specific* cross-linking *via* disulfide bond formation between $JMJD5^{\Delta 1\text{-}182}$ and $RpS6_{129\text{-}144}$, seven cysteine-variants of $JMJD5^{\Delta 1\text{-}182}$ ($JMJD5^{\Delta 1\text{-}182}$Q275C, $JMJD5^{\Delta 1\text{-}182}$Q277C, $JMJD5^{\Delta 1\text{-}182}$D280C, $JMJD5^{\Delta 1\text{-}182}$T306C, $JMJD5^{\Delta 1\text{-}182}$N308C, $JMJD5^{\Delta 1\text{-}182}$P324C, and $JMJD5^{\Delta 1\text{-}182}$W414C) and fifteen cysteine variants of $RpS6_{129\text{-}144}$ were employed (Table 7.2, Figure 7.4). Cysteine variants of $JMJD5^{\Delta 1\text{-}182}$ were produced following the same procedure as used to produce the wild-type (**Chapter 10**). Cysteine variants of $RpS6_{129\text{-}144}$ peptides were synthesised by Dr. Sarah Wilkins.

Table 7.2. List of cysteine variants of JMJD5 and RpS6 used in crystallography with their calculated/predicted masses.

Protein	Mass (Da)*	Peptide	Sequence	Mass (Da)
JMJD5$^{\Delta 1\text{-}182}$ (wt)	29699.60	RpS6$_{129\text{-}144}$ (wt)	VPRRLGPK**R**ASRIRKL	1903.35
JMJD5$^{\Delta 1\text{-}182}$.Q275C	29674.60	RpS6$_{129\text{-}144}$.V129C	**C**PRRLGPK**R**ASRIRKL	1907.36
JMJD5$^{\Delta 1\text{-}182}$.Q277C	29674.60	RpS6$_{129\text{-}144}$.P130C	V**C**RRLGPK**R**ASRIRKL	1909.38
JMJD5$^{\Delta 1\text{-}182}$.D280C	29687.65	RpS6$_{129\text{-}144}$.R131C	VP**C**RLGPK**R**ASRIRKL	1850.31
JMJD5$^{\Delta 1\text{-}182}$.T306C	29701.63	RpS6$_{129\text{-}144}$.R132C	VPR**C**LGPK**R**ASRIRKL	1850.31
JMJD5$^{\Delta 1\text{-}182}$.N308C	29688.63	RpS6$_{129\text{-}144}$.L133C	VPRR**C**GPK**R**ASRIRKL	1893.33
JMJD5$^{\Delta 1\text{-}182}$.P324C	29705.62	RpS6$_{129\text{-}144}$.G134C	VPRRL**C**PK**R**ASRIRKL	1949.44
JMJD5$^{\Delta 1\text{-}182}$.W414C	29616.52	RpS6$_{129\text{-}144}$.P135C	VPRRLG**C**K**R**ASRIRKL	1909.38
		RpS6$_{129\text{-}144}$.K136C	VPRRLGP**C**R**R**ASRIRKL	1878.32
		RpS6$_{129\text{-}144}$.A138C	VPRRLGPK**R**C**C**SRIRKL	1935.41
		RpS6$_{129\text{-}144}$.S139C	VPRRLGPK**R**A**C**RIRKL	1919.41
		RpS6$_{129\text{-}144}$.R140C	VPRRLGPK**R**AS**C**IRKL	1850.31
		RpS6$_{129\text{-}144}$.I141C	VPRRLGPK**R**ASR**C**RKL	1893.33
		RpS6$_{129\text{-}144}$.R142C	VPRRLGPK**R**ASRI**C**KL	1850.31
		RpS6$_{129\text{-}144}$.K143C	VPRRLGPK**R**ASRIR**C**L	1878.32
		RpS6$_{129\text{-}144}$.L144C	VPRRLGPK**R**ASRIRK**C**	1893.33

* includes the His$_6$-Tag.

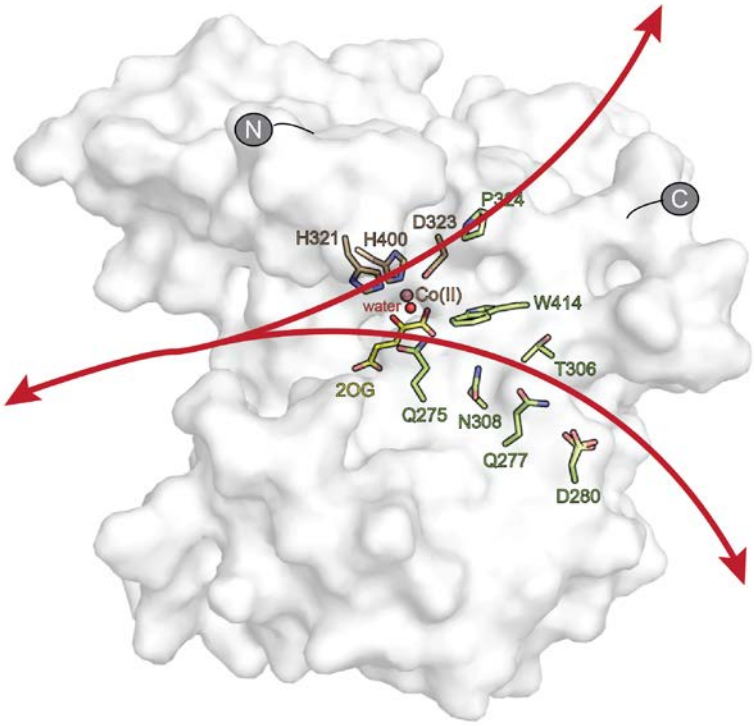

FIGURE 7.4. **Residues in JMJD5$^{\Delta 1\text{-}182}$ structure substituted to cysteine for cross-linking studies**. Views from a crystal structure of JMJD5$^{\Delta 1\text{-}182}$ (PDB: 4GJZ) showing the residues (lime sticks) in the likely substrate-binding grooves (red arrows) that were mutated to cysteine for cross-linking studies. Color code: metal binding residues, sand sticks; Co(II), light pink sphere; water, red sphere; 2OG, yellow.

In order to identify appropriately positioned pairs of JMJD5$^{\Delta 1\text{-}182}$XnC and RpS6$_{129\text{-}144}$XnC (where X and n represent the name and residue number, respectively, targeted for replacement with cysteine) that could form stable complex *via* disulfide bonds, cysteine variants of JMJD5$^{\Delta 1\text{-}182}$.XnC were incubated with cysteine variants of RpS6$_{129\text{-}144}$.XnC in the presence of Mn(II) and NOG (both in 5-fold excess). The mass of each possible JMJD5.RpS6 complex was then measured by denaturing mass spectrometry (**Chapter 10**). Complexes of JMJD5 and RpS6 were also treated with various concentrations of the reducing agent, TCEP (tris(2-carboxyethyl)phosphine hydrochloride) in the control reactions (Figure 7.5).

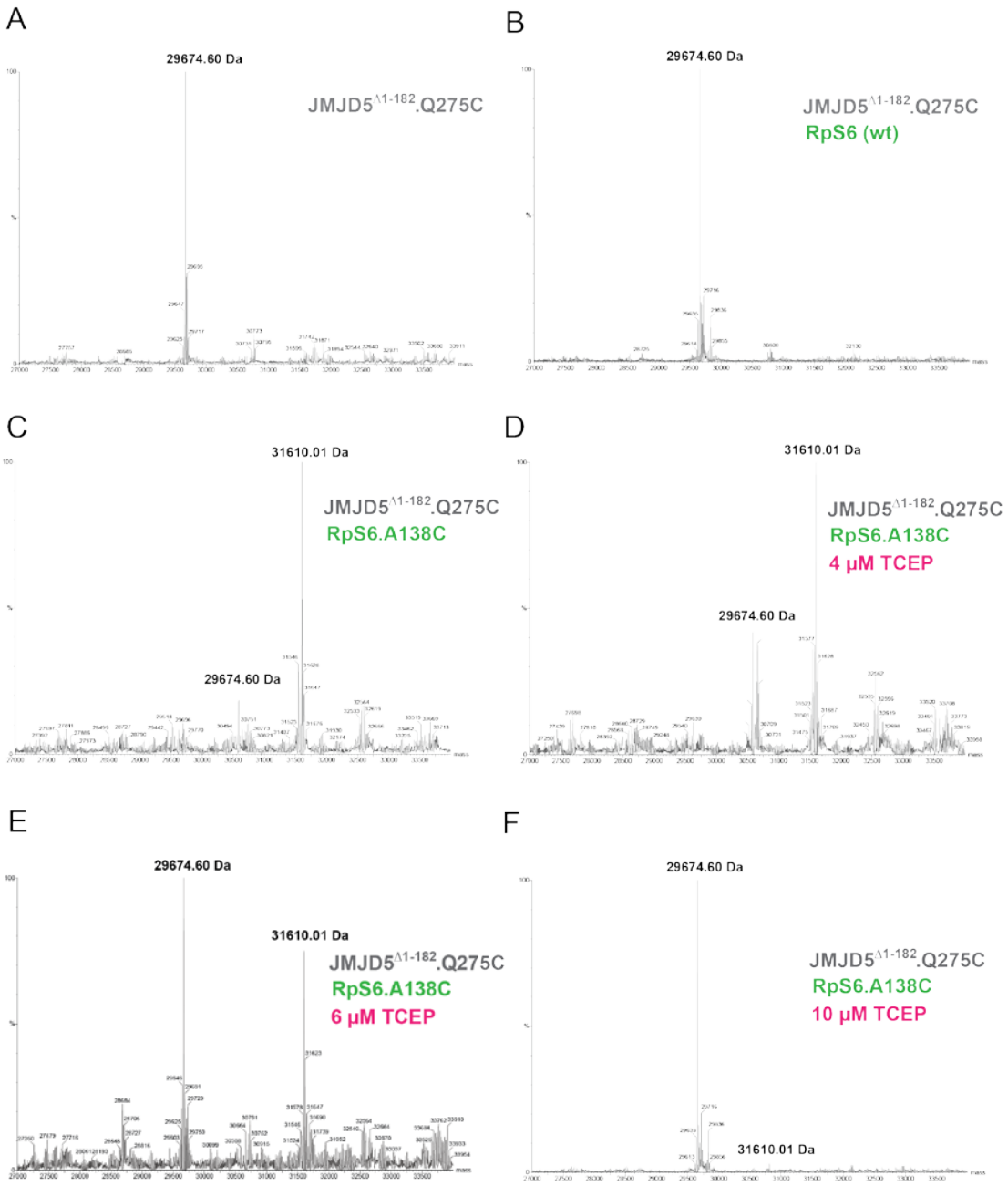

FIGURE 7.5. **MS spectra of JMJD5$^{\Delta 1\text{-}182}$.RpS6$_{129\text{-}144}$ complexes**. MS spectra of: (A) JMJD5$^{\Delta 1\text{-}182}$.Q275C, (B) JMJD5$^{\Delta 1\text{-}182}$.Q275C and wt RpS6$_{129\text{-}144}$, (C) JMJD5$^{\Delta 1\text{-}182}$.Q275C and RpS6$_{129\text{-}144}$.A138C, (D-F) JMJD5$^{\Delta 1\text{-}182}$.Q275C and RpS6$_{129\text{-}144}$.A138C in the presence of various concentrations of TCEP. Note that JMJD5$^{\Delta 1\text{-}182}$.Q275C does not form an apparent complex with wt RpS6$_{129\text{-}144}$ (B), whereas a complex was formed between cysteine variants JMJD5$^{\Delta 1\text{-}182}$.Q275C and RpS6$_{129\text{-}144}$.A138C (C). Complex formation was inhibited completely by addition of 10 µM TCEP (F).

MS analyses of the samples revealed masses corresponding to those for the predicted enzyme-substrate complex in most cases (Figure 7.5 shows representative spectra). For example, MS analysis of JMJD5$^{\Delta 1\text{-}182}$.Q275C/RpS6$_{129\text{-}144}$.A138C mixtures revealed near to complete complex formation in the absence of TCEP (Figure 7.5**C**), while the complex was not formed in the presence of 10 μM TCEP (Figure 7.5**F**). Crystallographic attempts were made using JMJD5$^{\Delta 1\text{-}182}$XnC and RpS6$_{129\text{-}144}$XnC and evidence for the formation of complex was observed in the corresponding mass spectra. Unfortunately, no evidence for any of the RpS6$_{129\text{-}144}$XnC peptide bound at the active site of JMJD5$^{\Delta 1\text{-}182}$XnC was observed in the crystal structures. This result is consistent with possible non-specific complex formation, perhaps due to reaction with one of the four native cysteine residues in JMJD5$^{\Delta 1\text{-}182}$ (Figure 7.6).

To address this issue, a more intensive approach was performed. Alanine variants of JMJD5$^{\Delta 1\text{-}182}$ replacing systematically the native cysteine residues in the JMJD5$^{\Delta 1\text{-}182}$XnC constructs were made and each variant was produced by using the same purification procedure as before (**Chapter 10**). Each JMJD5$^{\Delta 1\text{-}182}$XnC variant (28 in total) was incubated with each of the RpS6$_{129\text{-}144}$XnC variants (15 variants). Upon careful examination of the MS spectra of the complexes, it was observed that complexes were formed successfully and reproducibly when the peptides were incubated with JMJD5$^{\Delta 1\text{-}182}$XnC having all of its native cysteine residues substituted for alanine (Figure 7.7).

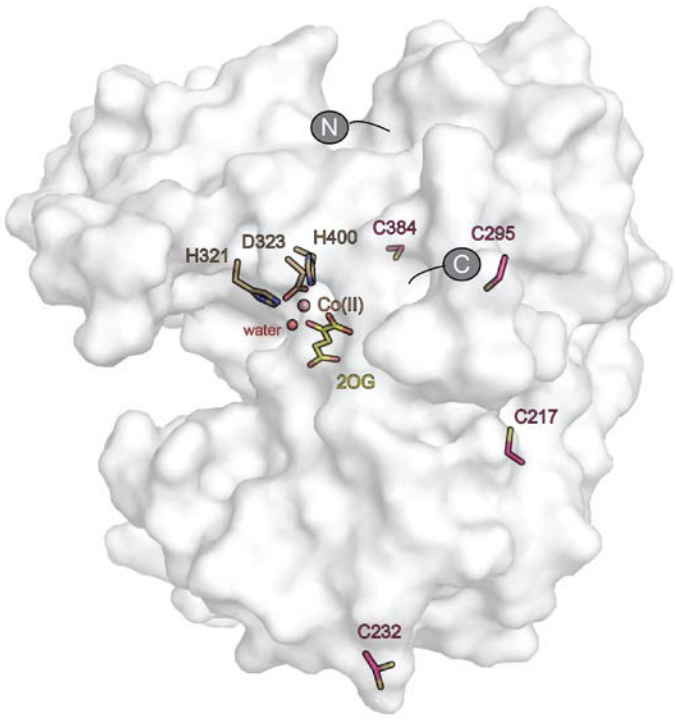

FIGURE 7.6. **Cysteine residues in JMJD5$^{\Delta 1\text{-}182}$**. View from a crystal structure of JMJD5$^{\Delta 1\text{-}182}$ (PDB: 4GJZ) showing its four cysteine residues (pink sticks). Color code: metal binding residues, sand sticks; Co(II), light pink sphere; water, red sphere; 2OG, yellow.

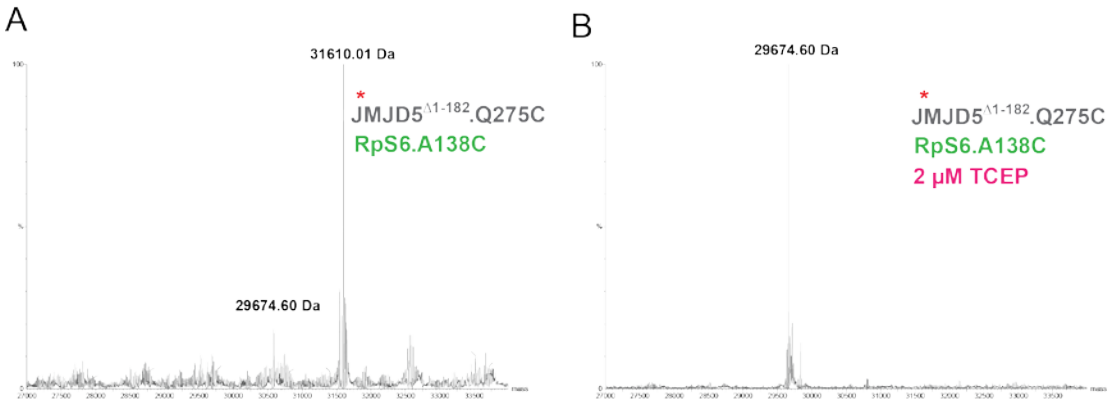

FIGURE 7.7. **MS spectra of putative JMJD5$^{\Delta 1\text{-}182}$.RpS6$_{129\text{-}144}$ complexes using JMJD5 with all of its native cysteine residues substituted for alanine**. MS spectra of JMJD5$^{\Delta 1\text{-}182}$.Q275C/RpS6$_{129\text{-}144}$ complexes in the presence of (A) 0 µM and (B) 2 µM TCEP. *Residues Cys^{217}, Cys^{232}, Cys^{295}, and Cys^{384} were substituted by alanine.

Crystallographic attempts were then made using JMJD5$^{\Delta 1\text{-}182}$XnC (C217A, C232A, C295A, and C384A) and RpS6$_{129\text{-}144}$XnC. Peptide fragments of 5-residues long from both RpS6 and RCCD1 (RpS6$_{135\text{-}139}$: PKRAS and RCCD1$_{139\text{-}143}$: CARAY) were also used in crystallographic attempts.

7.6. Crystallographic Studies of JMJD5.Substrate Complexes formed by Cross-Linking

Attempts were made to form JMJD5.substrate complexes using the procedures as before. A crystal structure was determined for the complex JMJD5$^{\Delta 1\text{-}182}$/Q275C.Mn(II).NOG. RpS6$_{129\text{-}144}$/A138C (Complex 2, Figure 7.8). Unfortunately again, no electron density for RpS6$_{129\text{-}144}$.A138C at the active-site of JMJD5$^{\Delta 1\text{-}182}$ was observed, except for the targeted Arg^{137} (Figure 7.8**A**). Further, the observed position of Arg^{137} C-3 was found too far from the metal centre (> 6.0 Å) suggesting that this conformation of Arg^{137} possibly is non-productive or may represent a product release conformation (analogous to that of complex 1, Figure 7.3). However, residues Glu^{238} and Tyr^{243} were found to provide support to Arg^{137} to bind at the active-site *via* salt bridge and π-stacking, respectively (Figure 7.8**A**).

A crystal structure of another cysteine-variant JMJD5$^{\Delta 1\text{-}182}$.N308C was also determined in complex with RCCD1$_{139\text{-}143}$ (CARAY) (Complex 3, Figure 7.8**B**). Interestingly, the native Cys^{139} of RCCD1$_{139\text{-}143}$ was found to form a disulfide bond with unnatural Cys^{308} of JMJD5; this interaction apparently helps the peptide fragment to bind to JMJD5 (Figure 7.8**B**). Unlike in substrate complex 2 (Figure 7.8**A**), Arg^{141} of RCCD1 inside this complex is apparently observed in a catalytically favourable conformation with its C-3 projecting toward the metal centre (Figure 7.8**B**), similarly to that of complex 1 (Figure 7.3).

These structures together reveal features of JMJD5.substrate complexes including snap shots of both substrate entry and product release conformations of the

substrate (R^{137}_{RpS6} or R^{141}_{RCCD1}). Crystallographic studies further implied that residues Glu^{238}, Tyr^{243}, Gln^{275}, and Trp^{310} would be the residues responsible for substrate-binding.

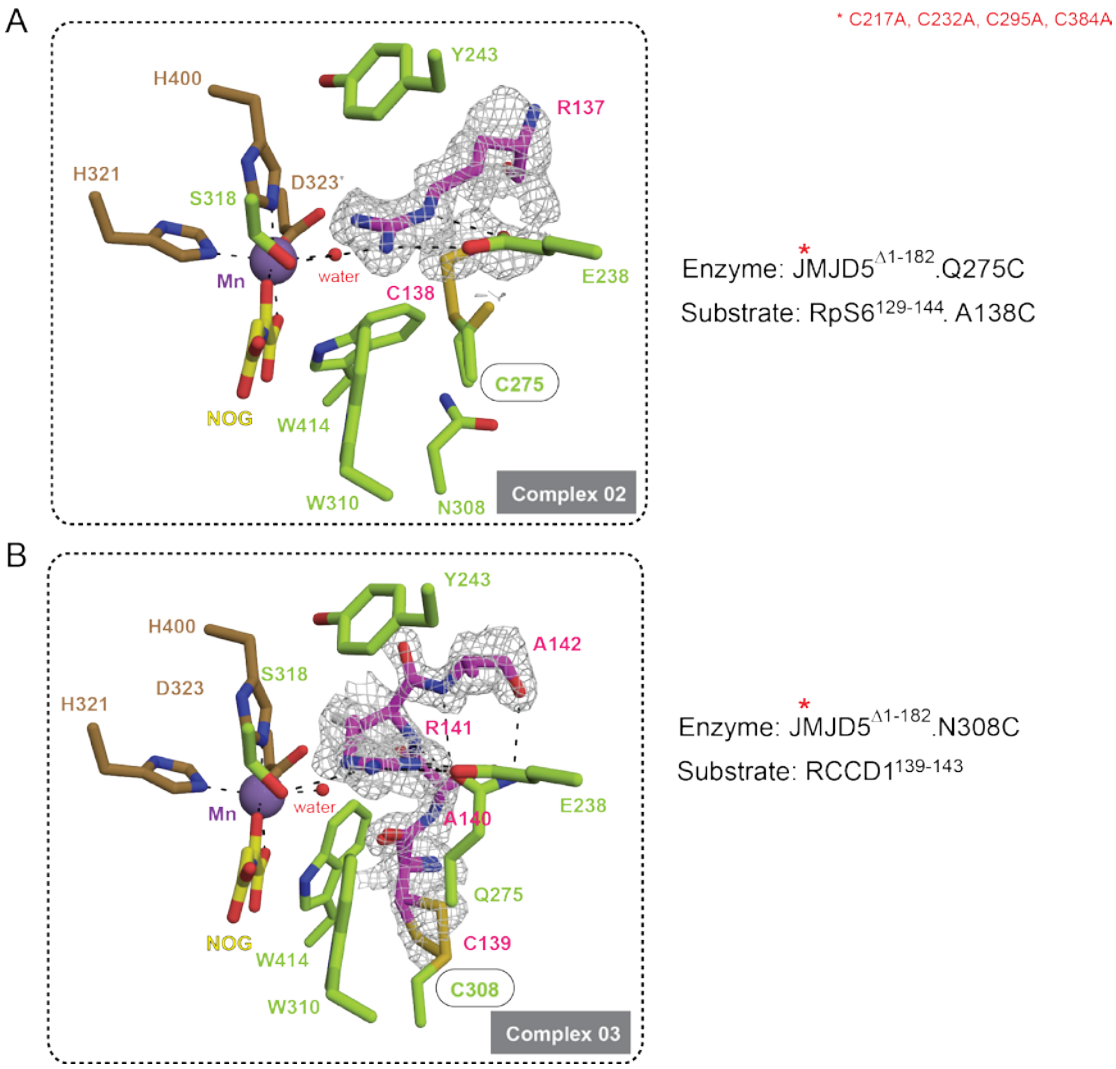

FIGURE 7.8. **JMJD5.RpS6/RCCD1 complex structures.** Views from crystal structures of JMJD5 variants in complex with (A) $RpS6_{129-144}$.A138C and (B) $RCCD1_{139-143}$. Note the targeted arginine residue (Arg^{137}_{RpS6} or Arg^{141}_{RCCD1}) was captured with both (B) productive as well as (A) non-productive conformations of its side-chain. Difference map of electron density (F_o-F_c omit map, grey) for substrates are contoured to 3σ.

7.7. Structure-guided Investigation of Substrate-Binding Residues in JMJD5

Based on the structures of the JMJD5 and RpS6/RCCD1 complexes (Figure 7.3 and 7.8), six alanine variants of wild-type $JMJD5^{FL}$ were made targeting residues around the active-

site pocket: JMJD5^{FL}.E238A, JMJD5^{FL}.Y243A, JMJD5^{FL}.Q275A, JMJD5^{FL}.W310A, JMJD5^{FL}.L356A, and JMJD5^{FL}.W414A (Figure 7.9**A**). These variants were purified following the same procedure as before (**Chapter 10**). Hydroxylation assays were performed with RpS6$_{129\text{-}144}$ and the JMJD5^{FL} mutants using MALDI-TOF MS. However, under conditions that led to near complete hydroxylation of RpS6$_{129\text{-}144}$ by wild-type JMJD5^{FL}, no hydroxylation was observed for JMJD5$_{E238A}$, JMJD5$_{Y243A}$, JMJD5$_{Q275A}$ or JMJD5$_{W310A}$ (Figure 7.9). These results suggest that E238, Y243, Q275, and W310 play roles in substrate-binding and thus catalysis (Figure 7.9). JMJD5$_{L356A}$ and JMJD5$_{W414A}$ showed partial argininyl-hydroxylase activity, suggesting that the corresponding residues (L356 and W414) are not so important (Figure 7.9).

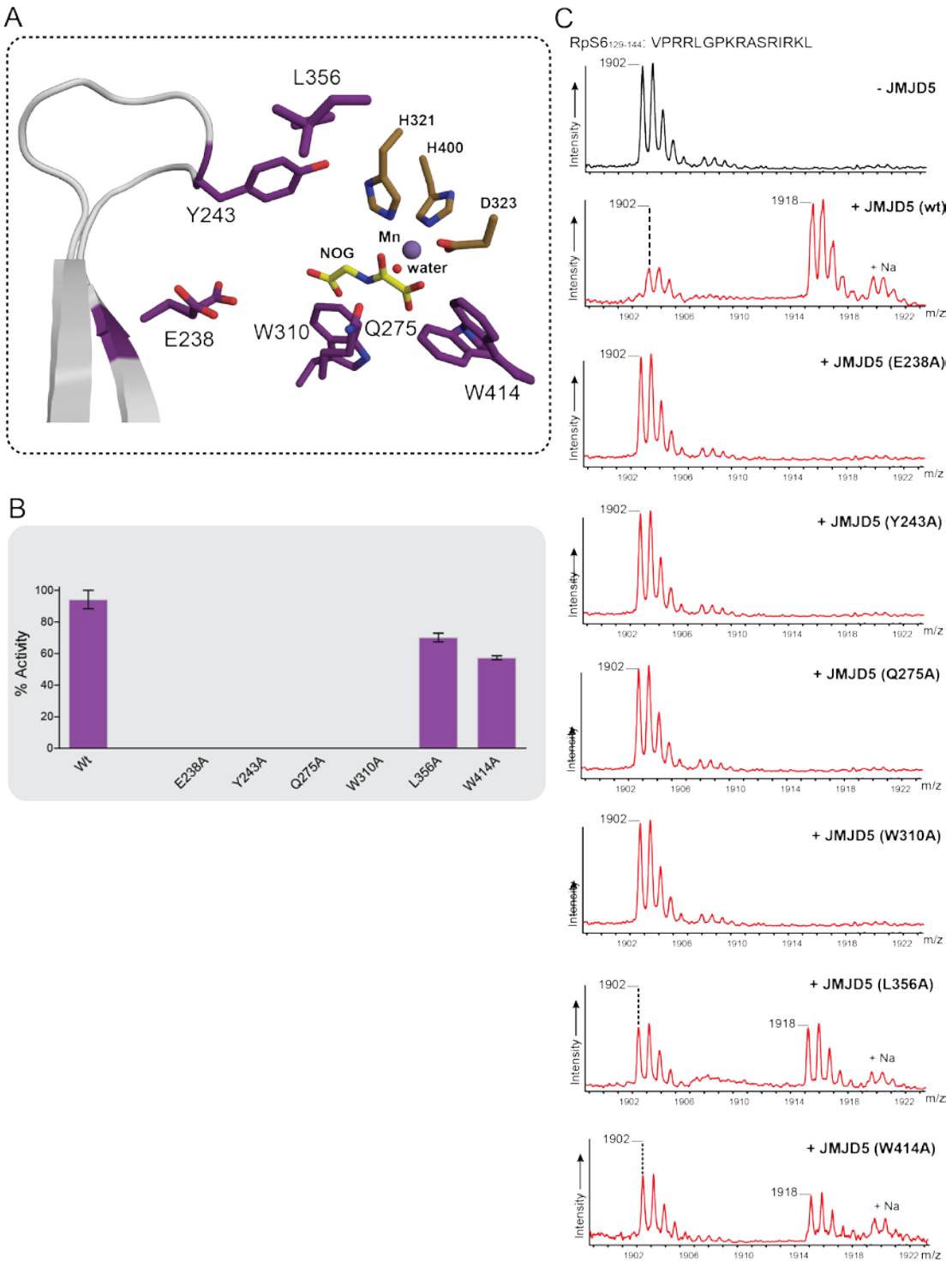

FIGURE 7.9. **Investigating substrate-binding residues in JMJD5 structure.** (A) Residues at the active site that were substituted by alanine. (B) Bar charts showing the relative extent of hydroxylation of $RpS6_{129-144}$ catalysed by wild-type and alanine variants of $JMJD5^{FL}$. (C) MALDI-TOF spectra showing the $JMJD5^{FL}$-dependent +16 Da modifications on $RpS6_{129-144}$. Values represent mean ± SD.

Table 7.3. Crystallographic data collection and refinement statistics.

	COMPLEX 1	**COMPLEX 2**	**COMPLEX 3**
X-Ray Source	DLS IO3	DLS IO3	DLS IO3
Wavelength (Å)	0.9795	0.9795	0.9795
Resolution (Å)	32.46 – 1.45 (1.50 – 1.45)*	49.91 – 1.12 (1.16 – 1.12)*	49.84 – 1.30 (1.35 – 1.30)*
Space Group	$P2_12_12_1$	$P2_12_12_1$	$P2_12_12_1$
Unit Cell Dimensions			
a, b, c	49.28, 64.93, 78.04	49.41, 65.07, 77.77	49.43, 64.81, 77.98
α, β, λ	90, 90, 90	90, 90, 90	90, 90, 90
Molecules per ASU	**1**	**1**	**1**
Wilson B Factor (A^2)	17.5	12.8	15.6
Reflections	44727 (4347)*	95694 (9219)*	62115 (6098)*
Completeness	98.8 (97.7)*	98.7 (96.3)*	100 (100)*
Multiplicity	8.8 (8.4)*	11.1 (9.9)*	9.0 (8.8)*
I/sI	19.0 (1.8)*	32.9 (2.2)*	24.3 (1.7)*
R_{merge}	0.090 (1.2)*	0.067 (1.1)*	0.079 (1.2)*
CC half	0.997 (0.634)*	0.999 (0.707)*	0.998 (0.568)*
R_{cryst}	0.146	0.140	0.143
R_{free}	0.168	0.155	0.164
Deviation from Idealized Geometry			
Bond Length (Å)	0.011	0.014	0.017
Bond angles (°)	1.064	1.289	1.479
Average B Factors			
All atoms	30.35	22.46	25.35
Protein	27.66	20.26	22.43
Ligand	31.09	29.58	25.25
Metal	12.95	9.95	11.24
Water	48.91	36.48	44.03
Ramachandran Plot			
Favored (%)	98.28	99.14	98.72
Allowed (%)	1.72	0.43	1.28
Disallowed (%)	0.00	0.00	0.00
Outlier (%)	0.00	0.43	0.00

* High resolution bin.
Complex 1: JMJD5$^{\Delta 1\text{-}182}$.Mn(II).RpS6$_{129\text{-}144}$
Complex 2: JMJD5$^{\Delta 1\text{-}182}$.Mn(II).RpS6$_{129\text{-}144}$.A138C
Complex 3: JMJD5$^{\Delta 1\text{-}182}$.Mn(II). RCCD1$_{139\text{-}143}$

Chapter 08: Inhibition Studies of JMJD5

8.1. Introduction

As already discussed in Chapter 05 and 06, 2OG (2-oxoglutarate) oxygenases have been targeted for therapeutic inhibition (4). The biochemical assignment of JMJD5 as an argininyl-hydroxylase has opened new scopes for further studies with JMJD5 for therapeutic inhibition (26). The work described in this chapter was carried out to identify potential inhibitors of JMJD5 that could lead to compound for use in the functional assignment of JMJD5 and essentially be exploited in the treatment of diseases associated with impaired regulation of JMJD5 catalysis, including cancer (47,48,73,113-115).

8.2. MALDI-TOF-based Investigation of Inhibitor Selectivity of JMJD5

Similar to JMJD6-inhibition study, a MALDI-TOF (matrix-assisted laser desorption ionization-time of flight) mass spectrometry was used to assay JMJD5-inhibition also (59-61,108).

In order to identify JMJD5 inhibitor, a set of compounds ranging from broad spectrum to subfamily specific inhibitors were tested (4,83,84,116). Broad spectrum 2OG oxygenase inhibitors included structural analogues of 2OG, pyridine- and isoquinoline-derivatives, daminozide, and TCA (tricarboxylic acid) cycle intermediates (Figure 8.1) (4). The tested 'selective 2OG oxygenase inhibitors' included selective PHD inhibitors in the clinical trials for use in anaemia treatment (83) and the selective KDM inhibitors (Figure 8.1) (84,116).

8.2.1. End-point Inhibition Assay

Initially, end-point inhibition assays were carried out using full-length JMJD5 (aa 1-416, $JMJD5^{FL}$) and $RpS6_{129-144}$ (VPRRLGPKRASRIRKL) in the presence of three concentrations of inhibitors: 0.1, 1, and 10 mM (10-1000 fold excess compared to K_m of 2OG). Of the non-specific 2OG oxygenase inhibitors/2OG analogues tested, NOG

showed 78% inhibition of JMJD5^{FL}-activity at a 0.1 mM concentration. The inhibition by NOG was found as an order of magnitude higher than those displayed by N-oxalyl-D-alanine (NODA) and N-oxalyl-L-alanine (NOLA) (6% and 8%, respectively) (Figure 8.2), suggesting that JMJD5-activity is sensitive to changes in the structures of inhibitors. The 2OG analogues **1**, **2,** and **3** were also found as inhibitors (20%, 21%, and 19%, respectively) under the same conditions (Figure 8.2).

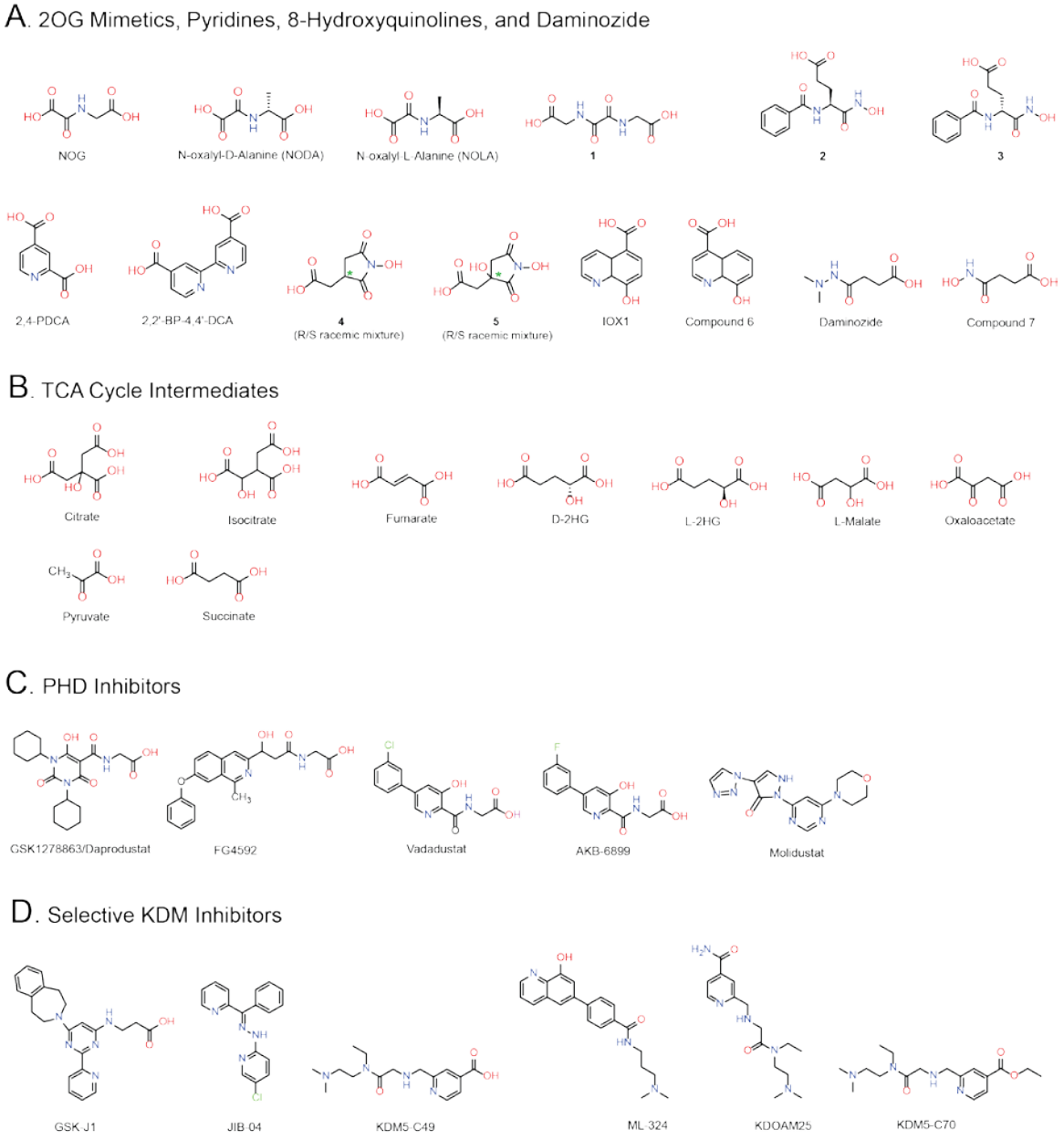

FIGURE 8.1. **Compounds tested for JMJD5 inhibition.** Structures of inhibitors screened against JMJD5^{FL} included (A) 2OG-, pyridine-, quinoline-derivatives,

daminozide, (B) TCA cycle intermediates, (C) reported selective PHD inhibitors, and (D) reported selective KDM inhibitors. * Denotes a chiral centre in a compound tested as a racemic mixture.

In comparison, **4** appeared to be a better inhibitor inhibiting 78% of JMJD5^{FL}-activity, which was similar to that of NOG but an order of magnitude higher than that of **5** (1.5%) (Figure 8.2), albeit both share a nearly identical chemical structure (Figure 8.1). This again indicates that inhibition of JMJD5-activity can be regulated *via* very subtle changes in the inhibitor structures. However, both daminozide and its structural analogue **7** appeared as relatively weak/no inhibitor. In contrast, inhibition by the pyridine-inhibitors 2,4-PDCA (pyridine-2,4-dicarboxylic acid) and 2,4-BPDCA (2,2'-bipyridyl-4,4-dicarboxylic acid) was found to be strong causing 86% and 85% inhibition, respectively at a 0.1 mM concentration (Figure 8.2). Similarly but in contrast to its structural analogue **6**, IOX1 inhibited with relatively high potency (72%) (Figure 8.2).

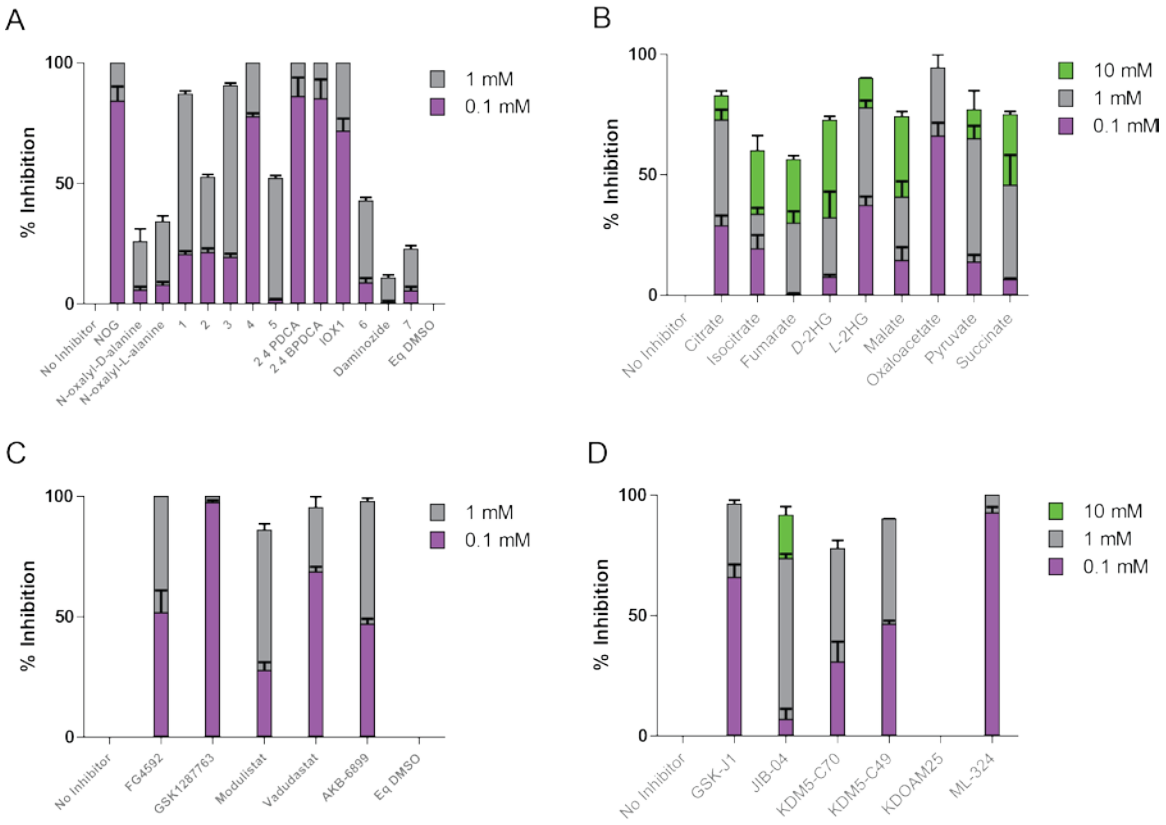

Figure 8.2. **End-point analyses of JMJD5 inhibition**. End-point assays using (A) 2OG structural mimetics, (B) TCA cycle intermediates, selective inhibitors of (C) PHD, and (D) KDM. Assays used MALDI-TOF MS with 10 µM $JMJD5^{FL}$, 100 µM Fe(II), 400 µM ascorbate, 50 µM 2OG and 100 µM substrate $RpS6_{129-144}$ (VPRRLGPKRASRIRKL) as described in Chapter 10. Values represent mean (n = 3) ± standard deviation (SD).

Amongst the TCA cycle intermediates, citrate, L-2HG and oxaloacetate showed relatively strong inhibition with 29%, 37%, and 66% inhibition, respectively (Figure 8.2). Inhibition studies with the reported selective PHD and KDM inhibitors revealed that most were inactive against JMJD5. Interestingly, one PHD inhibitor GSK1278863/Daprodustat (in clinical trials) (83) and one KDM inhibitor ML-324 (proposed to be useful in viral infection treatment) (84,116) caused near to complete inhibition of $JMJD5^{FL}$ under the experimental conditions used (Figure 8.2).

8.2.2. IC_{50} Values Determination of the JMJD5 Inhibitors

Inhibitors showing ≥ 50% inhibition at 0.1 mM concentration were considered for determining their half-maximal inhibitory concentration (IC_{50}) values. Experiments to determine the IC_{50} values were carried out using $JMJD5^{FL}$ and substrate $RpS6_{129-144}$ (VPRRLGPKRASRIRKL) in the presence of varied inhibitor concentrations (0-10 mM) (**Chapter 10**). The measured IC_{50} values for NOG and **4** were found to be 6 µM and 53 µm, respectively (Table 8.1, Figure 8.3). A final IC_{50} value of 12 µM was found for 2,4-PDCA, suggesting that $JMJD5^{FL}$ is more susceptible to inhibition by 2,4-PDCA than by 2,4-BPDCA (66 µM) (Table 8.1, Figure 8.3). Consistent with the end-point inhibition assay results, a final IC_{50} value of 96 µM was obtained for IOX1 (Table 8.1, Figure 8.3), suggesting that $JMJD5^{FL}$ could be targeted by isoquinoline inhibitors.

Table 8.1. IC_{50} values of the inhibitors tested against JMJD5^{L}. The IC_{50} values were determined using MALDI-TOF-based hydroxylation assays with 10 µM JMJD5^{FL}, 100 µM Fe(II), 400 µM ascorbate, 50 µM 2OG and 100 µM substrate RpS6$_{129-144}$ (VPRRLGPKRASRIRKL) in the presence of varied concentrations of inhibitors (0-10 mM) as described in Chapter 10. Values represent mean (n = 3) ± SD.

TCA Cycle Intermediates	**IC_{50} (µM)**	**PHD2 Inhibitors**	**IC_{50} (µM)**
Citrate	820 ± 1.8	GSK1278863	9 ± 1.2
Fumarate	1161 ± .1.4	FG4592	239 ± 1.9
D-2HG	1268 ± 1.5	Vadadustat	54 ± 1.5
Isocitrate	1294 ± 2	AKB-6899	288 ± 1.5
L-2HG	340 ± 1.3		
Malate	1604 ± 1.4	**KDM Inhibitors**	**IC_{50} (µM)**
Oxaloacetate	85 ± 1.4	GSK-J1	67 ± 1.5
Pyruvate	500 ± 1.6	KDM5-C49	621 ± 1.4
Succinate	840 ± 1.4	ML-324	15 ± 1.4
2OG Mimetics	**IC_{50} (µM)**		
NOG	6 ± 1.4		
2.4-PDCA	12 ± 1.4		
2.4-BPDCA	66 ± 1.5		
4	53 ± 1.4		
IOX1	96 ± 1.7		

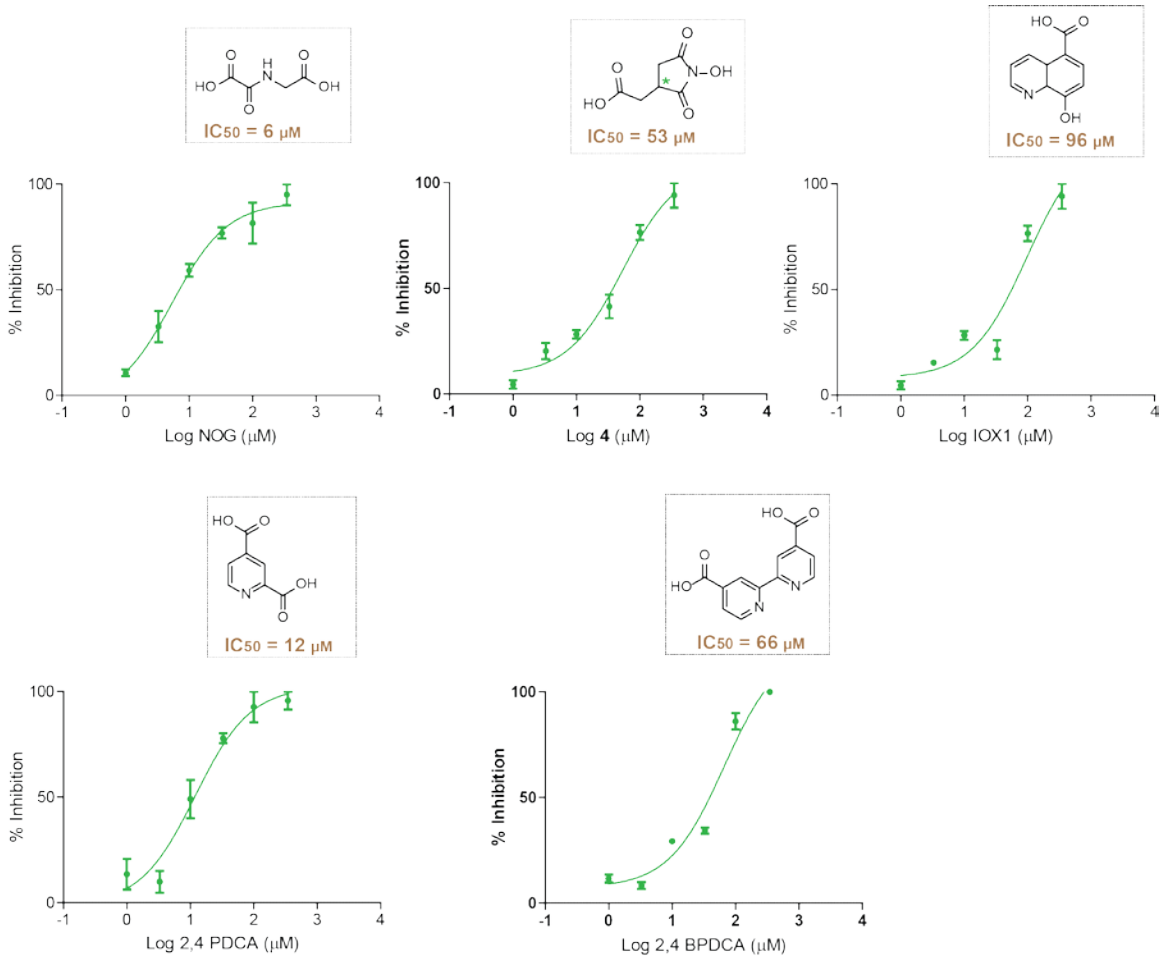

Figure 8.3. ***IC*$_{50}$ values of the 2OG analogues against JMJD5**. The *IC*$_{50}$ values were determined using MALDI-TOF-based hydroxylation assays with 10 μM JMJD5^{FL}, 100 μM Fe(II), 400 μM ascorbate, 50 μM 2OG and 100 μM substrate RpS6$_{129-144}$ (VPRRLGPKRASRIRKL) in the presence of varied concentrations of inhibitors (0-10 mM) as described in Chapter 10. Values represent mean (n = 3) ± SD.

Despite their weak inhibition properties observed in the end-point inhibition experiment (Figure 8.2), TCA cycle intermediates were also considered to determine their *IC*$_{50}$ values owing to their biological importance (90-92,108). Of the compounds tested, oxaloacetate and L-2HG gave *IC*$_{50}$ values of 85 and 340 μM, respectively (Table 8.1, Figure 8.4). By contrast, the *IC*$_{50}$ values of rest of the compounds were all ≥ 500 μM (Table 8.1, Figure 8.4). The *IC*$_{50}$ values for Daprodustat and ML-324 were 9 and 15 μM, respectively (Table 8.1, Figure 8.5 and 8.6), suggesting potent inhibition.

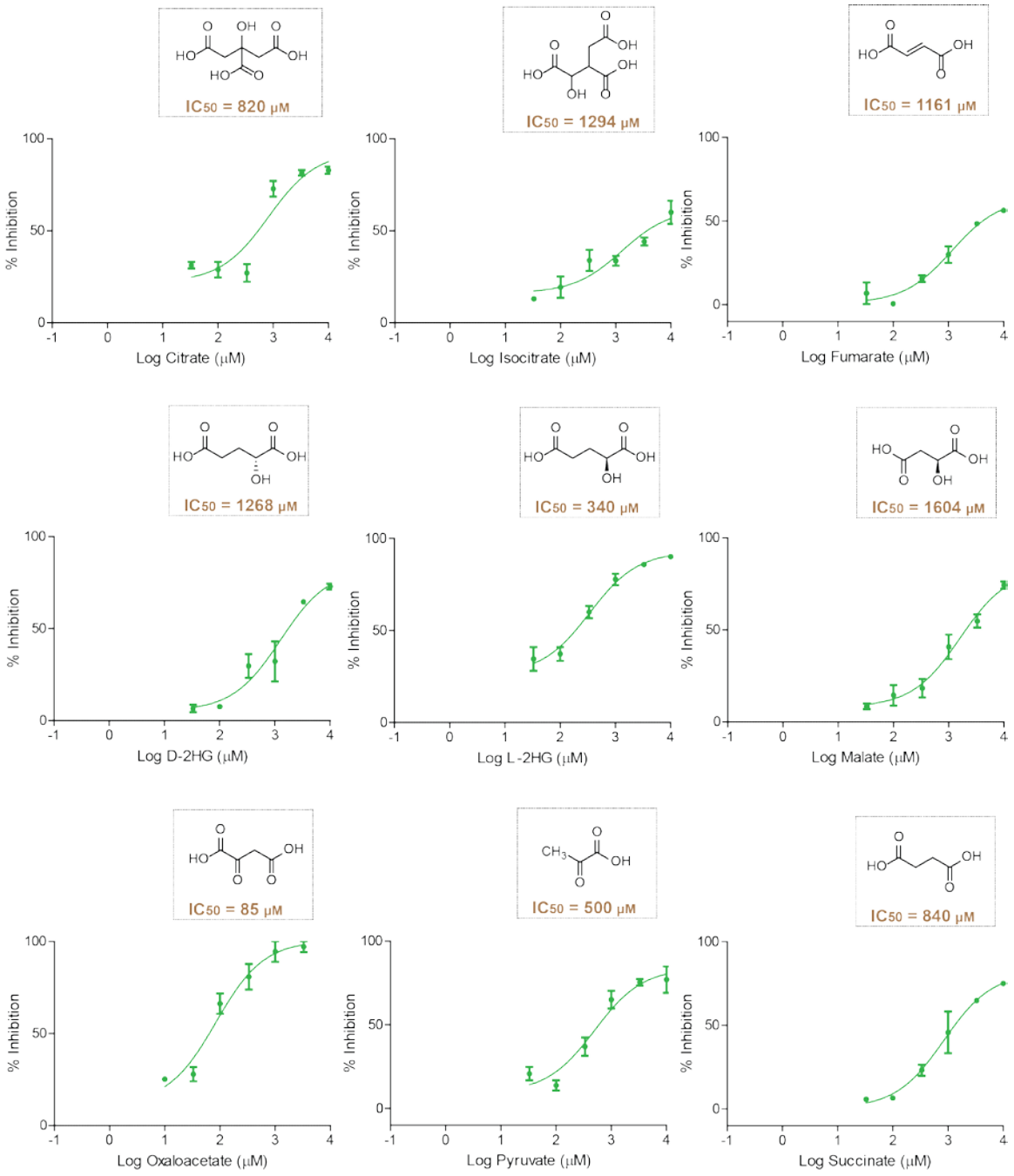

Figure 8.4. ***IC*$_{50}$ values of the TCA cycle intermediates against JMJD5**. The *IC*$_{50}$ values were determined using MALDI-TOF-based hydroxylation assays with 10 µM JMJD5^{FL}, 100 µM Fe(II), 400 µM ascorbate, 50 µM 2OG and 100 µM substrate RpS6$_{129-144}$ (VPRRLGPKRASRIRKL) in the presence of varied concentrations of inhibitors (0-10 mM) as described in Chapter 10. Values represent mean (n = 3) ± SD.

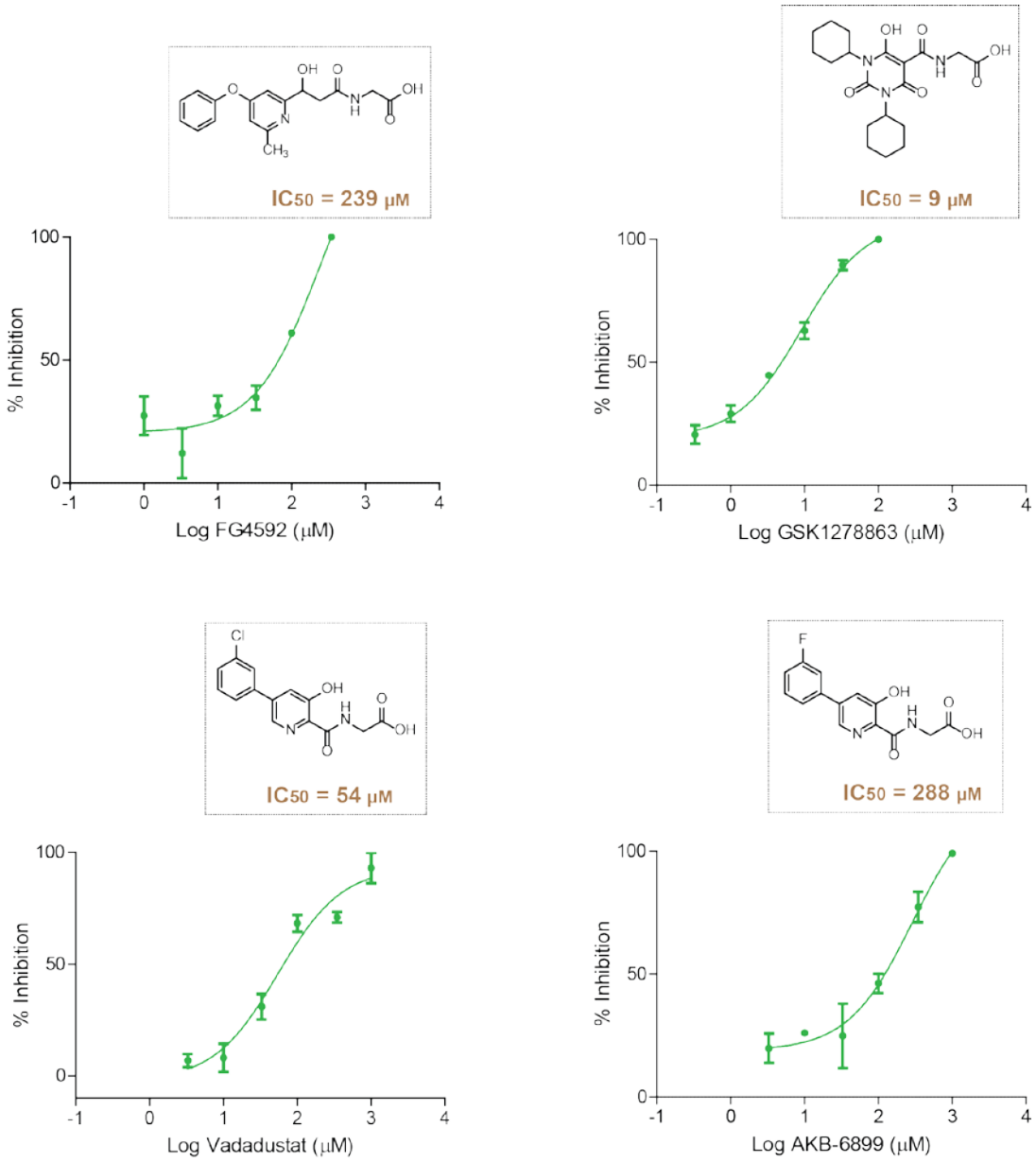

Figure 8.5. ***IC*$_{50}$ values of the selective PHD inhibitors against JMJD5.** The *IC*$_{50}$ values were determined using MALDI-TOF-based hydroxylation assays with 10 µM JMJD5^{FL}, 100 µM Fe(II), 400 µM ascorbate, 50 µM 2OG and 100 µM substrate RpS6$_{129-144}$ (VPRRLGPKRASRIRKL) in the presence of varied concentrations of inhibitors (0-10 mM) as described in Chapter 10. Values represent mean (n = 3) ± SD.

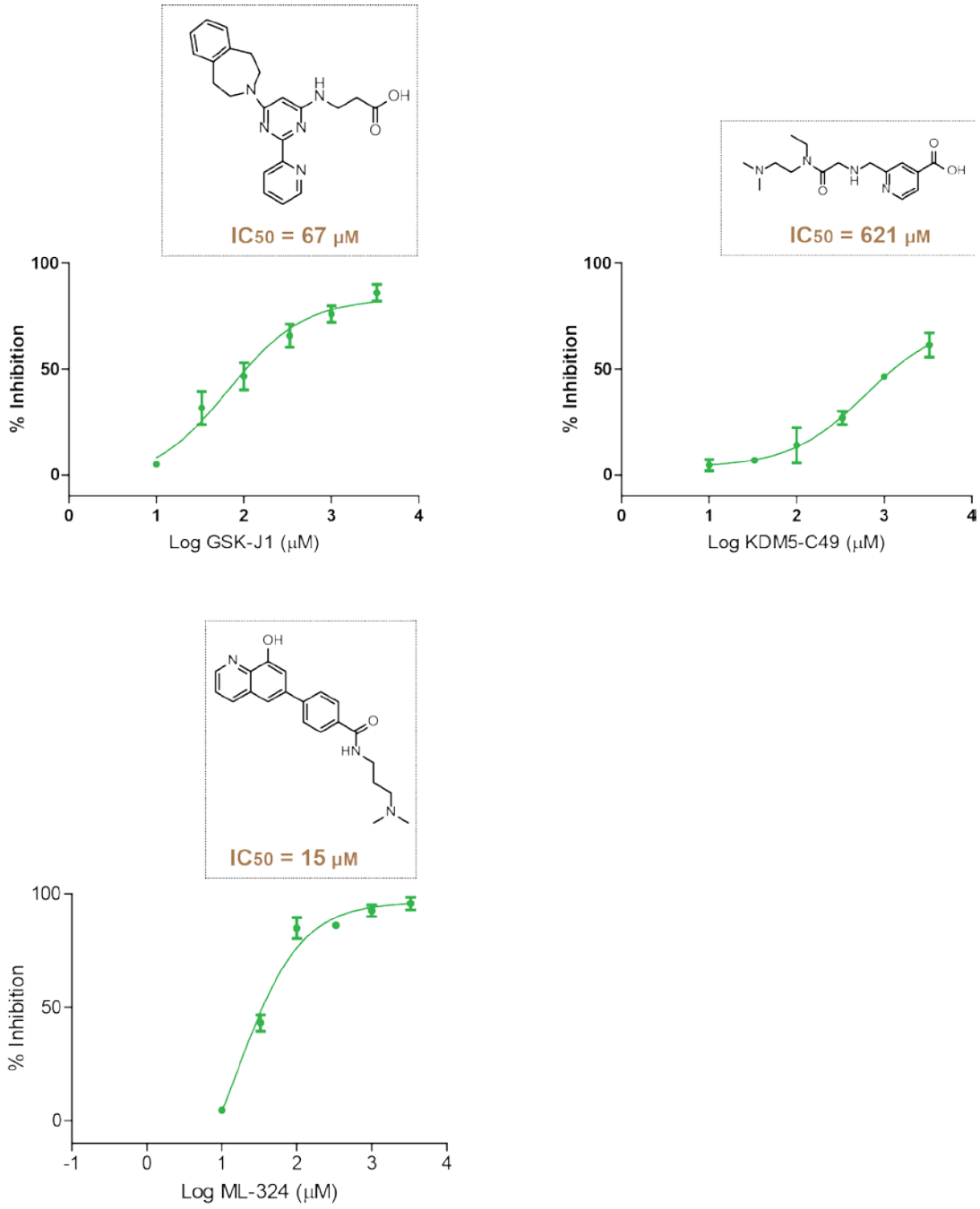

Figure 8.6. ***IC*$_{50}$ values of the selective KDM inhibitors against JMJD5.** The *IC*$_{50}$ values were determined using MALDI-TOF-based hydroxylation assays with 10 µM JMJD5^{FL}, 100 µM Fe(II), 400 µM ascorbate, 50 µM 2OG and 100 µM substrate RpS6$_{129-144}$ (VPRRLGPKRASRIRKL) in the presence of varied concentrations of inhibitors (0-10 mM) as described in Chapter 10. Values represent mean (n = 3) ± SD.

Overall, moderate to strong inhibition of $JMJD5^{FL}$ was observed by the inhibitors tested. Studies were then carried out to investigate the structural basis of the JMJD5-inhibition.

8.3. X-ray Crystallographic Studies for Investigating Inhibitor Selectivity of JMJD5

Crystallographic studies were performed by Dr. Rasheduzzaman Chowdhury (Chemistry Research Laboratory, University of Oxford) to investigate the structure-activity-relationship (SAR) of the inhibitors identified in this study and to identify important pharmacophore features. Crystallographic attempts were initiated to grow crystals of JMJD5.inhibitors complexes by applying sitting-drop vapour-diffusion method (78) using *N*-terminally truncated JMJD5 ($JMJD5^{\Delta 1-182}$) and Mn(II) and NOG replacing Fe(II) and 2OG, respectively.

Of the inhibitors tested, crystal structures of 2,4-PDCA, D-2HG, L-2HG, **1**, and **4** complexed to $JMJD5^{\Delta 1-182}$ were determined (Table 8.2, Figure 8.7). PHASER was used for molecular replacement (MR) using the crystal structure of $JMJD5^{\Delta 1-182}$.Co(II).2OG (PDB: 4GJZ) as a search model (49,79,80). Data collection and refinement statistics are given in table 8.2. In the structures, electron density maps $(F_o\text{-}F_c)$ clearly revealed the localisation of the individual inhibitor at the active-site of JMJD5, except in case of **1** where, density was observed only for part of the compound (Figure 8.7).

Typical 2OG/ligand binding residues that are conserved within the 2OG oxygenases are also observed in JMJD5 structures (Figure 8.7). Consistent with the observations from the reported literatures, the metal binding residues, His^{321}, Asp^{323}, and His^{400} coordinate the active-site metal, Mn(II) (the oxidation state is assumed) (Figure 8.7). Octahedral type co-ordination of the metal is enabled by the oxygen atoms from the 2OG C-1 carboxylate and C-2 carbonyl groups, except in the case of inhibitor **4** (Figure 8.7). Tyr^{272}, Ser^{318}, and Lys^{336} appear to interact with the 2OG C-5 carboxylate/equivalent of the ligands (Figure 8.7). Residues Asn^{327} and Trp^{414} are observed to interact with the

2OG C-1 carboxylate/equivalent moiety of the inhibitors. Binding of hydrophobic elements of the inhibitors is further supported by the hydrophobic side chains of Trp^{310}, Leu^{329}, and Val^{402} (Figure 8.7).

Table 8.2. Crystallographic data collection and refinement statistics.

Protein	JMJD5.Mn(II).**1**	JMJD5.Mn(II).**4**	JMJD5.Mn(II). 2,4-PDCA	JMJD5.Mn(II). D-2HG	JMJD6.Mn(II). L-2HG
X-Ray Source	DLS IO4	DLS IO2	DLS IO4-1	DLS IO2	DLS IO4-1
Wavelength (Å)	0.97949	0.98	0.91741	0.98	0.91741
Resolution (Å)	35.09-2.10 (2.16-2.10)*	78.20-1.49 (1.52-1.49)*	50.00-1.53 (1.58-1.53)*	50.00-1.65 (1.71-1.65)*	50.00-1.36 (1.41-1.36)*
Space Group	$P2_12_12_1$	$P2_12_12_1$	$P2_12_12_1$	$P2_12_12_1$	$P2_12_12_1$
Unit Cell Dimensions					
a, b, c	49.4, 64.5, 78.2	49.4, 64.6, 78.2	49.5, 64.8, 77.9	49.5, 64.6, 77.4	49.6, 64.4, 77.5
α, β, λ	90, 90, 90	90, 90, 90	90, 90, 90	90, 90, 90	90, 90, 90
Molecules per ASU	**1**	**1**	**1**	**1**	**1**
Wilson B Factor (A^2)	20.63	11.86	12.52	18.24	
Reflections	15196 (1231)*	41816 (2058)*	38444 (3781)*	30597 (2984)*	53414 (5302)*
Completeness	99.9 (99.9)*	100 (100)*	99.6 (99.7)*	99.8 (99.2)*	98.8 (99.4)*
Multiplicity	5.0 (5.0)*	7.0 (7.0)*	6.2 (5.6)*	6.7 (6.2)*	9.6 (8.9)*
I/sI	5.8 (1.9)*	15.0 (2.7)*	17.6 (6.6)*	18.17 (3.18)*	24.1 (4.2)*
R_{merge}	0.137 (0.671)*	0.094 (0.776)*	0.119 (0.55)*	0.108 (0.78)*	0.081 (0.529)*
R_{meas}(I)	0.169 (0.833)*	0.110 (0.907)*	0.13 (0.605)*		0.086 (0.561)*
CC half	0.989 (0.643)*	0.996 (0.796)*	0.989 (0.898)*		0.997 (0.934)*
R_{cryst}	0.1966	0.1992	0.1464	0.148	0.149
R_{free}	0.2320 (4.9)¥	0.21 (4.9)¥	0.1638 (4.91)¥	0.182 (4.9)¥	0.158 (4.9)¥
Deviation from Idealized Geometry					
Bond Length (Å)	0.006	0.009	0.008	0.012	0.008
Bond angles (°)	1.24	1.46	0.949	1.179	1.0
Average B Factors					
All atoms	26.0	18.7	18	21.5	23.7
Protein	24.9	16.7	7.2	19.3	21.8
Ligand	20.9	16.4	15.8	12.9	15.3
Metal	10.7	10.2	8.2	11.6	12.6
Water	38.4	31.4	31.8	35.9	38.4
Ramachandran Plot					
Favoured (%)	95.73	97.77	99.21	98.3	98.4
Allowed (%)	4.27	2.23	0.79	1.22	1.6
Disallowed (%)	0.0	0.0	0.0	0.0	0.0
Outlier (%)	0.0	0.0	0.0	0.41	0.0

* High resolution bin.

¥ Percentage of the total reflections used for R_{free} calculations.

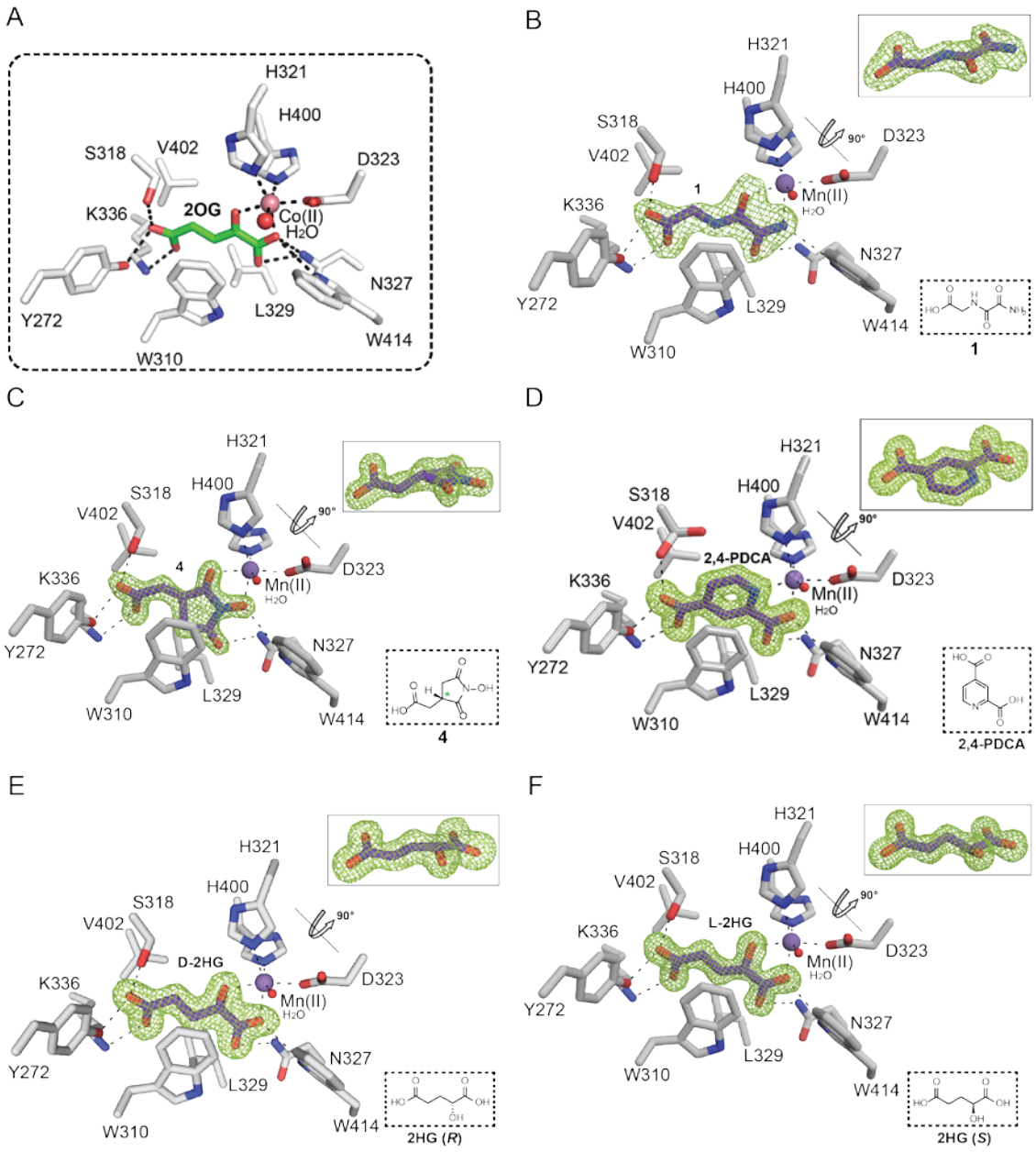

Figure 8.7. **Views from crystal structures of JMJD5 in complex with inhibitors.** (A) Stick-view of the active-site of JMJD5$^{\Delta 1\text{-}181}$ complexed with Co(II) and 2OG (PDB: 4GJZ). Stick-views of active-site of JMJD5$^{\Delta 1\text{-}181}$ complexed to inhibitors (B) **1**, (C) **4**, (D) 2,4-PDCA, (E) D-2HG, and (F) L-2HG. Insets show 90° rotation following views of ligands along with their ChemDraw structures. Asterisk (*) denotes chiral centre. Difference electron density (F_o-F_c omit map, lime) for inhibitors are contoured to 3σ.

8.4. Comparative Studies between the Active-site of JMJD5 and other 2OG Oxygenases

A comparative study of crystal structures of JMJD5 with other 2OG oxygenases revealed that relative conformations of the metal binding triads of JMJD5 are similar to those of other JmjC 2OG oxygenases (Figure 8.8). Oxygen atoms of the C-1 carboxylate of 2OG in JMJD5 is positioned *trans* to the proximal histidine ($H321_{JMJD5}$) (Figure 8.8), similar to FIH ($H199_{FIH}$), KDM4A ($H188_{JMJD2A}$), and PHF8 ($H247_{PHF8}$), but different from the non-JmjC hydroxylase PHD2 in which case, the equivalent oxygen atom is positioned *trans* to the distal histidine ($H313_{PHD2}$) (Figure 8.8). This type of rearrangement of ligands at the metal centre, a noteworthy characteristic of Fe(II)- and 2OG-dependent oxygenases, has been reported previously for other oxygenases including CAS (clavaminic acid synthase) (9).

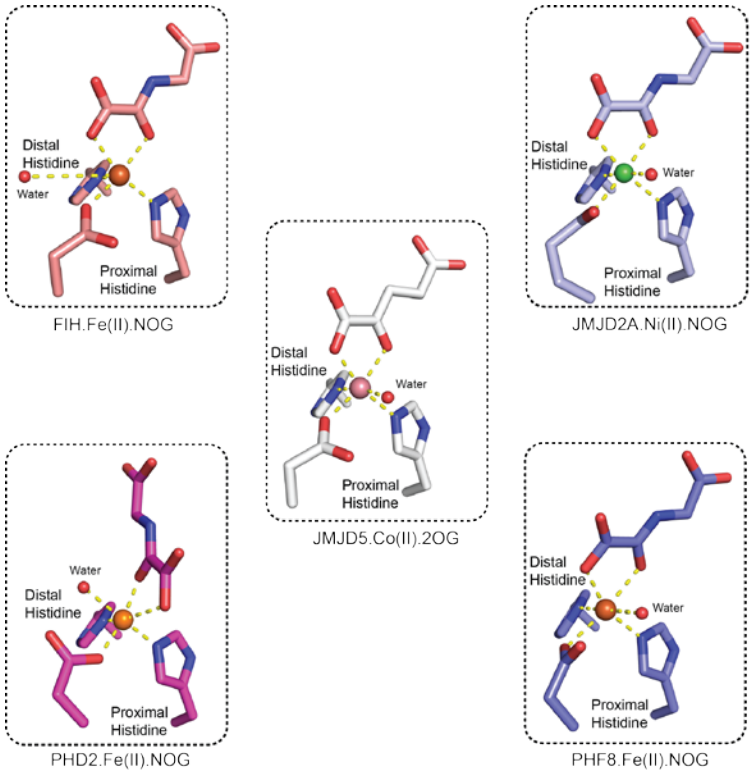

Figure 8.8. **Binding modes of the ligand with JMJD5 and other 2OG oxygenases.** An oxygen atom from the C-1 carboxylate of 2OG in the JMJD5.Co(II).2OG (PDB: 4GJZ) complex is positioned *trans* to the proximal histidine, as observed for FIH.Fe(II).NOG

(PDB: 1H2K), JMJD2A.Ni(II).NOG (2OX0), and PHF8.Fe(II).NOG (PDB: 3KV4) complexes, but not in the PHD2.Fe(II).NOG complex (PDB: 3HQR), where the equivalent oxygen atom from C-1 carboxylate is positioned *trans* to the distal histidine.

8.5. Comparison of Ligand-Binding Modes between JMJD5 and other 2OG Oxygenases

Analyses of the crystal structures of JMJD5.inhibitor complexes further reveal that, like KDM4A, JMJD5 utilizes multiple residues for ligand binding (Figure 8.7). $Y132_{KDM4A}$, $Y177_{KDM4A}$, $F185_{KDM4A}$, $N198_{KDM4A}$, $K206_{KDM4A}$, $W208_{KDM4A}$, and $K241_{KDM4A}$ from KDM4A were found to interact with 2,4-PDCA, while only residues $Y145_{FIH}$, $T196_{FIH}$, and $K214_{FIH}$ from FIH interact with 2,4-PDCA (Figure 8.9). The interaction may reflect the observed inhibition property of this inhibitor, which is relatively more potent against KDM4A (0.7 μM) (116) and JMJD5 (12 μM) than FIH (30 μM) (117).

The IC_{50} value obtained for NOG (6 μM) is even lower than the IC_{50} value obtained for 2,4-PDCA, suggesting that the overall structure of JMJD5 may have some features permitting smaller ligands like NOG to bind with more ease than the ligands like 2,4-PDCA having relatively bigger side chains. Comparisons of the crystal structures of JMJD5, PHD2, FIH and KDM4A revealed that the ligand-binding groove of JMJD5 is indeed different from that of the others (Figure 8.10). The ligand-binding groove of JMJD5 is relatively narrower and shallower than (in an increasing order) PHD2 >FIH >KDM4A (Figure 8.10), suggesting that JMJD5 and PHD2, although from different subfamily of 2OG oxygenase (4), apparently have similarly tight binding pockets. Further, the reported IC_{50} value of NOG against PHD2 (8 μM) supports this argument (4).

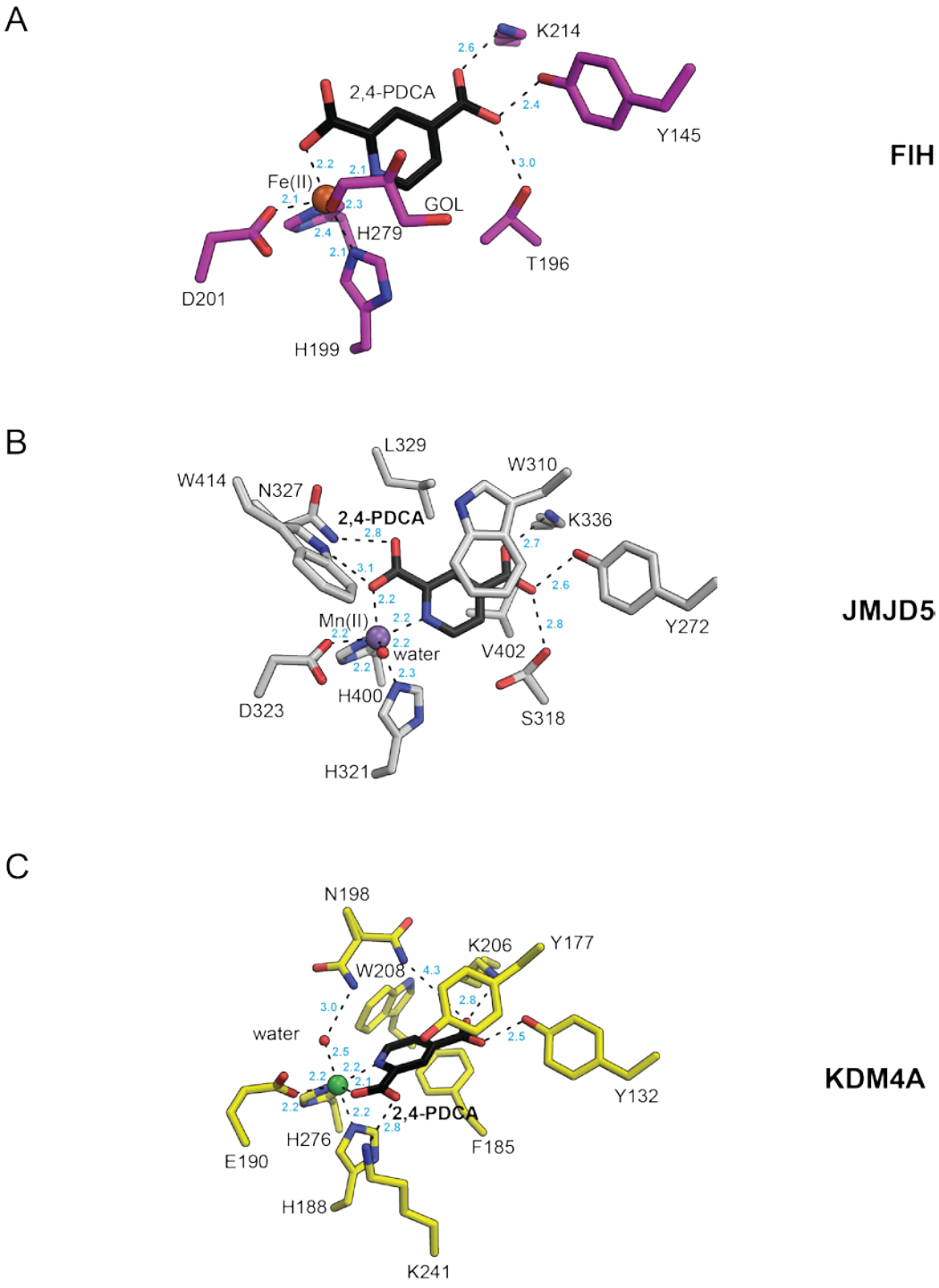

Figure 8.9. **Comparison of views from crystal structures of JMJD5 with FIH and KDM4A in complex with 2,4-PDCA**. Views of stick representation from structures of 2,4-PDCA bound to the active-sites of (A) FIH (PDB: 2W0X), (B) JMJD5, and (C) KDM4A (PDB: 2VD7).

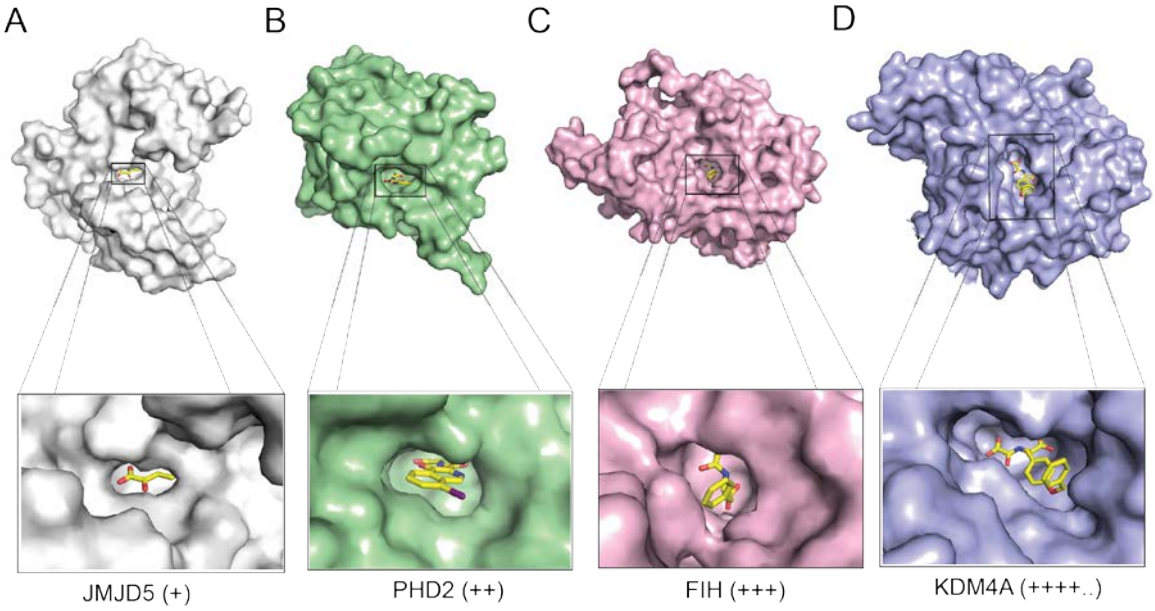

Figure 8.10. **Comparison of the ligand-binding groove of JMJD5 with those of other 2OG oxygenases**. Surface views from crystal structures of (A) JMJD5 (PDB: 4GJZ) (B) PHD2 (PDB: 2G1M), (C) FIH (PDB: 1YCI), and (D) KDM4A (2WWJ); inset shows the ligand-binding grooves increase in size in the order: JMJD5 >PHD2 >FIH >JMJD2A.

By contrast with JMJD5, the ligand-binding groove of KDM4A is apparently wider and deeper. This may in part explain why inhibitors like 2,4-PDCA, 2,4-BPDCA and their structural analogues bind to KDM4A and other KDMs more tightly than to other 2OG oxygenases (116). Notably, one bi-pyridine derivative, 4'-[(2-aminoethyl)carbamoyl]-2,2'-bipyridine-4-carboxylic acid, has also been reported to inhibit KDM4A, selectively (101). By contrast, 2,4-BPDCA showed relatively weaker inhibition of JMJD5 activity (66 µM).

Like 2,4-BPDCA, isoquinoline inhibitors IOX1 and **6,** which are more active against KDM4A than JMJD5, showed weak inhibition of JMJD5-activity. Further, neither daminozide nor its structural derivative **7** appeared as inhibitor of JMJD5, even though their structures resemble that of NOG. Daminozide is a selective inhibitor of KDM2/7 subfamily enzymes (97). Crystal structures of daminozide with KDM4A/PHF8 reveal that a hydrophobic ligand-binding pocket at the active-site of these enzymes, which enables binding of the dimethyl amino groups of daminozide. By contrast, the ligand-binding

pocket of JMJD5 is relatively less hydrophobic (Figure 8.11). This may explain why daminozide is selective inhibitor of KDM2/7s over JMJD5 and over other 2OG oxygenases including other KDMs (97).

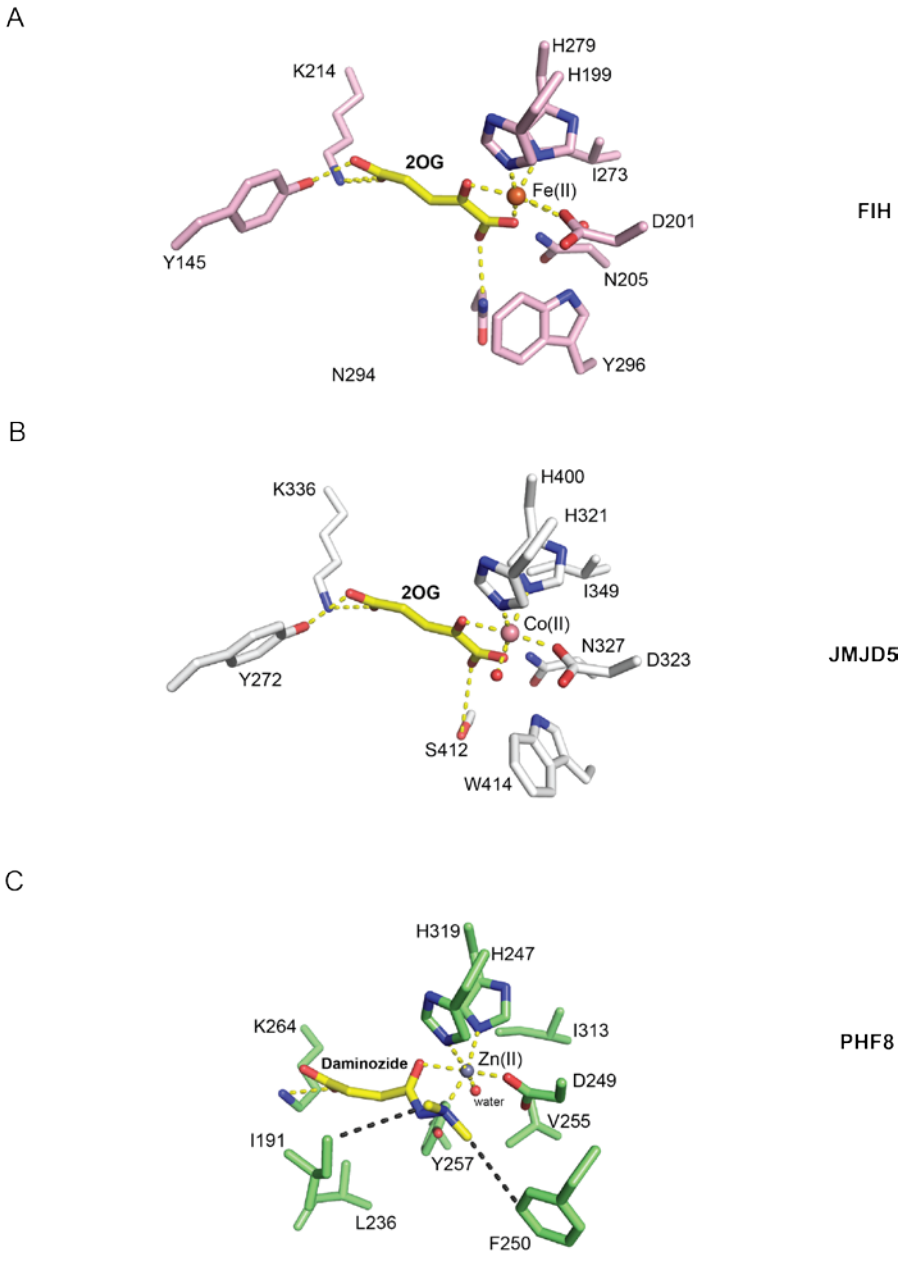

Figure 8.11. **Comparison of ligand-binding pocket between PHF8, JMJD5 and FIH**. Views from crystal structures showing binding of PHF8 (PDB: 4DO0) with daminozide by a unique hydrophobic pocket (shown as black dotted lines) that is absent in other 2OG oxygenases including FIH (PDB: 1H2L) and JMJD5 (PDB: 4GJZ).

Of the other 2OG oxygenase inhibitors tested, **4** showed moderate inhibition (Table 8.1, Figure 8.7). In contrast, **5** is relatively a weak inhibitor of JMJD5. A crystal structure of JMJD5 in complex with **4** was determined. The only difference between **4** and **5** is the presence of an extra hydroxyl group at C3-position of the pyrrole-2,5-dione ring of **5** (Figure 8.1), which likely makes **5** more hydrophilic than **4**. These results further suggest that the active-site pocket of JMJD5 is sensitive to subtle change in the inhibitor structures. Both **4** and **5** have a chiral centre at C3 of the pyrrole ring and were tested as racemic mixture of *R*-/*S*-stereoisomers. This demonstrates that the observed inhibition of JMJD5 by these compounds may either be by only the *S*- or *R*-stereoisomer of the compound.

Inhibition studies with the TCA cycle intermediates further supported the proposal that the inhibition of JMJD5 can be modulated by small changes in the inhibitor structure. The (*S*)-enantiomer of 2-hydroxyglutarate (L-2HG) (IC_{50} = 340 µM) was found to be better inhibitor for JMJD5 than the (*R*)-enantiomer (D-2HG) (IC_{50} = 1268 µM) (Table 8.1). Crystallographic analyses further showed that the hydrocarbon backbone of L-2HG is slightly shifted towards the hydrophobic residue W310, which may help L-2HG to form a stronger complex than D-2HG (Figure 8.7). Previous studies also showed that the (*S*)-form of 2HG is the better inhibitor of (most) 2OG oxygenases than the (*R*)-form, while the concentrations of both may reach levels in cell sufficient for inhibition (91). In the case of JMJD5, the obtained IC_{50} values were higher than those reported for other 2OG oxygenases (4). Nonetheless, their potential to inhibit JMJD5 at high concentrations may be an important consideration in certain biological contexts; for example, cancer cells carrying mutations in isocitrate dehydrogenase (IDH) exhibit substantially elevated levels of 2HG, which can in some cases reach millimolar concentrations (90-92).

While the inhibition studies using 2OG analogues and TCA cycle intermediates reveal that JMJD5 shows stereo selectivity towards small ligands for inhibition, studies using selective inhibitors of PHD and KDM reveal that JMJD5 is inhibited by Daprodustat

and ML-324 (Table 8.1, Figure 8.6). However, the binding modes of these inhibitors are still unknown. Furthermore, inhibition by ejecting the active-site Fe(II) may also be possible; one such example for KDM inhibitor has been reported previously (98). Further studies by crystallography or NMR are therefore required to uncover the inhibition mechanism by these inhibitors.

CHAPTER 09: Biochemical Characterisation of Human HPPD

9.1. Introduction

4-Hydroxyphenylpyruvate dioxygenase (HPPD) is a non-haem Fe(II)- and oxoacid-dependent oxygenase that catalyses the conversion of 4-hydroxyphenylpyruvic acid (HPPA) to homogentisic acid (HMGA; 2,5-dihydroxyphenylacetic acid), the second step of tyrosine catabolism in all aerobic metabolisms (Figure 9.1) (15). Unlike the 2-oxoglutarate (2OG)-dependent oxygenases, most of which use 2OG as a cosubstrate, HPPD requires only molecular oxygen for catalysis, *i.e*., it does not require 2OG. The oxoacid functionality of 2OG is in effect contained within the structure of HPPA (Figure 9.2) (15). The reaction catalysed by HPPD involves oxidative decarboxylation, aromatic ring hydroxylation, and substituent migration to yield the product HMGA (Figure 9.2); the migration process shows similarity to the NIH (National Institute of Health) shift observed for some P450 hydroxylases and pterin-dependent oxygenases (15).

HPPD has been targeted for both herbicidal and medicinal purposes (15). In animals, several hereditary diseases are caused by defects relating to enzymes in the tyrosine catabolism pathway (Figure 9.1) (15). For example, type I tyrosinemia, which is associated with kidney failure and liver cancer, is caused by a deficiency in fumarylacetoacetase (FAA, Figure 9.1) (15). Similarly, patients suffering from type II tyrosinemia can have a deficiency of tyrosine aminotransferase (TAT, Figure 9.1) (15). The symptoms of type II tyrosinemia are indistinguishable from those of another hereditary disease, type III tyrosinemia, which is caused by disruption of HPPD (15). Individuals with type III tyrosinemia produce HPPD with an alanine to valine substitution at position 268 (15). Further, a single mutation in human HPPD (Ala^{33} to Thr^{33}) causes hawkinsinuria, the symptoms of which include metabolic acidosis and severe stunting (15). Alkaptonuria is a related inborn defect occurring in individuals deficient in the activity of homogentisate 1,2-dioxygenase (HGD, Figure 9.1), also involved in tyrosine catabolism (15).

In plants, HPPD forms secondary metabolites (*e.g.* plastoquinone, tocopherols) essential for photosynthesis (Figure 9.1) (15). This step of tyrosine catabolism has been targeted by the agrochemical industry, leading to the development of important herbicides including mesotrione, nitisinone, and sulcotrione. Nitisinone, or 2-[2-nitro-4-(trifluoromethyl)benzoyl]-1,3-cyclohexanedione (NTBC), is approved by the FDA (US Food and Drug Administration) for the treatment of alkaptonuria and type I tyrosinemia by inhibiting human HPPD (15). These HPPD inhibitors block the production of toxic metabolites such as homogentisate, maleylacetoacetate, and fumarylacetoacetate (Figure 9.1), the accumulation of which can be fatal if left untreated.

Although the development of HPPD-inhibitors has targeted plant HPPD, less focus has been paid to the biochemical characterisation of human HPPD. Furthermore, there are no reports on how inhibitors of other human 2OG oxygenases, including those in clinical trials, interact with the mechanistically related enzyme HPPD. The work, carried out in this study, describes kinetic and structural characterisation of human HPPD as well as inhibitor profiling.

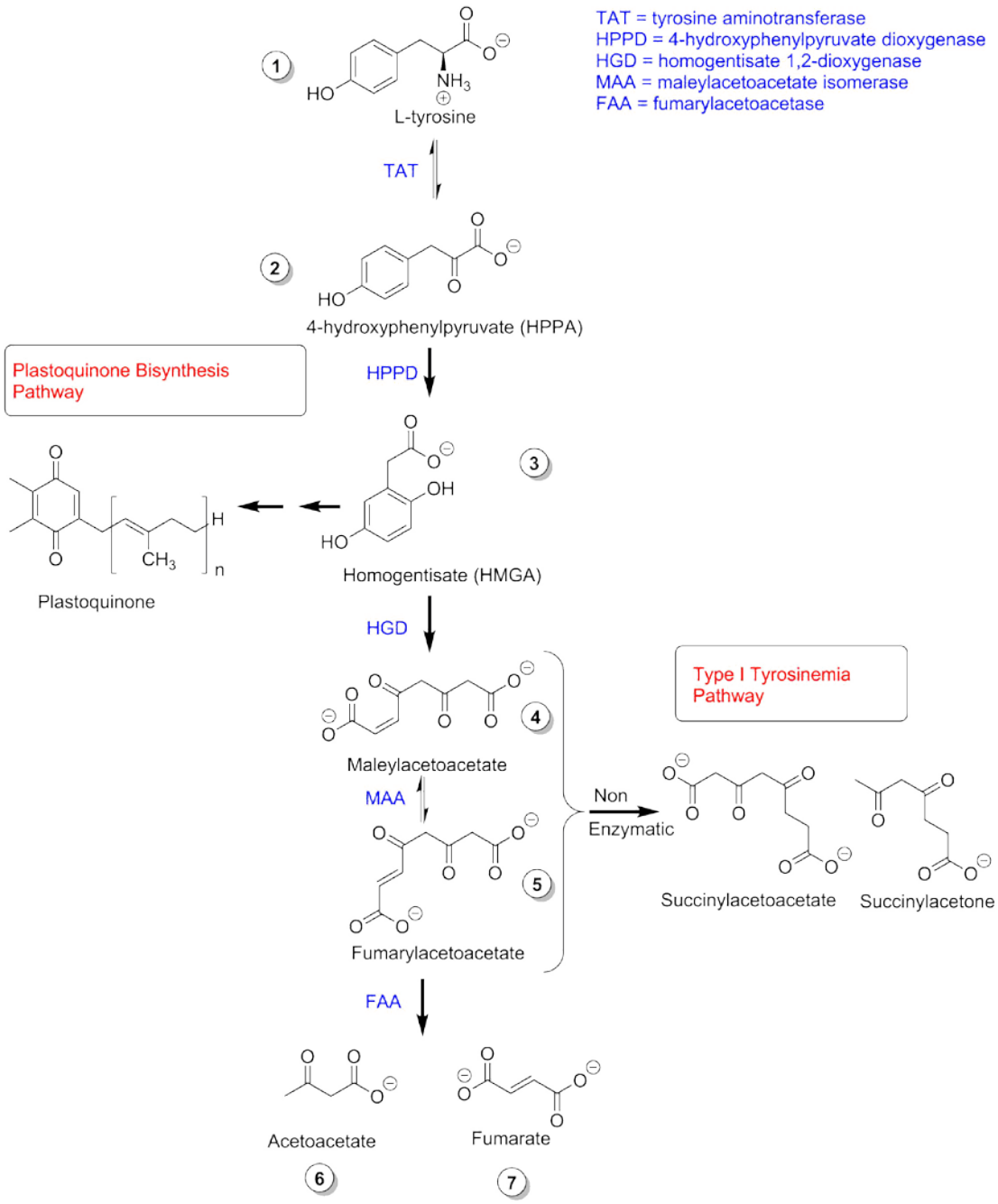

FIGURE 9.1. **The tyrosine catabolism pathway present in all aerobic metabolism.** The scheme shows the important role of HPPD catalysis in the degradation of tyrosine. This scheme is modified from Moran *et al.* (15).

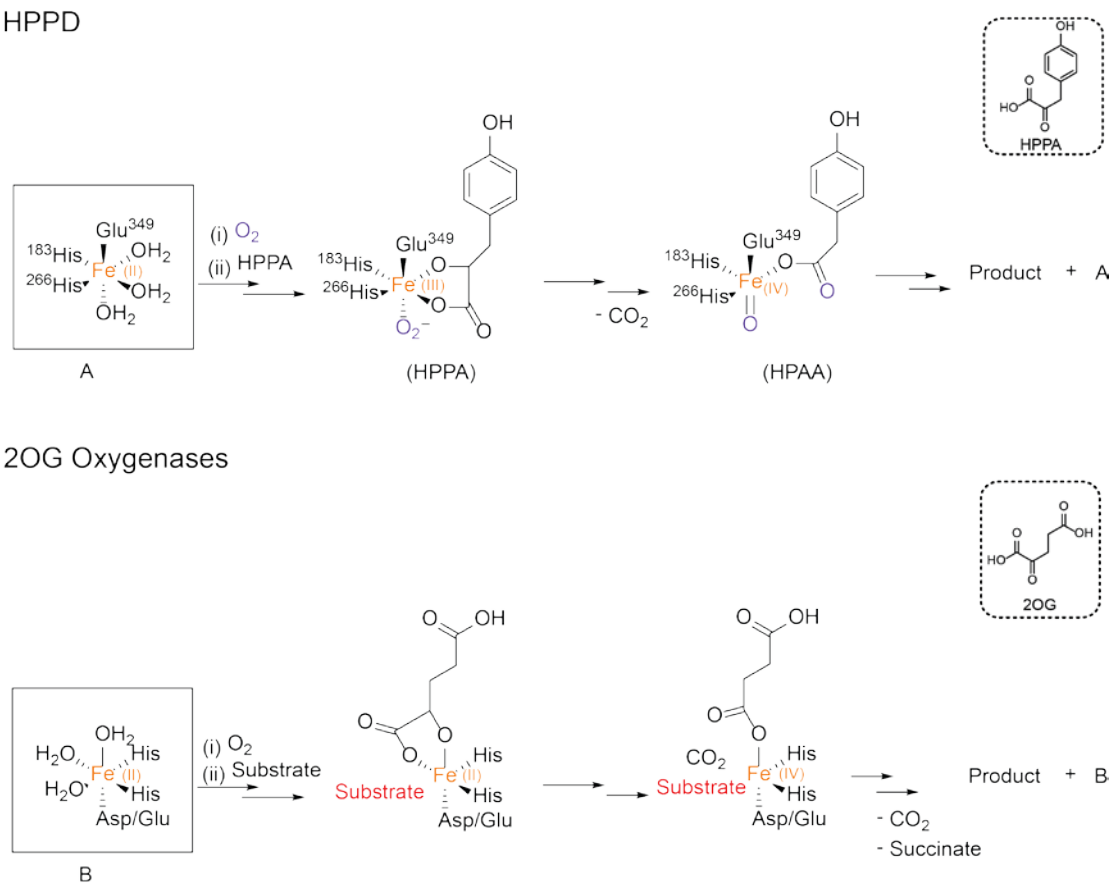

FIGURE 9.2. **Outline catalytic mechanisms for HPPD and comparison with that for the 2OG oxygenases.**

9.2. Production and Initial Characterisation of Wild-type Human HPPD

This work began with the production and purification of recombinant human HPPD, according to the procedure developed by the Structural Genomics Consortium (SGC, Oxford, UK) (150). The activity of purified human HPPD was then assayed by nuclear magnetic resonance (NMR) spectroscopy (**Chapter 10**). To date, various methods have been used to assay HPPD activity, including UV-visible spectrophotometry monitoring product formation (at 308 or 288 nm) (118-121), use of electrodes monitoring O_2 consumption or CO_2 release (122-125), and high performance liquid chromatography (HPLC) (125-127). However, no reported HPPD assays have employed NMR

spectroscopy. In the studies described herein, the ^{1}H signals of the HPPD substrate and the product were monitored using 700 MHz NMR spectrometers.

HPPD-catalysed formation of HMGA (compound **3**, Figure 9.1) from HPPA (compound **2** Figure 9.1) was observed by NMR. The reaction mixture contained purified human HPPD, ascorbate, and Fe(II) (Figure 9.3). The presence of HPPA and HMGA was confirmed by comparing the corresponding ^{1}H NMR (700 MHz) spectra with those of standards (Figure 9.3**B**). Based on comparison with these standards, the ^{1}H NMR spectra showed that the formation of HMGA from HPPA was HPPD-dependent (Table 9.1, Figure 9.3). Further, the time-dependent formation of HMGA catalysed by HPPD was observed. Collectively, these observations demonstrate the activity of the human HPPD (Figure 9.3**B** and 9.3**C**) purified in this work.

Unexpected ^{1}H signals (δ_H 6.84 ppm and 6.55 ppm) were observed, which occurred only after the addition of Fe(II) [$(NH_4)_2Fe(SO_4)_2.6H_2O$] to HPPA. These observed signals are distinct from the signals corresponding to HPPA (δ_H 6.97 ppm and 6.73 ppm) and HMGA (δ_H 6.63 ppm and 6.54 ppm) (Figure 9.3). This likely indicates a metal complex.

Table 9.1. Activity testing of wild-type and mutant human HPPD. Activity testing of wild type and alanine variants of human HPPD was carried out following the NMR-based assay as described in Chapter 10. Briefly, 500 µM of HPPA was allowed to react with 0.5 µM human HPPD in the presence of 100 µM Fe(II) and 400 µM ascorbate at room temperature. Values represent mean (n = 3) ± standard deviation (SD).

HPPD Variant	**HMGA (µM/2 min)**	**HMGA (µM/60 min)**	**Kinetic Parameters**				
			K_a **(µM)**	V_{max} **(µM.s^{-1})**	K_m **(µM)**	k_{cat} **(s^{-1})**	k_{cat}/K_m **(µM^{-1} s^{-1})**
WT	209	500	0.8	3.1	165	6.3	0.04
H183A	0	0	ND				
H266A	0	0	ND				
E349A	0	0	ND				

ND = not determined

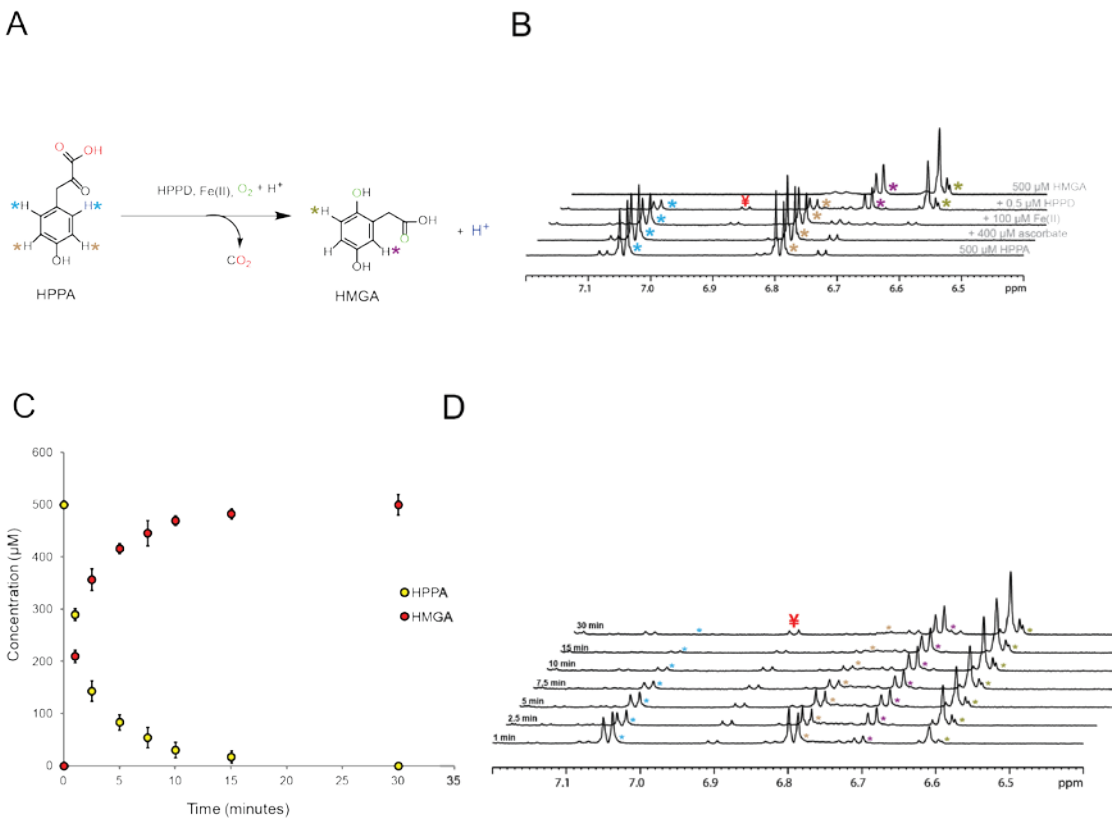

FIGURE 9.3. **Analysis of HPPD catalysis by ^{1}H NMR**. (A) Reaction scheme showing the conversion of HPPA to HMGA as catalysed by human HPPD. (B) ^{1}H NMR (700 MHz) spectra showing the signals corresponding to HPPA (δ_H 6.97 and 6.73 ppm) and HMGA (δ_H 6.63 and 6.54 ppm) (C) Plot showing the HPPD-dependent consumption of HPPA and formation of HMGA over time. (D) ^{1}H NMR spectra showing substrate consumption and product formation during HPPD catalysis. The activity testing and time course studies were carried out as described in Chapter 10. Values represent mean (n = 3) ± SD.

9.3. Kinetic studies of human HPPD

The interactions between HPPD and its substrate HPPA were studied in more detail by NMR. The binding constant (K_D) of HPPA was determined using CPMG (Carr-Purcell-Meiboom-Gill)-edited ^{1}H NMR experiments (56,57) as described in Chapter 10. Although

binding studies with HPPD and its inhibitors were performed previously (123), binding studies between HPPD and HPPA have not yet been reported. In this work, a 20 µM HPPA solution was titrated against human HPPD [HPPD.Zn(II)] until the ^{1}H signals for HPPA disappeared (**Chapter 10**). The relative amount of the HPPD.Zn(II).HPPA complex was then plotted against the concentration of HPPD using Origin™ (Figure 9.4). The apparent K_D value was determined by following the method of Morton *et al.* (58) (**Chapter 10**) and was 0.8 µM ± 0.15 µM (Table 9.1, Figure 9.4). This suggests very tight binding between human HPPD and HPPA, at least with Zn(II) bound (Figure 9.4).

A *steady-state* kinetic study of HPPD-catalysed conversion of HPPA to HMGA was then performed. Previous kinetic studies of HPPD from different species had employed methods such as HPLC (128), electrodes (126), and stopped-flow spectrophotometry (124). In this work, an NMR-based assay was used. The formation of HMGA from the reactions between 0.5 µM human HPPD and varied concentrations of HPPA (0-500 µM) was monitored (**Chapter 10**). Each reaction was monitored within the linear kinetic range (Figure 9.3) and each experiment was performed in triplicate. Finally, the rates of HMGA formation (v_0) were plotted against the concentration of HPPA, yielding a K_m value of 165 µM for HPPA (Table 9.1, Figure 9.4).

The K_m value of HPPA with human HPPD is relatively high (165 µM), contrasting the relatively low K_D value (0.8 µM). This may likely be due to the slow dissociation of HPPA from the HPPD.Zn(II).HPPA complex when compared to the complex of HPPD.Fe(II).HPPA. Previously reported work on human HPPD also found relatively high K_m values; *i.e.*, 80 (125) or 200 µM (128) against 5 µg of human HPPD enzyme. In comparison, the K_m values of HPPA were found to be 142, 27, and 6.9 µM against 0.5 µM archaeal HPPD (*Picrophilus torridus*), 1-2 µM bacterial HPPD (*Streptomyces avermitilis*), and 2.01 mM plant HPPD (*Arabidopsis thaliana*), respectively (124-126). Overall, these values suggest that HPPA is required in excess for efficient catalysis by HPPD. Notably, the K_m value of HPPA for *Arabisopsis*-HPPD was relatively low. However, variation in the

K_m values of HPPA against HPPD from various species further suggests that HPPA has different binding affinities towards HPPD from various species, although they share a highly conserved catalytic site (15). Moreover, variation in the *N*-termini of HPPD among various species might also impact the K_m values of HPPA (124-126). Note, the methods employed for these kinetic studies were also different, which may be another contributing factor in the different reported K_m values (124-126).

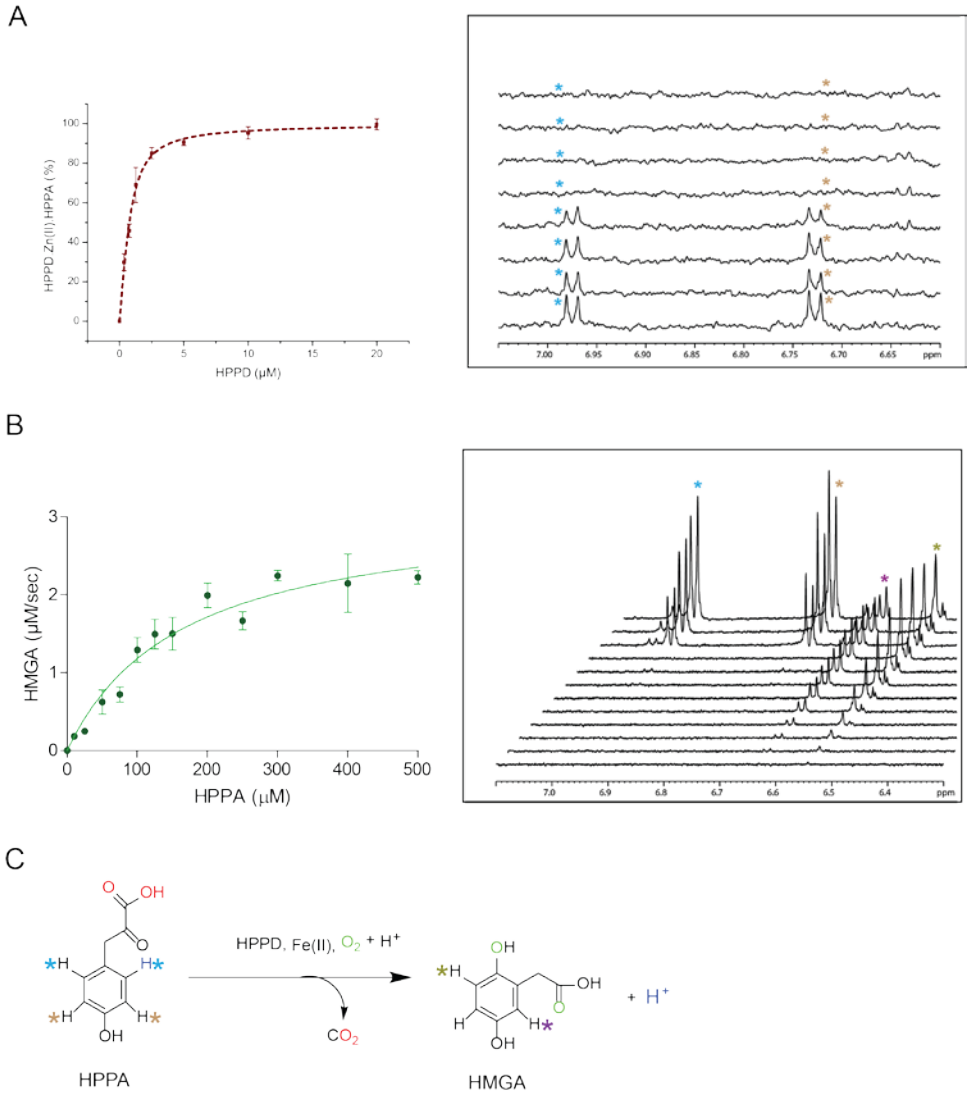

FIGURE 9.4. **Investigating binding of HPPA to human HPPD**. (A) Plot showing the titration of HPPD to a solution of HPPA as measured by CPMG NMR spectra to determine the K_D of HPPA; inset shows the gradual disappearance of ^{1}H signals of HPPA (δ_H 6.97 and 6.73 ppm) upon titration with human HPPD [HPPD.Zn(II) complex]. (B)

Michaelis-Menten plot showing the initial reaction rate of HPPD-catalysed HMGA formation as a function of HPPA concentration; inset shows the corresponding ^{1}H signals of HPPA (δ_H 6.97 and 6.73 ppm) and HMGA (δ_H 6.63 and 6.54 ppm). (C) The reaction catalysed by HPPD highlighting the protons from HPPA and HMGA used for NMR studies by asterisks. Experiments were carried out following the NMR-based assay described in Chapter 10. Values represent mean (n = 3) ± SD.

9.4. Activity Testing of Catalytic Variants of Human HPPD

The activities of metal binding variants of human HPPD were next investigated. Comparison of the plant and human HPPD amino acid sequences, with consideration of the structure of the former (129), implies that metal binding in human HPPD involves two histidine residues (His^{183} and His^{266}) and one glutamate (Glu^{349}) residue (129). Crystallographic studies have revealed their location on the β9, β13, and β16 strands of the *C*-terminal region of human HPPD, respectively (Figure 9.5) (15). Mutants wherein these three residues were substituted with alanine residues were cloned, produced in *Escherichia coli*, and purified according to the same procedure as used for wild-type HPPD (**Chapter 10**). ^{1}H NMR-based activity assays with these three mutants showed no substrate turnover (Table 9.1, Figure 9.5). Even after prolonged incubation (60 minutes), no HMGA formation was observed (Table 9.1, Figure 9.5). These results suggest that the catalytic activity of human HPPD depends on all three metal binding residues. This contrasts with previously reported work (128); human HPPD was found to be inactive when His^{266} or Glu^{349} were mutated to alanine residues. But the mutant H183A was found to retain some (low) catalytic activity (1.2% compared to wild-type). Further, activity of the mutant E349A was also found to be recovered when E349 was mutated to either glycine (E349G, 4.7% activity of wild-type) or glutamine (E349Q, 1.2% activity of the wild-type) (128).

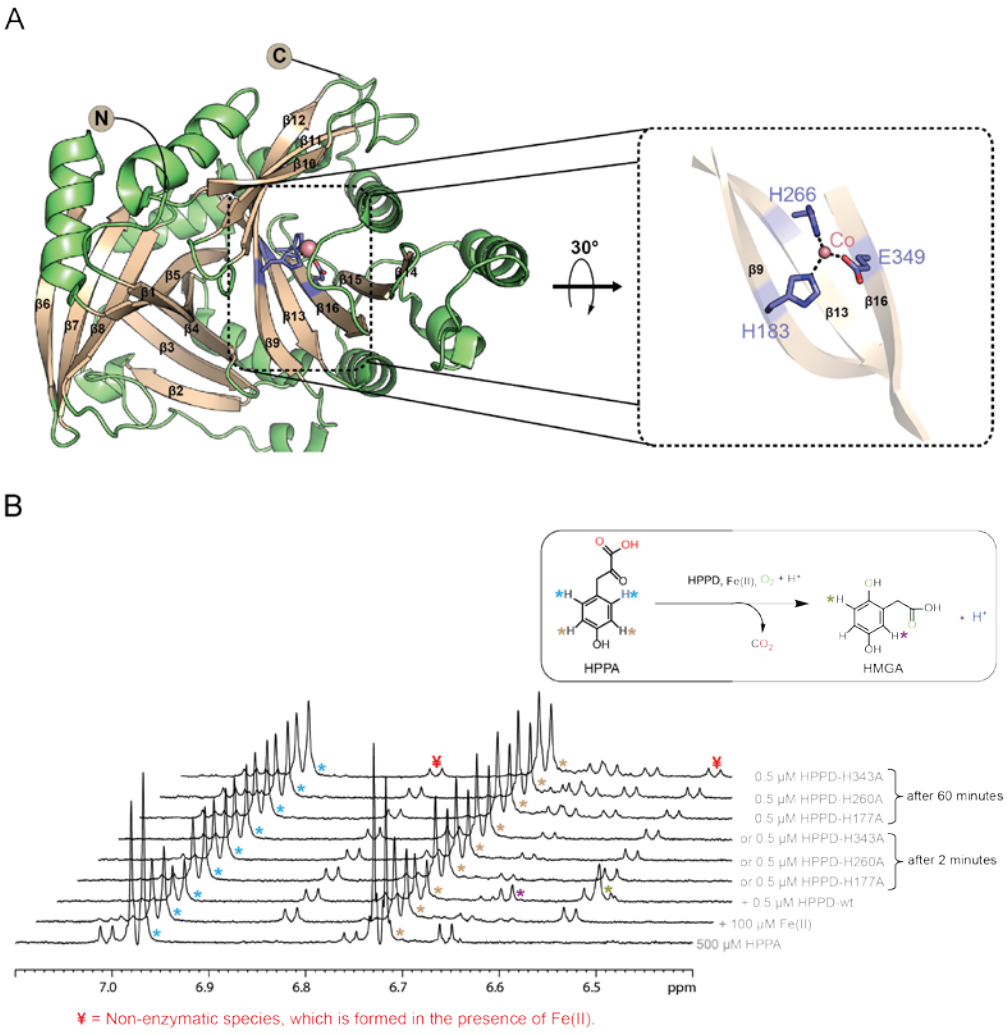

FIGURE 9.5. **Activity testing of the metal binding variants of human HPPD**. (A) Cartoon view from a crystal structure of wild type human HPPD (PDB: 3ISQ) showing the α-helices (green), β-sheets (wheat), active-site Co(II) (light pink sphere), and the metal binding residues (slate sticks); the inset highlights the metal binding residues which were substituted by alanine. (B) ^{1}H NMR (700 MHz) spectra showing the assay reaction mixture with either wild-type or mutant human HPPD; inset shows the reaction scheme of HPPD catalysis. Activity testing was carried out following the NMR-based assay as described in Chapter 10.

9.5. Screening of Alternative Substrates

HPPD has been previously shown to modify substrates other than HPPA. In particular, HPPD from various species showed decarboxylase and dioxygenase activities towards a range of α-keto acids, including α-ketoisocaproate (rat HPPD), 2-oxo-5-thiahexanoic acid (rat-HPPD), and phenylpyruvate (*Pseudomonas*, pig, and human HPPD) (15). However, the HPPD from a *Streptomyces* spp. showed neither decarboxylase nor dioxygenase activity towards phenylpyruvate (15).

To further explore the substrate-scope of human HPPD, a series of HPPA analogues were synthesized (compounds **1-10**, Table 9.2) (by Dr. Marios Markoulides, Chemistry Research Laboratory, University of Oxford). The binding properties of these compounds were tested with human HPPD using an NMR-based reporter displacement experiment (55). The extent to which these analogues displaced HPPA (in this case is the reporter ligand) from HPPD was measured. The Zn(II) complex of HPPD was used in this study to prevent substrate turnover, and the proton signals from HPPA were measured using a CPMG-edited ^{1}H NMR (56,57). Each of the compounds **1-10** showed competition with HPPA under these conditions. As a positive control, known inhibitors of HPPD (nitisinone or mesotrione) were used, which effectively displaced HPPA from HPPD (Figure 9.6). As compounds **1-10** refrained HPPA from binding to the active site of HPPD (Figure 9.6), these compounds likely did bind at the active site of HPPD. Importantly, the extent to which **1** displaced HPPA was similar to that observed in case of mesotrione and nitisinone (Figure 9.6), suggesting **1** can be a strong binder (either substrate or inhibitor) for human HPPD.

Another series of HPPA derivatives (compounds **11-20**, Table 9.2), in which the pyruvate functionality of HPPA was replaced with an oxazolone ring, was synthesized (by Dr. Marios Markoulides, Chemistry Research Laboratory, University of Oxford). Unlike compounds **1-10,** compounds **11-20** did not show any competition with HPPA (Figure 9.7), suggesting that none of these compounds bind to the HPPD.

These observations suggest that the pyruvate group of HPPA is important for binding to human HPPD. Compounds **1-10** closely resemble HPPA, differing only by the substitution of fluorine or chlorine atoms on the aromatic ring. In contrast, compounds **11-20**, in which the pyruvate group is replaced with oxazolone ring, appears to lack the functionality important for binding.

Compounds **1-10** were next tested with human HPPD as alternative substrates. These compounds were incubated with human HPPD in the presence of Fe(II) and ascorbate under the assay conditions as described elsewhere (**Chapter 10**), product formation was monitored by NMR spectroscopy. However, no evidence for HPPD-mediated formation of new chemical species was observed. This suggests that none of the compounds **1-10** are substrates of human HPPD.

Table 9.2. Structures of substrate analogues tested against human HPPD. Binding assays for compounds **1-20** with human HPPD were carried out following the 'Reporter Displacement Experiment' method described in Chapter 10.

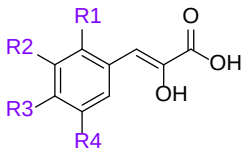

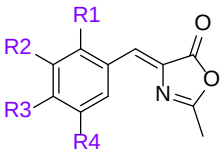

Compound	R1	R2	R3	R4	Competition*	Compound	R1	R2	R3	R4	Competition*
1	H	Cl	H	Cl	Yes	**11**	H	Cl	H	Cl	No
2	H	H	F	H	Yes	**12**	H	H	F	H	No
3	F	-H	-H	H	Yes	**13**	F	H	H	H	No
4	H	F	H	H	Yes	**14**	H	F	H	H	No
5	F	F	H	H	Yes	**15**	F	F	H	H	No
6	F	H	F	H	Yes	**16**	F	H	F	H	No
7	F	H	H	F	Yes	**17**	F	H	H	F	No
8	H	F	H	F	Yes	**18**	H	F	H	F	No
9	F	H	OH	H	Yes	**19**	F	H		H	No
10	H	F	OH	H	Yes	**20**	H	F		H	No

***** Competition was investigated with respect to HPPA-displacement for binding with human HPPD.

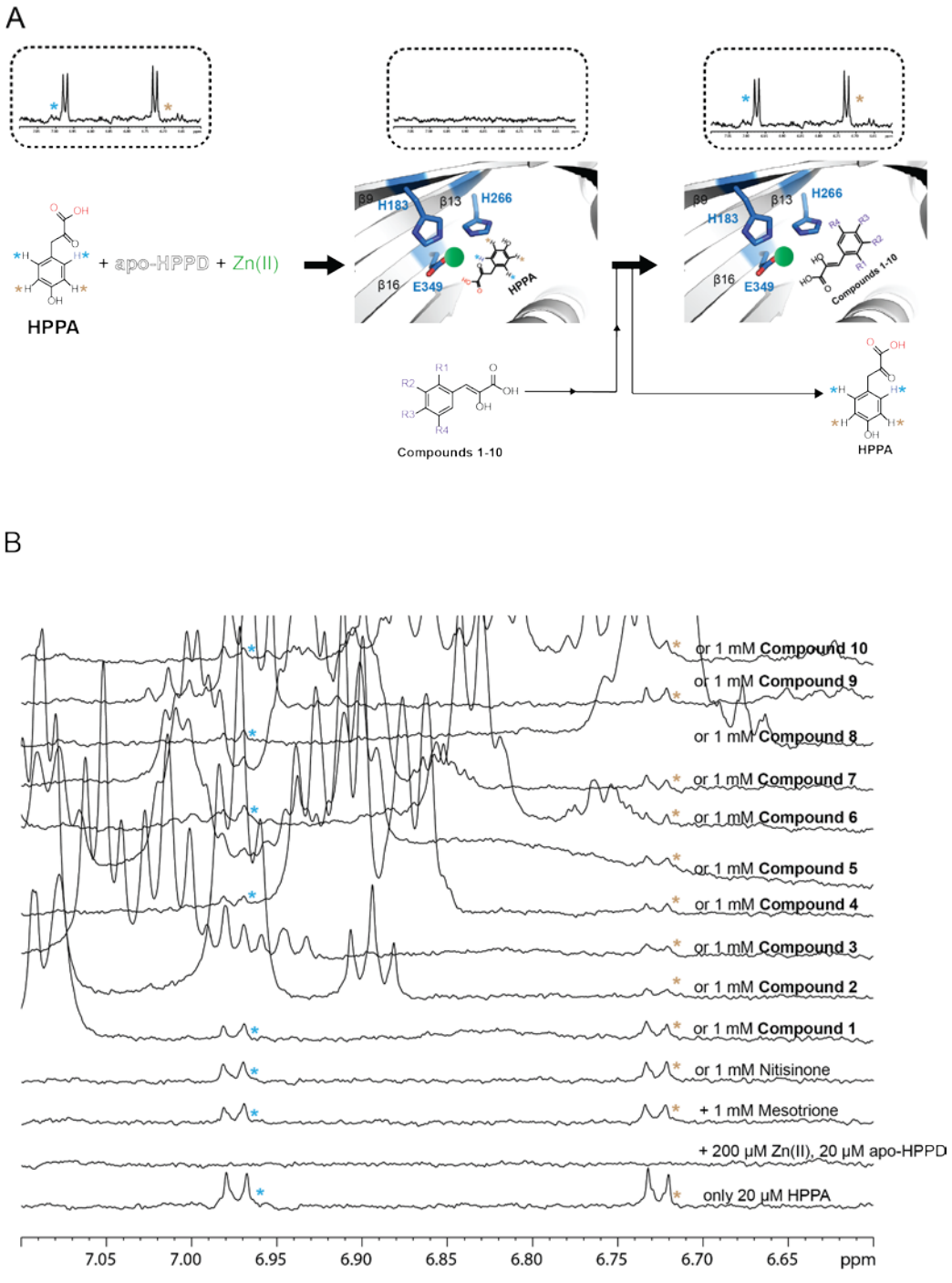

FIGURE 9.6. **Binding studies of substrate analogues with human HPPD**. (A) Model showing HPPA bound to the active site of human HPPD. Compounds **1**-**10** appeared to compete with HPPA for binding to the active-site of human HPPD, which results in the recovery of HPPA signals (inset). (B) ^{1}H NMR (700 MHz) spectra showing the

appearance of signals corresponding to HPPA (δ_H 6.97 and 6.73 ppm) upon addition of compounds **1**-**10**.

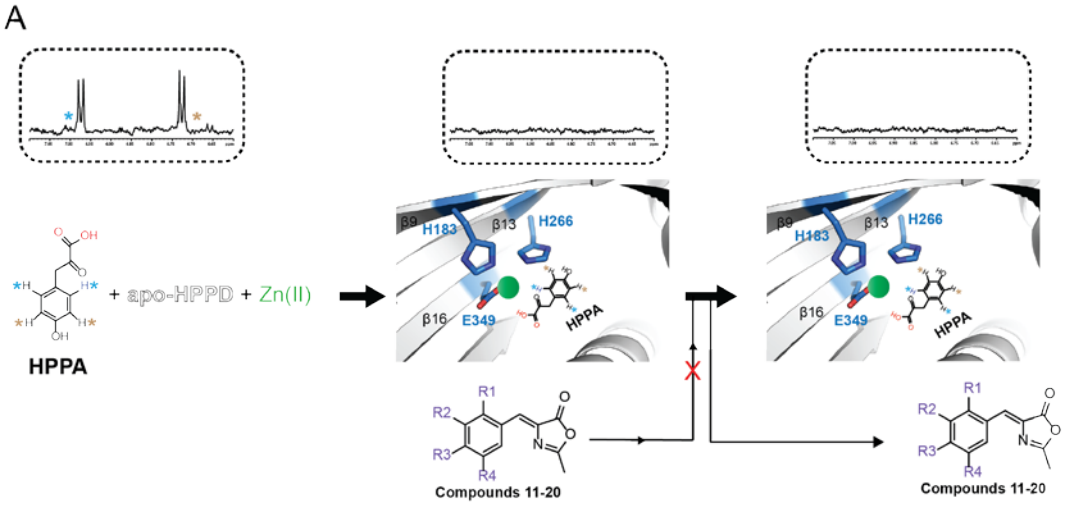

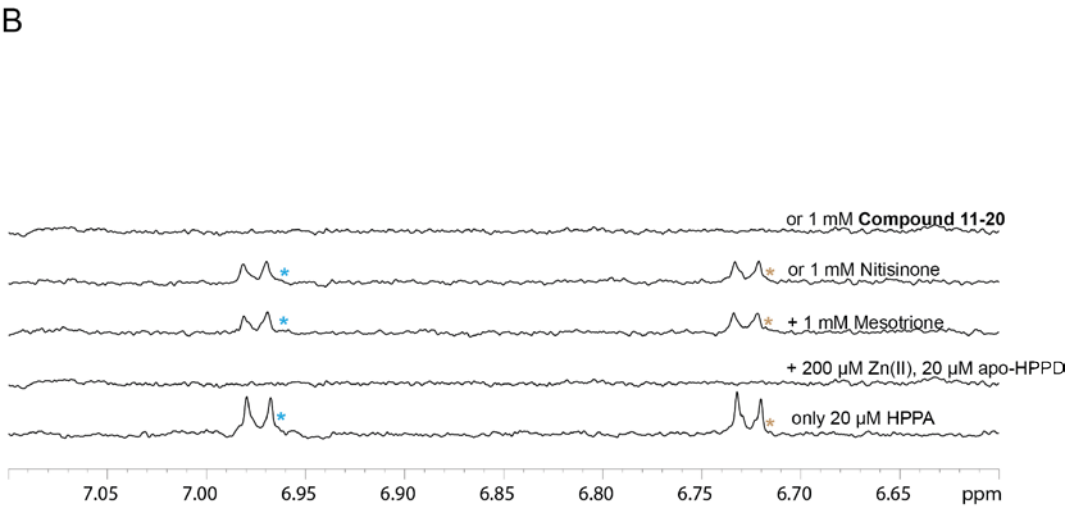

FIGURE 9.7. **Binding studies of substrate analogues with human HPPD**. (A) Model showing HPPA bound at the active site of human HPPD. HPPA was not displaced following the addition of compounds **11-20**. (B) ^{1}H NMR (700 MHz) spectra showing the appearance of signals corresponding to HPPA (δ_H 6.97 and 6.73 ppm) upon addition of mesotrione or nitisinone, but not compounds **11-20.**

9.6. Kinetic Studies on Reported HPPD Inhibitors

Although the inhibition of HPPD may cause side effects mimicking those of type II and III tyrosinemia, targeting this step of tyrosine catabolism may have benefits for patients with type I tyrosinemia, alkaptonuria, hawkinsinuria, and Parkinson's disease (15,130). To date, potential HPPD-inhibitors have been developed *e.g.* mesotrione, nitisinone, and sulcotrione, which are used as herbicides and medicine (15). Nonetheless, little is known about the binding affinities of these inhibitors to human HPPD enzymes; a previous study reported a high binding constant (K = 1.25 mM) for NTBC with *Sterptomyces* HPPD (*S. avermitilis*) (123). Therefore, a kinetic study using these inhibitors was carried out on human HPPD with an aim to understand better the inhibition of properties of these inhibitors against human HPPD.

9.6.1. Binding Experiments between Human HPPD and HPPD Inhibitors

First of all, a binding study was performed using NMR, as was performed for the substrate HPPA (section 9.3). A 20 μM solution of each inhibitor was titrated against human HPPD [as the HPPD.Zn(II) complex] until the inhibitor signals (^{1}H or ^{19}F where appropriate) disappeared (**Chapter 10**). Then, the apparent binding constant (K_D) values of the inhibitors were determined using the same procedure as for HPPA. The K_D values obtained thereafter were 16.6, 26 (^{1}H)/16.3 (^{19}F), and 3.4 for mesotrione, nitisinone, and sulcotrione, respectively (Table 9.3, Figure 9.8).

Table 9.3. Kinetic parameters of HPPD-inhibitors tested against human HPPD. Experiments were carried out following the NMR-based assay procedure described in Chapter 10. Values represent mean (n = 3) ± SD.

Inhibitor	K_D (μM)	IC_{50} (μM)
Mesotrione	16.6 ± 2.1	0.31 ± 1.3
Nitisinone	26 ± 2.5 (^{1}H), 16.3 ± 3.4 (^{19}F)	0.45 ± 1.3
Sulcotrione	3.4 ± 1.4	0.3 ± 1.3

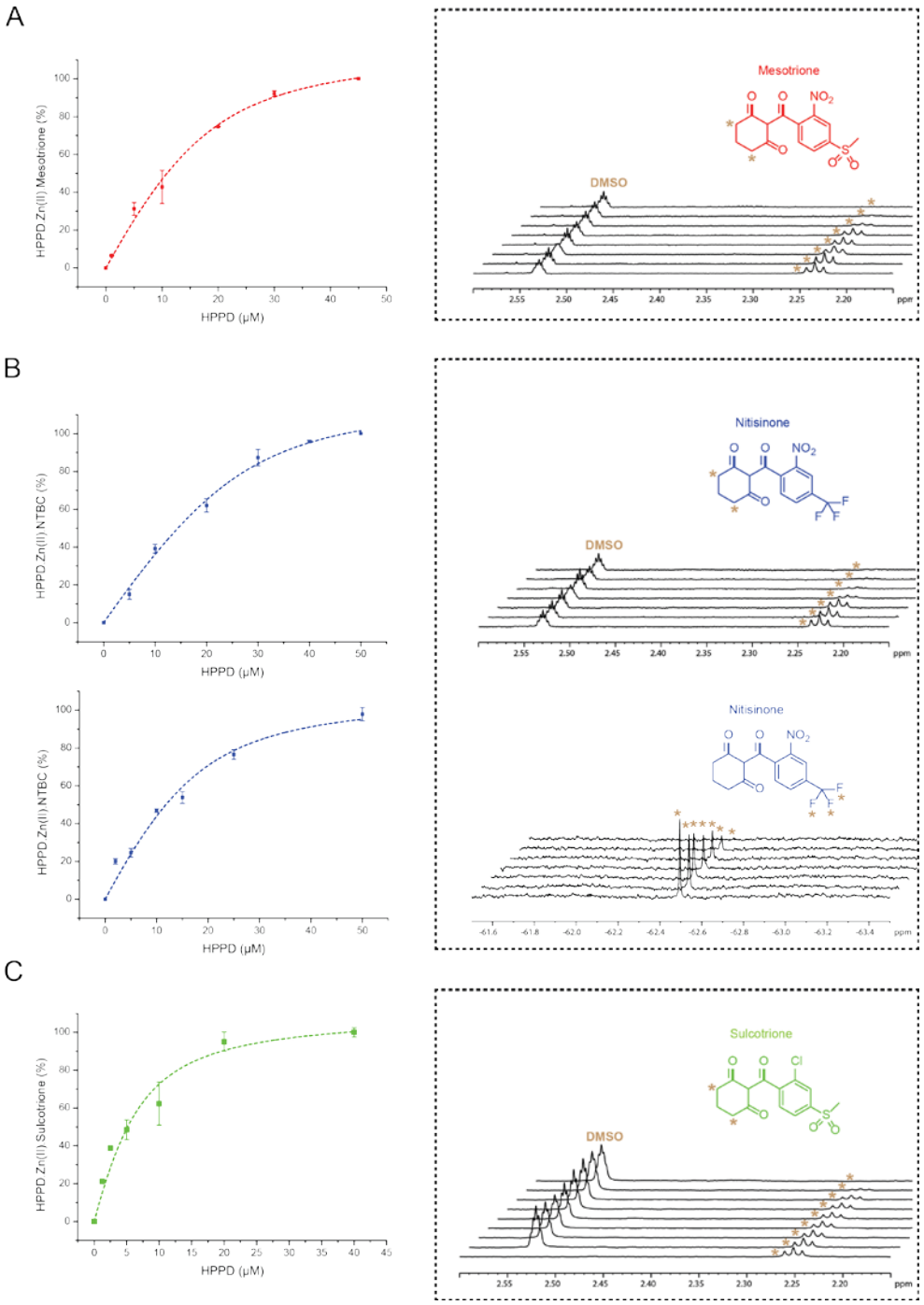

FIGURE 9.8. **Determination of binding constants for HPPD inhibitors**. Curves showing the titration of inhibitors (A) mesotrione, (B) nitisinone, and (C) sulcotrione with [HPPD.Zn(II)] to determine K_D values; insets show the disappearance of ^{1}H and ^{19}F signals for the inhibitors (δ_H 2.25 and δ_F -62.49 ppm) resulting from titration with human HPPD.Zn(II) complex (from 0-50 μM concentration). Values represent mean (n = 3) ± SD.

9.6.2. Inhibition Studies with human HPPD using HPPD Inhibitors

Next, the inhibitory properties of these inhibitors against human HPPD were investigated. First, an initial end-point inhibition assay was performed with 10, 100, and 1000 nM inhibitor (Figure 9.9).

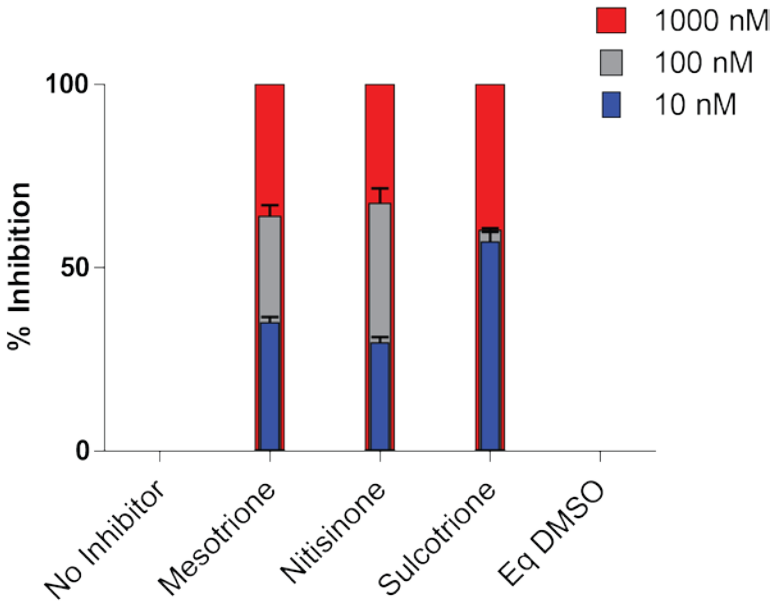

FIGURE 9.9. **Inhibition studies of human HPPD with reported HPPD inhibitors.** Bar charts showing the end-point inhibition assay results using 0.5 µM human [HPPD.Fe(II)] and 500 µM HPPA. Reaction using equivalent amount of DMSO (dimethyl sulfoxide) in place of inhibitor solution was also carried out, which confirmed no inhibition of HPPD activity due to DMSO. Experiments were carried out following the NMR-based assay procedure as described in Chapter 10. Values represent mean (n = 3) ± SD.

Based on these results, further inhibition studies were carried out to determine the half-maximal inhibitory concentration (IC_{50}) values of these inhibitors. Reactions between 0.5 µM human HPPD and 500 µM HPPA in the presence of varying concentrations of inhibitors (0.33-1000 nM) were monitored by NMR. IC_{50} values were then determined from the resultant curves, which were constructed by plotting percent inhibition against inhibitor concentration using GraphPad PRISM. The measured IC_{50} values were within the range of 300-500 nM, with sulcotrione exhibiting the lowest IC_{50} value of 300 nM

(Table 9.3, Figure 9.10). The apparent stronger binding property of sulcotrione with human HPPD (lowest K_D value, Table 9.3) might contribute to its relatively potent inhibitory property (Table 9.3).

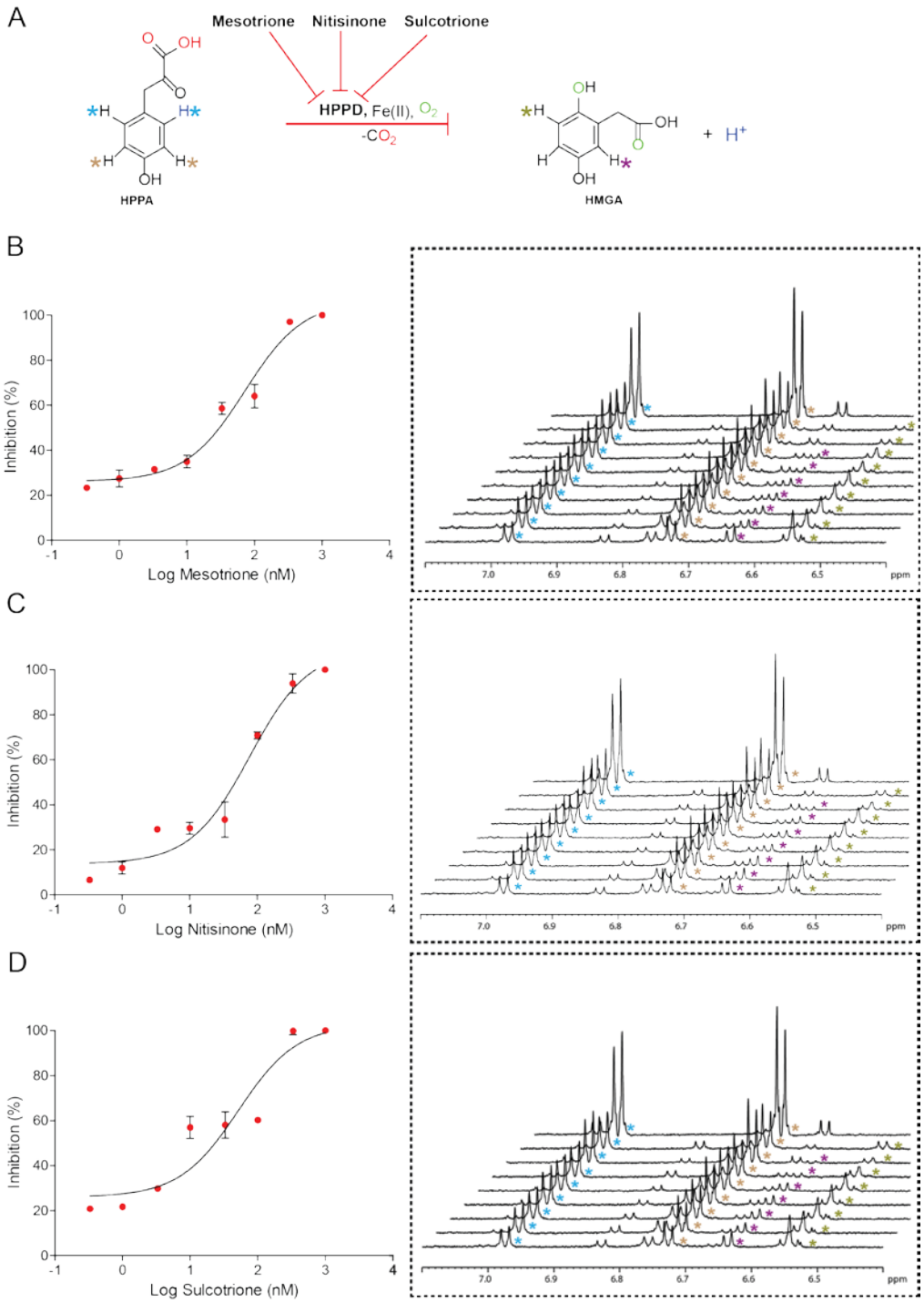

FIGURE 9.10. **Determination of *IC*$_{50}$ values for reported HPPD inhibitors with human HPPD**. (A) Reaction scheme showing the basis of HPPD inhibition. *IC*$_{50}$ curves of (B)

mesotrione, (C) nitisinone, and (D) sulcotrione as determined using 0.5 µM human HPPD [HPPD.Fe(II) complex], 500 µM HPPA, and a series of inhibitor concentrations as described in Chapter 10. Values represent mean (n = 3) ± SD.

The IC_{50} values for mesotrione and nitisinone were also in the nanomolar range, although their overall inhibitory potencies appeared to be relatively weaker compared to those reported against HPPD from other non-human species (**Appendix 06**) (130). For example, nitisinone was found to have IC_{50} values of 40, 50, and 68 nM against pig-liver HPPD (131), rat-liver HPPD (122), and isolated human HPPD (132), respectively; these measurement are about 10-fold lower than the IC_{50} value obtained from this work.

This variation in IC_{50} values might arise due to multiple reasons. First, the reactions in this study were carried out at room temperature (20 °C) without any pre-incubation of HPPD with the inhibitors, unlike the previously reported works where a 10-minute pre-incubation step between enzyme and inhibitor was performed at 37 °C before the addition of substrate (122,131,132). This pre-incubation step might help the inhibitors to bind to HPPD strongly since the binding of several HPPD inhibitors has been reported to be time-dependent (122). The techniques used to monitor the inhibition result are also different between these studies (**Appendix 06**), which might also influence the obtained results (130).

9.7. Screening of Potential HPPD Inhibitors

Next, inhibition studies using compounds **1-10** were carried out as these compounds demonstrated binding to human HPPD (section 9.5). The IC_{50} values of these compounds were measured by the NMR-based assay. The IC_{50} value for **1** was 86 µM whereas the IC_{50} values of **2-10** were all >100 µM (Table 9.4). These observations are consistent with the NMR binding studies where **1** showed the greatest competition with HPPA (Figure 9.6).

It is reported that the 2-benzoylethen-1-ol pharmacophore is the minimum requirement for potent inhibitors of HPPD (130). Despite the absence of this pharmacophore, compound **1** displayed a moderate level of potency against human HPPD (Table 9.4). This may be due to the presence of the pyruvate structural moiety which mimics HPPA (and hence, may be 2OG), and thus likely competes with substrate binding. Moreover, the presence of an electronegative (and hydrophobic) group (*i.e.*, a chlorine atom) might further facilitate the binding of **1** with human HPPD, as was observed with some other potential HPPD inhibitors (130).

Table 9.4. Structures and inhibition results for compounds 1-10 with human HPPD. IC_{50} values were determined using the NMR-based inhibition assay with 0.5 µM human HPPD [HPPD.Fe(II)], 500 µM HPPA, and various concentrations of the inhibitors (Chapter 10). Values represent mean (n = 3) ± SD.

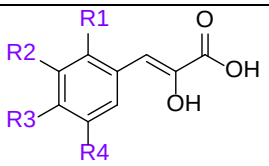

Compound	R1	R2	R3	R4	IC_{50} (µM)
1	H	Cl	H	Cl	86 ± 1.4
2	H	H	F	H	> 100
3	F	-H	-H	H	> 100
4	H	F	H	H	> 100
5	F	F	H	H	> 100
6	F	H	F	H	> 100
7	F	H	H	F	> 100
8	H	F	H	F	> 100
9	F	H	OH	H	> 100
10	H	F	OH	H	> 100

The inhibition studies were further extended using phenol derivatives (synthesised in the laboratory of Dr. John Sorensen, Department of Chemistry, University of Manitoba, Canada) and tri-carbonyl compounds (synthesised by Dr. Cyrille Thinnes, Chemistry Research Laboratory, University of Oxford) (Table 9.5). Note that some of the tri-carbonyl inhibitors are known to act as 2OG oxygenase inhibitors (DPhil Thesis, Cyrille Thinnes,

Chemistry Research Laboratory, University of Oxford). Before conducting the inhibition studies, the interaction between these compounds and human HPPD was investigated using the 'Reporter Displacement Assay' (**Chapter 10**). Amongst the compounds tested, only phenol derivatives **24**, **27**, **29** and tri-carbonyl derivatives **31**, **32** impacted on HPPA binding to human HPPD (Figure 9.11 and 9.12). The IC_{50} values of these compounds were next determined following NMR-based assay (**Chapter 10**). The measured IC_{50} values were 877, 165, 338, 12, and 18 μM, for **24**, **27**, **29**, **31**, and **32**, respectively (Table 9.5). Notably, the tri-carbonyl inhibitors **31** and **32** showed the greatest inhibition of human HPPD.

These observations support the proposal that the 2-benzoylethen-1-ol pharmacophore is a key component of HPPD inhibitors since both the tri-carbonyl inhibitors **31** and **32** have the substructure mimicking that of the 2-benzoylethen-1-ol pharmacophore (Figure 9.13). Based on these studies, modification of either HPPA- or tri-carbonyl-derivatives could be considered as a route to develop more potent inhibitors of human HPPD (Figure 9.13).

Table 9.5. Structures and inhibition results for compounds 21-35 with human HPPD. *IC_{50}* values were determined using the NMR-based inhibition assay using 0.5 µM human HPPD, 500 µM HPPA and various concentrations of the inhibitors (**Chapter 10**). Values represent mean (n = 3) ± SD.

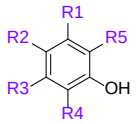

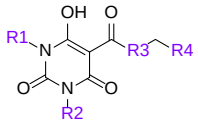

Compound	R1	R2	R3	R4	R5	Competition/IC_{50} (µM)	Compound	R1	R2	R3	R4	Competition/IC_{50} (µM)
21	H	OH	H	OH	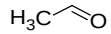	No/ND	**31**	CH_3	CH_3	H		Yes/12 ±1.3
22	CH_3	OH	H	OH	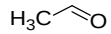	No/ND	**32**	CH_3	CH_3	H		Yes/18 ±1.3
23	H	OH	H	OH	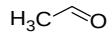	No/ND	**33**			NH	COOH	ND
24	H	OH	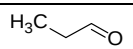	OH	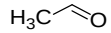	Yes/877±1.3	**34**	H	H	NH	COC_2H_5	ND
25	CH_3	OH	H	OH	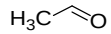	No/ND	**35**	CH_3	CH_3	NH	COC_2H_5	ND
26	H	OH	H	OH	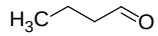	No/ND						
27	H	OH	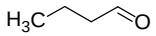	OH	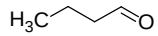	Yes/165±1.5						
28	H	OH	H	OH	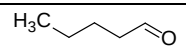	No/ND						
29	H	OH	H	OH	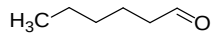	Yes/338±1.3						
30	H	OH	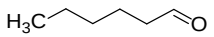	OH	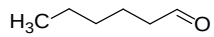	No/ND						

ND = not determined

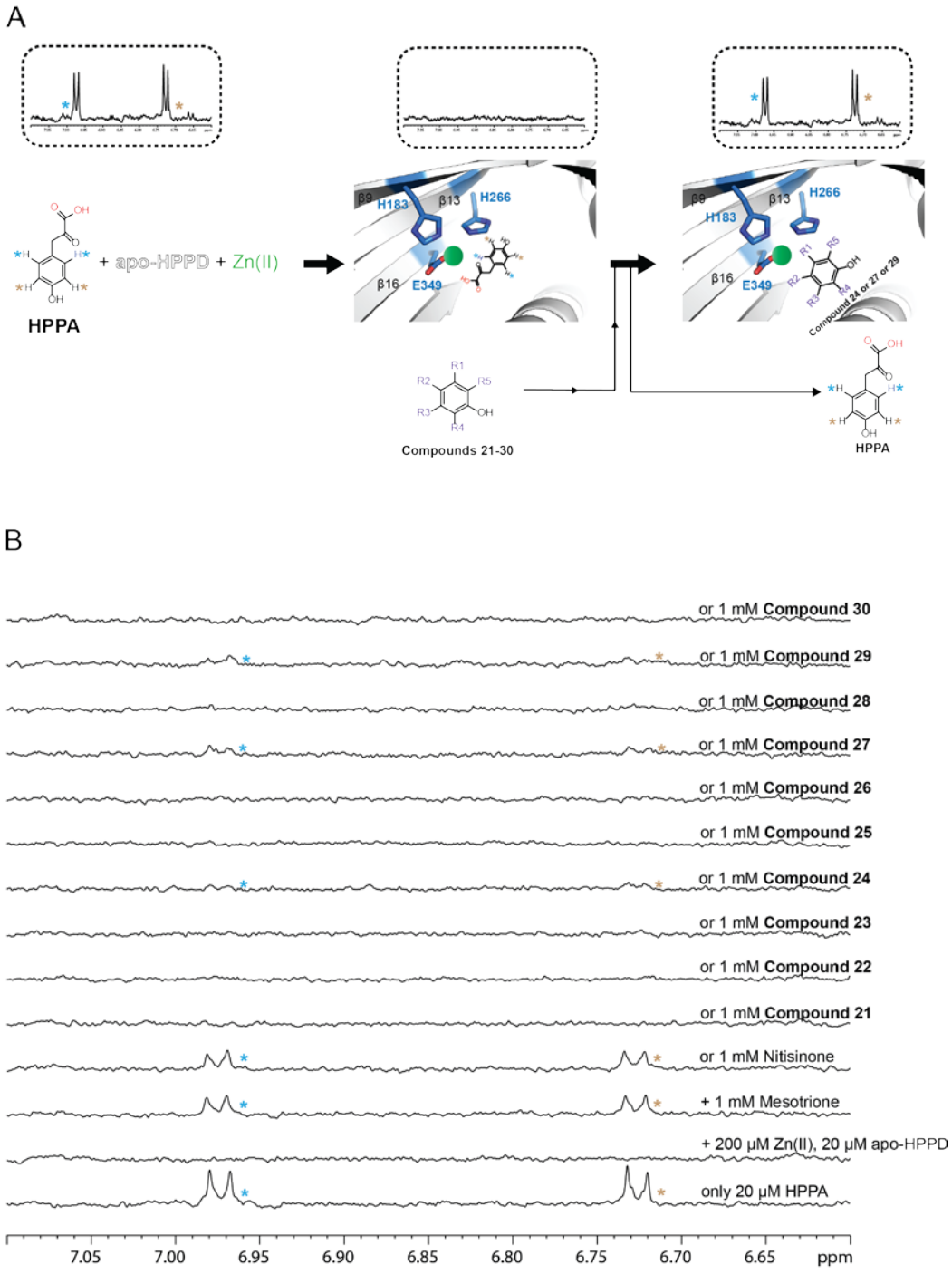

FIGURE 9.11. **HPPA displacement assays of human HPPD with phenol derivatives**. (A) Model showing the HPPA bound at the active-site of human HPPD, which was displaced by some phenol derivatives (insets show the ^{1}H NMR signals). (B) ^{1}H NMR (700 MHz) spectra showing the recovery of HPPA signals (δ_H 6.97 and 6.73 ppm) upon addition of mesotrione, nitisinone, and compounds **24**, **27**, and **29**.

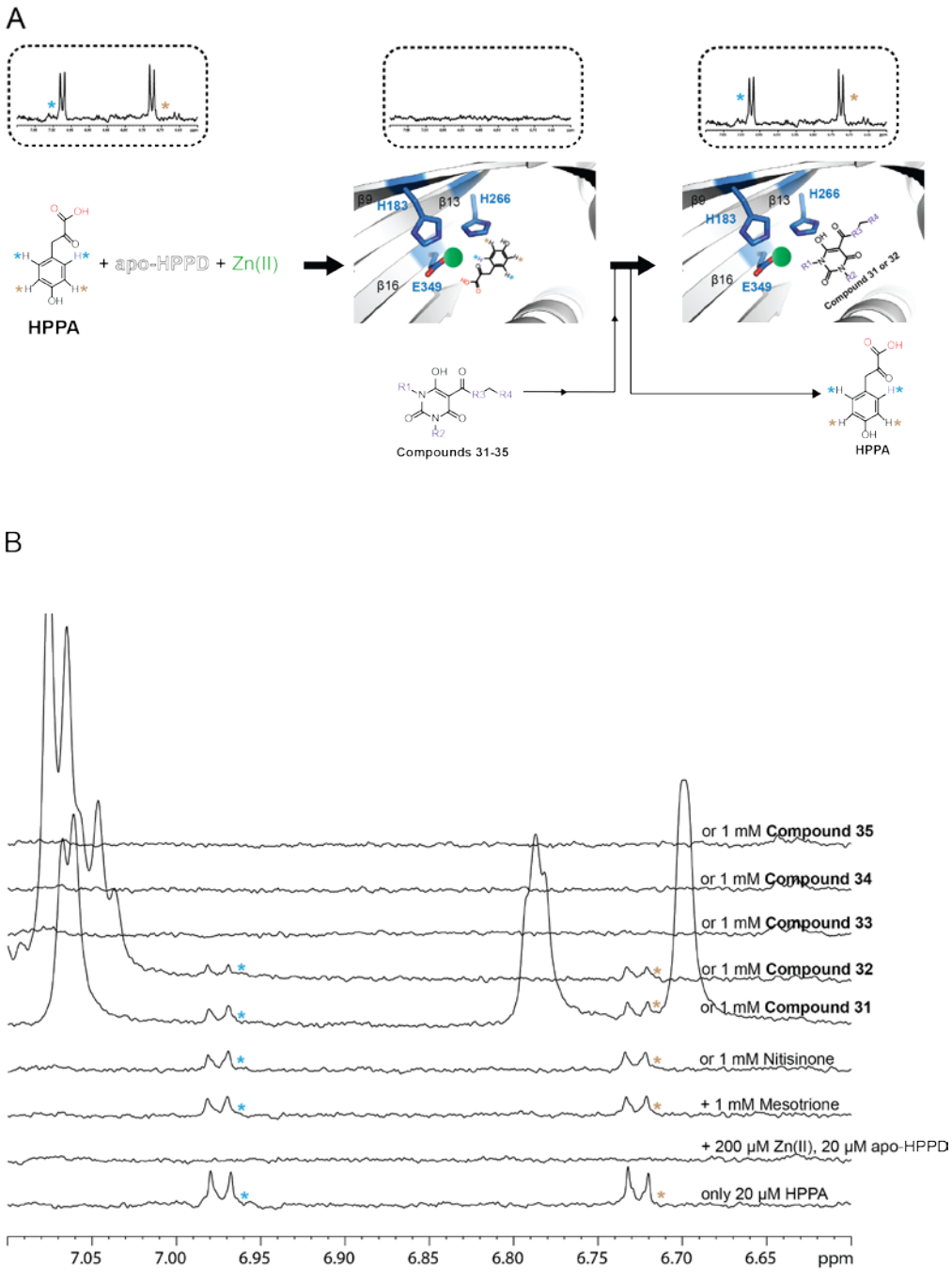

FIGURE 9.12. **HPPA displacement assays of human-HPPD with tri-carbonyl derivatives**. (A) Model showing HPPA bound at the active site of human HPPD, which was displaced upon addition of some tri-carbonyl compounds (insets show the ^{1}H NMR signals). (B) ^{1}H NMR (700 MHz) spectra showing the appearance of HPPA signals (δ_H 6.97 and 6.73 ppm) upon addition of mesotrione, nitisinone, and compounds **31** and **32**.

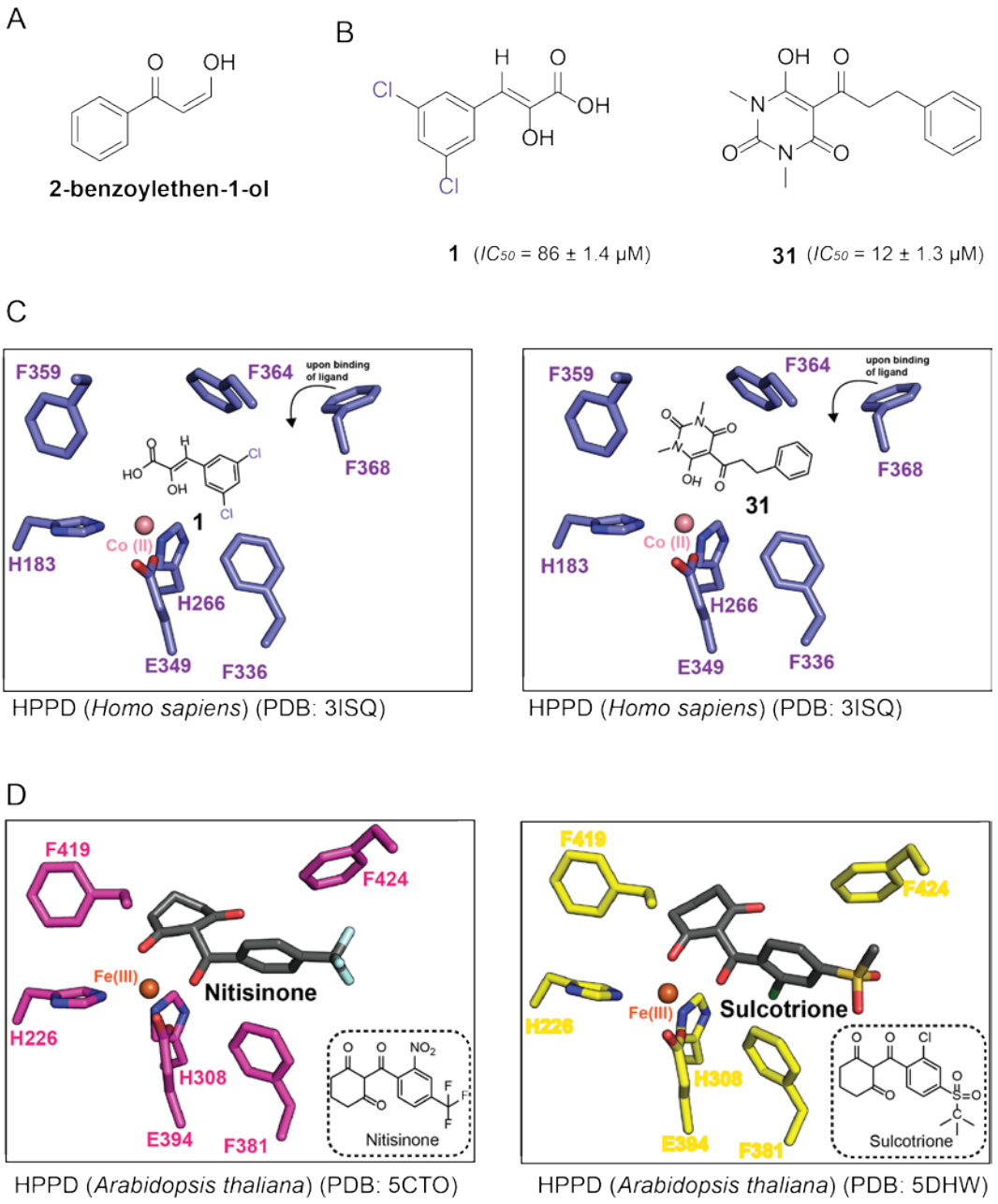

FIGURE 9.13. **Reported binding modes for HPPD inhibitors**. (A) The pharmacophore 2-benzoylethen-1-ol is present in several reported HPPD inhibitors. (B) Human HPPD inhibitions identified in this work. (C) Proposed mode of binding of **1** and **31** at the active-site of human HPPD. (D) Observed binding mode of inhibitors nitisinone (PDB: 5CTO) and sulcotrione (PDB: 5DHW) at the active-site of HPPD from *A. thaliana* (99).

9.8. Investigation of the Oligomeric State of Human HPPD

The oligomeric state of HPPD from various organisms has been described previously (130). HPPD from mammals, plants and *Streptomyces avermitilis* have been reported to be homodimers, whereas HPPD from *Pseudomonas fluorescens* is a homotetramer in solution. Variations in the interfaces between two monomers has also been observed in HPPD from various species (15,130). HPPD purified from human liver was found to be dimeric by size-exclusion chromatography (SEC) (119). In this work, the oligomeric status of human HPPD was examined by nano electrospray ionisation-mass spectrometry (nESI-MS) and SEC.

First, the oligomerisation status of human HPPD was investigated using analytical SEC. Purified human HPPD was loaded onto an analytical SEC column pre-equilibrated in the desired buffer (**Chapter 10**). The molecular mass of human HPPD was then calculated relative to the standard molecular mass markers (**Chapter 10**), which were cocurrently run on the same column. The results imply that human HPPD is dimeric in solution (Figure 9.14**A**) in agreement with the findings of Lindblad *et al*. (119).

The oligomeric staus of human HPPD was then investigated by non-denaturing mass spectrometry and for this purpose, a nESI-MS was used (Dr. Joseph Gault, Professor Dame Carol Robinson Group, Chemistry Research Laboratory, University of Oxford) (**Chapter 10**). The nESI-MS spectrum of human HPPD revealed a mass of ~90 kDa, corresponding to the dimeric form of human HPPD (Figure 9.14**B**).

A

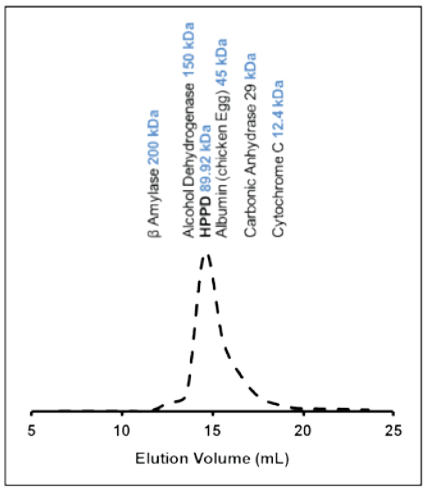

B

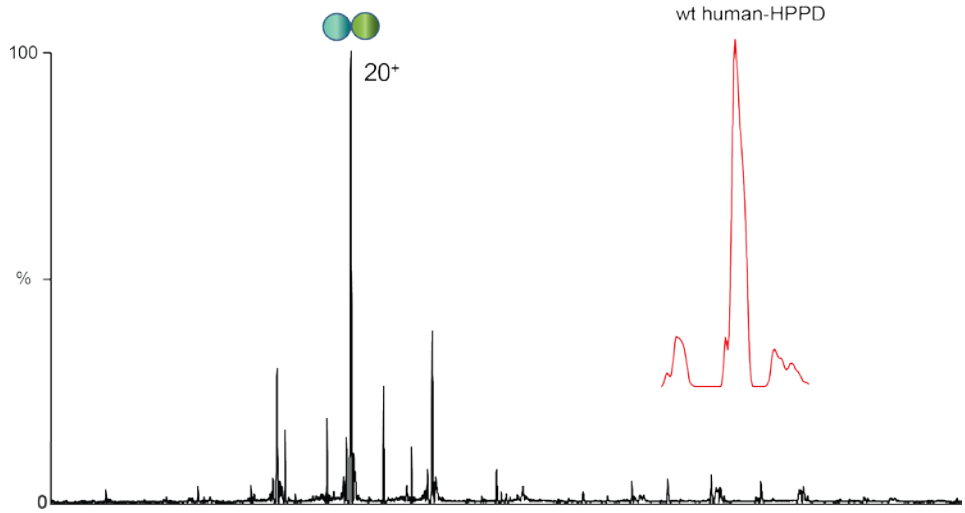

FIGURE 9.14. **Investigation of the oligomeric state of human HPPD in solution**. (A) Chromatogram of human HPPD on an analytical SEC column, showing that human HPPD elutes at a position corresponding to a dimeric form. (B) nESI-MS spectrum of wild-type full-length human HPPD showing that human HPPD is dimeric in solution.

9.9. Metal Binding Studies with Human HPPD

As discussed in Chapter 04, DSF (Differential Scanning Fluorometry) can be a useful technique for investigating the interaction of proteins with metal ions (76). A MiniOpticon PCR machine was used to investigate the binding affinities of metals with human HPPD

(**Chapter 10**). The results, using various metals [Co(II), Cu(II), Fe(II), Mn(II), Ni(II), and Zn(II)] and an apo-form of human HPPD, revealed that the apparent melting temperature (T_m) of apo-HPPD increased substantially in the presence of Ni(II) (ΔT_m = +3.2 °C), Mn(II) (ΔT_m = +1.4 °C), and Zn(II) (ΔT_m = +0.8 °C), but not in the presence of Fe(II) (ΔT_m = -0.1 °C), Co(II) (ΔT_m = -4.6 °C) and Cu(II) (ΔT_m = -6.1 °C) (Table 9.6, Figure 9.15).

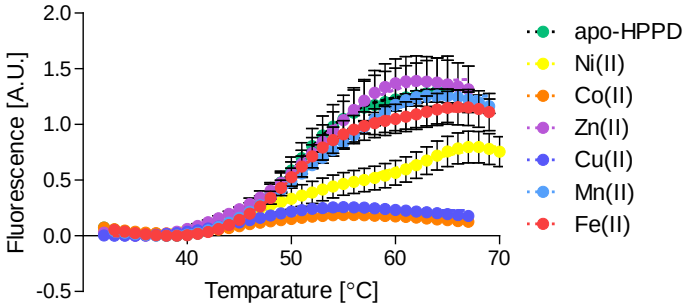

FIGURE 9.15. **DSF screening of metal binding to human HPPD**. Plots showing the melting curves of human HPPD in the absence and presence of a panel of metal ions.

Table 9.6. Metal Screening Results for human HPPD. Experiments were carried out following the procedure described in Chapter 10. Values represent mean (n = 3) ± SD.

Metal	T_m (°C)	ΔT_m (°C)
No metal (apo-HPPD)	50.6 ± 0.83	-
Ni(II)	53.8 ± 0.91	+ 3.2
Co(II)	46.0 ± 0.71	- 4.6
Zn(II)	51.4 ± 0.39	+ 0.8
Cu(II)	44.5 ± 1.03	- 6.1
Mn(II)	52.0 ± 0.32	+ 1.4
Fe(II)	50.5 ± 0.46	- 0.1

9.10. Structural Studies of Human HPPD

Twelve X-ray crystal structures of HPPD enzyme from multiple species have been reported: three from mammals including *Homo sapiens* (PDB: 3ISQ and 5EC3) (99) and *Rattus norvegicus* (PDB: 1SQI) (133), seven from plants including *Arabidopsis thaliana* (PDB: 1SP9, 1SQD, 1TFZ, 1TG5, 5CTO, and 5DHW) (99,134) and *Zea mais* (PDB: 1SP8) (134), two from bacteria including *Streptomyces avermitlis* (PDB: 1T47) (135) and *Pseudomonas fluorescens* (PDB: 1CJX) (136) (Figure 9.16). Work on human HPPD has also been carried out in Oxford, resulting in the deposition of a structure to the PDB (PDB: 3ISQ) (99); another group has deposited a crystal structure of human HPPD (PDB: 5EC3) (99) (Figure 9.16). Nevertheless, none of these structures is in complex with the substrate HPPA or with an inhibitor (99), suggesting that determining the crystal structures of human HPPD.substrate/inhibitor complexes is difficult. In this work, crystallographic studies of human HPPD were performed with an aim to determine the crystal structure of human HPPD in complex with its substrate and inhibitors.

Attempts were made to crystallize full-length human HPPD by the sitting-drop vapor diffusion method (78). HPPD (25 mg/mL) was incubated with either Mn(II) or Co(II) (at a 5:1 ratio of metal to enzyme) on ice for approximately 1 hour; crystallisation plates were laid following the procedures described in Chapter 10. Although HPPD was not apparently stabilised by Co(II) observed in the metal screening assay (section 9.9), Co(II) was used for crystallographic studies as the previously reported X-ray crystal structures of HPPD were in complex with either Fe(II), Fe(III), or Co(II) (Figure 9.16). Crystallisation attempts were performed using commercially available crystallisation screens: JCSG-plus, Pact Premier, Index, PEG Ion, Salt Rx, and Crystal Screen. Crystals of HPPD.Mn(II)/Co(II) complexes grew at 20 °C after 3-6 months, but the crystals were of poor diffraction quality. After numerous attempts, a diffractable crystal of human HPPD was obtained after six months (incubation temperature 20 °C and crystallisation condition #74 of Pact Premier), which was in complex with Mn(II) and was diffracted to 2.5 Å

resolution after subjecting to X-ray diffraction at the Diamond Light Source (DLS) synchrotron facility (data collection and molecular replacement were performed by Dr. Rasheduzzaman Chowdhury, Chemistry Research Laboratory).

The structure was solved using a previously reported crystal structure of human HPPD (PDB: 3ISQ) (99) as the reference structure. MR (molecular replacement) by PHASER (79) followed by iterative cycles of model-building using COOT and refinement using PHENIX (80) revealed the crystal structure of the human HPPD in a primitive triclinic space group (*P1*) with two monomers in the ASU (asymmetric unit) (Table 9.7, Figure 9.16). The crystal-packing of human HPPD is consistent with the observed dimeric oligomeric status of human HPPD in solution (section 9.8). Further analyses of this structure also revealed an apparent tight binding between the two monomers (chain A and chain B) (Figure 9.17). When the interfaces between two monomers were calculated by PISA (82), a calculated buried surface area of 3328 $Å^2$ was found, with a thermodynamically favourable $\Delta^i G$ value (-13.2 kcal mol^{-1}), suggesting the formation of a stable complex.

Table 9.7. Crystallographic data collection and refinement statistics.

Protein	HPPD.Mn(II)
X-Ray Source	IO2
Wavelength (Å)	0.9795
Resolution (Å)	50.00-2.50 (2.59-2.50)*
Space Group	*P1*
Unit Cell Dimensions	
a, b, c	46.4, 49.7, 77.0
α, β, λ	103.6, 102.4, 107.5
Molecules per ASU	**2**
Wilson B Factor (A^2)	58.15
Reflections	20194 (1900)*
Completeness	95.8 (88.5)*
Multiplicity	2.6 (2.2)*
I/sI	16.3 (16.22)*
R_{merge}	0.069 (0.466)*
R_{meas}(I)	0.085 (0.589)*
CC half	0.99 (0.767)*
R_{cryst}	0.1944
R_{free}	0.2256 (4.7)¥
Deviation from Idealized Geometry	
Bond Length (Å)	0.003
Bond angles (°)	0.590
Average B Factors	
All atoms	61.25
Protein	61.33
Metal	48.08
Water	53.9
Ramachandran Plot	
Favored	94.47
Allowed	5.34
Disallowed	0
Outlier	0.19

* High resolution bin.

¥ Percentage of the total reflections used for R_{free} calculations.

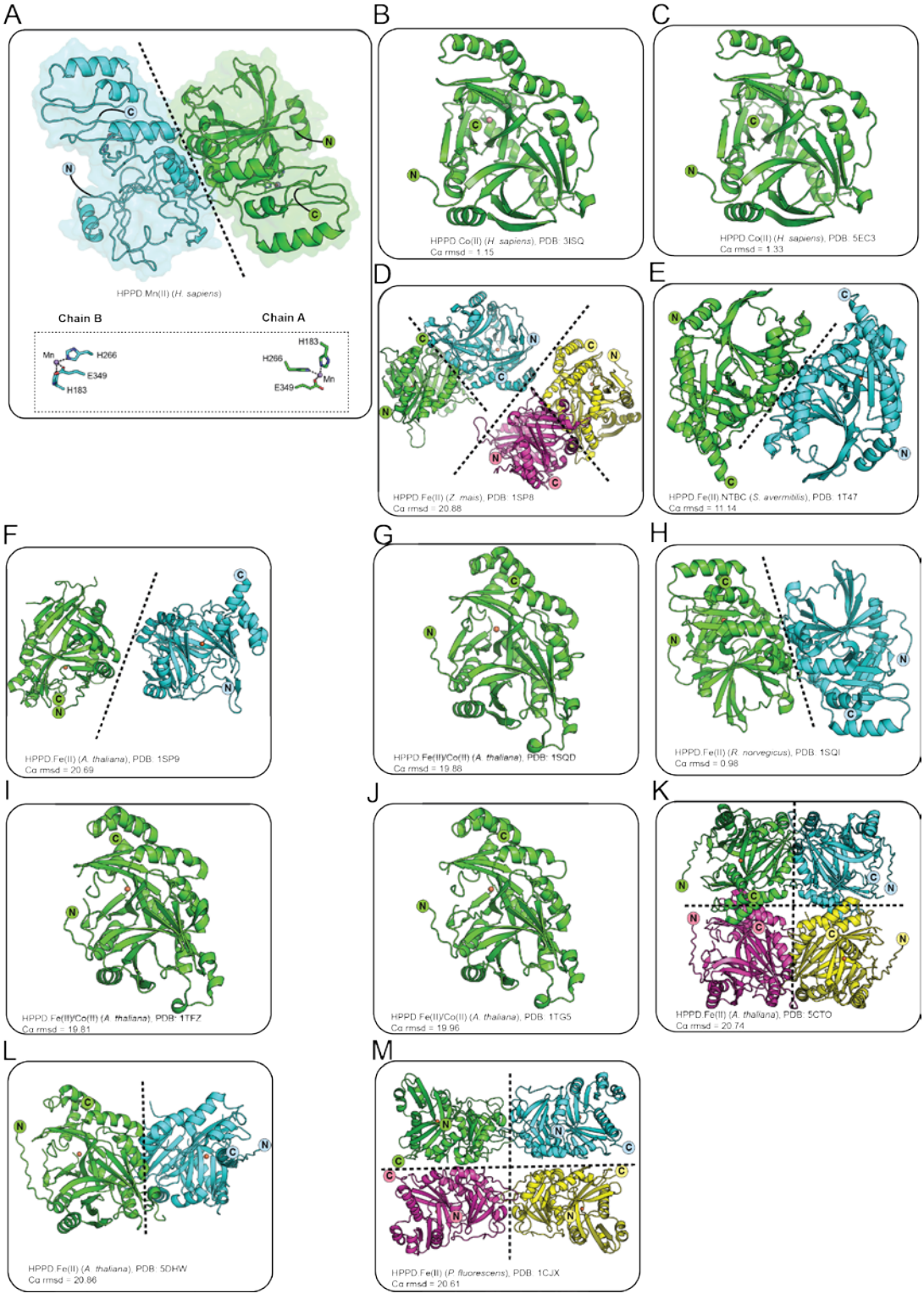

FIGURE 9.16. **Comparison of HPPD crystal packing**. (A) Cartoon view of a crystal structure of the human HPPD.Mn(II) complex determined in this work; the inset shows the metal binding residues. Cartoon views of previously reported crystal structures of HPPD from (B, C) *Homo sapiens,* (D) *Zea mais,* (E) *Streptomyces avermitilis,* (F) *Rattus*

norvegicus, (G) *Pseudomonas fluorescens*, and (H-M) *Arabidopsis thaliana*. Colour coding: green/cyan sticks, metal binding residues; chain A, green; chain B, cyan; chain C, magenta; chain D, yellow; Mn(II), Fe(II)/Co(II), purple, and orange sphere, respectively.

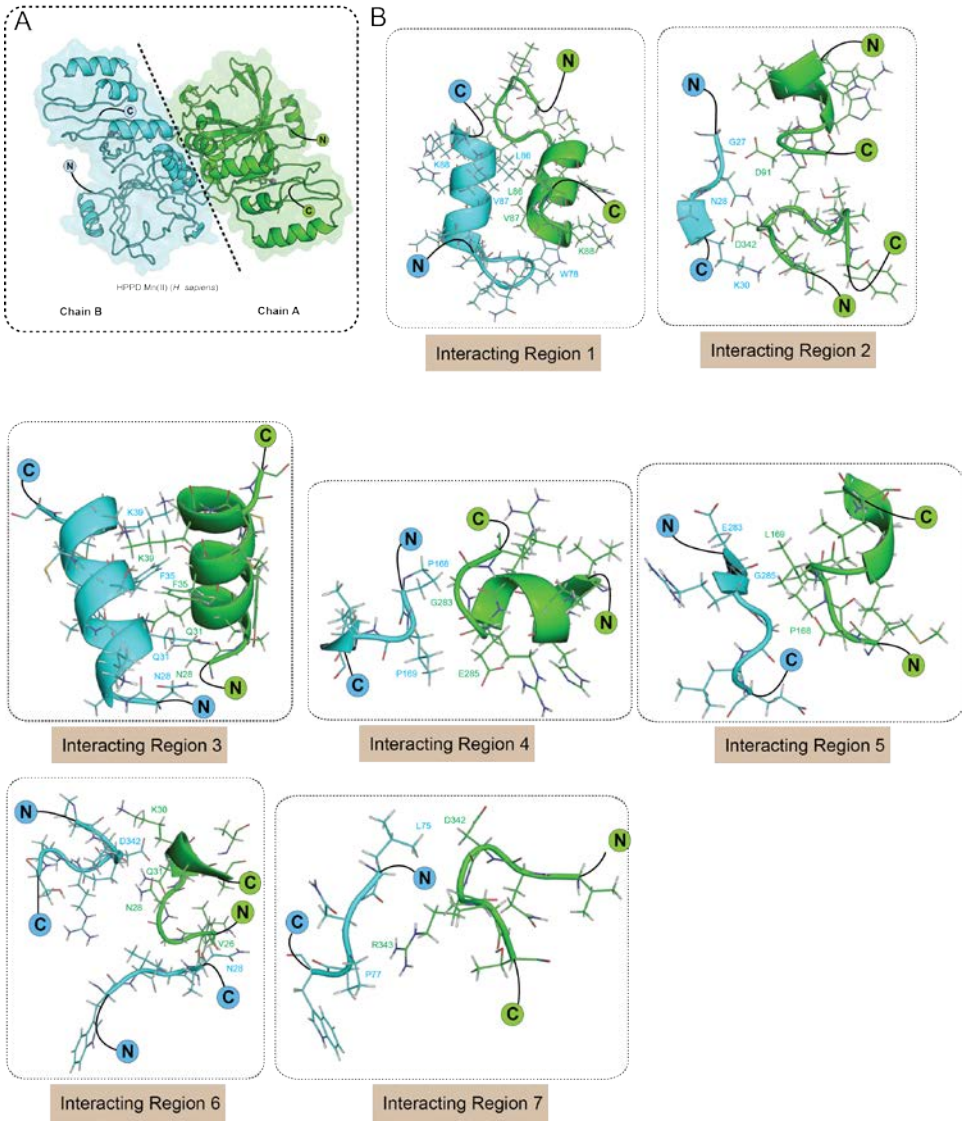

FIGURE 9.17. **Investigating the interfaces between the molecules inside the ASU of human HPPD as revealed by crystallography.** Cartoon views showing the interacting regions responsible for the formation of dimeric state of human HPPD.Mn(II) in the crystal packing.

A comparative study between the crystal structure of the HPPD.Mn(II) complex determined in this work was carried out with the HPPD.Co(II) complex (PDB: 3ISQ) reported previously (99). The analysis revealed that the HPPD.Mn(II) complex has an apparent missing region encompassing residues 188-262 (Figure 9.18). This indicates that this region is disordered, or possibly underwent fragmentation during the course of crystallisation. SDS-PAGE analysis of purified human HPPD indicated that degradation of human HPPD occurs in the course of purification (**Appendix 07**). This type of degradation of human HPPD has also been observed previously for the H183A variant (128). Fragmentation close to the catalytic site has also been observed for TfdA (2,4-dichlorophenoxyacetate/2OG dioxygenase) and ACCO (1-aminocyclopropane-1-carboxylate oxidase); in the case of TfdA and ACCO, fragmentation was reported to be stimulated by the active-site metal (137,138).

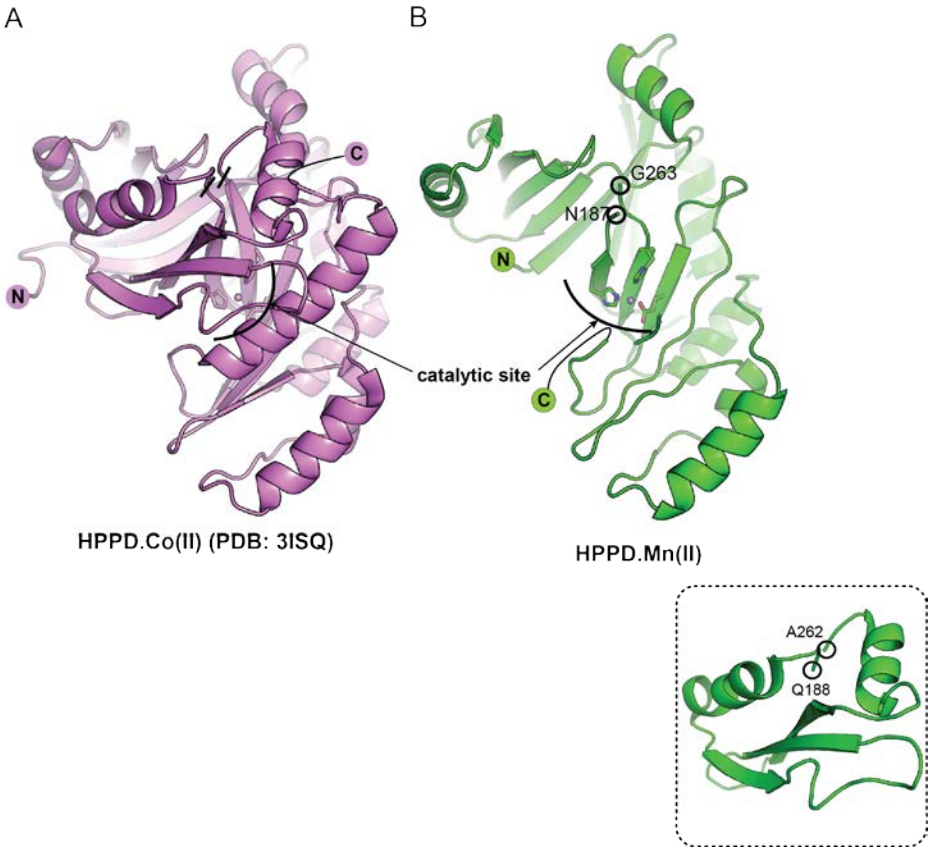

FIGURE 9.18. **Comparison between views from HPPD.Co(II) and HPPD.Mn(II) complex structures**. Cartoon views of crystal structures of HPPD in complex with (A)

Co(II) (PDB: 3ISQ) and (B) Mn(II). Note an apparent missing sequence in the HPPD.Mn(II) complex structure, comprising 76 residues (Q188-A262) (inset), which is present in the HPPD.Co(II) complex. Moreover, 16 residues from the *N*-terminus and 25 residues from the *C*-terminus were not visible in the HPPD.Mn(II) complex structure (B).

9.11. Optimisation of Purification Conditions for Human HPPD

Attempts were then made to optimise the crystallisation conditions so as to obtain crystals of human HPPD in a shorter period of time. First, the purification conditions were optimised, as the initially employed procedures (SGC, Oxford) (150) comprised several steps resulting in a longer purification time. Therefore, both the expression as well as the purification conditions of human HPPD was considered for optimisation. Based on the results obtained from small scale trials (**Appendix 08**), the gene encoding human HPPD was expressed in *E. coli*, and HPPD was purified following the optimised procedures (**Chapter 10**). The yield of HPPD was found to be substantially higher than that obtained according to the reported procedure (Figure 9.19).

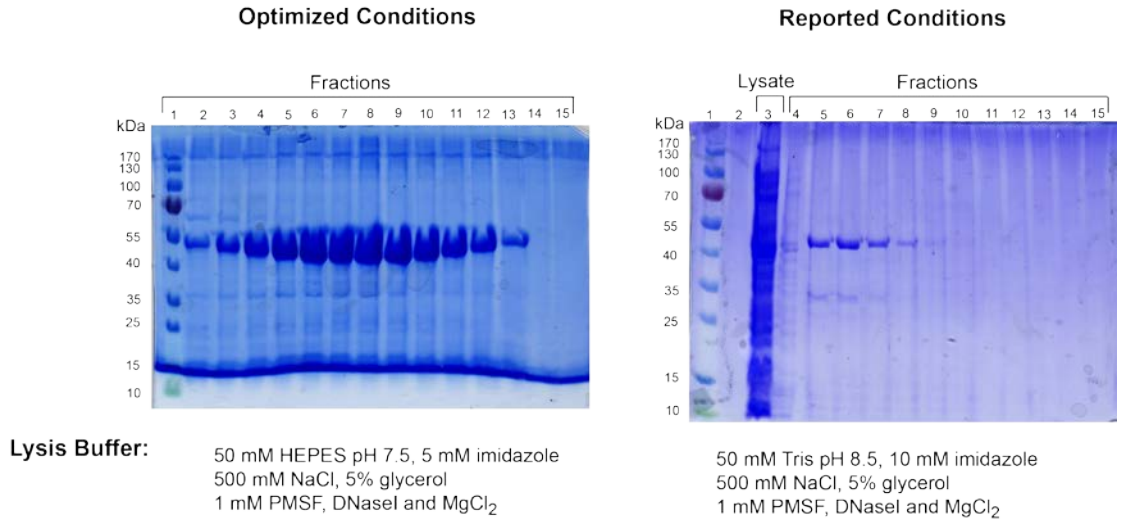

FIGURE 9.19. **Comparison of yield of human HPPD enzyme obtained from reported and optimised procedures.**

9.12. Crystallographic Studies with Human HPPD Purified following the Optimised Conditions

Crystallisation attempts were thereafter made using human HPPD purified according to the optimised procedures. From the crystallisation attempts using commercial broad screens, a suitable hit was obtained from condition #18 (0.1 M phosphate/citrate, pH 4.2, 40% (v/v) ethanol) of the JCSG-plus screen (Molecular Dimension). The crystals grew after 1-2 weeks (compared to 6 months of SGC procedure) and diffracted to a resolution of 3.1 Å at the DLS synchrotron facility. This JCSG-plus condition was therefore considered for further optimization. Eventually, crystals of human HPPD.Mn(II)/Co(II) complexes of larger size and of better diffraction quality were obtained, which diffracted to higher resolution (*i.e.*, 1.5 - 2.5 Å). Unfortunately, at the time of writing, it has not been possible to solve crystal structure of human HPPD from these data owing to problems like twinning and mosaicity (Figure 9.20).

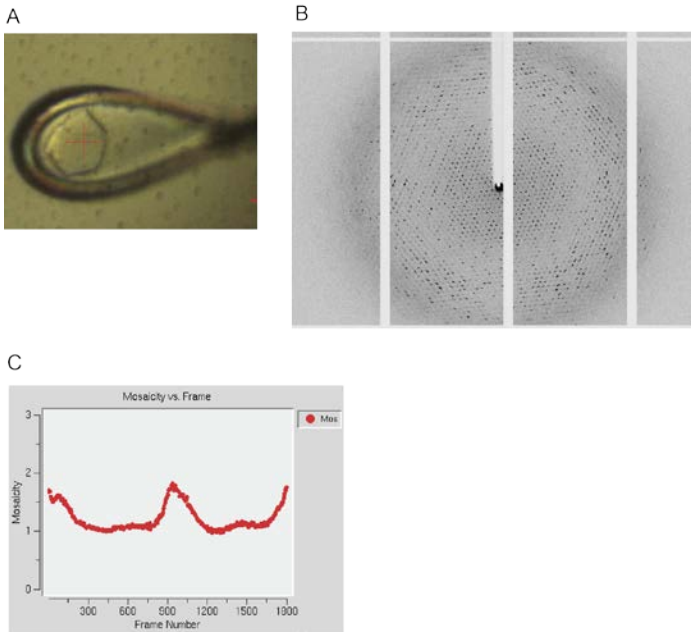

FIGURE 9.20. **X-ray data collection of crystal of human HPPD.** (A) Photograph of a crystal of human HPPD in complex with Mn(II), which diffracted to (B) 2.15 Å when subjected to X-ray diffraction at the DLS synchrotron facilities. (C) Curve showing the presence of high mosaicity in the acquired data.

CHAPTER 10: Materials and Methods

10.1. Water Purification

Two types of purified water were used: Elix Water® and MilliQ® water. Elix water® (purification grade Type 2) was produced using the Elix® High-throughput Water Purification System (Merck Millipore). MilliQ® ultrapure water (purification grade Type 1) was purified using the MilliQ® Integral Water Purification System (Merck Millipore).

10.2. Weighing

Weighing of compounds was performed using a Sartorius Basic Balance (Sartorius, Germany), or a Sartorius Analytical Balance (Sartorius, Germany).

10.3. Stirring/ Vortexing

Mixing was performed using the vortex mixer Genie 2 Vortex Mixer (Scientific Laboratory Supplies, UK).

10.4. Water Bath

A Grant W14 water bath was used for incubation at 42 °C and a Grant Y14 water bath was used for incubation at 37 °C.

10.5. pH Measurement

pH measurements were performed using a Hanna Instruments HI 9321 microprocessor pH meter fitted with a 5 mm diameter electrode. Before use, the probe was calibrated in either the range pH 4-7 or pH 7-10 as appropriate using standard calibration solutions (Fisher Scientific). The probe is usually stored in 4 M KCl solution between uses. The pH of solutions was adjusted with stock solutions of HCl or NaOH or NH_4OH as appropriate.

10.6. UV-VIS Spectroscopic Observation

To measure the optical density at 600 nm (OD_{600}) of the cell culture, a UV spectrometer (Innova® 44) was used. 1.0 mL size cuvette (Fisherbrand) was used; only the medium was used as a blank.

10.7. Centrifugation

Samples of small volume (≤ 1.5 mL) were centrifuged using a bench-top centrifuge either at 4 °C (Microfuge® 22R Microcentrifuge, Beckman Coulter) or at room temperature (Micro AccuSpin™, Fisher Scientific). Samples of medium volume (≤ 50 mL) were centrifuged using either the benchtop or a heavy-duty centrifuge as appropriate. For the purposes of protein concentration, peptide cleavage, cell pellets, a benchtop centrifuge was used (Allegra X-30R Centrifuge, Beckman Coulter), either at 4 °C or at room temperature. In case of lysates of proteins (≤ 40 mL) requiring rotation speed of 22,000 rpm and large-scale cell cultures (≥50 mL) requiring rotation speed of 8,000 rpm, a heavy duty Avanti centrifuge (Avanti J-26S XP, Beckman Coulter) was used.

10.8. Plasmid Constructs

DNA encoding for full-length and truncated versions of *N*-terminally His_6-Tagged JMJD6 protein (*Homo sapiens*) was inserted into the pET28a(+) expression vector by Dr. Celia J. Webby (Chemistry Research Laboratory, University of Oxford). DNA encoding for full-length and truncated versions of *N*-terminally His_6-Tagged JMJD5 protein (*Homo sapiens*) was inserted into the pNIC28-Bsa4 expression vector by Dr. Sarah Wilkins (Chemistry Research Laboratory, University of Oxford). DNA encoding for full-length *C*-terminally His_6-Tagged HPPD protein (*Homo sapiens*) was in the expression vector pNIC-CH and was obtained from the laboratory of Professor Udo Oppermann, Old Road Campus Research Building, University of Oxford.

10.9. Preparation of Oligonucleotides

Oligonucleotide primers were purchased from Sigma Life Science in the form of lyophilized pellets (0.025 µmol scale) and were resuspended in sterile MilliQ water following the manufacturers' protocol to give a concentration of 100 µM. Before making the stock solution, the tubes containing the pellets were centrifuged using a bench-top centrifuge (Micro AccuSpin™, Fisher Scientific) to avoid loss.

10.10. Site-directed Mutagenesis (SDM)

Table 10.1. List of components of the PCR mixtures used for SDM.

Reagent	Amount
ds DNA template	25-40 ng
Primer: 5' to 3' (10 µM stock)	1.25 µL
Primer: 3' to 5' (10 µM stock)	1.25 µL
Q5 Reaction buffer	5.0 µL
Q5 GC Enhancer	5.0 µL
dNTP Mix (10 mM stock)	1.0 µL
Q5 DNA Polymerase	0.5 µL
Sterile MilliQ Water	Up to 25 µL

Table 10.2. Thermal cycles used to carry out the SDM.

Step	Temperature (°C)	Duration
01	94	2 minutes
02	94	45 seconds
03	62	1 minute
04	72	20 minutes
05	72	20 minutes
05	4	Hold

*A total of 19 cycles were used for steps 02-04.

SDM was carried out following the procedure of QuickChange™ site-directed mutagenesis kit from Stratagene. Primers containing the desired mutation were used to amplify the full vector and insert sequence. Thermal cycles were carried out using a Techne Genius PCR (polymerase chain reaction) machine.

10.11. DpnI Digestion (139)

Since DpnI works on methylated/hemimethylated DNAs, the plasmid DNA templates were isolated from a dam$^+$ *E. coli* strain so that the parent DNA could be digested (139). In order to carry out the digestion process, reaction products obtained from the PCR machine were treated with the restriction enzyme DpnI to get rid of from the parental DNA (non-mutated). 0.5-1 µL DpnI enzyme was added to each PCR product, and then incubated at 37 °C for 2-3 hours.

10.12. Agarose Gel Electrophoresis

Table 10.3. TAE running buffer (x 50) (for 1 L).

Reagent	Amount
Tris HCl	242 gm
EDTA	14.6 gm
Glacial Acetic Acid	57.1 mL

Table 10.4. DNA sample loading buffer (x 5).

Reagent	Amount/volume
Glycerol	30% (v/v)
Xylene Cyanol FF	0.25% (v/v)
Bromophenol Blue	0.25% (w/v)
TAE Buffer	2% (v/v)

0.8-1% agarose gels were used to visualize DNA. Briefly, the appropriate amount of agarose (Bioline) was dissolved in an appropriate amount of TAE buffer (Table 10.3) by

heating (SuperWave 750 Microwave, Tecnolec). After cooling to ~60 °C, 4 µL SYBR Safe™ DNA gel stain was added. Gels were cast in an H2-SET gel tray (Anachem) to a depth of 0.7 cm with a comb inserted at one end of the gel to enable sample loading and allowed to cool at room temperature for the gel to set. Gels were run on a Bio-Rad system at a constant potential of 100 V for approximately 1 hour. Samples were run against a 2-log DNA Ladder 0.1-10 kb (Invitrogen) allowing molecular weight determination. Bands were visualized by UV light illumination using a Gel Imaging System (Bio-Rad).

10.13. Preparation of Competent Cells

Competent cells from commercial source were streaked on to an agar plate containing the appropriate antibiotic. Colonies were observed after overnight growth at 37 °C. One colony was picked with a loop and released into 15 mL of LB medium (with antibiotic where applies) and colonies were grown at 37 °C overnight with shaking at 200 rpm. 6 mL of overnight culture was added to 300 mL of LB medium and was grown to optical density (OD_{600}) of 0.45. Cell suspensions were then decanted into 6x50 mL tubes and cooled on ice for 15 minutes with occasional swirling of the tubes. Tubes were then centrifuged at 2500 rpm for 15 minutes in a bench-top centrifuge (Allegra X-30R Centrifuge, Beckman Coulter). Supernatants were removed completely using a pipette; the cell-pellets were resuspended in 15 mL ice-cold 100 mM $MgCl_2$ with gentle vortexing. The contained cell suspensions were placed into two tubes and were again centrifuged as before. Supernatant was removed using a pipette; the cell-pellets were then resuspended in 20 mL ice-cold 100 mM $CaCl_2$ with gentle vortexing. The tubes were then incubated on ice for 20 minutes and were centrifuged as before. The supernatants were removed completely and the cell-pellets were resuspended in 100 mM $CaCl_2$ solution containing 15% glycerol and combined into one tube. 100 µL aliquots of competent cells were then transferred in microcentrifuge tubes, snap-freezed in liquid nitrogen and freezed at -80°C until further use.

10.14. Transformation

The appropriate plasmid construct or the PCR product (mutation), was transformed into the desired competent cells (XL10 gold for sequencing or strains BL21(DE3), Rosetta2(DE3), Rosetta2(DE3)pLysS for expression). Plasmid equivalent to 40-50 ng was mixed with an aliquot of competent cells (45-50µL); the mixture was chilled on ice for ~30 minutes. Then a heat-shock at 42 °C for 30 seconds was given to the competent cells to take up the plasmid DNA. The cells were again chilled on ice for 2-5 minutes, then were incubated with an addition of 200 µL of LB media for 1 hour at 37 °C. This mixture was plated on LB-agar plate with appropriate antibiotic(s). The plate was then left in an incubator at 37 °C for overnight growth of the bacterial colony.

10.15. Plasmid Purification

Under sterile conditions, a single colony from the agar plate was picked up using a loop and then inoculated into 15 mL LB medium supplemented with appropriate antibiotic(s). The bacterial cells were then allowed to grow overnight in a thermal shaker at 37 °C with a shaking at 200 rpm. Next morning, the bacterial cell pellets were recovered by centrifugation and plasmid DNA was purified by using Qiagen Miniprep Kit.

10.16. DNA Concentration Determination

DNA concentration was determined by measuring the absorbance at 260 nm (A_{260}) in a Nanodrop ND-100 spectrophotometer (NanoDrop Technologies, USA). The concentration of the DNA is calculated based on the following equation:

$$A_{260}/\varepsilon_0 = [\text{DNA}]\ (\text{mM}) \ldots\ldots\ldots\

Base	Contribution to ε_0
T	8.8 $mM^{-1}.cm^{-1}$
C	7.3 $mM^{-1}.cm^{-1}$
G	11.7 $mM^{-1}.cm^{-1}$
A	15.4 $mM^{-1}.cm^{-1}$

10.17. DNA Sequence Verification

DNA sequences were assigned by Sanger Sequencing Service, Department of Biochemistry, University of Oxford.

10.18. Recombinant Enzyme Expression in *Escherichia coli*

Table 10.5. List of vectors.

Vector	Antibiotic	Tag	Tag Cleavage Site	Promoter	Protein
pET28a(+)	Kanamycin	*N*-terminal His_6-Tag	Thrombin	T7	JMJD6
pNIC28-Bsa4	Kanamycin	*N*-terminal His_6-Tag	TEV	T7	JMJD5
pNIC-CH	Kanamycin	*C*-terminal His_6-Tag	TEV	T7	HPPD

Table 10.6. 2TY media (for 1 L) [Media were prepared by Mr. H. M. Jubier].

Reagent	Amount
Bacto-tryptone	16 gm
Yeast extract	10 gm
NaCl	5 gm

To prepare solid medium for agar plate, 20 gm agar was added to the liquid before autoclaving.

Table 10.7. Terrific-broth (TB) media (for 1 L).

Reagent	Amount
Bacto-tryptone	12 gm
Yeast extract	24 g
Glycerol	4 mL

Solids were dissolved in 900 mL water. After autoclaving, 100 mL filter-sterilized 0.17 M KH_2PO_4, and 0.72 M K_2HPO_4 solutions were added.

10.18.1. Starter Culture

100 mL LB media supplemented with appropriate antibiotic was inoculated with a single colony from an agar plate or scraping from a glycerol stock. The bacterial cells were then allowed to grow at 37 °C for overnight with a shaking at 200 rpm in a New Brunswick Scientific G25 environmental shaker.

10.18.2. Glycerol Stocks

Sample (0.5 mL) from the starter culture was mixed in a sterile Eppendorf with sterile glycerol (0.5 mL) and flash frozen in liquid nitrogen before storage at -80 °C.

10.18.3. Expression Trials

1 mL of 'overnight' starter culture was added to 100 mL growth media in 500 mL flask supplemented with appropriate antibiotic(s). The bacterial growth started by incubating the flasks at 37 °C with shaking in a New Brunswick Series 25 shaker. Cells were induced with 0.2-1 mM IPTG (isopropyl β-D-1-thiogalactopyranoside) and allowed for further growth using various conditions (at 37 °C for next 4 hours or at 16/18 °C for next 16-18 hours). 1.5 mL of each culture was transferred to a 1.5 mL Eppendorf tube and pelleted. The supernatant was removed from the cell pellets and pellets were resuspended in the HisTrap column binding buffer. 25 µL from cell extract was separated as whole and the remainder was lysed by sonication (10 x 5s with 10s interval) on ice. Cell debris was

removed by centrifugation and the supernatant removed for analysis as cell lysates. Soluble expression levels were assessed by SDS-PAGE gel electrophoresis using 15 µL samples of the whole cell extract and cell lysates.

10.18.4. Large-Scale Production

Large-scale incubations were carried out in 600-1000 mL media (either 2TY or TB). 6-10 mL of overnight starter culture was added to the growth media supplemented with appropriate antibiotic(s). *E. coli* cells were allowed to grow at 37 °C with shaking at 200 rpm in an incubator shaker (Innova® 44). The cells were induced with 0.1-0.5 mM IPTG at the OD_{600} 1.0-2.0. Growth continued for 14-16 hours at 16/18 °C. Cells were then pelleted by centrifugation and stored in a resealabale plastic bag at -80 °C.

10.18.5. Recombinant Enzyme Purification

Table 10.8. Recipe of the buffer solution for IMAC* used to purify JMJD6.

Reagent	Charge	Binding	Wash	Elution	Strip
Tris/HEPES /Phosphate pH 7.5	-	50 mM	50 mM	50 mM	
NaCl	-	200-300 mM	200-300 mM	200-300 mM	
Imidazole	-	10 mM	50-500 mM	500 mM	-
$NiSO_4$	400 mM	-	-	-	
EDTA	-	-	-	-	100 mM
Glycerol	-	10%	10%	5%	-

* IMAC = immobilized metal ion affinity chromatography

Table 10.9. Recipe of the buffer solution for IMAC used to purify JMJD5.

Reagent	Charge	Binding	Wash	Elution	Strip
HEPES pH 7.5		50 mM	50 mM	50 mM	
NaCl	-	200 mM	200 mM	200 mM	
Imidazole	-	10 mM	50-500 mM	500 mM	-
$NiSO_4$	100 mM	-	-	-	
EDTA	-	-	-	-	100 mM
Glycerol	-	5%	5%	5%	-

Table 10.10. Recipe of the buffer solution for IMAC used to purify HPPD.

Reagent	Charge	Binding	Wash	Elution	Strip
HEPES/ Tris pH 7.5		50 mM	50 mM	50 mM	
NaCl	-	200-500 mM	200-500 mM	200-500 mM	
Imidazole	-	10 mM	50 mM	500 mM	-
$NiSO_4$	100 mM	-	-	-	
EDTA	-	-	-	-	100 mM
Glycerol	-	5%	5%	5%	-

Table 10.11. Recipe of the buffer solution for SEC*.

Reagent	JMJD6	JMJD5	HPPD
Tris/HEPES	50	50 mM	50 mM
NaCl	200-300 mM	200 mM	200-500 mM
Glycerol	5%	5%	5%

***** SEC = size exclusion chromatography

Table 10.12. Recipe of the buffer solution for ion exchange chromatography used to purify HPPD.

Reagent	Binding	Wash	Elution	Strip
Tri pH 7.5	50 mM	50 mM	50 mM	
NaCl	100 mM	100 mM	1000 mM	
EDTA	-	-	-	100 mM
Glycerol	5%	5%	5%	-

10.18.6. Purification

Cell pellets were suspended in binding buffer containing 10 µg/mL DNaseI, $MgCl_2$ and protease inhibitor tablet (Roche) and lysed on ice by sonication (6 min of 9s on, 9s off) using a Vibra Cell VCX 500 with a 13 mm probe. Cell debris was separated by

centrifugation and supernatants filtered through 0.45 µm filter (Minisart® Syringe Filter, Sartorius).

10.18.7. His_6-tagged Protein Purification

Cell lysates were loaded on either a 5 mL nickel affinity HisTrap (Novagen) or a 10 mL Ni-TED column. Buffers were run at 1-2.5 mL/min. Resin was prepared (in the case of HisTrap column) by washing with 5 column volume (CV) MilliQ water, then 3 CV charge buffer, then 5 CV MilliQ water, then 10 CV binding buffer before the cell lysate was applied on to the column. In the case of Ni-TED (tris-carboxymethyl ethylene diamine) column, the column was equilibrated in binding buffer before the lysates were loaded. However, the column was washed with 10 CV wash buffer before protein elution in 5 mL fractions with elution buffer using gradient elution (100% elution buffer in 20 minutes). Positive fractions were identified by analyzing the samples by UV spectroscopy and by SDS-PAGE gel electrophoresis, then concentrated down to 2-10 mL for further purification.

10.18.8. Cleavage of His_6-Tag

Proteins with a thrombin cleavable His_6-Tag were treated by restriction grade thrombin (Merck Millipore) by mixing at a ratio of 1:10 (w/w) and incubated at 4 °C for overnight. In the case of TEV (tobacco itch virus)-cleavable His_6-Tag, purified TEV (12 mg/mL) was added to the protein eluted from Ni-affinity chromatography at a ratio of 1:20 (w/w) and incubated at 4 °C for overnight. To isolate the tag-cleaved protein, protein solution was diluted into binding buffer without any imidazole and thereafter reapplied to a pre-charged HisTrap column. Cleaved proteins were collected from flow-through and were purified further.

10.18.9. Size-exclusion Chromatography

Protein samples were purified by size-exclusion chromatography (SEC) either by using Superdex® 200 26/60 or Superdex® 75 26/60 resins (Amershem Bioscience) connected to

Äkta purifier (GE Healthcare Life Sciences). 2-10 mL of protein was loaded on to the column using appropriate loop (2.5, 5, or 10 mL). Before loading the sample, the column was equilibrated with 2 CV of MilliQ water and 1 CV of gel filtration buffer. Fractions were collected in 5 mL tubes based on the UV trace. Positive fractions, after being examined by SDS-PAGE gel electrophoresis, were pooled together and concentrated down to 12-25 mg/mL using 30-50 kDa MWCO filter (Amicon), snap-freezed on liquid nitrogen and freezed at -80 °C.

In case of HPPD, proteins eluted from SEC were further treated for buffer-exchange into a storage buffer, which is 10 mM HEPES pH 7.5, 100 mM NaCl.

10.18.10. Ion Exchange Chromatography

Protein eluted from either HisTrap or SEC column was diluted into ion exchange buffer and loaded onto either Mono Q or S Sepharose column. After washing the column with 10 CV washing buffer, protein was eluted in elution buffer by a gradient elution of up to 1000 mM NaCl over 10 CV. Pure protein was concentrated and frozen in aliquots at -80 °C for further use.

10.18.11. Making the Apo-form of Proteins

To make the apo-form, proteins eluted from the HisTrap column were diluted with the appropriate buffer up to 0.5 mg/mL and were treated by 200 mM EDTA (ethylenediaminetetraacetic acid) for overnight at 4 °C. EDTA-treated protein samples were loaded onto SEC column to get rid of the EDTA.

10.18.12. Protein Concentration Determination

Protein concentrations were determined using 1.5 µL protein solution on a NanoDrop ND-1000 UV/Vis Spectrophotometer to measure the absorbance at 280 nm. Ɛ was calculated using the ProtParam tool on the ExPasy Proteomics Server and concentration calculated using the following equation:

$$A = \varepsilon.c.l \quad \text{… … … …

Table 10.16. Recipe for staining and destaining buffer for SDS-PAGE.

Reagents	Staining Buffer	Destaining Buffer
Comassie Brilliant Blue	0.5%	-
Methanol	50%	10%
Glacial Acetic Acid	10%	10%
MilliQ	39.5%	80%

Sodium dodecyl sulphate-polyacrylamide gel electrophoresis (SDS-PAGE) analysis of expression levels as well as protein samples was performed. SDS is an anionic detergent which binds in a non-sequence specific manner to denatured proteins in the presence of a reducing agent β-mercaptoethanol (140). The resultant SDS-polypeptides are separated on polyacrylamide gel according to their molecular weights. The molecular weights of the protein samples can therefore be approximated when compared with standard protein ladders. Briefly, bi-layered gels are run in a reservoir containing running buffer of a different pH and ionic strength so that the negatively charged SDS-polypeptide migrates through a porous stacking gel, followed by a resolving gel with higher acrylamide content to separate the samples (140). The polyacrylamide gels were made using the Bio-Rad Mini Protean II system. 15 µL of protein sample was mixed with 5 µL of loading buffer and heated at 110 °C for 10 minutes. Samples were then loaded on gels casted previously. Gels were run in the running buffer on a Bio-Rad Mini Protean II system at a constant potential of 160 V for 50 minutes. In each run, 5-10 µL of prestained protein ladder (PageRuler, Thermo Fisher) was used. The gel was then stained by the staining buffer for about 30 minutes followed by destaining.

10.20. Denaturing Mass Spectrometry

Denaturing mass spectrometry of protein samples (0.05-0.1 mg/mL) was performed using a Fisons Platform Quadrupole mass spectrometer equipped with an electrospray ionisation-mass spectrometry (ESI-MS) source fitted to an Agilent autosampler inlet. The

sample was quenched in a mixture of 50% acetonitrile/0.1% formic acid in water with a cone voltage of 30 V.

10.21. Non-denaturing Mass Spectrometry (68)

Prior to MS analysis, samples were buffer exchanged into 200 mM ammonium acetate, pH 8.0 using Micro Bio-Spin 6 columns (BioRad, Digilab Division, Cambridge, USA) (68). For all experiments, protein concentrations ranging from 1.5-2.0 mg/mL were considered. nESI-MS (nano-electrospray ionization-mass spectrometry) spectra were obtained according to a previously published protocol on an orthogonal time-of-flight mass spectrometer with a Z-spray source (LCT, Waters, Manchester, UK) in positive ion mode using the following parameters: capillary voltage, 1500 V; sample cone voltage, 120 V (unless otherwise specified); extraction cone voltage, 1 V; and ion transfer stage pressure, 8.8 mbar. Spectra were calibrated externally using a 33 mg/mL solution of cesium iodide. Data were acquired and processed with MassLynx^{TM} software (Waters, Manchester, UK), and are shown with minimal smoothing and without background subtraction. The relative abundances of the different oligomeric states were estimated from the intensities of the most abundant charge states for each construct and are expressed as a percentage of the total intensity.

10.22. MALDI-TOF MS

Table 10.17. MALDI matrix CHCA solution.

Reagent	Amount (0.5 mL)
CHCA (ALDRICH)	5 µg
Acetonitrile	350 µL
Trifluoroacetic acid	0.5 µL
MilliQ water	150 µL

Mass analysis of peptides was carried out using a MALDI (matrix-assisted laser desorption/ionization) micro Mx™ mass spectrometer (Waters Corporation) (61). A 96-

well MALDI plate (Waters Corporation) was used to carry the samples. Samples were analysed in the MALDI-MS using the positive reflectron mode. Instrument parameters were as follows: LASER energy 180-220, Pulse 2800, Detector 2000, and Suppression 800. Spectra were deconvoluted using MassLynx™ v4.0.

10.23. LC-MS/MS (141)

Peptides were analyzed on a NanoAcquity-UPLC system (Waters) connected to an Orbitrap Elite mass spectrometer (Thermo Fischer Scientific) possessing an EASY-Spray nano-electrospray ion source (Thermo Fischer Scientific). The peptides were trapped on an in-house packed guard column (75 µm i.d. x 20 mm, Acclaim PepMap C18, 3µm, 100 Å) using solvent A (0.1% Formic Acid in water) at a pressure of 140 bar. The peptides were separated on an EASY-spray Acclaim PepMap® analytical column (75 µm i.d. × 15 mm, RSLC C18, 3 µm, 100 Å) using a linear gradient (length: 100 minutes, 3 % to 60 % solvent B (0.1% formic acid in acetonitrile), flow rate: 300 nL/min). The separated peptides were electrosprayed directly into the mass spectrometer operating in a data-dependent mode using a CID/ETD (collision induced dissociation/electron transfer dissociation) based method. Full scan MS spectra (scan range 150-2000 m/z, resolution 30000, AGC target 1e6, maximum injection time 250 ms) and subsequent CID MS/MS spectra (AGC target 3e4, maximum injection time 500 ms) of 10 most intense peaks were acquired in the Orbitrap. CID fragmentation was performed at 35% of normalized collision energy and the signal intensity threshold was kept at 500 counts. ETD spectra (AGC cation target 5e4, AGC anion target 2e5, cation maximum injection time 100 ms) were acquired in the Iontrap.

10.23.1. Data analysis (141)

PEAKS 8.0 software was used to analyse the raw data. The raw MS file was searched against the respective protein sequence. NONE was selected as the protease. Demethylation and hydroxylation were set as variable modifications. Precursor mass

tolerance was set as 15 ppm. Fragment mass tolerance for CID and ETD were set to 0.8 Da. All spectra were manually validated.

10.24. Quantitative Size-exclusion Chromatography (65,66)

Quantitative SEC was performed using a 30 mL Superdex® 200 10/300 GL size-exclusion column (GE Healthcare Life Sciences) following a modified procedure of the SIGMA-ALDRICH protocol and previous literatures (65,66). For each sample, 30 µM of JMJD6 was injected in 300 µL and the column was washed with 2 CV of the gel-filtration buffer in between the loading of each sample. As standards, Cytochrome C, Carbonic Anhydrase (bovine erythrocytes), Bovine Serum Albumin (BSA), Alcohol Dehydrogenase (yeast), β-Amylase (sweet potato) and Blue Dextran were injected onto the column.

10.25. Circular Dichroism Spectroscopy (53,142)

Circular dichroism (CD) spectra were collected using a Jasco J-815 spectrometer (Jasco). Protein solutions were buffered with 10 mM phosphate buffer, pH 8.0. Optical density of the buffers really matters in case of CD experiment and 10 mM phosphate buffer is reported to have the least optical density and is an ideal buffer for CD experiment as well . Spectra were acquired using a quartz cuvette with a 0.1 cm path length. The spectra were collected between 260-185 nm at 0.2 $nm.min^{-1}$ increments with a response time of 1 second and a data pitch of 0.5 nm. Base lines were collected in the same manner using 10 mm sodium phosphate buffer, pH 8.0. Spectra were averaged over four scans, and then corrected for solvent background and smoothness. To determine secondary structure components, CDSSTR deconvolution method was applied to the data, which were accessed using the DICHROWEB server (142).

10.26. Differential Scanning Fluorimetry (76)

Differential Scanning Fluorimetry (DSF) was used to investigate the T_m values of the enzymes (76). It was performed using a MiniOpticon™ Real-Time PCR Detection System (BioRad). The assay was carried out in a white 8x6 wells PCR plates (Star Lab). The total

assay volume per well was 50 µL. SYPRO Orange dye (Invitrogen) was used for non-specific binding to hydrophobic residues and its increase in fluorescence was monitored as a function of temperature. 5 µL of compound stock solution (0.02 mM) was individually dispensed into the PCR wells to obtain a final compound concentration of 0.002 mM in the assay (Table 18). The dye stock solution in DMSO (5000x concentrate) was first diluted by adding 5 µL to 2.5 ml of buffer to produce a 10x concentrated solution. This SYPRO Orange buffer solution was used to make up an enzyme mixture solution to get a final assay concentration of 2 µM enzyme and 50 µM $MnCl_2$. 45 µL of this enzyme mixture solution were dispensed to each well with the compound solution to give a total volume of 50 µL.

The fluorescence readings were taken between 25 °C and 80 °C, increasing the temperature linearly in steps of 1 °C every minute (52). For determination of T_m values, melting curves for each triplicate data set were exported into GraphPad PRISM. A Boltzmann curve was fitted between the values of minimum and maximum intensities. The midpoint (*i. e.*, the T_m value) was calculated by the software.

Table 10.18. List of reagents and their concentrations used for DSF.

Assay Reagent	Stock Concentration (mM)	Final Concentration (mM)
Enzyme	0.01	0.002
Metal	1.0 mM in Buffers	0.05
SYPRO	10X in buffer	1X

10.27. Isothermal Titration Calorimetry (77)

To determine thermodynamics of binding of metal to the apo-protein, isothermal titration calorimetry (ITC) analysis was performed (77). Aliquots of proteins were buffer exchanged using Bio-Rad Micro Bio-Spin column P6 at 4 °C according to the manufacturers' protocol (5x0.5 mL equilibration). The concentration of the combined buffer-exchanged protein aliquots was determined using NanoDrop followed by diluting

the protein to the adequate concentration (40 μM) using buffer. Metals were dissolved and diluted (400 μM) in the identical buffer. ITC analysis was executed on full automated MicroCal PEAQ-ITC in duplicate under the same conditions (ITC, buffer, temperature, etc.) for each experiment. The observed data were analysed with MicroCal PEAQ-ITC analysis software (1.1.0). Buffer used for ITC experiment was: 50 mM Tris pH 7.5, 200 mM NaCl. Metals used included: $Ni(II)Cl_2.6H_2O$ (≥97%), $Co(II)Cl_2.6H_2O$ (99.1%), $Cu(II)SO_4.5H_2O$ (≥98%).

10.28. ITC settings

Automation method: plate pre-rinse syringe clean, ITC method: 19 injections, reference power: 10 μcal/sec, cell: 280 μL, cell temperature: 25 °C, initial delays: 60 s, stirring speed: 750 rpm, 19 injections, 2.0 μL per injection over 4 s (first injection is 0.4 μL), spacing between injections: 150 s, feedback: high, tray temperature: 10 °C.

10.29. Peptide Synthesis in Peptide Synthesizer (143)

Peptides were mainly purchased from GL Biochem (Shanghai, China).

Peptides were also synthesized by following solid phase peptide synthesis (SPPS) procedure (143) on a CS-Bio automated solid phase peptide synthesizer (CS-Bio 336S and CS_Bio 336X). All amino acids were supplied as 9-fluorenylmethyloxycarbonyl (Fmoc) protected amino acids. Standard amino acids were supplied by CS-Bio.

Peptide synthesis was carried out in dimethylformamide (DMF), unless otherwise stated. Fmoc Rink Amide MDHA resin (CS-Bio) was used for synthesis. Typically, synthesis was carried out using 100 μmol resins. Amino acids were used at 10x excess (1 mmol), and activating reagents (di-isopropylcarbodiimide (DIC), 1-hydroxybenzotriazole (HOBt) were also used at 1 mmol. The reaction was started with swelling of 100 μmol resin in 2 mL DMF by shaking for 1 hour. Activation of amino acids was carried out using HOBt (0.5 M solution in DMF) and DIC (0.5 M solution in di-methyl sulfoxide). Amino acids were dissolved in DMF. DIC and HOBt (2 mL) solutions were added immediately to

the resin. The activation reaction was carried out by shaking for 30 minutes. Each amino acid was allowed to react with the resin for 2 hours, with constant shaking, after which the resin was washed with DMF. Fmoc group on amino acid was removed by treatment with 20% piperidine for 8 min so that free amino group of amino acid attached to peptide could couple with free carboxylic acid on newly added Fmoc protected amino acid. Next Fmoc-protected activated amino acid was added, the entire cycle was repeated. After the coupling of last amino acid, the *N*-terminal Fmoc group was removed by 20% piperidine.

After synthesis, the resin was transferred to a filter using DMF and then washed 3x by dichloromethane (DCM) to remove any remaining DMF from resin. The resin was then dried overnight in a vacuum desiccator. Peptides were cleaved from the resin and all side-chain protecting groups were removed by soaking the resin in 5 mL of cleavage cocktail (2.5% tri-isopropyl silane (TIPS) in trifluoroacetic acid, TFA) for 3 hours. For peptides containing methionine or cysteine residues, the cleavage cocktail was amended slightly to TFA (88%), water (5%), phenol (5%) and triisopropylsilane (2%). After 3 hours, the TFA solution containing free peptide was filtered and the TFA volume was reduced to 0.5 mL by bubbling N_2 gas through the solution. The peptide was then precipitated from solution by adding 10 mL ice-cold diethyl ether which was further centrifuged at 2400 rpm for 2 minutes and the supernatant ether was decanted. The solid peptide was then lyophilized in water with 0.1% TFA and freeze-dried overnight. Peptides were purified by HPLC and the mass of the peptides was confirmed by MALDI-TOF MS.

10.30. Lyophilization

Samples were frozen at -80 °C before being lyophilized at room temperature and 4 mBar using a Micro Modulyo freeze drier. Samples remained on the machine until only a powder remained.

10.31. Hydroxylation Assay (16,17,40,60,61)

Hydroxylation assays were performed using MALDI-TOF MS (MALDI Micro MX™, Waters Corporation). 10 µM of enzyme was added in a standard assay mixture of 400 µM L-sodium ascorbate (SIGMA-ALDRICH), 100 µM of ammonium iron (II) sulfate hexahydrate ($(NH_4)_2Fe(SO_4)_2.6H_2O$, SIGMA-ALDRICH) in 50 mM Tris buffer pH 7.5. Finally, a mixture of 500 µM 2-oxoglutarate (2OG, Fluka) and 50-100 µM of substrate-peptide were added to initiate the reaction at 37 ºC. The reaction mixture was quenched by adding equivolume of 1% formic acid solution. In a 96-well MALDI plate (Waters Corporation), 0.8 µL of CHCA (α-cyano-4-hydroxycinnamic acid, ALDRICH) (1 µg in 0.1 mL CHCA solvent) and 0.6 µL of quenched mixture were dropped in a single well. After being dried completely, samples were analysed by MALDI-MS using the conditions mentioned below.

In case of time-course hydroxylation assay, reactions were carried out using standard assay procedures. 5 mL sample was withdrawn at each time point (2, 4, 6, 8, 12, 15, and 30 minutes) and was quenched by 1% formic acid.

10.32. *Steady-state* Kinetic Studies (59,60,72)

For the K_m value determination of Fe(II), concentration of $(NH_4)_2Fe(SO_4)_2$ was varied between 0-150 µM, while keeping the concentrations of 2OG and ascorbate as standard. Enzyme and substrate concentrations were 10 µM and 50-100 µM, respectively. To determine the K_m of 2OG, concentration of 2OG was varied between 0-150 µM whilst keeping the concentrations of other components unchanged. To determine the kinetic parameters of the substrate peptides, reactions were carried out in presence of various concentrations of peptide (40-fold excess) ensuring that the substrate remains in excess in the reaction mixture in order to comply with the Michaelis-Menten kinetics (60,61,71).

In all cases, reactions were quenched within the linear range of time-course hydroxylation curve (typically 2 to 6 minutes). Initial reaction rate (v_0) was then plotted as

a function of concentration of the variables (either 2OG or Fe(II) or substrate peptide) by using GraphPad PRISM and kinetic parameters were calculated by the Michaelis-Menten equation:

$$v = \frac{d[P]}{dt} = \frac{V_{max}[S]}{K_m + [S]} \quad \ldots\ldots\ldots\ldots\ldots (3)$$

10.33. Inhibition Kinetics (59-61)

To determine the IC_{50} values of the inhibitors, standard hydroxylation assay procedure was followed in the presence of various concentrations of inhibitors (0-10 mM). Values of percent inhibition of hydroxylation were plotted as a function of inhibitor concentration (log-values) by using GraphPad PRISM and IC_{50} values were thus calculated.

10.34. Demethylation Assay (29,32,39)

To carry out the demethylation assay with JMJD6, 10 µM enzyme was mixed with 20-100 µM Fe(II), 400 µM ascorbate in 50 mM HEPES-KOH pH 8.0. Mixture of 500-1000 µM 2OG and 100 µM peptide was finally added to it to initiate the reaction, which was allowed to continue for 0.5-2 hours at 37 °C. Reaction samples were quenched by equivolume of 1% formic acid, spotted on MALDI target plate, and then analysed by MALDI-TOF MS following the same procedure as before.

10.35. NMR-based Assay (55)

Table 10.19. List of special reagents used in NMR experiment.

Reagent	Manufacturer
Tris-D11	Cambridge Isotope Laboratories or Euriso-Top
DMSO-D6	Merck Chemicals

All NMR experiments were carried out in solution buffered with 50 mM deuterated tris(hydroxymethyl)aminomethane (Tris-D11; pH 7.5). Buffers were made up in MilliQ water and pH was adjusted using HCl.

NMR experiments were performed using a Bruker Avance AV111 700 MHz spectrometer equipped with an inverse TCI CryoProbe, optimized for ^{1}H observation, and installed with Topspin 4.0 software. The ^{1}H pulse tip-angle was calibrated using the single-pulse nutation methods with the NMR sample or with the NMR buffer prior to the actual experiment. Experiments were carried out either in 2 or 3 mm NMR tube (Wilgenberg) and the solvent deuterium signal was used as an internal lock signal. NMR parameters such as water suppression, sample temperature, number of transients, acquisition time and mixing time were determined on a per sample basis, although typically the number of transients usually varied between 32 to 64, and the relaxation delay usually between 1 and 2 seconds. Typically, water suppression was achieved using the excitation sculpting method (2 ms Sinc1.1000 pulse)

10.36. Activity Assay for HPPD

Reaction between purified 0.5 µM HPPD and 500 µM HPPA was allowed to occur inside 2/3 mm NMR tube or 1.5 mL Eppendorf tube at room temperature in the presence of 100 µM of Fe(II) and 400 µM ascorbate. ^{1}H signals obtained from the reaction samples were then compared with ^{1}H signals of the standards. Complete turnover of HPPA to HMGA was achieved between 1 to 5 minutes based on the efficiency of the purified human HPPD.

10.37. Time Course Assay

Time course experiments were monitored by ^{1}H NMR. The lag time between sample mixing and end of the first experiment was usually between 3.5 and 5 minutes. However in case of experiments involving HPPD, reactions appeared to be stopped inside the NMR tube. In case of JMJD6, all the reactions were carried out inside NMR and multiple ^{1}H signals of succinate were recorded over time. Typically, the total experiment time for each spectrum was shorter than 3 minutes. Initial rates were calculated by linear fitting

using Excel 2003 for data points of up to 20% turnover to ensure that the reaction was in the linear range (only applicable for experiments involving HPPD).

10.38. K_m Determination of HPP

Reactions between 0.5 µM HPPD and various concentration of HPPA were allowed to occur under the same condition as used for activity assay. Each reaction was allowed to occur at room temperature for 2 minutes and reaction products were analysed by ^{1}H NMR (700 MHz). Initial reaction rate (v_0) was then plotted as a function of HPPA concentration by using GraphPad PRISM and the kinetic parameters were calculated from the Michaelis-Menten equation (equation 3, section 10.32).

10.39. CPMG Displacement Experiment (56,57)

The CPMG (Carr-Purcell-Meiboom-Gill) displacement experiments were conducted using the AV700 instrument. The PROJECT(Periodic Refocusing of J Evolution by Coherence Transfer)-CPMG sequence ($90°_x – [\tau – 180°_y – \tau – 90°_y – \tau – 180°_y – \tau]_n$ – acq) was applied as described by Aguilar *et al.* (144). Typical experimental parameters were as follows: total echo time 48 ms (τ = 2 ms, n = 6), acquisition time 2.94 seconds, relaxation delay 2 seconds, number of transients 128. Water suppression was achieved by presaturation.

10.40. 2OG Turnover Assay with JMJD6 (10)

JMJD6 (10 µL), Fe(II) (100 µM) and ascorbate (400 µM) were mixed in deuterated Tris-D11 pH 7.5 in a 1.5 mL Eppendorf tube. Substrate (either only 500 µM 2OG or mixture of 500 µM 2OG and 100 µM LUC7L2$_{267-278}$) was added finally to initiate the reaction. The mixture was immediately transferred into a 2 mm NMR tube and the acquisition of the ^{1}H signal was started after 3.5-5minutes. The total run time for each sample was 2 minutes 45 seconds. Intensity for succinate formed over time and catalysed by JMJD6 from each chromatogram was plotted as a function of temperature in Excel 2003 to calculate the rate of succinate formation.

10.41. Binding Constant Measurement (JMJD6 and HPPD) (58)

10-20 µM ligand and 200 µM Zn(II) was mixed in deuterated Tris-D11 pH 7.5 and the $^{1}H/^{19}F$ signals for the ligand were recorded by using AV 700 MHz/AV 600 MHz. Ligand was then titrated against EDTA-treated enzyme (0-150 µM) until the signal for ligand fully disappeared, suggesting complete enzyme.ligand complex formation. The percentage of enzyme.Zn(II).ligand was plotted as a function of enzyme concentration using Origin™ and the apparent binding constant (K_D^{app}) was measured using the following equation described by Morton *et al.*

$$\Delta_{obs} = \Delta_{max} \times \frac{(K_D^{app} + [L]_0 + [P]_0) - \sqrt{\{(K_D^{app} + [L]_0 + [P]_0)^2 - 4 \times [L]_0 \times [P]_0\}}}{2 \times [P]_0} \quad \ldots\ldots\ldots (4)$$

where, Δ_{obs} represents change in any observable NMR parameter from the titration, Δ_{max} represents the maximum change of the monitored NMR parameter, $[L]_0$ represents the titrated ligand concentration, $[P]_0$ represents the protein concentration. Typically, a 5-10% error was allowed in the curve fitting process.

10.42. Reporter Displacement Experiment (55)

Reporter ligand experiment was adopted to calculate the percent displacement of reporter compound (2OG in case of JMJD6 and HPPA in case of HPPD) done by the 'ligand of interest'. To avoid the enzymatic catalytic activity, diamagnetic Zn(II) was used in excess and presumably the binding ability of the ligand, including 2OG and HPP, was not substantially affected by the use of Zn(II) as the active site metal. In order to see the signal of reporter ligand and to attenuate the protein resonances, CPMG-PROJECT method was used. This method helped to differentiate free from bound signal of reporter ligand. However, when the reporter ligand formed full complex with the enzyme, CPMG-edited ^{1}H spectrum showed complete/near to complete diminution of its signals, which

eventually reappeared upon addition of a true competitor for the same active-site pocket of the enzyme.

Initial recovery of HPPA signal was the basis for screening new inhibitor/binder for HPPD. On the other hand, percentage of 2OG displaced by the ligand calculated by using the following equation was the basis for identifying potent inhibitor of JMJD6.

$$\% \text{ 2OG Displacement} = \frac{I_{2OG} - I_{2OG(0)}}{I_{2OG(blank)} - I_{2OG(0)}} \text{ X } 100\% \quad \ldots \quad (5)$$

where, I_{2OG} is the integral of 2OG ^{1}H signal in the presence of both inhibitor and the protein, $I_{2OG(0)}$ is the integral of 2OG in the presence of the protein but in the absence of inhibitor, $I_{2OG(blank)}$ is the integral of 2OG in the absence of both protein and inhibitor. For the ideal scenario in which the 2OG signal is fully attenuated in the presence of protein (and absence of inhibitor), $I_{2OG(0)}$ should tend toward zero.

10.43. Crystallization Trials

Proteins of high purity (≥ 95%, confirmed by SDS-PAGE analysis) and at higher concentration ≥ 25 mg/mL (500-600 µM) were used for crystallographic attempts. Enzyme.metal.ligand/substrate complexes were formed by incubating the mixture on ice for ~1 hour. Typically, the components were used in 5-fold excess of the protein concentration. However, a Phoneix™ RE crystallization robot and a Minstrel-HT™ platform with CrystalTrek™ from Rigaku Inc. were used to lay down crystallization plates (Art Robbins Instruments). In each reservoir, the dispenser poured 80 µL of the crystallization buffer. In each well, 0.3 µL of crystallization solutions were poured at ratios of 2:1 (0.2 µL of protein solution and 0.1 µL of crystallization buffer), 1:1 (0.1 µL of protein solution and 0.1 µL of crystallization buffer), and 1:2 (0.1µL of protein solution and 0.2 µL of crystallization buffer).

In the case of crystallization attempts under anaerobic conditions, plates were laid inside a hypoxic chamber. Initially, the stock solutions including protein, ligand, metal, substrate, and buffer were equilibrated under the anaerobic condition. Then, the protein solution, pre-incubated with appropriate component (metal or ligand or substrate or all), was mixed with the crystallisation buffer (at a 1:1 ratio) in a sitting drop 24-well crystallisation plate. In each reservoir of the plate, 500 µL of the crystallisation buffer was also poured.

In both cases (aerobic and anaerobic condition), crystals were allowed to grow by sitting-drop vapor diffusion method. Crystallisation plates were regularly examined under optical microscope (Leica Microsystems, Germany) for hits. Crystals were cryo-protected using a mixture of reservoir solution diluted to either 20-25% (v/v) glycerol (JMJD5 and JMJD6) or 20% (v/v) ethylene glycol (HPPD). Diffraction data were collected at the DLS (Diamond Light Source) synchrotron facility. PHASER was used for molecular replacement (MR) and structural models were improved by iterative cycles of manual building in COOT and crystallographic refinement in PHENIX (79,80).

CHAPTER 11: Summary and Conclusions

The work presented in this thesis attempted to address the on-going issues related to the functional assignment of 2 members of 2OG-dependent oxygenases: JMJD6 (JmjC domain containing protein 6) and JMJD5 (JmjC domain containing protein 5). Based on the results obtained, it can now be said that a comprehensive knowledge on both of these two enzymes is now available.

First, it was identified from the studies with JMJD6 that the *C*-terminal polyS domain has a strong impact on the substrate-recognition property of JMJD6. Studies involving the variants of JMJD6 with and without the polyS domain clearly revealed that the catalytic activities of JMJD6 including binding with 2OG, conversion of 2OG to succinate and lysyl-hydroxylation are regulated by the *C*-terminal polyS domain. The oligomerisation property of JMJD6 was also found to be regulated by the *C*-terminal regions including the polyS domain, in accord with the previous literature (33). Further, the lysyl-hydroxylase activity of JMJD6 on two of its reported substrates ($LUC7L2_{267\text{-}278}$ and $H4_{1\text{-}15}$) was found not to depend on ascorbate. Kinetic studies of JMJD6 using the isolated peptide-substrates of histones next revealed that JMJD6 is not an arginine demethylase but a lysyl-hydroxylase. Interestingly, the lysyl-hydroxylase activity on the splicing regulatory (SR) proteins was found to be dependent on the relative position of the lysine residue (*N*- vs *C*-terminus), the presence of other lysine residue(s) next to the targeted lysine, the length of the peptide sequence, and the hydrophilicity of the peptide. Studies with isolated peptide-fragments further showed that the JMJD6-VHL/ERα interactions mediate *via* the JMJD6-catalysed hydroxylation of lysine residues within the sequence of these proteins ($K171_{VHL}$, $K252_{ER\alpha}$, and $K257_{ER\alpha}$). Further, studies with $LUC7L2_{267\text{-}278}$ with various lysine analogues at position 269 (K269) led to the finding that JMJD6 hydroxylates only the L-lysine, not any of the other tested lysine analogues. More studies on the reported substrates as well as on those identified in this work therefore would be of future interest to further investigate the substrate-scope of JMJD6. Next,

crystallographic attempts with both full length (JMJD6^{FL}) and truncated (JMJD6$^{\Delta 344\text{-}403}$) JMJD6 led to the determination of crystal structures of JMJD6 in complex with various metals and ligands including the complex structures of JMJD6$^{\Delta 344\text{-}403}$.Fe(II).2OG, JMJD6$^{\Delta 344\text{-}403}$.Ni(II).2OG, JMJD6$^{\Delta 344\text{-}403}$.Mn(II).NOG, JMJD6$^{\Delta 344\text{-}403}$.Mn(II).2,4-PDCA, JMJD6$^{\Delta 344\text{-}403}$.Mn(II).fumarate, JMJD6$^{\Delta 344\text{-}403}$.Mn(II).succinate, and JMJD6^{FL}.Mn(II).NOG. These structures reveal that the binding mode of the C-1 carboxylate of 2OG/NOG/ligand to JMJD6 is similar to that of PHD2 and PHF8 but different from FIH and KDM4A. The crystallographic studies with full-length JMJD6 has further revealed an additional and still unprecedented property of JMJD6, which is fragmentation in solution catalysed by *C*-terminal region including the polyS domain. Although the JMJD6^{FL}.Mn(II).NOG complex structure was solved from a high resolution dataset (1.6 Å), the structure of the *C*-terminal region of full-length JMJD6 comprising the residues Ser^{335}-Arg^{403} including the polyS domain is not visible in the electron density maps. Partial and inconclusive evidence for residues that may correspond to the *C*-terminal region is found close to the *N*-terminal region of the chains within the crystal structure of JMJD6^{FL}. This gives an indication of possible degradation of JMJD6 across its *C*-terminus. SDS-PAGE and MS analyses of JMJD6-variants with and without a *C*-terminal region including the polyS domain further confirmed that JMJD6 indeed underwent self-cleavage likely catalysed by the polyS domain during the crystallisation process. This property of JMJD6 can now be exploited in future crystallographic studies with JMJD6.substrate complex as the polyS domain has significant impact on the substrate-recognition by JMJD6. Inhibition studies with JMJD6 identified the non-selective 2OG oxygenase inhibitors 2,4-PDCA, 2,4-BPDCA, IOX1, **2**, **3**, selective PHD inhibitors FG4592, AKB-6899, Vadadustat, GSK1278863, GSK1278863 analogues **5**, **6**, **8**, and **14** as moderate to potential inhibitors for JMJD6. These data together suggest that potent inhibitors for JMJD6 would now possibly be developed by modulating the pharmacophoric properties of these inhibitors. Most importantly, weak inhibition by D- and L-2HG indicates a possible connection between JMJD6 and cancer,

which corroborates the previously reported literature in which a possible role of JMJD6 as potential biomarker in cancer prognosis was mentioned. Overall, these results should be validated inside cells, though the inhibition data generated throughout this work can be considered as a good starting point to develop potential JMJD6-inhibitors.

Kinetic studies with JMJD5 using isolated peptide-fragments led to the identification of two new substrates for JMJD5: RpS6 (40S ribosomal protein) and RCCD1 (regulator of chromosome condensation domain-containing protein 1), where JMJD5 was observed to catalyse the hydroxylation of $R137_{RpS6}$ and $R141_{RCCD1}$. However, no evidence for the demethylase activity of JMJD5 on its reported histone-substrates was found under the conditions used. Furthermore, crystal structures of multiple constructs of JMJD5 in complex with peptide-fragments of RpS6 and RCCD1 were determined, which further supports our proposal that JMJD5 is indeed a JmjC hydroxylase, not a demethylase. These findings together indicate again the functional diversities of 2OG oxygenases including various post-translational modifications (PTMs), which can possibly be extended up to the regulation of ribosomal functions and chromosomal stability. Next, structure-guided mutagenesis studies identified the substrate-binding residues in JMJD5 structure, which should potentially be exploited to unveil the substrate-recognition property of JMJD5 at a further advanced level. An inhibition study with JMJD5 was also performed using broad spectrum 2OG oxygenase, selective KDM and selective PHD inhibitors. It identified the template structures that would be directional to develop potent and selective JMJD5-inhibitors. Although, previous structural work by Rizzo *et al.* revealed the binding mode of the broad spectrum inhibitor NOG with JMJD5 (49), the results presented here provide additional insights into the coordination chemistry between JMJD5 and its newly-identified inhibitors. Of particular interest, given the biological importance of JMJD5, is its inhibition by certain citric acid cycle (TCA cycle)-intermediates and 2-hydroxyglutarate (2HG). The results raise the possibility that (some) of the

pathophysiological effects of TCA cycle intermediates/2HG levels are mediated by JMJD5 inhibition.

Biochemical studies on human 4-hydroxyphenylpyruvate dioxygenase (HPPD) revealed the unprecedented property of human HPPD that it requires all of its metal binding residues to catalyse the conversion of HPPA to HMGA. An NMR-based method was developed throughout this work to assay the functional properties of human HPPD. Using this method, comprehensive kinetic studies of human HPPD with its substrate (HPPA) and reported inhibitors (mesotrione, nitisinone/NTBC, and sulcotrione) were carried out. The NMR-based assay reveals a low K_D (0.8 µM) but a relatively high K_m value (165 µM) of HPPA, although the obtained K_m value is consistent with the literatures (125,128). NMR-based assays also revealed relatively high IC_{50} values of the inhibitors compared to the reported-values. However, none of the reported works used NMR for IC_{50} value determination of HPPD-inhibitors; therefore, the IC_{50} values of the HPPD-inhibitors obtained from this work are not comparable with those reported in the literature (130). Based on a screening assay of various HPPA-derivatives and 2OG oxygenase inhibitors, three new inhibitors (**1**, **31**, and **32**) were identified for human HPPD. Nevertheless, further structural modifications on these inhibitors are required to achieve more potency. Crystallographic studies with human HPPD further led to the structure determination of human HPPD. In the structure, residues Q188-A262 are not visible, which may likely be due to the fragmentation of human HPPD. Furthermore, oligomerisation property of human HPPD enzyme was also investigated in this work, which revealed the dimeric status of human HPPD in solution. Overall, these results present functional and structural properties of human HPPD, which has not been reported previously. Importantly, inhibition studies with synthetic compounds led to the identification of new pharmacophores for human HPPD-inhibitors, which now need to be tested against other homologues of HPPD.

Appendix 01

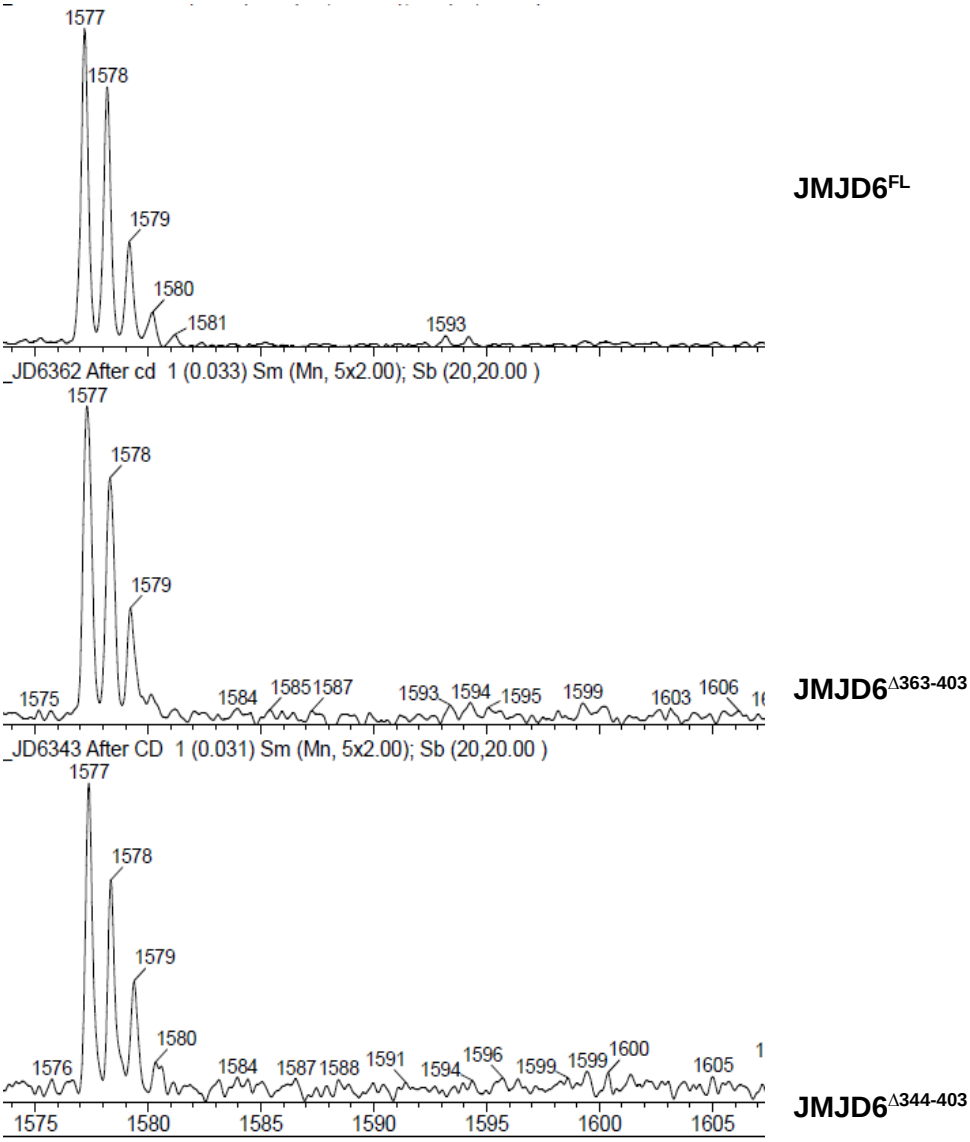

FIGURE 12.1. **Activity testing of JMJD6 variants.** MALDI-TOF spectra showing little/no hydroxylation of LUC7L2$_{267-278}$ (NPKRSRSREHRR) as catalysed by the JMJD6 variants obtained after thermal refolding. Experiments were carried out following the hydroxylation assay procedure described in Chapter 10.

Appendix 02

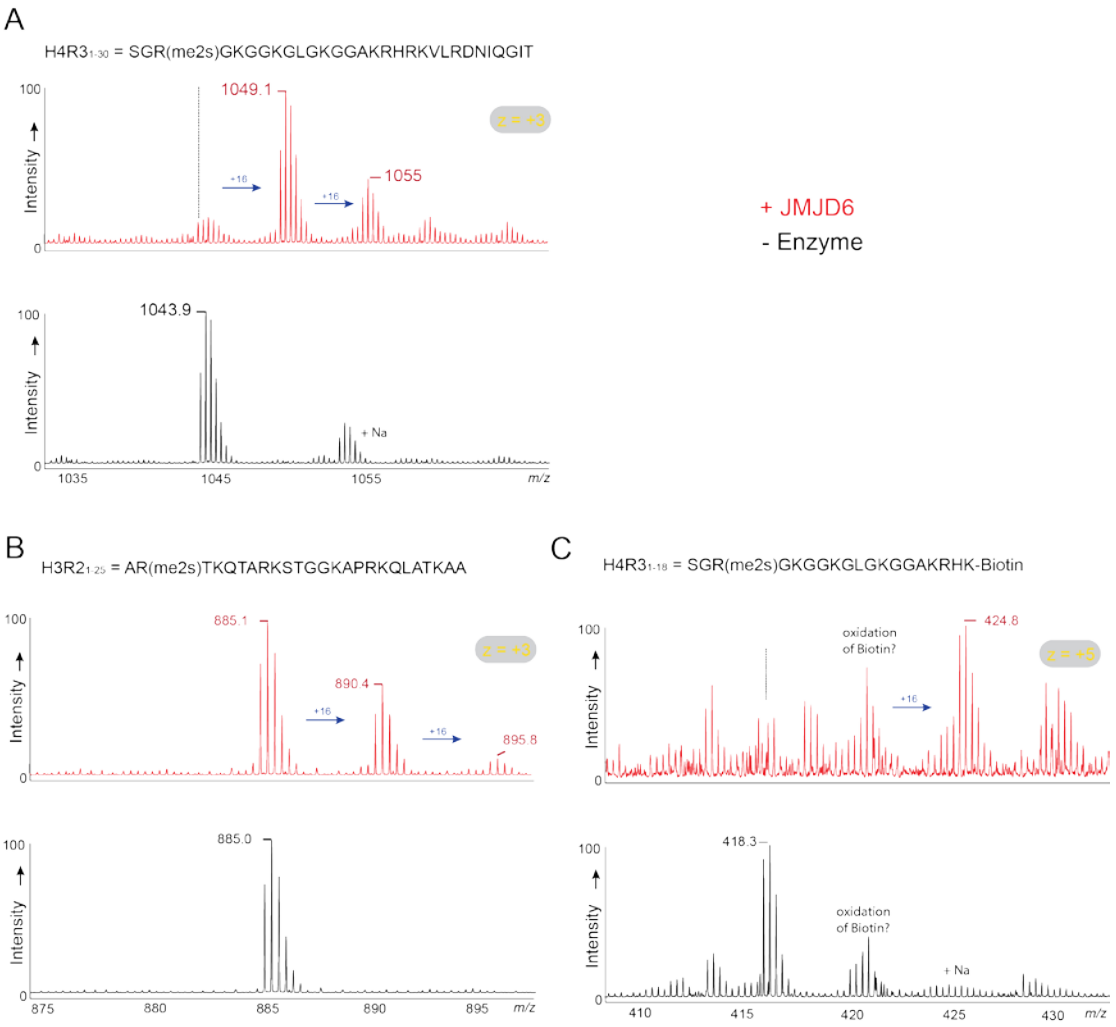

FIGURE 12.2. **JMJD6 is a lysyl-hydroxylase**. MALDI-TOF spectra showing the appearance of peaks with +16 Da shift in mass demonstrating hydroxylation in JMJD6$^{\Delta 363\text{-}403}$-treated histone peptides (red spectra). Black spectra are of the peptides in the presence of other reaction components except enzyme. Note the lack of evidence for demethylation by JMJD6$^{\Delta 363\text{-}403}$, which was purified following the reported procedures (29,32,39). Experiments were carried out following the demethylation assay procedure described in Chapter 10.

Appendix 03

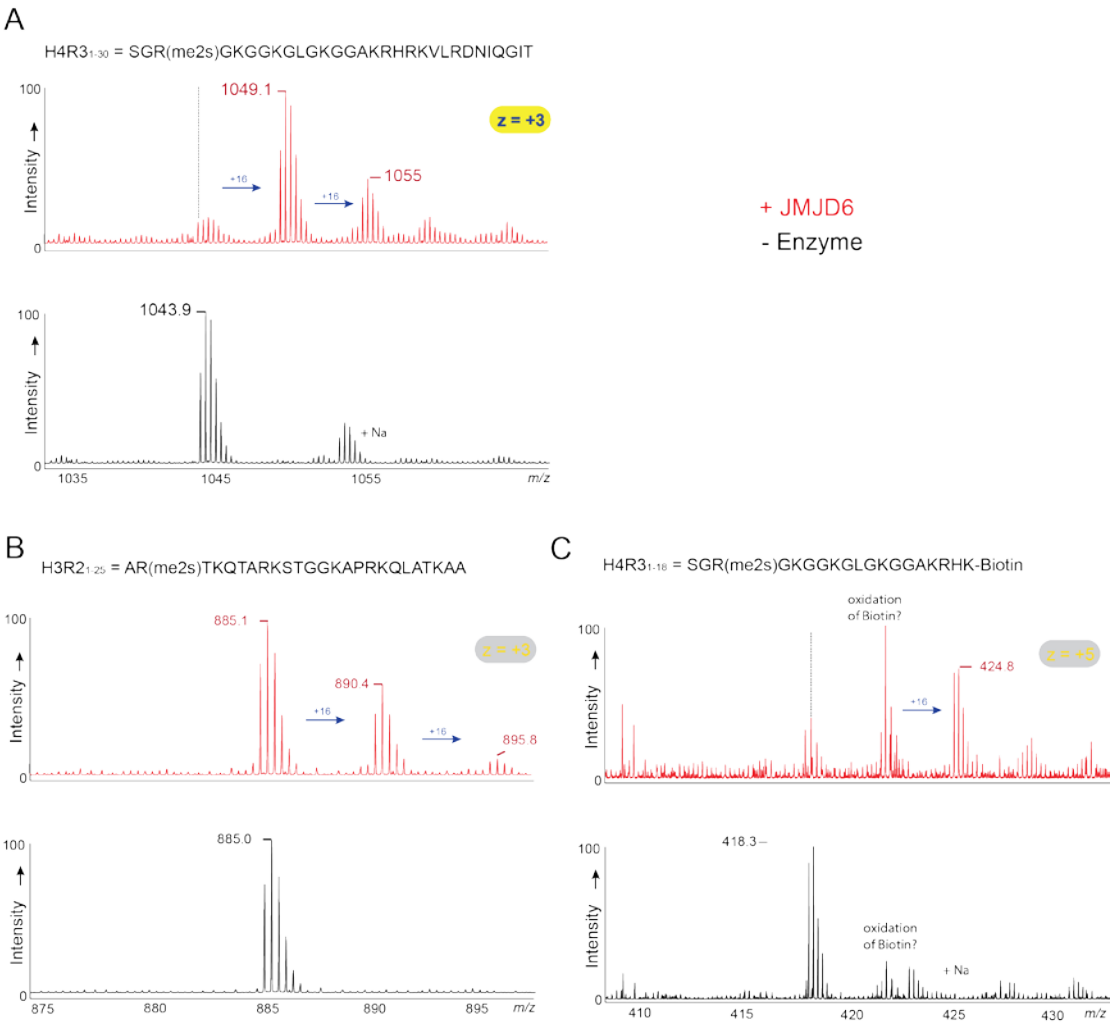

FIGURE 12.3.1**. Investigation of demethylation activity of JMJD6^{FL} on histone peptides.** MALDI-TOF spectra showing the appearance of peaks with +16 Da shift in mass demonstrating hydroxylation in JMJD6^{FL}-treated histone peptides (red spectra). Black spectra are of the peptides in the presence of other reaction components except enzyme. Note the lack of evidence for demethylation by JMJD6^{FL}. Experiments were carried out following the demethylation assay procedure described in Chapter 10.

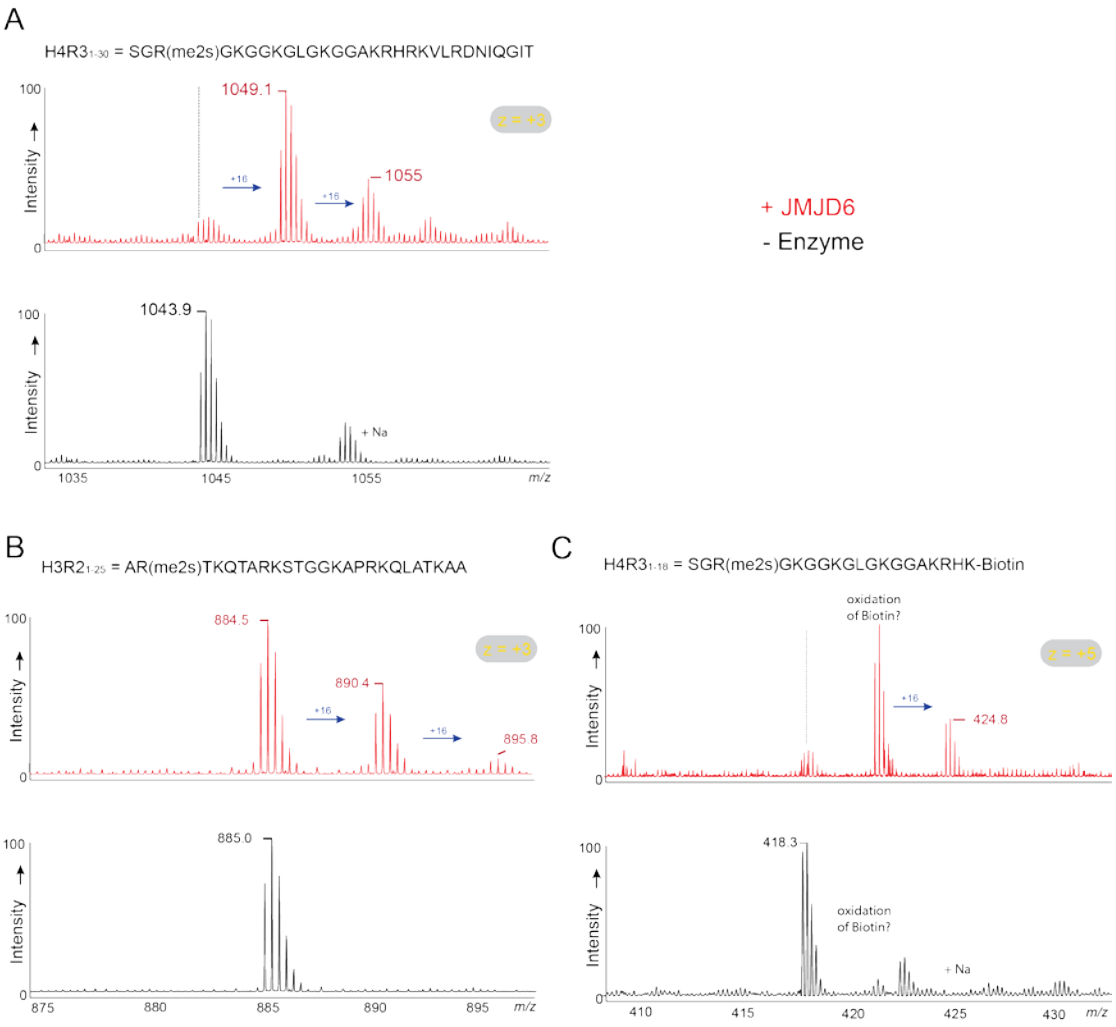

FIGURE 12.3.2. **Investigation of demethylation activity of JMJD6$^{\Delta 344\text{-}403}$ on histone peptides.** MALDI-TOF spectra showing the appearance of peaks with +16 Da shift in mass demonstrating hydroxylation in JMJD6$^{\Delta 344\text{-}403}$-treated histone peptides (red spectra). Black spectra are of the peptides in the presence of other reaction components except enzyme. Note the lack of evidence for demethylation by JMJD6$^{\Delta 344\text{-}403}$. Experiments were carried out following the demethylation assay procedure described in Chapter 10.

Appendix 04

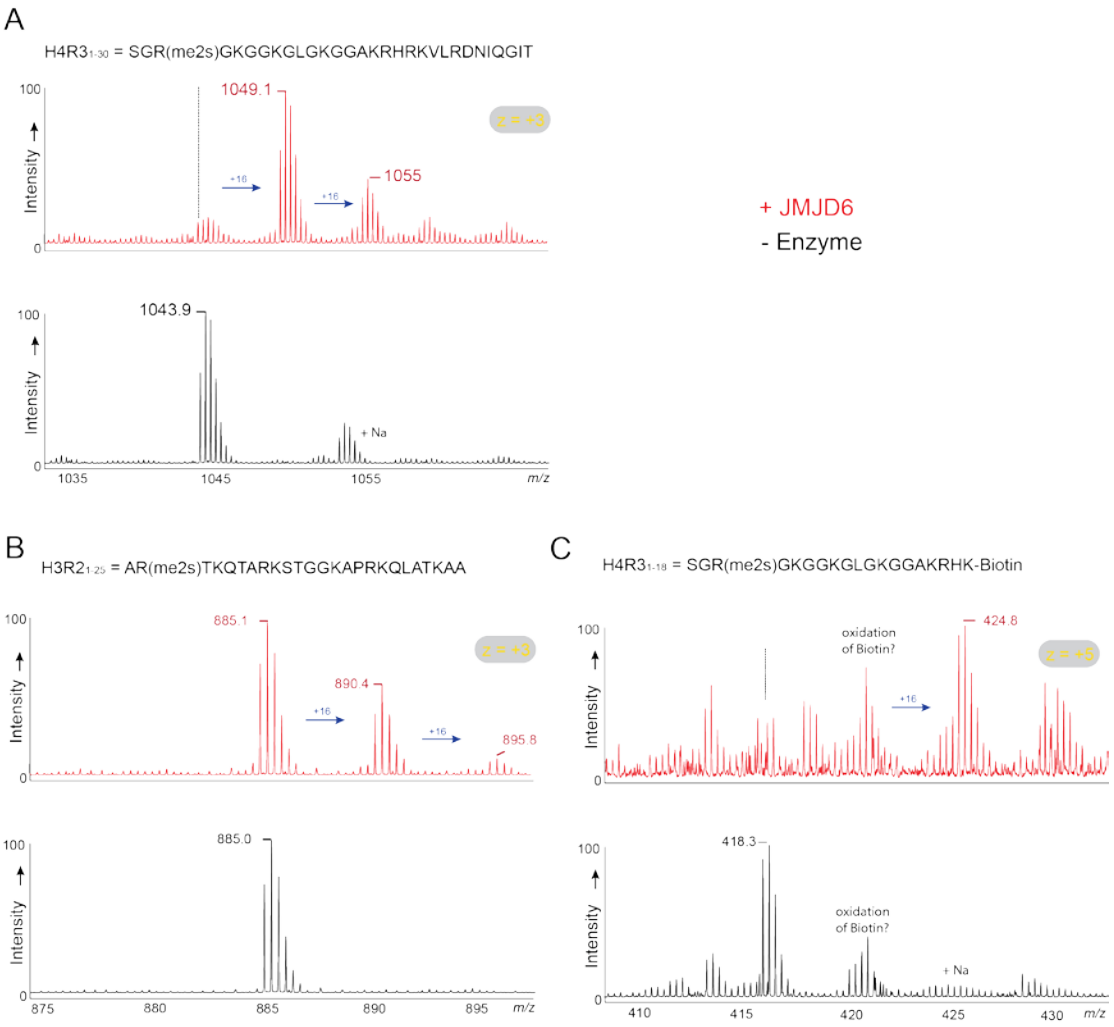

FIGURE 12.4. **Investigation of lysyl-hydroxylase activity of JMJD6 on histone peptides without ascorbate**. MALDI-TOF spectra showing the appearance of peaks with +16 Da shift in mass demonstrating hydroxylation in JMJD6$^{\Delta 363\text{-}403}$-treated histone peptides (red spectra) without ascorbate in the reaction buffer. Black spectra are of the peptides in the presence of other reaction components except enzyme. Experiments were carried out following the hydroxylation assay procedure described in Chapter 10.

Appendix 05

A

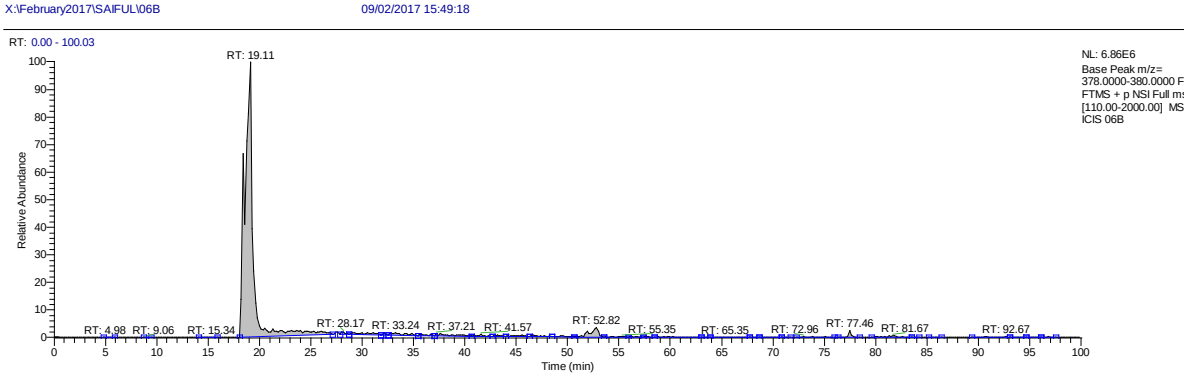

B

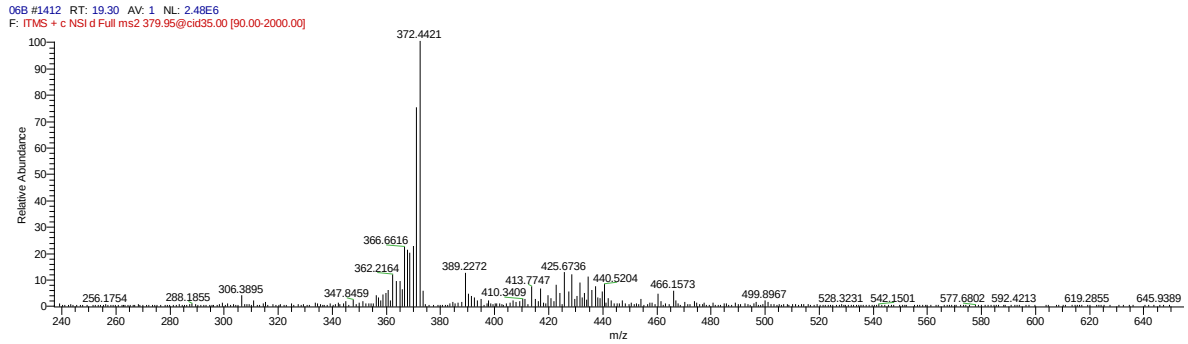

C

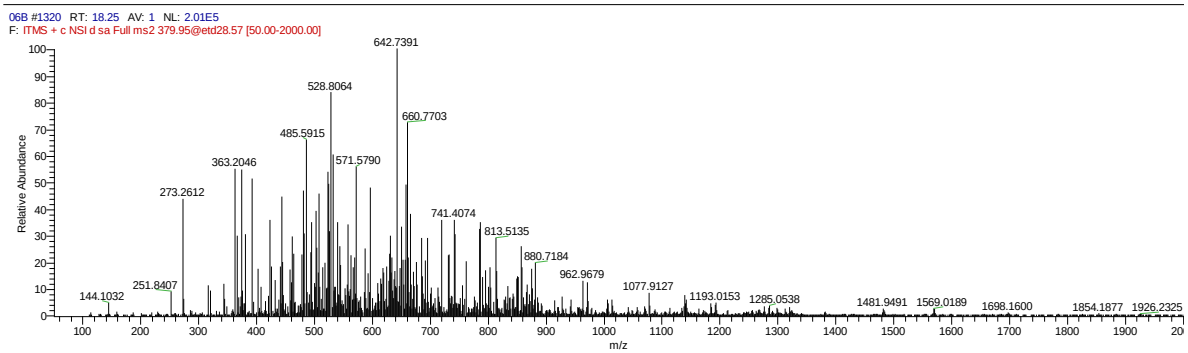

FIGURE 12.5.1 **LC-MS/MS analysis of H3R2(me2s)$_{1-25}$: AR(me2s)TKQTARKSTG GKAPRKQLATKAA without enzyme treatment.** (A) LC-MS chromatogram. Fragmentation of the peptide (m/z = 379.9) by applying (B) CID and (C) ETD. Results represent technical triplicate (n = 3).

A

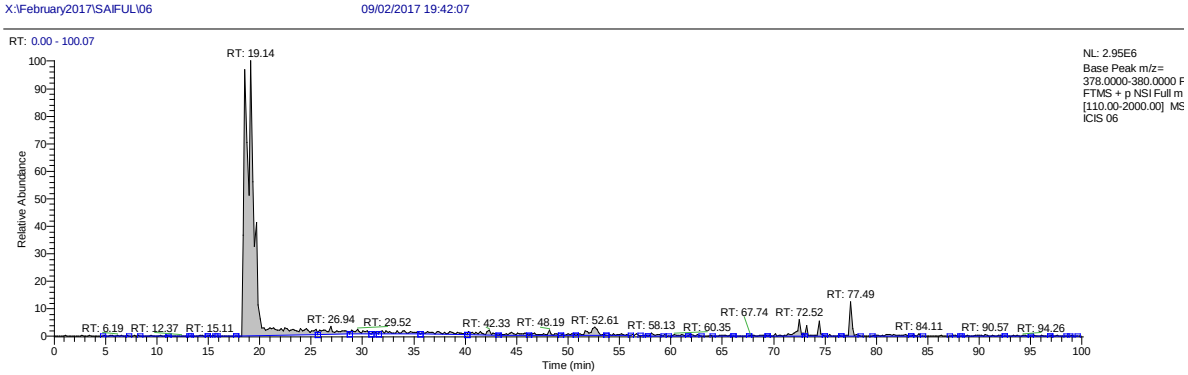

B

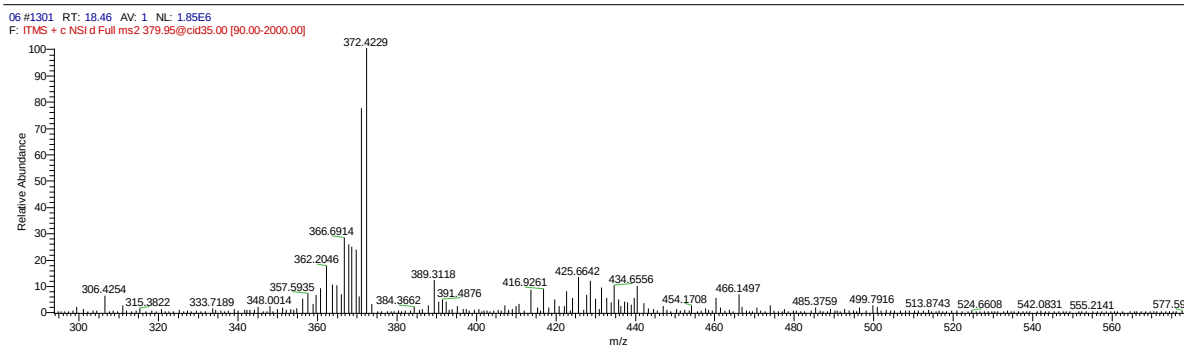

C

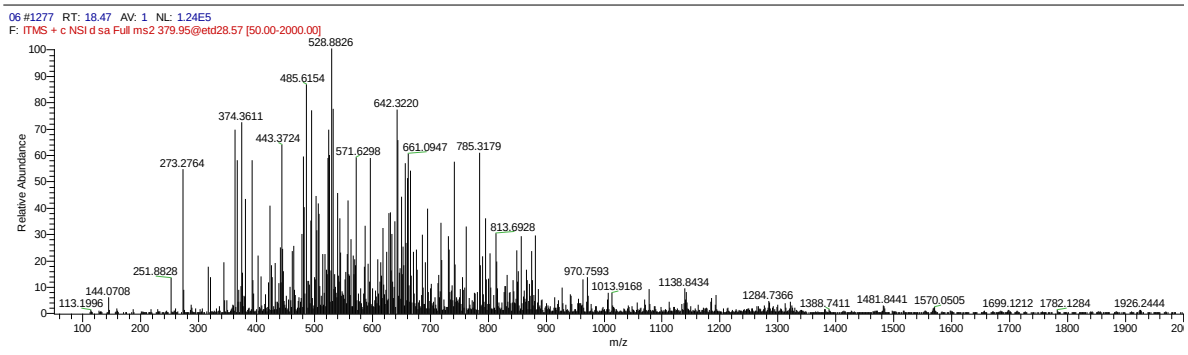

FIGURE 12.5.2. **LC-MS/MS analysis of JMJD6-treated H3R2(me2s)$_{1\text{-}25}$: AR(me2s)TKQTARKSTGGKAPRKQLATKAA.** (A) LC-MS chromatogram. Fragmentation of the unmodified peptide (m/z = 379.95) by applying (B) CID and (C) ETD. Results represent technical triplicate (n = 3).

A

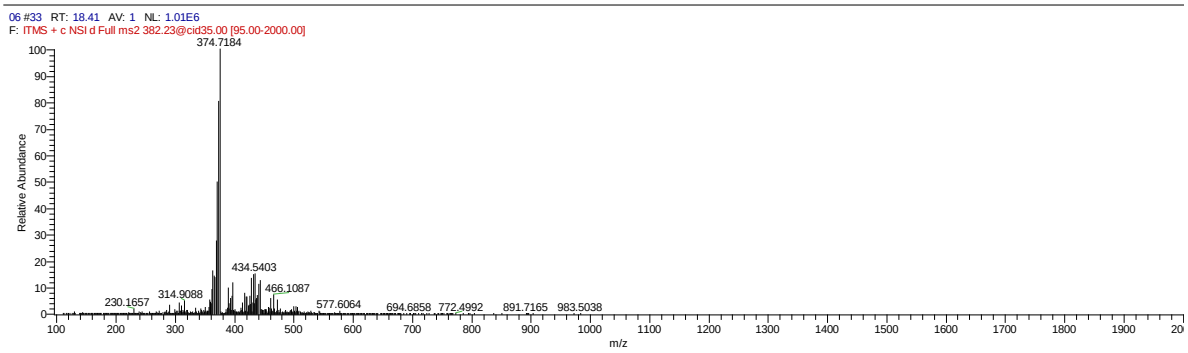

B

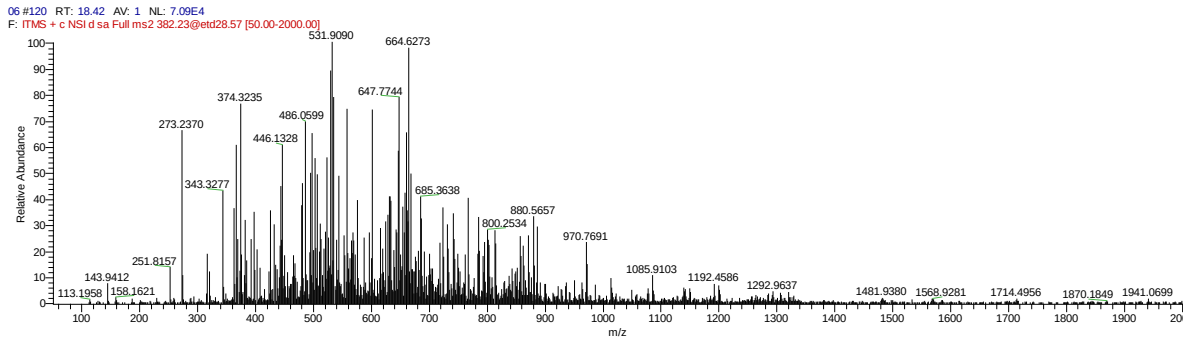

FIGURE 12.5.3. **LC-MS/MS analysis of JMJD6-treated H3R2(me2s)$_{1\text{-}25}$: AR(me2s)TKQTARKSTGGKAPRKQLATKAA.** Fragmentation of the hydroxylated peptide (m/z = 382.23) by applying (A) CID and (B) ETD. Results represent technical triplicate (n = 3).

A

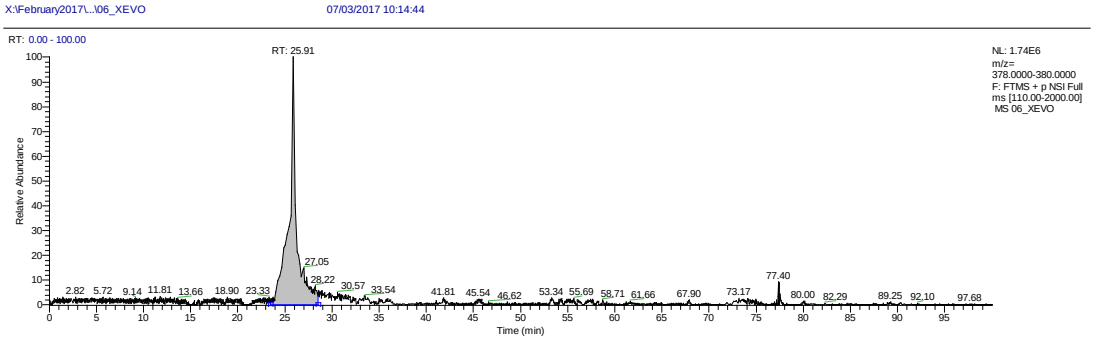

B

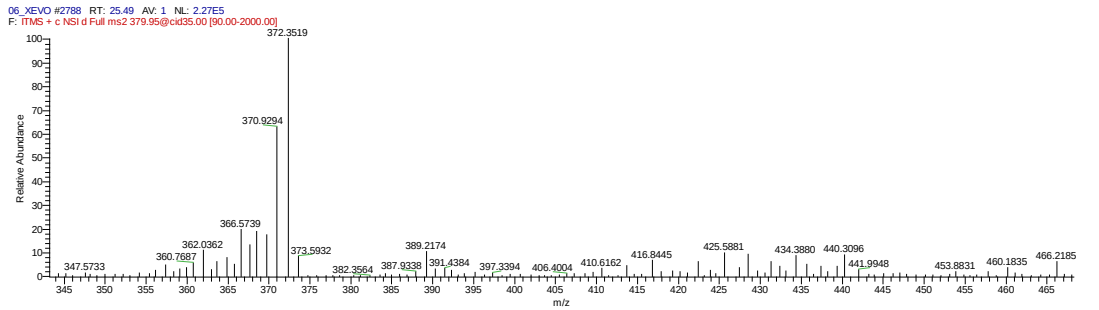

C

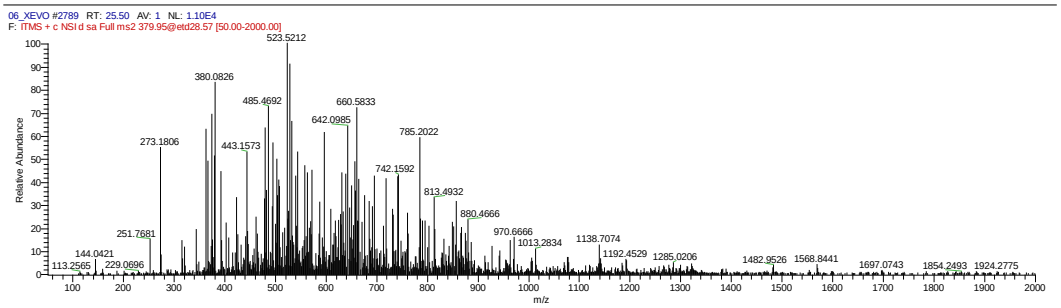

FIGURE 12.5.4. **LC-MS/MS analysis of JMJD2E-treated H3R2(me2s)$_{1-25}$: AR(me2s)TKQTARKSTGGKAPRKQLATKAA.** (A) LC-MS chromatogram. Fragmentation of the unmodified peptide (m/z = 379.95) by applying (B) CID and (C) ETD. Results represent technical triplicate (n = 3).

A

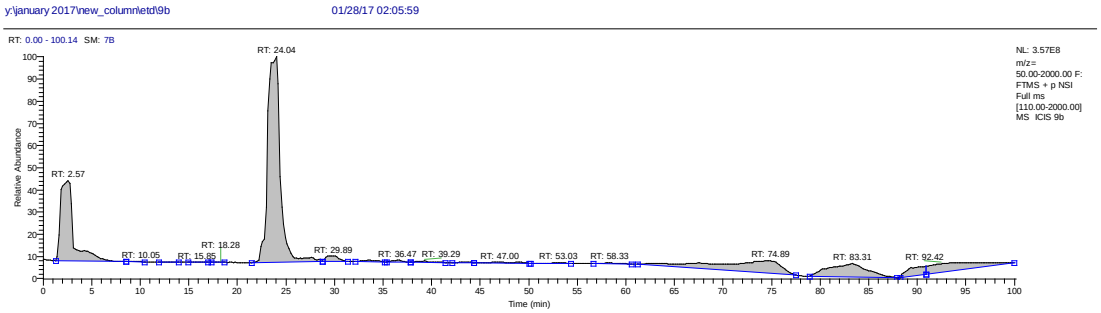

B

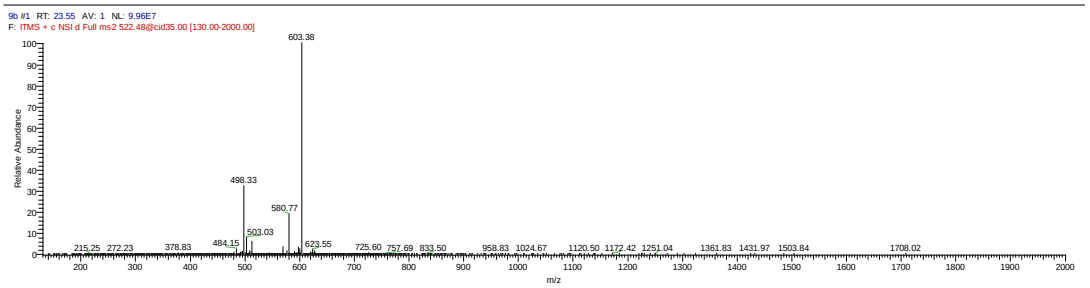

C

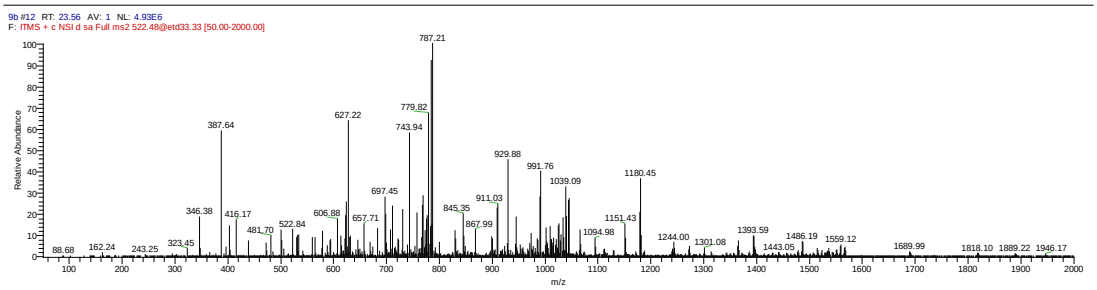

FIGURE 12.5.5. **LC-MS/MS analysis of H4R3(me2s)$_{1-30}$: SGR(ms2s)GKGGKGLGKGG AKRHRKVLRDNIQGIT without enzyme treatment.** (A) LC-MS chromatogram. Fragmentation of the peptide (m/z = 522.47) by applying (B) CID and (C) ETD. Results represent technical triplicate (n = 3).

A

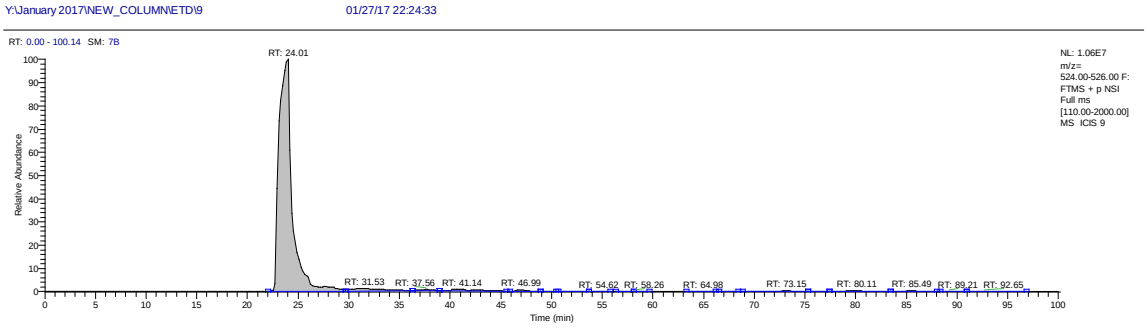

B

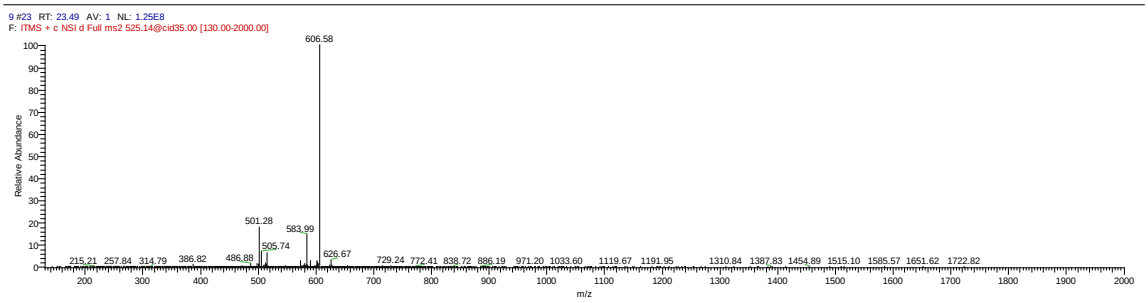

C

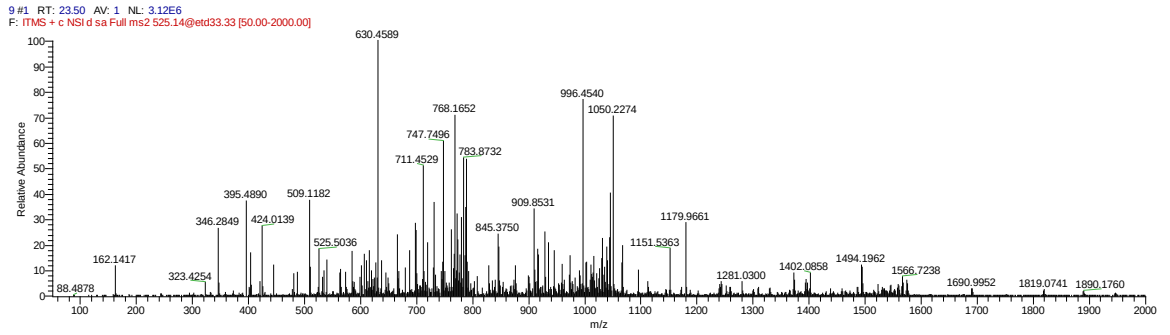

FIGURE 12.5.6. **LC-MS/MS analysis of JMJD6-treated H4R3(me2s)$_{1-30}$: SGR(ms2s)GKGGKGLGKGGAKRHRKVLRDNIQGIT.** (A) LC-MS chromatogram. Fragmentation of the hydroxylated peptide (m/z = 525.14) by applying (B) CID and (C) ETD. Results represent technical triplicate (n = 3).

A

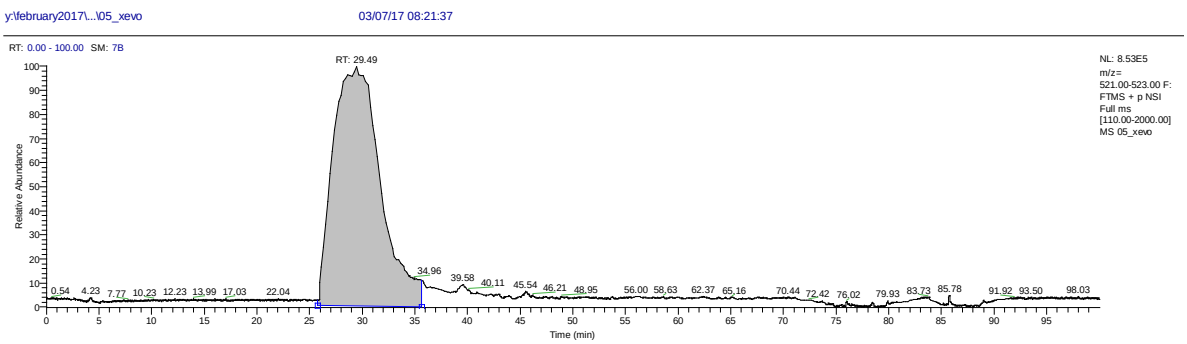

B

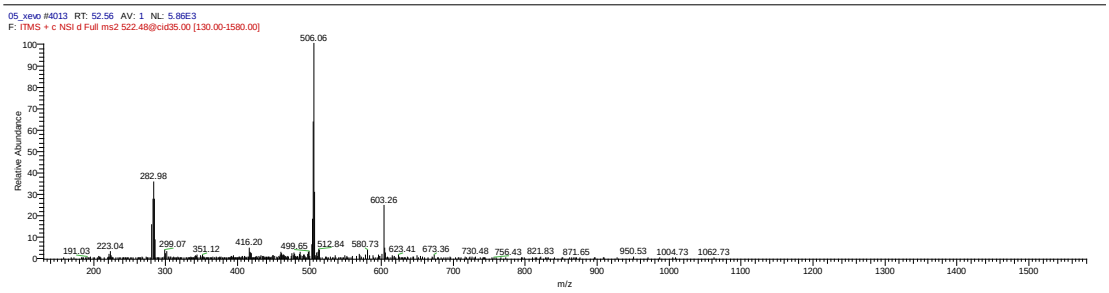

C

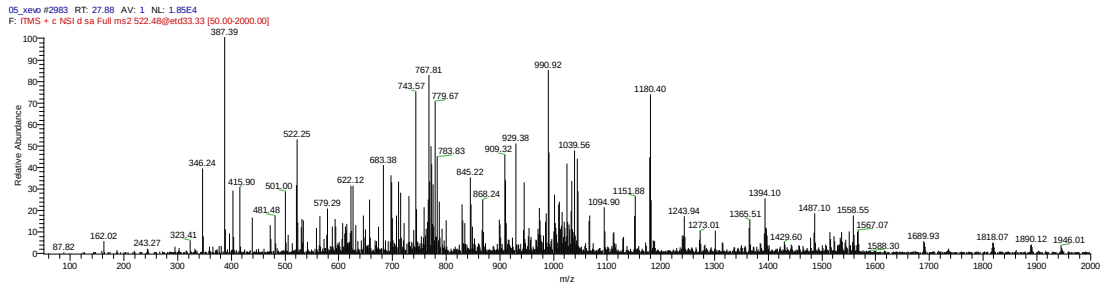

FIGURE 12.5.7. **LC-MS/MS analysis of JMJD2E-treated H4R3(me2s)$_{1-30}$: SGR(ms2s)GKGGKGLGKGGAKRHRKVLRDNIQGIT.** (A) LC-MS chromatogram. Fragmentation of the unmodified peptide (m/z = 522.48) by applying (B) CID and (C) ETD. Results represent technical triplicate (n = 3).

A

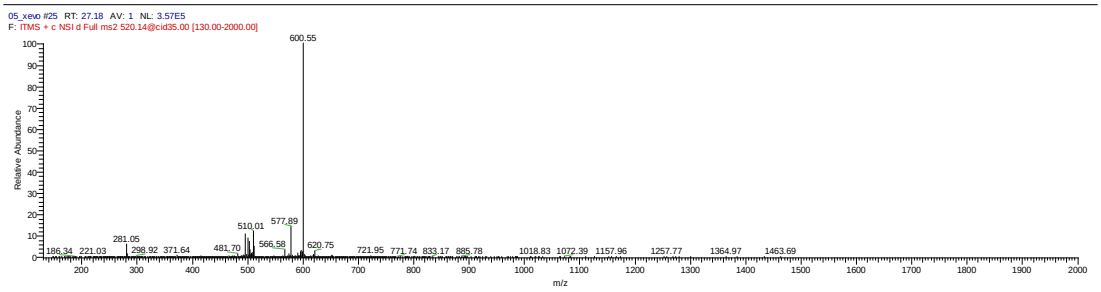

B

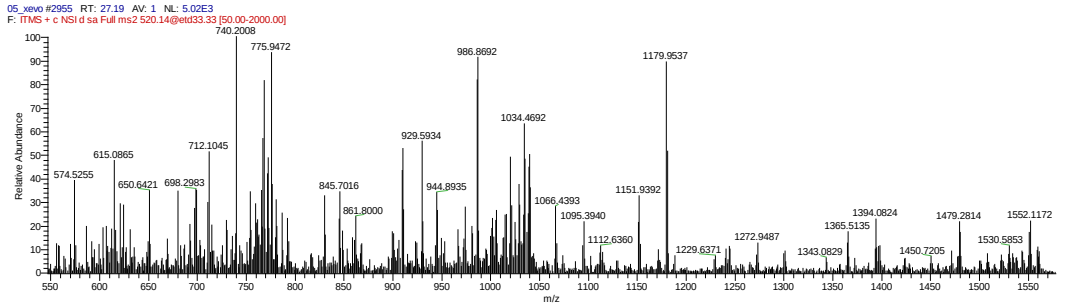

FIGURE 12.5.8. **LC-MS/MS analysis of JMJD2E-treated H4R3(me2s)$_{1\text{-}30}$: SGR(ms2s)GKGGKGLGKGGAKRHRKVLRDNIQGIT.** Fragmentation of the demethylated peptide (m/z = 520.14) by applying (A) CID and (B) ETD. Results represent technical triplicate (n = 3).

A

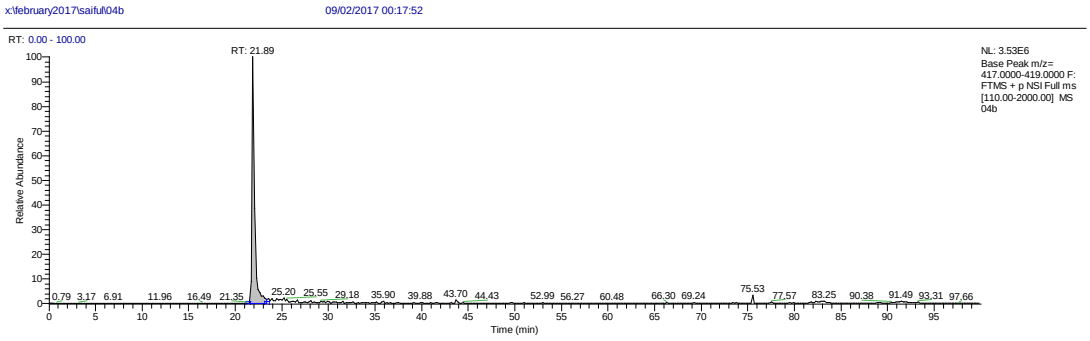

B

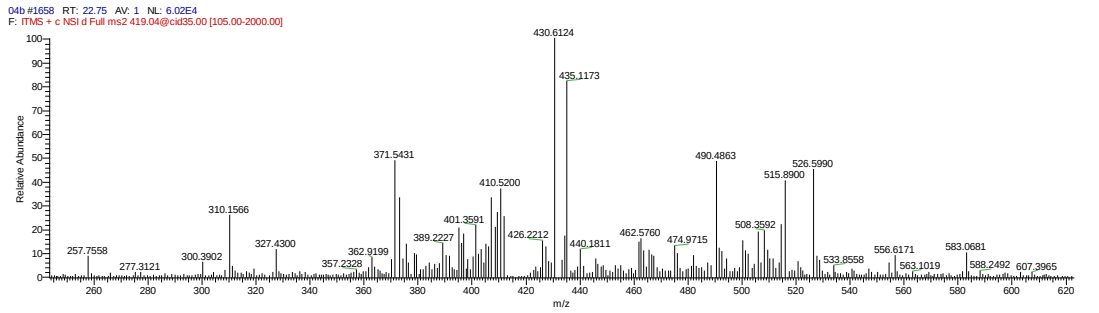

C

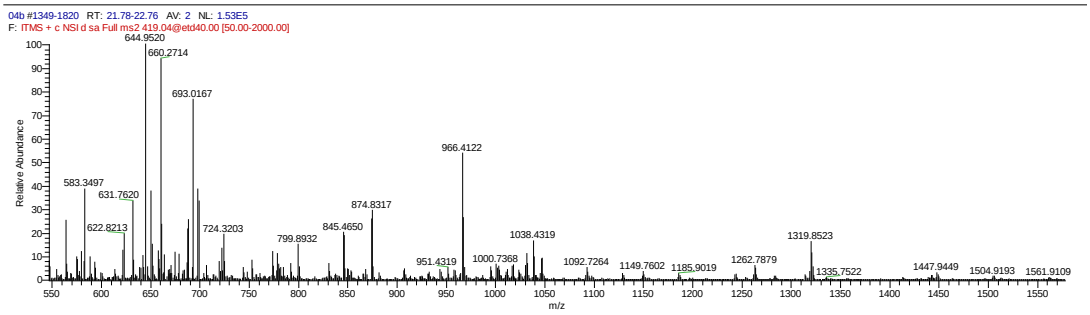

FIGURE 12.5.9. **LC-MS/MS analysis of H4R3(me2s)$_{1-19}$: SGR(ms2s)GKGGKGLGK GGAKRHK-Biotin without enzyme treatment.** (A) LC-MS chromatogram. Fragmentation of the peptide (m/z = 419.04) by applying (B) CID and (C) ETD. Results represent technical triplicate (n = 3).

A

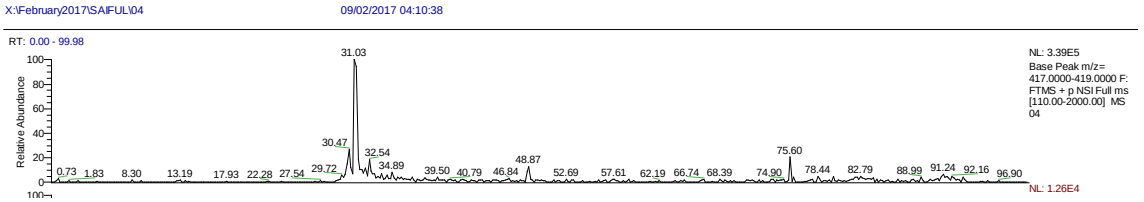

B

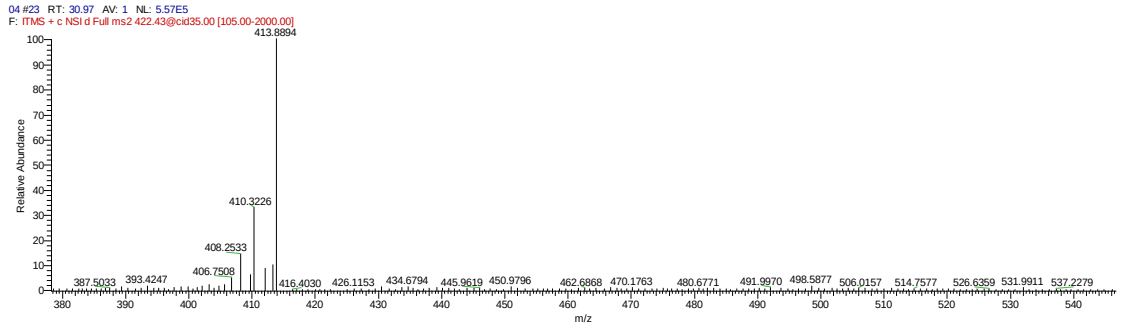

C

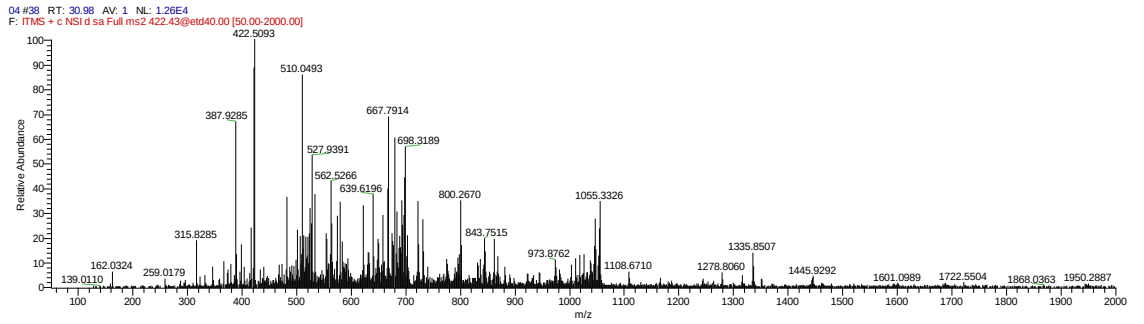

FIGURE 12.5.10. **LC-MS/MS analysis of JMJD6-treated H4R3(me2s)$_{1-19}$: SGR(ms2s)GKGGKGLGKGGAKRHK-Biotin.** (A) LC-MS chromatogram. Fragmentation of the hydroxylated peptide (m/z = 422.43) by applying (B) CID and (C) ETD. Results represent technical triplicate (n = 3).

A

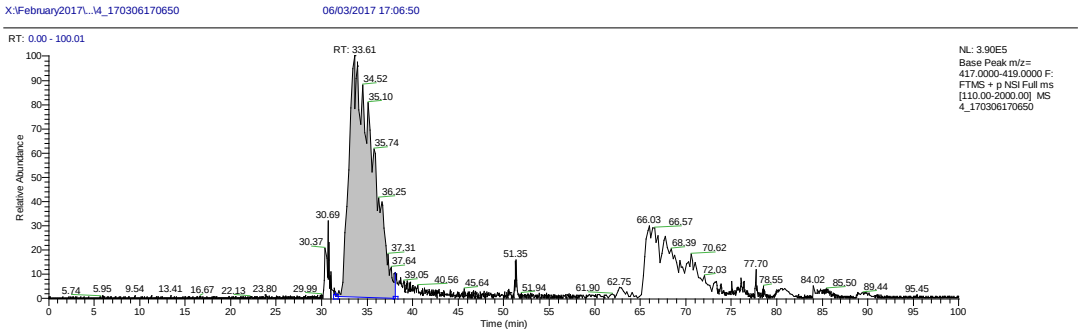

B

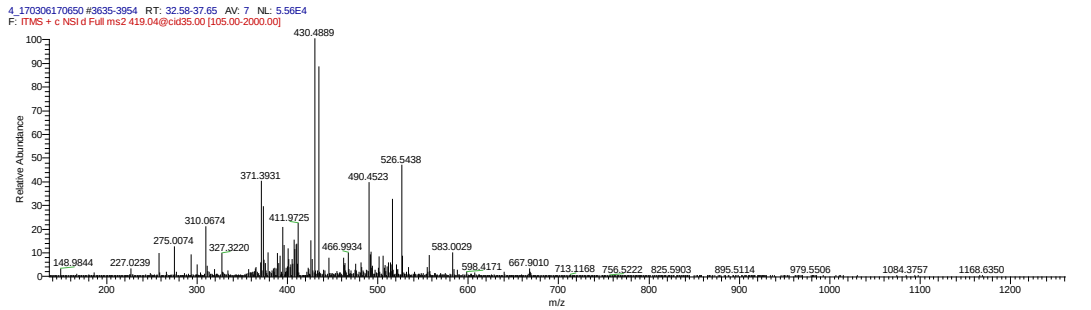

C

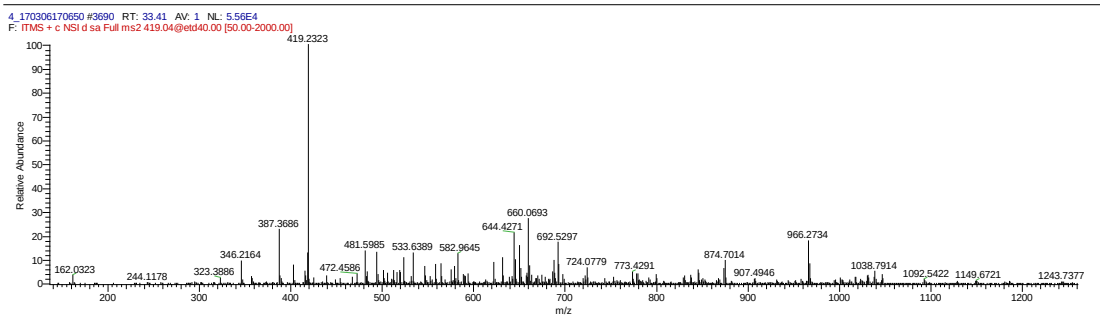

FIGURE 12.5.11. **LC-MS/MS analysis of JMJD2E-treated H4R3(me2s)$_{1-19}$: SGR(ms2s)GKGGKGLGKGGAKRHK-Biotin.** (A) LC-MS chromatogram. Fragmentation of the unmodified peptide (m/z = 419.04) by applying (B) CID and (C) ETD. Results represent technical triplicate (n = 3).

Appendix 06

Table 12.1. List of *IC_{50}* values/inhibition constants of the HPPD inhibitors reported in the literatures.

Compound	Chemical Structures	Functional Groups	IC_{50}/K_i (µM)	Source	Method
Usnic Acid (145)	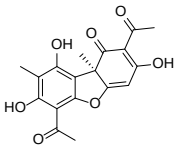	-	0.07/ -	*A. thaliana*	HPLC, monitoring the formation of HMGA
Pinocembrin (130)	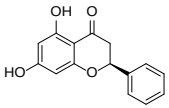	-	73/13.7	Pig liver	
Leptospermone (146)	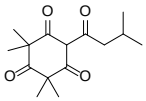	-	3.1/ -	*A. thaliana*	HPLC, monitoring the formation of HMGA
Grandiflorone (146)	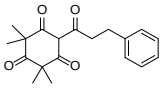	-	0.22/ -	*A. thaliana*	
HPPA Analogues (147)	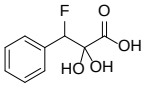	-	10/ -	Pig liver	Spectrophotometry/ Enol borate method
Triketone Derivatives	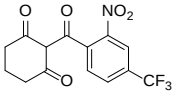 Nitisinone/NTBC (131)		0.04	Pig liver	Spectrophotometry/ Enol borate method
	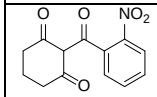 NTBC analogue 1 (131)		0.16		

	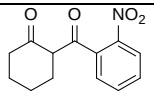 NTBC analogue 2 (131)		0.7		
	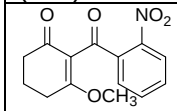 NTBC analogue 3 (131)		52		
	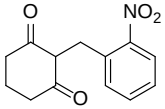 NTBC analogue 4 (131)		126		
	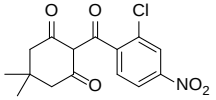 NTBC analogue 5 (131)		36		
	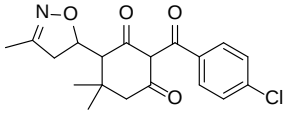 NTBC analogue 6 (131)		60		
Benzoylcyclohexane-1,3-doine derivatives (148)	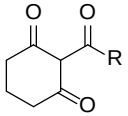 NTBC analogue	R = iPr	93/ -	Pig liver	Spectrophotometry/ Enol borate method
		R = cPr	6/ -		

Cyclohex-2-en-1-one esters (149)	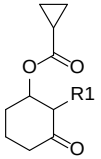	n = 1, R1 = H n = 1, R1 = Cl n = 1, R1 = Br n = 0, R1 = H	0.03 0.015 0.028 0.07	Pig liver	Spectrophotometry/ Enol borate method
Benzoyl-benzothiazines (130)	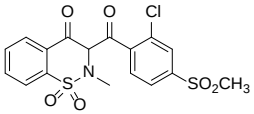		0.48/ -	*A. thaliana*	Spectrophotometry/ Enol borate method
Pyrazole-Quinazolone (130)	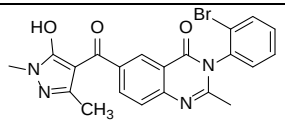		0.011	*H. sapiens*	Spectrophotometry/ Enol borate method
Pyrazole-Benzimidazolone (130)	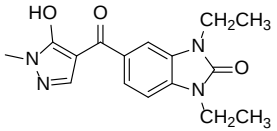		0.021	*H. sapiens*	Spectrophotometry/ Enol borate method

Appendix 07

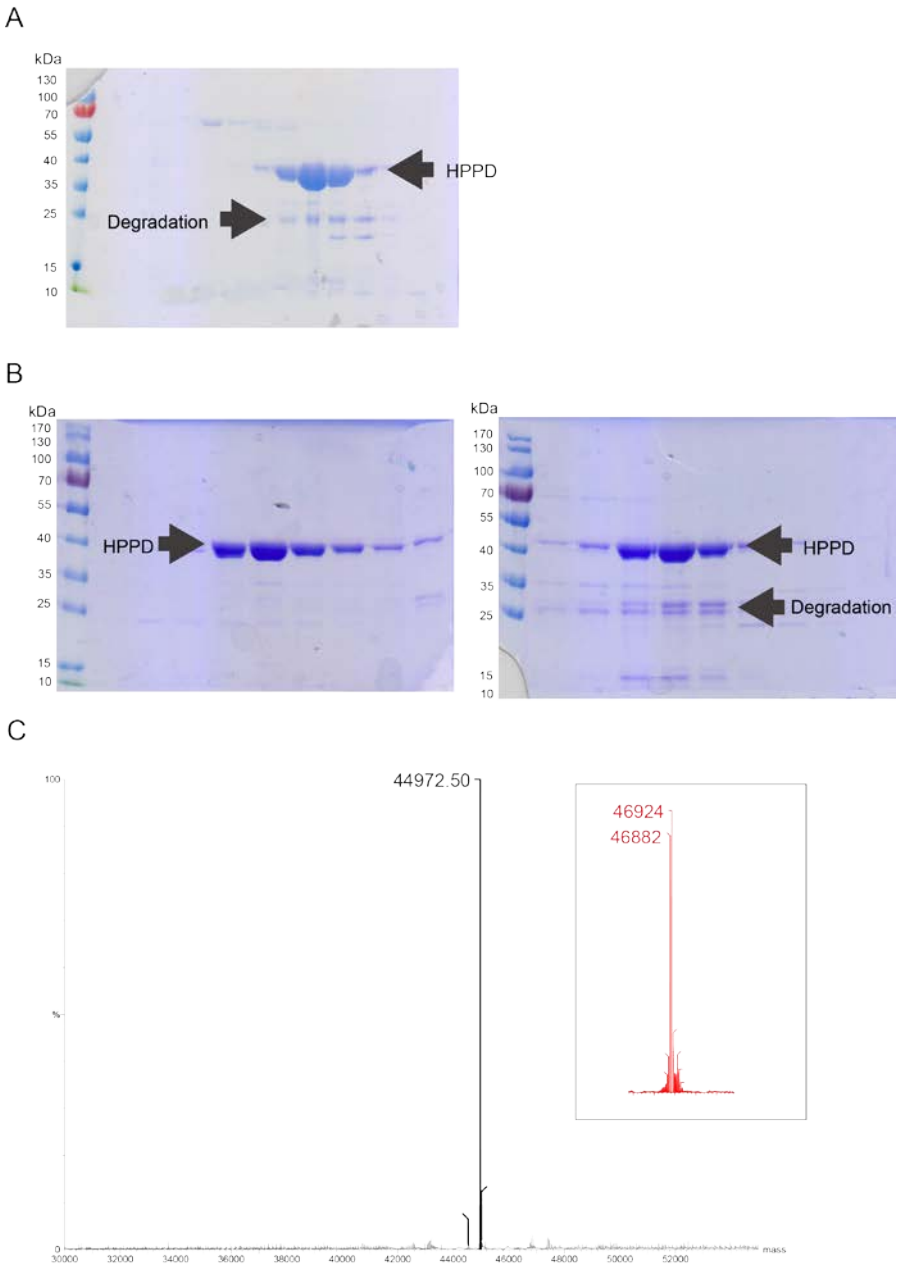

FIGURE 12.6. **Analysis of purified human HPPD by SDS-PAGE and mass spectrometry**. (A) SDS-PAGE gel showing the bands corresponding to human HPPD and possibly degraded products. (B) SDS-PAGE gels showing the bands corresponding to human HPPD purified by HisTrap followed by SEC (left gel) and finally Ion-exchange chromatography (right gel). (C) Mass spectra of human HPPD with and without the His_6-tag.

Appendix 08

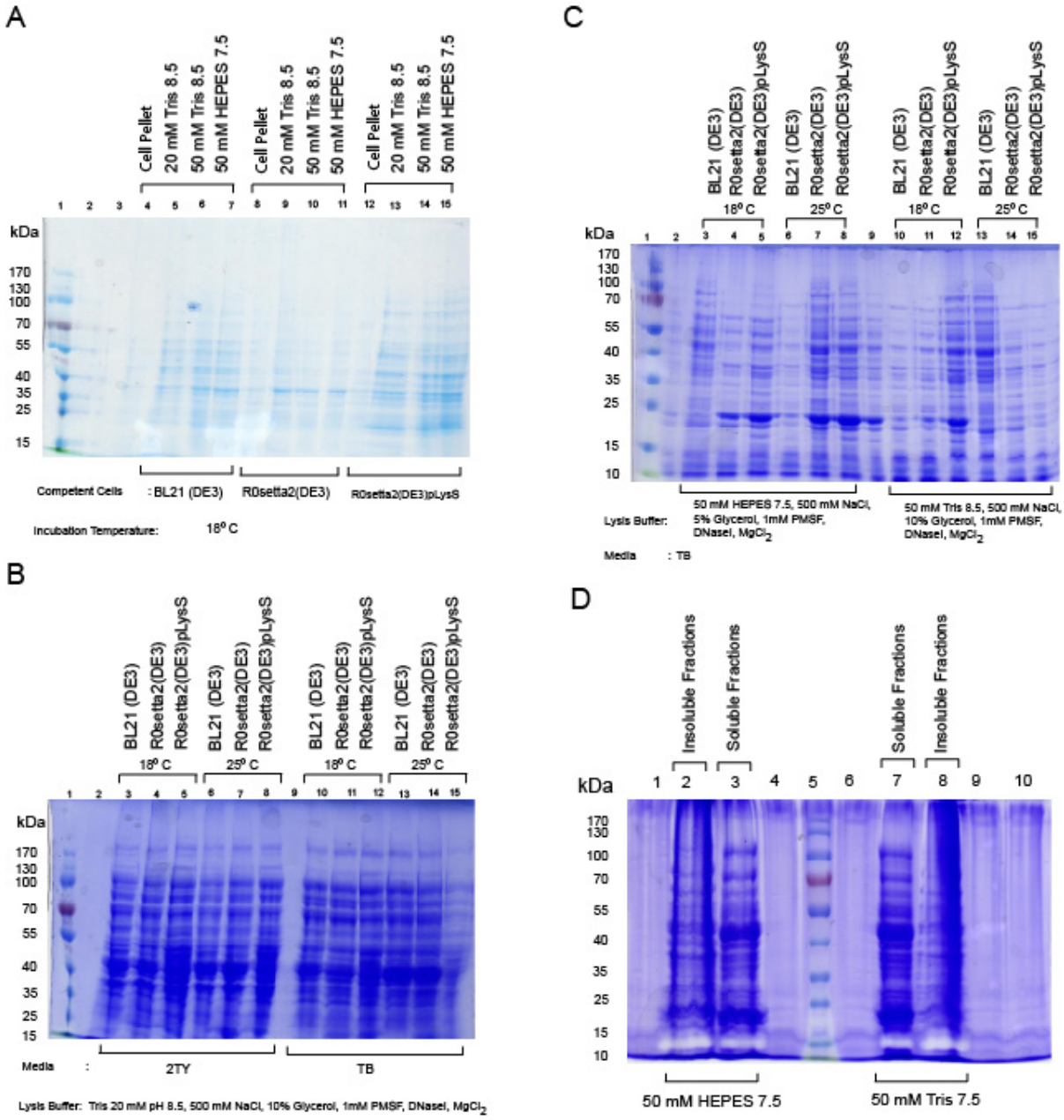

FIGURE 12.7. **Expression and purification trials of human HPPD.**

CHAPTER 13: References

1. Schofield, C. J., and Zhang, Z. (1999) Structural and mechanistic studies on 2-oxoglutarate-dependent oxygenases and related enzymes. *Curr. Opin. Struct. Biol.* **9**, 722-731

2. Schofield, C. J., and Ratcliffe, P. J. (2004) Oxygen sensing by HIF hydroxylases. *Nat. Rev. Mol. Cell Biol.* **5**, 343-354

3. Islam, M. S., Hopkinson, R., Leissing, T. M., Chowdhury, R., and Schofield, C. J. (2017) 2-Oxoglutarate dependent oxygenases. *Ann. Rev. Biochem*. **87.**

4. Rose, N. R., McDonough, M. A., King, O. N. F., Kawamura, A., and Schofield, C. J. (2011) Inhibition of 2-oxoglutarate dependent oxygenases. *Chem. Soc. Rev.* **40**, 4364-4397

5. Franklin, T. J. (1997) Therapeutic approaches to organ fibrosis. *Int. J. Biochem. & Cell Biol.* **29**, 79-89

6. Myllyharju, J. (2015) CHAPTER 5 Collagen Hydroxylases. in *2-Oxoglutarate-Dependent Oxygenases*, The Royal Society of Chemistry. pp 149-168

7. Myllyharju, J., and Kivirikko, K. I. (2001) Collagens and collagen-related diseases. *Ann. Med.* **33**, 7-21

8. McDonough, M. A., Loenarz, C., Chowdhury, R., Clifton, I. J., and Schofield, C. J. (2010) Structural studies on human 2-oxoglutarate dependent oxygenases. *Curr. Opin. Struct. Biol.* **20**, 659-672

9. Zhang, Z., Ren, J., Harlos, K., McKinnon, C. H., Clifton, I. J., and Schofield, C. J. (2002) Crystal structure of a clavaminate synthase-Fe(II)-2-oxoglutarate-substrate-NO complex: evidence for metal centered rearrangements. *FEBS Lett.* **517**, 7-12

10. Hausinger, R. P. (2004) FeII/alpha-ketoglutarate-dependent hydroxylases and related enzymes. *Crit. Rev. Biochem. Mol. Biol.* **39**, 21-68

11. Loenarz, C., and Schofield, C. J. (2008) Expanding chemical biology of 2-oxoglutarate oxygenases. *Nat. Chem. Biol.* **4**, 152-156

12. Han, M. V., and Zmasek, C. M. (2009) phyloXML: XML for evolutionary biology and comparative genomics. *BMC Bioinformatics* **10**, 356

13. Larkin, M. A., Blackshields, G., Brown, N. P., Chenna, R., McGettigan, P. A., McWilliam, H., Valentin, F., Wallace, I. M., Wilm, A., Lopez, R., Thompson, J. D.,

Gibson, T. J., and Higgins, D. G. (2007) Clustal W and Clustal X version 2.0. *Bioinformatics* **23**, 2947-2948

14. Klose, R. J., Kallin, E. M., and Zhang, Y. (2006) JmjC-domain-containing proteins and histone demethylation. *Nat. Rev. Gen.* **7**, 715-727

15. Moran, G. R. (2005) 4-Hydroxyphenylpyruvate dioxygenase. *Arch. Biochem. Biophys.* **433**, 117-128

16. Webby, C. J., Wolf, A., Gromak, N., Dreger, M., Kramer, H., Kessler, B., Nielsen, M. L., Schmitz, C., Butler, D. S., Yates, J. R., 3rd, Delahunty, C. M., Hahn, P., Lengeling, A., Mann, M., Proudfoot, N. J., Schofield, C. J., and Bottger, A. (2009) Jmjd6 catalyses lysyl-hydroxylation of U2AF65, a protein associated with RNA splicing. *Science* **325**, 90-93

17. Wang, F., He, L., Huangyang, P., Liang, J., Si, W., Yan, R., Han, X., Liu, S., Gui, B., Li, W., Miao, D., Jing, C., Liu, Z., Pei, F., Sun, L., and Shang, Y. (2014) JMJD6 promotes colon carcinogenesis through negative regulation of p53 by hydroxylation. *PLoS Biol.* **12**, e1001819

18. Alahari, S., Post, M., and Caniggia, I. (2015) Jumonji Domain Containing Protein 6: A Novel Oxygen Sensor in the Human Placenta. *Endocrinology* **156**, 3012-3025

19. Marcolovic, S., et al. (2017) (3S)-Lysyl hydroxylation of TRAFAC GTPases is catalysed by the human Jumonji-C oxygenase JMJD7. *Nat Chem. Biol*.: Submitted

20. Feng, T., Yamamoto, A., Wilkins, S. E., Sokolova, E., Yates, L. A., Munzel, M., Singh, P., Hopkinson, R. J., Fischer, R., Cockman, M. E., Shelley, J., Trudgian, D. C., Schodel, J., McCullagh, J. S., Ge, W., Kessler, B. M., Gilbert, R. J., Frolova, L. Y., Alkalaeva, E., Ratcliffe, P. J., Schofield, C. J., and Coleman, M. L. (2014) Optimal translational termination requires C4 lysyl hydroxylation of eRF1. *Mol. Cell.* **53**, 645-654

21. Schofield, C. J., and Ratcliffe, P. J. (2005) Signalling hypoxia by HIF hydroxylases. *Biochem. Biophys. Res. Commun.* **338**, 617-626

22. Chowdhury, R., Leung, I. K., Tian, Y. M., Abboud, M. I., Ge, W., Domene, C., Cantrelle, F. X., Landrieu, I., Hardy, A. P., Pugh, C. W., Ratcliffe, P. J., Claridge, T. D., and Schofield, C. J. (2016) Structural basis for oxygen degradation domain selectivity of the HIF prolyl hydroxylases. *Nat. Commun.* **7**, 12673

23. Hewitson, K. S., McNeill, L. A., Riordan, M. V., Tian, Y. M., Bullock, A. N., Welford, R. W., Elkins, J. M., Oldham, N. J., Bhattacharya, S., Gleadle, J. M.,

Ratcliffe, P. J., Pugh, C. W., and Schofield, C. J. (2002) Hypoxia-inducible factor (HIF) asparagine hydroxylase is identical to factor inhibiting HIF (FIH) and is related to the cupin structural family. *J. Biol. Chem.* **277**, 26351-26355

24. Singleton, R. S., Liu-Yi, P., Formenti, F., Ge, W., Sekirnik, R., Fischer, R., Adam, J., Pollard, P. J., Wolf, A., Thalhammer, A., Loenarz, C., Flashman, E., Yamamoto, A., Coleman, M. L., Kessler, B. M., Wappner, P., Schofield, C. J., Ratcliffe, P. J., and Cockman, M. E. (2014) OGFOD1 catalyzes prolyl hydroxylation of RPS23 and is involved in translation control and stress granule formation. *Proc. Natl. Acad. Sci. U.S.A.* **111**, 4031-4036

25. Chowdhury, R., Sekirnik, R., Brissett, N. C., Krojer, T., Ho, C. H., Ng, S. S., Clifton, I. J., Ge, W., Kershaw, N. J., Fox, G. C., Muniz, J. R., Vollmar, M., Phillips, C., Pilka, E. S., Kavanagh, K. L., von Delft, F., Oppermann, U., McDonough, M. A., Doherty, A. J., and Schofield, C. J. (2014) Ribosomal oxygenases are structurally conserved from prokaryotes to humans. *Nature* **510**, 422-426

26. Wilkins, S., Islam, M. S., Markolovic, S., Hopkinson, R., Ganon, J., Ge, W., Schofield, C. J., Chowdhury, R. (2017) JMJD5 is a human arginyl C-3 hydroxylase. *Nat. Commun.* : Submitted

27. Youn, M.-Y., Yokoyama, A., Fujiyama-Nakamura, S., Ohtake, F., Minehata, K.-i., Yasuda, H., Suzuki, T., Kato, S., and Imai, Y. (2012) JMJD5, a Jumonji C (JmjC) Domain-containing Protein, Negatively Regulates Osteoclastogenesis by Facilitating NFATc1 Protein Degradation. *J. Biol. Chem.* **287**, 12994-13004

28. Walport, L. J., Hopkinson, R. J., Chowdhury, R., Schiller, R., Ge, W., Kawamura, A., and Schofield, C. J. (2016) Arginine demethylation is catalysed by a subset of JmjC histone lysine demethylases. *Nat. Commun.* **7**, 11974

29. Chang, B., Chen, Y., Zhao, Y., and Bruick, R. K. (2007) JMJD6 is a histone arginine demethylase. *Science* **318**, 444-447

30. Poulard, C., Rambaud, J., Hussein, N., Corbo, L., and Le Romancer, M. (2014) JMJD6 Regulates ERα Methylation on Arginine. *PloS one* **9**, e87982

31. Lawrence, P., Conderino, J. S., and Rieder, E. (2014) Redistribution of demethylated RNA helicase A during foot-and-mouth disease virus infection: Role of Jumonji C-domain containing protein 6 in RHA demethylation. *Virology* **452–453**, 1-11

32. Gao, W.-w., Xiao, R.-q., Peng, B.-l., Xu, H.-t., Shen, H.-f., Huang, M.-f., Shi, T.-t., Yi, J., Zhang, W.-j., Wu, X.-n., Gao, X., Lin, X.-z., Dorrestein, P. C., Rosenfeld, M. G., and Liu, W. (2015) Arginine methylation of HSP70 regulates retinoid acid-mediated RARβ2 gene activation. *Proc. Natl. Acad. Sci. U.S.A.* **112**, E3327-E3336

33. Bottger, A., Islam, M. S., Chowdhury, R., Schofield, C. J., and Wolf, A. (2015) The oxygenase Jmjd6--a case study in conflicting assignments. *Biochem. J.* **468**, 191-202

34. Fadok, V. A., Bratton, D. L., Rose, D. M., Pearson, A., Ezekewitz, R. A., and Henson, P. M. (2000) A receptor for phosphatidylserine-specific clearance of apoptotic cells. *Nature* **405**, 85-90

35. Cikala, M., Alexandrova, O., David, C. N., Pröschel, M., Stiening, B., Cramer, P., and Böttger, A. (2004) The phosphatidylserine receptor from Hydra is a nuclear protein with potential Fe(II) dependent oxygenase activity. *BMC Cell Biol.* **5**, 26

36. Mantri, M., Krojer, T., Bagg, E. A., Webby, C. A., Butler, D. S., Kochan, G., Kavanagh, K. L., Oppermann, U., McDonough, M. A., and Schofield, C. J. (2010) Crystal Structure of the 2-Oxoglutarate- and Fe(II)-Dependent Lysyl Hydroxylase JMJD6. *J. Mol. Biol.* **401**, 211-222

37. Böse, J., Gruber, A. D., Helming, L., Schiebe, S., Wegener, I., Hafner, M., Beales, M., Köntgen, F., and Lengeling, A. (2004) The phosphatidylserine receptor has essential functions during embryogenesis but not in apoptotic cell removal. *J. Biol.* **3**, 15

38. Boeckel, J.-N., Guarani, V., Koyanagi, M., Roexe, T., Lengeling, A., Schermuly, R. T., Gellert, P., Braun, T., Zeiher, A., and Dimmeler, S. (2011) Jumonji domain-containing protein 6 (Jmjd6) is required for angiogenic sprouting and regulates splicing of VEGF-receptor 1. *Proc. Natl. Acad. Sci. U.S.A.* **108**, 3276-3281

39. Liu, W., Ma, Q., Wong, K., Li, W., Ohgi, K., Zhang, J., Aggarwal, A. K., and Rosenfeld, M. G. (2013) Brd4 and JMJD6-associated anti-pause enhancers in regulation of transcriptional pause release. *Cell* **155**, 1581-1595

40. Unoki, M., Masuda, A., Dohmae, N., Arita, K., Yoshimatsu, M., Iwai, Y., Fukui, Y., Ueda, K., Hamamoto, R., Shirakawa, M., Sasaki, H., and Nakamura, Y. (2013) Lysyl 5-hydroxylation, a novel histone modification, by Jumonji domain containing 6 (JMJD6). *J. Biol. Chem.* **288**, 6053-6062

41. Ishimura, A., Terashima, M., Tange, S., and Suzuki, T. (2016) Jmjd5 functions as a regulator of p53 signaling during mouse embryogenesis. *Cell Tissue Res.* **363**, 723-733

42. Oh, S., and Janknecht, R. (2012) Histone demethylase JMJD5 is essential for embryonic development. *Biochem. Biophys. Res. Commun.* **420**, 61-65

43. Jones, M. A., Covington, M. F., DiTacchio, L., Vollmers, C., Panda, S., and Harmer, S. L. (2010) Jumonji domain protein JMJD5 functions in both the plant and human circadian systems. *Proc. Natl. Acad. Sci. U. S. A.* **107**, 21623-21628

44. Wang, H.-J., Hsieh, Y.-J., Cheng, W.-C., Lin, C.-P., Lin, Y.-s., Yang, S.-F., Chen, C.-C., Izumiya, Y., Yu, J.-S., Kung, H.-J., and Wang, W.-C. (2014) JMJD5 regulates PKM2 nuclear translocation and reprograms HIF-1α–mediated glucose metabolism. *Proceedings of the National Academy of Sciences* **111**, 279-284

45. Marcon, E., Ni, Z., Pu, S., Turinsky, Andrei L., Trimble, Sandra S., Olsen, Jonathan B., Silverman-Gavrila, R., Silverman-Gavrila, L., Phanse, S., Guo, H., Zhong, G., Guo, X., Young, P., Bailey, S., Roudeva, D., Zhao, D., Hewel, J., Li, J., Gräslund, S., Paduch, M., Kossiakoff, Anthony A., Lupien, M., Emili, A., Wodak, Shoshana J., and Greenblatt, J. (2014) Human-Chromatin-Related Protein Interactions Identify a Demethylase Complex Required for Chromosome Segregation. *Cell Rep.* **8**, 297-310

46. Huang, X., Zhang, S., Qi, H., Wang, Z., Chen, H.-W., Shao, J., and Shen, J. (2015) JMJD5 interacts with p53 and negatively regulates p53 function in control of cell cycle and proliferation. *Biochimica et Biophysica Acta (BBA) - Mol. Cell Res.* **1853**, 2286-2295

47. Zhang, R., Huang, Q., Li, Y., Song, Y., and Li, Y. (2015) JMJD5 is a potential oncogene for colon carcinogenesis. *Int. J. Clin. Exp. Pathol.* **8**, 6482-6489

48. Zhao, Z., Sun, C., Li, F., Han, J., Li, X., and Song, Z. (2015) Overexpression of histone demethylase JMJD5 promotes metastasis and indicates a poor prognosis in breast cancer. *Int. J. Clin. Exp. Pathol.* **8**, 10325-10334

49. Del Rizzo, P. A., Krishnan, S., and Trievel, R. C. (2012) Crystal Structure and Functional Analysis of JMJD5 Indicate an Alternate Specificity and Function. *Mol. Cell Biol.* **32**, 4044-4052

50. Cui, P., Qin, B., Liu, N., Pan, G., and Pei, D. (2004) Nuclear localization of the phosphatidylserine receptor protein via multiple nuclear localization signals. *Exp. Cell Res.* **293**

51. Wolf, A., Mantri, M., Heim, A., Müller, U., Fichter, E., Mackeen, Mukram M., Schermelleh, L., Dadie, G., Leonhardt, H., Vénien-Bryan, C., Kessler, Benedikt M., Schofield, Christopher J., and Böttger, A. (2013) The polyserine domain of the lysyl-5 hydroxylase Jmjd6 mediates subnuclear localization. *Biochem. J.* **453**, 357-370

52. Ebbinghaus, S., Dhar, A., McDonald, J. D., and Gruebele, M. (2010) Protein folding stability and dynamics imaged in a living cell. *Nat. Meth.* **7**, 319-323

53. Greenfield, N. J. (2007) Using circular dichroism collected as a function of temperature to determine the thermodynamics of protein unfolding and binding interactions. *Nat. Protocols* **1**, 2527-2535

54. Dalvit, C., Flocco, M., Knapp, S., Mostardini, M., Perego, R., Stockman, B. J., Veronesi, M., and Varasi, M. (2002) High-Throughput NMR-Based Screening with Competition Binding Experiments. *J. Am. Chem. Soc.* **124**, 7702-7709

55. Leung, I. K., Demetriades, M., Hardy, A. P., Lejeune, C., Smart, T. J., Szollossi, A., Kawamura, A., Schofield, C. J., and Claridge, T. D. (2013) Reporter ligand NMR screening method for 2-oxoglutarate oxygenase inhibitors. *J. Med. Chem.* **56**, 547-555

56. Carr, H. Y., and Purcell, E. M. (1954) Effects of Diffusion on Free Precession in Nuclear Magnetic Resonance Experiments. *Phys. Rev.* **94**, 630-638

57. Meiboom, S., and Gill, D. (1958) Modified Spin-Echo Method for Measuring Nuclear Relaxation Times. *Rev. Sci. Instr.* **29**, 688-691

58. Morton, C. J., Pugh, D. J. R., Brown, E. L. J., Kahmann, J. D., Renzoni, D. A. C., and Campbell, I. D. (1996) Solution structure and peptide binding of the SH3 domain from human Fyn. *Structure* **4**, 705-714

59. Horita, S., Scotti, J. S., Thinnes, C., Mottaghi-Taromsari, Y. S., Thalhammer, A., Ge, W., Aik, W., Loenarz, C., Schofield, C. J., and McDonough, M. A. (2015) Structure of the ribosomal oxygenase OGFOD1 provides insights into the regio- and stereoselectivity of prolyl hydroxylases. *Structure* **23**, 639-652

60. Tarhonskaya, H., Hardy, A. P., Howe, E. A., Loik, N. D., Kramer, H. B., McCullagh, J. S. O., Schofield, C. J., and Flashman, E. (2015) Kinetic

Investigations of the Role of Factor Inhibiting Hypoxia-Inducible Factor (FIH) as an Oxygen Sensor. *J. Biol. Chem.*

61. Tarhonskaya, H., Nowak, R. P., Johansson, C., Szykowska, A., Tumber, A., Hancock, R. L., Lang, P., Flashman, E., Oppermann, U., Schofield, C. J., and Kawamura, A. (2017) Studies on the Interaction of the Histone Demethylase KDM5B with Tricarboxylic Acid Cycle Intermediates. *J. Mol. Biol.*

62. Clifton, I. J., McDonough, M. A., Ehrismann, D., Kershaw, N. J., Granatino, N., and Schofield, C. J. (2006) Structural studies on 2-oxoglutarate oxygenases and related double-stranded beta-helix fold proteins. *J. Inorg. Biochem.* **100**, 644-669

63. Leung, I. K., Krojer, T. J., Kochan, G. T., Henry, L., von Delft, F., Claridge, T. D., Oppermann, U., McDonough, M. A., and Schofield, C. J. (2010) Structural and mechanistic studies on gamma-butyrobetaine hydroxylase. *Chem. Biol.* **17**, 1316-1324

64. Elkins, J. M., Hewitson, K. S., McNeill, L. A., Seibel, J. F., Schlemminger, I., Pugh, C. W., Ratcliffe, P. J., and Schofield, C. J. (2003) Structure of factor-inhibiting hypoxia-inducible factor (HIF) reveals mechanism of oxidative modification of HIF-1 alpha. *J. Biol. Chem.* **278**, 1802-1806

65. Andrews, P. (1964) Estimation of the molecular weights of proteins by Sephadex gel-filtration. *Biochem. J.* **91**, 222-233

66. Randelj, O., Rassow, J., and Motz, C. (2007) Separation of Proteins by Blue Native Electrophoresis. in *Protein Targeting Protocols* (van der Giezen, M. ed.), Humana Press, Totowa, NJ. pp 417-427

67. Almén, M. S., Nordström, K. J., Fredriksson, R., and Schiöth, H. B. (2009) Mapping the human membrane proteome: a majority of the human membrane proteins can be classified according to function and evolutionary origin. *BMC Biol.* **7**, 50

68. Gault, J., Donlan, J. A. C., Liko, I., Hopper, J. T. S., Gupta, K., Housden, N. G., Struwe, W. B., Marty, M. T., Mize, T., Bechara, C., Zhu, Y., Wu, B., Kleanthous, C., Belov, M., Damoc, E., Makarov, A., and Robinson, C. V. (2016) High-resolution mass spectrometry of small molecules bound to membrane proteins. *Nat. Meth.* **13**, 333-336

69. Yi, J., Shen, H.-F., Qiu, J.-S., Huang, M.-F., Zhang, W.-J., Ding, J.-C., Zhu, X.-Y., Zhou, Y., Fu, X.-D., and Liu, W. (2017) JMJD6 and U2AF65 co-regulate

alternative splicing in both JMJD6 enzymatic activity dependent and independent manner. *Nucleic Acids Res.* **45**, 3503-3518

70. Heim, A., Grimm, C., Müller, U., Häußler, S., Mackeen, M. M., Merl, J., Hauck, S. M., Kessler, B. M., Schofield, C. J., Wolf, A., and Böttger, A. (2014) Jumonji domain containing protein 6 (Jmjd6) modulates splicing and specifically interacts with arginine–serine-rich (RS) domains of SR- and SR-like proteins. *Nucleic Acids Res.* **42**, 7833-7850

71. Tarhonskaya, H., Chowdhury, R., Leung, I. K., Loik, N. D., McCullagh, J. S., Claridge, T. D., Schofield, C. J., and Flashman, E. (2014) Investigating the contribution of the active site environment to the slow reaction of hypoxia-inducible factor prolyl hydroxylase domain 2 with oxygen. *Biochem. J.* **463**, 363-372

72. Koivunen, P., Hirsilä, M., Kivirikko, K. I., and Myllyharju, J. (2006) The Length of Peptide Substrates Has a Marked Effect on Hydroxylation by the Hypoxia-inducible Factor Prolyl 4-Hydroxylases. *J. Biol. Chem.* **281**, 28712-28720

73. Bieging, K. T., Mello, S. S., and Attardi, L. D. (2014) Unravelling mechanisms of p53-mediated tumour suppression. *Nat. Rev. Cancer* **14**, 359-370

74. Saibil, H. (2013) Chaperone machines for protein folding, unfolding and disaggregation. *Nat. Rev. Mol. Cell Biol.* **14**, 630-642

75. Hong, X., Zang, J., White, J., Wang, C., Pan, C. H., Zhao, R., Murphy, R. C., Dai, S., Henson, P., Kappler, J. W., Hagman, J., and Zhang, G. (2010) Interaction of JMJD6 with single-stranded RNA. *Proc. Natl. Acad. Sci. U. S. A.* **107**, 14568-14572

76. Niesen, F. H., Berglund, H., and Vedadi, M. (2007) The use of differential scanning fluorimetry to detect ligand interactions that promote protein stability. *Nat. Protocols* **2**, 2212-2221

77. Bleijlevens, B., Shivarattan, T., Flashman, E., Yang, Y., Simpson, P. J., Koivisto, P., Sedgwick, B., Schofield, C. J., and Matthews, S. J. (2008) Dynamic states of the DNA repair enzyme AlkB regulate product release. *EMBO reports* **9**, 872-877

78. Dessau, M. A., and Modis, Y. (2011) Protein Crystallization for X-ray Crystallography. *J. Visual. Exp.* , 2285

79. Adams, P. D., Grosse-Kunstleve, R. W., Hung, L.-W., Ioerger, T. R., McCoy, A. J., Moriarty, N. W., Read, R. J., Sacchettini, J. C., Sauter, N. K., and Terwilliger, T. C.

(2002) PHENIX: building new software for automated crystallographic structure determination. *Acta Cryst. Section D* **58**, 1948-1954

80. Terwilliger, T. (2003) Improving macromolecular atomic models at moderate resolution by automated iterative model building, statistical density modification and refinement. *Acta Cryst. Section D* **59**, 1174-1182

81. Han, G., Li, J., Wang, Y., Li, X., Mao, H., Liu, Y., and Chen, C. D. (2012) The hydroxylation activity of Jmjd6 is required for its homo-oligomerization. *J. Cell. Biochem.* **113**, 1663-1670

82. Krissinel, E., and Henrick, K. (2007) Inference of Macromolecular Assemblies from Crystalline State. *J. Mol. Biol.* **372**, 774-797

83. Maxwell, P. H., and Eckardt, K.-U. (2016) HIF prolyl hydroxylase inhibitors for the treatment of renal anaemia and beyond. *Nat. Rev. Nephrol.* **12**, 157-168

84. McAllister, T. E., England, K. S., Hopkinson, R. J., Brennan, P. E., Kawamura, A., and Schofield, C. J. (2016) Recent Progress in Histone Demethylase Inhibitors. *J. Med. Chem.* **59**, 1308-1329

85. Henry, L., Leung, I. K., Claridge, T. D., and Schofield, C. J. (2012) γ-Butyrobetaine hydroxylase catalyses a Stevens type rearrangement. *Bioorg. Med. Chem. Lett.* **22**, 4975-4978

86. Rydzik, A. M., Leung, I. K., Kochan, G. T., Loik, N. D., Henry, L., McDonough, M. A., Claridge, T. D., and Schofield, C. J. (2014) Comparison of the substrate selectivity and biochemical properties of human and bacterial gamma-butyrobetaine hydroxylase. *Org. Biomol. Chem.* **12**, 6354-6358

87. King, O. N. F., Li, X. S., Sakurai, M., Kawamura, A., Rose, N. R., Ng, S. S., Quinn, A. M., Rai, G., Mott, B. T., Beswick, P., Klose, R. J., Oppermann, U., Jadhav, A., Heightman, T. D., Maloney, D. J., Schofield, C. J., and Simeonov, A. (2010) Quantitative High-Throughput Screening Identifies 8-Hydroxyquinolines as Cell-Active Histone Demethylase Inhibitors. *PloS one* **5**, e15535

88. Hewitson, K. S., Lienard, B. M., McDonough, M. A., Clifton, I. J., Butler, D., Soares, A. S., Oldham, N. J., McNeill, L. A., and Schofield, C. J. (2007) Structural and mechanistic studies on the inhibition of the hypoxia-inducible transcription factor hydroxylases by tricarboxylic acid cycle intermediates. *J. Biol. Chem.* **282**, 3293-3301

89. McNeill, L. A., Flashman, E., Buck, M. R., Hewitson, K. S., Clifton, I. J., Jeschke, G., Claridge, T. D., Ehrismann, D., Oldham, N. J., and Schofield, C. J. (2005) Hypoxia-inducible factor prolyl hydroxylase 2 has a high affinity for ferrous iron and 2-oxoglutarate. *Mol. Biosyst.* **1**, 321-324

90. Dang, L., White, D. W., Gross, S., Bennett, B. D., Bittinger, M. A., Driggers, E. M., Fantin, V. R., Jang, H. G., Jin, S., Keenan, M. C., Marks, K. M., Prins, R. M., Ward, P. S., Yen, K. E., Liau, L. M., Rabinowitz, J. D., Cantley, L. C., Thompson, C. B., Vander Heiden, M. G., and Su, S. M. (2010) Cancer-associated IDH1 mutations produce 2-hydroxyglutarate. *Nature* **465**, 966-966

91. Koivunen, P., Lee, S., Duncan, C. G., Lopez, G., Lu, G., Ramkissoon, S., Losman, J. A., Joensuu, P., Bergmann, U., Gross, S., Travins, J., Weiss, S., Looper, R., Ligon, K. L., Verhaak, R. G., Yan, H., and Kaelin, W. G., Jr. (2012) Transformation by the (R)-enantiomer of 2-hydroxyglutarate linked to EGLN activation. *Nature* **483**, 484-488

92. Yang, H., Ye, D., Guan, K.-L., and Xiong, Y. (2012) IDH1 and IDH2 mutations in tumorigenesis: mechanistic insights and clinical perspectives. *Clinical cancer research : an official journal of the American Association for Cancer Research* **18**, 5562-5571

93. Chang, K.-H., King, O. N. F., Tumber, A., Woon, E. C. Y., Heightman, T. D., McDonough, M. A., Schofield, C. J., and Rose, N. R. (2011) Inhibition of Histone Demethylases by 4-Carboxy-2,2′-Bipyridyl Compounds. *ChemMedChem* **6**, 759-764

94. Banerji, B., Conejo-Garcia, A., McNeill, L. A., McDonough, M. A., Buck, M. R. G., Hewitson, K. S., Oldham, N. J., and Schofield, C. J. (2005) The inhibition of factor inhibiting hypoxia-inducible factor (FIH) by [small beta]-oxocarboxylic acids. *Chem. Commun.* , 5438-5440

95. Hales, N. J., and Beattie, J. F. (1993) Novel inhibitors of prolyl 4-hydroxylase. 5. The intriguing structure-activity relationships seen with 2,2'-bipyridine and its 5,5'-dicarboxylic acid derivatives. *J. Med. Chem.* **36**, 3853-3858

96. Hirsilä, M., Koivunen, P., Günzler, V., Kivirikko, K. I., and Myllyharju, J. (2003) Characterization of the Human Prolyl 4-Hydroxylases That Modify the Hypoxia-inducible Factor. *J. Biol. Chem.* **278**, 30772-30780

97. Rose, N. R., Woon, E. C., Tumber, A., Walport, L. J., Chowdhury, R., Li, X. S., King, O. N., Lejeune, C., Ng, S. S., Krojer, T., Chan, M. C., Rydzik, A. M.,

Hopkinson, R. J., Che, K. H., Daniel, M., Strain-Damerell, C., Gileadi, C., Kochan, G., Leung, I. K., Dunford, J., Yeoh, K. K., Ratcliffe, P. J., Burgess-Brown, N., von Delft, F., Muller, S., Marsden, B., Brennan, P. E., McDonough, M. A., Oppermann, U., Klose, R. J., Schofield, C. J., and Kawamura, A. (2012) Plant growth regulator daminozide is a selective inhibitor of human KDM2/7 histone demethylases. *J. Med. Chem.* **55**, 6639-6643

98. Sekirnik, R., Rose, N. R., Thalhammer, A., Seden, P. T., Mecinovic, J., and Schofield, C. J. (2009) Inhibition of the histone lysine demethylase JMJD2A by ejection of structural Zn(ii). *Chem. Commun.*, 6376-6378

99. Berman, H. M., Westbrook, J., Feng, Z., Gilliland, G., Bhat, T. N., Weissig, H., Shindyalov, I. N., and Bourne, P. E. (2000) The Protein Data Bank. *Nucleic Acids Res.* **28**, 235-242

100. McDonough, M. A., McNeill, L. A., Tilliet, M., Papamicael, C. A., Chen, Q. Y., Banerji, B., Hewitson, K. S., and Schofield, C. J. (2005) Selective inhibition of factor inhibiting hypoxia-inducible factor. *J. Am. Chem. Soc.* **127**, 7680-7681

101. Rose, N. R., Woon, E. C. Y., Kingham, G. L., King, O. N. F., Mecinović, J., Clifton, I. J., Ng, S. S., Talib-Hardy, J., Oppermann, U., McDonough, M. A., and Schofield, C. J. (2010) Selective Inhibitors of the JMJD2 Histone Demethylases: Combined Nondenaturing Mass Spectrometric Screening and Crystallographic Approaches. *J. Med. Chem.* **53**, 1810-1818

102. Chowdhury, R., McDonough, M. A., Mecinovic, J., Loenarz, C., Flashman, E., Hewitson, K. S., Domene, C., and Schofield, C. J. (2009) Structural basis for binding of hypoxia-inducible factor to the oxygen-sensing prolyl hydroxylases. *Structure* **17**, 981-989

103. Conejo-Garcia, A., McDonough, M. A., Loenarz, C., McNeill, L. A., Hewitson, K. S., Ge, W., Liénard, B. M., Schofield, C. J., and Clifton, I. J. (2010) Structural basis for binding of cyclic 2-oxoglutarate analogues to factor-inhibiting hypoxia-inducible factor. *Bioorg. & Med. Chem. Lett.* **20**, 6125-6128

104. Chen, Z., Zang, J., Kappler, J., Hong, X., Crawford, F., Wang, Q., Lan, F., Jiang, C., Whetstine, J., Dai, S., Hansen, K., Shi, Y., and Zhang, G. (2007) Structural basis of the recognition of a methylated histone tail by JMJD2A. *Proc. Natl. Acad. Sci.* **104**, 10818-10823

105. Rose, N. R., Ng, S. S., Mecinović, J., Liénard, B. M. R., Bello, S. H., Sun, Z., McDonough, M. A., Oppermann, U., and Schofield, C. J. (2008) Inhibitor Scaffolds

for 2-Oxoglutarate-Dependent Histone Lysine Demethylases. *J. Med. Chem.* **51**, 7053-7056

106. Aik, W., Demetriades, M., Hamdan, M. K. K., Bagg, E. A. L., Yeoh, K. K., Lejeune, C., Zhang, Z., McDonough, M. A., and Schofield, C. J. (2013) Structural Basis for Inhibition of the Fat Mass and Obesity Associated Protein (FTO). *J. Med. Chem.* **56**, 3680-3688

107. Feng, C., Liu, Y., Wang, G., Deng, Z., Zhang, Q., Wu, W., Tong, Y., Cheng, C., and Chen, Z. (2014) Crystal Structures of the Human RNA Demethylase Alkbh5 Reveal Basis for Substrate Recognition. *J. Biol. Chem.* **289**, 11571-11583

108. Chowdhury, R., Yeoh, K. K., Tian, Y. M., Hillringhaus, L., Bagg, E. A., Rose, N. R., Leung, I. K. H., Li, X. S., Woon, E. C. Y., Yang, M., McDonough, M. A., King, O. N., Clifton, I. J., Klose, R. J., Claridge, T. D. W., Ratcliffe, P. J., Schofield, C. J., and Kawamura, A. (2011) The oncometabolite 2-hydroxyglutarate inhibits histone lysine demethylases. *EMBO reports* **12**, 463-469

109. Cunliffe, C. J., Franklin, T. J., Hales, N. J., and Hill, G. B. (1992) Novel inhibitors of prolyl 4-hydroxylase. 3. Inhibition by the substrate analog N-oxaloglycine and its derivatives. *J. Med. Chem.* **35**, 2652-2658

110. Hsia, D. A., Tepper, C. G., Pochampalli, M. R., Hsia, E. Y. C., Izumiya, C., Huerta, S. B., Wright, M. E., Chen, H.-W., Kung, H.-J., and Izumiya, Y. (2010) KDM8, a H3K36me2 histone demethylase that acts in the cyclin A1 coding region to regulate cancer cell proliferation. *Proc. Natl. Acad. Sci.* **107**, 9671-9676

111. Ishimura, A., Minehata, K.-i., Terashima, M., Kondoh, G., Hara, T., and Suzuki, T. (2012) Jmjd5, an H3K36me2 histone demethylase, modulates embryonic cell proliferation through the regulation of Cdkn1a expression. *Development* **139**, 749-759

112. Wu, J., He, Z., Yang, X.-M., Li, K.-L., Wang, D.-L., and Sun, F.-L. (2017) RCCD1 depletion attenuates TGF-β-induced EMT and cell migration by stabilizing cytoskeletal microtubules in NSCLC cells. *Cancer Lett.* **400**, 18-29

113. Kouwaki, T., Okamoto, T., Ito, A., Sugiyama, Y., Yamashita, K., Suzuki, T., Kusakabe, S., Hirano, J., Fukuhara, T., Yamashita, A., Saito, K., Okuzaki, D., Watashi, K., Sugiyama, M., Yoshio, S., Standley, D. M., Kanto, T., Mizokami, M., Moriishi, K., and Matsuura, Y. (2016) Hepatocyte Factor JMJD5 Regulates Hepatitis B Virus Replication through Interaction with HBx. *Journal of Virology* **90**, 3530-3542

114. Wang, H., Zhou, X., Wu, M., Wang, C., Zhang, X., Tao, Y., Chen, N., and Zang, J. (2013) Structure of the JmjC-domain-containing protein JMJD5. *Acta Crystall. Section D* **69**, 1911-1920

115. Wu, J., He, Z., Wang, D.-L., and Sun, F.-L. (2016) Depletion of JMJD5 sensitizes tumor cells to microtubule-destabilizing agents by altering microtubule stability. *Cell Cycle* **15**, 2980-2991

116. Suzuki, T., and Miyata, N. (2011) Lysine Demethylases Inhibitors. *J. Med. Chem.* **54**, 8236-8250

117. Koivunen, P., Hirsilä, M., Günzler, V., Kivirikko, K. I., and Myllyharju, J. (2004) Catalytic Properties of the Asparaginyl Hydroxylase (FIH) in the Oxygen Sensing Pathway Are Distinct from Those of Its Prolyl 4-Hydroxylases. *J. Biol. Chem.* **279**, 9899-9904

118. Johnson-Winters, K., Purpero, V. M., Kavana, M., Nelson, T., and Moran, G. R. (2003) (4-Hydroxyphenyl)pyruvate Dioxygenase from Streptomyces avermitilis: The Basis for Ordered Substrate Addition. *Biochemistry* **42**, 2072-2080

119. Lindblad, B., Lindstedt, G., Lindstedt, S., and Rundgren, M. (1977) Purification and some properties of human 4-hydroxyphenylpyruvate dioxygenase (I). *J. Biol. Chem.* **252**, 5073-5084

120. Lindstedt, S., and Rundgren, M. (1982) Blue color, metal content, and substrate binding in 4-hydroxyphenylpyruvate dioxygenase from Pseudomonas sp. strain P. J. 874. *J. Biol. Chem.* **257**, 11922-11931

121. Schmidt, S. R., Müller, C. R., and Kress, W. (1995) Murine Liver Homogentisate 1,2-Dioxygenase. *Eur. J. Biochem.* **228**, 425-430

122. Ellis, M. K., Whitfield, A. C., Gowans, L. A., Auton, T. R., Provan, W. M., Lock, E. A., and Smith, L. L. (1995) Inhibition of 4-Hydroxyphenylpyruvate Dioxygenase by 2-(2-Nitro-4-trifluoromethylbenzoyl)-cyclohexane-1,3-dione and 2-(2-Chloro-4-methanesulfonylbenzoyl)-cyclohexane-1,3-dione. *Toxicol. Appl. Pharmacol.* **133**, 12-19

123. Kavana, M., and Moran, G. R. (2003) Interaction of (4-Hydroxyphenyl)pyruvate Dioxygenase with the Specific Inhibitor 2-[2-Nitro-4-(trifluoromethyl)benzoyl]-1,3-cyclohexanedione. *Biochemistry* **42**, 10238-10245

124. Purpero, V. M., and Moran, G. R. (2006) Catalytic, NonCatalytic, and Inhibitory Phenomena: Kinetic Analysis of (4-Hydroxyphenyl)pyruvate Dioxygenase from Arabidopsis thaliana. *Biochemistry* **45**, 6044-6055

125. Shah, D. D., Conrad, J. A., Heinz, B., Brownlee, J. M., and Moran, G. R. (2011) Evidence for the Mechanism of Hydroxylation by 4-Hydroxyphenylpyruvate Dioxygenase and Hydroxymandelate Synthase from Intermediate Partitioning in Active Site Variants. *Biochemistry* **50**, 7694-7704

126. Frick, E., Spatzal, T., Gerhardt, S., Krämer, A., Einsle, O., and Hüttel, W. (2014) Structural and functional characterization of 4-hydroxyphenylpyruvate dioxygenase from the thermoacidophilic archaeon Picrophilus torridus. *Extremophiles* **18**, 641-651

127. Gunsior, M., Ravel, J., Challis, G. L., and Townsend, C. A. (2004) Engineering p-Hydroxyphenylpyruvate Dioxygenase to a p-Hydroxymandelate Synthase and Evidence for the Proposed Benzene Oxide Intermediate in Homogentisate Formation. *Biochemistry* **43**, 663-674

128. Huang, C.-W., Liu, H.-C., Shen, C.-P., Chen, Y.-T., Lee, S.-J., Lloyd, Matthew D., and Lee, H.-J. (2016) The different catalytic roles of the metal-binding ligands in human 4-hydroxyphenylpyruvate dioxygenase. *Biochem. J.* **473**, 1179-1189

129. Rüetschi, U., Rymo, L., and Lindstedt, S. (1997) Human 4-Hydroxyphenylpyruvate Dioxygenase Gene (HPD). *Genomics* **44**, 292-299

130. Santucci, A., Bernardini, G., Braconi, D., Petricci, E., and Manetti, F. (2017) 4-Hydroxyphenylpyruvate Dioxygenase and Its Inhibition in Plants and Animals: Small Molecules as Herbicides and Agents for the Treatment of Human Inherited Diseases. *J. Med. Chem.* **60**, 4101-4125

131. Wu, C.-S., Huang, J.-L., Sun, Y.-S., and Yang, D.-Y. (2002) Mode of Action of 4-Hydroxyphenylpyruvate Dioxygenase Inhibition by Triketone-type Inhibitors. *J. Med. Chem.* **45**, 2222-2228

132. Xu, Y.-L., Lin, H.-Y., Ruan, X., Yang, S.-G., Hao, G.-F., Yang, W.-C., and Yang, G.-F. (2015) Synthesis and bioevaluation of pyrazole-benzimidazolone hybrids as novel human 4-Hydroxyphenylpyruvate dioxygenase inhibitors. *Eur. J. Med. Chem.* **92**, 427-438

133. Yang, C., Pflugrath, J. W., Camper, D. L., Foster, M. L., Pernich, D. J., and Walsh, T. A. (2004) Structural Basis for Herbicidal Inhibitor Selectivity Revealed by

Comparison of Crystal Structures of Plant and Mammalian 4-Hydroxyphenylpyruvate Dioxygenases. *Biochemistry* **43**, 10414-10423

134. Fritze, I. M., Linden, L., Freigang, J., Auerbach, G., Huber, R., and Steinbacher, S. (2004) The Crystal Structures of Zea mays and Arabidopsis 4-Hydroxyphenylpyruvate Dioxygenase. *Plant Physiol.* **134**, 1388-1400

135. Brownlee, J. M., Johnson-Winters, K., Harrison, D. H. T., and Moran, G. R. (2004) Structure of the Ferrous Form of (4-Hydroxyphenyl)pyruvate Dioxygenase from Streptomyces avermitilis in Complex with the Therapeutic Herbicide, NTBC. *Biochemistry* **43**, 6370-6377

136. Serre, L., Sailland, A., Sy, D., Boudec, P., Rolland, A., Pebay-Peyroula, E., and Cohen-Addad, C. (1999) Crystal structure of Pseudomonas fluorescens 4-hydroxyphenylpyruvate dioxygenase: an enzyme involved in the tyrosine degradation pathway. *Structure* **7**, 977-988

137. Liu, A., Ho, R. Y. N., Que, L., Ryle, M. J., Phinney, B. S., and Hausinger, R. P. (2001) Alternative Reactivity of an α-Ketoglutarate-Dependent Iron(II) Oxygenase: Enzyme Self-Hydroxylation. *J. Am. Chem. Soc.* **123**, 5126-5127

138. Zhang, Z., Barlow, J. N., Baldwin, J. E., and Schofield, C. J. (1997) Metal-Catalyzed Oxidation and Mutagenesis Studies on the Iron(II) Binding Site of 1-Aminocyclopropane-1-carboxylate Oxidase. *Biochemistry* **36**, 15999-16007

139. Pingoud, A., and Jeltsch, A. (2001) Structure and function of type II restriction endonucleases. *Nucleic Acids Res* **29**, 3705-3727

140. Banga, J. P. (1998) SDS-Polyacrylamide Gel Electrophoresis (SDS-Page) A2 - Delves, Peter J. in *Encyclopedia of Immunology (Second Edition)*, Elsevier, Oxford. pp 2143-2144

141. Sobott, F., Watt, S. J., Smith, J., Edelmann, M. J., Kramer, H. B., and Kessler, B. M. (2009) Comparison of CID Versus ETD Based MS/MS Fragmentation for the Analysis of Protein Ubiquitination. *J. Am. Soc. Mass Spec.* **20**, 1652-1659

142. Whitmore, L., and Wallace, B. A. (2004) DICHROWEB, an online server for protein secondary structure analyses from circular dichroism spectroscopic data. *Nucleic Acids Res.* **32**, W668-W673

143. Behrendt, R., White, P., and Offer, J. (2016) Advances in Fmoc solid-phase peptide synthesis. *J. Pept. Sci.* **22**, 4-27

144. Aguilar, J. A., Nilsson, M., Bodenhausen, G., and Morris, G. A. (2012) Spin echo NMR spectra without J modulation. *Chem. Commun.* **48**, 811-813

145. Romagni, J. G., Meazza, G., Nanayakkara, N. P. D., and Dayan, F. E. (2000) The phytotoxic lichen metabolite, usnic acid, is a potent inhibitor of plant p-hydroxyphenylpyruvate dioxygenase. *FEBS letters* **480**, 301-305

146. Dayan, F. E., Duke, S. O., Sauldubois, A., Singh, N., McCurdy, C., and Cantrell, C. (2007) p-Hydroxyphenylpyruvate dioxygenase is a herbicidal target site for β-triketones from Leptospermum scoparium. *Phytochemistry* **68**, 2004-2014

147. Ling, T.-s., Shiu, S., and Yang, D.-y. (1999) Design and synthesis of 3-fluoro-2-oxo-3-phenylpropionic acid derivatives as potent inhibitors of 4-hydroxyphenylpyruvate dioxygenase from pig liver. *Bioorg. & Med. Chem.* **7**, 1459-1465

148. Lin, Y.-l., Wu, C.-s., Lin, S.-w., and Yang, D.-y. (2000) SAR studies of 2-o-substituted-benzoyl- and 2-alkanoyl-cyclohexane-1,3-diones as inhibitors of 4-hydroxyphenylpyruvate dioxygenase. *Bioorg. & Med. Chem. Lett.* **10**, 843-845

149. Lin, S. W., Lin, Y. L., Lin, T. C., and Yang, D. Y. (2000) Discovery of a potent, non-triketone type inhibitor of 4-hydroxyphenylpyruvate dioxygenase. *Bioorg. & Med. Chem. Lett.* **10**, 1297-1298

150. http://www.thesgc.org/structures/3isq